UNIVERSITY OF LIVERPOOL

Identification and characterisation of microtubule binding proteins

Hannah Glover

Thesis submitted in accordance with the requirements of University of Liverpool for the Degree of Doctor in Philosophy

April 2023

Identification and characterisation of microtubule binding proteins

Hannah Glover

Abstract

Microtubules are an essential component of the cytoskeleton and help facilitate a wide variety of functions including cellular division, transport of cargo, cell migration and maintaining cell shape. They are formed from α-tubulin and β-tubulin subunits which dimerise and then polymerise to form microtubules lattices. A plethora of microtubule binding proteins can associate with these structures and are required to regulate microtubule organisation and to allow for their diverse array of functions. Identifying the complete microtubule proteome is therefore crucial for understanding the full extent of microtubule function. This work describes a method for identifying novel microtubule binding proteins directly from cells and their subsequent characterisation. Furthermore, additional characterisation of the poorly researched deubiquitylase enzyme, USP31, which has also been shown to associate with microtubules, was undertaken.

Several proteomic studies have been previously performed in a variety of model species to identify microtubule-associated proteins, however the majority of these studies preceded major advances in the sensitivity of mass spectrometry instruments and the adoption of isotopic labelling procedures (e.g. SILAC) that provide more quantitative data. To identify novel microtubule binding proteins, I have developed an unbiased biochemical assay which utilises differential extraction to allow for removal of cytosolic proteins whilst retaining microtubule networks for collection. I have conducted triplex mass spectrometric analysis which quantitates the sensitivity of microtubule protein extraction from U2OS cells following manipulation of the network by microtubule-depolymerising (nocodazole) or microtubule-stabilising (Taxol) drugs. This method can be easily transferred to other cell types. This approach is benchmarked by co-segregation of tubulin and previously established microtubule-binding proteins. I have identified several candidate proteins which have not been previously described as microtubule binding proteins using this method. Not only has this allowed for identification of the microtubule proteome, but it has also provided an inventory for the most Taxol-sensitive and nocodazole-sensitive proteins within the cell.

By using this novel method for microtubule binding protein extraction, I have successfully identified a selection of novel candidates including the ubiquitin E3 ligase, TRIM3 (Tripartite motif-containing protein) and galectin-related protein, LGALSL. Both have been confirmed in this work to localise with the microtubule network. I have focused on TRIM3 and shown that it can also be seen to associate with the mitotic spindle throughout the entirety of mitosis. Microtubule localisation has been mapped to the C-terminal NHL repeats, a domain which is required but is not sufficient alone for microtubule localisation. Additionally, I have identified a functional role for TRIM3 in the regulation of the acetylated tubulin network. TRIM3 depletion prevents the accumulation of acetylation under conditions of Taxol stabilisation by regulating the expression levels of the α-tubulin acetyl-transferase enzyme, αTAT1.

A second line of enquiry described in this thesis involves the further characterisation of a previously established microtubule binding protein. USP31 is a deubiquitylase (DUB) that associates with microtubules and has been previously found to regulate mitotic progression. I have undertaken further investigations into its role within mitosis. I have shown that USP31 expression levels differ throughout the cell cycle, with a 2- to 3-fold increase being seen during mitosis compared to asynchronous cells, particularly in prometaphase and metaphase. Upon entry into mitosis, USP31 is phosphorylated in a CDK1-dependent manner and dephosphorylated upon mitotic exit, with a rapid relocalisation onto the central spindle observed during anaphase. Catalytic-inactive mutants of USP31 display cytokinesis defects, leading me to investigate the involvement of USP31 with the chromosomal passenger complex (CPC): a main regulator of the cell cycle and cytokinesis. I have shown that in prometaphase arrested cells, components of the CPC, including INCENP and aurora B, display decreased expression levels. Under anaphase-like conditions, USP31 depleted cells present with mislocalisation of the CPC components at the spindle midzone in a CDK1-dependent manner. Furthermore, USP31 depletion causes a specific delay in the transition of ectopically expressed INCENP from the inner centromeres to the spindle midzone.

Table of Contents

Abstract.....2

Table of contents.....4

List of Figures.....9

List of Tables.....13

Abbreviations.....14

Acknowledgements.....17

1 Chapter 1 - Introduction ***18***

1.1 Microtubules **18**

1.1.1 Tubulin and microtubule discovery 18

1.1.2 Tubulin proteins 19

1.1.3 Microtubule polymerisation.....21

1.1.4 Dynamic instability 22

1.1.5 Microtubule drugs.....25

1.1.6 Nucleation and the centrosome.....27

1.1.7 Microtubule branching.....30

1.1.8 Microtubule motor proteins.....31

1.1.8.1 Kinesin 32

1.1.8.2 Dynein.....34

1.1.9 Microtubule associated proteins 37

1.1.9.1 Structural MAPs 37

1.1.9.2 Plus-end tracking proteins (+TIPs) 39

1.1.10 The tubulin code 42

1.1.10.1 Microtubule isotypes 42

1.1.10.2 Microtubule post-translational modifications.....43

1.1.10.3 Detyrosination 44

1.1.10.4 Tyrosination 47

1.1.10.5 Δ2-tubulin.....47

1.1.10.6 Acetylation 48

1.1.10.7 Glutamylation and glycylation.....51

1.1.10.8 Other tubulin modifications.....53

1.1.10.9 Neurons and the tubulin code 54

1.2 Mitosis **55**

1.2.1 Microtubules and the mitotic spindle 55

1.2.2 Mitotic regulation and the spindle assembly checkpoint 58

1.2.3 Mitotic kinases 60

1.2.4 The chromosomal passenger complex.....61

1.3 The ubiquitin proteasome system **63**

1.3.1 Ubiquitin.....63

1.3.2 Ubiquitin conjugation.....64

1.3.3 Ubiquitin signalling 66

1.3.4 Deubiquitylases and ubiquitin removal 67

1.3.5 Proteasomal degradation 67

1.3.6 TRIM family of E3 ligases....68
1.3.7 Ubiquitin specific proteases....72
1.3.8 Ubiquitin-associated proteins and microtubules....72

1.4 Proteomics....73
1.4.1 Edman degradation....74
1.4.2 Advances in protein MS....74
1.4.3 Electrospray ionisation....75
1.4.4 Tandem Mass Spectrometry....76
1.4.5 Computational advances....77
1.4.6 2D gel electrophoresis....78
1.4.7 Quantitative mass spectrometry....79
1.4.8 Non-gel-based techniques....80
1.4.8.1 ICAT labelling....81
1.4.8.2 SILAC labelling....82
1.4.8.3 TMT labelling....83
1.4.8.4 The microtubule proteome....84

1.5 Purpose of this study and summary of chapters....85

2 Chapter 2 – Materials and Methods....86

2.1 Cell biology....86
2.1.1 Materials and Reagents....86
2.1.2 Cell lines....86
2.1.3 Plasmid DNA transfection....87
2.1.4 siRNA transfection....87
2.1.5 Live cell imaging....88
2.1.6 Fixed cell imaging....88
2.1.7 Drug treatments....89
2.1.8 Microtubule cold-induced polymerisation....89
2.1.9 MitoTracker™ Green FM staining....89
2.1.10 Cell synchronisation....89

2.2 Analysis....90
2.2.1 Microtubule network density....90
2.2.2 Corrected total cell fluorescence....90
2.2.3 MiNa plugin analysis....90
2.2.4 Colocalisation analysis....91
2.2.5 Statistical analysis....91

2.3 Molecular Biology....92
2.3.1 Reagents....92
2.3.2 PCR for cloning and subcloning....92
2.3.3 Overlapping PCR....94
2.3.4 Site directed mutagenesis....95
2.3.5 TOPO TA cloning....97
2.3.6 Bacterial transformation and glycerol stocks....97
2.3.7 Agarose gel electrophoresis....98
2.3.8 Restriction digestion....98
2.3.9 Ligation....98

2.3.10 mRNA extraction and reverse transcription 99
2.3.11 Quantitative real-time polymerase chain reaction (qRT-PCR) 99

2.4 Biochemistry 100
2.4.1 Materials and Reagents 100
2.4.2 Cell lysis 101
2.4.3 Protein assay and sample preparation 101
2.4.4 Sodium dodecyl sulphate-polyacrylamide gel electrophoresis (SDS-PAGE) 102
2.4.5 Coomassie staining 102
2.4.6 Western blotting 102
2.4.7 Immunofluorescence 104
2.4.8 Initial microtubule extraction protocol 105
2.4.9 Optimised microtubule extraction protocol 106
2.4.10 Analysis of stable microtubules 106
2.4.11 Lambda phosphatase treatment 106

2.5 Mass spectrometry 107
2.5.1 Materials and reagents 107
2.5.2 Stable Isotopic Labelling by Amino Acids in cell culture (SILAC) 107
2.5.3 Cell lysis and sample preparation 107
2.5.4 In gel digest 108
2.5.5 Mass spectrometry for phospho-proteomics 108
2.5.6 Luxembourg facility protocols and procedures 109
2.5.6.1 Sample resuspension 109
2.5.6.2 Peptide fractionation and LC/MS injection 109
2.5.6.3 MaxQuant analysis 110

3 Chapter 3 – Determination of the microtubule proteome 111

3.1 Introduction 111

3.2 Expression of microtubule modifications across a cell line panel 112

3.3 Initial trial of microtubule extraction protocol 112

3.4 Optimisation of the microtubule extraction protocol 115
3.4.1 Optimisation of nocodazole treatment 115
3.4.2 Optimisation of removal of cytosolic proteins 117
3.4.3 Optimisation of microtubule collection 118
3.4.4 Alternative method for microtubule extraction 119
3.4.5 Immunofluorescence of the microtubule extraction protocol 121
3.4.6 Immunofluorescence of retained MAPs 123
3.4.7 Test of alternative lysis buffers for microtubule collection 124
3.4.8 Microtubule extraction protocol in alternative cell lines 124

3.5 Identification of the microtubule proteome using SILAC isotopic labelling 125
3.5.1 Workflow for obtaining the microtubule proteome 126
3.5.2 Quality control 126
3.5.3 Data analysis 128
3.5.4 Data visualisation 129

3.5.5 Initial analysis of outlying proteins 133
3.5.6 Data sorting and selection 135
3.5.7 Comparison with other microtubule proteomes 138
3.5.8 Network visualisation 139
3.5.9 Selection of hits for further characterisation 140
3.5.10 Taxol enriched proteins 144
3.5.11 Dynein and dynactin are enriched in nocodazole-treated fractions 146

3.6 Discussion 149

4 Chapter 4 – Characterisation of novel microtubule binding proteins 153

4.1 Introduction 153

4.2 LGALSL 154
4.2.1 Structure and function of LGALSL 154
4.2.2 Cloning and generation of GFP tagged LGALSL 155
4.2.3 LGALSL displays microtubule localisation 155

4.3 RMDN3 157
4.3.1 Structure and function of RMDN3 157
4.3.2 Alignment of RMDN3 and RMDN1 158
4.3.3 RMDN3 localises to mitochondria 159
4.3.4 Cloning and generation of GFP tagged RMDN3 161
4.3.5 C-terminally tagged RMDN3 localises to mitochondria via the transmembrane domain 161
4.3.6 N-terminally tagged RMDN3 localises to microtubules 163
4.3.7 GFP-RMDN3 stabilises microtubules and prevents their depolymerisation 163
4.3.8 GFP-RMDN3 localises to modified microtubules 166
4.3.9 GFP-RMDN3 does not localise to the centrosome 166
4.3.10 Taxol affects the mitochondria network 168

4.4 TRIM3 169
4.4.1 Introduction to TRIM3 170
4.4.2 TRIM3 gene and protein 171
4.4.3 TRIM3 expression levels in different cell lines 173
4.4.4 TRIM3 is extracted in a nocodazole-sensitive manner 174
4.4.5 TRIM3 localisation 174
4.4.5.1 TRIM3 localises to microtubules 174
4.4.5.2 TRIM2 also colocalises with microtubules 177
4.4.5.3 TRIM3 does not bind to the centrosome 177
4.4.5.4 TRIM3 colocalises to the whole microtubule network 179
4.4.5.5 TRIM3 colocalises with the mitotic spindle 181
4.4.5.6 The TRIM family cos box domain 182
4.4.5.7 Generation of TRIM3 truncations and deletion mutations 184
4.4.5.8 TRIM3 localises to microtubules via the NHL repeats 186
4.4.5.9 TRIM3 colocalises with HRS 186
4.4.5.10 TRIM3 may colocalise with actin 187
4.4.6 Phenotypic effects of TRIM3 depletion 188
4.4.6.1 TRIM3 depletion and tubulin levels 188

4.4.6.2 TRIM3 affects the accumulation of acetylation on α-tubulin.....190
4.4.6.3 TRIM3 depletion affects the acetylation of stable microtubules 193
4.4.6.4 TRIM3 depletion affects ATAT1 expression levels 195
4.4.6.5 TRIM3 does not affect the stability of ATAT1 196
4.4.6.6 TRIM3 does not affect EB1 distribution on microtubule plus ends 198
4.4.6.7 TRIM3 and microtubule dynamics 199
4.4.6.8 TRIM3 depletion does not affect mitotic progression 200

4.5 Discussion 203
4.5.1 LGALSL 203
4.5.2 RMDN3 204
4.5.3 TRIM3 206

5 Chapter 5 – USP31 and its role in mitosis.....209

5.1 Introduction 209

5.2 USP31 expression during mitosis 209
5.2.1 USP31 levels increase during mitosis 209
5.2.2 USP31 displays a shift in molecular weight during mitosis 211

5.3 USP31 is phosphorylated in mitosis 213
5.3.1 Kinase activity during mitosis 213
5.3.2 USP31 is phosphorylated by CDK1.....214
5.3.3 GFP-USP31 in the stable cell lines is also phosphorylated during mitosis ……..216
5.3.4 USP31 phosphorylation may regulate its localisation to the mitotic spindle 219
5.3.5 Localisation of USP31 on the mitotic spindle is controlled by CDK1 222

5.4 Determination of USP31 phosphorylation sites 223
5.4.1 Conjugating the GFP nanobody to the beads.....223
5.4.2 Phosphoproteomics of USP31 224
5.4.3 Generation of USP31 phospho-mutants.....226

5.5 USP31 and the chromosomal passenger complex 230
5.5.1 USP31 catalytic inactive mutant displays ectopic furrowing during anaphase-like conditions 230
5.5.2 USP31 depletion causes reduced levels of the CPC and the associated motor proteins in mitosis 231
5.5.3 USP31 depletion causes mislocalisation of the CPC components in a CDK1 dependent manner 232
5.5.4 Aurora B inhibition does not lead to mislocalisation of the CPC proteins in USP31 depleted cells.....233
5.5.5 USP31 depletion does not cause this effect on the CPC by disrupting the detyrosinated or acetylated networks.....235
5.5.6 USP31 affects the CPC expression and localisation during anaphase but not telophase 238
5.5.7 USP31 does not affect cytokinesis 240
5.5.8 USP31 depletion leads to a delay in the transition of INCENP from the centromeres to the spindle midzone 241

5.6 Discussion 244
5.6.1 USP31 expression levels 244
5.6.2 USP31 phosphorylation 245
5.6.3 USP31 and the chromosomal passenger complex 246
5.6.4 Next steps for USP31 249
6 Chapter 6 - Conclusions 250
6.1 Novel microtubule binding proteins 250
6.2 Future applications for microtubule differential extraction 250
6.2.1 The tubulin code 250
6.2.2 The neuronal microtubule proteome 252
6.3 TRIMs and microtubules 252
6.4 TRIM3 in neurons 253
6.5 USP31 in neurons 254
6.6 Microtubule-related diseases 254
6.7 USP31 as a drug target 255
References 257

List of Figures

Figure 1.1 - Tubulin structure 20
Figure 1.2 - Chromosome mapping of human tubulin genes 21
Figure 1.3 - Microtubule dynamic instability 23
Figure 1.4 - Microtubule nucleation 29
Figure 1.5 – Motor protein structure and transport along microtubules 33
Figure 1.6 – Microtubule associated proteins 40
Figure 1.7 - Microtubule post-translational modifications 44
Figure 1.8 - Detyrosination controls chromosome transport during mitosis 46
Figure 1.9 – Microtubule acetylation prevents mechanical breakage 49
Figure 1.10 - Tubulin modifications and responsible enzymes 50
Figure 1.11 - Glutamylation affects spastin severing activity 52
Figure 1.12 - Structure of the mitotic spindle 56
Figure 1.13 – The SAC is regulated by kinetochore attachments 59
Figure 1.14 – The CPC is regulated in a spatiotemporal manner during mitosis 62
Figure 1.15 – Ubiquitin as a reversible post translational modification 65
Figure 1.16 – TRIM superfamily domain maps 70
Figure 1.17 - Techniques for relative protein quantification 81

Figure 2.1 – MiNa plugin analysis of acetylated tubulin network 91
Figure 2.2 – Schematic for the cloning process for GFP-tagged constructs 94
Figure 3.1 – Expression of tubulin modifications across a panel of cell lines.....113
Figure 3.2 - Test of the microtubule extraction protocol 114
Figure 3.3 – Optimisation of nocodazole treatment 116
Figure 3.4 - Optimisation of removal of cytosolic proteins 118
Figure 3.5 – Optimisation of microtubule collection 119
Figure 3.6 – Schematic of alternative microtubule extraction protocol.....121
Figure 3.7 – Differential extraction of microtubules and binding proteins.....122
Figure 3.8 – MAP4 is retained on microtubules during the microtubule extraction protocol.....123
Figure 3.9 – 8M urea extraction buffer does not affect microtubule extraction.....124
Figure 3.10 - Microtubule extraction is robust across different cell lines.....125
Figure 3.11 – Schematic showing SILAC mass spectrometry workflow 127
Figure 3.12 – Quality control of microtubule extraction protocol for MS analysis ...128
Figure 3.13 – Proteome distribution of U2OS cells following microtubule extraction protocol compared to nocodazole- or Taxol-treated cells 130
Figure 3.14 – Fold change of the proteome distribution of U2OS cells following microtubule extraction in 3 different conditions depicted against the sum of the intensities.....131
Figure 3.15 – Volcano plot of the proteome composition of U2OS cells following microtubule extraction compared to the significance (p-value) 132
Figure 3.16 – Tubulin and microtubule binding proteins are enriched >2-fold 134
Figure 3.17 – Mass spectrometry analysis identifies potential novel microtubule binding proteins 136
Figure 3.18 – Heat map of hits identified across the 3 repeats.....137
Figure 3.19 – Comparison with other microtubule proteomes 138
Figure 3.20 – Cytoscape network showing interactions between hits identified in the proteome 140
Figure 3.21 – Intensities of unique peptide of selected proteins in each condition.142
Figure 3.22 – Mitochondrial proteins identified in the mass spectrometry dataset .143
Figure 3.23 – Proteins enriched and depleted following taxol treatment.....145
Figure 3.24 – Dynein and dynactin proteins are enriched in nocodazole-treated cells 147
Figure 3.25 – Confirmation of dynein enrichment following nocodazole treatment 148
Figure 4.1 – LGALSL domain map and structure 154
Figure 4.2 – LGALSL may localise to microtubules.....155

Figure 4.3 – GFP-LGALSL shows clear colocalisation with microtubules.....156
Figure 4.4 – RMDN3 domain map and structure.....157
Figure 4.5 – Alignment of human RMDN1 and RMDN3.....159
Figure 4.6 – RMDN3 colocalises with the mitochondrial network.....160
Figure 4.7 – Generated GFP-tagged RMDN3 constructs.....161
Figure 4.8 – Removal of the RMDN3 transmembrane domain prevents mitochondrial localisation.....162
Figure 4.9 – GFP-RMDN3 localises to microtubules.....164
Figure 4.10 – GFP-RMDN3 localisation is not lost with nocodazole or cold treatment 165
Figure 4.11 – RMDN3 localises on acetylated and detyrosinated microtubules 167
Figure 4.12 – GFP-RMDN3 does not bind to the centrosome.....168
Figure 4.13 – Mitochondrial network is disrupted after Taxol treatment.....169
Figure 4.14 – Structure of TRIM3.....170
Figure 4.15 – Alignment of TRIM3 across species.....172
Figure 4.16 – Normalised expression levels of TRIM proteins in U2OS cells 173
Figure 4.17 – Confirmation of TRIM3 extraction in control and taxol treated cells .175
Figure 4.18 – TRIM3 localises to microtubules 176
Figure 4.19 – TRIM3 localisation is lost with cold-induced microtubule depolymerisation.....177
Figure 4.20 – TRIM2 localises to microtubules 178
Figure 4.21 – TRIM3 and TRIM2 do not localise to the centrosome.....178
Figure 4.22 – TRIM3 and TRIM3 colocalise with modified microtubules 180
Figure 4.23 – TRIM3 localises to the mitotic spindle 181
Figure 4.24 – TRIM3 does not contain a cos-box domain 183
Figure 4.25 – Generation of TRIM3 truncations and deletions 184
Figure 4.26 – TRIM3 localises to microtubules via the NHL repeats 185
Figure 4.27 – TRIM3 colocalises with Hrs.....187
Figure 4.28 – TRIM3 may also colocalise with actin.....188
Figure 4.29 – TRIM3 depletion does not affect tubulin levels 189
Figure 4.30 – TRIM3 and the microtubule density.....190
Figure 4.31 – TRIM3 depletion prevents accumulation of acetylated α-tubulin.....191
Figure 4.32 – TRIM3 depletion and visualisation of accumulation of acetylated α-tubulin.....192
Figure 4.33 – TRIM3 depletion affects the stable acetylated tubulin network 194
Figure 4.34 – TRIM3 depletion affects ATAT1 expression levels 195
Figure 4.35 – TRIM3 regulates ATAT1 levels on a post-transcriptional level.....196

Figure 4.36 – TRIM3 does not change the protein stability of ATAT1.....197
Figure 4.37 – TRIM3 depletion does not affect EB1-cap length 198
Figure 4.38 – TRIM3 depletion does not regulate microtubule dynamics 199
Figure 4.39 – TRIM3 depletion does not affect mitotic progression.....201
Figure 4.40 – TRIM3 depletion does not affect chromosome segregation.....202
Figure 5.1 – USP31 expression levels increase during mitosis 210
Figure 5.2 – USP31 is phosphorylated during mitosis.....212
Figure 5.3 – USP31 is not phosphorylated by PLK1 215
Figure 5.4 –USP31 is phosphorylated by CDK1 during mitosis.....217
Figure 5.5 – GFP-tagged USP31 in stably expressing cell lines is phosphorylated in mitosis by CDK1 218
Figure 5.6 – GFP-USP31 relocalises to the central spindle during anaphase 220
Figure 5.7 – USP31 expression levels in U2OS cells stably expressing GFP-USP31 221
Figure 5.8 – Localisation of USP31 on the spindle is controlled by CDK1.....222
Figure 5.9 – Generation of GFP pulldown beads 223
Figure 5.10 – GFP-USP31 pulldown workflow 225
Figure 5.11 - Generation of USP31 phospho-mutants 227
Figure 5.12 – USP31 phospho-mutants all localise to microtubules.....228
Figure 5.13 - USP31 phospho-mutants all localise to the spindle.....229
Figure 5.14 – USP31 CA1 cells show ectopic furrowing during cytokinesis.....230
Figure 5.15 – USP31 depletion affects CPC protein levels 232
Figure 5.16 – USP31 depletion affects CPC localisation.....234
Figure 5.17 – Aurora B inhibition does not affect the localisation of the CPC in USP31 depleted cells.....235
Figure 5.18 – Disruption of the detyrosinated and acetylated microtubule networks does not affect CPC mislocalisation.....237
Figure 5.19 – CPC localisation during anaphase and telophase 239
Figure 5.20 – USP31 depletion does not affect centrosome number.....240
Figure 5.21 – USP31 depletion effects the transition of GFP-INCENP.....242
Figure 6.1 – Detyrosination networks in TTL and VASH1/2 knock-out cell lines....251

List of Tables

Table 1.1 - Microtubule binding drugs 25
Table 1.2 - Motor protein family members, functions and structural features.....36
Table 1.3 - Half-lives of different microtubules during different cell states 55
Table 2.1 – siRNA oligo sequences 88
Table 2.2 – Reaction mix for PCR-up.....93
Table 2.3 – PCR thermocycler programme for PCR-up 93
Table 2.4 – PCR thermocycler programme for overlapping PCR 95
Table 2.5 – Reaction mix for SDM 95
Table 2.6 – PCR thermocycler programme for SDM 96
Table 2.7 – Primers used for cloning.....96
Table 2.8 – Reaction mix for reverse transcriptase 99
Table 2.9 - Primers used for RT-qPCR 100
Table 2.10 – Reaction mix for qPCR.....100
Table 2.11 – Thermocycler programme for qPCR.....100
Table 2.12 – Primary antibodies used for western blotting 103
Table 2.13 – Secondary antibodies used for Western Blotting 104
Table 2.14 – Primary antibodies used for immunofluorescence 105
Table 2.15 – Secondary antibodies used for immunofluorescence 105
Table 5.1 – Phospho-proteomics of USP31 during mitosis 224

Abbreviations

+TIP	plus-end-tracking proteins
2DE	2-dimensional gel electrophoresis
ACN	Acetonitrile
ALS	Amyotrophic Lateral Sclerosis
APC/C	Anaphase-promoting complex
ATAT1	Alpha tubulin acetyl-transferase
ADP	Adenosine diphosphate
ATP	Adenosine triphosphate
BB2	B-Box 2
BICD2	Bicaudal D2
CAMSAP	Calmodulin-regulated spectrin-associated protein
CAP-Gly	Cytoskeleton-associated protein-Glycine rich
CART	Cytoskeleton-associated recycling or transport
CCP	Cytosolic carboxypeptidase
CDC	Cell division cycle protein
CDK1	Cyclin dependent kinase 1
CDK5RAP2	CDK5 regulatory subunit-associated protein 2
CENP	Centromere protein
CHX	Cycloheximide
CLASP	Cytoplasmic linker associated protein
CLIP	Cytoplasmic linker protein
CPC	Chromosomal passenger complex
CRD	Carbohydrate recognition domain
CRMP2	Collapsin response mediator protein 2
CTCF	Corrected total cell fluorescence
CYLD	Cylindromatosis
DMEM	Dulbecco’s Modified Eagle Medium (DMEM)
DNA	Deoxyribonucleic acid
DPYSL	Dihydropyrimidinase-related protein
DUB	Deubiquitylase
EB	End-binding
EBH	End-binding homology
EML4	Echinoderm microtubule-associated protein-like 4
ER	Endoplasmic reticulum
ESCRT	Endosomal sorting complexes required for transport

FA	Formic acid
FBS	Foetal bovine serum
GDP	Guanosine diphosphate
GFP	Green fluorescent protein
GTP	Guanosine triphosphate
HA	Hemagglutinin
HDAC6	Histone deacetylase 6
HPLC	High performance liquid chromatography
INCENP	Inner centromere protein
iPSCs	Induced pluripotent stem cells
KO	Knockout
LC-MS/MS	Liquid chromatography-tandem mass spectrometry
LGALSL	Lectin galactoside-binding-like protein
MAP	Microtubule associated protein
MAPRE3	Microtubule associated protein RP/EB family member 3
MATCAP	Microtubule associated tyrosine carboxypeptidase
MCAK	Mitotic centromere-associated kinesin, KIF2C
MCC	Mitotic checkpoint complex
MiNA	Mitochondrial network analysis
MISP	Mitotic spindle positioning protein
MKLP	Mitotic kinesin-like protein
MQ	MaxQuant
mRNA	messenger RNA
MS	Mass spectrometry
MT	Microtubule
MTOC	Microtubule organising centre
NHL	NCL-1, HT2A and LIN-41
ORP	Oxysterol-binding protein (OSBP)-related proteins
PBS	Phosphate-buffered saline
PCNT	Pericentrin
PLK1	Polo-like kinase 1
PTM	Post-translational modification
PTPIP51	Protein tyrosine phosphatase-interacting protein 51
qRT-PCR	Quantitative reverse transcription-polymerase chain reaction
RBR	Ring between ring
RING	Really interesting new gene
RMDN3	Regulator of microtubule dynamics protein 3

RNA	Ribonucleic acid
RSLC	Rapid separation liquid chromatography
SAC	Spindle assembly checkpoint
SDS-PAGE	Sodium dodecyl sulphate polyacrylamide electrophoresis
SILAC	Stable isotope labelling by amino acids in cell culture
siRNA	Small interfering RNA
SUMO	Small ubiquitin-like modifier
SVBP	Small vasohibin binding protein
TLR3	Toll like receptor 3
TOG	Tumour overexpressed gene
TPPP	Tubulin polymerase promoting protein
TPR	Tetratricopeptide repeat
TPX2	Targeting Protein for Xklp2
TRIM	Tripartite motif containing protein
TTL	Tubulin tyrosine ligase
TTLL	Tubulin tyrosine ligase-like
γ-TuRC	γ-tubulin ring complex
γ-TuSC	γ-tubulin small complex
UBD	Ubiquitin binding domain
USP	Ubiquitin-specific proteases
VAPB	Vesicle-associated membrane protein-associated protein B
VASH1/2	Vasohibin1/2
WT	Wild type

Acknowledgements

I have thoroughly enjoyed these last few years whilst completing my PhD, and although it has been challenging at times, I could not have got here without the support from so many people.

Firstly, I would like to thank my supervisors Professor Michael Clague and Professor Sylvie Urbé for the huge amount of time, patience and guidance they have given over the past few years. Their lab has been such a great working environment with a huge number of opportunities available which I am grateful for. Thanks to Professor Gunnar Dittmar and Dr Marta Mendes for allowing the use of their mass spectrometry machine. Much of this work would not have been possible without it. I would also like to thank the Wellcome Trust for supporting me throughout my research.

I would like to give a special thanks to Joana Gomes Neto for keeping me sane while working on USP31 and all the chaos it brought with it – thanks for the late night and early morning drug treatments, helping seed 483647 dishes for a single mitotic shake off and for taking over when I could no longer cope using the sonicator. Thanks to Emma Rusilowicz-Jones for providing me with my initial training when I first joined the lab during my MRes, and all the moral support she gave when I was analysing my mass spec data. Thanks to Erithelgi Bertsoulaki for all her help and guidance on the microscope and working in mitosis which I really enjoyed doing and became a huge part of my project. Thanks to Anne Clancy for answering all my stupid questions. Thanks to Hannah Elcocks for being a motivational gym buddy and giving me an excuse to leave the lab in the evenings. I would also like to thank the rest of MCSU lab and the rest of 5th floor for providing such a great working environment.

I would also like to thank a number of people outside the lab for all their support despite having no idea what I was talking about half the time. Firstly, to Rachel and Ishbel for being here in Liverpool with me and making my time here all that more enjoyable. A special thanks to Luke for being an excellent house husband and having my tea ready and waiting for when I returned from the lab each day. Thanks for listening while I chat on about lab-related annoyances. To my friends Grace, Emma and Jen who I know are always there whenever I need them. To both my parents, I will always be grateful for your support throughout my whole academic life. And finally, to my Greenbank netball girls who have provided me with the full scouse experience and a great escape when time in the lab was tough.

Chapter 1 - Introduction

The cytoskeleton is a large, complex network which provides the cell with its mechanical support and framework. 3 major classes of intracellular filamentous protein structures make up the cytoskeleton, namely actin filaments, intermediate filaments and microtubules, all of which are formed by the polymerisation of specific protein subunits. Actin filaments and microtubules are both polarised and are formed from globular protein subunits named actin and tubulin respectively, whereas intermediate filaments are unpolarised networks formed from multiple classes of protein dimers (Wickstead and Gull, 2011).

1.1 Microtubules

All our cells contain mesh-like networks that are formed from tube-shaped protein structures called microtubules. They are hollow structures and measure approximately 25 nm in diameter (Brinkley, 1997). These microtubules contribute to a wide variety of cellular functions such as maintaining cell shape, allowing cell movement, facilitating cell division and they provide the main structural unit for flagella and cilia. Additionally, they are frequently compared to railway tracks as specific proteins termed motor proteins (detailed in section 1.1.8) can travel along them to transport their cargo to specific areas of the cell. The microtubule network has the ability to perform all of these different functions because of their plethora of associated proteins and their dynamic nature: they are able to rapidly grow, collapse and reform to suit the cells needs and requirements (Nogales, 2000).

1.1.1 Tubulin and microtubule discovery

Microtubules were first described in the early 1950's when mitotic spindles were extracted from sea urchin eggs by Mazia and Dan. Spindle structures were analysed by electron microscopy (EM), and a protein accounting for the majority of the mass of the mitotic spindle was isolated by isoelectric precipitation (Mazia and Dan, 1952). A second early study which highlighted the presence of microtubules was during the EM analysis of ciliary apparatus of epithelial cells (Fawcett and Porter, 1954). In this study, Don Fawcett and Keith Porter described all cilia as being structurally similar, consisting of longitudinal columns formed from 9 doublet pairs and 2 singlet filaments. A decade later, further structural insights were obtained including the work by Ledbetter and Porter which described microtubules of plant cells existing as 13 protofilaments *in vivo* (Ledbetter and Porter, 1964). The microtubule subunit was

finally discovered in 1968 by Weisenberg and Borisy, following tubulin purification using a drug called colchicine, known to disrupt the mitotic spindle (Taylor, 1965; Borisy and Taylor, 1967). They were able to saturate tubulin with radioactive colchicine and use gel filtration to determine the amount of bound colchicine. Purification was then achieved using gradient elution from Sephadex columns. Their results showed that the purified protein obtained had similar properties such as molecular weight, amino acid composition and sedimentation constant, to the microtubule subunits seen in brain cells, cilia, and sperm tails. This protein was originally named the 'colchicine-binding protein' (Weisenberg et al., 1968; Borisy and Taylor, 1967). Around the same time, a further important discovery by Stevens, Renaud and Gibbons confirmed that the structural units of cilia and flagellum associate with guanine nucleotides (Stevens et al., 1967). The term "tubulin" was eventually adopted following the independent isolation of the microtubule building blocks in 1968 (Mohri, 1968; Yanagisawa et al., 1968).

It was from this point that research into tubulin and microtubules significantly picked up. In 1972, microtubules were formed *in vitro* from porcine brain homogenates, highlighting microtubules' ability to spontaneously assemble in the presence of GTP and a calcium chelator only (Weisenberg, 1972; Borisy and Olmsted, 1972). These *in vitro* microtubule preparations remain largely in use today to facilitate microtubule investigations. A further milestone in the discovery of microtubules was the determination of the tubulin 3D structure in the presence of Taxol in 1998 by Eva Nogales and Kenneth Downing. Electron crystallography was used to determine a structure with a resolution of 3.7Å, allowing both α- and β-tubulin to be described similarly as being compact with a nucleotide-binding region at the amino terminus, a Taxol-binding intermediate domain and a motor protein binding surface at the carboxy terminus (Nogales et al., 1998, 1999).

1.1.2 Tubulin proteins

Tubulin is a superfamily of globular proteins. α- and β-tubulin proteins each have a molecular weight of ~50kDa and are highly conserved. They contain 451 and 445 amino acids respectively and display 41% sequence homology (Ponstingl et al., 1981; Krauhs et al., 1981). Despite differences at the primary sequence, their overall structures are almost identical (Figure 1.1). They are compact protein structures which consist of 3 functional core domains. The N-terminal region spans from residues 1-205 and contains the nucleotide-binding binding domain, facilitated by a Rossmann

fold. This is composed of 6 parallel β-sheets and 5 α-helices arranged in an alternate fashion and is present in multiple nucleotide-binding proteins. The globular intermediate domain spans from residues 206-381 and consists of a mixed β-sheet surrounded by 5 α-helices. The final region at the C-terminus consists of 2 overlapping α-helices which sit on the surface of the globular domain. This region associates with other tubulin proteins in the microtubule structure, as well as facilitating binding of microtubule-associated proteins. Despite there being 3 sequential domains, structurally there are no definitive boundaries to each component (Nogales, 1998).

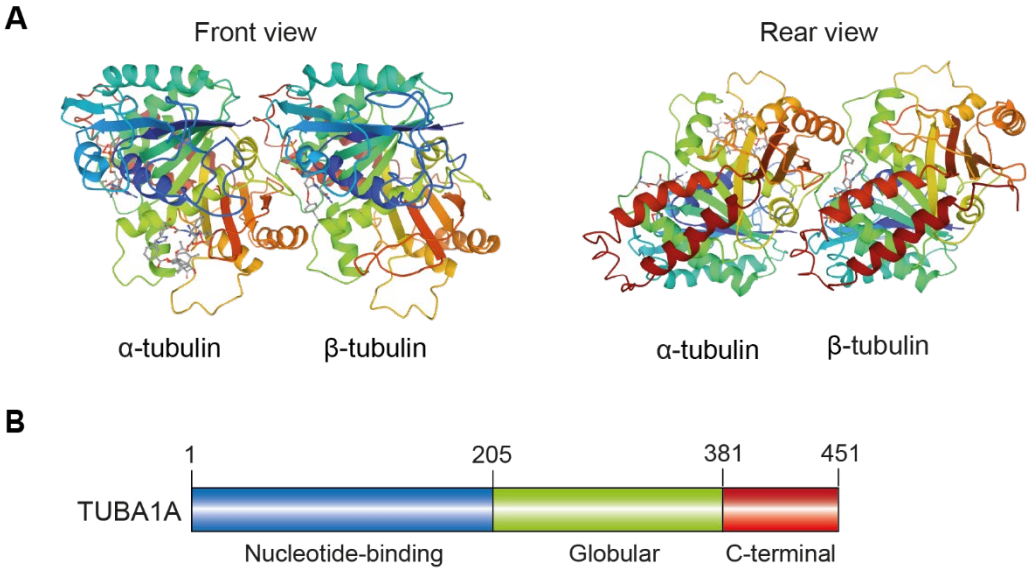

Figure 1.1 - Tubulin structure

A: Flat ribbon cartoon structure of the α- and β-tubulin subunits, with their front (left) and rear (right) views shown. Structural data was obtained from PDB database. PBD ID: 1TUB. **B**: Schematic representation of tubulin functional domains. Residue numbers refer to those of the TUBA1A gene.

In eukaryotes, there are 6 major subclasses of tubulin proteins: 5 of them are found in humans including α, β, γ, δ and ε, and the final subclass, ζ, is exclusive to kinetoplastids (Findeisen et al., 2014). α- and β-tubulin are the main tubulin proteins as they are ubiquitously expressed and associate together to form the basic structural unit of microtubules. γ-tubulin is also ubiquitously expressed however it is located at the microtubule organising centre (MTOC) and functions by nucleating formed microtubules. δ- and ε-tubulin are conserved across all eukaryotes which contain centrioles/ciliated cells (Wickstead and Gull, 2011) and are located at the

centrosomes, thought to facilitate centriole structure and function (Chang and Stearns, 2000). 23 tubulin genes and a least 48 pseudogenes are found within the human genome and are spread across all 24 chromosomes. There are therefore multiple genes encoding for each different tubulin subclass, with 9 α, 10 β, 2 γ, and 1 each of δ and ε, expressing different tubulin isotypes, with the majority of sequence differences occurring at the C-terminus (Findeisen et al., 2014).

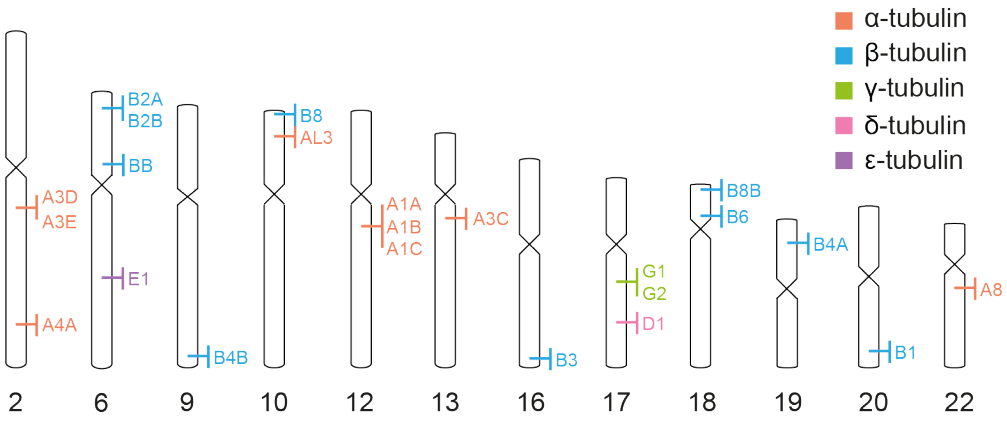

Figure 1.2 - Chromosome mapping of human tubulin genes

The human tubulin genes are distributed across 12 different chromosomes. Some genes occur in clusters, thought to have occurred through gene duplication. Coding genes only are displayed here and not pseudogenes which span across all other chromosomes not displayed.

1.1.3 Microtubule polymerisation

α- and β-tubulin spontaneously dimerise before polymerising into microtubule lattices (Akhmanova and Maiato, 2017). Lattices usually contain 13 protofilaments (although 10-15 protofilaments have been observed across a number of organisms) which are laterally associated to form hollow cylindrical structures (Wickstead and Gull, 2011; Chalfie and Thomson, 1982). Microtubules are polarised structures and consist of a plus end and a minus end. The plus-end is the major microtubule elongation site whereas the minus-end is usually stabilised at their origin (Mitchison, 1993), however it can also slowly contribute to the addition of heterodimers *in vitro* (Martin and Akhmanova, 2018). Tubulin proteins are capable of binding GTP. α-tubulin has a non-exchangeable site (N-site) trapped between the interface of both subunits, where GTP cannot be hydrolysed to GDP. β-tubulin has an exchangeable site (E-site) capable of facilitating GTP hydrolysis, facing the plus end (Desai and Mitchison, 1997). When a

new tubulin dimer loaded with GTP approaches the β-tubulin at growing end, the contacts occurring within and between the heterodimers straighten, allowing for lateral contacts to occur between adjacent protofilaments. Further addition allows for further straightening and the eventual closure of the microtubule cylinder (Wang and Nogales, 2005). Simultaneously, as the new GTP-tubulin molecule is added, hydrolysis of the GTP to GDP within the preceding heterodimer is enhanced. The new tubulin dimer still contains GTP-β-tubulin, and this therefore caps the polymer as it grows, retaining the straightened conformation and hence the lateral contacts.

1.1.4 Dynamic instability

Microtubules are dynamic and can grow and shrink constantly for the continuous remodelling of the cytoskeleton, referred to as dynamic instability (Figure 1.3). This property allows them to alter their shape, length and localisation for rapid regulation of cellular function (Mitchison and Kirschner, 1984). As microtubule polymerisation slows, catastrophe can occur, which is the sudden depolymerisation of microtubules. The mechanistic ideas are related to the GTP cap present at the growing end, an idea that was first proposed in 1981 by Carlier and Pantaloni. They showed that one molecule of GTP was hydrolysed per tubulin heterodimer, and the process of tubulin addition and GTP hydrolysis occurs in 2 subsequent steps (Carlier and Pantaloni, 1981). When the pool of free tubulin diminishes, polymerisation rate decreases and eventually pauses. Hydrolysis of all the previously bound GTP-tubulin within the lattice occurs quickly to give GDP-bound tubulin. This reveals an unstable GDP-tubulin dimer at the plus end (Mitchison and Kirschner, 1984) which causes a bend between the adjacent monomers that is not compatible with the lateral contacts occurring between protofilaments. The destabilised lattice therefore converts from a growing state to a paused state, and eventually to a depolymerising state called catastrophe (Gardner et al., 2013; Wang and Nogales, 2005). Upon initiation, protofilaments peel away from the microtubule lattice and depolymerise independently (Nogales, 2000). The occurrence of catastrophe is greater within longer microtubules and those closer to the periphery of the cell as these are more dynamic to allow for rapid remodelling to assist with cell movement and shape (Gardner et al., 2013). This mechanism is shown in Figure 1.3.

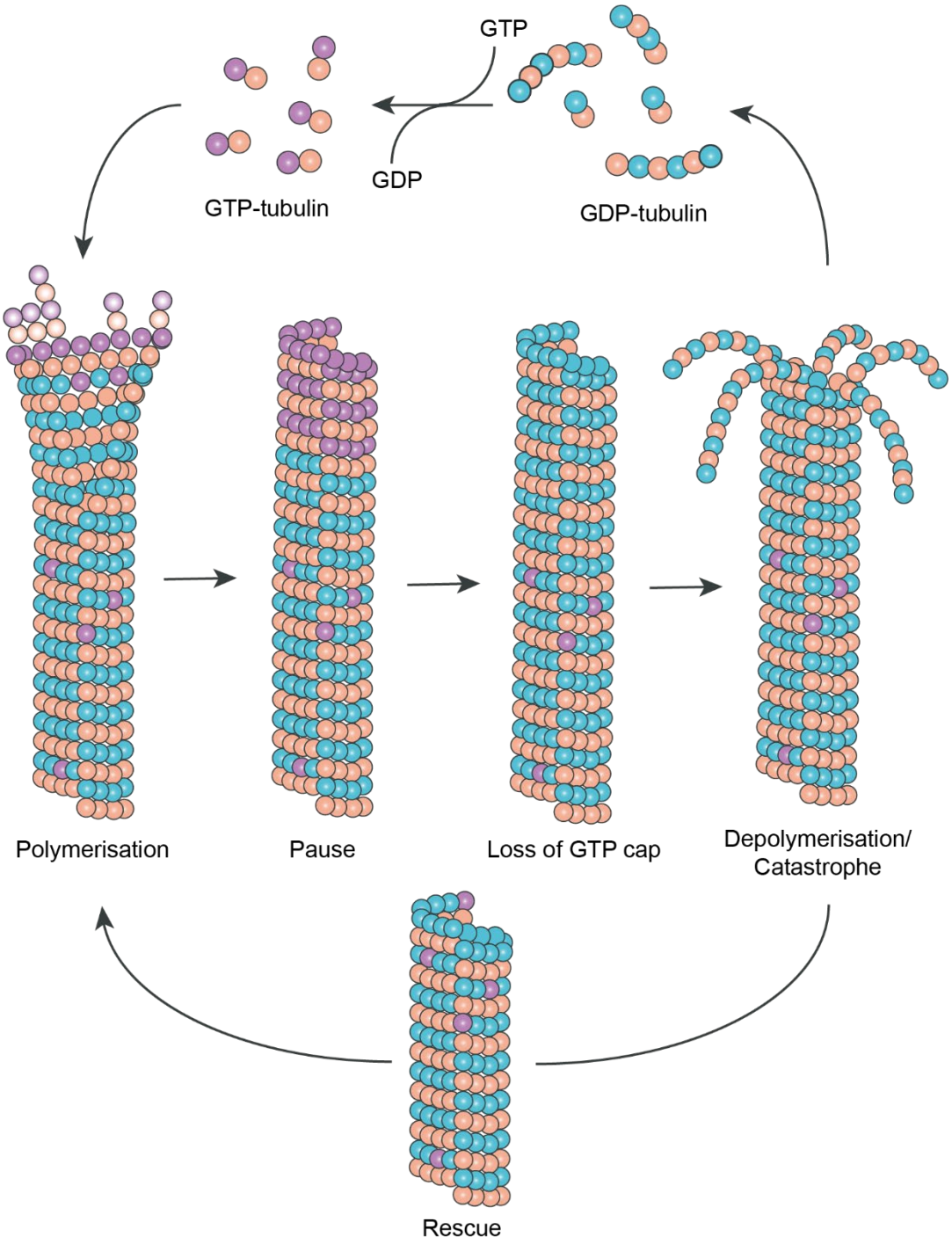

Figure 1.3 - Microtubule dynamic instability

Microtubules form from polymerisation of GTP-bound heterodimers of α- and β-tubulin. GTP hydrolysis occurs in previously added heterodimers as new ones are added and a GTP cap at the end is present to stabilise microtubules. As polymerisation slows, GTP hydrolysis catches up and the GTP cap is lost, the microtubules destabilise and peel away from the lattice, causing depolymerisation. Shrinking microtubules can either be rescued for regrowth, or their subunits can be harvested, GDP exchanged for GTP, and polymerisation of a new microtubule can begin.

When catastrophe does occur, this rapid shrinkage can be rescued, allowing the existing microtubule to begin growing again. These events are thought to be relatively rare however (Gardner et al., 2013). It was originally thought that an increase in free tubulin concentration may cause microtubule regrowth following catastrophe, however this was shown early on to not be sufficient (Walker et al., 1988). The presence of microtubule binding proteins which act to stabilise and destabilise has been suggested to play a role within these dynamic instability events. For example, cytoplasmic linker associated proteins (CLASPs) can stably bind to the microtubule lattice and recruit soluble tubulin to facilitate the rescue and regrowth events (Al-Bassam et al., 2010). Another possible reason for these rescue events is the presence of GTP-tubulin within the lattice itself, retained due to incomplete hydrolysis. These are termed 'GTP remnants' and can become exposed as depolymerisation occurs. This would in turn recreate the GTP cap at the plus end during depolymerisation and stabilise the microtubule, allowing for rescue and regrowth to occur. Dimitrov *et al.* developed a GTP-tubulin specific antibody which was used to show its presence throughout the microtubule lattice and not just at the plus ends (Dimitrov et al., 2008). This suggestion has been independently verified by another group who were investigating the function of the E3 ligase, Von Hippel-Lindau tumour suppressor protein, as a microtubule associated protein (MAP). They showed that this protein acts as a strong promotor for microtubule stability by inhibiting GTP hydrolysis activity at the plus end and along the lattice, creating a GTP cap and GTP remnants respectively, both *in vitro* and *in vivo*. This thereby reduces catastrophe and increases rescue events (Thoma et al., 2010). Further verification of this theory and the presence of GTP remnants has also been seen along the axon of neuronal cells (Nakata et al., 2011).

A study performed in 2015 by Schaedel *et al*. provided an alternative mechanism for the incorporation of GTP remnants. They showed that microtubules can display structural defects, leading to weakened areas and eventual damage. They demonstrated that if microtubules were subjected to rounds of bending cycles to induce damage *in vivo*, they were able to repair themselves and regain their stiffness. Pulse lasers were used to induce microtubule defects and fluorescent-labelled tubulin was specifically incorporated into the damaged region in the middle of the lattice (Schaedel et al., 2015). A follow up study confirmed that rescue events occurred more frequently at these sites of self-repair. Furthermore, these sites contained GTP-bound tubulin and were capable of recruiting MAPs with an increased affinity for GTP tubulin

such as end-binding protein 3 (EB3) and CLASP (described in section 1.1.9.2, possibly contributing to the increase in rescue events (Aumeier et al., 2016).

1.1.5 Microtubule drugs

Microtubules are targets for numerous drugs which alter their dynamics. Microtubule-stabilising drugs associate with free tubulin dimers to increase polymerisation, and with the microtubule lattice to prevent depolymerisation. Conversely, microtubule-destabilising drugs induce depolymerisation and prevent further polymerisation. These drugs are frequently used as anti-cancer drugs. Microtubule destabilising Vinca alkaloids are prescribed to cancer patients to inhibit proper formation of the mitotic spindle and prevent cellular division (Donoso et al., 1977). Paclitaxel, more commonly known as Taxol, stabilises microtubules, arresting cells in G2/M phase and inducing cell death (Horwitz, 1994). Alongside their therapeutic uses, microtubule drugs are frequently used within scientific research both *in vivo* and *in vitro*. Commonly used microtubule binding drugs are detailed in Table 1.1.

Table 1.1 - Microtubule binding drugs

Name	Binding site	Action	Uses
Colchicine	Colchicine	Depolymerisation	Gout, arthritis
Colcemid	Colchicine	Depolymerisation	Metastatic breast cancer
Nocodazole	Colchicine	Depolymerisation	Microtubule research – cell cycle synchronisation
Paclitaxel	Taxane	Polymerisation and stability	Ovarian, breast and non-small cell lung cancers
Docetaxel	Taxane	Polymerisation	Breast, prostate gastric adenocarcinoma and non-small cell lung cancers
Vinblastine	Vinca	Depolymerisation	Testicular cancer, Hodgkin's disease
Vincristine	Vinca	Depolymerisation	Paediatric malignancies (leukaemia, lymphoma)
Eribulin	Microtubule plus ends	Depolymerisation	Breast cancer, liposarcoma
Estramustine	Alternative site	Depolymerisation	Prostate cancer

Colchicine is the microtubule-depolymerising drug which lead to the discovery of tubulin as the microtubule subunit (Weisenberg et al., 1968). The colchicine binding site was identified by developing an assay which allowed tubulin to copurify with

radiolabelled colchicine (Borisy and Taylor, 1967). This therefore highlights the importance of microtubule-binding drugs within research. Colchicine causes depolymerisation by binding to the colchicine-binding site on β-tubulin within free dimers and lattices. Upon binding it induces a conformational change that switches the polymer from a straight conformation into a curved one. This reduces the lateral contacts between the subunits and protofilaments, causing rapid depolymerisation and mimicking the GDP-tubulin state (Ravelli et al., 2004). Although nocodazole has become the primary drug for microtubule depolymerisation today, colchicine is still used as a treatment for gout and other inflammatory conditions (Dalbeth et al., 2014).

Nocodazole is a microtubule-depolymerising drug which acts similarly to colchicine. It was identified as a microtubule binding drug following an antimitotic drug screen (De Brabander et al., 1975), and was shown to inhibit polymerisation of tubulin isolated from rat brains in a readily reversible manner with a stoichiometry of one to one (Hoebeke et al., 1976). Nocodazole binds to the β-tubulin subunit and competitively inhibits colchicine binding. Following use of this drug, the addition of GTP and microtubule-associated proteins involved in polymerisation are insufficient to stimulate the microtubule reformation (Lee et al., 1980). Specificity to different tubulin isotypes has also been observed, with the greatest binding affinity occurring with αβIV and the lowest with αβIII (Xu et al., 2002). Treatment with nocodazole *in vivo* leads to rapid depolymerisation within 20 minutes, however exposure times after 2-5 hours can lead to altered cell morphology (Lee et al., 1980). Nocodazole is therefore useful for studying microtubule dynamics and is also frequently used within cell biology to synchronise cells to prometaphase (Blajeski et al., 2002).

Taxol was first isolated from Taxus brevifolia plants (Wani et al., 1971) before being confirmed to enhance microtubule stabilisation and nucleation later that decade (Schiff and Horwitz, 1980). It is the major microtubule-stabilising drug used within research. Taxol binds specifically and reversibly to the β-tubulin subunit of both free and polymerised tubulin (Rao et al., 1992). Application *in vitro* induces microtubule rearrangement, causing them to bundle and stabilise, with cold temperatures being insufficient to cause depolymerisation (Schiff and Horwitz, 1980). Induction of polymerisation can occur in the absence of both microtubule binding proteins and GTP (Kumar, 1981; Schiff and Horwitz, 1981). Taxol binding induces a conformational change causing tubulin filaments to adopt a straightened conformation, mimicking the action imposed from the addition of GTP-tubulin, preventing curling within the lattice ends and increasing the lateral contacts. This therefore increases stability and

reduces catastrophe events (Arnal and Wade, 1995). Taxol has aided a number of major tubulin and microtubule discoveries including the determination of the structure of both tubulin subunits (Nogales, 1998).

1.1.6 Nucleation and the centrosome

Polymerisation of microtubules *in vitro* can occur spontaneously in the presence of GTP and a calcium chelator only when the concentration of tubulin dimers is above the critical concentration of 5 μM (Walker et al., 1988). In *vivo* however, for initiation of polymerisation to occur, a nucleation factor is required (Borisy and Olmsted, 1972).

Most microtubules originate from microtubule organising centres (MTOC) following their nucleation. They are anchored here by their minus ends, with their plus ends protruding out into the cytoplasm as they polymerise. The dominant MTOC is the centrosome, which is a complex, globular structure that is made up of 2 centrioles, the mother and the daughter, and organises microtubules by controlling their nucleation and anchoring. Each centriole is formed from 9 sets of microtubule triplets arranged with radial symmetry into a cylinder. Surrounding these centrioles is the pericentriolar material which contains high levels of proteins required for nucleation, growth and anchoring of microtubules (Martin and Akhmanova, 2018). The centrosome also plays a crucial role during cell division, with it being duplicated to form a daughter centrosome during S phase of every cycle. Nucleation can then occur at each individual centrosome to form the mitotic spindle (Fu et al., 2015).

The formation of new microtubules from free tubulin dimers is a regulated, multi-step process that is kinetically unfavourable. Templates from either γ-tubulin oligomers or the severed ends of pre-existing microtubules are therefore required (Wieczorek et al., 2015). γ-tubulin was first discovered in 1989 by Oakley and Oakley when looking at mutations within a previously identified microtubule interacting protein, mipA. By cloning and sequencing they discovered that mipA and β-tubulin shared 33.3% sequence similarity, indicating they are part of the same superfamily. This discovery was the key finding to understanding how microtubules nucleate (Oakley and Oakley, 1989). γ-tubulin associates with multiple proteins called γ-tubulin complex proteins (GCPs), which come together in a ring-shaped structure called the γ-tubulin ring complexes (γTuRC). This acts like a scaffold to facilitate microtubule nucleation (Zheng et al., 1995). In yeast, this structure is termed the γ-tubulin small complex (γTuSC) and has been shown by EM to consist of two γ-tubulin subunits, and one

each of GCP2 and GCP3 (Kollman et al., 2010). The human structure is formed from GCP2-6 proteins which associate directly to 14 γ-tubulins. GCP's all contain a Grip1 motif for lateral association to each other, and a Grip2 motif to bind to γ-tubulin. The completed structure resembles a single helical turn (Kollman et al., 2010), and mimics the microtubule plus-end, thereby acting as a ring-like template. Multiple recent studies have described the cryo-EM structures for γTuRC (Würtz et al., 2022) allowing the arrangement of GCP proteins to finally be determined (Liu et al., 2020; Consolati et al., 2020; Zimmermann et al., 2020). The structure mainly contains GCP2 and GCP3 molecules, with 2 GCP4 and one each of GCP5 and 6 (Consolati et al., 2020; Würtz et al., 2022). These structural studies also all revealed the presence of a single actin molecule within the structure, thought to regulate its geometry (Würtz et al., 2022) and also stabilise the closed conformation (Consolati et al., 2020). Additionally, MZT2 molecules were also shown to crosslink GCP interfaces, stabilising the interactions (Consolati et al., 2020). This structure is illustrated in Figure 1.4.

Once the γTuRC cone-like cap structure has been formed, αβ-tubulin dimers are then recruited and nucleated to form the minus end of the microtubule. Nucleation is dependent on the conformation of a hinge within GCP3 which either leaves a gap within the γTuRC or provides a template with the exact spacing of microtubule filaments, allowing the formation of 13 protofilaments (Petry and Vale, 2015; Kollman et al., 2010). Once elongation has been initiated, the minus end of the newly formed microtubule is anchored to the centrosome to stabilise microtubule structures (Oakley et al., 2015). Anchoring is facilitated by the major microtubule-anchoring structures, the subdistal appendages, which contains multiple proteins including ninein to bridge the nucleation and anchoring processes together (Delgehyr et al., 2005).

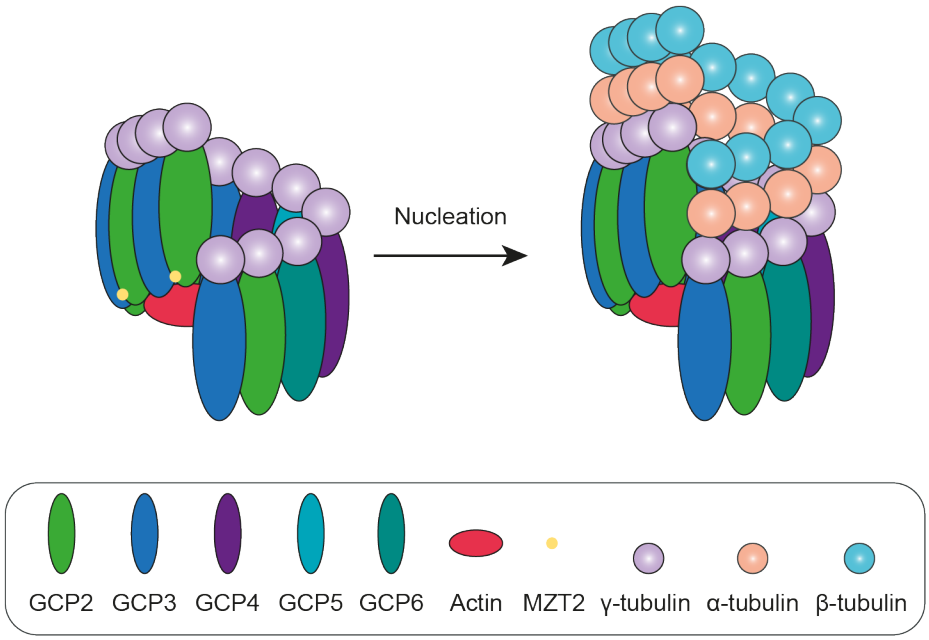

Figure 1.4 - Microtubule nucleation

Schematic diagram showing the γTuRC structure and the nucleation of tubulin dimers to initiate microtubule formation. GCP2-6 proteins each associate to one of 14 γ-tubulin molecules and then laterally associate to form a single helical structure. A single actin molecule is found within the structure, and MZT2 proteins crosslink the GCP proteins at the perimeter. αβ-tubulin dimers can then associate to initiate microtubule formation from the minus end.

In addition to the core complex, other essential proteins are required for the localisation and activation of the γTuRC before nucleation can occur. For example, depletion of GCP-WD has been seen to abolish correct localisation of γ-tubulin prior to nucleation (Lüders et al., 2006). Pericentrin and AKAP450 proteins contribute to complex localisation via their PACT (pericintrin-AKAP450 centrosomal targeting) domains (Gillingham and Munro, 2000). Furthermore, activation factor CDK5RAP2 facilitates centrosomal attachment of γTuRC and increases the nucleating capacity by ~7-fold (Choi et al., 2010). Data from my host laboratory has also highlighted the involvement of USP21 in nucleation and regrowth of microtubules at the centrosome. Microtubule regrowth occurs after 2.5 minutes following cold depolymerisation, however when USP21 is depleted this is impaired (Urbé et al., 2012). The nucleation step of microtubules is therefore dependent on the regulation of a complex network of proteins.

Non-centrosomal MTOCs also exist which can facilitate microtubule nucleation at alternative cellular regions (Petry and Vale, 2015). The Golgi apparatus can nucleate microtubules in a γ-tubulin dependent manner, with several proteins observed in

centrosomal-nucleation also being recruited here, including CDK5RAP2 and AKAP450 (Wang et al., 2010). These microtubules are generally important for cell polarity and migration, and are optimal for trafficking of cargo to and from the Golgi (Martin and Akhmanova, 2018). Microtubules formed at the centrosome can be severed and transported via motor-driven transport to other areas of the cell (Petry and Vale, 2015). Ninein can translocate with these microtubules and facilitate the capping and anchorage of their minus ends at apical sites of the plasma membrane of epithelial cells (Mogensen et al., 2000). This reorganisation is thought to influence apical-basal polarisation, cell differentiation and cell shape in epithelial cells (Goldspink et al., 2017). Further microtubule nucleation sites have also been described during spindle formation. Quantitative analysis confirms that microtubule density is greater within the chromosome ring compared to at the spindle poles, suggesting microtubules must originate from an additional site, thought to be the kinetochores. Multiple short, non-centrosomal microtubules are observed in contact with the kinetochores shortly after spindle formation (Sikirzhytski et al., 2018). The mechanisms involved are not completely understood however this process is hypothesised to be promoted by the accumulation of RanGTP and RanGTP-dependent nucleation and stabilisation factors (Torosantucci et al., 2008; Petry and Vale, 2015).

1.1.7 Microtubule branching

Microtubule nucleation can occur from pre-existing microtubules, allowing for the formation of a branched network. Microtubule branching was first visualised in plant cells by Murta *et al.* and nucleation was facilitated by recruitment of γ-tubulin to these branch points. These new microtubules can protrude from the side of an existing one at a 42° angle (Murata et al., 2005).

Microtubule branching has also been observed within the mitotic spindle during cellular division, with γ-tubulin being localised to the spindle body. This may partly explain how microtubules can be rapidly formed within the spindle during mitosis and meiosis (Goshima et al., 2008). Augmin is an 8-subunit complex which plays a key role within lateral nucleation of microtubules within the spindles of *Xenopus* egg extracts. Augmin is required, in conjunction with γ-tubulin and TPX2, to initiate branch nucleation and elongation, and its depletion disrupts their formation. By following the plus tip end-binding protein 1 (EB1), the newly created daughter microtubules were

confirmed to display the same polarity as their mother microtubules (Petry et al., 2013).

Microtubule-dependent nucleation is also crucial within neuronal cells. Neurons are highly polarised cells which make direct contacts with many other cells in order to pass on their signals. The occurrence of microtubule branching here aids axonal outgrowth, determines the shape of the axon and promotes neuronal development. This mechanism is independent of γ-tubulin and requires the recruitment of the microtubule-remodelling factor, SSNA1. SSNA1 can self-assemble into fibrils and bind at branch points, causing the growing microtubule to split in two. Separate branches can then form rather than nucleating the side of a pre-existing lattice. Mutations within SSNA1 cause disruptions to branching initiation and hinder axon development (Basnet et al., 2018).

1.1.8 Microtubule motor proteins

A major function for microtubules is for the transport of cargo to specific cellular locations. Such cargo includes organelles, other membranous vesicles, signalling proteins and adaptor proteins, all of which are too large to diffuse through the cell themselves (Endow et al., 2010). This function is facilitated by two families of motor proteins, kinesin and cytoplasmic dynein, which ‘walk’ along the microtubule lattices, pulling their bound cargo with them (Schroer, 2000). This guided transport relies on microtubule polarity to direct them to the correct locations, with conventional kinesin motors travelling towards the plus end at the cell periphery (anterograde), and the cytoplasmic dynein travelling towards the minus end nearer the perinuclear region (retrograde). Furthermore, these motor families display different affinities towards different cargos, adding another level of regulation to ensure correct positioning of cellular components (Lane and Allan, 1998). This regulated transport of organelles was observed before the identity of these motor proteins was determined. However, as all cargo was seen to travel along microtubules at the same velocity regardless of size, it was hypothesised that the same type of motor was responsible for interacting with and transporting a variety of organelles and vesicles (Ronald D Vale et al., 1985a).

1.1.8.1 Kinesin

Conventional kinesin (kinesin-1) was the first to be discovered in 1985 by two independent laboratories. Scott Brady isolated a microtubule associated ATPase from chicken brain (Brady, 1985) which fitted the predicted characteristics of the ATP-dependent motor protein required for axonal transport (Brady et al., 1985; Lasek and Brady, 1985). The discovery of kinesin in 1985 by Ronald Vale was performed using giant squid axon where it was shown that beads could be transported along axonal microtubules only with the addition of a soluble protein fraction. They confirmed that the beads were interacting with a motor protein from this protein mix, which was in turn identified as kinesin after purification using a microtubule-affinity purification technique (Vale et al., 1985b; c). It was this group which named the protein 'kinesin' (Vale et al., 1985a). The sequence for kinesin-1 was first determined in Drosophila, and this allowed for the protein structure to be identified, revealing an ATP-binding domain and microtubule-binding activity. Structural determination revealed that this motor protein had a similar organisation to the actin-dependent motor protein, myosin, despite sharing no sequence similarity (Yang et al., 1989). Following the determination of the sequence and structure of kinesin-1, ~50 other kinesin-related proteins (KRPs) were identified in the early 1990's. There are now 15 known groups of kinesin proteins within this family, detailed within Table 1.2 (Endow et al., 2010).

Kinesin-1 is a hetero-tetramer consisting of 2 identical heavy chains and a pair of identical globular light chains (Figure 1.5A). The heavy chains each contain an α-helical central stalk region required for dimerisation, connected to an N-terminal motor domain head via a neck linker. Heavy chains facilitate microtubule binding and coordinate the walking motion, whereas the light chains allow for cargo binding (Lane and Allan, 1998; Shao and Gao, 2006). X-ray crystallography of the kinesin heavy chain revealed that the catalytic motor domain is composed of an 8-stranded β-sheet and 3 α-helices, with the nucleotide binding cleft positioned to one side and the microtubule binding site to the other (Kull et al., 1996). Kinesin family members differ based on the heavy chains involved and the non-motor accessory proteins which join them (Endow et al., 2010). For example, kinesin-2 forms a heterotrimer from 2 different heavy chain motor domains and a single light chain that associates with the cargo (Scholey, 1996). Kinesin-13 members possess an unconventional structure, with the motor domain is present within the middle of the polypeptide. These family members differ from other kinesins as they do not display directionality but instead induce depolymerisation (Moores and Milligan, 2006).

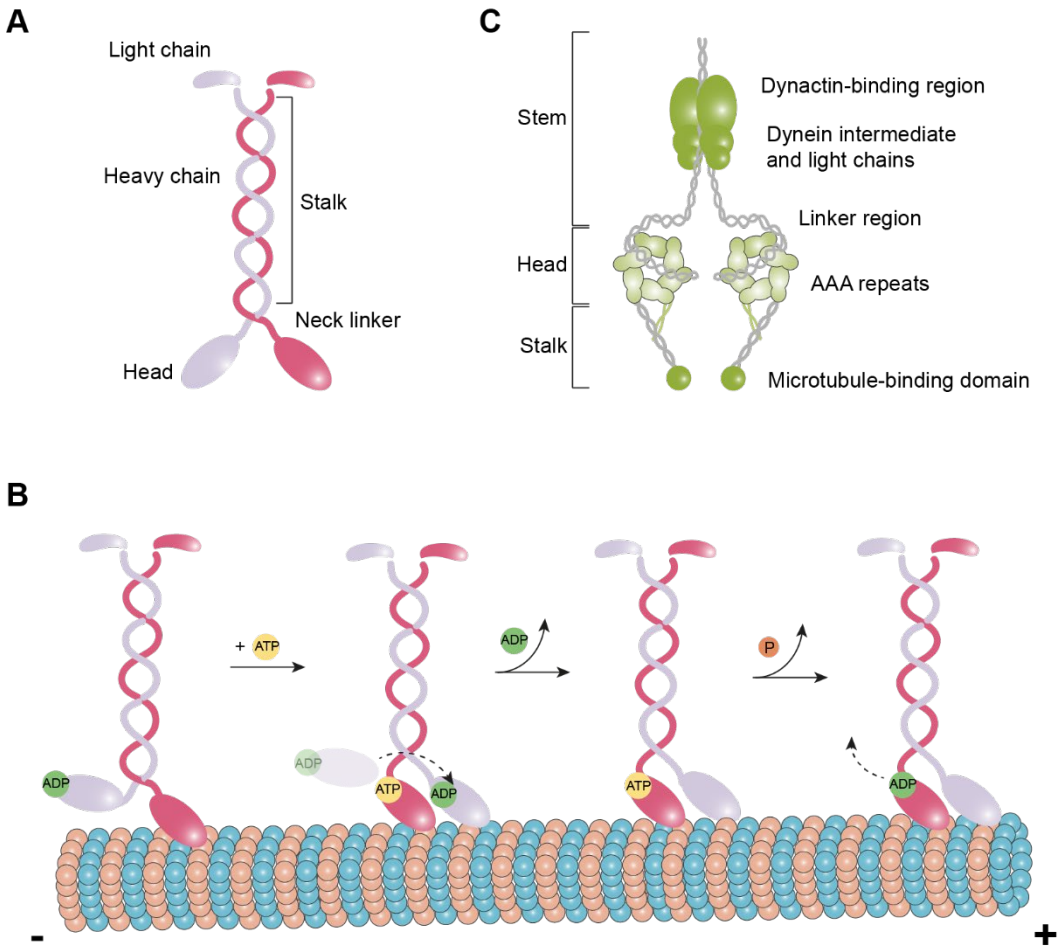

Figure 1.5 – Motor protein structure and transport along microtubules

A. Kinesin proteins are formed from 2 light chains for cargo binding, and 2 heavy chains which each have a stalk for dimerisation, and a head for microtubule binding, joined together via a neck linker. **B.** Kinesin is able to walk along microtubules in an ATP-dependent manner using the head domains. The back ADP-containing head is weakly bound. ATP binding to the front head induces a conformational change and the back head swings in front. ADP is then released from the front whilst ATP hydrolysis of the one at the back then occurs. The leading head is then ready to accept ATP to take another step. **C.** Cytoplasmic dynein is a large multi-subunit protein containing a pair of heavy, intermediate, intermediate light and light chains. The intermediate and light chains make up the stalk for binding dynactin and cargo. Each heavy chain contains 6 AAA repeats which make up the motor head, connected by a linker to the microtubule-binding region in the stalk.

Kinesins transport their cargo in an ATP-dependent manner (Figure 1.5B). ATP derived energy is converted into mechanical work, and the two motor heads, one from each heavy chain, function in a highly coordinated ‘hand-over-hand’ mechanism to walk down the microtubule without completely dissociating (Kaseda et al., 2003). As

the motor protein walks along, the leading head is associated tightly to microtubules in a nucleotide-free state, whereas the rear head is weakly associated in an ADP-bound state. ATP can then bind to the front motor head, inducing a large conformational change in the neck linker region of the heavy chain, causing it to lean forward and 'dock' into the front motor head. Simultaneously, the weakly bound rear head is immobilised, and swings forward to become the new front motor, binding to the next site along the lattice. This movement and reattachment cause the release of the ADP from the new leading head, and the ATP hydrolysis of the now rear head. The front motor head is now in a nucleotide-free state ready to bind another ATP molecule to initiate another step along the microtubules. With each step, one motor head remains tightly bound to the microtubule lattice whilst the other takes a 17 nm step forward (Rice et al., 1999; Endow et al., 2010; Shao and Gao, 2006). This mechanism is therefore dependent on the binding and hydrolysis of ATP to produce the force required for driving the movement, but also to specify the direction of travel (Rice et al., 1999; Endow et al., 2010).

1.1.8.2 Dynein

Dynein is the second family of motor proteins and displays minus end directed transport (retrograde) (Höök and Vallee, 2006). In comparison to the large kinesin family, there are only 2 members of the cytoplasmic dynein family, cytoplasmic dynein and axonemal dynein. Axonemal dynein was first reported by Ian Gibbons as an ATP-dependent motor which facilitates cilia bending (Gibbons, 1963; Gibbons and Rowe, 1965). This enzyme was thought to have a similar structure to the axoneme arms which link the microtubule doublets within the cilia structure (Gibbons, 1981). It localises exclusively to the cilia and flagellar base and allows cilia microtubules to slide against each other for cilia beating (Höök and Vallee, 2006). Cytoplasmic dynein, is responsible for intracellular transport, mitosis, polarisation and cell movement, and was identified later in 1987 (Paschal et al., 1987). It can enable the microtubule-dependent transport of the Golgi, lysosomes and late endosomes, alongside other microtubules, mRNA and viruses (Reck-Peterson et al., 2018). Additionally, it also associates with chromosome kinetochores and the cell cortex during cell division (Barisic and Maiato, 2016).

Dynein is a very large multi-protein subunit formed from a pair of heavy chains and multiple accessory proteins termed intermediate, light intermediate and light chains (Vallee et al., 2004), with the heavy chains containing ~4600 amino acids (Asai and

Koonce, 2001). Although dynein shares some resemblance to kinesin and myosin, it does contain structural differences which highlight it as a unique motor (Asai and Koonce, 2001). The N-terminal domain forms the stem required for dimerisation and the binding of accessory proteins (Habura et al., 1999). This contains ~1300 residues, with the remaining residues all contributing to the motor domain, which are connected together via a linker. The motor head domain is formed from ring of 6 repeated AAA (ATPases Associated diverse cellular Activities) modules containing multiple nucleotide binding sites (Asai and Koonce, 2001) and a microtubule-binding region, termed the stalk, between the 4th and 5th AAA repeats (Goodenough and Heuser, 1984). This is illustrated in Figure 1.5C.

Unlike kinesin and myosin, dynein cannot produce force and travel along microtubules in a similar manner. It exists in two conformational states based on the presence and absence of ATP and ADP. Movement begins with both stalks bound tightly to the microtubule, and the motor domains in an ADP-bound state. ATP binding within the front head induces a conformational change within the AAA ring structure and the stalk, causing it to dissociate and lean forwards (Bhabha et al., 2016). ATP binding occurs at the AAA1 repeat within the motor and coordinates the microtubule affinity change, with the tail swinging forward (Imamula et al., 2007). This dissociation induces a conformational change within the linker region to AAA2/3 and the ring rotates, causing this released stalk to rebind to the microtubule closer to the minus end. This rebinding event stimulates ATP hydrolysis in the front motor, allowing it to bind with greater affinity (Carter et al., 2011). Following rebinding, the linker shifts towards the AAA4/5 repeats and induces tension between the front and the rear motor head domains. This tension then causes the rear motor to undergo the same mechanistic sequence to allow it to step forward and relieve the tension between the 2 heavy chains. Unlike with kinesin, it remains unclear how dynein displays a stepping bias towards the minus end however (Bhabha et al., 2016).

In order for dynein to become activated and transport cargo, an additional protein complex termed dynactin (developed from dynein activator) is required (Gill et al., 1991; Schroer and Sheetz, 1991). Dynein remains largely inactive in the absence of these additional factors, with its transport along microtubules *in vitro* lacking processivity (McKenney et al., 2014). Dynactin is a multimeric protein complex which includes proteins such as dynamitin, $p150^{Glued}$ for associating with dynein and microtubules, and actin-related proteins (ARPs) for regulating transport activity and cargo binding (Lane and Allan, 1998). For stable assembly and activation of the

dynein-dynactin complex however, a coiled-coil adaptor protein is required. The most studied adaptor protein is BicD2 which allows the two complexes to interact, and also associates dynein with membranous organelles (McKenney et al., 2014). Additional adaptor proteins such as Hook3, RILP and FIP3 have also been identified which allow stable association and allosteric activation (Schroeder and Vale, 2016). Dynein activation is achieved when both factors are present, causing the dynein heads to shift to the correct orientation for motility (Olenick and Holzbaur, 2019). Furthermore, LIS1 protein promotes the formation of dynein-dynactin-adaptor complexes (Splinter et al., 2012). Despite a great indication that these factors are required for successful activation and motor transport (Lane and Allan, 1998), recent research has revealed an alternative mechanism for dynein activation. It has been reported that dynein heavy chain dimers can cross-bridge with neighbouring microtubules, leading to autoactivation due to their separation, allowing dynein to function without the requirement for dynactin (Chakraborty et al., 2020).

Table 1.2 - Motor protein family members, functions and structural features

Adapted from Miki *et al* (2005).

Name	Members	Functions	Structural features
Kinesin-1	KIF5A/B/C, KHC	Organelle transport, nuclear movement	Neck β-sheet, conserved coiled-coil stalk
Kinesin-2	KIF3A, KIF3B/C, KIF17, Krp85/95	Organelle transport, intra-flagellar transport, spermatogenesis	Clusters of charged residues after the neck β-sheet
Kinesin-3	KIF1, KIF13, KIF14, KIF16, KIF28, NcKIF1C/Klp7	Organelle transport	β-sheet and helix in neck region, forkhead-associated domain, monomeric/homodimer
Kinesin-4	KIF4, KIF7, KIF21, KIF27, NcKIF21A	Organelle transport, chromosomal movement	Conserved neck β-sheet and coiled-coil
Kinesin-5	KIF11, Eg5, BimC	Bipolar spindle formation	Family-specific neck, catalytic core, BimC box domain, sparse coiled-coils, homotetramers
Kinesin-6	Rab6Kinesin, KIF20, KIF23, MKLP1	Cytokinesis, microtubule transport	Loosely conserved neck region, long insert in catalytic core
Kinesin-7	CENP-E, KIF10, KIP2, CMET, CANA	Microtubule-kinetochore capture, nuclear migration	Long, family-specific neck, abundant coiled-coils
Kinesin-8	KIF18, KIF19, Kip3, Klp67A	Mitochondrial transport, chromosome segregation, nuclear migration	Helical family-specific neck

Kinesin-9	KIF6, KIF9, KRP3, CrKLP1	Functions within cilia and flagellar, uncharacterised	Conserved sequence of neck region
Kinesin-10	KIF22, KID, Nod	Chromosome binding, cell division	Helix-hairpin-helix DNA binding motif
Kinesin-11	Smy1, VAB8, KIF26A, KIF26B	Signal transduction	Divergent catalytic core
Kinesin-12	KIF12, AtPAKRP1, KIF15, Xklp2, HKLP2	Organelle transport, neuronal development, cell division	Homologous sequence at C-terminal, coiled-coils
Kinesin-13	MCAK, KIF2, KIF24, PrKin1, XKCM1	Vesicle transport, microtubule depolymerising activity, cellular division, neuronal development,	Catalytic core in middle of protein, conserved positively charged helical neck
Kinesin-14A	CHO2, KIFC1, Kar3, KatA, Ncd	Yeast nuclear fusion, mitosis	Family-specific neck helix
Kinesin-14B	KIFC2/3, KatD, KCBP, KIF25	Organelle transport, endocytosis	Family-specific helical neck region, calponin homology domain
Orphans	CeKLP10, CeKP18, Ddk9	Uncharacterised	n/a
Axonemal dynein	DHC9, DHC11, DHC5, DHC8, DHC7, DHC3	Microtubule sliding	
Cytoplasmic dynein	Dynein 1, Dynein 2	Retrograde transport, microtubule-kinetochore capture, spindle orientation, axonemal maintenance	

1.1.9 Microtubule associated proteins

In addition to the microtubule motor proteins, there is also a plethora of other proteins which bind to microtubules. These are known as microtubule-associated proteins (MAPs) and have been categorised into 4 groups based on their functions: 1) proteins that nucleate microtubules and initiate their elongation (section 1.1.6); 2) end-binding proteins; 3) structural MAPs; and 4) microtubule-severing proteins. Originally, for a protein to be defined as a MAP, the protein in question must not bind to any other subcellular fractions and must colocalise with tubulin following multiple rounds of polymerisation/depolymerisation cycles *in vitro* (Bodakuntla et al., 2019).

1.1.9.1 Structural MAPs

Structural MAPs were given their name due to their overall function of binding to microtubules and assisting with their polymerisation, stability and bundling, thereby controlling microtubule structure and organisation (Bodakuntla et al., 2019). This

function was identified early on following the initial discoveries of MAP1 and MAP2 proteins from brain extracts (Sloboda et al., 1975), and the identification of tau where it was apparent that microtubule polymerisation of brain tubulin could not commence in its absence (Weingarten et al., 1975). The implications of these MAPs within microtubule bundling was observed by EM in the 1970's and was shown to be regulated differently based on MAP size: MAP2 is large and allows bundling to be more spaced out whereas tau is smaller and induces a more compact structure (Herzog and Weber, 1978). Tau has also been structurally shown to act as a microtubule 'staple' by spanning across 3 tubulin dimers upon association and holding the lattice together (Kellogg et al., 2018). Additionally, it is highly brain specific and has been associated with neurodegenerative disorders such as Alzheimer's disease (Iqbal et al., 2016). MAP4 and MAP7 were purified directly from Hela cells shortly after and were also observed to stimulate microtubule polymerisation (Bulinski and Borisy, 1979). MAP4 has not been implicated in bundling and may actually repel this action due to its long projection domain, forcing parallel microtubules apart (Figure 1.6B) (Iida et al., 2002). MAP1A and 1B, which possess very similar properties (Garner et al., 1990), and the family of echinoderm microtubule associated protein (EMAP)-like proteins (EMLs) were identified shortly after, with the latter family also displaying microtubule bundling effects (Vallee and Bloom, 1983). During initial MAP discoveries, it was also noticed that some microtubules were insensitive to the cycles of polymerisation and depolymerisation and remained in a polymerised state, highlighting their increase in stability. Stable tubule only peptide (STOP), later renamed as MAP6, was identified as the culprit for this enhanced stability under cold conditions (Delphin et al., 2012).

Additional roles have also been documented for structural MAPs. Firstly, they facilitate the interactions between microtubules and the other two components of the cytoskeleton: actin and intermediate filaments. The engineered protein TipAct is able to associate with EB proteins at the growing plus end and crosslink with actin simultaneously, causing microtubule growth to align with the existing actin filament (Figure 1.6B). Microtubules can then assist with actin structures by inducing their transport, stretching and bundling (López et al., 2014). Second, most MAPs are involved in cargo transport regulation by controlling motor protein activity. Overexpression of tau proteins reduces the velocity of intracellular trafficking in a kinesin-dependent manner, and has been suggested as a possible cause for tau-dependent neurodegeneration (Ebneth et al., 1998). Furthermore, Xenopus MAP4 proteins have been reported to increase the processivity of kinesin-2 motors whilst

simultaneously inhibiting dynein transport when overexpressed (Semenova et al., 2014). Therefore, decorating microtubules with structural MAPs can cause both physical prevention of vesicular transport by reducing the contacts of motor proteins with the microtubule lattice, but in other cases enhance this function. A final role for these structural MAPs is the protection they provide from microtubule-severing proteins. Overexpression of MAP2 reduces the efficiency of katanin-dependent severing of neuronal microtubules within mammalian fibroblasts, and the depletion of tau allows katanin to sever axonal microtubules into short pieces (Figure 1.6D) (Qiang et al., 2006).

1.1.9.2 Plus-end tracking proteins (+TIPs)

Plus-end tracking proteins (+TIPs) are a structurally and functionally diverse group of MAPs which specifically associate with the dynamic growing ends of microtubules (Figure 1.6B) (Akhmanova and Steinmetz, 2010). These proteins generally target polymerising microtubules as opposed to those which are shrinking, however tracking of shrinking microtubules has been observed in yeast cells by the Dam1 complex (Lampert et al., 2010). +TIPs can associate with microtubules either autonomously or with the aid of an adaptor protein (commonly another +TIP) and they are divided into different categories based on their binding motifs or their functions (Akhmanova and Steinmetz, 2010).

End-binding (EB) proteins are a family of +TIPs which are highly conserved, found within yeast through to humans. They can interact independently with microtubule tips, with EB1 being frequently referred to as the master plus-end tracking protein due to its ability to associate with most other +TIPs (Dixit et al., 2009; Fong et al., 2017). EB proteins have a highly conserved N-terminal domain containing a calponin homology fold crucial for microtubule binding. Furthermore, they contain a coiled-coil domain for dimerisation, an EB homology (EBH) domain and a C-terminal tail containing an EEY/F sequence motif, which resembles that of tyrosinated α-tubulin, to allow interactions with other +TIPs (Buey et al., 2011). EB binding has been shown to require GTP hydrolysis, with binding being abolished when a slow hydrolysing GTP analogue was substituted, explaining their specificity to plus tips. They have also been reported to rapidly turnover at the plus tip by binding and dissociating repeatedly for multiple seconds at a time, allowing the GTP ends to be tracked as they polymerise (Dixit et al., 2009). Work carried out in Thomas Surrey's lab showed that the abundance of EB1 proteins at microtubule plus tips are indicative of microtubule

dynamics, with larger caps representing greater microtubule stability (Duellberg et al., 2016).

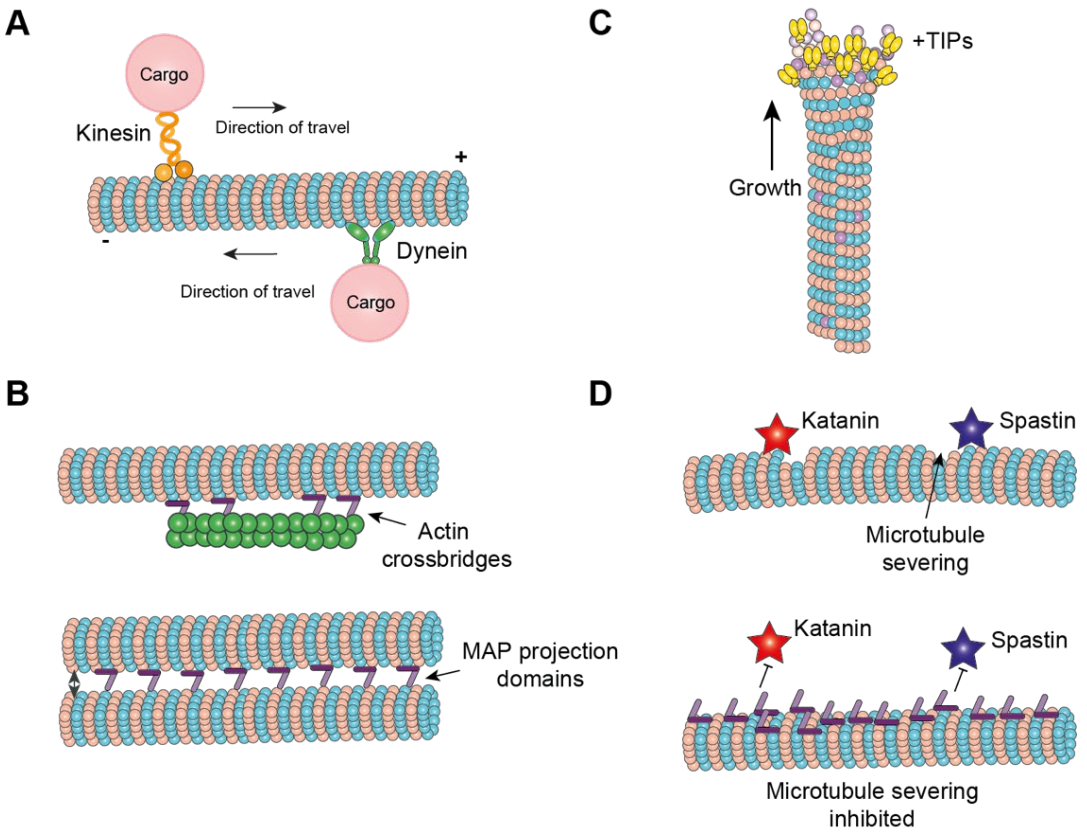

Figure 1.6 – Microtubule associated proteins

Examples of different microtubule associated proteins (MAPS). **A.** Kinesin and dynein motor proteins transporting cargo along microtubule lattices. **B.** Structural MAPs facilitating actin cross bridges and preventing microtubule bundling. **C.** Plus-end tracking proteins (+TIPs) localising to the growing microtubule end. **D.** Katanin and spastin severing proteins and how they can be inhibited by structural MAPs.

The second class of +TIPs includes the cytoplasmic-linker protein 170 (CLIP-170)-which was the first +TIP to be identified (Perez et al., 1999). Other members include CLIP-115, the dynactin subunit p150^{glued} and the deubiquitylase enzyme CYLD. They all contain a CAP-gly (cytoskeleton-associated protein glycine-rich) domain to facilitate microtubule binding (Peris et al., 2006; Gao et al., 2008). This domain consists of glycine residues and a hydrophobic cavity that allows association with the EEY/F motif present within both α-tubulin tails and EB proteins (Weisbrich et al.,

2007). This basic domain neutralises the acidic C-terminal tail of tubulin subunits, reducing electrostatic repulsion between adjacent microtubules to facilitate microtubule bundling (Wang et al., 2014). CAP-gly proteins are unable to associate directly with the microtubule plus tips alone and rely on the presence of EB proteins to form a composite binding site. They thereby 'hitch-hike' upon other autonomously binding proteins (Bieling et al., 2008; Akhmanova and Steinmetz, 2010). Furthermore, this class of +TIPs display a preference to tyrosinated microtubules, with detyrosination disrupting their interaction (Peris et al., 2006). Despite this same EEY/F motif being present within EB1, this is not subjected to detyrosination as a regulatory mechanism (Bosson et al., 2012).

The largest class of +TIPs are those containing an SxIP motif (Ser-x-Ile-Pro, where x represents any amino acid) (Honnappa et al., 2009). Included in this group is the tumour suppressor adenomatous polyposis coli (APC) and the kinesin-13 protein MCAK (Akhmanova and Steinmetz, 2010). These sequence motifs can bind directly to the EBH domain within EB proteins to indirectly interact with microtubules (Honnappa et al., 2009). Finally, +TIPs can also bind to microtubule plus ends via TOG (tumour overexpressed gene) or TOG-like domains, originally discovered within ch-TOG proteins. These are found within the family of rescue promoters CLASP (CLIP-associating protein), and the microtubule polymerase XMAP125/Dis1. XMAP125 contains 5 TOG repeats whereas CLASP only contains 1 TOG domain and 2 TOG-like domains (Slep, 2009) and therefore requires the addition of an SxIP motif for complete binding to microtubule tips (Akhmanova and Steinmetz, 2010).

Many +TIP proteins have a role in regulating microtubule dynamics due to their localisation at the lattice growing end. They consist of proteins which promote growth such as XMAP215 (Fox et al., 2014) and those which lead to depolymerisation and catastrophe such as MCAK and Kip3 (Peris et al., 2009; Gardner et al., 2013). Additionally, CLIP-170 and CLASP proteins promote rescue events, thereby reducing catastrophes and increasing microtubule stability (Dixit et al., 2009; Al-Bassam et al., 2010). +TIPs can also induce interactions between microtubule growing ends and other cellular structures. CLIP-170 and CLASP proteins localise to kinetochore microtubules to allow binding and stabilisation to the kinetochores of sister chromatids (Tanenbaum et al., 2006). Furthermore, +TIPS, CLIP-170 in particular, can recruit dynein to the plus ends (Nirschl et al., 2016) and assist with its cargo loading for transportation (Akhmanova and Steinmetz, 2010). EB1 also acts to associate microtubule plus tips with the ER Ca^{2+} sensor STIM1 (Friedman et al., 2010). EB1 can

restrict STIM1 from associating with ER-plasma membrane junctions, regulating the dynamic contacts between them and microtubules. This delay in STIM1 translocation contributes to regulation of Ca^{2+} by reducing excess influx (Chang et al., 2018). A final role for these proteins is their possible involvement in microtubule nucleation and anchoring as high levels of EB proteins have been observed within the centrosome (Louie et al., 2004).

1.1.10 The tubulin code

1.1.10.1 Microtubule isotypes

Despite microtubule's highly conserved and uniform structure, they are capable of performing a large range of physiological functions. As mentioned in section 1.1.2, there are 9 α-tubulin and 10 β-tubulin isotypes which can all be incorporated into microtubule lattices. Their presence was not fully confirmed until the determination of the α- and β-tubulin amino acid sequences in 1981 which highlighted the occurrence of heterogenous sequences (Ponstingl et al., 1981; Krauhs et al., 1981). Differential incorporation of these isotypes may contribute to their wide variety of functions. It was originally hypothesised that different tubulin isotypes must make up different microtubule structures such as those found within flagellar/cilia and in mitotic spindles (Greer and Shepherd, 1982), however research in *Drosophila* found the same β-tubulin isotype to be present across both differential structures (Kemphues et al., 1982). It was also shown that all isotypes contributed to microtubule formation in cultured mammalian cells (Lopata and Cleveland, 1987). There is however evidence to suggest that specific isotypes affect microtubule assembly properties: microtubules formed using only TUBB3 display faster polymerisation and depolymerisation in comparison to those formed with a homogenous mixture of TUBB2, TUBB3 and TUBB4. This therefore suggests that TUBB3 may be favourably incorporated into microtubule structures which require rapid remodelling (Tischfield and Engle, 2010). It is this incorporation bias that makes the use of cycles of polymerisation and depolymerisation in microtubule research questionable, possibly leading to incorrect conclusions (Souphron et al., 2019).

TUBB3 is a neuron-specific isotype (Latremoliere et al., 2018), thought to be involved in neuronal development as TUBB3 mutations lead to brain malformations in patients (Park et al., 2021). It has been shown to be differentially expressed during neuronal development, with high levels during outgrowth and reduced levels in mature neurons (Hausrat et al., 2021). Reduced TUBB3 expression levels have recently been shown

to decrease tubulin polyglutamylation modifications whilst also increasing the motility of the kinesin KIF5C. This study concluded that TUBB3 expression levels are sensitive to changes in neuronal activity (Radwitz et al., 2022). A further study recently reported that TUBB3 is not required for neuronal function but it is required to ensure proper axonal growth following injury (Latremoliere et al., 2018). Research is therefore still required to elucidate the functional roles of TUBB3 within neuron development.

1.1.10.2 Microtubule post-translational modifications

Tubulin proteins are highly decorated with post translational modifications (PTMs) (Figure 1.7). The histone code is a well-recognised model which describes how chromatin functions are regulated by the presence of multiple PTMs. For microtubules, this has therefore been termed the 'tubulin code' due to the observed parallels between chromatin and microtubules (Verhey and Gaertig, 2007). Identified modifications include: phosphorylation, acetylation, glutamylation, glycylation, ubiquitylation, sumoylation, methylation and palmitoylation (Yu et al., 2015; Liu et al., 2015), alongside the tubulin specific modification: detyrosination (section 1.1.10.3) (Nieuwenhuis and Brummelkamp, 2018). Most modifications exist on the C-terminus of both tubulin subunits on microtubule lattices, which are involved in interacting with microtubule-associated proteins (MAPs). Despite unique modifications being discovered many years ago, their complexity is only just being unravelled. It is hypothesised that PTMs regulate interactions with(MAPs. This in turn leads to changes in dynamics, contacts with other cellular components and the generation of polarity (Gadadhar et al., 2017a). Much work has been performed to unravel the specialised function of the tubulin code within neuronal cells (Moutin et al., 2020) however their roles within epithelial cells remains largely unresolved other than a specific role in mitosis. These modifications and their enzymes are illustrated in Figure 1.10.

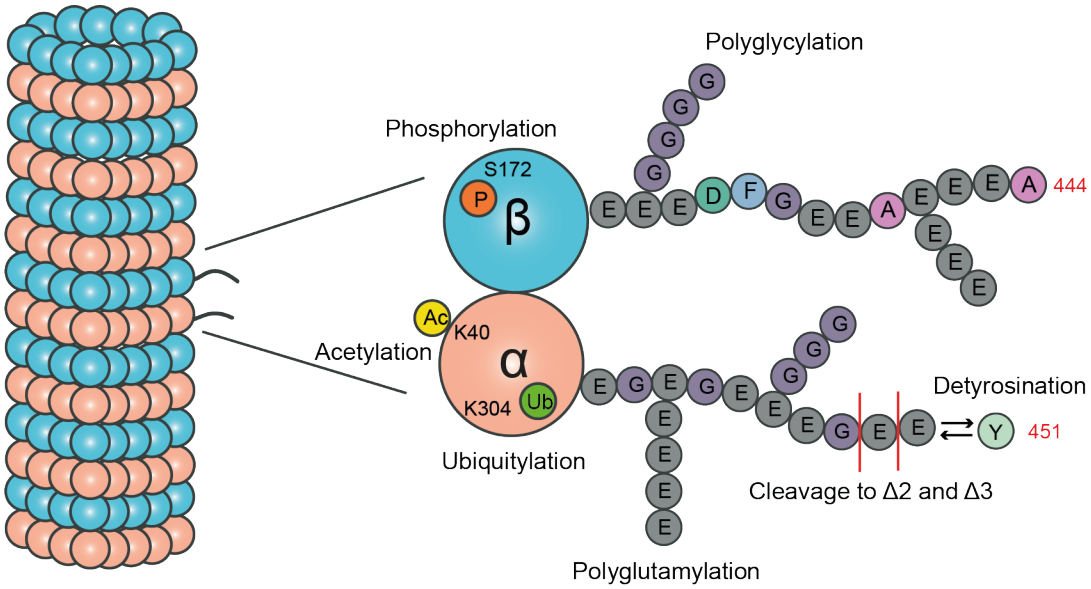

Figure 1.7 - Microtubule post-translational modifications

Modifications accumulate on microtubule structures and are highly concentrated on their C-terminal tails. Modifications consist of but are not limited to phosphorylation, polyglycylation, polyglutamylation, acetylation, ubiquitylation, and detyrosination. Adapted from Gadadhar et al., (2017).

1.1.10.3 Detyrosination

Detyrosination was the first tubulin PTM to be discovered almost 50 years ago when tyrosine addition to α-tubulin was observed following a general amino acid incorporation screen (Barra et al., 1974; Arce et al., 1975, 1978). Detyrosination is the reversible removal of the C-terminal tyrosine of α-tubulin. Once heterodimers are incorporated into the microtubule lattice, this terminal tyrosine is cleaved by carboxypeptidase enzymes, VASH1 and VASH2 (Vasohibins), in conjunction with the small vasohibin binding protein (SVBP) (Nieuwenhuis et al., 2017; Aillaud et al., 2017). It has recently been revealed that these two enzymes modify different tubulin subpopulations, with VASH1-SVBP driving global modifications and VASH2-SVBP driving local modifications, orchestrated by their different binding configurations. Short and frequent binding was seen for VASH1-SVBP across the network whereas longer less frequent binding was observed locally for VASH2-SVBP (Ramirez-Rios et al., 2023). MATCAP (microtubule associated tyrosine carboxypeptidase), was recently identified as a 3rd detyrosinating enzyme via a haploid genetic screen (Landskron et al., 2022). Tyrosine removal by these enzymes reveals a C-terminal glutamate residue which can either be cleaved again to produce irreversible Δ2 or tyrosine can be re-ligated by tubulin tyrosine ligase (TTL) (Wloga et al., 2017a). TTL functions

primarily on depolymerised tubulin dimers (Raybin and Flavin, 1977). Together, these 2 reactions form the detyrosination cycle (Nieuwenhuis et al., 2017; Aillaud et al., 2017). Most tubulin subunits are encoded with a C-terminal tyrosine with the exceptions of TUBA8 which has a phenylalanine and TUBA4A which completely omits this final residue. These isotypes however have the ability to be cleaved or have a tyrosine added to the C-terminal respectively, and can therefore both take part in the detyrosination cycle (Nieuwenhuis and Brummelkamp, 2018).

As mentioned previously, detyrosination is the only microtubule PTM specific to α-tubulin, highlighting its importance within the microtubule lattice. It was the research on detyrosinated microtubules by Gunderson and Bulinski that first provided the idea that PTMs are enriched on specific microtubule subsets rather than being scattered across the network in a random fashion (Gundersen and Bulinski, 1986; Gundersen et al., 1984). Detyrosination occurs on many different microtubule structures such as the cytoskeleton during interphase, on the mitotic spindle, at the centrosome and on primary cilium (Poole et al., 1997; Gundersen et al., 1984). Detyrosination is enriched on stable microtubules, with it being generally accepted that this is a consequence of their stability, rather than a causative effect, as it accumulates as the microtubules grow (Khawaja et al., 1988).

Functional relevance for detyrosination has been identified during mitosis (Barisic and Maiato, 2016; Ferreira et al., 2020). Within the mitotic spindle, astral microtubules are tyrosinated, whereas kinetochore microtubules are detyrosinated. This spatial organisation ensures that chromosomes are transported to the correct location during cell division. Dynein motor proteins capture the chromosomes and transport them to the spindle pole along tyrosinated astral microtubules. The kinesin-7 motor protein, CENP-E then takes over and transports the chromosomes to the cell equator via detyrosinated kinetochore microtubules. Both motor proteins therefore hold differential preferences and affinities to tyrosinated and detyrosinated microtubules to guide them and the chromosomes to the correct location. Perturbation of detyrosination levels resulted in disrupted chromosome congression (Barisic and Maiato, 2016). A second reported mechanism for detyrosination is during mitotic error correction. The kinesin-13 microtubule depolymerase MCAK displays a preference towards tyrosinated microtubules (Peris et al., 2009) and is inhibited on detyrosinated microtubules (Ferreira et al., 2020). Detyrosination accumulates on correct, stable microtubule-kinetochore attachments. These microtubules therefore do not require microtubule depolymerisation, allowing MCAK to move on to incorrect microtubule-

kinetochore attachments that require its error correcting activity (section 1.2.1) (Ferreira et al., 2020).

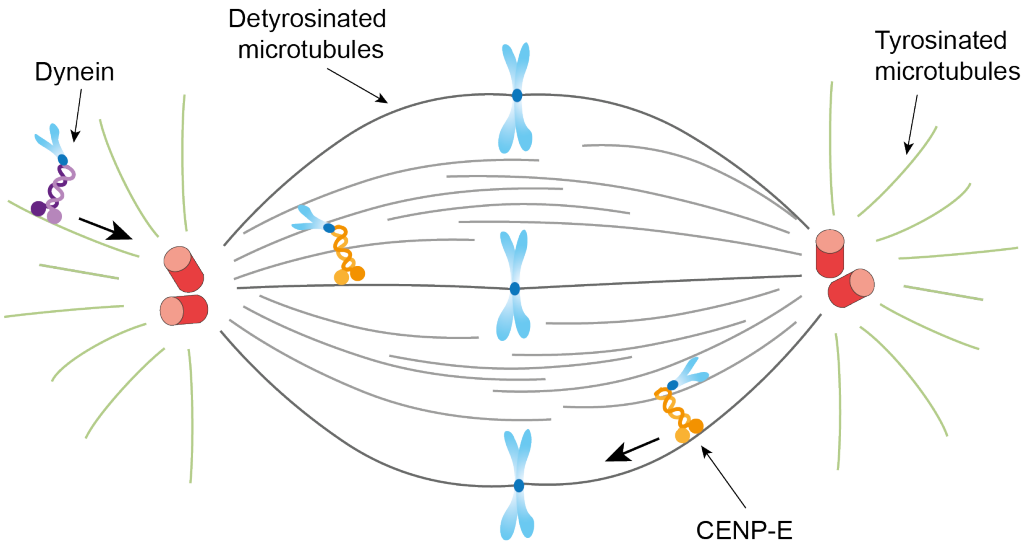

Figure 1.8 - Detyrosination controls chromosome transport during mitosis

Astral microtubules are tyrosinated (green) and dynein transports chromosomes along them towards the spindle pole. CENP-E then transports them along detyrosinated kinetochore microtubules (grey) to the cell equator before chromosome segregation (Barisic et al., 2015).

An additional function for detyrosinated microtubules is for the spatial concentration of lysosome and autophagosome interactions (Mohan et al., 2019). Lysosomes are transported along detyrosinated microtubules to autophagosomes during autophagy. A 3-fold increase in their presence has been observed on this particular microtubule subset, with their motility also being impaired in its absence. Furthermore, live cell imaging indicates that lysosome-autophagosome fusion occurs along these microtubules. This subset of microtubules therefore spatially confines lysosomes and their autophagy machinery to facilitate interactions. Lysosome transport was shown to be kinesin-1 dependent, with knockdown of this motor protein reducing autophagy occurrences (Mohan et al., 2019). Preference for kinesin-1 for detyrosinated microtubules has also been reported by multiple studies (Dunn et al., 2008; Liao and Gundersen, 1998; Lin et al., 2002; Verhey and Hammond, 2009).

1.1.10.4 Tyrosination

Alongside its role in providing directionality for CENP-E-dependent chromosome transport (Barisic et al., 2015), tyrosinated microtubules also display enhanced recruitment of +TIP proteins to the growing ends of microtubules. This spatial regulation from tyrosinated microtubules was first described in budding yeast when investigating the CLIP170 yeast ortholog, Bik1p, which was shown to have reduced interaction with plus tips in the presence of detyrosination (Badin-Larçon et al., 2004; Bieling et al., 2008). This specific recruitment was confirmed for other +TIPs including CLIP-115 and $p150^{Glued}$, which like CLIP-170 contain a CAP-Gly domain (Peris et al., 2006). To further support this conclusion, other +TIPs such as EB1, EB3 and CLASP which lack the CAP-Gly domain were insensitive to tubulin tyrosination status (Peris et al., 2006; Erck et al., 2005). Tyrosination and detyrosination therefore allow for spatiotemporal regulation of microtubules, which impacts their functions.

1.1.10.5 Δ2-tubulin

Upon producing detyrosinated tubulin, further cleavage of the penultimate glutamate residue of α-tubulin can result in the formation of Δ2-tubulin. This is an irreversible reaction catalysed by the deglutamylating enzyme cytoplasmic carboxypeptidase 1 enzyme (CCP1), detailed below in section 1.1.10.7. (Rogowski et al., 2010). This modification was discovered in 1991 when it was found that brain tubulin protein could not be re-ligated with tyrosine (Paturle-Lafanechère et al., 1991). Its irreversibility has been attributed to structural constraints within the TTL enzyme which re-ligates tyrosine. For re-ligation of detyrosinated tubulin, hydrogen bonds form between the penultimate glutamine of α-tubulin and residues within the active site of TTL, required for complete enzymatic activity. As this glutamine is absent, the C-terminal tail cannot reach the active site properly, preventing tyrosine addition (Prota et al., 2013). Δ2-tubulin accumulates on known stable microtubule structures such as cilia, flagellar and those within neurons, making it a marker of very long-lived microtubules. Furthermore, it has been suggested that these sequential modifications may act as a grading system for microtubule maturation, with tyrosinated being immature, detyrosinated being mature, and Δ2-tubulin showing full maturation (Paturle-Lafanechère et al., 1994). No specific functional role has reported for this irreversible modification (Peris et al., 2022).

1.1.10.6 Acetylation

Acetylation is the process by which an acetyl group is reversibly added to the ε-amino group of a conserved lysine residue (Howes et al., 2014; Jenkins et al., 2017). It is a well-recognised PTM and is frequently involved in protein cellular activities and functional regulation (Liu et al., 2015). Acetylation of lysine 40 of the α-tubulin subunit (K40) was the second microtubule PTM to be discovered (L'Hernault and Rosenbaum, 1985, 1983; LeDizet and Piperno, 1987). This modification is unique as it is located within the microtubule luminal interface as opposed to the outer lattice surface (Fernández-Barrera and Alonso, 2018). This modification is added by α-tubulin N-acetyltransferase 1 (αTAT1) (Akella et al., 2010; Shida et al., 2010) and removed by the deacetylases histone deacetylase class II enzyme (HDAC6) and sirtuin-2 (SIRT2) (Hubbert et al., 2002; North et al., 2003). αTAT1 is thought to gain access to the microtubule lumen via the microtubule ends and diffuses down the lumen, scanning the subunits for acetylation sites (Kull and Sloboda, 2014). A second model suggests that αTAT1 accesses the lumen via bends and breaks within the microtubule lattice (Coombes et al., 2016). It is likely that access occurs via a combination of these methods (Janke and Montagnac, 2017).

K40 acetylation accumulates on stable microtubules, and it was originally under debate as to whether it causes stabilisation or whether it is purely a marker of stability (Jenkins et al., 2017; Perdiz et al., 2011; Wloga et al., 2017a). The idea that it was just a consequence of microtubule stability was originally the front runner based on the fact that drug-induced stabilisation causes acetylation accumulation, whereas increasing acetylation levels did not appear to alter the stability (Palazzo et al., 2003). Furthermore, initial investigations concluded there were no differences in the protofilament structure (Howes et al., 2014). However, it is now accepted that K40 acetylation protects microtubules from mechanical ageing by weakening the inter-protofilament interactions, allowing for enhanced flexibility and resilience against mechanical stress (Xu et al., 2017; Portran et al., 2017). More recent structural analysis revealed that K40 acetylation induces a conformational change in the unstructured M-loop it resides in. This in turn reduces protofilament interactions, increases microtubule flexibility and causes mechanical resistance (Eshun-Wilson et al., 2019). Acetylation is found in greater numbers at curved regions where breakages in the lattice can occur (Xu et al., 2017) suggesting that αTAT1 can enter at these points, locally acetylate α-tubulin subunits and allow lattice repair, illustrated in Figure 1.9 (Schaedel et al., 2015; Janke and Montagnac, 2017).

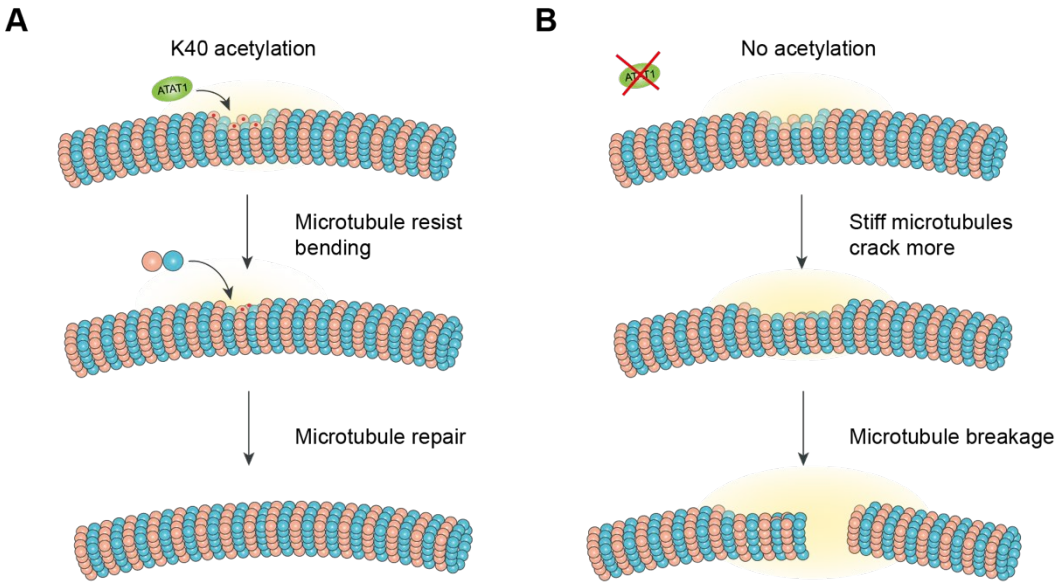

Figure 1.9 – Microtubule acetylation prevents mechanical breakage

When microtubules are bent, they are exposed to mechanical stress which can create cracks in the lattice. **A.** The ATAT1 enzyme can enter the microtubule lumen by these breaks and locally acetylate the α-tubulin subunits. This increases the microtubule flexibility and prevents further breakage and allow for self-repair by the addition of new tubulin dimers. **B.** In the absence of ATAT1, acetylation does not occur, and microtubules are still exposed to mechanical stress. Cracks get larger and eventually the microtubule snaps, leading to complete depolymerisation. Adapted from Janke and Montagnac (2017).

Multiple suggestions that microtubule K40 acetylation affects the binding of MAPs, motor proteins and other microtubule-binding proteins have also been put forward. Kinesin-1 binding and transport was proposed to be increased by acetylation (Reed et al., 2006). Clear colocalisation of acetylated microtubules and kinesin-1 was observed in rat primary hippocampal neurons which guides the motor out of the dendrites and into the axons (Tas et al., 2017). Other investigations however have concluded that acetylation alone does not increase motor processivity but it may do so in combination with other factors such as by inducing microtubule bundling (Balabanian et al., 2017; Kaul et al., 2014; Walter et al., 2012). Other functions have been suggested for K40 acetylation such as: the interaction and inhibition of membrane ATPases (Arce et al., 2008); interaction with HSP90 in macrophages for enhanced recruitment of Akt/PKB and p53 signalling (Giustiniani et al., 2009); and in touch sensation in mice (Morley et al., 2016) and *C. elegans* (Shida et al., 2010).

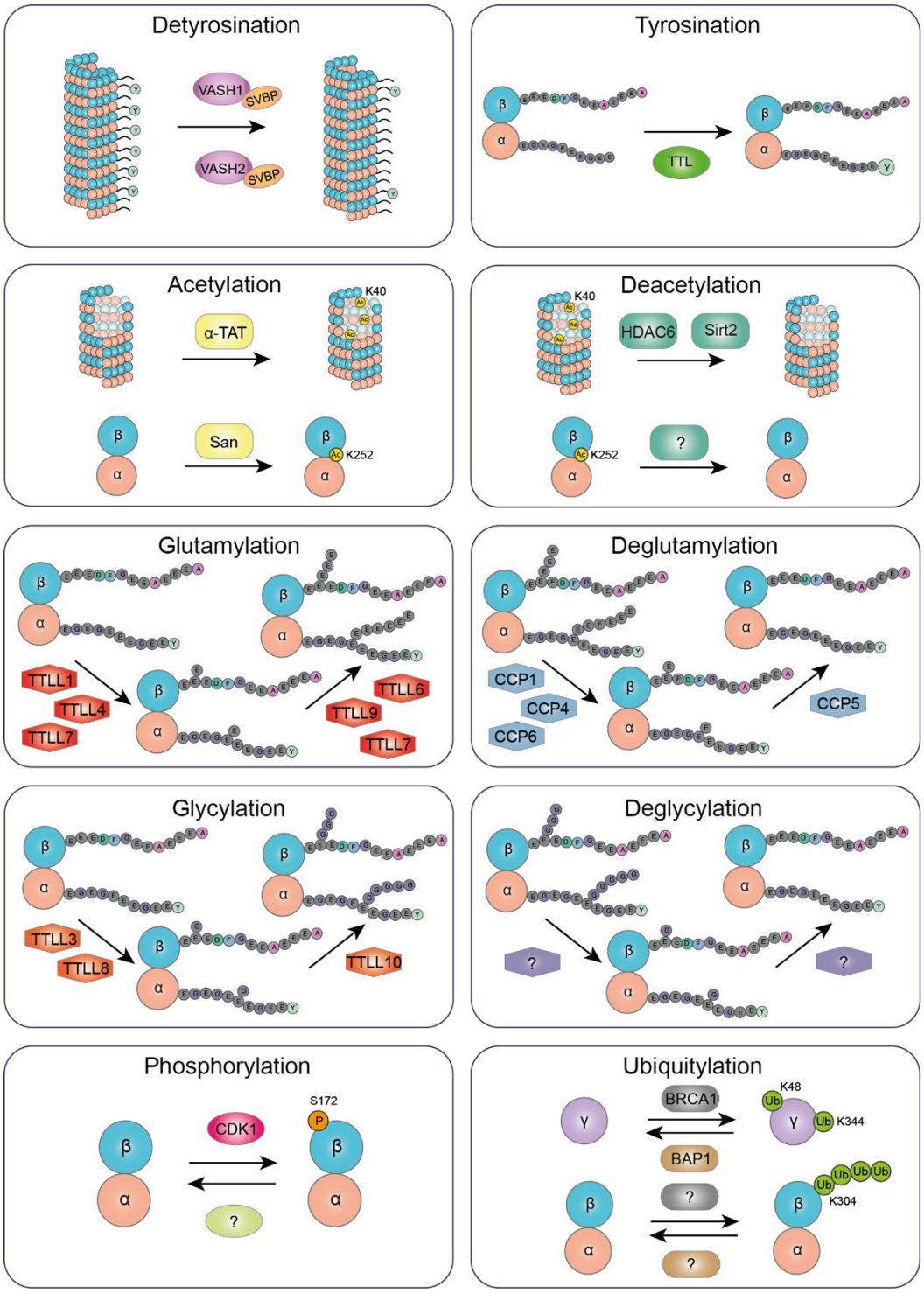

Figure 1.10 - Tubulin modifications and responsible enzymes

Schematic diagram of specific examples of the many modifications that occur on both tubulin subunits and microtubule polymers and their responsible enzymes where known.

Additional acetylation sites have been reported on both tubulin subunits however their importance and functional relevance are yet to explored due to most sites not being conserved (Liu et al., 2015; Howes et al., 2014). One site on the β-tubulin subunit that has been investigated further is the acetylation of position K252. This acetyl addition performed by San acetyltransferase occurs within the globular domain between the α/β-tubulin dimer interface, on soluble tubulin heterodimers. This PTM neutralises the positive charge of the lysine residue and also interacts with the α-tubulin GTP phosphate group, inducing a conformational change which impedes dimer association, regulating the polymerisation kinetics (Chu et al., 2011).

1.1.10.7 Glutamylation and glycylation

Tubulin glutamylation and glycylation is the addition of glutamyl or glycyl groups, respectively, to the γ-carboxyl group of glutamate residues present within the C-terminal tails of both α- and β-tubulin via an isopeptide bond (Gadadhar et al., 2017a). Both tubulin monomers have multiple glutamate residues within these tails, thereby allowing various docking sites for these modifications. These modifications were first discovered in the early 90's and were originally thought to be a tubulin-specific modification, however they have now been identified on other proteins as well (Gadadhar et al., 2017a; Eddé et al., 1990; Redeker et al., 1994). Subsequent addition of multiple glutamyl/glycyl groups produces polyglutamylated or polyglycylated chains, with different chain lengths thought to induce different protein-protein interactions. The enzymes that catalyse these reactions are similar to tubulin tyrosine ligase (TTL), due to them possessing a TTL domain, and are therefore named TTL-like (TTLL) proteins (Janke et al., 2005). Unlike for detyrosination, there are multiple TTLL proteins expressed which can add glutamyl or glycyl groups onto tubulin tails. Each display a preference for either α- or β- tubulin (Janke et al., 2005), with some initiating the first group addition whilst others elongate the chain. In mammalian cells, TTLL1, and 4 initiate glutamylation whereas TTLL6 and 9 display elongation activities (Wloga et al., 2008, 2017a). TTLL7 can initiate and elongate glutamylation chains on β-tubulin tails (Mukai et al., 2009). For glycylation, TTLL3 and 8 initiate chain formation, whereas TTLL10 can elongate them in most mammalian cells (Rogowski et al., 2009; Ikegami and Setou, 2009; Wloga et al., 2009). In humans however, the expressed TTLL10 contains an inhibitory mutation, meaning side chains are limited to monoglycylation (Rogowski et al., 2009). The addition of these side chains is reversible, and their removal can be catalysed by cytoplasmic carboxypeptidases (CCP) called tubulin deglutamylases/deglycylases. Enzymes catalysing

deglutamylation have been discovered: CCP1, 4 and 6 function to shorten the polyglutamyl chains, whereas CCP5 removes the final group from the branch point. The deglycylation enzymes are yet to be identified (Magiera et al., 2018).

Glutamylation is a relatively uncommon tubulin PTM, only appearing on specific microtubule subsets such as axonemes, centrioles and within neuronal cells (Bobinnec et al., 1998; Rogowski et al., 2010; Wloga et al., 2008). Its presence has been correlated with regulating microtubule stability and network density by influencing microtubule severing proteins spastin (Lacroix et al., 2010) and katanin (Szczesna et al., 2022; Genova et al., 2023). Glutamate chain lengths provide a graded regulation of this severing promotion (Figure 1.11): as chain length increases, spastin severing activity also increases up until 6 glutamate residues where an inhibitory effect on spastin is observed (Valenstein and Roll-Mecak, 2016). Polyglutamylation is observed within the mitotic spindle (Bobinnec et al., 1998) and may regulate spindle length by altering severing activity (Janke and Bulinski, 2011). A second function has been proposed in cilia and flagellar motility and structure. A loss off TTLL6 function causes reduced cilia movement (Linck et al., 2014) whilst overexpression has been correlated with cilia shortening (Wloga et al., 2017b). Fine tuning of glutamylation is therefore required for normal axoneme function. Finally, polyglutamylation has been correlated with increased velocity and processivity of kinesin-2 *in vitro,* with increased chain lengths causing further enhanced transport (Sirajuddin et al., 2014).

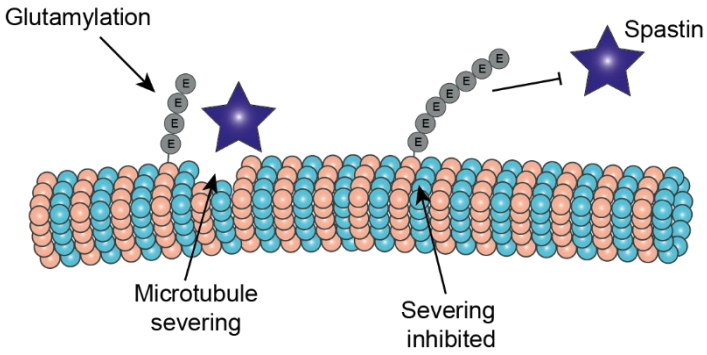

Figure 1.11 - Glutamylation affects spastin severing activity

Glutamylation leads to increased levels of spastin-dependent microtubule severing. As chain length increases, spastin activity increases. When chain length exceeds 6 glutamate resides then spastin is inhibited giving a graded regulatory mechanism.

Glycylation has only been observed on outer doublet microtubules of axoneme structures (Wloga et al., 2009). Glycylation levels regulate the overall length of the primary cilia, and any deviations in these modifications causes length alterations (Gadadhar et al., 2017b). Loss of TTLL3 reduces cilia formation within Zebrafish and affects axoneme length and structure in Tetrahymena. Interestingly, glycylation is predominantly found on the outer doublets however it is the central microtubules which displayed assembly defects, suggesting cilia formation is dependent on contributions from the outside doublets in a glycylation-dependent manner (Wloga et al., 2009). Increased glutamylation and decreased glycylation therefore both lead to cilia shortening, suggesting there is some competition but also cooperation between these modifications (Wloga et al., 2017b; Rogowski et al., 2010; Kimura et al., 2010).

1.1.10.8 Other tubulin modifications

Other common modifications have been identified on tubulin subunits such as phosphorylation, ubiquitylation, palmitoylation and SUMOylation however their functional roles remain largely unknown (Janke and Bulinski, 2011). The most well characterised instance of tubulin phosphorylation occurs at the conserved site of Ser172 on the β-tubulin subunit by cyclin-dependent kinase 1 (CDK1) (Fourest-Lieuvin et al., 2006). Phosphorylation is added onto free tubulin subunits as opposed to tubulin dimers within the microtubule lattice (Wloga et al., 2010). This residue is located near the GTP-binding pocket (Ramkumar et al., 2018) and may cause disruptions with GTP-binding and the interactions with other tubulin dimers, thereby preventing its incorporation into microtubule structures. These modified tubulin subunits are found within the soluble fraction during mitosis, indicating that CDK1 may regulate microtubule dynamics during cell division (Fourest-Lieuvin et al., 2006). Other phosphorylation sites have been reported such as S444 and Ser446 within the β-tubulin C-terminal tail, however their functional relevance remains unexplored (Liu et al., 2015; Ramkumar et al., 2018).

Ubiquitylation has also been observed on both α- and β- tubulin subunits (Liu et al., 2015). Ubiquitylation of α-tubulin has been connected to cilia disassembly, with ubiquitylation levels increasing as disassembly occurs. Lysine 304 becomes decorated with K63 polyubiquitin chains, which is thought to alter the lattice structure and initiate axoneme disassembly (Wang et al., 2019b). As multiple sites for each of these modifications have been observed, it seems likely that their functional significance is greater than what is currently reported (Liu et al., 2015). Additionally,

γ-tubulin is ubiquitylated by the E3 ubiquitin ligase BRCA1 and is required for centrosome regulation. Knockdown of BRCA1 leads to a hyperactivity at the centrosome, leading to centrosome amplification, increased nucleation events and larger aster formations. γ-tubulin ubiquitylation therefore prevents microtubule nucleation (Sankaran et al., 2006; Starita et al., 2004).

1.1.10.9 Neurons and the tubulin code

Microtubule function is critical within neuronal architecture and development as they make up the structural component of the axon and facilitate cargo transport. In neurons anterograde transport is required for transporting lipids and proteins to the distal axons whereas retrograde transport facilitates the removal of organelles and aged proteins from the distal regions for their recycling and degradation. Defects on cargo transport have been associated with neurodegenerative and neurodevelopmental diseases (Maday et al., 2014).

The tubulin code plays a role in regulating neuronal development and function. During the early stages of development, microtubules are mixed-polarity and mainly tyrosinated, with detyrosination found in the inner neurites. The axon is then highly enriched in both detyrosinated and Δ2 microtubules. In mature neurons dendrites are composed of tyrosinated microtubules at their distal locations whereas detyrosinated and Δ2 microtubules are found at their inner regions. This balance between tyrosinated and detyrosinated microtubules is crucial for vesicular trafficking down the axon (Nirschl et al., 2016). Alterations into the tyrosination-detyrosination cycle have also been associated with differential defects (Moutin et al., 2020). Most research has been performed using neurons derived from knockout (KO) mouse models. Mice which are null for the TTL enzyme are seen to die shortly after birth. Hippocampal neurons derived from these mice display significantly high levels of detyrosinated microtubules which have a disordered microtubule network and undergo premature differentiation (Erck et al., 2005). Another study showed that in comparison, SVBP KO mice hippocampal neurons display high levels of tyrosinated tubulin and low detyrosinated tubulin, with modification levels increasing as the neurons mature. This suggests another enzyme may be responsible for detyrosination but not until the later stages of development. These KO mouse derived neurons displayed much shorter or even absent axons and increased branching (Pagnamenta et al., 2019). Another study reported that in mouse hippocampal neurons, depletion of SVBP reduced axon development, and those which overexpressed SVBP had large and even multiple

axons, further supporting the role for detyrosination in neuronal development (Wang et al., 2019a).

1.2 Mitosis

1.2.1 Microtubules and the mitotic spindle

Microtubules play a crucial role within one of the most important mechanisms to occur within a cell's lifecycle: mitosis. They are the structures, along with 1000's of other proteins, that form the mitotic spindle required for aligning and segregating chromosomes to ensure successful division. Although a lot of the mechanisms regarding this process have been identified, there are still gaps within the literature. The main reasons for this are due to the large number of microtubules involved in the mitotic spindle, the density of the network, and its dynamic nature: microtubules are able to assemble and disassemble completely within an hour (Petry, 2016). Microtubules involved in spindle formation are illustrated in Figure 1.12, and their half-lives are detailed in Table 1.3.

Table 1.3 - Half-lives of different microtubules during different cell states

Type of microtubule	Half-life (min)			
	Interphase	Prometaphase	Metaphase	Anaphase
Cytoskeletal	10	/	/	/
Astral	10	0.3	0.9	0.9
Interpolar	/	0.3	0.9	0.9
Kinetochore	/	3	7.1	37.5
Axonal	130	/	/	/

The overall structure of the mitotic spindle has been well defined. It consists of 2 centrosomes at opposite ends of the structures, known as the spindle poles, which are formed from the duplication of the centrosome during S-phase. These centrosomes are the origin for the majority of microtubule structures present within the mitotic spindle (Fu et al., 2015). During prophase, the microtubule network present during interphase is rapidly replaced with more dynamic microtubules. Astral microtubules are initially nucleated, which are then transported to opposite sides of the nucleus to separate the centrosomes. This action is facilitated by dynein motor proteins, using the nuclear envelope to guide them. The astral microtubules can then attach the spindle poles to the cell cortex via the dynein-dynactin complex, allowing for further centrosome separation and spindle organisation (Markus and Lee, 2011).

This attachment also functions to orientate the spindle axis to ensure successful chromosome separation and cell division (Rosenblatt, 2005). The kinesin-5 family member Eg5/Kif11 also functions within this process of spindle formation by inducing microtubule sliding between anti-parallel interpolar microtubules, pushing them apart to induce spindle pole separation (Kapitein et al., 2005).

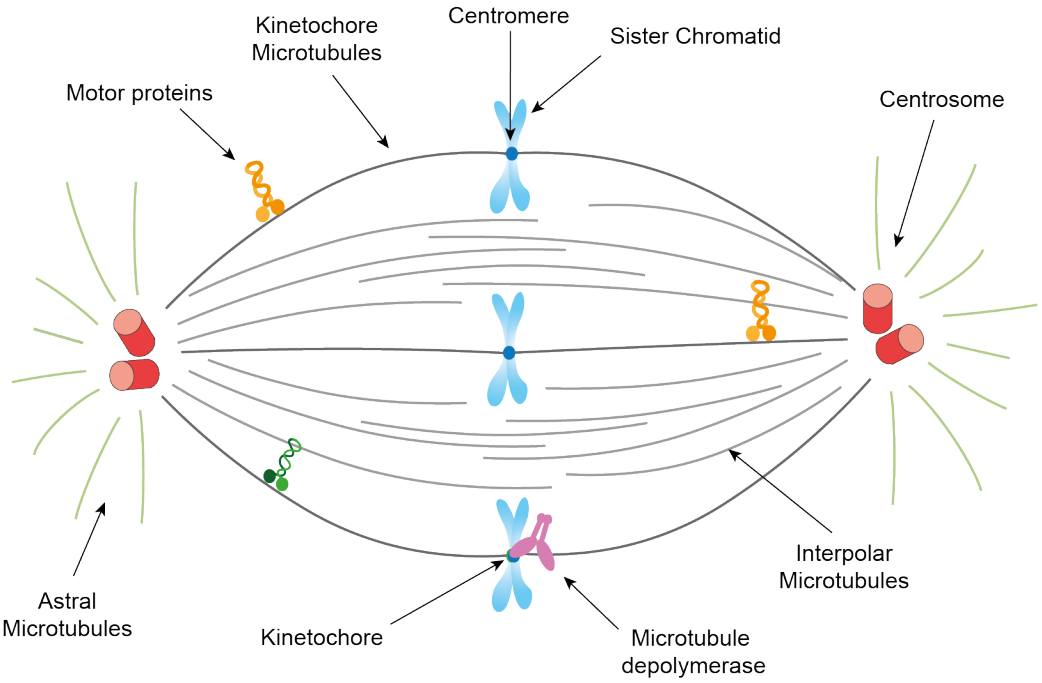

Figure 1.12 - Structure of the mitotic spindle

The mitotic spindle is generally nucleated from the duplicated centrosomes positioned either side at the spindle poles. Spindle orientation is controlled by the astral microtubules. Kinetochore microtubules extend from the centrosomes to 'search-and-capture' the sister chromatids and associate with kinetochores bound to the centromere. Interpolar microtubules occurring from the centrosomes and via microtubule-dependent nucleation maintain the bipolarity of the structure. Motor proteins are present along microtubules to maintain the structure and guide chromosomes to the correct location. Microtubule depolymerising proteins act to facilitate chromosome segregation.

Once the spindle poles are in place, kinetochore microtubules can be nucleated to form the bulk of the mitotic spindle. These originate from the centrosomes and grow from their plus ends into the centre of the spindle to search for and capture the chromosomes (Kirschner and Mitchison, 1986; Heald and Khodjakov, 2015). They bind to the chromosomes via a complex of proteins which associate at their

centromeres, termed kinetochores. Microtubules associate with kinetochores via their plus ends or laterally, with around 20 microtubules thought to associate with each in humans (Biggins and Walczak, 2003). This group of bundled kinetochore microtubules are termed K-fibres and are the most stable form of microtubules within the spindle structure with a half-life of 4-8 minutes (Zhai et al., 1995; Meunier and Vernos, 2012). Ran-GTP is present in high levels on these kinetochore structures which induces the association of microtubule-stabilising factors to these kinetochore microtubules, biasing their growth towards them and facilitating the search-and-capture model (Meunier and Vernos, 2012; Caudron et al., 2005). In addition to the kinetochore microtubules, interpolar microtubules are also present. These microtubules extend from each centrosome towards the opposite pole and interact with each other in the centre in an anti-parallel manner. Their main function is to maintain the spindle bipolarity. These microtubules are the most dynamic within the spindle with a half-life of 30 seconds to 1 minute (Zhai et al., 1995; Meunier and Vernos, 2012).

Once end-on attachments to kinetochores are formed, microtubule binding proteins stabilise these interactions to prevent catastrophe and ensure prolonged attachment to the sister chromatids. If merotelic attachment occurs (where a single kinetochore is bound to K fibres from both spindle poles) MCAK proteins can initiate slight microtubule depolymerisation to allow them to unbind and rebind to the correct kinetochore, preventing mitotic errors (Ferreira et al., 2020). Microtubule binding proteins then function to transport the chromosomes to the metaphase plate ready for segregation (Monda and Cheeseman, 2018). To further increase the density of microtubules within the mitotic spindle, microtubule-dependent nucleation (described in section 1.1.7) also occurs here, and is thought to explain the rapid formation of the spindle structure, whilst maintaining the overall bipolarity (Petry et al., 2013; Goshima et al., 2008). Once the chromosomes are aligned at the metaphase plate and correctly attached, sister chromatids are segregated to opposite poles of the cell. Dynein-dynactin motor proteins bind to the kinetochore after microtubule attachment and are able to facilitate the transport of chromosomes down these kinetochore microtubules towards their minus ends at either pole (Sharp et al., 2000). The pull on the sister chromatids causes tension on the centromere and eventually separates the sister chromatids. This action is further facilitated by simultaneous microtubule shortening. Kinesin-13 family proteins, such as KLP59C and KLP10A in Drosophila, initiate microtubule depolymerisation from the plus and minus ends respectively in a ‘poleward flux’ model to assist with chromatid sister separation (Rogers et al., 2004;

Mitchison, 1989; Peris et al., 2009). In addition, spindle elongation occurs to pull the chromosomes apart (Brust-Mascher and Scholey, 2011).

Microtubule dynamics play an important role within both the formation and the function of the mitotic spindle. Microtubules have to be rapidly depleted and formed to allow for complete reorganisation from the normal interphase microtubule network to create the highly structured spindle during mitosis. Dynamic instability is required in mitosis to regulate the number of microtubules present, their different lengths throughout the structure, the positioning of the spindle poles and the chromosomes, and their overall segregation to either side of the cell. Due to the vast number of overlapping microtubules present within the spindle structure, determining their individual dynamics is difficult (Petry, 2016). The importance of dynamics here is highlighted by the implications seen when microtubule drugs are applied. Microtubule depolymerisation drugs such as vinblastine and nocodazole (section 1.1.5) induce mitotic arrest when supplied in low doses by inhibiting the spindle dynamics (Jordan et al., 1992). It is thought that reduced dynamics can prevent microtubules from associating with kinetochores, hence preventing completion of the spindle assembly checkpoint, and halting mitosis (Wendell et al., 1993).

1.2.2 Mitotic regulation and the spindle assembly checkpoint

Mitosis can be separated into 6 different stages which include: prophase where the nuclear envelope begins to break down and the chromosomes start to condense; prometaphase where the microtubules reorganise themselves to attach to the kinetochores of chromosomes; metaphase where the mitotic spindle is fully formed and the connections between the microtubules and the chromosome kinetochores are correct and stable; anaphase where the microtubules separate the sister chromatids by pulling them to opposite spindle poles of the cell; telophase where the chromosomes begin to decondense and the nuclear envelope starts to reform; and finally cytokinesis which is the complete division of the cytoplasm, resulting in 2 separate daughter cells. All these different stages are tightly regulated and are distinct from each other based on the proteins that are expressed and activated during each stage (Schmit and Ahmad, 2007).

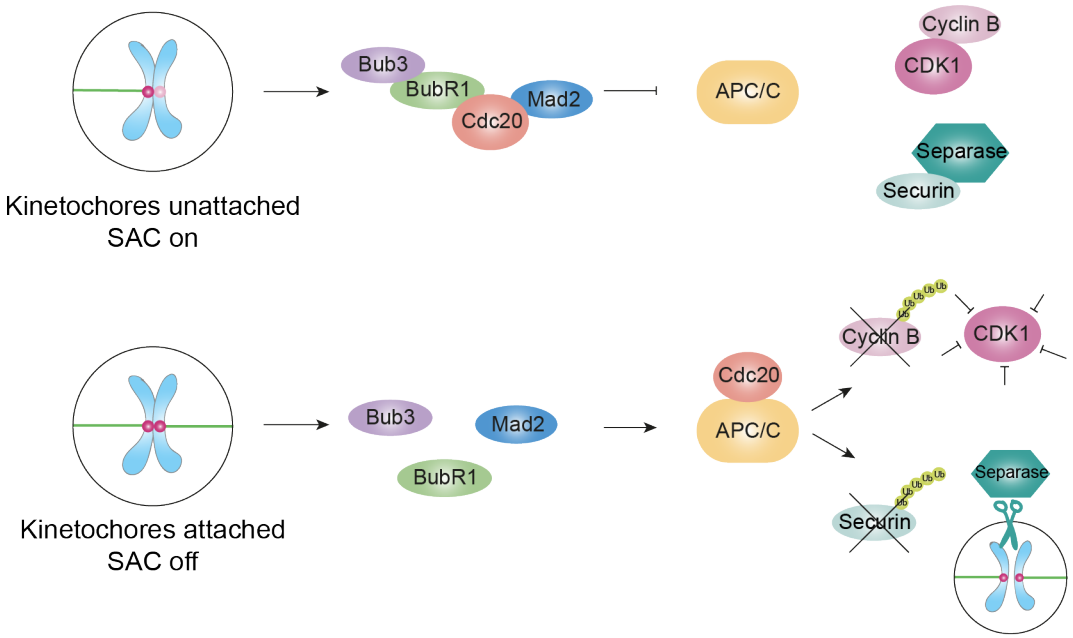

Figure 1.13 – The SAC is regulated by kinetochore attachments

The spindle assembly checkpoint acts as a safeguard between metaphase and anaphase. When kinetochores are not attached to microtubules the SAC is turned on and the mitotic checkpoint complex containing Bub2, BubRI, Mad2 and CDC20 is formed. The APC/C E3 ligase is inactive and CDK1 activity remains high and separase is inhibited by securin binding. When all kinetochores are attached the SAC is turned off and the mitotic checkpoint complex is abolished. This allows CDC20 to associate with and activate the APC/C, leading the degradation of both cyclin B and securin which inactivates CDK1 and activates separase respectively. Anaphase onset can now commence.

The spindle assembly checkpoint (SAC) is a highly regulated safety device which maintains genomic stability during cell division (Figure 1.13). This checkpoint occurs between metaphase and anaphase onset and monitors the attachments of microtubules to kinetochores, ensuring chromosome segregation only occurs when all kinetochores are correctly attached (Lara-Gonzalez et al., 2021). The anaphase-promoting complex/cyclosome (APC/C) is an E3 ligase enzyme which controls the transition from metaphase into anaphase onset (Watson et al., 2019). When the SAC is switched on and kinetochores are not all attached, the mitotic checkpoint complex (MCC) is formed. This is a tetrameric complex consisting of the kinetochore proteins Mad2, BubRI and Bub3, and the APC/C activator Cdc20 (Liu and Zhang, 2016). This sequestration of Cdc20 leads to APC/C inhibition and prevents anaphase onset (Watson et al., 2019). When kinetochores are all fully attached and the SAC has been satisfied however, Cdc20 is released from the MCC due to disassembly of the

complex and inhibition of *de novo* MCC formation (Liu and Zhang, 2016). Active APC/C-Cdc20 can then facilitate the ubiquitination and degradation of two key substrates, cyclin B and securin. Cyclin B degradation causes inactivation of the main mitotic kinase, CDK1, allowing inactivation of early mitotic proteins (Peters, 2006). The degradation of securin allows for the cleavage and activation of separase, which can in turn go on to cleave cohesin which holds the sister chromatids together, allowing them to segregate and be pulled to opposite poles (Waizenegger et al., 2002). Satisfaction of the SAC and subsequent activation of the APC/C therefore leads to anaphase onset via a tightly regulated mechanism (Lara-Gonzalez et al., 2021).

1.2.3 Mitotic kinases

Phosphorylation is a key regulator of mitotic entry and progression, controlling both activation and/or localisation of a large number of proteins. There are various kinases known to function within mitosis including the cyclin-dependent kinases, Polo kinases and aurora kinases. They are all tightly regulated via spatiotemporal mechanisms to allow for precise chromosome segregation (Nigg, 2001). Cyclin-dependent kinases (CDK) are a family of kinases which phosphorylate serine/threonine residues on their substrates and are each activated at specific timings throughout the cell cycle via their interactions with different cyclins and are inactivated by CDK inhibitors. CDK1 is known as the major mitotic kinase and promotes entry into mitosis. It is first activated in G2 phase by cyclin A association, and its activity is maintained by cyclin B in the initial stages of mitosis until it is inactivated at anaphase onset due to cyclin B degradation. CDK1 phosphorylation events lead to nuclear envelop breakdown, chromosome condensation, kinetochore function and the formation of the mitotic spindle (Ding et al., 2020). Polo-like kinases (PLK) are another family of serine/threonine kinase which also regulate different aspects of the cell cycle. PLK1 is the family member which acts during mitosis. It is required to stabilise kinetochore-microtubule attachments by phosphorylating kinetochore proteins involved in the spindle assembly checkpoint (SAC) such as Mad3 and BubR1 (Elowe et al., 2007). It is also required in mitotic exit and cytokinesis where it phosphorylates motor proteins MKLP2 and RacGAP1 which are crucial for the correct position of the chromosomal passenger complex for cytokinesis initiation (Neef et al., 2003; Adriaans et al., 2019), and for cleavage furrow formation, respectively (Zitouni et al., 2014). Aurora kinases make up a 3rd family of serine/threonine kinases which are also involved in mitotic entry and progression. This family consists of 3 members: aurora kinase A, B and C.

Aurora A and B both play a role within mitosis, whereas aurora C is restricted to meiosis within germ cells. Aurora B comes together with INCENP, Borealin and Survivin to make the chromosomal passenger complex, which is a core mitotic regulator further described within the next section (Willems et al., 2018). Kinase activity is therefore tightly regulated throughout the whole of the cell cycle to ensure events occur at the correct time (Nigg, 2001).

1.2.4 The chromosomal passenger complex

The chromosomal passenger complex (CPC) is a key regulator of mitosis. It is a heterotetrametric complex which consists of 4 proteins. The inner centromere protein (INCENP) is the scaffold protein that holds the complex together, aurora B provides the catalytic activity and survivin and borealin/DasraB are the targeting proteins (Carmena et al., 2012). INCENP was the first CPC protein to be identified and was shown to reside at the inner centromeres in early mitosis before transitioning to the spindle midzone and midbody in late mitosis (Cooke et al., 1987). Its association with the aurora B kinase was then later identified in *Xenopus* eggs (Adams et al., 2000) and *C. elegans* (Kaitna et al., 2000) and was shown to be evolutionary conserved and hence biologically relevant (Adams et al., 2000). Shortly after, the presence of both survivin (Carvalho et al., 2003) and borealin (Gassmann et al., 2004) within this complex were also identified. These 2 subunits come together to form a 3-helix bundle via the N-terminal region of INCENP which is required for regulating the activity and localisation of the aurora B kinase component (Jeyaprakash et al., 2007).

This complex is required at multiple locations at specific times throughout cellular mitosis to ensure precise regulation of chromosome segregation and cytokinesis, illustrated in Figure 1.14 (Carmena et al., 2012). It localises to the centromeres during the early stages of mitosis, promoted by the K63 ubiquitination of survivin by the E3 ligase Ufd1 (Vong et al., 2005). Once the SAC has been satisfied, the CPC is translocated to the central spindle midzone during anaphase onset. This relocalisation is facilitated by the deubiquitylation of survivin by USP9X (Vong et al., 2005), and the ubiquitylation of aurora B by the cullin 3 (CUL3) E3 ubiquitin ligase complexes CUL3-KLHL9-KLHL13 and CUL3-KLHL21, initiating its release from the centromeres (Sumara et al., 2007; Maerki et al., 2009). The CPC is then transported to the central spindle via the motor protein, MKLP2 (Gruneberg et al., 2004), and eventually to the cleavage furrow during late mitosis (Adams et al., 2000; Jeyaprakash et al., 2007). This localisation regulation adds an extra layer of complexity to controlling the CPC

activity, ensuring that events occur within a spatiotemporal manner (Carmena et al., 2012; Aleem et al., 2015).

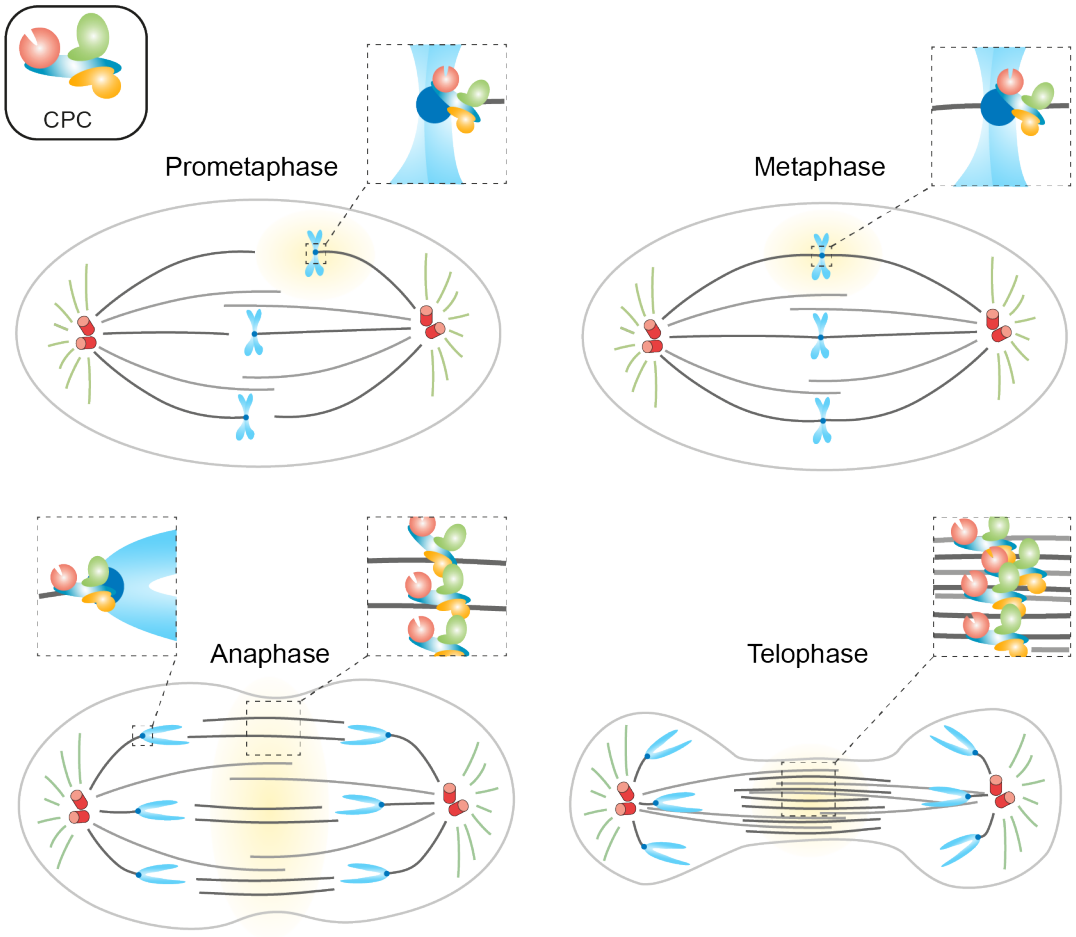

Figure 1.14 – The CPC is regulated in a spatiotemporal manner during mitosis

The CPC is formed from INCENP (blue), aurora B (red), borealin (green) and survivn (yellow). The localisation of the CPC is regulated throughout mitosis to ensure that it can carry out the correct function at the correct time. During prometaphase it localises to the centromeres of the chromosomes being transported to the cell equator. At metaphase it is found at the centromeres. During anaphase onset it transitions from the centromeres to the spindle midzone. Then finally during telophase it is present at the midzone within the cleavage furrow.

Aurora B is one of the most highly studied serine/threonine kinases and is a master regulator of mitotic progression (Carmena et al., 2009). Its activation occurs in a complex, multistep process, first initiated by its association with INCENP (Honda et al., 2003). This in turn initiates the phosphorylation of both INCENP and the T-loop within aurora B, leading to its full activation (Bishop and Schuniacher, 2002). Upon

activation of aurora B, the functions of the CPC can be performed. In early mitosis, one of the major roles of aurora B is the regulation of kinetochore-microtubule attachments by phosphorylating multiple kinetochore proteins prior to formation of correct attachments (Welburn et al., 2010). These include components of the KNL1, Mis12 and NDC80 complexes which are key microtubule-binding proteins of the kinetochore (Petrovic et al., 2016). Aurora B activity also promotes disruption of incorrect microtubule-kinetochore attachments until correct and stable ones have been formed (Tanaka et al., 2002). It does this by inhibiting the microtubule depolymerisation activity and localisation of the kinesin-13 member, mitotic centromere-associated kinesin (MCAK), when correct kinetochore-microtubule attachments are achieved (Andrews et al., 2004). Additionally, aurora B recruits the components of the MCC to the kinetochores when the SAC is activated (Ditchfield et al., 2003).

Upon anaphase onset, CPC function is then required at the central spindle midzone. Here it facilitates the localisation of the centralspindlin complex, formed from MKLP1 and the Rho GTPase activating protein MgcRacGAP (Zhu et al., 2005). Following aurora B phosphorylation, the centralspindlin then initiates microtubule bundling to stabilise the central spindle and furrow regression occurs (Douglas et al., 2010). As the cell progresses into telophase and cytokinesis, the CPC is first involved in contractile ring formation (Carmena et al., 2012). This occurs through the indirect regulation of the small GTPase protein Rho A which activates myosin II and induces actin polymerisation to form a compact mature ring required for cytokinesis (Lewellyn et al., 2011; Miller, 2011). The final role for the CPC is in regulating abscission. Aurora B activity is required to monitor the clearance of chromosomes into each daughter cell, ensuring that cytokinesis only occurs after they have all migrated to their respective poles (Norden et al., 2006). The function of the CPC is ultimately terminated when aurora B is targeted for proteasomal degradation by the APC/C and its activator, Cdh1, upon completion of cytokinesis (Stewart and Fang, 2005).

1.3 The ubiquitin proteasome system

1.3.1 Ubiquitin

Ubiquitin is an ~ 8 kDa protein consisting of 76 amino acids which can be attached to lysine residues of substrate. Ubiquitin can be added as either a single moiety to create mono-ubiquitylation or chains can be extended to create poly-ubiquitylation (Komander and Rape, 2012). Ubiquitin adopts what has been termed a ubiquitin fold

motif which consists of 5 β-sheets, a 3_{10} helix and a short 3.5-turn α-helix (Dikic et al., 2009). Ubiquitin is conjugated to proteins via its C-terminal glycine residue to create an isopeptide bond. Additional ubiquitin subunits can then be added at positions K6, K11, K27, K29, K48, K63 and M1 in the previous ubiquitin (Akutsu et al., 2016). Mono- and poly-ubiquitin can then be recognised by other proteins via their ubiquitin-binding domains (UBDs).

1.3.2 Ubiquitin conjugation

Ubiquitin is conjugated to its target proteins via a series of catalytic reactions. The first stage is performed by E1 ubiquitin activating enzymes via a two-step reaction. There are only two found in mammalian cells; UBA1 and UBA6 (Jin et al., 2007). The role of these enzymes is to activate the ubiquitin moieties by first catalysing the formation of an acyl-adenylate intermediate at the C-terminal of ubiquitin using ATP •Mg2+. The catalytic cysteine of the E1 enzyme is then used to create a thioester-bond between it and the ubiquitin (Schulman and Wade Harper, 2009).

E2 conjugating enzymes can then accept the activated ubiquitin at their catalytic cysteine residues via a transthiolation reaction. Humans have ~ 40 E2 enzymes which are involved in this ubiquitin transfer (Stewart et al., 2016). E2 enzymes are then recruited by an E3 ubiquitin ligase enzyme which interacts with the target protein, allowing for the direct or indirect transfer of the ubiquitin moiety from the E2 onto the substrate (Yang et al., 2021). There is estimated to be between 600 and 700 E3 ligase enzymes in mammalian cells which makes up around 5% of the genome (Jaishankar et al., 2018). Each E2 enzyme can associate with multiple E3 ligase enzymes. Some E2 enzymes when they are paired with certain E3 ligases can be seen to dictate the chain specificity of the linkage and hence decide the fate of that substrate (Wijk and Timmers, 2010; Clague et al., 2015). There are also some E2 enzymes which are only capable of catalysing ubiquitin addition directly onto the substrate, leading to the formation of monoubiquitylation only, whereas others can only facilitate polyubiquitin elongation by only adding ubiquitin onto other moieties (Ye and Rape, 2009).

E3 ligase enzymes can be subdivided into 3 different families which include the HECT (homologous to E6AP carboxy terminus), the RING (really interesting new gene) and the RBR (RING between RING) families. HECT and RBR enzymes are able to accept ubiquitin subunits at a conserved cysteine residue in a similar manner to the E2 enzymes, before then transferring it onto their substrates (Rotin and Kumar, 2009).

RING E3 ligases however acts as a scaffold to provide specificity by bringing the E2 and the substrate closer together to facilitate direct transfer of ubiquitin from the E2 onto the substrate (Clague et al., 2015; Metzger et al., 2014). This mechanism is illustrated in Figure 1.15.

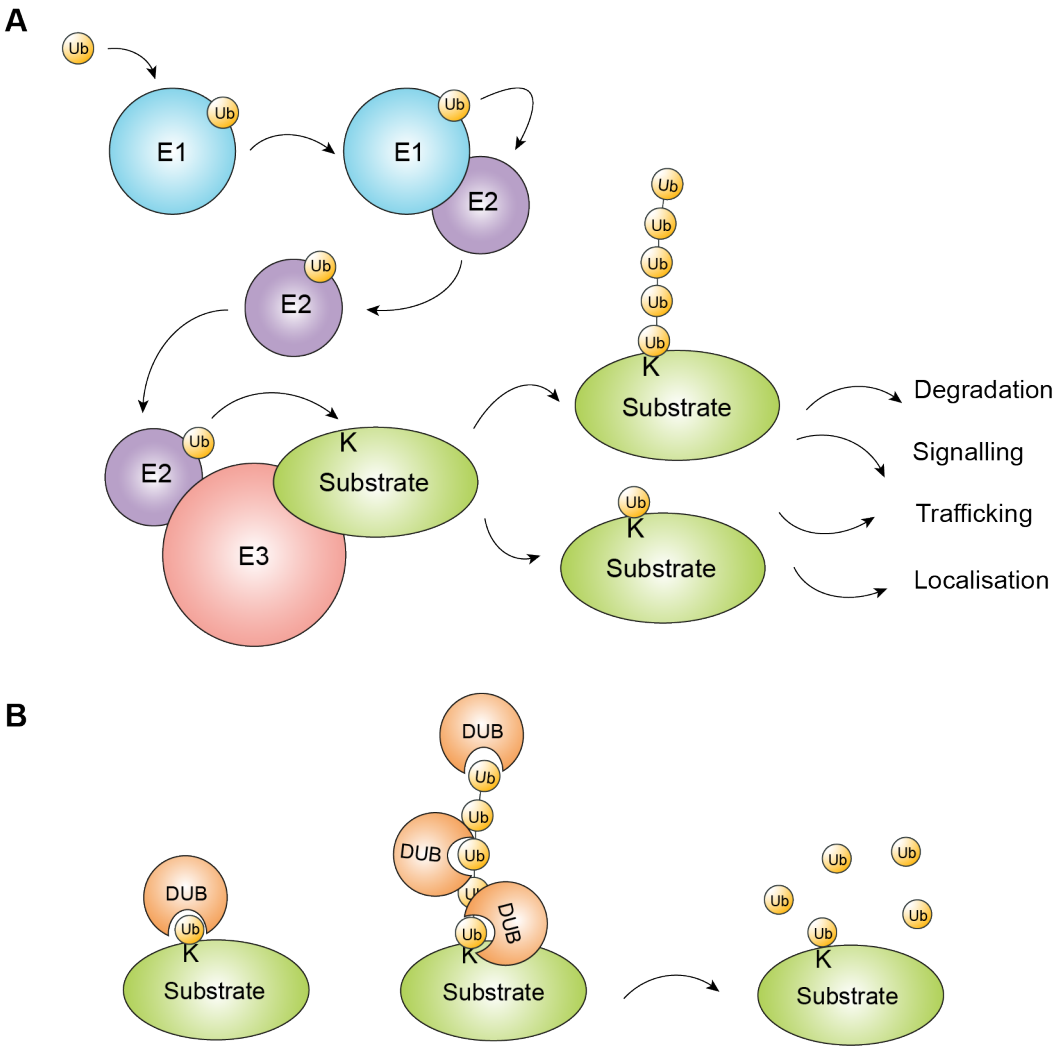

Figure 1.15 – Ubiquitin as a reversible post translational modification

A. The ubiquitin conjugation cascade is performed by the stepwise activation of 3 enzymes including the E1 ubiquitin activating enzymes, E2 ubiquitin conjugating enzymes and E3 ubiquitin ligase enzymes. The E1 conjugates first associates with and activates the ubiquitin moiety before it is passed onto the catalytic cysteine of the E2 enzyme. The E3 enzymes can then interact with both the substrate and the E2 to facilitate the transfer of ubiquitin onto lysine residues of its substrates. Mono- and poly-ubiquitination chains can be made leading to a range of downstream signals such as degradation, signalling, trafficking and localisation. **B.** Deubiquitylase enzymes (DUBs) remove mono- and poly-ubiquitin off their substrates.

1.3.3 Ubiquitin signalling

The complexity and diversity that is provided by this PTM has been termed the ubiquitin code and allows ubiquitin signalling to be involved in many different areas of cell biology (Komander and Rape, 2012). As mentioned above, polyubiquitin chains can be made using different lysine residues within the ubiquitin subunits. K48, K63 and K11 are the most abundant within eukaryotic cells (Peng et al., 2003; Clague et al., 2015), with K48 and K63 being known as the canonical linkage chains (Tracz and Bialek, 2021). The use of different residues can create chains with different topologies to increase the plethora of proteins able to interact with them (Dikic et al., 2009). For example, K48 chains can pack up tightly (Cook et al., 1994) whereas K63 chains adopt a more linear structure (Komander et al., 2009b). To further increase the complexity, chains can also be made using multiple linkages and branching by the use of different lysine residues (Kolla et al., 2022).

Chains formed from K48 linkages are well known to be associated with proteasomal degradation (Lee et al., 1989; Thrower et al., 2000), although most topologies except K63 chains have now been linked with protein degradation (Xu et al., 2009). The mechanisms involved in ubiquitin-dependent proteasomal degradation are described in further detail in section 1.3.5. K63 chains are also commonly found within eukaryotes, and have been involved in trafficking (Dósa and Csizmadia, 2022), DNA damage repair (Liu et al., 2018) and innate immunity (Madiraju et al., 2022). For example, it plays a role in IKK activation via interleukin-1 and Toll-like receptor pathways: TRAF6 is recruited upon receptor activation, leading to autoubiquitylation via K63 chains, which in turn act as a scaffold for the TAK1 kinase complex and hence further downstream signals (Chen and Sun, 2009; Deng et al., 2000).

Functional roles for non-canonical ubiquitylation chains (K6, K11, K27 K29, K33 and M1) have also been identified (Tracz and Bialek, 2021). K6 chains have been reported to regulate the DNA damage response, as BRCA1-BARD1 autoubiquitination leads to the formation of K6 chains at the site of damage (Wu-Baer et al., 2003). Additionally, K6 chains, alongside K11 and K63 have been shown to facilitate the clearance of damaged mitochondria via mitophagy with the DUB USP30 which opposes this mitophagy signal displaying a strong preference for K6 chains (Cunningham et al., 2015). K11 chains also play a crucial role during mitotic progression. The E3 ligase APC/C, alongside the E2 enzyme UBE2S, catalyses the addition of K11 chains onto mitotic checkpoint proteins to initiate their degradation and allow for progression into anaphase (Wu et al., 2010). Finally, monoubiquitylation

is also able to facilitate a number of downstream signalling responses (Hicke, 2001). Monoubiquitylation of histone proteins H2A and H2B is involved in regulating gene expression (Spencer and Davie, 1999), and have also been shown to be required for meiosis in yeast (Robzyk et al., 2000). Endocytosis is also promoted by monoubiquitylation, with multiple mono-ubiquitin moieties being sufficient for internalisation, recycling and degradation of receptor tyrosine kinases (Haglund et al., 2003). Critically, monoubiquitylation is also involved in the spatial regulation of the chromosomal passenger complex (section 1.2.4) during mitosis (Maerki et al., 2009; Sumara and Peter, 2007).

1.3.4 Deubiquitylases and ubiquitin removal

Whilst the E1, E2 and E3 enzymes are responsible for adding ubiquitin moieties to substrates, deubiquitylase enzymes (DUBs) are required for removing them. These enzymes are able to cleave the isopeptide bonds between a ubiquitin subunit and its substrate or between two ubiquitin subunits, either associated to a substrate or within free ubiquitin chains. They cleave with either an exo or an endo-peptidase action by cleaving at the end of the chain or within the chain respectively (Figure 1.15). There are approximately 100 members of the DUB family which can be divided into 7 evolutionarily conserved families. 6 of these 7 families, including USPs, UCHs, Josephins, OTUs, MINDYs and ZUPI, are cysteine proteases and therefore catalyse the breakage of isopeptide bonds using a catalytic cysteine residue, whereas the JAMM family are zinc-dependent metalloproteases (Clague et al., 2019).

1.3.5 Proteasomal degradation

To maintain cellular homeostasis, protein turnover is critical. This involves the whole life cycle of a protein which spans from synthesis, to folding and trafficking, and finally degradation (Hipp et al., 2019). The ubiquitin proteasome system is involved in the degradation of proteins. Tagging of substrates with ubiquitin via E3 ligases can induce them to be degraded whereas the removal of these ubiquitin subunits by DUBs leads to substrate stability. Protein turnover is essential for healthy maintenance of the cell and disruption can lead to a number of neurological diseases (Tai and Schuman, 2008).

The proteasome is a large multi-subunit structure which is involved in the degradation of proteins. Its main role is to cleave ubiquitylated proteins targeted for degradation into small peptides. The 26S proteasome is a cylindrical shaped organelle which is

formed from a 20S catalytic core particle and one or two 19S regulatory complex which come together to generate a 2.5MDa multi-catalytic protein degrading machine (Tanaka, 2009). The 19S regulatory complex contains ~ 20 different subunits and regulates the activity of the catalytic core by recognising the ubiquitin tagged proteins being targeted there. It is formed from lid and base subcomplexes which assist with the removal of ubiquitin chains, and protein unfolding and subsequent translocation into the core of the complex respectively (Bard et al., 2018). There are 6 subunits within the cap which can hydrolyse ATP, providing the energy for unfolding and transferring proteins (Martinez-Fonts et al., 2020). Subunits Rpn10, Rpn13 and Rpn1 are able to recognise ubiquitin chains on the surface of the substrate proteins targeted for degradation (Martinez-Fonts et al., 2020). The Zn^{2+}-dependent metalloprotease, Rpn11, cleaves the polyubiquitin chains to recycle the ubiquitin subunits (Worden et al., 2017). The 20S catalytic core consists of 28 subunits, arranged in 4 rings to form a chamber. The 2 outer rings consist of α subunits and the 2 inner rings contain the β subunits which contain 3 proteolytic active sites per ring. The α rings regulate protein entry into the proteolytic chamber where protein cleavage takes place (Kunjappu and Hochstrasser, 2014). The majority of proteins can be degraded via this organelle due to the catalytic proteases being able to cleave after basic, acidic and hydrophobic residues (Arendt and Hochstrasser, 1997). Once proteins have been cleaved into shorter peptides, these can exit the chamber into the cytosol where complete cleavage into ‘free’ amino acids for recycling occurs.

Changes in expression levels of E3 ligases and DUBs will therefore alter the ubiquitylation of their substrates, ultimately affecting their stability. Depletion of E3 ligases will lead to an increase in their substrate expression levels as ubiquitylation will be reduced and substrates will not be targeted for degradation. On the reverse side, depletion of a DUB will increase substrate ubiquitylation, decreasing expression.

1.3.6 TRIM family of E3 ligases

The largest family of E3 ligases are those which contain a RING domain. This type of E3 ligase catalyses the addition of ubiquitin to its substrates by orchestrating the direct transfer from the E2 conjugating enzyme. They facilitate this via their 2 Zn^{2+} ions which can interact with the E2 enzyme (Deshaies and Joazeiro, 2009). Tripartite motif containing proteins (TRIMs) are a large family of RING containing E3 ligase enzymes (Meroni and Diez-Roux, 2005), with more than 80 members being found within humans (Hatakeyama, 2017).

TRIM/RBCC proteins get their name by the presence of their highly conserved domains which are found in almost all members. These domains include the RING domain (R), either one or two zinc-binding B-box (B) domain followed by a coiled-coil (CC) (Torok and Etkin, 2001). The B-box domain is a defining component of the tripartite motif. Similar to the RING domain, it also utilises Zn^{2+} ions to coordinate cysteine or histidine residues (Borden et al., 1993). The second coordination residue involved is what differentiates the B-box 1 from the B-box 2 domain, with the B-box 1 containing a cysteine and the B-box 2 containing a histidine. TRIM members have been found to contain both B-box domains, however in those that have only one, it is typically the B-box 2 which is found. The coiled-coil domain which follows is required for dimerisation (Meroni and Diez-Roux, 2005). These domains are always located at the N-terminus in this order with the spacing between each domain being highly conserved across members (Tocchini and Ciosk, 2015). Family members are then differentiated by the varying domains at their C-terminus, allowing them to be structurally classified into 11 different subfamilies, as shown in Figure 1.16A. E3 ligase activity can be facilitated via the RING domain, provided they possess a cysteine residue followed by a proline required for their catalytic activity (Budhidarmo et al., 2012). There are however some family members which lack this RING domain, but do still contain the B-box like domains and the coiled-coil with their highly conserved spacing (Williams et al., 2019). There are 7 proteins which fit into this classification as shown in Figure 1.16B.

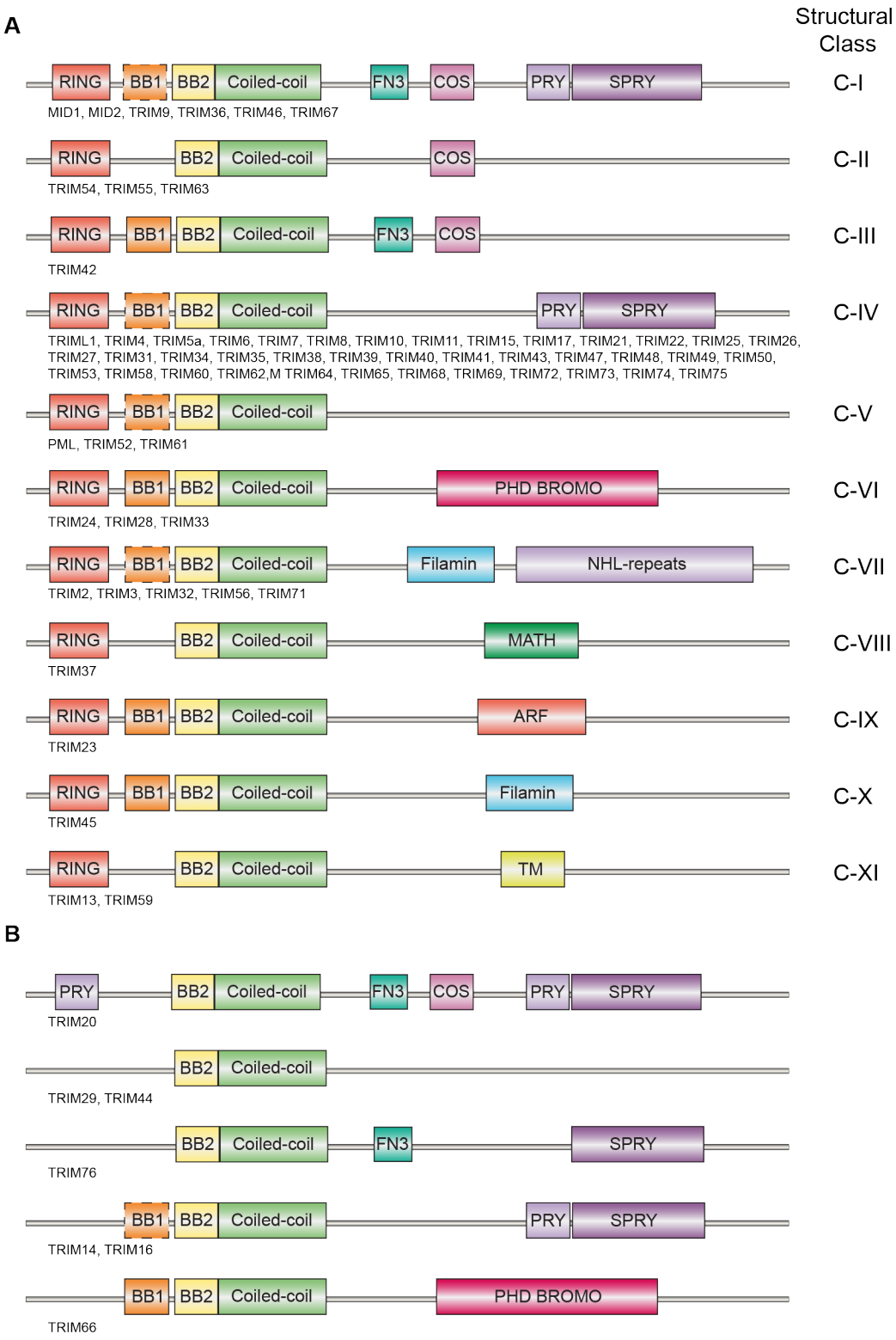

Figure 1.16 – TRIM superfamily domain maps

Domain maps of the **A.** RBCC and **B.** BCC motif containing TRIM proteins. Members of each classification are detailed. Adapted from Williams et al., (2019). Schematics are not to scale.

TRIM protein members carry out a wide variety of different functions and are active across all stages of the cell cycle (Venuto and Merla, 2019). Many TRIM proteins are induced by type I and type II interferons (IFN) and are therefore involved in the innate immune response (Ozato et al., 2008). TRIM21 interacts with and ubiquitylates the IRF8 transcription factor following IFN stimulation, leading to the increased expression of cytokines (Kong et al., 2007). TRIM21 may also be involved in the activation of T cells, further supporting its role within immunity (Ishii et al., 2003). TRIM8 has been reported to influence immunity by preventing the attenuation of IFN induced signalling by interacting with SOCS1 (suppressor of cytokine signalling 1), thereby promoting prolonged inflammatory responses (Toniato et al., 2002). In addition to roles in innate immunity, three related TRIM proteins have been reported to be involved in the turnover of muscle proteins. These are TRIM63, TRIM55 and TRIM54, also known as MURF1, 2 and 3 (muscle RING finger protein) respectively. They are expressed in skeletal and cardiac muscle tissues and are involved in remodelling muscles by inducing degradation of sarcomere muscle proteins such as troponin I (Kedar et al., 2004; Witt et al., 2005). MURF2 and 3 have also been found in association with glutamylated microtubules, myosin and titin during the formation of the sarcomere (Pizon et al., 2002).

Many TRIM proteins have been directly associated with a number of human diseases. Some TRIM members are involved in the development and progression of cancerous tumours. p53 stability and regulation is affected by a number of TRIMs including TRIM13, TRIM19, TRIM24, TRIM28 and TRIM29 (Hatakeyama, 2011). For example, TRIM13 can directly associate with the negative regulator of p53, MDM2, leading to its degradation. TRIM13 is known to be downregulated in different cancer types. This thereby leads to increased levels of MDM2, decreased levels of p53 and hence tumour progression (Joo et al., 2011). Other diseases have also been connected to TRIM proteins. Point mutations within different regions of TRIM32 lead to different disease phenotypes. Those found within the C-terminal NHL domain of TRIM32 have been associated with limb-girdle muscular dystrophy type 2H (Frosk et al., 2002), whereas point mutations within the B-Box domain lead to Bardet-Biedl syndrome (Chiang et al., 2006).

1.3.7 Ubiquitin specific proteases

The ubiquitin-specific protease (USP) enzymes make up the largest family of DUBs with ~50 members. They are cysteine proteases which utilise critical amino acid residues to create their catalytic site, termed either the catalytic diad or triad. This includes the catalytic cysteine in close proximity to a histidine, and in some cases either an aspartic acid or an asparagine residue (Komander et al., 2009a). The cysteine peptidase reaction was investigated in much detail using the papain family. The mechanism involves the nucleophilic attack of the isopeptide bond from the thiol group within the catalytic cysteine. This leads to the formation of a covalent acyl intermediate formed with the cysteine within the DUB and the glycine residue on the distal ubiquitin. A water molecule is then required to hydrolyse this intermediate and complete the isopeptide cleavage (Komander et al., 2009a; Cstorer and Ménard, 1994). The histidine residue is required for lowering the pKa of the cysteine, allowing for it to perform a nucleophilic attack of the isopeptide bond, and an Asp or Asn residue aligns and polarises this histidine (Clague et al., 2013).

In general, USP DUBs do not display a preference for a specific type of ubiquitin linkage, with most being able to cleave any type of chain (Faesen et al., 2011). There are however some exceptions to this statement, with the mitochondrial localising DUB, USP30, displaying a preference for K6 chains (Cunningham et al., 2015), and the microtubule localising DUB, CYLD, having a preference for K63 and Met-1 linked ubiquitin (Hrdinka et al., 2016).

1.3.8 Ubiquitin-associated proteins and microtubules

A number of proteins involved in the ubiquitin machinery have been reported to localise to microtubules. 9 members of the TRIM family of E3 ligases contain a cos-box domain which is required for their microtubule localising capabilities (Short and Cox, 2006). This includes members within the C-I and C-II subclasses. TRIM42 within the C-III subclass also contains a cos-box domain however microtubule localisation has not been confirmed. The best studied of these TRIM proteins are MID1 and MID2 (TRIM18 and TRIM1 respectively) which have shown to be involved in cytokinesis. Astrin, which stabilises kinetochore-microtubule attachments before chromosome segregation (Dunsch et al., 2011), is ubiquitylated by MID2 during mitotic exit to target the it for proterasomal degradation and facilitate cytokinesis (Gholkar et al., 2016).
Some deubiquitylase enzymes are also known to localise to microtubules. The first to be identified was the familial cylindromatosis tumour suppressor, CYLD. It interacts

with microtubules via its CAP-Gly domains (detailed in section 1.1.9.2) and regulates microtubule dynamics and cell migration (Gao et al., 2008). Additionally, CYLD inhibits the activity of HDAC6, leading to an increase in microtubule acetylation levels and negatively-regulating cell cycle progression (Wickström et al., 2010). USP21 was the second DUB shown to associate with both microtubules and the centrosome (Urbé et al., 2012; Heride et al., 2016). This DUB is involved in regulating microtubule dynamics as its depletion leads to reduced microtubule extension following cold-induced microtubule depolymerisation. A functional role in primary cilia formation was also identified (Urbé et al., 2012). Finally, a previous PhD student from my host laboratory has provided the first characterisation of the 3rd microtubule localising DUB, USP31 (Bertsoulaki, 2018). Erithelgi Bertsoulaki showed that USP31 decorates modified microtubules as well as associating with the mitotic spindle and that its depletion leads to altered microtubule dynamics, a change in the length of the EB1 plus end cap and fragmentation of both the acetylated and detyrosinated microtubule networks (Bertsoulaki, 2018). Further characterisation of this protein, and its involvement within mitosis is reported in Chapter 5.

1.4 Proteomics

The term proteomics describes the analysis of the total proteins present in a sample collected under specified conditions. Over the past 20 years, the technologies available to facilitate the formation of proteomic data has increased significantly with key milestones which lead to advancements within this area. Many methods for detecting gene expression had been developed such as large-scale sequencing and cDNA microarrays, and as useful as these are, they do not consider regulation of expression at the protein level. Studies at a genome level therefore omit information provided from half-lives and post-translational modifications which regulate expression, highlighting the importance for more research within this area (Gygi et al., 2000). Despite this, protein identification via its amino acid sequence has only become possible due to the Human Genome Project and the complete sequencing of the human genome, as this forms the databases used for peptide identification.

Mass spectrometry (MS) was originally used in protein biology to identify a specific protein of interest following its association to a certain biological activity (Aebersold, 2003). Being able to quickly identify a protein of interest was a main driver for the development of these high throughput, high-sensitivity technologies. Further uses for

MS include looking at protein expression levels, modifications, protein-protein interactions, subcellular localisation determination and investigation of protein complexes (Henzel et al., 2003). Proteomics is dependent on the combination of 3 technologies including: a method to separate and fractionate the complex protein mixtures obtained; mass spectrometry or tandem mass spectrometry machinery to detect and identify the proteins present; and bioinformatics resources to interpret and analyse the resulting data. All 3 of these areas have been advanced over the past 20-30 years so we can now identify proteins of interest in a quantitative, reproducible manner.

1.4.1 Edman degradation

Typically, to identify a protein or peptide, the primary amino acid sequence must first be decoded. In the 1980's the main method for protein identification was Edman degradation, originally developed by Pehr Edman (Edman, 1949). Identification via this technique is facilitated by degrading each amino acid in turn from the N-terminal of a peptide and individually identifying them. The basic method involves 3 steps: coupling, cleavage and conversion (Edman and Begg, 1967). The first step is to couple the N-terminal amino acid with a phenyl isothiocyanate to produce a phenylthiocarbamyl derivative group. Cleavage of this first peptide bond can then be achieved under acidic conditions to give an anilinothiazolinone molecule and a shortened peptide. Conversion of this residue to a more stable phenylthiohydantoin form under aqueous acid conditions is then required to allow for better analysis. This resulting residue can then be resolved via reverse-phase high-performance liquid chromatography (HPLC) and identified by comparison to standards. This is repeated for all amino acids within the peptide to determine the complete sequence (Smith, 2001). This was the standard method at the time and was used to sequence a number of proteins, including both α- and β- tubulin subunits (Ponstingl et al., 1981; Krauhs et al., 1981). Despite its robustness, this was a time-consuming process, with each chemical cycle requiring 20 minutes (Smith, 2001). Furthermore, this method often failed to identify peptides if modifications such as acetylation were present at their amino terminus (Steen and Mann, 2004).

1.4.2 Advances in protein MS

To allow for the quick identification of multiple proteins, technologies surrounding MS techniques were developed and eventually displaced the Edman degradation method in the 1990's (Steen and Mann, 2004). For successful MS analysis, samples of

interest are required within the gaseous ionic phase. Methods such as chemical and electrical ionisation had been developed for this purpose however these were not compatible with proteins. As proteins are non-volatile and polar structures, they were susceptible to destruction when subjected to these ionisation techniques (Banerjee and Mazumdar, 2012). A new ionisation technique called fast atom bombardment (FAB) was developed in 1981 to combat these problems. Ionisation was achieved however only singly charged analytes were formed, making their high mass to charge ratios (m/z values) difficult to measure with current analysers. Furthermore, protein digestion was required to measure those with molecular weights higher than 1000Da (Barber et al., 1981). In the late 1980's/early 1990's, all these problems were overcome by the development of the ionisation techniques electrospray ionisation (ESI) (Fenn et al., 1989) and matrix-assisted laser desorption/ionisation (MALDI) (Karas and Hillenkamp, 1988). ESI gained popularity due to its ability to integrate with many existing liquid-phase separation techniques already being used and allowed for production of multiply charged gaseous protein ions for easy identification. MALDI was also frequently used due to it being simple, sensitive, providing a large mass range, and its generation of easy-to-interpret data (Aebersold, 2003).

1.4.3 Electrospray ionisation

ESI is a soft ionisation technique that allows the conversion of liquid-phase ions to gaseous ions of large biomolecules without causing their fragmentation and destruction (Fenn et al., 1989). The technique was developed by John Bennett Fenn for which he was awarded a Nobel Prize in Chemistry for in 2002 alongside Koichi Tanaka for his contribution to MALDI (Grayson, 2011). What made ESI superior to the FAB ionisation technique was its ability to create multiply charged gaseous ions which allows their m/z values to drop to a suitable range that can be measured by the common mass analysers being used in MS machineries (Banerjee and Mazumdar, 2012). Furthermore, it is also capable of retaining native protein structures and activities, allowing interpretations of their 3D structures, PTM's and non-covalent interactions (Ouyang et al., 2003). The basic method of ESI involves samples being injected into an ioniser at a low flow rate before a comparatively high voltage is applied, creating a strong electric field. This causes sample dispersion to occur, forming an electrospray of highly charged droplets of 1-2 μm in diameter which are directed towards the mass spectrometer. A high vacuum and a high temperature are then applied to facilitate the release of charged analytes from the droplets and their complete desolvation into a gas phase (Banerjee and Mazumdar, 2012). These

charged ions are obtained from doubly protonating the digested peptides within the sample (Steen and Mann, 2004). These formed multiply charged ions are then compatible with most common MS analysers, where the peptides are separated based on their m/z ratio before they are passed to the detector for measuring (Banerjee and Mazumdar, 2012).

Developments of different electrosprays have been developed since ESI first emerged, with the most popular today being the nanoelectrospray which was developed by Matthias Wilm and Matthias Mann (Wilm and Mann, 1996). As suggested by its name, aspects from ESI have been adapted on a nanoscale. The flow rate has been reduced from 1-20 μL/min to 20-50 nL/min, a low sample concentration of nanomole/ml is required and the droplet diameter is reduced to <200nm, making them significantly smaller than with ESI (Wilm and Mann, 1996; Banerjee and Mazumdar, 2012). This development therefore improved the sensitivity of ESI-MS. Protein samples were therefore obtained and digested using trypsin before being subjected to ESI-MS and collision activation. The resulting spectra provided the peptide fingerprints, with the mass differences between fragments being used to determine the amino acid sequences. Bioinformatic tools are then required to determine the protein identity from these peptide sequences. The determination of a protein in a sample from its sequence is known as ‘bottom up’ proteomics (Banerjee and Mazumdar, 2012).

1.4.4 Tandem Mass Spectrometry

Following on from ESI and the initial determination of the m/z values of each trypsinised peptide, another round of MS is performed to determine the primary structure of each peptide. This is referred to as tandem MS or MS/MS. Individual peptides are separated and subjected to collision-induced dissociation and allowed to collide with an inert gas such as nitrogen, helium or argon, causing them to fragment further (Steen and Mann, 2004). Multiple rounds of collisions are performed to create different fragmented ions corresponding to all different lengths of the peptide which differ by one amino acid each time (Mitchell Wells and McLuckey, 2005). These fragmented peptides can then be sent to the detector again to identify their m/z ratios. The differences in mass between each sequential peptide can then be used to determine which amino acid has been lost and hence the primary sequence can be resolved. Manual analysis of these peaks can lead to the incorrect sequence being determined. For example, the mass of one asparagine residue is equal to the mass

of two glycine residues, and a very small peak occurring in the middle of two large peaks may be missed, causing the sequence to be recorded as one amino acid change rather than two (Steen and Mann, 2004). This problem, along with the ability to analyse a large amount of data within a short amount of time, can be overcome by the use of computational analysis to identify the peptide sequence.

1.4.5 Computational advances

A major advancement for the proteomics field was the development of computational algorithms to allow for quick and reliable analysis of proteomic data. One of the first programmes developed was named FragFit and was combined with MALDI-MS to identify proteins using peptide mass fingerprinting. This software was capable of using the masses of each peptide produced to identify the protein in which it originated from by searching a database which contained 91,000 different protein sequences (Henzel et al., 1993). This was one of the first studies that allowed protein identification from MS. Despite this, as ESI combined with tandem MS had proved more popular than MALDI, an identification algorithm called SEQUEST was developed by Eng *et al.* shortly after to allow identification of peptides by comparing the spectra produced to a theoretical spectra within the GenPept database (Eng et al., 1994). Further developments in computer algorithms for protein identification were developed as the requirement for high-throughput proteomic data increased. The development of Mascot allowed for the integration of the search criteria used within both FragFit and SEQUEST, allowing for overall peptide mass and amino acid sequence to both be used for identification, and included probability-based scoring to reduce false positive identification (Perkins et al., 1999). Both SEQUEST and Mascot were frequently used tool for proteomic data analysis however other computer algorithms are also available including Sonar ms/m, PeptideSearch and ProteinProspector which all require a sequence database as a reference (Steen and Mann, 2004).

There are a number of computational software platforms available for MS-based proteomics including MS Quant (Schulze and Mann, 2004) and MaxQuant (Cox and Mann, 2008) which both allow for peptide identification and quantification. The most commonly used computational platform today is MaxQuant which was released in 2008 by Jurgen Cox and Matthias Mann (Cox and Mann, 2008). This platform incorporates a set of algorithms which can extract raw MS data, allowing for identification of peptides at a high-accuracy rate within a short time. Upon its release it was shown to identify >4000 proteins at any one time from mammalian cell lysates,

with the newest release now being capable of recognising >25,000 peptides within one single run (Wichmann et al., 2019). Originally, the previously developed Mascot algorithm was integrated within the software to allow for peptide identification, however it now incorporates its own search engine, Andromeda, which performs equally as well as Mascot but also accommodates and assigns complex PTM patterns and allows identification of a greater number of peptides (Cox et al., 2011b). MaxQuant has been continually developed and displays advanced mass precision and accuracy (Cox and Mann, 2009; Cox et al., 2011a). It facilitates the analysis of multiple methods of quantification in addition to SILAC, which was incorporated within the first release (Cox and Mann, 2008), such as label-free, tandem mass tags (TMT) and isobaric tags for relative and absolute quantification (iTRAQ). Additionally, it can also be integrated with a number of other MS platforms, further increasing its usability (Tyanova et al., 2016). The development of MaxQuant therefore provided a huge boost to overcome the many challenges faced when analysing data produced from MS-based 'bottom-up' proteomics experiments. There are also a number of other software which have been developed to assist with proteomic research, many of which have come from Steven Gygi's lab. These include various Smart-TMT applications such as Real-Time-Search which provides fragment spectra identification as they are acquired (Schweppe et al., 2020; Erickson et al., 2019) and GoDig which allows targeted analysis for hypothesis-driven research (Yu et al., 2023).

1.4.6 2D gel electrophoresis

Another important milestone in the proteomics field was the development of 2-dimensional gel electrophoresis systems (2DE), which was introduced by 2 independent groups in 1975 (Klose, 1975; O'Farrell, 1975). The idea of separating proteins out using 2 electrophoresis protocols had been proposed prior to these publications however they did not show resolution of many proteins (Smithies and Poulik, 1956). Proteins were first separated via their isoelectric point, followed by their separation via their molecular weight in the second dimension using SDS-PAGE. This method uses the idea that most proteins will have different physiochemical properties, and therefore be efficiently separated from each other. Individual proteins were detected using various visualisation techniques to produce a gel with individual spots at specific locations, their size proportional to their expression levels. This technique resolved >1000 proteins from one sample with high resolution, high sensitivity and the ability to reproduce results (O'Farrell, 1975). It was considered one of the most valuable tools for separating and visualising proteins (Issaq and Veenstra, 2008).

1.4.7 Quantitative mass spectrometry

The most important yet challenging area of proteomics was the quantification of protein expression between 2 or more physiological states. Unfortunately, peak intensities are not always proportional to the amount of peptide present due to peptide solubility, protease accessibility and ionisation efficiency for particular peptides, and therefore peaks cannot be used to directly compare protein expression levels. The ability to therefore apply quantifiable applications to 2DE was desirable as this was thought to be the most comprehensive method available for protein detection and identification. In order to do this, different samples were resolved on individual gels in parallel and their spots visualised. Alignment methods allow matching of spots and their intensities can be compared to provide a quantitative measure of their abundance. All matched spots of interest were labelled, excised from the gels and subjected to MS to confirm their identification (Issaq and Veenstra, 2008). This technique was widely used for quantitative proteomic analysis including within microtubule related studies. For example, the differences in microtubule binding proteins at 0hr and 12hr of post-diapause development in Artemia franciscana was determined via this method (O'Connell et al., 2006). The possible issue with this method however is that running samples on different 2DE gels may induce differences relating to the separation or the staining. This may affect the intensities observed or even lead to some spots being incorrectly paired together. In addition, multiple proteins can be present at the same spot due to their similar properties which may lead to alterations in spot intensities and hence the quantification of results (Issaq and Veenstra, 2008; Magdeldin et al., 2014; Gygi et al., 2000).

Advances were made to try and overcome any issues occurring from the use of individual gels. In 1997, different fluorescent cyanine tags to distinguish between samples was utilised. This technique was named 'differential imaging gel electrophoresis' and allowed for up to 3 different samples of equal concentration to be run on one gel and imaged to calculate any differences in protein abundance (Ünlü et al., 1997). Scanning of the gel at the 3 different wavelengths allows specific visualisation of all the proteins in each sample. Images were then merged and computational analysis matched the spots between samples to measure their intensities and determine protein expression changes (Ünlü et al., 1997; Issaq and Veenstra, 2008). This technique contributed significantly to the advancement of 2DE as all samples were resolved on the same gel, allowing for better comparison between them as misalignment errors are reduced, ensuring accurate quantitation (Issaq and Veenstra, 2008).

Despite this technique being powerful at the time, there are some limitations. Proteins with low abundance are not always detected as there is too little material for spots to be visualised. This could therefore lead to some proteins of interest not being excised from the gel and identified via MS. This was observed during an evaluation of its use for protein detection from total cell yeast lysates: only abundant proteins were identified. In order to visualise these, large amounts of starting material are required which is a limitation in itself as resolution is reduced (Gygi et al., 2000). Similarly, despite much optimisation into the resolving technique, some insoluble proteins or those high in either basic or acidic amino acids remain difficult to detect as they do not migrate through the gel successfully (Wilkins et al., 1998). It therefore became apparent that the use of 2DE in combination with MS was not suitable for detecting and identifying every protein within a sample (Gygi et al., 2000).

1.4.8 Non-gel-based techniques

As 2DE became too limiting for full analysis of complex samples, alternative techniques were developed. Isotopic labelling became the new ‘big thing’ for quantitative analysis of MS data, selected due to their identical chemical and physical properties to the naturally occurring equivalents (Zhu et al., 2010). Around this time, isotopic labelling of drug analogues was already being used to measure precise levels of drugs and their metabolites using quantitative MS techniques (de Leenheer and Thienpont, 1992; Browne et al., 1981). Isotopic labelling was first introduced to proteomic investigations in 1999 by 3 independent research groups. The first used culture media containing 15N isotopes to metabolically label bacterial cells with stable isotopes (Oda et al., 1999). The second depleted any naturally occurring stable isotopes from one sample to achieve a similar result (Paša-Tolic et al., 1999). The 3rd introduced the idea of isotope-coded affinity tags (ICAT), where tags are enzymatically labelled and then separated by affinity chromatography before MS analysis (Gygi et al., 1999). In later years, more approaches utilising stable isotopes were also developed including Stable Isotope Labelling by Amino Acids in Cell Culture (SILAC) (Ong et al., 2002), Tandem Mass Tags (TMT) (Thompson et al., 2003), Isotope Coded Protein Labelling (ICPL) and Isobaric Tags for Relative and Absolute Quantification (iTRAQ) (Zhu et al., 2010).

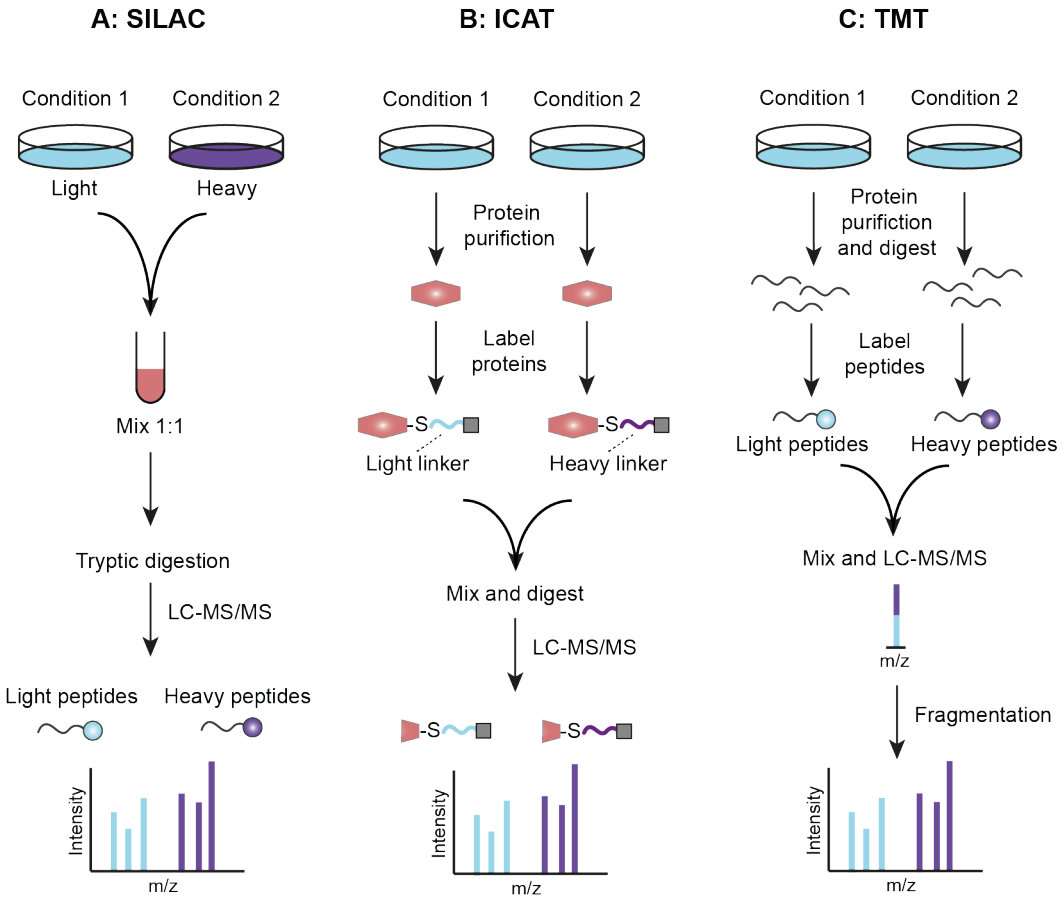

Figure 1.17 - Techniques for relative protein quantification

A: Schematic displaying SILAC (stable isotope labelling of amino acids in cell culture) labelling. Different conditions are metabolically labelled with either light or heavy (or medium, not shown) amino acids supplied in the cell culture media. **B:** Schematic displaying ICAT (isotope-coded affinity tag) method. Purified proteins from different conditions are labelled with affinity tags containing either light or heavy linkers. **C:** Schematic displaying TMT (tandem mass tags) method. Digested peptides from different conditions are labelled with either of a pair of tags containing different isotopic labels and a mass normalisation group to equalise the mass of the tags, ensuring coelution of peptides.

1.4.8.1 ICAT labelling

ICAT introduces isotope labelled affinity tags into peptides present within a protein sample of interest (Gygi et al., 1999). The basic method illustrated in Figure 1.17B includes a tag which contains a biotin affinity moiety for purification of peptides, a thiol-specific reactive group for labelling reduced cysteine side chains and an isotopically coded linker binding the 2, which exists in a light and a heavy form. Protein samples are specifically labelled and combined in a 1:1 ratio, before being enzymatically

cleaved with trypsin to produce peptide fragments between 5 and 25 residues. Avidin affinity chromatography is then performed to isolate any biotin-labelled peptides for MS identification. Quantification is achieved by determining ratios between the intensities of the same peptides from each condition, allowing a measure of protein abundance. This method achieves accurate measurement of small changes in protein levels as the overall complexity of the sample is restricted to those only containing cysteine residues, increasing their chance of detection (Gygi et al., 1999). This idea however also poses as a limitation: the frequency of cysteine residues within proteins is approximately 2% compared to other amino acids such as leucine which has a frequency of 10% (Ong et al., 2002). Furthermore, some proteins do not contain cysteine residues, and these therefore cannot be identified or quantified.

1.4.8.2 SILAC labelling

An advancement in the use of stable isotopes for metabolic labelling of proteins was that developed shortly after in Matthius Mann's laboratory termed 'stable isotopic labelling by amino acids in cell culture, or SILAC (Figure 1.17A) (Ong et al., 2002). Cell culture media containing either L-lysine or deuterium-labelled L-leucine-5,5,5-D3 were utilised on different samples for incorporation during protein synthesis to produce 'light' and 'heavy' peptides respectively. The 2 samples are then differentially treated as desired, combined in a 1:1 ratio and digested with trypsin prior to quantitation by MS. The peptides produced in each sample are therefore chemically identical, however their mass changes can still be detected. Quantification data is provided by determining the ratios of peak intensities of each peptide between conditions (Ong et al., 2002). There are numerous advantages to this method, and it is still widely used today for quantitative MS investigations (Schubert et al., 2017). Peptide labelling steps are not required as labels are incorporated during protein synthesis, reducing any differences that may be acquired during this stage. ~ 98% incorporation of stable isotopes can be achieved following 5 doublings of cells. Labelling is sequence specific and several peptides from the same protein can be analysed. Additionally, small changes in protein expression can be detected using this method, increasing the information obtained (Ong et al., 2002). Today, lysine and arginine isotopes are typically used due to trypsin digestion occurring adjacent to these residues, ensuring every peptide fragment contains at least one isotopic label (Bantscheff et al., 2007; Ong et al., 2003). Although this method is limited by only having 3 different labels, early combination of samples makes it one of the most

accurate measurers of protein expression. In addition, all 3 samples can be analysed at once, reducing experimental time (Bantscheff et al., 2007).

1.4.8.3 TMT labelling

The use of isotope labelling with both ICAT and SILAC methods allows peptides from different samples to be chemically identical however they carry a different mass, causing heavier peptides to migrate faster through liquid chromatography columns. This causes comparable peptides to elute at different times, possibly as different fractions, and may lead to ionisation suppression during ESI if another peptide were to coelute with it. The development of tandem mass tags (TMT) (Figure 1.17C) has provided an additional quantitative method for MS analysis that overcomes this differential elution issue, whilst also providing additional advantages (Thompson et al., 2003). TMT was developed in 2003 and uses isobaric labelling to differentiate between conditions: these labels are identical both chemically and by their mass. TMT tag pairs are made up of a sensitisation enhancement group, which has guanidino functionality, attached to an amino acid which is tagged with a deuterium group within one pair. They then contain a fragmentation enhancement group consisting of a proline residue, followed by a mass normalisation group. This mass normalisation group is required to balance out the difference present within the tagged amino acid. Digested peptides from each condition are tagged with a different label, with attachment occurring at the α-amino group, before being combined and analysed by LC-ESI-MS/MS. Collision-induced dissociation is required to fragment the TMT label and produce a peptide with a specific m/z value which is then detected whilst easily avoiding the untagged material (Thompson et al., 2003). An advantage this method has over both ICAT and SILAC labelling is that multiplexing can be performed, with up to 18 conditions being analysed at the same time, making this method a popular choice for quantitative proteomic analysis (Li et al., 2021). Different tags can be produced by changing the fragmentation enhance to aspartic acid, adding a biotin tag or altering the position of the heavy isotopes incorporated, maintaining the mass and chemical structure but creating a unique tag (Thompson et al., 2003). A limitation to this method however is that labelling is not as efficient as metabolic labelling, with some peptides going undetected (Ong et al., 2002).

1.4.8.4 The microtubule proteome

Microtubules are known to interact with a large plethora of proteins. Several proteomic studies have been performed in a variety of species to identify microtubule-associated proteins, primarily using *in-vitro* techniques. Over 250 MAPs were identified from early Drosophila embryos using taxol- and GTP-stabilised endogenous tubulin preparations, followed by 2D gel electrophoresis (Hughes et al., 2008). In another study, macrophage extracts were incubated with the microtubule stabilising drug, taxol, and purified bovine brain tubulin before being eluted for analysis via mass spectrometry and quantification via spectral counting. This led to the identification of 406 microtubule-binding proteins in macrophages, with 52 of these being up-regulated upon microtubule stability, and 42 being down-regulated (Patel et al., 2009). In 2010, 318 proteins from meiotic *Xenopus* egg extracts were found to bind to taxol-stabilised bovine brain tubulin (Gache et al., 2010). Another example published in 2011 identified 1155 proteins as binding to the metaphase spindle in Chinese hamster ovary cells using Multi-dimensional Protein Identification Technology, providing the first mitotic spindle-associated proteins within these cells. Synchronised cells were treated with taxol and phalloidin before being lysed and spindles pelleted for analysis (Bonner et al., 2011). A final example was that performed by Rosas-Salvans *et al.* which investigated the proteins involved in driving microtubule self-organisation in mitotic cells in *Xenopus* egg extracts (Rosas-Salvans et al., 2018). This study identified 1262 proteins involved in RanGTP-dependent microtubule assemblies and also provided a comparison of its proteins identified compared to those found within other spindle proteomes. This comparison revealed that 431 were exclusively identified in that proteome providing a greater comprehensive list of spindle associated proteins than before (Rosas-Salvans et al., 2018).

The majority of these studies preceded major advances in the sensitivity of mass spectrometry instruments and the adoption of isotopic labelling procedures (Patel et al., 2009). Additionally, many involve the manipulation of the microtubule network *in-vitro* and/or the addition of exogenous tubulin, thereby incompletely capturing the intracellular architecture and environment. Furthermore, a number of studies have focused on only spindle associated proteins as opposed to the interphase microtubule network, where identification of different proteins would occur (Rosas-Salvans et al., 2018; Bonner et al., 2011; Sauer et al., 2005; Rao et al., 2016). The requirement for a more comprehensive proteomic analysis of microtubule binding proteins during interphase is therefore required.

1.5 Purpose of this study and summary of chapters

Microtubules are an essential component of the cytoskeleton, and their functions and kinetics are regulated by a plethora of microtubule binding proteins. Identification of a complete microtubule proteome is therefore required to understand the wide array of functions performed by microtubules. This work describes a method for identifying microtubule binding proteins directly from cells and the subsequent characterisation of novel candidates. It thereby satisfies the unmet need for up-to-date proteomic analysis of microtubule binding proteins during interphase utilising modern quantitative mass spectrometry techniques.

In Chapter 3 I optimise a novel method to differentially extract microtubules and their binding proteins directly from cells. I then conducted quantitative mass spectrometry proteomics to determine a microtubule proteome and identify novel microtubule binding proteins.

In Chapter 4 I go on to characterise 3 proteins selected from those identified within the proteome from Chapter 3. Specifically, I further investigate TRIM3 as a novel microtubule binding protein. Prior to this study, a number of TRIM proteins have been reported to localise to microtubules, and I show that TRIM3 is also capable of microtubule association via an alternative domain. I then describe the effects that TRIM3 depletion has on the microtubule network and the enzyme responsible for catalysing microtubule acetylation, ATAT1.

In Chapter 5 I then follow a different line of enquiry which involves characterisation of another microtubule localising protein: the poorly characterised DUB, USP31. Initial characterisation of this protein performed by a previous PhD student, Erithelgi Bertsoulaki revealed USP31 depletion caused mitotic defects. I therefore further investigate the roles of USP31 in mitosis and provide a functional role in regulating the chromosomal passenger complex.

Chapter 2 – Materials and Methods

2.1 Cell biology

2.1.1 Materials and Reagents

Most plasticware for general tissue culture was purchased from Starlabs. µ-Dish 35mm (81156) were purchased from Ibidi (Thistle Scientific LTD) and plasticware for mass spectrometry was purchased from Corning Inc (NY, USA). Cell culture media was supplied by Gibco (Thermo Fisher Scientific): Dulbecco's Modified Eagle Medium (DMEM) + GlutaMAX-I (31966-021); DMEM/F-12 Nutrient Mixture (DMEM/F12) + GlutaMAX-I (31331-028); Minimum Essential Medium/Non-Essential Amino Acids (MEM/NEAA) (11140-035); and OptiMEM (409864). Dimethyl sulfoxide (D4540), Foetal Bovine Serum (FBS, 10437028) and Dulbecco's Phosphate Buffered Saline (PBS, 14080055) were also purchased from Gibco (Thermo Fisher Scientific). Trypsin-EDTA (15400) and the transfection reagents Lipofectamine RNAiMAX (13778150) and Lipofectamine 2000 (11668019) were obtained from Invitrogen (Thermo Fisher Scientific). G-418 solution (4727878001) was obtained from Roche Diagnostics. Thymidine (T1895-5G), Nocodazole (M1404), MG132 (474790), Paclitaxel (Taxol, T7402), CDK1 inhibitor RO3306 (SML0569), Aurora B inhibitor ZM447439 (189410), Dimethyl sulfoxide (D4540) and GeneJuice transfection reagent (70697) were purchased from Sigma Aldrich. PLK1 inhibitor BI2536 (S1109) was purchased from Selleck chem. The lambda protein phosphatase reaction kit (P0753) was purchased from New England Biolabs (NEB).

2.1.2 Cell lines

U2OS osteosarcoma cells were purchased from European Collection of Authenticated Cell Cultures (ECACC). SK-N-BE2 cells were purchased from American Type Culture Collection (ATCC). Parental human telomerase reverse transcriptase-immortalised retinal-pigment epithelial (hTERT-RPE1) containing the Flp-in system (hTERT-RPE1-FRT-TREX) cells were generously donated by Jonathon Pines (London) (Pagliuca et al., 2011). Hela cells stably expressing mCherry-α-tubulin were a kind gift from Prof. Anna Akhmanova (Utrecht University, The Netherlands). U2OS cells stably expressing mRFP-H2B, and those expressing mCherry-tubulin and GFP-CENPA were a kind gift from Dr Helder Maiato (CID/IBMC, Porto). U2OS cells stably expressing GFP-USP31 wild type (WT8, WT9, WT10 and WT13) and a catalytic inactive mutant (CA1) were made in the laboratory by Erithelgi Bertsoulaki (Bertsoulaki, 2018). U2OS cells with doxycycline inducible VSV-INCENP-GFP

expression were a kind gift of Dr Susanne Lens (Utrecht University; (van der Horst et al., 2015). All U2OS derived cell lines and Hela cells were grown in Dulbecco's Modified Eagle Medium (DMEM) whereas RPE1 and SK-N-BE2 cells were cultured in DMEM-F12 (1:1). Both types of media were supplemented with 10% heat-inactivated foetal bovine serum and 1x non-essential amino acids. Media for USP31 expressing cell lines and Hela cherry tubulin cells were also supplemented with 0.4mg/ml G418 selection. Cells were cultured in incubators at 37 °C with 5% CO2 and split every 2-3 days ranging from 1:2 or 1:10 dilutions as needed.

2.1.3 Plasmid DNA transfection

All plasmid DNA transfections were performed the day prior to collection of experimental data into either a 6-well plate for lysis or a 6-well plate or 35 mm ibidi dishes for live cell imaging, with cells at 60-80% confluency at the time of transfection. 100 µl OptiMEM was combined with either 3 µl GeneJuice or 3 µl Lipofectamine2000, vortexed and incubated at room temperature for 5 minutes. 1 µg of plasmid DNA was then added to the OptiMEM solution. This was then incubated at room temperature for 15 minutes before being added dropwise to each well.

2.1.4 siRNA transfection

All siRNA treatments were performed the day after cell seeding. For USP31 knockdowns, more cells were seeded in comparison to the control treatments due to slower growth and greater cell death occurring following transfection, to ensure equal confluency during the experiment. All siRNA protocols were performed using Lipofectamine RNAiMAX transfection reagent, in accordance with the manufacturer's protocol. For treatment of 6-well plate or 35 mm ibidi dishes, 83 µl OptiMEM was combined with 2 µl RNAiMAX, vortexed and incubated for 5 minutes at room temperature. 83 µl OptiMEM was added to 2 µl of 20 µM siRNA stock (40 nM final concentration) in parallel and also incubated for 5 minutes. Solutions were then combined, vortexted and incubated at room temperature for 20 minutes. 830 µl fresh culture media was added to each dish before the siRNA solution was added dropwise to a final volume of 1 ml. The reaction was added to cells for 24 hours before the media was exchanged. Reaction volumes were scaled up for use in larger dishes. Details of oligonucleotides used can be found in Table 2.1.

Table 2.1 – siRNA oligo sequences

Target	Cat. No.	Oligo name	Sequence
Non-targeting	D-001810-01	NT1	TGGTTTACATGTCGACTAA
ATAT1	L-014510-02	ATAT1	GUAGCUAGGUCCCGAUAUA GAGUAUAGCUAGAUCCCUU GGGAAACUCACCAGAACGA CUUGUGAGAUUGUCGAGAU
RMDN3	J-020973-10	RMDN3-10	CCUUAGACCUUGCUGAGAU
SVBP	J-032124-19	SVBP-19	GGAUAAAUCUGAACUCACU
TRIM3	L-006931-00	TRIM3	GUACAGCACAGGCGGCAAA, GCACAUAUGAGCUAGUGUA, GAGCGCCACUGCACACGAA, GAAUGAAAUUGUAGUAACG
USP31	SI00758415	Q1	CCCGAAATATTTAGGCCTGAA
USP31	SI00758429	Q4	GAGCGTCATCATCAGCCTCAA

2.1.5 Live cell imaging

Live cell imaging experiments were performed using either a 3i Marianas spinning disk confocal microscope (3i Intelligent Imaging innovations, Germany) or a NIKON Ti-Eclipse microscope, as specified in the resultant figure legends. All experiments took place in a humidified chamber at 37 °C with 5 % CO_2. For imaging on the Marianas spinning disk confocal microscope cells were seeded into 35 mm ibidi dishes and imaged using either a Plan-Apochromat 40x/1.3NA Oil Objective or a Plan-Apochromat 63x/1.4NA Oil Objective. For confocal images, the range and step size used is indicated in individual figures. For imaging on the NIKON TI-Eclipse, cells were seeded into 6 well plates and imaged using a CFI Plan Fluor ELWD ADM 20x objective. Perfect Focus System (PFS) was employed to ensure focus was maintained during long imaging series.

2.1.6 Fixed cell imaging

A NIKON TI-Eclipse microscope was used to acquire fluorescence images using either a CFI Plan Apo 40x objective or a CFI Plan Apochromat VC 60X objective lens. Confocal images were acquired using either a Marianas 3i spinning disc confocal microscope (3i, Intelligent Imaging Innovations, Germany) with a Plan-Apochromat 40x/1.3NA Oil Objective or a Plan-Apochromat 63x/1.4NA Oil Objective M27, or using

a Zeiss LSM900 with Airyscan confocal laser scanning microscope using a 63x x 1.4 NA Zeiss Plan Apochromat objective.

2.1.7 Drug treatments

All drug treatments were carried out in normal culture medium. Nocodazole was used at 100 ng/ml for synchronisation and 6 µM for microtubule depolymerisation. Taxol was used at 6 µM for microtubule stabilisation and 0.5 µg/ml for accumulation of modifications. All other drugs were used at the following concentrations: 2 mM thymidine, 5 µM MG132, 10 µM RO3306, 10 µM ZM447439, 100 nM BI2536, 100 µg/ml cycloheximide. The duration of treatments is detailed in respective figure legends.

2.1.8 Microtubule cold-induced polymerisation

To depolymerise microtubules using cold conditions, cells were incubated on ice on a metal plate inside the cold room at 4 ºC for 1 hour before being fixed with ice cold methanol for immunofluorescence as described (section 2.4.7).

2.1.9 MitoTracker™ Green FM staining

MitoTracker staining was performed as suggested in the manufacturer's instructions. Cells were seeded at the desired density into 35 mm glass-bottomed ibidi dishes and any prior treatment was carried out. On the day of imaging, fresh medium containing 50nM MitoTracker™ Green FM (Invitrogen, M7514) was added an hour before imaging. Media was exchanged to fresh DMEM before cells were transferred to the 3i Marianas spinning disk confocal microscope for live cell imaging. See section 2.1.5 for further details.

2.1.10 Cell synchronisation

For experiments requiring cells within a specific period of the cell cycle, cells were synchronised via 2 different methods. Cells were seeded in 10 cm dishes and incubated for 2 days until at least ~ 80% confluent before initiating synchronisation. For collection of cells within G1/S, S or G2 phase, cells were synchronised via double thymidine block. 2 mM thymidine was added to the cell culture medium and incubated for 16 hours. Thymidine was released using fresh medium for 8 hours before adding a further 2 mM for a further 16 hours. Cells were then released again into fresh

medium and then collected at G1 (0 hours), G1/Early S (2.5 hours), Late S (5.5 hours) or G2 (7.5 hours) and lysed in 8 M urea as described in section 2.4.2. For collection of cells in mitosis, with cells being synchronised and held at the prometaphase stage, cells were treated with 2 mM thymidine for 24 hours followed by release from thymidine into fresh medium containing 100 ng/ml nocodazole for 16 – 18 hours. To perform mitotic shake-off the current medium was used to wash the surface of the plate to detach rounded-up, prometaphase-arrested cells for collection whilst leaving behind adherent non-dividing cells. Mitotic cells were collected in falcon tubes and centrifuged at 200 g for 5 minutes to pellet the cells before resuspending in warmed fresh medium to release from nocodazole. The pellet was washed a further 2X in fresh medium before a final resuspension in DMEM containing 25 mM HEPES. Samples were either lysed immediately or incubated in a water bath at 37 °C for specified time points to allow cells to re-enter into mitosis before being lysed.

2.2 Analysis

2.2.1 Microtubule network density

Microtubule network density was analysed in Fiji by applying a threshold value to the images based on the control sample. This allows for the microtubule network to be visualised and the background to be excluded. Individual cells were drawn around and the area which had no signal (the empty space between microtubule lattices) was measured.

2.2.2 Corrected total cell fluorescence

The corrected total cell fluorescence (CTCF) of the microtubule network was analysed using Fiji. Cells were manually drawn around and area, integrated density and the mean grey value were selected and measured using the 'analyse' command. The same measurements were acquired for the background of each image: 3 separate background areas were selected, and the mean values calculated. The CTCF was then calculated using the following equation:

CTCF = integrated density – (area of selected cell x mean fluorescence background)

2.2.3 MiNa plugin analysis

The MiNa (Mitochondrial Network Analysis) plugin (Valente et al., 2017) for Fiji was utilised to characterise the interconnectivity of both the mitochondria and the

acetylated microtubule network. Both antibody stains can be recognised by the plugin as show in Figure 2.1. Individual cells were manually drawn around and the plugin applied to each individually. A contrast image is first generated before being converted into a binary image of the morphological skeleton which can then be analysed. Upon analysis, 9 different parameters are provided which can be used to interpret the connectivity of both the microtubule and mitochondrial network. Parameters used for the analysis here include the 'footprint' which shows the area of the cell that is occupied by signal, the 'mean branch network' which shows the mean number of branches per network and the branch length.

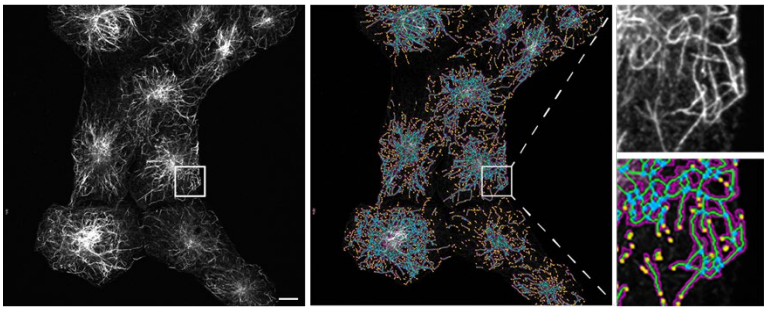

Figure 2.1 – MiNa plugin analysis of acetylated tubulin network

Example image. U2OS cells were fixed with ice cold MeOH and stained for acetylated tubulin. Images were acquired using a 3i spinning disc confocal microscope. The MiNa plugin in Fiji has been used to assess the acetylated tubulin network connectivity. The original image (left) and the overlayed image mapping the detected network (right) are shown. Scale bar = 10µm.

2.2.4 Colocalisation analysis

The colocalisation of 2 proteins visualised by immunofluorescence was analysed using the JalCoP plugin in Fiji (Bolte and Cordelières, 2006). Individual cells in both channels being analysed were manually drawn around and the Pearson's correlation coefficient was calculated.

2.2.5 Statistical analysis

For western blot quantifications, band intensities were measured using Image Studio Software. Intensity levels of INCENP expression during live-cell imaging was measured using ImageJ software. All statistical analysis was carried out using GraphPad Prism. Error bars: mean± SD. ns>0.05, *p≤0.05, **p≤0.01, ***p≤0.001, ****p≤0.0001).

2.3 Molecular Biology

2.3.1 Reagents

The HiSpeed Maxiprep kit (12633), HiSpeed Midi kit (12643), Miniprep kit (27106), QIAquick Gel Extraction Kit (28704), RNeasy Mini kit (74106), QIAshredder (79656) and the RNAse-free DNase set (79254) were purchased from Qiagen. Molecular biology grade ethanol and isopropanol were purchased from Sigma Aldrich. All primers for qPCR and cloning were ordered from Eurofins Scientific. All restriction digest enzymes, T4 DNA ligase reagents (M0202), 1kb DNA ladder (N3232) and 100bp DNA ladder (N3231) were ordered from New England Biolabs. TAE buffer was purchased from National Diagnostics. S.O.C. medium (1554-034), DH5α subcloning efficiency cells (18265-017), One Shot™ TOP10 chemically competent *E.coli* cells (C404006) SYBR Safe DNA gel stain (S33102) and electrophoresis grade agarose were purchased from Invitrogen. XL1-Blue supercompetent cells (200236), deoxynucleotide mix (PCR-grade, 100nM, 200415), Pfu Ultra II Fusion HF DNA polymerase (600670). PCR nucleotide mix (C1441) and RNasin plus RNAse inhibitor (N2611) were purchased from Promega alongside standard PCR reagents. Reverse transcriptase (10121360) and Reverse transcriptase buffer (10512703) were purchased from Fisher Scientific (Loughborough, UK). iTaq Universal SYBR Green Supermix was purchased from Bio-Rad. Nuclease free water (W4502) and all other required chemicals were purchased from Sigma-Aldrich.

2.3.2 PCR for cloning and subcloning

For this work, I generated EGFP-tagged versions of the proteins RMDN3 and LGALSL, and EGFP-tagged full length and truncations of TRIM3. The workflow for this procedure is illustrated in Figure 2.2 using GFP-TRIM3 as an example. The same steps were performed for all constructs generated. For this, the open reading frames (ORF) were amplified by PCR using the plasmids containing the construct DNA as a template. pBluescriptR-LGALSL was purchased from Horizon Discovery, pCMV5D-RMDN3-HA was purchased from MRC-PPU, Dundee, and the pcDNA3X(+)MyEGFP-mTRIM3 was a generous gift from Prof. Germana Meroni, Trieste. The primers used for amplification contained overhangs at the 5' ends with BglII being added within the sense primer, and SalI being added within the anti-sense primer in all instances. The reaction mix shown in Table 2.2 was prepared and incubated within the thermocycler for the specified times and temperatures described in Table 2.3. The full PCR products were then resolved on an agarose gel alongside molecular weight markers to confirm the product was the expected size. The band was excised and purified

using a DNA gel extraction before being incorporated into a pCR4-TOPO vector backbone and transformed into bacteria using the procedures described in section 2.3.5 and 2.3.6. Transformed bacteria pCR4-TOPO vectors were subjected to miniprep extraction and then analysed for the correct PCR insert product via diagnostic restriction digestion as described in section 2.3.8 and sequencing at the DNA Sequencing Service (MRC-PPU, Dundee). Correct products and the pEGFP-C1 or the pEGFP-N3 backbone, as required, were then digested using BglII and SalI to generate complementary overhangs before being resolved in an agarose gel for extraction of corresponding band. Gel extraction purification kit was used to purify the linearised pieces before being ligated together as described in section 2.3.9 to generate GFP-tagged constructs. All constructs were fully sequenced at MRC-PPU, Dundee as mentioned.

Table 2.2 – Reaction mix for PCR-up

Per reaction	µl
Water	Adjusted
10X Pfu Buffer	5
dNTPs (25 mM)	0.5
Primer Forward (10 mM)	1
Primer Reverse (10 mM)	1
DNA template (50 ng)	Adjusted
HS Ultra-II Pfu fusion	1
DMSO (5% final)	2.5
Total	50 µl

Table 2.3 – PCR thermocycler programme for PCR-up

No. of cycles	Temperature (ºC)	Time (minutes)
1	95	2
30	95	0.5
	55	0.5
	72	1
1	72	3

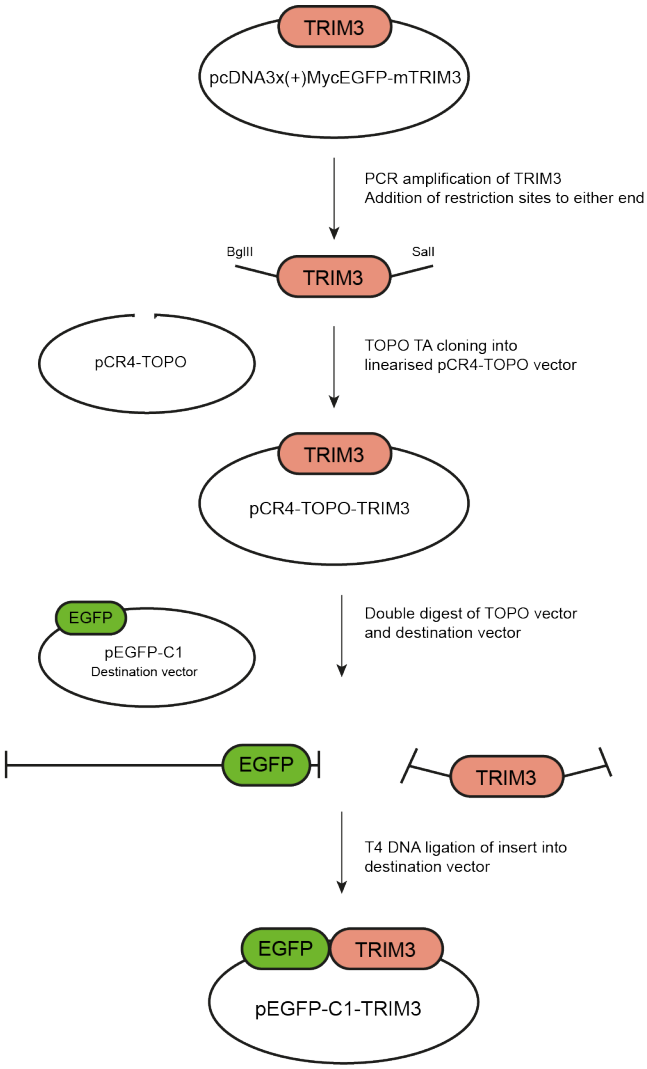

Figure 2.2 – Schematic for the cloning process for GFP-tagged constructs

The construct of interest (TRIM3 in this case) was amplified by PCR from the pcDNA3X(+)MycEGFP-mTRIM3 plasmid (gifted from Prof. Germana Meroni). Designed primers included a BglII restriction site at the 5' end and SalI site at the 3' end. The products were first incorporated into a pCR4-TOPO vector before being digested and ligated into the pEGFP-C1 vector.

2.3.3 Overlapping PCR

Overlapping PCR was used to make the TRIM3 deletion constructs, where domains within the middle of the protein where removed. Primers were designed to flank either side of the region to be deleted. An initial round of PCR was used to amplify two separate fragments: one for each end of the construct, stopping at either the start of the end of the region to be deleted. The protocol used is shown in Table 2.4. Products were then mixed together, and primers were added to allow for amplification of the full length. The amplified sequence was then inserted into a TOPO vector (2.3.5),

transformed into bacteria (2.3.6), digested using restriction enzymes incorporated into the 5' and 3' end primers (2.3.8) and finally ligated into the pEGFP-C1 vector (2.3.9).

Table 2.4 – PCR thermocycler programme for overlapping PCR

No. of cycles	Temperature (ºC)	Time (minutes)
1	95	2
25	95	0.5
	55	0.5
	72	1
1	72	10

2.3.4 Site directed mutagenesis

For introduction of point mutations, site directed mutagenesis (SDM) was performed using sense and anti-sense primers designed to contain the desired mutation and where possible, silent mutations to introduce or abolish restriction sites as a diagnostic. The reaction mix shown in Table 2.5 was prepared and incubated within the thermocycler for the specified times and temperatures described in Table 2.6. The reaction was then placed on ice before being treated with 1 µl of DpnI restriction enzyme for 1 hour at 37 ºC to digest the original plasmid. This original plasmid is targeted due to it being methylated from being produced in bacterial cells, whereas the produced product is not. The SDM product was then transformed into XL1-Blue competent bacterial cells as described in section 2.3.6. Linear PCR products transformed into bacteria will be repaired to form a circular plasmid.

Table 2.5 – Reaction mix for SDM

Per reaction	µl
Water	Adjusted
10X Pfu Buffer	5
dNTPs (25 mM)	0.5
Primer Forward (10 mM)	1
Primer Reverse (10 mM)	1
DNA template (50 ng)	Adjusted
HS Ultra-II Pfu fusion	1
DMSO (5% final)	2.5
Total	50 µl

Table 2.6 – PCR thermocycler programme for SDM

No. of cycles	Temperature (ºC)	Time (minutes)
1	95	2
18	95	0.5
	55	1
	72	9

Table 2.7 – Primers used for cloning

Gene	Primer no.	Used for	Sequence
TRIM3	3082	PCR-up	F- AGATCTGGGGAGCACCGTGAACAC
TRIM3	3083	PCR-up	R- GTCGACCTACTGGAGGTATCGATAGGCCTTAAAG
TRIM3	3084	PCR-up	F- AGATCTATGGCAAAGAGGGAGGACAGC
TRIM3	3085	PCR-up	R- GTCGACCTACCCCAGGTTGAGCACCGA
TRIM3	3086	PCR-up	F- AGATCTATGGCAAAGAGGGAGGACAG
TRIM3	3087	PCR-up	R- GTCGACCTACTGGGCATTCTCATGTGGC
TRIM3	3150	PCR-up	AGATCTATGGCAAAGAGGGAGGACAGCCC
TRIM3	3151	PCR-up	GTCGACCTAGGAAGGTGGCAGGTCCCCAG
TRIM3	3152	PCR-up	GTCGACCTATTCGTCTTCAATTGGATTGTCCTTC
TRIM3	3157	PCR-up	AGATCTGCCCAGCTGGAACTGGTC
TRIM3	3158	PCR-up	AGATCTGGGGCACTGCTCACCACCAG
TRIM3	3316	PCR-up	AGATCTCTCGTCTTTCGTGTTGGTAGTC
TRIM3	3153	Overlap	GATCGGTGCTCAACCTGGGGGCATCCCCAGATGATGTGAAGCG
TRIM3	3154	Overlap	CGCTTCACATCATCTGGGGATGCCCCCAGGTTGAGCACCGATC
TRIM3	3155	Overlap	CTGGAACTGGTCCTTGAAAACCTGGGGGCACTGCTC
TRIM3	3156	Overlap	GAGCAGTGCCCCCAGGTTTTCAAGGACCAGTTCCAG
LGALSL	3088	PCR-up	AGATCTATGGCGGGATCAGTGGCCGAC
LGALSL	3089	PCR-up	GTCGACTCAGCCAAGCTTGGTGATCTGGAGG
RMDN3	3090	PCR-up	AGATCTATGTCTAGACTGGGAGCCCTG
RMDN3	3091	PCR-up	GTCGACTCAGTCTCGTAAAATGACTTCCAGTTC
RMDN3	3365	PCR-up	AGATCTACCATGTCTAGACTGGGAGCCCTG
RMDN3	3366	PCR-up	GTCGACAGCGGCCGCGTCTCGTAAAATGACTTC
RMDN3	3367	PCR-up	AGATCTACCATGGGCCGCAGCCAGAGCCTGCCCAAC
USP31	2979	SDM	GATTATCATAGACTGTCTGCTCCTACACAAACAGCAGCAAAGC
USP31	2980	SDM	GCTTTGCTGCTGTTTGTGTAGGAGCAGACAGTCTATGATAATC
USP31	2981	SDM	GATTATCATAGACTGTCTGAACCTACACAAACAGCAGCAAAGC

USP31	2982	SDM	GCTTTGCTGCTGTTTGTGTAGGTTCAGACAGTCTATGATAATC
USP31	2983	SDM	CCTGTCTGCAAAGCTGCAGATGCGCTCCAATGCTCCATCCCG
USP31	2984	SDM	CGGGATGGAGCATTGGAGCGCATCTGCAGCTTTGCAGACAGG
USP31	2989	SDM	GATGCGCTCCAATGAACCATCGCGATTTTCAGG
USP31	2990	SDM	CCTGAAAATCGCGATGGTTCATTGGAGCGCATC
USP31	2993	SDM	GAGCGACTCCGTCGACAGCGCTCCAGTCAAAGAGG
USP31	2994	SDM	CCTCTTTGACTGGAGCGCTGTCGACGGAGTCGCTC
USP31	2997	SDM	GAGCGACTCCGTCGACAGCGAACCAGTCAAAGAGG
USP31	2998	SDM	CCTCTTTGACTGGTTCGCTGTCGACGGAGTCGCTC

2.3.5 TOPO TA cloning

TOPO TA cloning allows for direct insertion of PCR products into a plasmid vector to allow for sequencing and easy 'cut and paste' into multiple vector backbones. 2 µl of freshly produced PCR products were combined with salt solution containing 200 mM NaCl, 10 mM $MgCl_2$ and water to make the reaction mix up to 6 µl. 1 µl of the linearised TOPO vector (pCR4-TOPO) was then added, and the reaction was incubated for 5-15 minutes at room temperature. This reaction was then transformed into One Shot Top10 competent cells as described in 2.3.6

2.3.6 Bacterial transformation and glycerol stocks

DH5α *Escherichia coli* were primarily used for transformation of DNA. For site directed mutagenesis, XL1-Blue competent cells were used, and One stop TOP10 competent cells were used when transforming in DNA from TOPO TA cloning procedures or ligations. Cells were thawed on ice then incubated with 2 µl (~ 100 ng) specified plasmid for 30 minutes. Heat shock at 42°C was performed for 20-45 seconds in a water bath (dependent on the cells used, following manufacturers instructions), followed by 2 minutes incubation on ice. 250 µl of SOC medium was then added and cells were incubated at 37°C for 1 hour at 250 rpm. Cells were then distributed onto Luria broth [LB; 1% Bacto™ tryptone, 0.5% yeast extract, 1% NaCl] plates supplemented with 1.5% agar and either 50 µg/ml kanamycin or 100 µg/ml ampicillin and grown overnight at 37°C. Single colonies were selected and suspended in 5ml LB supplemented with antibiotic in sterile falcon tubes and incubated in a shaker at 37°C overnight. A proportion of bacteria was then subjected to DNA extraction via Qiagen MiniPrep kit for confirmation of plasmid first via restriction digestion, followed by DNA Sequencing Service (MRC-PPU, Dundee). The remaining culture, if confirmed positive, was then transferred to larger flasks of 100-250 ml LB

supplemented with antibiotic and incubated overnight in a shaker at either 30 or 37°C. 500 µl was combined with 500 µl 40% glycerol and stored at -80°C for future use, whilst the rest of the culture was used for further DNA extraction via Qiagen MiniPrep or a MaxiPrep kit.

2.3.7 Agarose gel electrophoresis

DNA plasmids and fragments were suspended in 1X DNA loading buffer (*Bioline:* 5% w/v glycerol, 0.1 mM EDTA, 0.04% w/v bromophenol blue) before being resolved on agarose gel for their analysis. Electrophoresis grade agarose was suspended in 100ml Tris-acetate-EDTA buffer (TAE; 40 mM Tris-base, 20 mM acetate, 1 mM EDTA) and heated in the microwave until agarose had dissolved. Upon brief cooling of the mixture, SYBR™ Safe DNA Gel Stain (1:10,000) dilution was added before pouring the mixture into a mould and left to set. Samples were loaded alongside Quick-Load Purple 2-log DNA ladder and resolved at 136 V in horizontal midi electrophoresis tanks (Fisher Scientific) in TAE buffer for ~ 45 minutes. DNA bands were visualised using ultraviolet light.

2.3.8 Restriction digestion

Restriction digestion was performed to confirm successful transformation and purification of plasmids, in addition to cutting out fragments prior to ligations. Individual reactions were adjusted to accommodate the selected restriction enzyme(s) but usually consisted of 1 µg DNA, 1X NEB CutSmart Buffer or 1X NEB 3.1 buffer, 10 units enzyme then incubated for at least 90 minutes at 37 °C. Enzymes used were purchased from NEB.

2.3.9 Ligation

For ligations, the insert of interest was digested from the pCR4-TOPO vector backbones they were previously placed in, described in section 2.3.5, and digested with BglII and SalI overnight. The pEGFP-C1 and pEGFP-N3 vectors were also digested overnight with the same restriction enzymes to make complementary overhangs (see section 2.3.8 for restriction digestion protocol). The linearised pieces were resolved on agarose gel to confirm successful digestion from the TOPO vectors, and the desired bands were cut out and subjected to gel extraction protocol following the manufacturer's instructions. The inserts of interest were then ligated together with the backbone using a T4 DNA ligase enzyme and incubated at room temperature for

10 minutes. Heat inactivation was carried out at 65 ºC for 10 minutes before being transformed into DH5α, TOP10 or XL1 Blue bacterial cells as described in section 2.3.6.

2.3.10 mRNA extraction and reverse transcription

mRNA was extracted from U2OS cells using the RNeasy mini kit as per the manufacturer's instructions. (RNease Mini kit, Qiagen). DNase incubation was performed during this procedure to prevent contamination from genomic DNA. The concentration and quality of the extracted mRNA was measured using a NanoDrop Spectrophotometer ND100 at 260 nM. 1 µg of mRNA was then used to carry out reverse transcriptase reaction to form cDNA. This was combined with 1 µl Oligo DT primers in a total volume of 11 µl and was incubated at 70 ºC for 5 minutes to prime the mRNA poly(A) tails. Nucleotide mix and RNasin were then added and samples were incubated at 37 ºC for 5 minutes. 1 µl (200 units) of MuL reverse transcriptase was then added and incubated at 42 ºC for 1 hour, followed by 72 ºC for 10 minutes. Samples were then held on ice for 5 minutes before being diluted up to 100 µl with H_2O. Reaction mix is detailed in Table 2.8.

Table 2.8 – Reaction mix for reverse transcriptase

Per reaction	Volume
5x Reverse Transcription buffer	4 µl
PCR nucleotide mix	2 µl
RNasin	0.5 µl
Nuclease free ddH_2O	1.5 µl

2.3.11 Quantitative real-time polymerase chain reaction (qRT-PCR)

To ensure the designed primers amplified only one amplicon of the desired size, primers were first tested using end-point PCR. Primers used are detailed in Table 2.9. Following primer confirmation, a reaction mixture was prepared for each primer set as described in Table 2.10 and 6 µl was added to each well of a white bottomed qPCR plate. 4 µl of the cDNA was then added and mixed by pipetting. qPCR was then performed using a CFX connect Real-time PCR detection system (Bio-rad) following the protocol as described in Table 2.11. The Ct values were analysed after 40 cycles by normalising to a house-keeping gene GAPDH to give ΔCt, transformed to $2^{-\Delta Ct}$ and then normalised to the control sample.

Table 2.9 - Primers used for RT-qPCR

Gene	Primer no.	Fw/Rv	Sequence
GAPDH	2100	Fw	CAATGACCCCTTCATTGACC
	2101	Rv	GACAAGCTTCCCGTTCTCAG
ATAT1	3368	Fw	GGCCCAGAATCTTTCCGCTC
	3369	Rv	GATGCAAAGTGGTTCTACCTCAT
TRIM3	3374	Fw	GTAGTAACGGACTTCCATAACC
	3375	Rv	TTCCATTGGAGTCCACAGCTAC

Table 2.10 – Reaction mix for qPCR

Per reaction and set of primers	Volume
H_2O	0.4 µl
iTaq universal SYBR Green supermix	5 µl
Forward primer (10µM)	0.3 µl
Reverse primer (10µM)	0.3 µl

Table 2.11 – Thermocycler programme for qPCR

No. of cycles	Temperature (ºC)	Time
1	95	3 minutes
40	95	10 seconds
	60	30 seconds
1	72	10 minutes

2.4 Biochemistry

2.4.1 Materials and Reagents

The majority of chemicals used were purchased from Sigma-Aldrich along with Bovine IgG (immunoglobulin B), Ponceau stain (P7170), Goat Serum Donor Herd (G6767), 2-mercaptoethanol (M6250) and mammalian protease inhibitors (P8340). BCA protein assay kit (23225) was ordered from Pierce Biotechnology (Rockford, IL, USA). Pierce™ 660nm protein assay kit (22662) was purchased from Thermo Fisher Scientific. NuPAGE Novex 4-12% Bis-Tris Gels (NP0321BOX, NP0322BOX, WG1402BOX), NuPAGE 3-(N-morpholino)propanesulfonic acid (MOPS) running buffer, SimplyBlue SafeStain (LC6060), DAPI (4'6-Diamidino-2-Phenylindole Dihydrochloride) (D1306) were purchased from Invitrogen (Paisley, UK). Amersham

Protran 0.45 µm nitrocellulose membrane (10600002) was purchased from GE healthcare. Mowiol (475904) was purchased from Merck Millipore (Darmstadt, Germany). Unstained broad range marker (P7704) was obtained from New England Biolabs. Full-range Rainbow™ molecular weight marker (RPN800E) was purchased from VWR. Marvel skimmed milk powder was obtained from Premier Brands, UK.

2.4.2 Cell lysis

Seeded cells were treated as indicated in figures for the required length of time. Dishes were then placed on a metal place on ice and washed twice with ice cold PBS. For lysis with RIPA buffer [150 mM NaCl, 1% Triton-X100, 0.1% SDS, 1% sodium deoxycholate, 10 mM Tris-HCL pH 7.5], samples were incubated on a rocker on ice for 15 minutes. RIPA was always supplemented with mammalian protease inhibitors (1:250 v/v). For lysis with 'hot SDS lysis buffer' [1 mM EDTA, 50 mM NaF, 2% SDS], samples were washed twice at RT with PBS before 110ºC preheated buffer was added to culture cell dishes placed on a 110ºC heat block. Cells were harvested using a cell scraper and collected in screw-top tubes. Samples were then heated to 110 ºC for 10 minutes, vortexing every 2 minutes to ensure complete lysis. For lysis with 8M urea [8 M Urea, 50 mM Tris-HCl, pH 8], ice cold PBS was added to the plate and the cells scraped using a rubber policeman and collected into a falcon tube. Samples were then centrifuged at 200 g for 5 minutes and the pellet resuspended in 100 µl lysis buffer. Samples were then sonicated using a sonicating probe on ice to break down the nucleic acids (5 times x 5 seconds with 5 second intervals). For both lysis methods, samples were then centrifuged at 14,000 rpm at 4 °C for 20 minutes to pellet any cell debris. For lysis of cells collected via mitotic shake off procedure, samples to be lysed were centrifuged at 1000g for 1min, washed in ice cold PBS and centrifuged again. The pellet was then resuspended in 100 µl of either 8 M urea lysis buffer or RIPA lysis buffer, as stated, depending on the protein of interest.

2.4.3 Protein assay and sample preparation

Protein concentration of lysates was determined using either a BCA protein assay or a Pierce 660 nm protein assay depending on what lysis buffer was used (for compatibility reasons), following the manufacturer's instructions. Both assays were performed in a 96-well plate. For the BCA, a standard curve was produced using Millipore water, the corresponding lysis buffer and Bovine IgG (1 mg/ml). Bovine IgG was used in 2 µg intervals between 0-10 µg and was carried out in duplicate. Pierce BCA/$CuSO_4$ solution (1:50) was then added and incubated for 30 minutes at 37ºC.

Absorbance was then measured at 562 nm. For the Pierce 660 nm, a standard curve was produced using the premade standards of Bovine serum albumin (BSA) diluted in 0.9% sodium chloride with sodium azide at the following µg/ml concentrations: 125, 250, 500, 750, 1000, 1500 and 2000. Pierce 660 nm reagent was then added for 5 minutes and absorbance was measured at 660 nm. Samples were assayed in triplicate for both assays and measurements were taken using a plate reader (Multiskan spectrum, Thermo Labsystems). The samples were then adjusted to equal concentrations using additional lysis buffer before being resuspended in 5X sample buffer [15 % SDS (w/v), 50 % glycerol, 16 % β-mercaptoethanol, 1.25 % bromophenol blue, 312.5 mM Tris HCl pH 6.8]. 'Hot lysis' samples were resuspended in hot lysis sample buffer [7 % SDS, 50 % glycerol, 16 % β-mercaptoethanol, 1.25 % bromophenol blue, 312.5 mM Tris HCl pH 6.8

2.4.4 Sodium dodecyl sulphate-polyacrylamide gel electrophoresis (SDS-PAGE)

All samples were suspended in 5X sample buffer, boiled (95 °C, 5 minutes) and either used straight away or retained at -20 °C until required. 10-20 µg protein (unless stated) was resolved with molecular weight markers on precast NuPAGE Novex 4-12% Bis-Tris Gels in 3-(*N*-morpholino)propanesulfonic acid (MOPS) buffer (*Invitrogen*). Electrophoresis was performed at 160 V until the bromophenol blue had just migrated off the gel. Gels were either subjected to western blotting procedures or Coomassie staining.

2.4.5 Coomassie staining

Samples resolved using SDS-PAGE were stained for 1 hour with SimplyBlue™ SafeStain (Invitrogen) before destaining in either distilled or HPLC water for 1 hour. Fresh water was then applied and left overnight. Gels were imaged using LI-COR Odyssey Imaging Software at 700 nm.

2.4.6 Western blotting

Samples resolved using SDS-PAGE were transferred to 0.45 nm nitrocellulose membrane (0.9A, 1 hour) in transfer buffer [0.2 M Glycine, 25 mM Tris, 20% methanol] then stained with Ponceau S to confirm successful transfer. Membranes were incubated in blocking solution (Tris buffered saline [TBS: 150 mM NaCL, 10 mM Tris, pH 7.5] supplemented with 0.1% Tween-20 [TBST, v/v], and 5% non-fat milk [w/v]) for

1 hour to prevent non-specific binding of antibodies. For some antibodies, blocking and antibody incubation was performed using 5% bovine serum albumin (BSA) in TBST. Membranes were then incubated with primary antibodies at times and concentrations specified in Table 2.12. Membranes were then washed X3 for 5 minutes in TBST before incubating in IRDye-conjugated secondary antibodies (detailed in Table 2.13) in blocking solution for 1 hour. Membranes were scanned using a LI-COR Odyssey Imaging Software at 800 nm or 680 nm for visualisation. Band intensities were quantitated using Image Studio Lite.

Table 2.12 – Primary antibodies used for western blotting

Protein	Species	Company	Catalogue	Conditions
a-tubulin	M	Sigma Aldrich	T5168	1:10,000 1hr
b-tubulin	R	Abcam	ab6046	1:500 o/n
Acetylated tubulin	M	Sigma Aldrich	T6793	1:1000 o/n
Actin	M	Proteintech	66009-1-Ig	1:10,000 1hr
Actin	R	Proteintech	20536-1-AP	1:10,000 1hr
ATAT1	R	Proteintech	28828-1-AP	1:500 o/n
Aurora B	M	BD Transduction	611083	1:1000 o/n
Borealin	M	Santa Cruz	SC-376635	1:1000 o/n
CDC27	M	BD Transduction	610454	1:1000 o/n
Cyclin A2	R	Abcam	ab32386	1:1000 o/n
Cyclin B1	M	Abcam	ab05373	1:1000 o/n
Detyrosinated tubulin	R	Abcam	ab48389	1:1000 o/n
DYNC1LI1	R	Atlas	HPA035013	1:1000 o/n
EB1	M	BD Transduction	610535	1:1000 o/n
EML4	R	CST	12156S	1:1000 o/n
GAPDH	R	Cell Signaling	2118S	1:1000 o/n
GFP	Sh	Home made	n/a	1:1000 o/n
H3-pSer10	M	Millipore	05-806	1:1000 o/n
HDAC6	M	Santa Cruz	SC-133106	1:500 o/n
INCENP	M	Santa Cruz	SC-376514	1:1000 o/n
KLHL21	R	Proteintech	16952-1-AP	1:1000 o/n
MAP4	R	Bethyl	A301-488A	1:1000 o/n
MKLP1	R	Abcam	ab174304	1:1000 o/n

MKLP2	R	Bethyl	A300-879A	1:1000 o/n
RMDN3	R	Atlas	HPA009975	1:1000 o/n
SAMM50	R	Abcam	ab133709	1:1000 o/n
Survivin	R	Novus Biologicals	NB500-201	1:1000 o/n
SVBP	R	Novus Biologicals	NBP1-81071	1:1000 o/n
TRIM3	R	Proteintech	28392-1-AP	1:1000 o/n
TTL	R	Proteintech	13618-1-AP	1:1000 o/n
USP31	M	Santa Cruz	SC-100634	1:200 o/n
VASH1	M	Santa Cruz	SC-365541	1:1000 o/n
VASH2	R	Abgent	AP13956b	1:1000 o/n

Table 2.13 – Secondary antibodies used for Western Blotting

Secondary Antibody	Company/ Catalogue	Conditions
Donkey anti-mouse IRDye 800CW	LICOR, 926-32212	1:10,000, 1h, RT
Donkey anti-mouse IRDye 680LT	LICOR, 926-68022	1:10,000, 1h, RT
Donkey anti-rabbit IRDye 800CW	LICOR, 926-32213	1:10,000, 1h, RT
Donkey anti-rabbit IRDye 680LT	LICOR, 926-68023	1:10,000, 1h, RT
Donkey anti-goat IRDye 800CW	LICOR, 926-32214	1:10,000, 1h, RT
Donkey anti-goat IRDye 680LT	LICOR, 926-68024	1:10,000, 1h, RT

2.4.7 Immunofluorescence

Cells were seeded onto 22 mm square coverslips in 6-well plates and cultured overnight under standard cell culture conditions. Cells were then fixed with ice cold methanol at -20 °C for 5 minutes to permeabilise and fix the cells. Cells were immediately washed in PBS before non-specific sites were blocked using 10% goat serum in PBS for 30 minutes. Primary antibodies in 5% goat serum were then applied at concentrations indicated in Table 2.14 and incubated for 1 hour. Coverslips were washed X3 for 4 minutes in PBS before incubating in Alexa-Fluor 488- and Alexa-Fluor 594- conjugated secondary antibodies in 5% goat serum (1:1000, 30 min). Coverslips were again washed 3X for 4 min in PBS before finally washing in Millipore water. Mowiol supplemented with DAPI was then used to mount to the coverslips to glass slides, which were left to dry overnight.

Table 2.14 – Primary antibodies used for immunofluorescence

Protein	Species	Company	Catalogue	Conditions
a-tubulin	Rat	Bio-Rad	MCA77G	1:500
b-tubulin	R	Abcam	ab6046	1:500
Acetylated tubulin	M	Sigma Aldrich	T6793	1:1000
Aurora B	M	BD Transduction	611083	1:1000
Borealin	M	Santa Cruz	SC-376635	1:1000
Detyrosinated tubulin	R	Abcam	ab48389	1:1000
DYNC1LI1	R	Atlas	HPA035013	1:1000
EB1	M	BD Transduction	610535	1:1000
HA	M	Covance	MMS-101P	1:500
HRS	R	Homemade	958/3	1:1000
INCENP	M	Santa Cruz	Sc-376514	1:50
MAP4	R	Bethyl	A301-488A	1:1000
Pericentrin	R	Abcam	ab4448	1:1000
Phalloidin-594	-	Invitrogen	A12381	1:2000
RMDN3	R	Atlas	HPA009975	1:200
TOMM20	M	BD Transduction	612278	1:500
TOMM20	R	Sigma Aldrich	HPA11562	1:500

Table 2.15 – Secondary antibodies used for immunofluorescence

Secondary Antibody	Company/ Catalogue	Conditions
Donkey anti-mouse AF488	Invitrogen	1:1000, 30 min, RT
Donkey anti-mouse AF594	Invitrogen	1:1000, 30 min, RT
Donkey anti-rabbit AF488	Invitrogen	1:1000, 30 min, RT
Donkey anti-rabbit AF594	Invitrogen	1:1000, 30 min, RT
Donkey anti-rat AF594	Invitrogen	1:1000, 30 min, RT

2.4.8 Initial microtubule extraction protocol

Cells were treated with 6 µM of Nocodazole or the equivalent volume of DMSO as a control and incubated for 30 minutes at 37 °C. The following steps were carried out in a water bath at 37 °C using buffers which were preheated to 37 °C. Cells were first washed in phosphate buffered saline (PBS) before being incubated in a microtubule stabilisation buffer [PM2G: 0.1 mM PIPES pH 6.9, 1 mM $MgSO_4$, 2 M glycerol, 2 mM

EGTA, 0.1% NP40 (v/v), 0.1% 2-mercaptoethanol (v/v)]. PM2G was added for specified times to wash away free tubulin and 75% of cell protein, lipid and small molecules, and was then retained. Excess calcium buffer [0.1 M PIPES pH 6.9, 1 mM $CaCl_2$] supplemented with 1:250 mammalian protease inhibitor (MPI) was added for 10 minutes to release the cytoskeleton. Release fractions were centrifuged at 13,500 rpm for 10 minutes at 4 °C and the supernatant retained. The remaining cells on the plates were then subjected to the hot lysis protocol.

2.4.9 Optimised microtubule extraction protocol

Cells were treated with 6 µM of Nocodazole for 1 hour or 6 µM of Taxol for 30 minutes at 37 °C alongside a DMSO control of equivalent volume. The following steps were either performed in a water bath at 37 °C using buffers which were preheated to 37 °C, or on ice using buffers precooled to 4 °C. Cells were washed in PBS before being incubated in Lysis and Microtubule Stabilisation buffer [LMS: 100 mM PIPES pH 6.9, 5 mM $MgCl_2$, 1 mM EGTA, 30% glycerol, 0.1% NP40, 0.1% Triton X-100, 0.1% Tween-20, 0.1% 2-mercaptoethanol (v/v)] supplemented with MPI (1:250) for 5 minutes and samples were collected. The remaining microtubules on the plates were then extracted using either hot lysis or 8 M urea.

2.4.10 Analysis of stable microtubules

U2OS cells were transfected with siRNA against TRIM3 and aTAT alongside a non-targeting control (NT1) as described in section 2.1.4 for 72 hr. Cells were then treated with 6 µM nocodazole for 1 hour to depolymerise the dynamic microtubules whilst maintaining nocodazole-resistant ones. Cells were then washed twice in a buffer containing PIPES, HEPES, EGTA and $MgSO_4$ [PHEM: 60 mM PIPES, 25 mM HEPES, 10 mM EGTA and 4 mM Mg SO_4] before treating cells with PHEM buffer containing 0.2% Triton-X 100 for 1 minute. This removes the cytosolic tubulin (depolymerised microtubules) whilst maintaining the intact stable microtubules. Cells were then fixed in ice cold MeOH and stained for the specified antibodies as described in section 2.4.7.

2.4.11 Lambda phosphatase treatment

For lambda phosphatase treatment, samples were lysed in 100 µl 2 % SDS lysis buffer (2 % SDS, 1 mM EDTA, 50 mM NaF) and sonicated before being subjected to a buffer exchange into lambda phosphatase buffer (150 mM NaCl, 1 mM EDTA, 1

mM EGTA, 1% Triton X-100, 20 mM Tris-HCl pH 7.5) using an Amicon® Ultra 0.5 ml Centrifugal Filter following the manufacturer's instructions. The remaining concentrated protein was rediluted using this compatible buffer back up to 100 µl and subjected to a protein assay (section 2.4.3). 20 µg of sample was made up to 40 µl for phosphatase treated samples and 5 µl NEBuffer for protein MetalloPhosphatases (PMP) and 5 µl of 10 mM $MnCl_2$ was added. 400 units of lambda phosphatase were then added to each treated sample. Control samples were made up identically but without the lambda phosphatase. Samples were incubated at 30 °C for 30 minutes then prepared in sample buffer for SDS-PAGE.

2.5 Mass spectrometry

2.5.1 Materials and reagents

DMEM for SILAC was purchased from Gibco (88364, Thermo Fisher Scientific). Dialysed Foetal Bovine Serum (FB-1001D/500) was purchased from BioSera. All amino acids were obtained from Sigma Aldrich. LowBind Eppendorf tubes (022431081) were purchased from Eppendorf (Hamburg, Germany).

2.5.2 Stable Isotopic Labelling by Amino Acids in cell culture (SILAC)

U2OS cells were cultured under standard conditions in DMEM for SILAC supplemented with 10% dialysed FBS and L-proline, Pro0 [200 µg/ml] to prevent conversion of arginine to proline. Differentially labelled amino acids were added to the media to generate 3 separate conditions: Light (L-lysine, Lys0; L-arginine, Arg0), Medium (L-lysine-$^{2}H_4$, Lys4; L-arginine-$^{13}C_6$, Arg6) and Heavy (L-lysine-$^{13}C_6$-$^{15}N_2$, Lys8; L-arginine-$^{13}C_6$-$^{15}N_4$, Arg10). L-lysine was supplemented at a final concentration of 146 µg/ml whereas L-arginine was supplemented at a final concentration of 84 µg/ml. Cells were cultured for a minimum of 6 passages and tested to confirm amino acid incorporation before experiments proceeded.

2.5.3 Cell lysis and sample preparation

Cells were seeded into 15 cm dishes and incubated for 2 days until >80% confluent. Cells were treated with 6 µM of Nocodazole for 1 hour or 6 µM of Taxol for 30 minutes at 37 °C alongside a DMSO control of equivalent volume. They were then placed on a metal plate on ice and washed twice in PBS before being incubated in Lysis and Microtubule Stabilisation buffer [LMS: 100 mM PIPES pH 6.9, 5 mM $MgCl_2$, 1 mM

EGTA, 30% glycerol, 0.1% NP40, 0.1% Triton X-100, 0.1% Tween-20, 0.1% 2-mercaptoethanol (v/v)] supplemented with MPI (1:250) for 5 minutes. LMS buffer was removed and collected before the remaining microtubules on the plates were collected using 8M urea. Extracted microtubules from each condition were combined in a 1:1:1 ratio and filtered through 15ml Amicon ultra centrifugal filters (10,000 MW) at 4000 g at RT until the minimum volume was retained.

2.5.4 In gel digest

Samples prepared in 2.5.3 were subjected to a Pierce 660 nm protein assay (section 2.4.3) to determine the protein concentration. 125 µg of protein was then resolved via SDS-PAGE (2.4.4) until proteins migrated 1/3 through the gel, followed by Coomassie staining (2.4.5). The sample lane was cut into 12 equal slices, then into 1 mm^2 cubes and destained using 50 mM Ammonium bicarbonate (Ambic) containing 50% Acetonitrile (ACN, v/v) at 37 °C in an Eppendorf ThermoMixer Compact at 900rpm. Samples were dehydrated (ACN, 5 minutes) and dried via Speedvac rotary evaporation. Peptides were reduced in 10 mM dithiothreitol (56 °C, 1 hour), alkylated in 55mM iodoacetamide (RT, 30 minutes), washed in 100mM Ambic (15 minutes) then repeated in 50 mM Ambic with 50 % ACN. Samples were dehydrated in ACN, followed by Speedvac evaporation. Peptides were cleaved with 3 µg trypsin per sample lane in 40 mM Ambic and 9% ACN (37 °C, overnight) then extracted using ACN (30 °C, 30 minutes), followed by 1 % formic acid (RT, 20 minutes) and then ACN again. Retained supernatants were dried in the speed vac overnight before freezing at -20 °C until required.

2.5.5 Mass spectrometry for phospho-proteomics

Dried peptides were resuspended in 1% (v/v) formic acid (FA) and vortexed for 2 minutes to ensure all peptides were obtained. Samples were centrifuged at 13,000 rpm for 10 minutes at 4°C to pellet cell debris. 5 µl of each sample was separated using a nanoACQUITY UPLC system (Waters), coupled to an LTQ Orbittrap XL mass spectrometer (Thermo Scientific) containing a Proxeon nanoelectrospray source. Samples were loaded onto a C18 symmetry trapping column (180 µm x 20 mm) (Waters) in 0.1% (v/v) FA and 1% (v/v) ACN at a flow rate of 10 µl/min for 5 min. Peptides were then resolved using a 25 cm x 75 µm column (Waters) using a 50-minute gradient of 7-35%m, 300 nL/min. The mass spectrometer acquired full MS survey scans in the Orbitrap (R = 30 000; m/z range 350–2000) and performed MSMS

on the top 6 multiple charged ions in the linear quadrupole ion trap (LQT) after fragmentation using collision-induced dissociation (30 ms at 35% energy). All spectra were collected using Xcalibur software (version 2.0.7, Thermo Fisher Scientific) and analysed using Maxquant version 1.6.17.0 using phosphorylation detection.

2.5.6 Luxembourg facility protocols and procedures

Samples were analysed at Luxembourg Institute of Health at the Quantitative Biology Unit through a collaboration with Professor Gunnar Dittmar. All sample preparation and MaxQuant searches were performed by Dr Marta Mendes.

2.5.6.1 Sample resuspension

Samples were desalted using C18 tips (Rappsilber et al., 2003). Briefly, samples were resuspended in 50 µl 0.1% FA. C18 tips were first activated with Methanol, equilibrated twice with 0.1% FA, then samples were loaded, and peptides were washed with 0.1% FA. Samples were then eluted with 80% ACN / 0.1% FA and dried in the speed vac. Finally, they were reconstituted in 0.1% FA.

2.5.6.2 Peptide fractionation and LC/MS injection

Peptides were fractionated on a QExactive HF Plus column coupled to a nanoHPLC Ultimate 3000 using a pre-concentration onto a nano-column configuration. An Acclaim PepMap 100 (75 µm, 2 cm) was used to do the pre-concentration and an Acclaim PepMap RSLC (Rapid separation liquid chromatography, 75 µm, 15 cm) was used for peptide separation. Total run time was of 118 minutes with a gradient from 4% to 40% Buffer B [Buffer B: 80% ACN / 0.1% FA], in the following steps: 2% for 8 minutes, 2% to 40% in 80 minutes, 90% for 10 minutes and an equilibration step with 2% for 20 minutes. The MS was operated in a data dependent manner using a loop count of 12. MS1 was acquired in a scan range from 375-1500 m/z, with a resolution of 120000, an AGC target of 3x106 and a maximum IT (injection time) of 120 ms. MS2 was acquired at a resolution of 17500, an AGC target of 1x105 and maximum IT time of 60 ms. Dynamic exclusion was set to 20s and ion with charge states of +1 and greater than +6 were excluded.

2.5.6.3 MaxQuant analysis

Searches were performed using MaxQuant, version 1.6.17.0, against the human database. Carbamidomethylation of cysteines (+57Da) was used as a fixed modification and oxidation of Methionine (+16Da) and Acetylation of the N-terminal (+42Da) as variable modifications. Multiplicity was set to 3 and the labels were as follow: Medium labels - Arg6;Lys4, Heavy labels - Arg10;Lys8.

Chapter 3 – Determination of the microtubule proteome

3.1 Introduction

Foundational studies which define the microtubule proteome predate modern techniques. The advancement of Liquid Chromatography-Tandem Mass Spectrometry (LC-MS/MS) has made the use of 2D gel electrophoresis as a means of protein separation redundant, by providing an increase in coverage and sensitivity of proteins identified via mass spectrometry. Another feature lacking in these prior attempts to define the microtubule proteome is quantitation: either no quantitative data is provided, or spectral counting is utilised. This technique is problematic due to the differences observed in the direct physical properties of each peptide not being accounted for, and the small dynamic range it achieves (Bantscheff et al., 2007). The development of quantitative techniques for mass spectrometry such as SILAC (stable isotope labelling by amino acids in cell culture) (Ong et al., 2002) and TMT (tandem mass tags) (Thompson et al., 2003), as described in section 1.4.8, have allowed for major advancements in proteomic studies by enabling direct comparisons of peptide intensities across conditions.

The aim of this work is therefore to revisit the microtubule proteome by introducing a modern approach for quantitative mass spectrometry. A new methodology, inspired by a paper published in 1981 by Ann Duerr, David Pallas and Frank Solomon (Duerr et al., 1981) will also be introduced. This method utilises differential extraction from microtubule-enriched and microtubule-depleted conditions to specifically identify microtubule binding proteins. Not only are prior attempts to establish a microtubule proteome lacking quantitative data, many are derived by performing rounds of polymerisation-depolymerisation in the presence of protein lysates (Souphron et al., 2019). This methodology utilises microtubule networks which have been assembled *in vitro*, as opposed to being obtained directly from cells. Furthermore, the use of brain extracts as a source of tubulin creates a bias towards specific tubulin isoforms, such as TUBB3 which is neuronal specific (Tischfield and Engle, 2010). Finally, taxol is frequently employed as a microtubule stabiliser, allowing for conformational changes within the microtubule lattices which may ultimately alter the binding proteins associated with them (Arnal and Wade, 1995).

I have therefore established and optimised a protocol which extracts microtubules and their binding proteins directly from cells using set criteria. Tubulin and EML4 (echinoderm microtubule-associated protein-like 4), a known microtubule binding protein (Houtman et al., 2007) were used as readouts of the dynamic range for successful optimisation. This methodology was then upscaled and mass spectrometry was performed to identify the microtubule proteome in which a number of novel microtubule binding proteins have been identified.

3.2 Expression of microtubule modifications across a cell line panel

Microtubules can be highly modified by various post-translational modifications (PTMs) as mentioned in section 1.1.10. They are thought to induce a so called 'tubulin code' which can alter the binding proteins which associate with the microtubule lattices (Gadadhar et al., 2017a). As the eventual goal was to obtain a microtubule proteome specifically for modified microtubules, a cell line expressing high levels of various microtubule PTMs was required. The levels of detyrosination and K40 acetylation of α-tubulin were therefore analysed across a variety of different cell lines. Figure 3.1 shows modification levels are variable across different cell lines, with acetylation being highest in HEK293T, MCF7, SKN-BE2 and U2OS, and detyrosination highest in U2OS and SKN-BE2. U2OS cells were selected due to their easy growth and their large flat nature which is better suited for cell imaging.

3.3 Initial trial of microtubule extraction protocol

The basic procedure used for microtubule extraction is illustrated in Figure 3.2A and consists of 1 condition being treated with a vehicle (DMSO, i, left panel) and another condition treated in parallel with a microtubule-depolymerising drug, nocodazole (i, right panel). This provides a microtubule enriched and a microtubule depleted condition respectively.

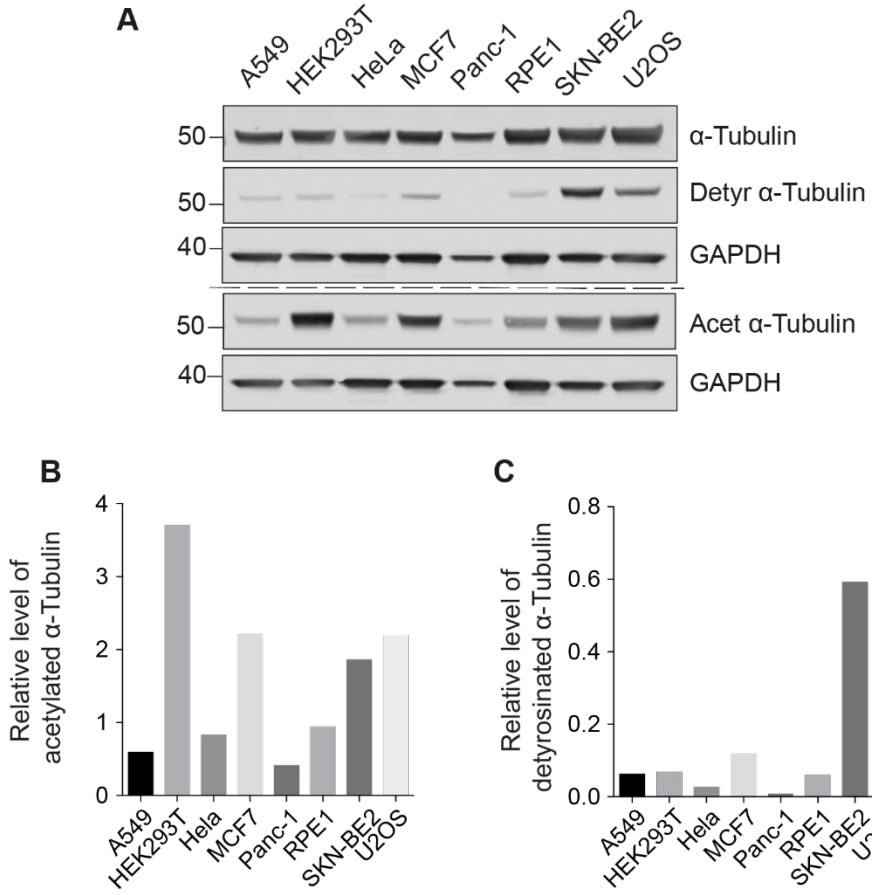

Figure 3.1 – Expression of tubulin modifications across a panel of cell lines

A: Western blot analysis of α-tubulin, acetylated α-tubulin and detyrosinated α-tubulin levels in 8 different cell lysates as indicated. GAPDH was used as a loading control. 15µg protein was loaded per well. **B&C:** Quantification of relative acetylated α-tubulin and detyrosinated α-tubulin levels respectively.

Lysis and microtubule stabilisation buffer (LMS) is then applied. LMS contains 4M glycerol for limiting the rates of polymerisation and depolymerisation (Keates, 1980), 5mM $MgCl_2$ which plays a critical role in assembly (Grover and Hamel, 1994; O'Brien et al., 1990), and 1mM EGTA for calcium chelation, as calcium causes loss of tubulin polymerisation (Sandoval and Weber, 1978). This buffer also contains mild detergent which allows for extraction of 75% of cytosolic proteins, lipids and small molecules, whilst maintaining the intact microtubule network and their binding proteins (Figure 3.2A ii, cytosol fraction). Microtubules are therefore retained in control cells, whereas all soluble, depolymerised tubulin is removed in nocodazole-treated cells. A buffer containing an excess of free calcium ions (1 mM) is then added to depolymerise any retained and intact microtubules and collect them along with their binding proteins (Figure 3.2A iii). Binding proteins extracted following this method must fit 2 criteria: 1) bind to intact microtubules and 2) dissociate following microtubule depolymerisation.

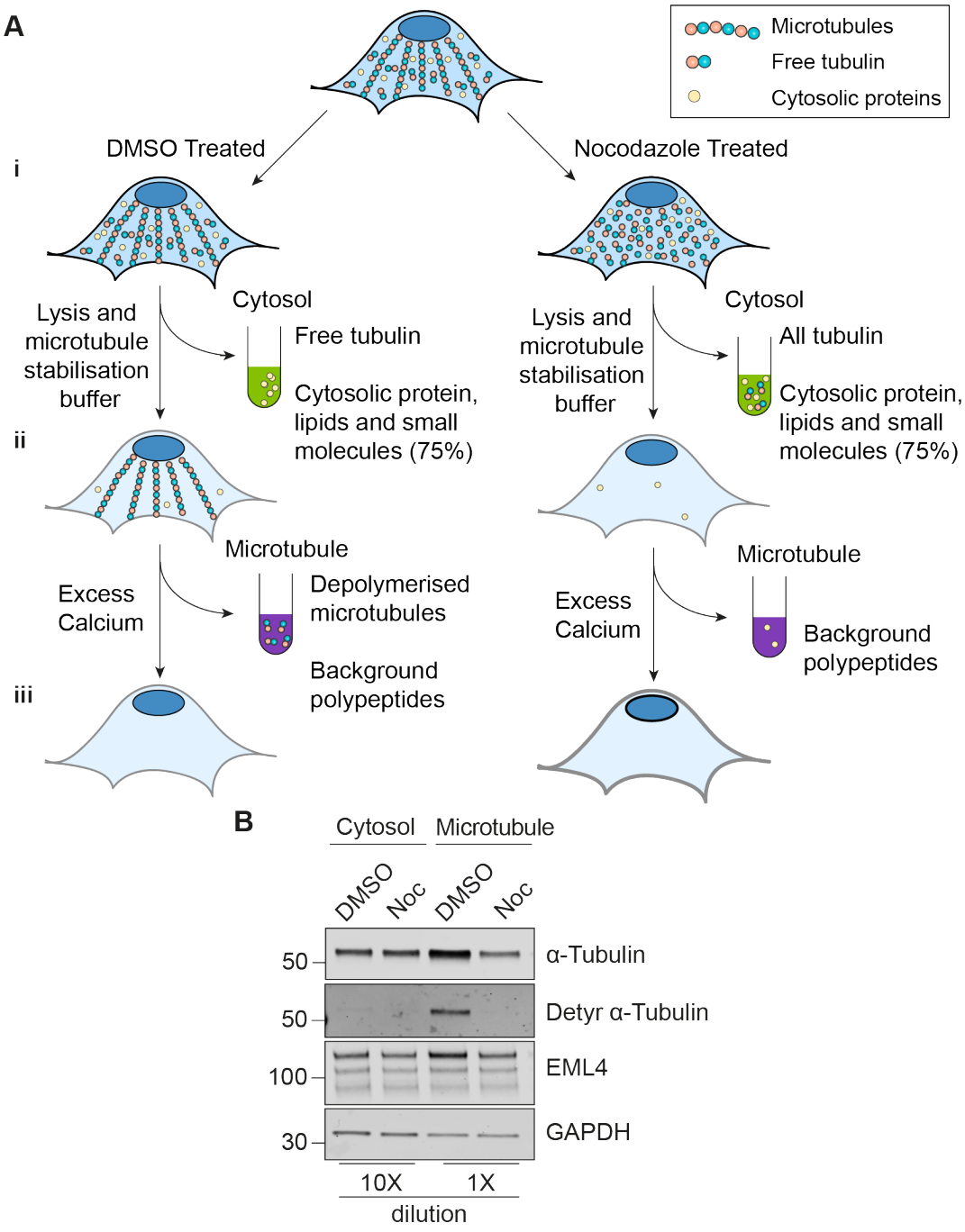

Figure 3.2 - Test of the microtubule extraction protocol

A: Schematic. U2OS cells were treated with DMSO (control, left) or Nocodazole (right), then extracted with LMS buffer, maintaining microtubule structures or eluting them respectively as a 'Cytosol' fraction. Free tubulin, cytosolic protein, lipids and small molecules were also collected. Excess calcium buffer then depolymerises microtubules in control cells and is retained with any binding proteins as a 'Microtubule' fraction along with background polypeptides. **B**: Microtubule extraction protocol was performed as described. LMS was applied for 15 minutes and calcium release for 10 minutes. Western blot analysis of α-tubulin, EML4 and GAPDH levels. Sample dilutions are as indicated.

Initially cells were treated with nocodazole for 2 hours, LMS for 15 minutes and excess calcium for 10 minutes. Buffer additions were performed in a water bath at 37 °C to maintain physiological conditions and prevent cold-dependent microtubule depolymerisation. The dynamic range of extraction was determined by immunoblotting for α-tubulin, EML4 as a microtubule binding protein marker and GAPDH as a cytosolic marker (Figure 3.2B). Greater levels of α-tubulin and EML4 are extracted within the control microtubule fraction compared to nocodazole-treated cells as anticipated. Detyrosinated α-tubulin levels were used to monitor polymerised microtubules due to its absence on soluble tubulin. Promisingly, the majority of detyrosinated α-tubulin was observed in the control microtubule fraction, confirming microtubule retention here and their loss following nocodazole treatment. In contrast, GAPDH appeared constant across both treatments, confirming nocodazole specifically acts on microtubules and associated proteins. These results are therefore promising however, to obtain a greater dynamic range of EML4 enrichment, optimisation of each step was required.

3.4 Optimisation of the microtubule extraction protocol

3.4.1 Optimisation of nocodazole treatment

To achieve the greatest dynamic range between conditions, nocodazole treatment had to be optimised. Increasing concentrations between 0 and 12 μM were tested and microtubule depolymerisation was analysed via immunofluorescence of α-tubulin (DM1α) (Figure 3.3A). 30 minutes was initially selected to determine whether complete depolymerisation was possible at a shorter incubation time point, and to prevent morphological changes induced from extended nocodazole treatment (Lee et al., 1980). As nocodazole concentration increases, microtubule depolymerisation increases, causing a disrupted network and an increase in free soluble tubulin. Some intact microtubules can be observed in all conditions due to some stable microtubules being resistant to nocodazole depolymerisation. 6 μM nocodazole was selected as a suitable concentration due to no noticeable increase in depolymerisation occurring with 12 μM.

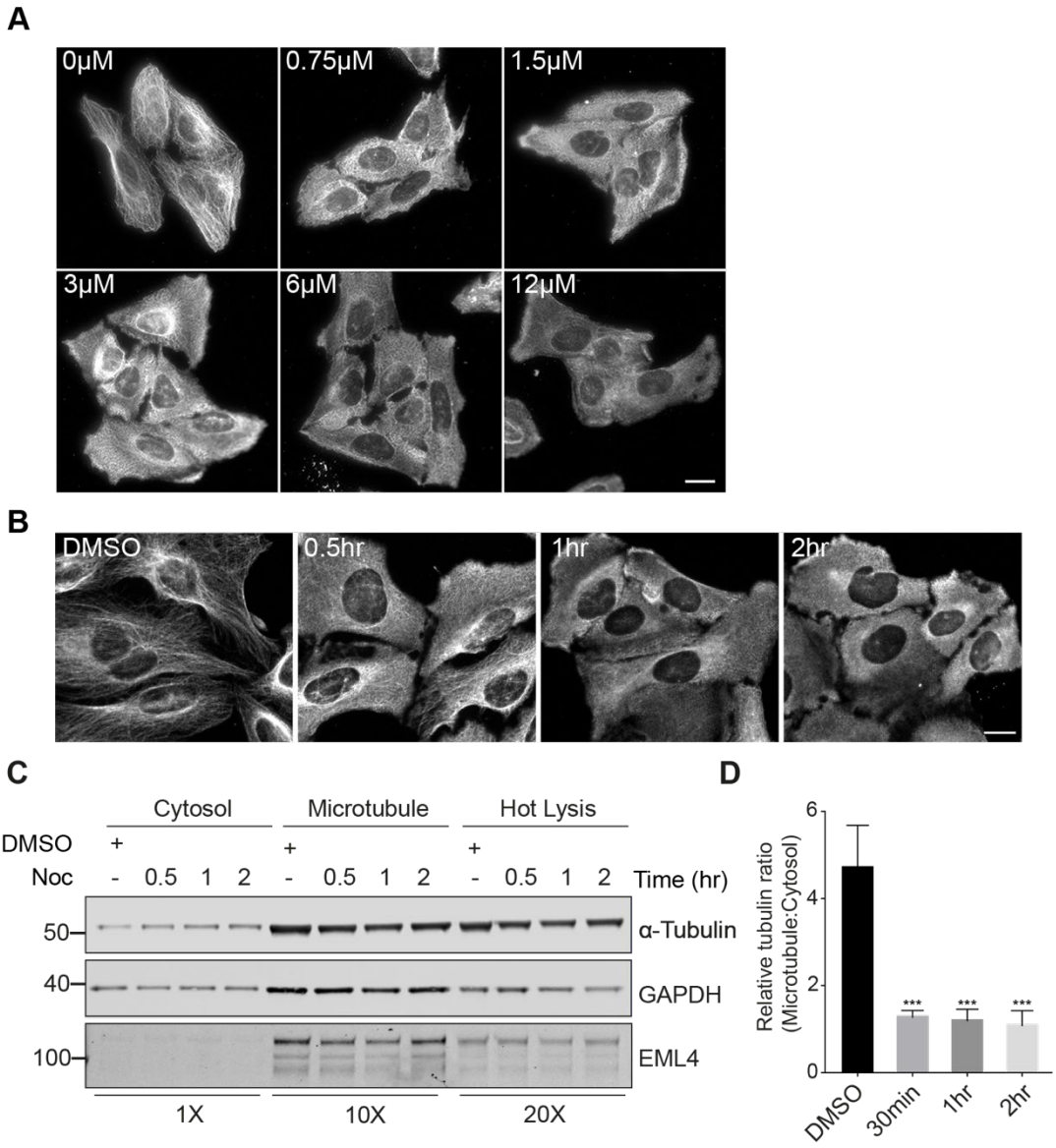

Figure 3.3 – Optimisation of nocodazole treatment

A: U2OS cells were treated with indicated concentrations of nocodazole at 37°C for 30 minutes. Cells were fixed with methanol and stained for α-tubulin. **B/C/D**: U2OS cells were treated with 6 μM Nocodazole for 30 minutes, 1 hour or 2 hours. DMSO treatment for 2 hours was used as a control. **B**: Immunofluorescence of the microtubule network. Scale bars = 20 μm. **C/D**: Microtubule stabilisation buffer LMS was added for 5 minutes followed by excess calcium for 10 minutes. Hot lysis was then performed to visualise the remaining proteins. C: Western blot analysis of α-tubulin, EML4 and GAPDH levels. Dilution of samples is as indicated. D: Ratios of Microtubule:Cytosol for α-tubulin. Visualisation was performed using a Nikon-TI eclipse microscope. Statistical analysis confirmed using one-way ANOVA test with Dunnett's multiple comparison: ***; $p \leq 0.001$

To determine the optimum incubation time for nocodazole treatment, cells were treated for indicated time points and the microtubule network visualised (Figure 3.3B). Significant disruption of the microtubule network is achieved after 30 minutes, however both longer time points display fewer intact microtubules. Biochemical analysis and quantitation using the extraction protocol detailed in section 3.3 shows no difference between extracted α-tubulin levels, with EML4 levels mirroring the same pattern (Figure 3.3C/D). The original protocol states that only 75% of soluble proteins are removed with LMS (Duerr et al., 1981). These results suggest this limit is reached after 30 minutes nocodazole treatment despite seeing greater disruption to the microtubule network with longer incubation times in Figure 3.3B. Despite no biochemical differences between timepoints, 1 hour was selected for subsequent experiments.

3.4.2 Optimisation of removal of cytosolic proteins

To maximise the removal of cytosolic proteins, whilst retaining intact microtubules and binding proteins, optimisation of LMS incubation time was required. Nocodazole-treated cells were used to observe maximum cytosol removal, and LMS was applied for indicated timepoints. Microtubules were then collected using excess calcium and residual proteins collected using hot SDS lysis buffer. Figure 3.4A shows that more α-tubulin, EML4 and GAPDH are extracted in the 'cytosol' fraction as LMS incubation time increases. Quantitation of the relative tubulin ratio confirms that maximum removal of tubulin was achieved after 5 minutes, with no further increase seen after 15 minutes (Figure 3.4B). Interestingly, all protein levels continue to decrease after 15 minutes in the 'microtubule' fraction, despite no change in the 'cytosolic' fraction. A similar pattern was observed within the hot lysis fractions. As there is no statistical difference in the relative tubulin ratio between the 5- and 15-minute incubation times, 5 minutes was selected as optimal. Furthermore, shorter incubation times were favourable to reduce the extent of microtubule binding protein detachment during these incubation steps.

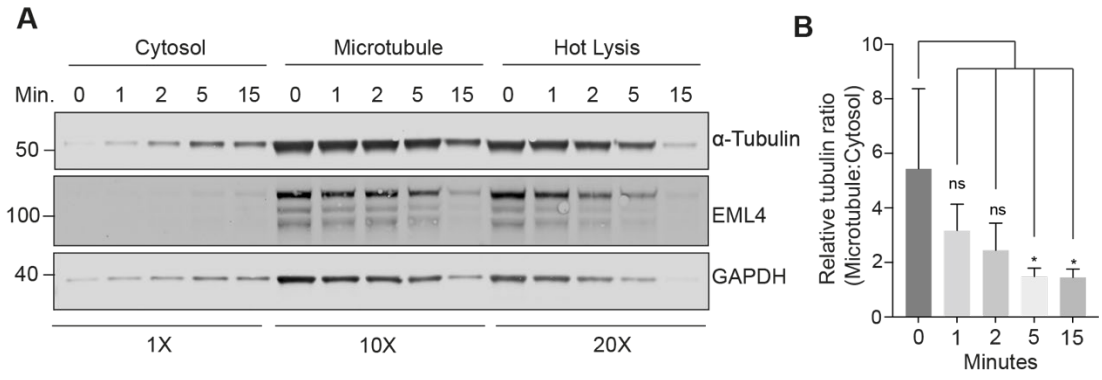

Figure 3.4 - Optimisation of removal of cytosolic proteins

A: U2OS cells were treated with 6 μM nocodazole for 30 minutes. Microtubule stabilisation buffer (LMS) was then added for specified times to collect the 'cytosol'. Excess calcium buffer was added for 10 minutes to collect the 'microtubules'. Hot lysis then collected the proteins remaining on the plate. Western blot analysis of α-tubulin, GAPDH and EML4. Sample proportions are as indicated. **B:** Ratios of Microtubule:Cytosol for α-tubulin levels: n=3. Statistical analysis confirmed using one-way ANOVA test with Dunnett's multiple comparison: *; $p \leq 0.05$.

3.4.3 Optimisation of microtubule collection

To maximise the collection of microtubules and their binding proteins, optimisation of excess calcium addition was also required. Untreated cells were used to observe maximum microtubule extraction, and calcium buffer was applied for indicated timepoints. Figure 3.5A shows all cytosolic fractions achieved the same levels of all proteins analysed, confirming this previously optimised step provides reproducible results. For the microtubule fractions an increase in α-tubulin levels is not observed with greater incubation times as expected, however a slight increase in EML4 can be seen. GAPDH levels remain unchanged across timepoints. Excess calcium buffer has been proposed to depolymerise microtubules (Timothy O'brien et al., 1997). However, as no noticeable difference in α-tubulin is seen between the 0 and 15-minute timepoints, this raised questions about the efficiency of the excess calcium buffer for collecting the microtubules. I therefore tested the excess calcium buffer against the LMS buffer as a control. Figure 3.5B shows that slightly greater levels of α-tubulin are extracted within the control compared to the nocodazole-treated cells in the 'cytosol' fractions as expected. Additionally, a small increase in the extraction of α-tubulin in control 'microtubule' fractions can be seen following the calcium buffer. EML4 levels remain unchanged with both buffers. Taken together, this indicated that in my hands, excess calcium does not efficiently depolymerise and collect microtubules and binding proteins. I thus set out to explore an alternative method.

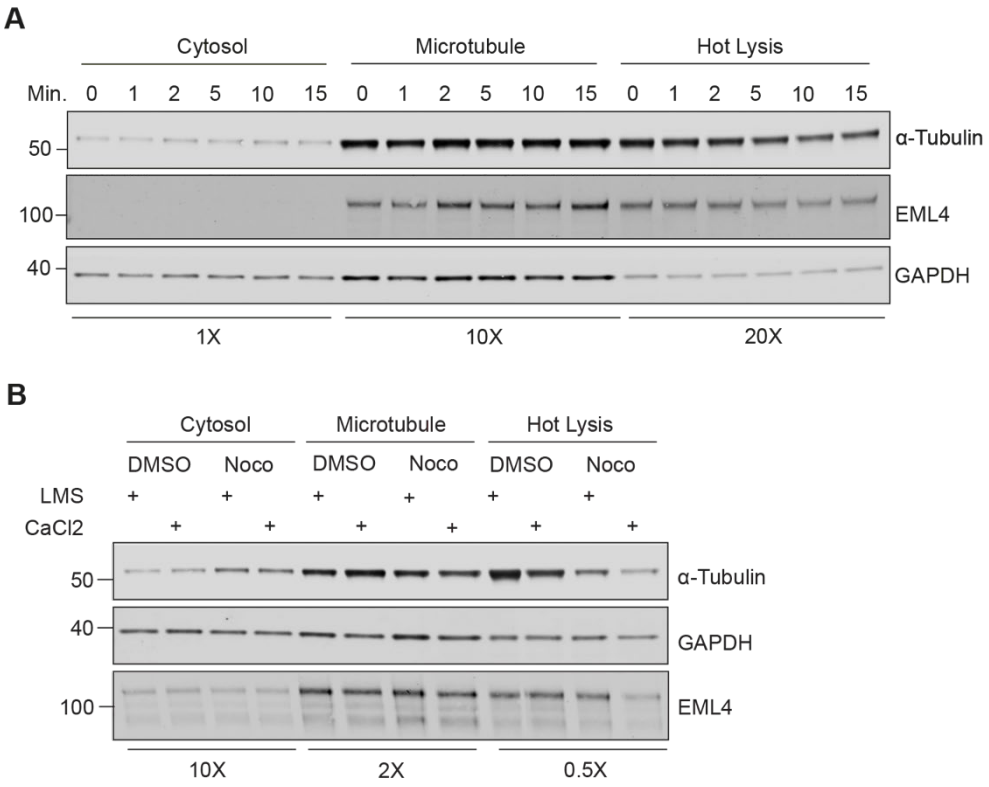

Figure 3.5 – Optimisation of microtubule collection

A/B: U2OS cells were washed with microtubule stabilisation buffer (LMS) for 5 minutes to remove the cytosolic proteins. **A:** Excess calcium buffer was then added for indicated times to extract the microtubules. The remaining cells on the plate were subjected to hot lysis. **B:** U2OS cells were treated with either DMSO or 6 μM Nocodazole for 1hr then washed with LMS. LMS or excess calcium buffer (10 min) was then used to extract microtubules. The remaining proteins on the plate were subjected to SDS hot lysis.

3.4.4 Alternative method for microtubule extraction

The originally tested protocol for microtubule extraction directly from cells proved to be unsuccessful as the excess calcium buffer provided inefficient microtubule collection, thereby reducing the dynamic range across conditions. An alternative method for microtubule collection was therefore desirable. To address this issue, I omitted the calcium depolymerisation step, and cells were simply lysed using hot SDS containing buffer. This therefore removes the requirement for microtubule depolymerisation and ensures that all retained microtubules and their binding proteins are collected. This will lead to an increase of background proteins, however labelling with different stable isotopes for each condition will allow for non-microtubule related proteins to be ratiometrically separated during subsequent quantitative mass

spectrometry analysis. Additionally, taxol treatment was added in as an additional condition. Taxol stabilises microtubules, as described in section 1.1.5, thereby introducing a microtubule enriched fraction to complement the nocodazole microtubule depleted fraction. The alternative protocol is illustrated in Figure 3.6.

I also evaluated the temperature for conducting this experiment. This protocol was performed in parallel at both 37°C and 4°C to determine which achieved the greatest dynamic range. The rationale for this was based on Taxol-treated microtubules being cold-stable and could therefore provide a greater dynamic range between control and taxol conditions. Figure 3.7A shows that successful differential extraction was achieved across all 3 treatments at both temperatures, with the greatest levels of α-tubulin and EML4 within the control and taxol 'microtubule' fractions at both temperatures. No α-tubulin was extracted in the cytosolic fraction following Taxol treatment, suggesting all free tubulin has polymerised. Incubation at 4°C achieved a greater dynamic range of EML4 suggesting microtubule binding proteins are more favourably extracted under these conditions. Furthermore, more GAPDH is removed following LMS incubation at 4°C compared with 37°C. This indicates fewer unwanted cytosolic proteins are present within the microtubule fraction, allowing for a purer sample. Although microtubule depolymerisation occurs under cold temperatures (4°C), immunofluorescence of the microtubule network shows this does not begin until after 10 minutes at this temperature (Figure 3.7B). The microtubule network is therefore unaffected after 5 minutes at this temperature.

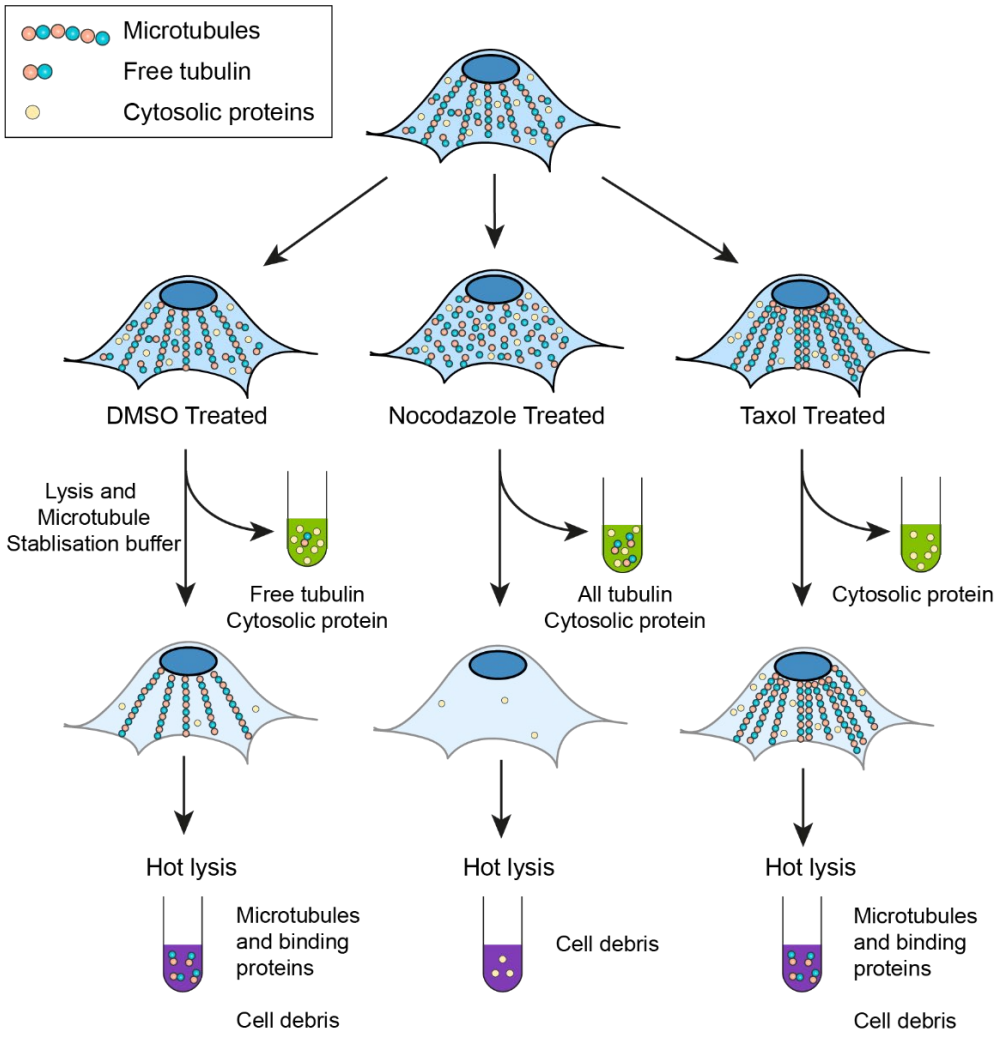

Figure 3.6 – Schematic of alternative microtubule extraction protocol

Schematic. U2OS cells were treated with DMSO (1 hour, left) or Nocodazole (1 hour, middle), or Taxol (30 minutes, right) then treated with LMS buffer at 4ºC for 5 minutes. This was then collected (shown in green) and microtubules and their associated proteins remain behind whereas the cytosol and any free tubulin are collected. Hot lysis is then added to the remaining microtubules on the dish to collect them (shown in purple), alongside any binding proteins.

3.4.5 Immunofluorescence of the microtubule extraction protocol

To visualise the microtubule network during this extraction protocol, immunofluorescence was performed after treatment with either DMSO, nocodazole or Taxol, and after LMS addition. Figure 3.7C confirms that control-treated cells retain their microtubule structures following removal of the cytosol. Treatment with nocodazole shows consistent loss of the microtubule network as previously seen in Figure 3.3, and subsequent incubation with LMS leads to a dramatic decrease in the levels of tubulin present. The remaining intact microtubules are presumed to be

stable, nocodazole-resistant microtubules (Xu et al., 2017) which may be masked by the large level of free α-tubulin seen before LMS addition. In addition, the remaining microtubules display a thicker structure than usual, possibly indicating microtubule bundling. Co-staining with acetylated α-tubulin, a modification which accumulates on stable microtubules, confirms this hypothesis. These results therefore show successful extraction of microtubules within control cells and significant loss following nocodazole treatment.

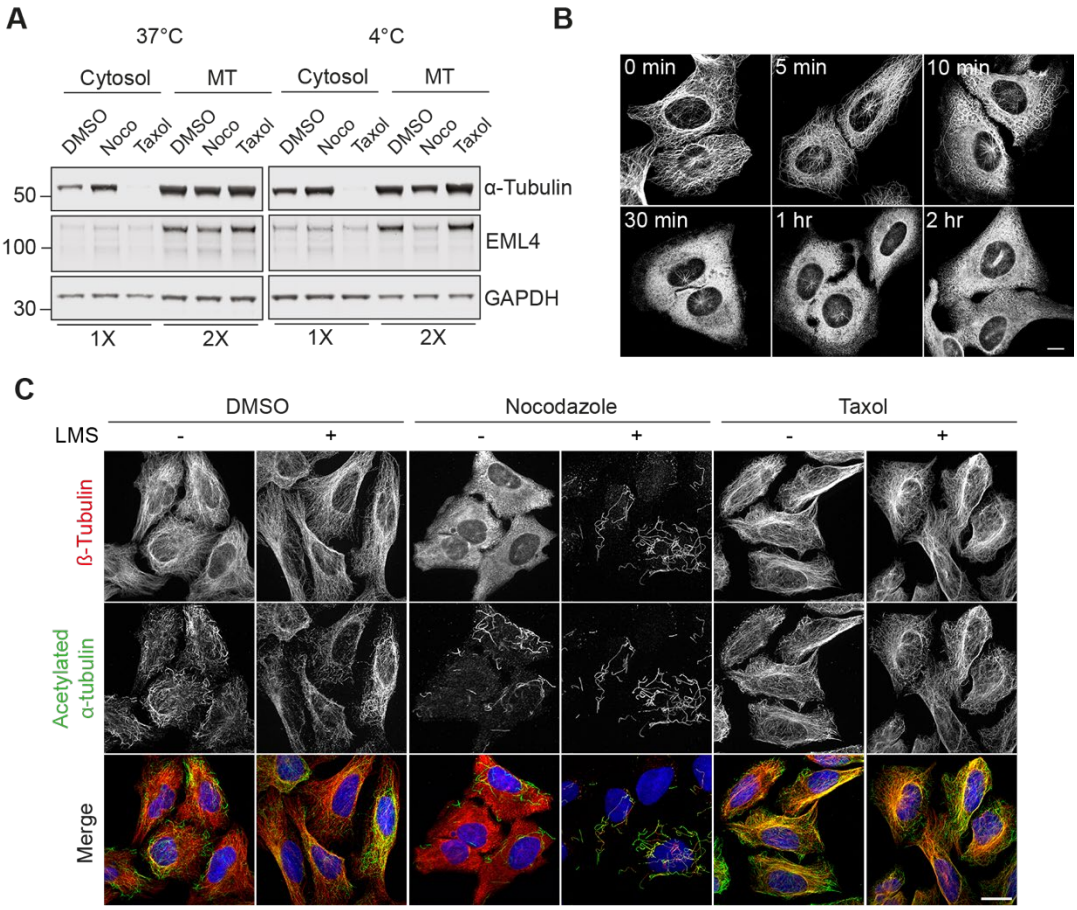

Figure 3.7 – Differential extraction of microtubules and binding proteins

A: U2OS cells were treated with either Nocodazole (6 µM, 1 hr), Taxol (6µM, 30min) or DMSO. Lysis and microtubule stabilisation buffer was then added (5min, 37°C or 4°C as indicated) to remove cytosolic proteins. Hot SDS lysis was then added to collect remaining microtubules on the plate. Sample concentrations are as indicated. **B:** Cells were incubated on ice for specified time points before being fixed and stained for α-tubulin. Images were acquired using Zeiss LSM 900 Airyscan confocal microscope. Scale bar = 10 µm. **C.** Cells were treated as in A, fixed with ice cold methanol before and after LMS buffer addition, and stained for β-tubulin (red) and acetylated α-tubulin (green) and DAPI (blue). Visualisation was performed with a 3i spinning disk confocal microscope. Scale bar = 20 µm.

3.4.6 Immunofluorescence of retained MAPs

To confirm that microtubule binding proteins are retained on the microtubule network during this protocol, I visualised the localisation of MAP4. MAP4 is a structural microtubule-associated protein (MAP) which binds along the whole of the microtubule lattice (section 1.1.9.1). Figure 3.8 confirms that retention of MAP4 is successful: colocalisation with α-tubulin can clearly be seen in control cells before and after LMS incubation. In contrast, MAP4 localisation was disrupted in nocodazole-treated cells. This further confirms this extraction method has been successfully optimised.

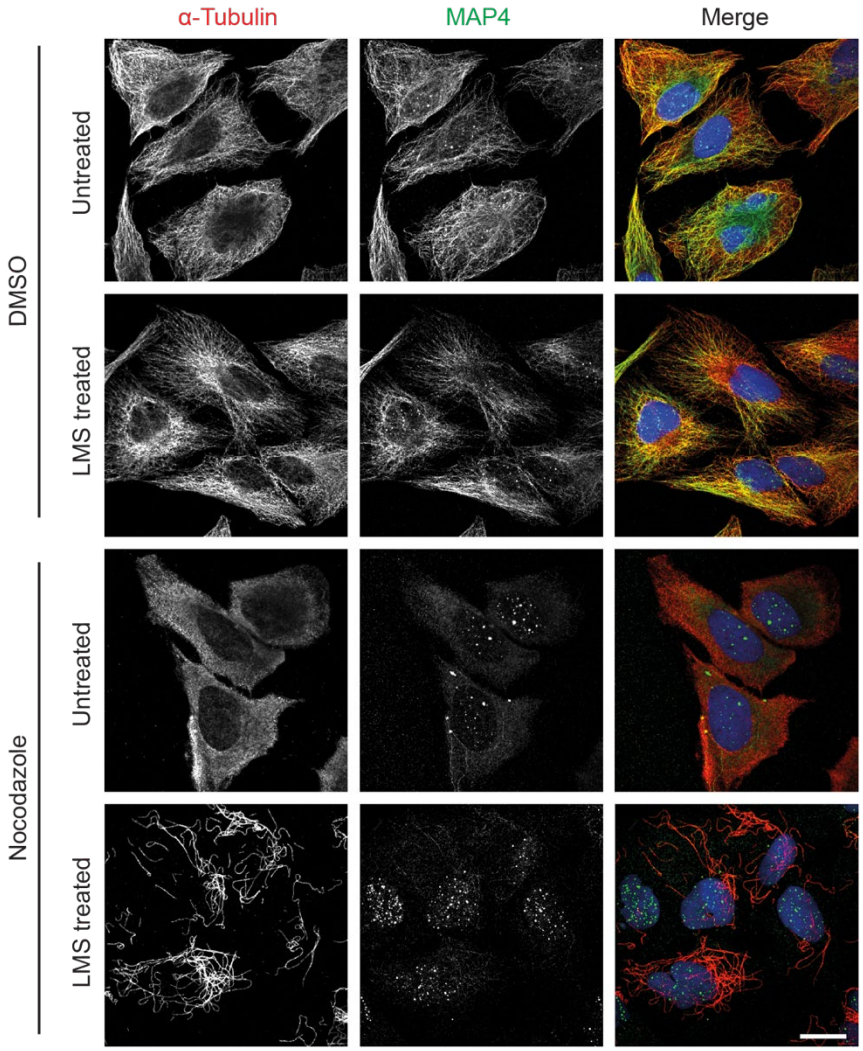

Figure 3.8 – MAP4 is retained on microtubules during the microtubule extraction protocol

U2OS cells were treated with 6 μM Nocodazole for 1 hour alongside a DMSO control. Lysis and microtubule stabilisation buffer (LMS) was then either added or not for 5 minutes at 4°C. Cells were then fixed with ice cold methanol and stained for α-tubulin (red) and MAP4 (green). Visualisation was performed with a 3i spinning disk confocal microscope. Scale bar = 20 μm.

3.4.7 Test of alternative lysis buffers for microtubule collection

To ensure extracted samples were compatible for mass spectrometry analysis, the maximum amount of detergent must be removed from the samples. As there are several detergents in the LMS buffer, a PBS wash step was incorporated after the removal of the LMS cytosolic fraction, and before the microtubule fraction was collected to remove residual LMS buffer. Figure 3.9A confirms this additional step does not affect the levels of α-tubulin and EML4 within the extracted fraction. GAPDH levels decrease slightly, indicating more cytosolic proteins can be removed without affecting the microtubules and binding proteins. This wash step was therefore incorporated into subsequent experiments. Additionally, as the hot lysis buffer used for microtubule collection contains high levels of detergent (2% SDS), 8M urea was tested as an alternative. Figure 3.9B confirm that comparable levels of both α-tubulin and EML4 are extracted using both buffers. Hot SDS lysis buffer was therefore substituted with 8M urea in all subsequent experiments.

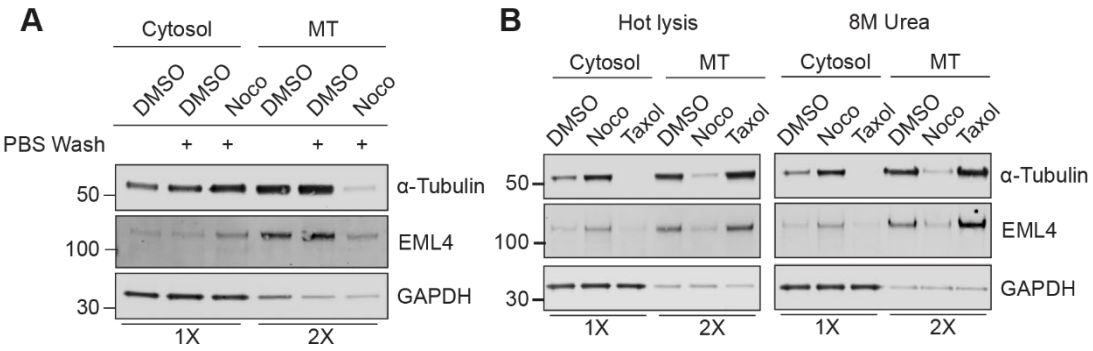

Figure 3.9 – 8M urea extraction buffer does not affect microtubule extraction

U2OS cells were treated with 6 μM Nocodazole or DMSO control for 1 hour. Lysis and microtubule stabilisation buffer was then added for 5 minutes at 4ºC to remove cytosolic proteins (cytosol). **A:** Cells were either washed or not with PBS before hot lysis buffer was added to collect the remaining microtubules on the dish (MT). **B:** Hot lysis buffer (left) or 8M urea (right) was used to collect the remaining microtubules on the dish. Western blot analysis of α-tubulin, GAPDH and EML4. Sample concentrations are as indicated.

3.4.8 Microtubule extraction protocol in alternative cell lines

To check whether this protocol was optimal for use on other cell lines, the optimised protocol was performed on SKN-BE2 and RPE1 FlpIn-TET cells. SKN-BE2 cells were selected as they displayed comparable levels of acetylated and detyrosinated α-tubulin, as shown within Figure 3.1, and RPE1 cells were selected as they are

commonly used within our laboratory. Figure 3.10 confirms this protocol can be applied to other cells lines and not just U2OS cells. For SKN-BE2 cells (Figure 3.10A) α-tubulin and EML4 and all enriched within the expected fractions. For RPE1 cells (Figure 3.10B), the dynamic range for α-tubulin levels however was reduced, with similar levels being seen across all 3 conditions in the microtubule fractions. EML4 however was specifically extracted within both control and Taxol-treated cells suggesting extraction of microtubule binding proteins can be achieved in this cell line using this protocol.

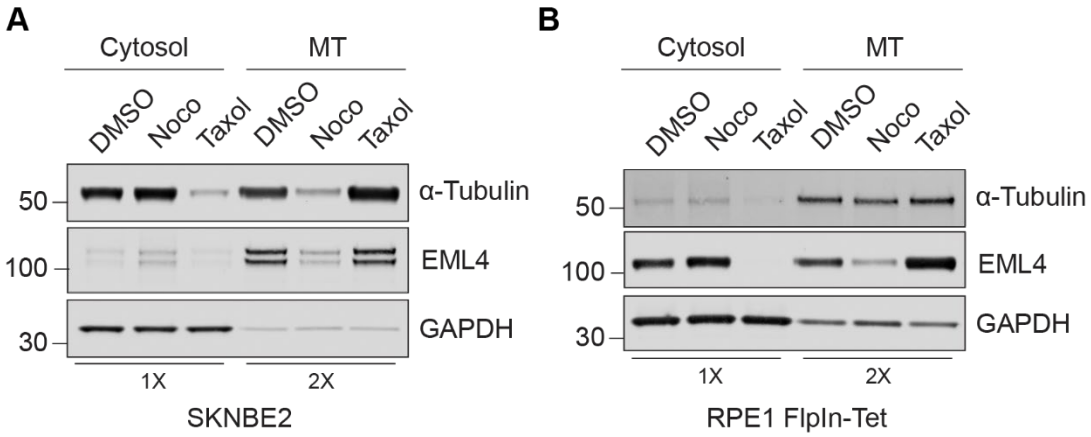

Figure 3.10 - Microtubule extraction is robust across different cell lines

SNKBE2 (**A**) and RPE1-FlpIn-TET (**B**) cells were treated with 6 μM Nocodazole for 1 hour or Taxol for 30 minutes alongside a DMSO control. Lysis and microtubule stabilisation buffer was then added (5min at 4°C) to remove cytosolic proteins. Remaining microtubules were then collected using 8M urea (MT). Western blot analysis of α-tubulin, GAPDH and EML4. Sample concentrations are as indicated.

3.5 Identification of the microtubule proteome using SILAC isotopic labelling

After successfully optimising a protocol for extracting microtubules and binding proteins, the next step was to identify the microtubule proteome using mass spectrometry analysis. To allow for a direct quantitative comparison of protein levels between microtubule fractions, Stable Isotope Labelling with Amino acids in Cell culture (SILAC) was utilised (section 1.4.8.2). This technique allows for the differential labelling of the amino acids, lysine and arginine, by incorporating 'light', 'medium' and 'heavy' isotopes into the culture medium, allowing different samples to be labelled

during protein synthesis. Samples to be compared are then combined in a 1:1:1 ratio before being subjected to mass spectrometry. This technique works by creating peptides which share the same amino acid sequence however their mass differs. This can be detected within the mass spectrometer to provide the relative abundance of the peptides identified (Ong et al., 2002). The use of SILAC within this research allows for the unbiased identification of microtubule binding proteins on a global scale directly from the cells.

3.5.1 Workflow for obtaining the microtubule proteome

A schematic for the workflow carried out is shown in Figure 3.11. The 'light' labelled cells were treated with DMSO for 1 hour, the 'medium' labelled cells were treated with nocodazole for 1 hour and the 'heavy' labelled cells were treated with Taxol for 30 minutes prior to performing the optimised microtubule extraction protocol. The details of the SILAC media composition can be found in section 2.5.2. The differentially labelled microtubule fractions obtained were combined in a 1:1:1 ratio, subjected to protein concentration as described in section 2.5.3 before being prepared via in gel digest for mass spectrometry analysis. Three independent repeats were analysed. Liquid chromatography and tandem mass spectrometry (LC MS/MS) was performed in Professor Gunnar Dittmar's lab in the Luxembourg Institute of Health by Dr Marta Mendes. To identify the proteins which are differentially enriched in each fraction, the normalised ratios of Medium/Light and Heavy/Light, which correspond to Nocodazole/DMSO and Taxol/DMSO respectively, were used.

3.5.2 Quality control

As a quality control measure, the levels of labelled amino acids within each condition were verified to confirm that sufficient incorporation had occurred in all 3, as unequal amounts of incorporation could lead to biased and inaccurate results. This check was performed by Erithelgi Bertsoulaki (former PhD student and post doc within the lab) as part of her PhD work and confirmed incorporation to be greater than 97% (Bertsoulaki, 2018). A second quality control measure that was taken was to confirm that the microtubule extraction protocol was successful for all 3 independent repeats being analysed. To do this, a small amount of lysate was taken prior to protein concentration and were analysed via western blotting. The results in Figure 3.12 confirm that the protocol was successful on all 3 cases, therefore proteomic analysis could proceed.

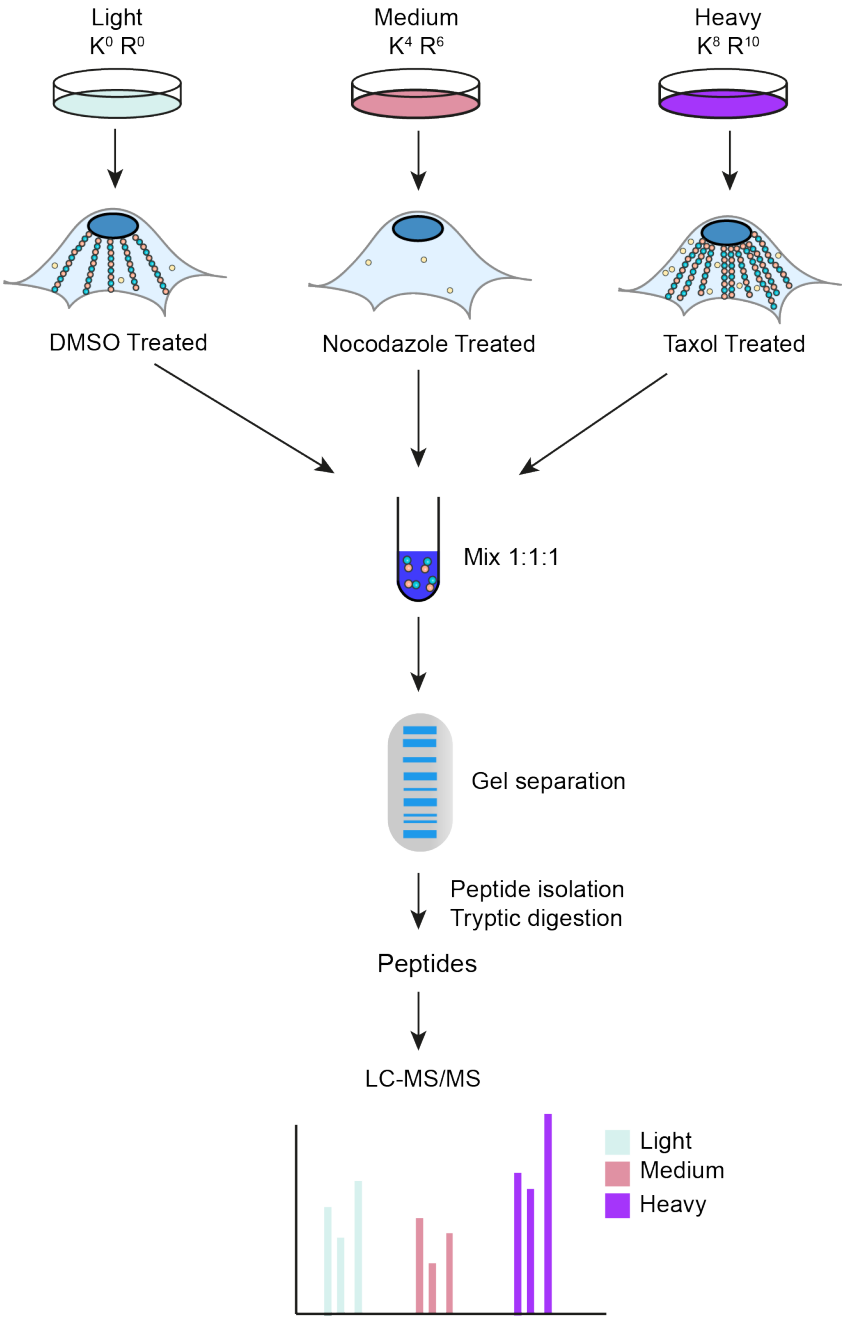

Figure 3.11 – Schematic showing SILAC mass spectrometry workflow

Schematic showing the workflow for SILAC mass spectrometry analysis. U2OS cells incubated with light (Lys0, Arg0), medium (Lys4, Arg6) or heavy (Lys8, Arg10) amino acids were treated with either DMSO, Nocodazole or Taxol respectively. Microtubule extraction was performed, and the microtubule fractions were mixed at a 1:1:1 volume ratio before being subjected to gel separation, peptide isolation and tryptic digestion. Peptides were then separated via liquid chromatography and analysed via mass spectrometry.

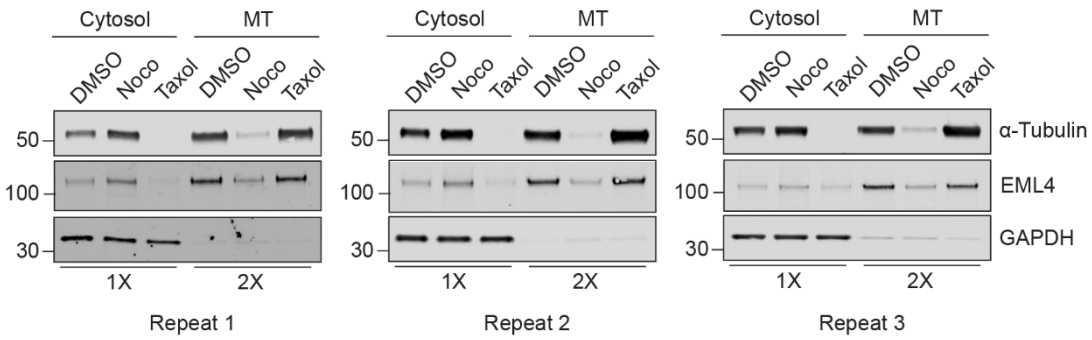

Figure 3.12 – Quality control of microtubule extraction protocol for MS analysis

SILAC labelled U2OS cells were treated with 6 μM Nocodazole for 1 hour (medium) or Taxol for 30 minutes (heavy) alongside a DMSO control (light). Lysis and microtubule stabilisation buffer was then added (5 minutes at 4°C) to remove cytosolic proteins (cytosol). Microtubules were then collected using 8 M urea lysis buffer (MT). Western blot analysis of α-tubulin, GAPDH and EML4 were performed for all 3 repeats. Sample proportions are as indicated.

3.5.3 Data analysis

Analysis of the 3 independent repeats was performed using MaxQuant as described in section 2.5.5.3. Initial observation of the raw data suggests that comparable numbers of peptides were identified within all 3 treatments. Looking at the intensity values, an average of 4189, 4144 and 4113 proteins across all 3 repeats were identified in the Light/DMSO, Medium/Nocodazole and Heavy/Taxol conditions respectively. This confirms that amino acid incorporation is equal across all conditions. As there was expected to have a slight skew to the data, with more proteins being enriched in the DMSO and Taxol fractions compared to the nocodazole fraction, the analysis was performed using the normalised ratios of the proteins, to ensure that the main cloud of unchanged proteins remained centrally distributed. The ratios are Medium/Light (M/L) and Heavy/Light (H/L) which correspond to Nocodazole/DMSO and Taxol/DMSO respectively and were used to identify proteins enriched in DMSO-treated cells compared to nocodazole- and Taxol-treated cells.

Across all 3 repeats, 4930 proteins were identified from a total of 410,788 total peptides, and 73,117 unique peptides. To obtain a ratio for every protein, each protein must be identified within all 3 conditions. Therefore, if a protein is missing from one of these conditions, then a ratio cannot be made against that sample, and that protein may therefore need to be excluded from the final analysis. After taking this into account, I noticed that repeat 1 and 3 achieved a similar number of identified proteins

(3510 in repeat 1 and 3471 in repeat 3), however much fewer proteins were identified within repeat 2 (2509). To reduce the number of proteins being excluded from the final analysis, and hence potentially losing proteins which are specifically associated with microtubules, proteins that were identified within at least 2 repeats in all conditions were retained for analysis. Any protein that was identified in only one repeat was excluded from the dataset. This resulted in 3544 of the 4930 proteins being taken forward for further analysis. To analyse the ratios and extract the quantitative data from the MaxQuant table, the average of the normalised ratios for M/L and H/L for each protein identified in at least 2 repeats was determined and then transformed into a $\log_2$. In addition, for each of the ratios calculated, the sum of the intensities for each protein were also calculated (eg Intensity M + Intensity L). This value was then transformed $\log_{10}$. These parameters were then used to plot the data using JMP 13.

3.5.4 Data visualisation

To easily visualise the protein distribution, the average M/L and H/L $\log_2$ of the normalised ratios were plotted on a scatter graph, shown in Figure 3.13. On the x-axis, proteins found to be enriched within the DMSO-treated fraction are shifted towards the left whereas those enriched in nocodazole-treated fraction are shifted to the right of the graph. On the y-axis, those found to be enriched in DMSO are shifted towards the bottom whereas those enriched in Taxol-treated cells are shifted towards the top of the graph. Most of the outlying proteins are distributed towards the left of the graph as opposed to the right, showing that fewer proteins are specifically extracted following nocodazole treatment. Furthermore, as these outlying proteins are not largely located within either the top left or the bottom left quadrant, it suggests there is no strong correlation observed between the nocodazole and taxol treatments. These drugs act independently from each other on a protein-protein bases.

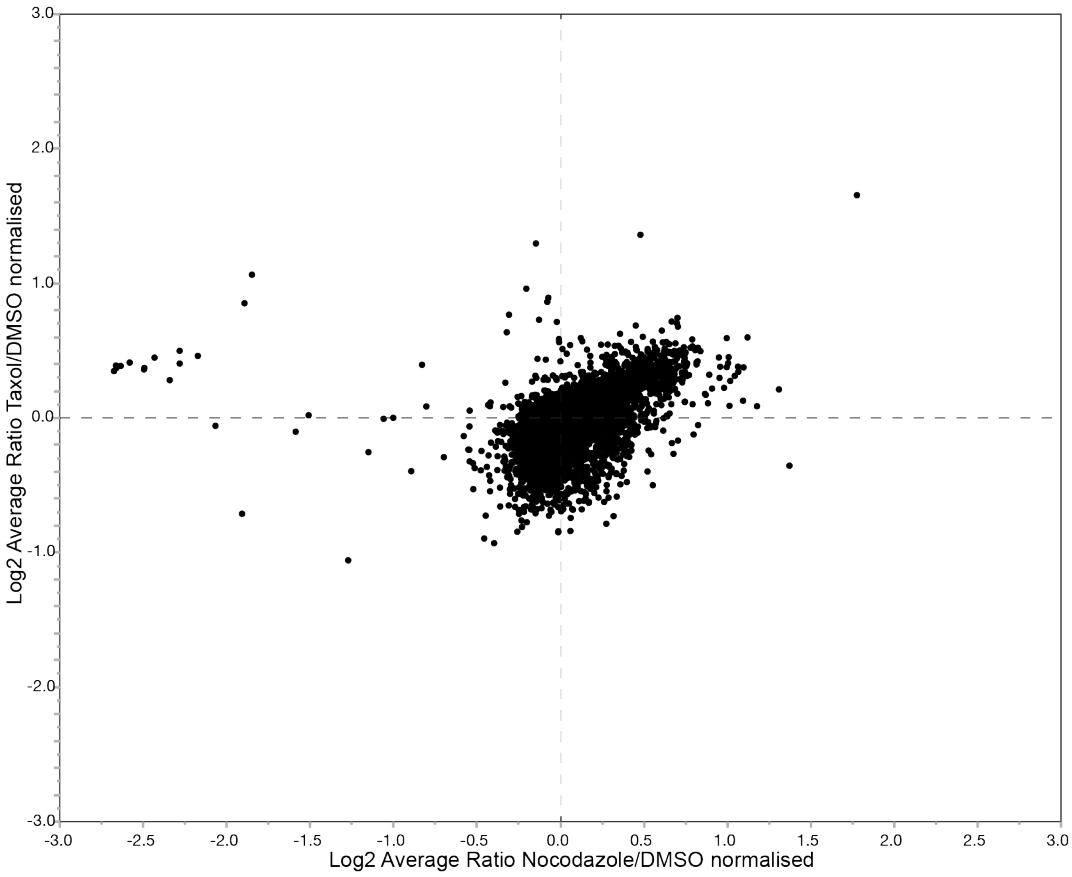

Figure 3.13 – Proteome distribution of U2OS cells following microtubule extraction protocol compared to nocodazole- or Taxol-treated cells

The logarithmic change (log_2) of the proteome composition following microtubule extraction in DMSO treated cells compared to nocodazole- and Taxol-treated cells. The average normalised ratios from at least 2 repeats are shown in the graph.

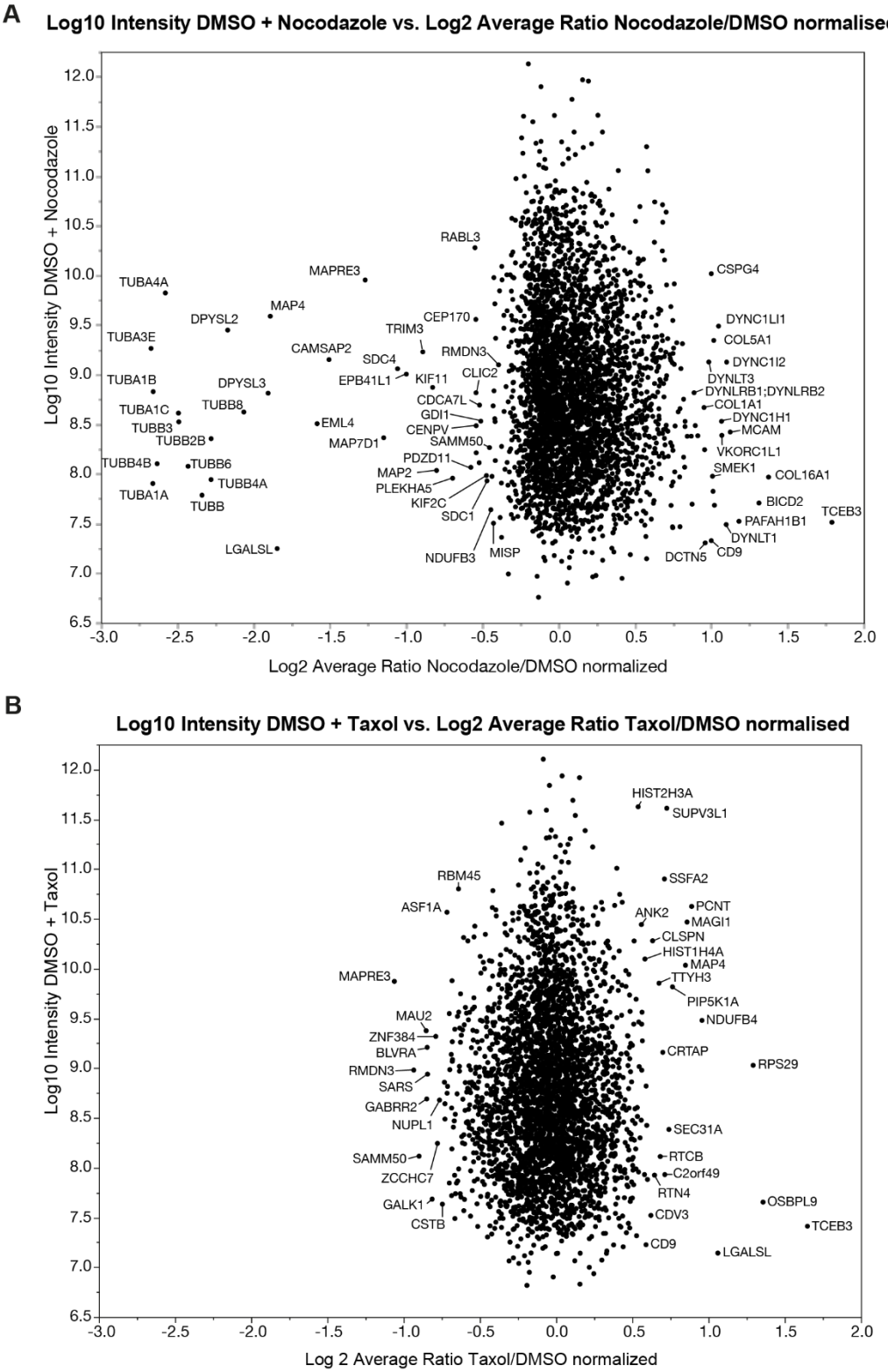

Figure 3.14 – Fold change of the proteome distribution of U2OS cells following microtubule extraction in 3 different conditions depicted against the sum of the intensities.

The graph shows the average of at least 2 repeats for the DMSO-treated cells against the nocodazole- (**A**) and Taxol- (**B**) treated cells. The logarithmic change (log_2) of the normalised ratios are plotted against the logarithmic sum (log_{10}) of the intensities.

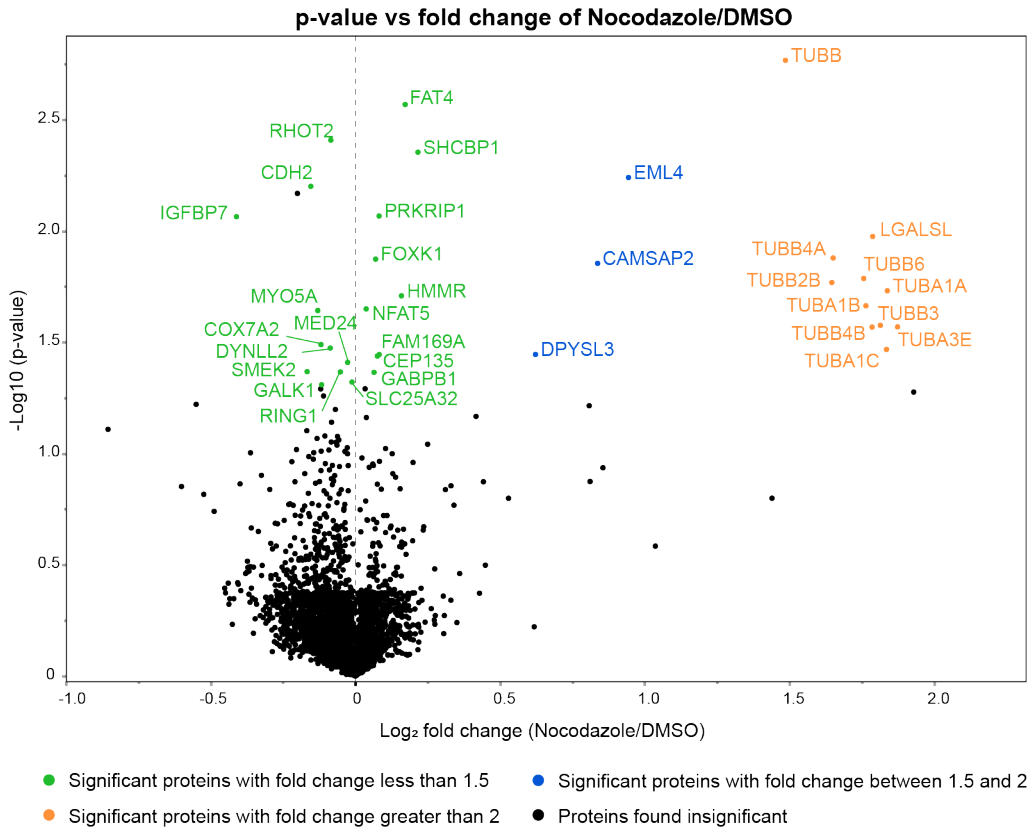

Figure 3.15 – Volcano plot of the proteome composition of U2OS cells following microtubule extraction compared to the significance (p-value)

The $\log_2$ fold change of the average ratio is plotted against the negative logarithm (log10) of the p-value for the DMSO compared to the nocodazole. Proteins which change significantly with a fold change greater than 2 are highlighted in orange, those between 1.5 and 2-fold in blue, and those with a fold change less than 1.5 are shown in green.

An additional graph was also plotted to display the $\log_2$ transformed average ratios for each condition against the $\log_{10}$ transformed intensities to see the differences of the enriched proteins compared to their protein abundance (Figure 3.14A/B). Points shown on the outskirts of the graphs have been labelled. Note, TCEB3 shown to be the most enriched protein in both taxol and nocodazole fractions (top right quadrant in Figure 3.13, bottom right in Figure 3.14), did not show consistent results across the 2 repeats it was identified in, with normalised ratios of 5.8 and 1.1 for M/L and 5.5 and 0.74 for H/L. This protein will therefore not be commented on in any further sections. To analyse the consistency of the ratios obtained across the 3 repeats for Nocodazole/DMSO, a t-test difference value was generated followed by a p-value of the t-test difference. This statistical test was performed using Perseus and the $\log_2$ fold change for each protein are plotted against the negative logarithm $\log_{10}$ of the p-

values, shown in Figure 3.15. Those indicated in colour represent proteins which are considered statistically significant to a p-value threshold of 5%, with the green ones showing significant proteins with a fold change between 0.5849 ($log_2$1.5) and -0.5849 ($log_2$0.666), blue ones representing a fold change above 0.5849 and orange ones representing a fold change above 1 ($log_2$2). Those with a 2-fold change in orange are all tubulin proteins except for 1 other and include 10 of the total 12 tubulin isoforms identified in the dataset.

3.5.5 Initial analysis of outlying proteins

As anticipated, the proteins shown to be most sensitive to nocodazole (those located to the left of the scatter plot shown in Figure 3.13), and are therefore enriched within the control fraction, are the tubulin proteins identified (Figure 3.16, labelled in blue). Of the 12 isoforms that were identified, all except TUBB8 are also enriched following taxol treatment. Clustered amongst the tubulin proteins is the structural microtubule associated protein, MAP4, which is known to localise along microtubule lattices, as confirmed in Figure 3.8. DPYSL2 (dihydropyrimidinase-related protein 2), also known as CRMP-2 (collapsin response mediator protein 2), which functions in promoting tubulin assembly by transporting tubulin heterodimers to the growing plus ends (Fukata et al., 2002), also clusters here. Other known microtubule binding proteins also displaying nocodazole sensitivity by at least 2-fold include EML4 CAMSAP2, MAP7D1, DPYSL3 and MAPRE3. EML4 (echinoderm microtubule associated protein) is known to stabilise microtubules (Houtman et al., 2007), and has been implicated in non-small cell lung cancer when expressed as a fusion protein with ALK (anaplastic lymphoma kinase) (Sasaki et al., 2010). MAP7D1 has functional roles in microtubule stabilisation (Kikuchi et al., 2022) and kinesin-1 dependent transport of mitochondria (Hooikaas et al., 2019). CAMSAP2 (calmodulin-regulated spectrin-associated protein 2) is sensitive to nocodazole only and specifically localises to minus-ends of non-centrosomal microtubules. It is important for maintaining the neuronal microtubule network and dendrite development (Yau et al., 2014). DPYSL3, also known as CRMP-4, regulates both the microtubule and actin cytoskeleton within the growth cone (Khazaei et al., 2014). Finally, MAPRE3 (microtubule associated protein RP/EB family member 3), more commonly known as end-binding protein 3 (EB3) is part of the core plus-tip tracking complex which associates with the growing ends of microtubules as they polymerise (Galjart, 2010). Furthermore, EB3 has been shown to regulate microtubule minus-ends decorated with CAMSAP2 proteins, causing detachment of Golgi-tethered microtubules (Yang et al., 2017). DPYSL3 and EB3 are also taxol

sensitive, with EB3 being the most taxol-sensitive protein in the whole dataset, indicating they lose their microtubule localisation when either drug is present. From this analysis of the most nocodazole sensitive proteins, I can confirm that tubulin and microtubule binding proteins are specifically extracted with this protocol.

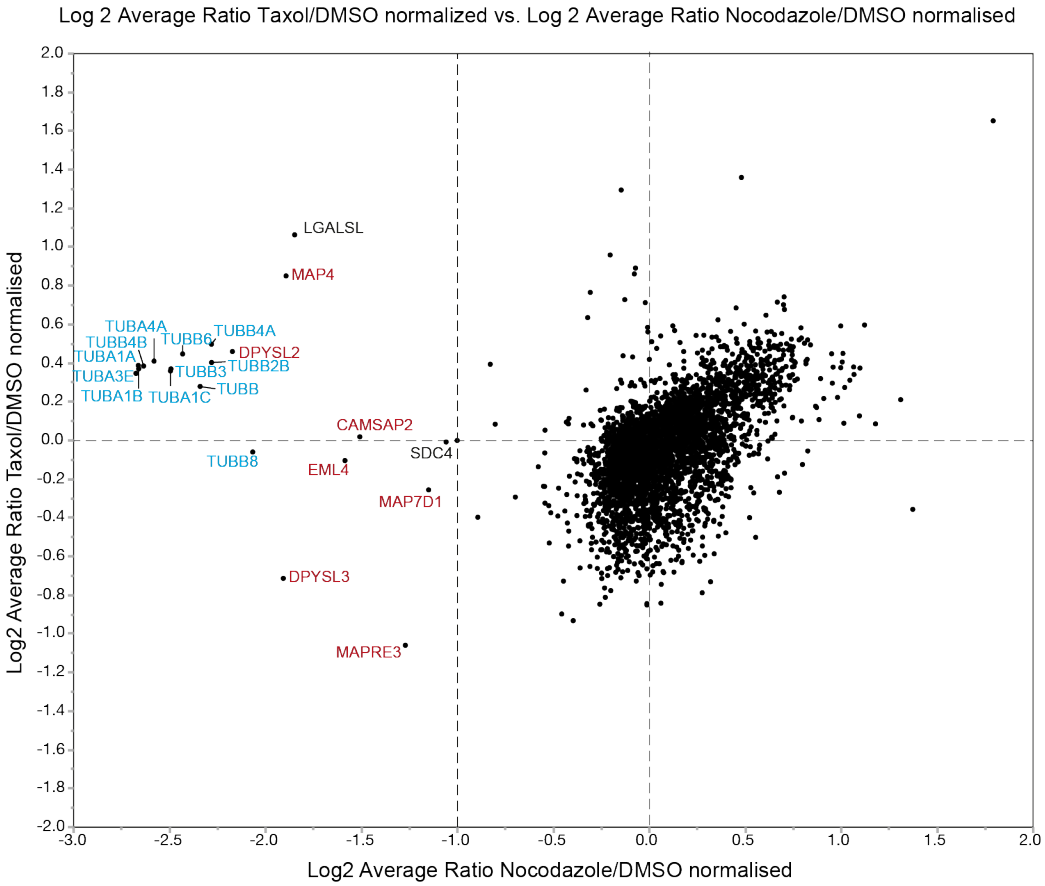

Figure 3.16 – Tubulin and microtubule binding proteins are enriched >2-fold

The logarithmic change (log_2) of the proteome composition following microtubule extraction in DMSO treated cells compared to nocodazole- and Taxol-treated cells. The average normalised ratios from at least 2 repeats are shown in the graph. Tubulin proteins are labelled in blue, known microtubule binding proteins are labelled in red.

3.5.6 Data sorting and selection

To select candidates for further analysis as novel microtubule binding proteins, a cut off threshold for hits of interest had to first be established. For this next section I will therefore focus on the proteins enriched in DMSO compared to nocodazole, located towards the left of the scatter plot in Figure 3.13. Ideally, a threshold level of at least a two-fold change, where the log_2 value is less than -1 ($log_20.5$) would be used. However, this would only result in a shortlist of 21 proteins in total, of which 12 are tubulin proteins (blue), and 7 are already known microtubule binding proteins (red). This would therefore leave only 2 proteins, Syndecan-4 (SDC4) and Galectin-related protein (LGALSL) as possible hits for further analysis (black). This is illustrated in Figure 3.16.

An alternative method for determining the cut-off for the shortlist was therefore utilised. The Database for Annotation, Visualisation and Integrated Discovery (DAVID) Bioinformatics Resources is an online resource which provides functional annotation tools for investigating the biological meaning behind large gene lists (Huang et al., 2009; Sherman et al., 2022). I used the functional annotation clustering tool to look for the enrichment score for microtubule or microtubule-binding proteins between a selection of the top changing proteins. Default settings were used which include the classification strategy as medium, a similarity term overlap of 3, a similarity threshold of 0.5 and an enrichment threshold of 1.0. The first 10 (proteins 1 to 10) were selected and their enrichment score was recorded. The selection then shifted down by 1 so this next 10 were analysed (proteins 2 to 11) and the score recorded. This selection process continued down the list of proteins in order starting with the lowest normalised ratio for nocodazole/DMSO until an enrichment score for either microtubule, microtubule cytoskeleton or microtubule binding category was not provided for 10 consecutive sets of 10. Once this was reached, the cut-off for the shortlisted proteins was made, leading to a nocodazole-specific microtubule proteome of 64 proteins. A heat map displaying enrichment scores is shown in Figure 3.17A. The overall enrichment score for all 64 proteins is 13.09, the highest category for enrichment shown, suggesting this protocol specifically enriches for microtubules and their binding proteins. Figure 3.17B shows the distribution of these proteins on the scatter plot displaying Log_2 Nocodazole/DMSO vs Taxol/DMSO.

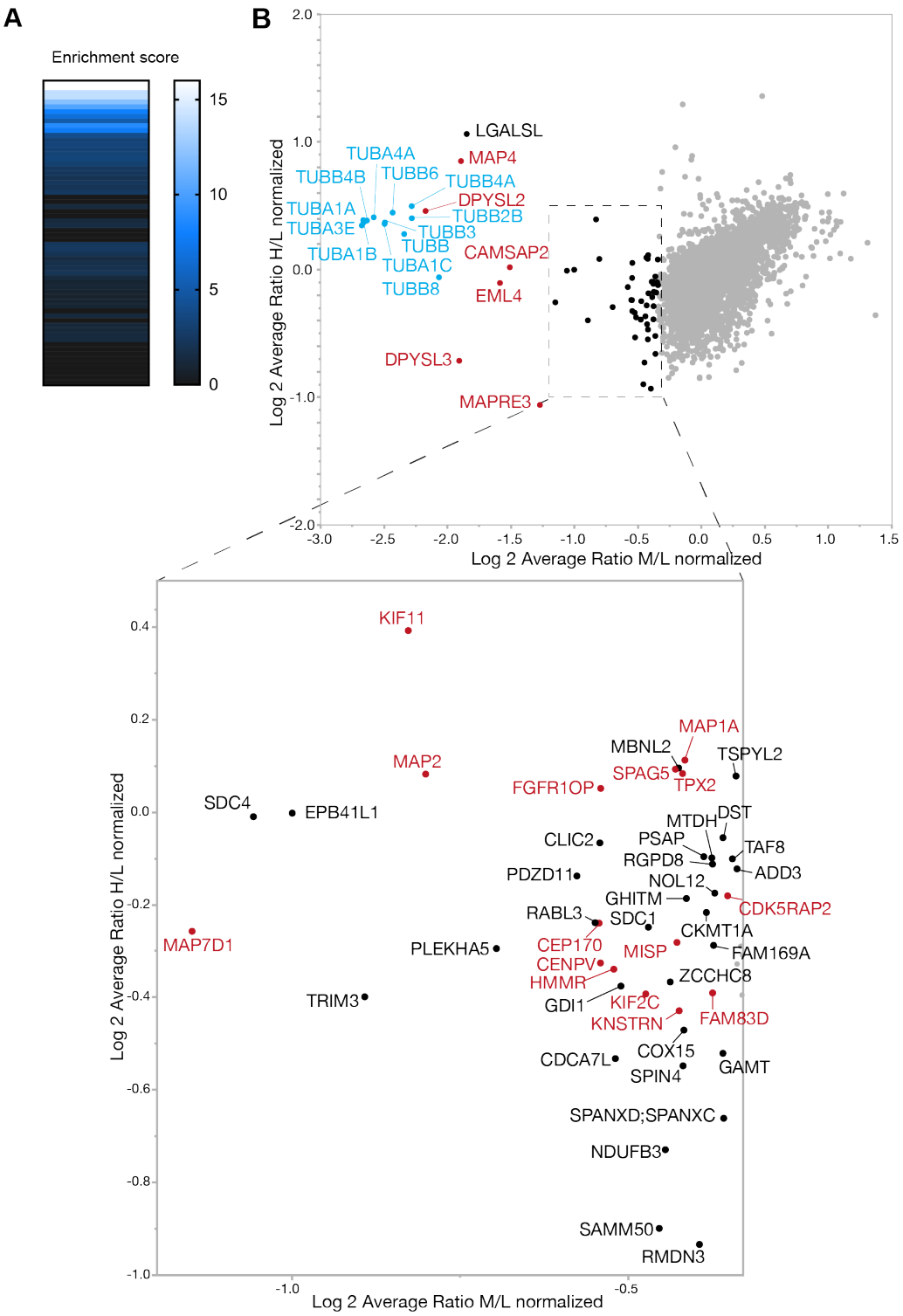

Figure 3.17 – Mass spectrometry analysis identifies potential novel microtubule binding proteins

A. Heat map showing the enrichment scores for microtubule related proteins. The top hits of the average log2 normalised Nocodazole/DMSO ratio (from ≥2 repeats) were analysed using DAVID Bioinformatics 6.8 Functional Annotation Clustering in groups of 10 starting with the most enriched. **B.** The ratiometric $\log_2$ of extracted proteins is shown. Proteins enriched in DMSO compared to nocodazole as defined in A are labelled: tubulin proteins (blue), known MAPs (red), potential candidates (black). Magnified view of indicated region shown.

Manual examination of these proteins was performed using uniprot, and the proteins were sorted into 3 categories: 1) tubulin proteins, 2) known microtubule binding proteins and 3) potential candidates for microtubule binding. These categories are illustrated in Figure 3.17B with tubulin proteins, known microtubule binding proteins and candidate proteins labelled in blue, red and black respectively. 21 proteins previously known to associate with microtubules, representing 33% of the proteome identified here, and 40% if tubulin proteins are excluded. This is quite a high proportion of this proteome, further confirming specific extraction. The remaining 31 proteins also identified are therefore thought of as novel candidate microtubule binding proteins.

As mentioned in section 3.5.3, proteins identified in at least 2 repeats were taken forward for analysis. Therefore, to confirm that consistency was seen across the repeats where values were included from, a heat map was produced to show the individual log2 Nocodazole/DMSO normalised ratios of the 52 proteins identified as either known or novel microtubule binding proteins. Figure 3.18 confirms that 22 of these 52 proteins are only observed in 2 repeats, with blank ratios shown in grey. Despite this, all are shown to have a negative $\log_2$ value in all repeats they are present in with the exception of GHITM in repeat 2 which displayed a $\log_2$ value of 0.033.

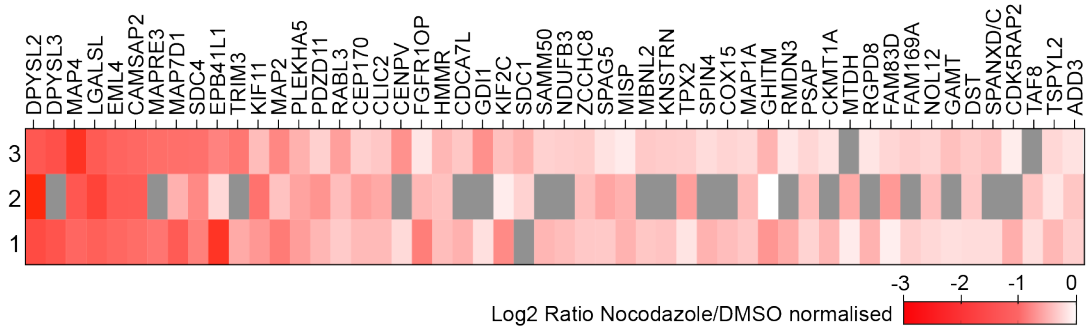

Figure 3.18 – Heat map of hits identified across the 3 repeats

Heat map showing the Log2 Nocodazole/DMSO normalised ratios of the proteins shown to be enriched in the DMSO fraction. Tubulin proteins have been excluded and only known microtubule binding proteins and potential novel binding proteins are shown. Grey boxes represent where a ratio was not provided within that repeat.

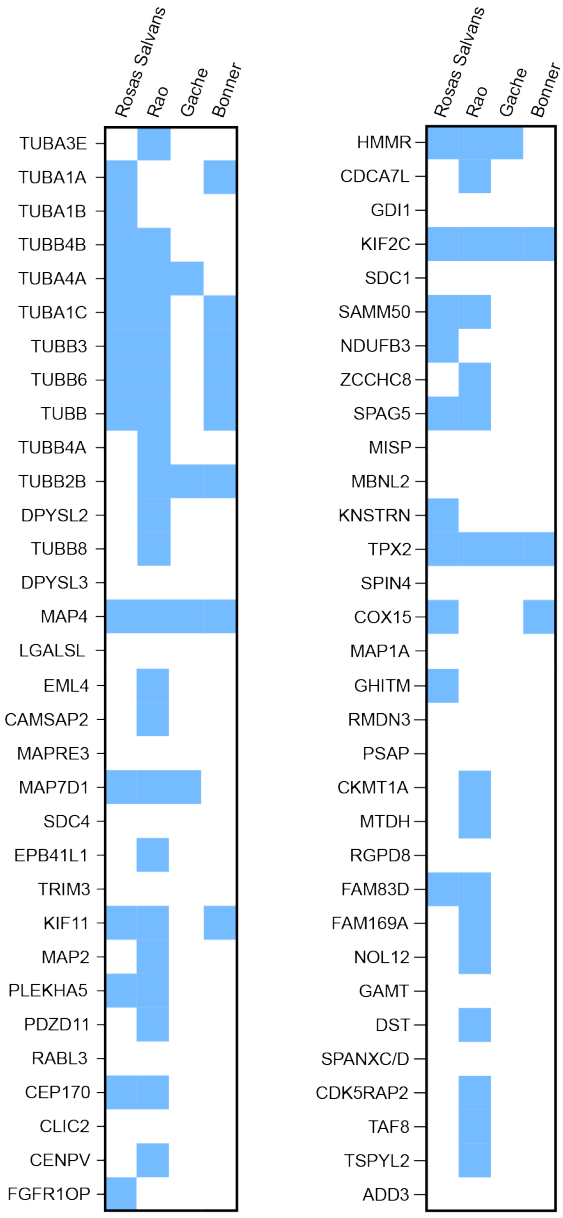

Figure 3.19 – Comparison with other microtubule proteomes

Schematic diagram showing the 64 proteins of interest in the proteome and their appearance in previously determined proteomes. Column 1: (Rosas-Salvans et al., 2018), Column 2: (Rao et al., 2016), Column 3: (Gache et al., 2010), Column 4: (Bonner et al., 2011).

3.5.7 Comparison with other microtubule proteomes

A series of other microtubules proteomes have been previously identified. I selected 4 of these to compare with the top 64 proteins that were identified as being enriched for in a nocodazole-sensitive manner (Figure 3.19). Rosas Salvans *et al* looked at proteins involved in self-organisation of microtubules in M phase of *Xenopus* egg extracts, and had 24 proteins in common (Rosas-Salvans et al., 2018). Rao *et al*

performed quantitative proteomic analysis, using dimethyl stable isotopes, to determine the clathrin dependent spindle proteome, identifying 38 of these proteins (Rao et al., 2016). The third study identified the meiotic microtubule-associated interactome within *Xenopus* eggs, of which only 7 proteins were also identified in my enriched proteome. Finally, I compared my 64 hits with those identified in a mitotic spindle proteome in Chinese hamster ovary cells, only finding 11 proteins in common (Bonner et al., 2011). It is interesting to note that some known microtubule binding proteins identified within my dataset were not observed in some of these other proteomes. For example, MAPRE3 (EB3) and MAP1A were not identified in any, whilst EML4 and MAP2 were only identified in Rao *et al*. These results confirm that my proteomic approach can identify similar proteins identified in other microtubule proteomes, whilst also identifying additional novel candidates.

3.5.8 Network visualisation

To see whether any identified hits were already known to be associated with each other, BioGRID 4.4.202 (The Biological General Repository for Interaction Datasets) was downloaded and utilised. This is a public dataset which includes protein interaction data from humans and other model organisms which have been confirmed using experimental techniques such as yeast-two hybrid, co-purification, FRET and Affinity Capture-MS. The BioGRID database was therefore filtered to show only interactions occurring within the 64 proteins of interest in the proteome, illustrated in Figure 3.17. This information was combined with their Log_2 Nocodazole/DMSO normalised ratios (shown by the colour of the nodes) as an indicator of whether proteins known to interact with each other were more likely to be enriched in a similar manner. As expected, all tubulin proteins interact with each other, as represented by the lines linking them all together. Known microtubule binding proteins such as MAP2, DPYSL2 and DPYSL3 are also shown to interact with the tubulin proteins identified. There is also a cluster of proteins shown towards the bottom left of the network which have been seen to associate with the centrosomal protein CEP170. All of these proteins, except RABL3 has been previously shown to localise to microtubules. RABL3 is involved in ciliogenesis but direct binding with microtubules has not been shown (Kobayashi et al., 2022). This result may therefore provide more evidence which supports RABL3 being a novel microtubule binding protein. There are however some known interactions which do not appear within the BioGRID dataset such as the interaction between MAPRE3 and tubulin proteins, and also MAP4 and tubulin. There may therefore be additional interactions which may facilitate with the selection of identified hits for further characterisation which are missing here.

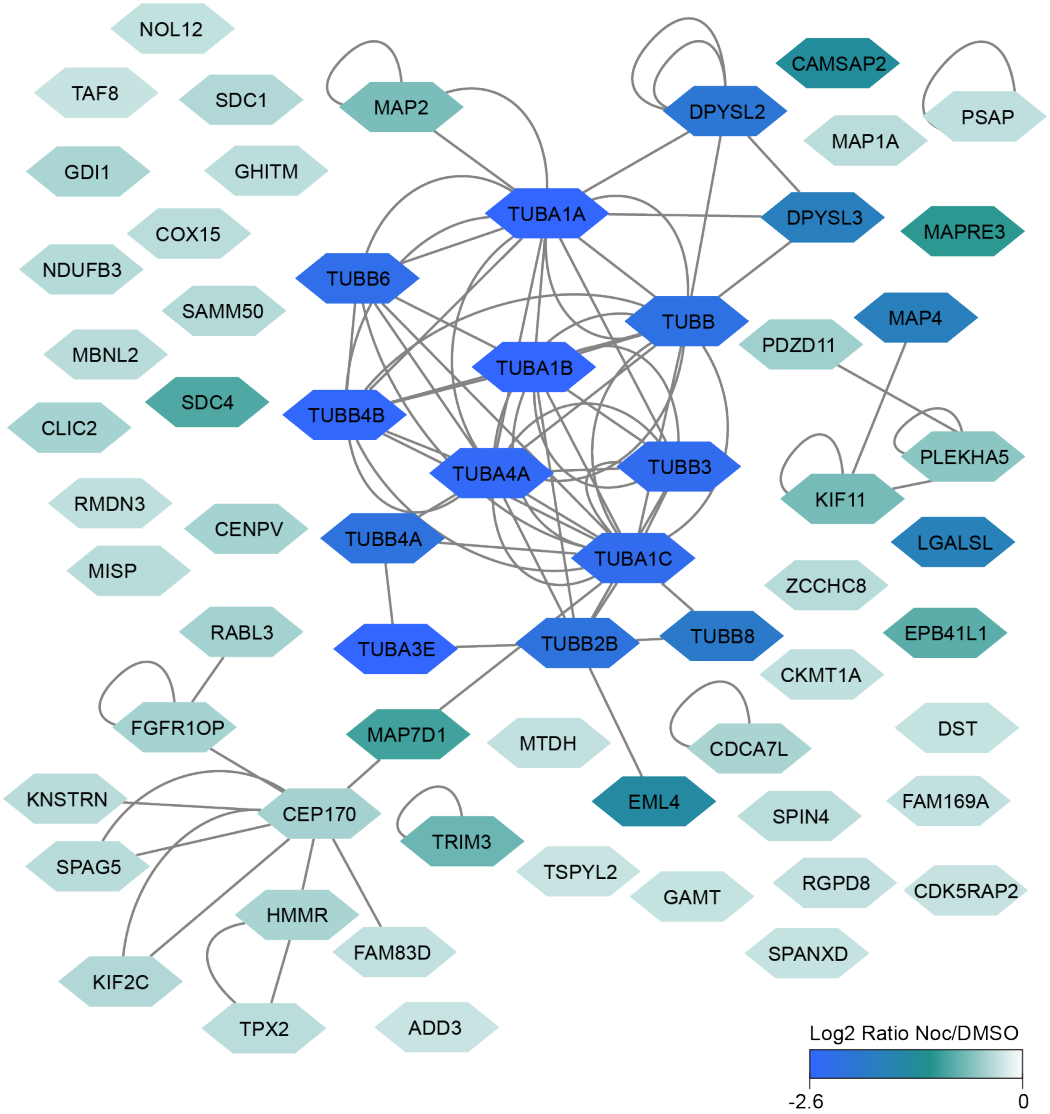

Figure 3.20 – Cytoscape network showing interactions between hits identified in the proteome

Proteins enriched in the DMSO fraction compared to the nocodazole fraction were extracted from BioGRID 4.4.202 and any confirmed interactions were mapped using cytoscape. Nodes are coloured depending on their Log_2 Nocodazole/DMSO normalised ratios as indicated in the scale bar.

3.5.9 Selection of hits for further characterisation

Of the proteins identified as being enriched in DMSO compared to nocodazole using DAVID bioinformatics analysis (shown in Figure 3.17), TRIM3, LGALSL, RMDN3 and SAMM50 were identified as proteins of interest. The log_{10} intensities of the unique peptides identified for these proteins are shown in Figure 3.21 alongside TUBA1A and EML4 for comparison. As expected, all TUBA1A and EML4 peptides displayed

greater intensities in DMSO and taxol compared to nocodazole. Similar results are observed for LGALSL which coincides with the ratio values observed in Figure 3.17B. TRIM3 showed that all peptides are de-enriched in nocodazole compared to DMSO, confirming specific extraction alongside microtubules, however the taxol intensities were somewhat variable. Finally, all peptide intensities for RMDN3 and SAMM50 coincides with the ratio values shown in Figure 3.17B, confirming their de-enrichment in both nocodazole and taxol.

TRIM3 (tripartite motif-containing protein 3) was of interest to me as this is a ubiquitin E3 ligase protein and my host laboratory has a strong focus on the ubiquitin system. TRIM proteins are a large family of E3 ligases, with more than 70 members in humans (Williams et al., 2019). 9 individuals have previously been shown to bind to microtubules (Williams et al., 2019; Short and Cox, 2006). Furthermore, TRIM3 has previously been shown to associate with and regulate the kinesin motor protein KIF21B (Labonté et al., 2013), so it is possible that it also has a direct association with microtubules. 8 peptides were identified for TRIM3 across 2 repeats. Further characterisation of TRIM3 will be explored in section 4.4.

LGALSL (Lectin Galactoside-Binding-Like Protein) also stood out as a possible protein of interest due to it being the biggest outlier of these 32 candidate proteins in the DMSO compared to Nocodazole fraction (M/L). Furthermore, it was consistently extracted across all 3 repeats, with a significant change of greater than 2-fold (Figure 3.15). It also displays sensitivity to Taxol treatment, indicating stronger association to microtubules following Taxol treatment. It was identified in all 3 repeats from 11 peptides and displayed ratio values of 0.322, 0.213 and 0.3. LGALSL, also known as galectin-related protein (GRP), is related to the galectin family of proteins which are known to bind carbohydrates (Johannes et al., 2018). LGALSL is highly conserved across vertebrates, and although it does contain a carbohydrate recognition domain at its C-terminus, its sequence is altered at 5 of the 7 resides required for carbohydrate binding. Carbohydrate binding is therefore not facilitated, indicating an alternative role for this protein which differs from other galectins (Zhou et al., 2008; Wälti et al., 2008). Additionally, LGALSL has been identified as a candidate gene for ALS (Amyotrophic lateral sclerosis) (Gelfman et al., 2019). This protein will be discussed more in section 4.2.

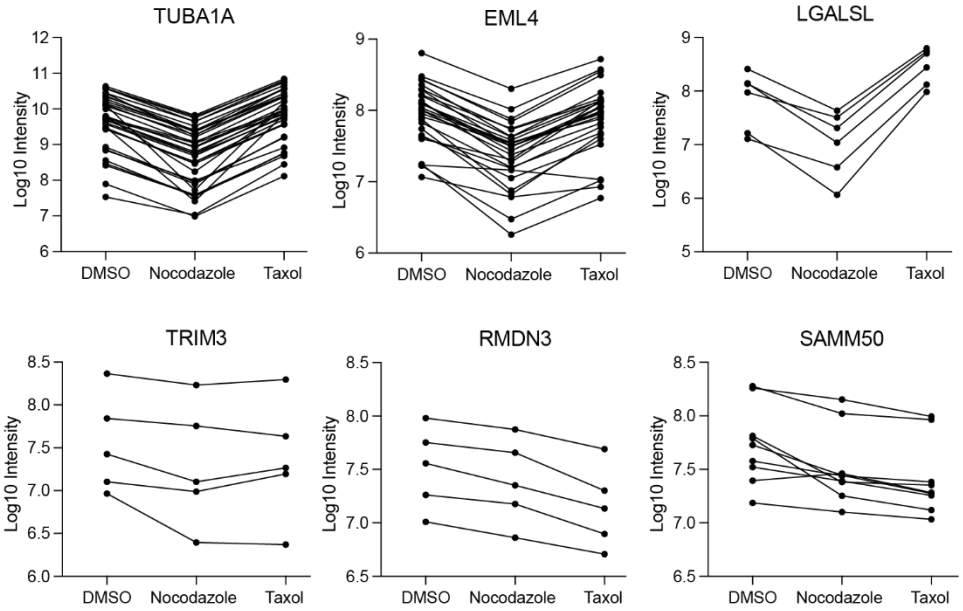

Figure 3.21 – Intensities of unique peptide of selected proteins in each condition

Log_{10} of intensity values across the DMSO (light), nocodazole (medium) and taxol (heavy) conditions for each unique peptide identified for the indicated proteins.

Finally, RMDN3 (Regulator of Microtubule Dynamics protein 3) was also identified as a potential protein of interest, with 6 peptides being identified. RMDN3, also known as PTPIP51, localises to the outer mitochondrial membrane (OMM) via its transmembrane domain and is involved in phospholipid transfer at ER-associated membranes (Yeo et al., 2021; Stoica et al., 2014). It has been shown to associate with oxysterol-binding protein (OSBP)-related proteins ORP5 and ORP8 at these locations (Galmes et al., 2016). It's family member RMDN1 associates with microtubules in *C. elegans* embryos, and possible localisation of human HA-RMDN3 to microtubules and the mitotic spindle in Hela cells is also suggested (Oishi et al., 2007). Despite this, no further evidence connecting RMDN3 and microtubules has been obtained. This protein will therefore be further characterised in section 4.3.

This data set may also allow us to infer possible interactions between proteins. SAMM50 (sorting and assembly machinery component 50 homolog), identified from 17 unique peptides, co-segregates with RMDN3 across both dimensions. This protein is also located in the OMM (Ott et al., 2012) and also associates with ORP5/ORP8 at the ER-associated membranes (Monteiro-Cardoso et al., 2022). This co-segregation and the sharing of interacting partners with RMDN3 also highlights SAMM50 as a protein of interest. Additionally, both proteins are 2 of the top 3 most Taxol-sensitive

hits within the data set: they lose their microtubule binding ability in the presence of taxol. I was therefore interested in the distribution of other mitochondrial proteins within the data set, as it is well known that mitochondria are transported along microtubule tracks (Melkov and Abdu, 2018). To do this, a scatter graph was plotted highlighting all mitochondrial proteins within the data set. Their distribution is illustrated in purple (Figure 3.22). Highlighted proteins were identified using the Human MitoCarta 3.0 and those lying outside the main cloud are labelled.

Figure 3.22 – Mitochondrial proteins identified in the mass spectrometry dataset

The logarithmic change (log_2) of the proteome composition following microtubule extraction in DMSO treated cells compared to nocodazole- and Taxol-treated cells. The average normalised ratios from at least 2 repeats are shown in the graph. Mitochondrial proteins are highlighted in purple. Mitochondrial proteins were identified using Human MitoCarta 3.0.

These highlighted proteins were identified using the Human MitoCarta 3.0 and includes 14 localising within the intermembrane space, 175 within the mitochondrial matrix, 39 at the OMM and 123 at the mitochondrial inner membrane (MIM). The

specific mitochondrial localisation for the final 15 proteins remains unknown. The majority of mitochondrial proteins are present within the main proteomic cloud. The labelled outliers include both NDUFB3 and NDUFB4 which are located within the MIM, SUPV3L1, C8orf82 and GRPEL1 which reside in the mitochondrial matrix and BCL2L1 which is at the OMM. This distribution suggests that co-extraction of RMDN3 and SAMM50 in a nocodazole- and taxol-sensitive manner is specific to these proteins rather than to mitochondria as a whole, further indicating these proteins may be specifically involved in microtubule binding.

3.5.10 Taxol enriched proteins

Taxol causes microtubule stabilisation, inducing a conformational change in the microtubule lattice (Arnal and Wade, 1995). Microtubule modifications such as acetylation and detyrosination, which accumulate on stable microtubules, have also been seen to accumulate on artificially stabilised microtubules following taxol treatment (Verhey and Gaertig, 2007). As microtubule modifications are thought to influence associations with binding proteins, the taxol condition may therefore identify novel candidates which specifically bind to or dissociate from modified microtubules. Interestingly, most known microtubule binding proteins identified did not display much sensitivity to taxol treatment, with their $\log_2$ values ranging between 0.39 and -0.43, with the exception of MAP4 and DPYSL2 which were enriched, and DPYSL3 and EB3 which were de-enriched. The top 20 proteins that were enriched and de-enriched are highlighted in Figure 3.23.

Those seen to be enriched in taxol-treated cells included LGALSL as mentioned in section 3.5.9. Other proteins include: PCNT (pericentrin) which plays a major role in centrosome biogenesis and promoting astral microtubule formation for spindle orientation in conjunction with CDK5RAP2 (Luo and Pelletier, 2014); SEC31A, a component of the Coat Protein Complex (COPII) which localises to vesicular structures (Tang et al., 2000) and is regulated by MAP1B expression levels (Takahara et al., 2018); RTN4 (Reticulon-4/Nogo-B) which links the microtubule and actin cytoskeletons in vascular smooth muscle cells and influences their dynamics (Rodríguez-Feo et al., 2016); and AP3D1, which is part of the adaptor protein-3 complex which is required for microtubule-dependent transport of lytic granules in synapses (Clark et al., 2003).

Those which were de-enriched following taxol treatment include RMDN3 and SAMM50 (3.5.9). Proteins also extracted in a similar manner include: the chromosome cohesion factor MAU2 require for cohesin loading to chromatin (Watrin et al., 2006) which in turn facilitates proper kinetochore-microtubule attachments during mitosis (Makrantoni and Marston, 2018); SHC1, an adaptor protein involved in the Raf-1/MAPK cascade (Ravichandran, 2001); and ACIN1, known as Acinus, which is a caspase-3 activated protein required for condensation of chromatin during apoptosis (Sahara et al., 1999), and is a substrate of kinases aurora A and aurora B (Hochegger et al., 2013).

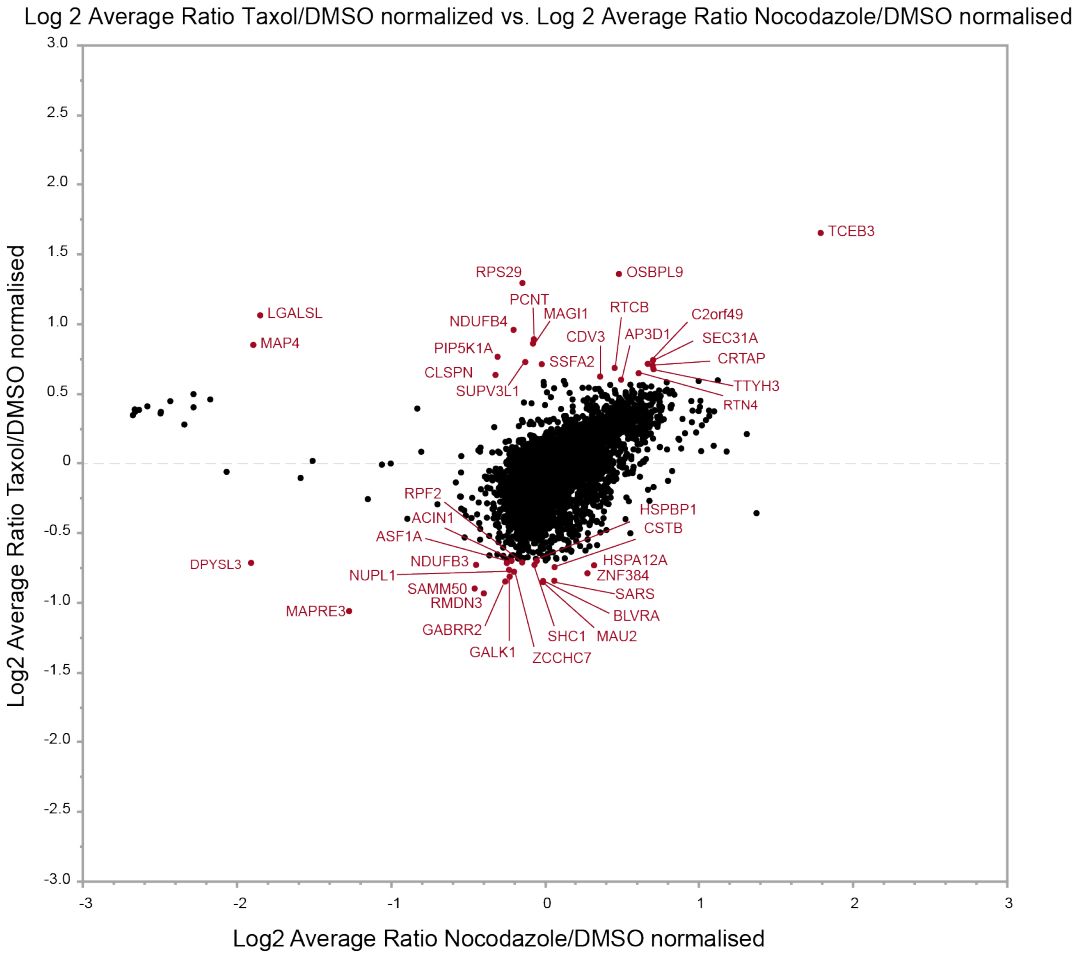

Figure 3.23 – Proteins enriched and depleted following taxol treatment

The logarithmic change (log_2) of the proteome composition following microtubule extraction in DMSO treated cells compared to nocodazole- and Taxol-treated cells. The average normalised ratios from at least 2 repeats are shown in the graph. Proteins enriched (top) and depleted (bottom) in taxol compared to DMSO are labelled in red.

3.5.11 Dynein and dynactin are enriched in nocodazole-treated fractions

Dynein is the major microtubule motor which transports cargo in a retrograde fashion (from the plus-end to the minus-end) (Höök and Vallee, 2006). Dynactin is an accessory protein required to facilitate this transport and scaffold dynein to its cargo (McKenney et al., 2014). These proteins displayed an unexpected behaviour as all were found to be enriched in the nocodazole fraction. The graph in Figure 3.24 shows the nocodazole-enriched outliers with those known to associate with microtubules labelled in green. These proteins include; dynactin subunits DCTN1, DCTN2, DCTN5 and DCTN3; cytoplasmic dynein subunits DYNC1LI1, DYNC1H, DYNLT1, DYNC1I2, DYNLRB1/DYNLRB2 and DYNLT3; BICD2 which links cargo to dynein motors; PAFAH1B1 (LIS1) which is required for dynein mediated transport (Splinter et al., 2012); and ACTR10 (Arp11) and ACTR1A (Arp1) which are both subunits of the dynactin and are involved in cargo-binding (Schroer, 2004).

To confirm this unexpected result, the $\log_{10}$ intensities of the unique peptides identified for DYNC1LI1 across each condition is shown in Figure 3.25A. The same pattern is observed for each peptide, with an enrichment observed following nocodazole treatment compared with both control and taxol cells. I therefore wanted to confirm this result by analysing the levels of DYNC1LI1 within each fraction. Figure 3.25B confirms that dynein proteins are indeed enriched following nocodazole treatment. A prior study of dynein has shown that nocodazole induces accumulation of dynein to the nuclear envelope (Gerlitz et al., 2013). This observation was therefore investigated by observing the localisation of DYNC1LI1 during the microtubule extraction protocol. Figure 3.25C confirms a relocalisation of dynein to the nuclear envelope following both nocodazole and taxol treatment, causing a ring to form around it, as indicated with the arrows. Furthermore, nuclear staining is stronger within both these conditions following LMS addition, explaining this unexpected result.

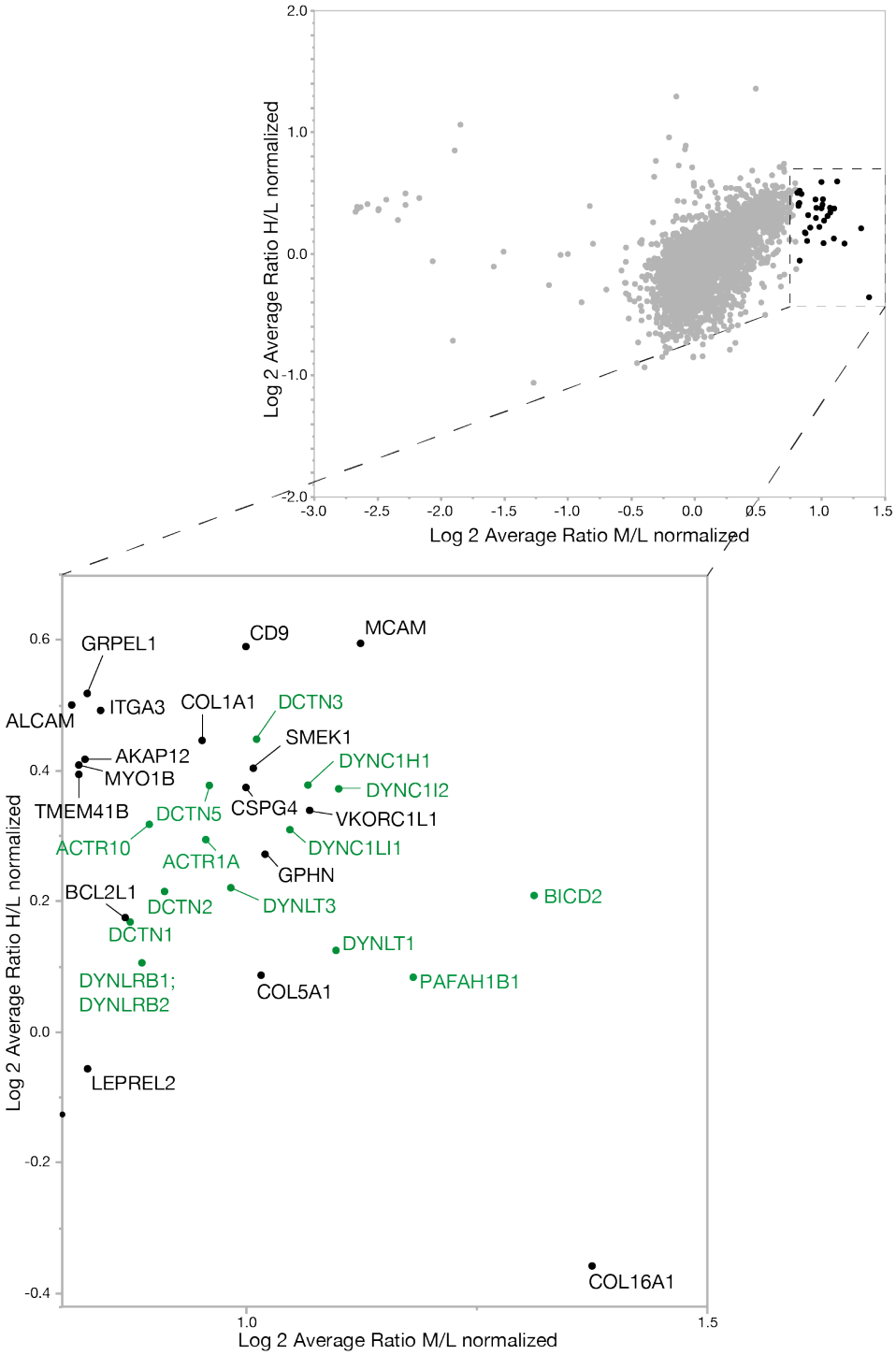

Figure 3.24 – Dynein and dynactin proteins are enriched in nocodazole-treated cells

The logarithmic change (log_2) of the proteome composition following microtubule extraction in DMSO treated cells compared to nocodazole- and Taxol-treated cells. The average normalised ratios from at least 2 repeats are shown in the graph. Proteins enriched in nocodazole compared to DMSO are labelled with dynein, dynactin or their adaptor proteins highlighted in green.

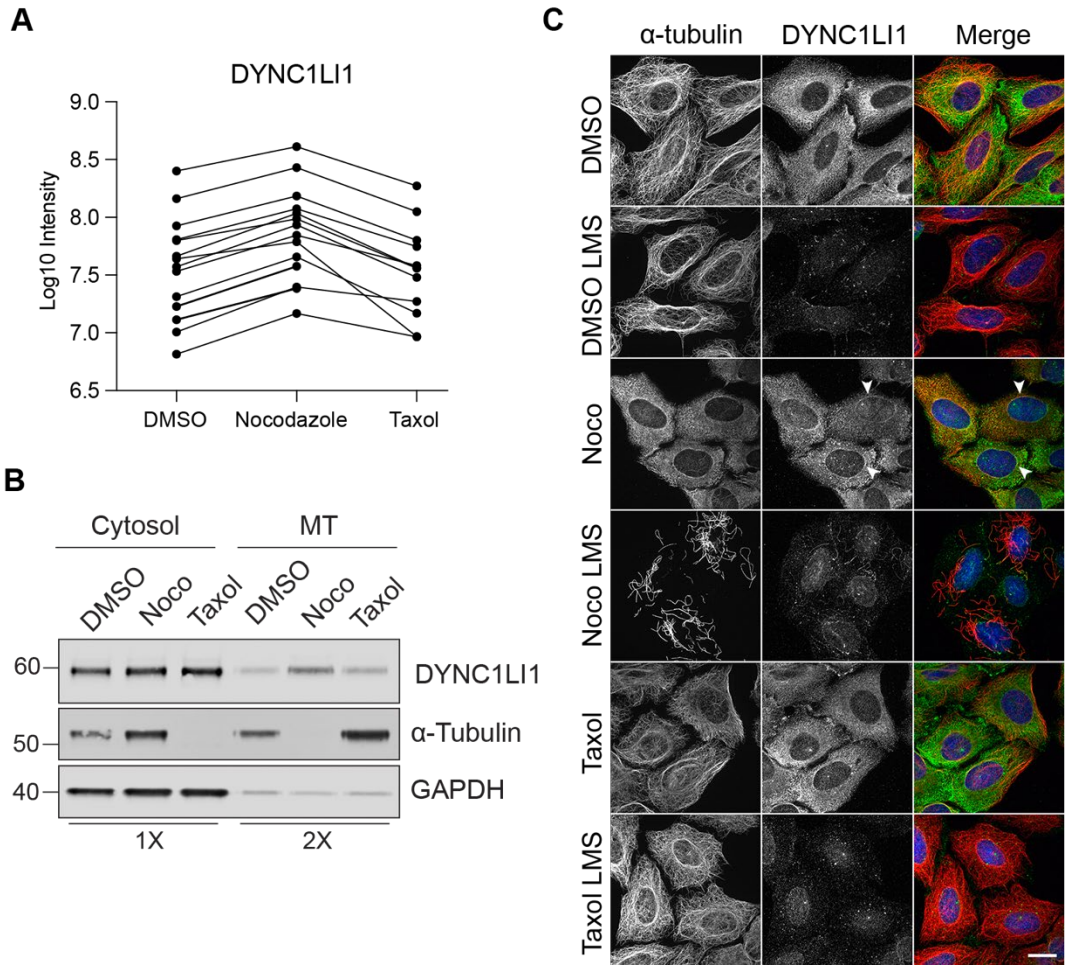

Figure 3.25 – Confirmation of dynein enrichment following nocodazole treatment

A. Log_{10} of intensity values across the DMSO (light), nocodazole (medium) and taxol (heavy) conditions for each unique peptide for DYNC1LI1. **B/C** U2OS cells were treated with 6 μM Nocodazole for 1 hour or Taxol for 30 minutes alongside a DMSO control. B**:** Lysis and microtubule stabilisation buffer (LMS) was then added (5 minutes, 4°C) to remove cytosolic proteins (cytosol). Microtubules were then collected using 8M urea (MT). Western blot analysis of α-tubulin, GAPDH and EML4. Sample proportions are as indicated. **C:** LMS buffer was either added or not (5 minutes, 4°C) before cells were fixed in ice cold methanol and stained for dynein (DYNC1LI1, green) α-tubulin (red) and DNA (DAPI, blue).

3.6 Discussion

In the work described in this chapter, I have successfully established and optimised a new methodology to specifically extract microtubule binding proteins directly from cells. U2OS cells were either treated with nocodazole, taxol or DMSO as a control in a SILAC configuration. They were then incubated with a lysis and microtubule stabilisation buffer which allows for the maintenance of intact microtubules and their binding proteins, whilst removing cytosolic proteins. Remaining microtubule fractions were then collected and analysed by LC-MS/MS. The independent repeats were performed that were analysed via MaxQuant. This analysis has allowed for the generation of quantitative microtubule proteome in an unbiased fashion. 64 of these identified proteins are specifically enriched for in a nocodazole-sensitive manner, of which 31 are novel candidate microtubule binding proteins, and some of these will be further explored in Chapter 4.

Of these 64 proteins found to be enriched, 21 are known microtubule binding proteins, thereby serving as a control for successful enrichment. It was expected that structural MAPs such as MAP4 (Iida et al., 2002) and EML4 (Houtman et al., 2007), which are known to bind along the whole microtubule lattice, would be specifically enriched for in this study. Other types of microtubule binding proteins were also identified including plus-tip binding proteins, minus-end binding proteins and kinesin motor proteins. EB3 (MAPRE3) is a plus-tip binding protein which tracks the growing end of microtubules as they polymerise (Galjart, 2010). CDK5RAP2 (CDK5 regulatory subunit-associated protein 2) is another plus tip identified which interacts with EB1 via its SxIP sequence motif (Fong et al., 2017). It has also been shown to associate with the γ-tubulin ring complex (γTuRC) and functions to regulate γTuRC-mediated microtubule nucleation (Choi et al., 2010). Minus-end localising proteins such as CAMSAP2 (Yau et al., 2014) and TPX2 (Targeting Protein for Xklp2) (Alfaro-Aco and Petry, 2017) are also extracted in a nocodazole-sensitive manner. Finally, kinesin motor proteins including KIF2C, also known as mitotic centromere-associated kinesin (MCAK), and KIF11 (Eg5). This methodology can therefore be used to extract a wide range of different microtubule binding proteins.

There are however known microtubule binding proteins which are absent within this proteome. EB2 was not present within the dataset, and EB1, although identified, was not greatly enriched for, only achieving a $\log_2$ value of -0.27. This may be explained by EB3 having the highest affinity and binding site density at the plus tip of all three

EB proteins (Roth et al., 2019). Cytoplasmic linker proteins (CLIP) CLIP170 and CLIP115 are examples of other known plus tips which are absent from the dataset. CLIP170 binds to both EB1 and EB3 at the plus tips where they regulate its dissociation from growing microtubule ends (Komarova et al., 2005). Whereas EB1 can autonomously associate with microtubule plus ends, CLIP170 requires EB1 for its tracking ability (Bieling et al., 2008) and transiently interacts with the plus tips (Komarova et al., 2005). This transient association may explain the absence of this protein. It should therefore be expected that some novel microtubule binding proteins will be missed using this protocol.

Of these 21 known microtubule binding proteins identified, many function within mitosis. The kinesin MCAK (KIF2C) is a microtubule depolymerase that regulates the attachment of microtubules to kinetochores (Ferreira et al., 2020). It functions in combination with EB3 at plus-ends to generate highly dynamic microtubules (Montenegro Gouveia et al., 2010). Other mitotic proteins include KIF11 (Eg5) which is crucial for microtubule sliding, the formation of bipolar spindles and regulation of spindle length (Kapitein et al., 2005), TPX2 which stimulates nucleation of spindle microtubules (Alfaro-Aco and Petry, 2017) and MISP (mitotic interactor and substrate of PLK1) which is an actin cytoskeleton and focal adhesion associated protein which interacts with EB1 and the dynein/dynactin complex to link with microtubules and regulate spindle positioning (Maier et al., 2013). Additionally, SPAG5, also known as astrin, and KNSTRN (kinastrin) are targeted to plus ends to regulate kinetochore-microtubule attachments and facilitate chromosome segregation (Dunsch et al., 2011; Thein et al., 2007). Nocodazole treatment induces an enrichment of mitotic proteins due to low levels causing cells to arrest in prometaphase: microtubules are depolymerised, the spindle cannot form, and mitosis cannot progress. Despite there being an expected increase in mitotic cells following nocodazole treatment, the extraction protocol will remove these proteins from this fraction whilst retaining them within the control fraction. Differential analysis will therefore show increased mitotic proteins in the control compared to nocodazole, making them identifiable outliers. Additionally, many mitotic proteins display low levels during interphase and elevated levels during M phase which may further increase the ratios obtained. Both MCAK (Ganguly et al., 2008) and TPX2 (Neumayer et al., 2014) have been shown to respond in this manner, further indicating why multiple mitotic proteins have been extracted. This marked increase in the detection of mitotic proteins suggests that this protocol could be utilised to investigate spindle binding proteins by combining this with cell synchronisation protocols to enrich for mitotic cells.

Taxol is known to induce microtubule stabilisation by inducing polymerisation and preventing depolymerisation (Horwitz, 1994). These stable microtubules are able to accumulate multiple tubulin PTMs such as acetylation and detyrosination of the α-tubulin subunit (Verhey and Gaertig, 2007). Both stability and the presence of modifications have been implicated in regulating the interactions between microtubules and associated proteins (Janke and Magiera, 2020). RTN4 was shown to be enriched following Taxol treatment, but despite being previously linked with microtubules, it did not display sensitivity to nocodazole. Furthermore, a connection with microtubule acetylation has also been highlighted with this protein: a reduction in HDAC6, the major tubulin de-acetylase (Hubbert et al., 2002), combined with an increase in acetylation is observed when RTN4 is depleted (Rodríguez-Feo et al., 2016). Since acetylation and RTN4 are both increased following taxol treatment, this suggests there is a possible inverse relationship occurring between microtubule dynamics and stability and the expression and/or association of RTN4 and microtubules. Additionally, the adaptor protein SHC1 is reduced here in response to taxol treatment. Previous research has shown that taxol increases tyrosine phosphorylation of SHC1 causing the SHC1-Grb2 complex to form and activate the MAP kinase pathway (Wolfson et al., 1997). Furthermore, additional effects which are distinct from microtubule stability, such as altering cytokine synthesis, have been observed (White et al., 1998). As the majority of these proteins do not display differential extraction with nocodazole as well, it can therefore be hypothesised that some proteins which display taxol-sensitivity do so via a distinct pathway unconnected to microtubule stability.

Dynein is a very large multi-protein subunit, made up from a pair of heavy chains and multiple accessory proteins termed intermediate, light intermediate and light chains (Vallee et al., 2004). This motor protein interacts with multiple adaptor proteins, such as the dynactin complex, which are required to regulate its activation and localisation (Kardon and Vale, 2009). A number of these proteins including dynein heavy and light chains, dynactin subunits and BICD2 (Bicaudal D2) were enriched within the nocodazole-treated fraction. This was intriguing as they are well characterised microtubule binding proteins. Previous studies have shown that dynein and its interactors are relocated to the nuclear envelope following nocodazole treatment (Gerlitz et al., 2013; Raaijmakers et al., 2013) and was confirmed by my data shown in Figure 3.25. Under physiological conditions, dynein is recruited to the nuclear envelope in G2/prophase in a BICD2 dependent manner (Raaijmakers et al., 2013; Splinter et al., 2010). Furthermore, during the transition from interphase into mitosis,

microtubules undergo a large amount of reorganisation (Petry, 2016). Interphase microtubules first undergo partial disassembly at the periphery during prophase. Then when nuclear envelope breakdown occurs, a process which requires cytoplasmic dynein (Salina et al., 2002), a rapid disassembly in tubulin polymers is seen (Petry, 2016). It is therefore possible that nocodazole-treatment mimics the early stages of mitosis by inducing the loss of microtubule structures and hence the recruitment of dynein and its adaptors proteins to the nuclear envelope, explaining this observed phenotype.

This work presents the first attempt to determine a microtubule proteome directly from cells in interphase in a quantitative manner. This may then go on to open up new biology following further confirmation and characterisation of these candidate novel microtubule binding proteins.

Chapter 4 – Characterisation of novel microtubule binding proteins

4.1 Introduction

In the previous chapter I described the successful optimisation of a protocol using a new methodology to extract and identify potential novel microtubule binding proteins. In this chapter, I describe my further investigations of these candidates to firstly confirm their microtubule binding ability, and secondly identify any phenotypic effects observed on the microtubule network from manipulating these proteins. Microtubule binding proteins play a crucial role in regulating the differential functions of the cytoskeleton. As the microtubule network is widespread throughout the cell, it can be speculated that there is a large and ever-growing list of proteins known to associate and interact with them to some degree. As it is the binding proteins which regulate the dynamics and functions of microtubules, identifying and characterising them will help us to better understand the microtubule network.

Proteins were selected for further characterisation based on available tools and reagents, as well as those which fit best with the current interests of my host laboratory. These included LGALSL, RMDN3 and TRIM3. LGALSL was selected as this was the greatest outlier of novel candidates within the proteome and was identified to a similar degree in all 3 repeats. RMDN3 was selected for further analysis as it's gene abbreviation stands for 'regulator of microtubule dynamics 3', however a limited connection to microtubules has been observed, with RMDN3 localising to the outer mitochondrial membrane (OMM). Furthermore, the fact that it was extracted in a similar manner to SAMM50 was interesting to me: both are sensitive to nocodazole and taxol by a comparable degree. These are both OMM proteins and share common binding partners including oxysterol-binding protein (OSBP)-related proteins ORP5 and ORP8 (Galmes et al., 2016; Monteiro-Cardoso et al., 2022). Finally, TRIM3 was selected as this is an E3-ligase enzyme and my host laboratory has an interest within the ubiquitin system. Furthermore, a selection of other TRIM proteins have been previously shown to associate with microtubules, making TRIM3 a prime candidate as a novel binding protein.

4.2 LGALSL

From the proteomic results displayed in section 3.5.4, LGALSL was enriched in the control microtubule fraction compared to nocodazole. It was the most significant hit identified which is not already annotated as a microtubule binding protein. Furthermore, it is also taxol sensitive, with more LGALSL being extracted following treatment of taxol compared to the control. As this was the most significant and consistent novel microtubule binding protein identified, further characterisation of it was performed in this chapter.

4.2.1 Structure and function of LGALSL

LGALSL, also known as Galectin Related Protein (GRP) and HSPC159, is a member of the galectin family of proteins which are known to bind carbohydrates on glycoproteins (Johannes et al., 2018). LGALSL is highly conserved across vertebrates. It is a relatively small protein consisting of only 172 amino acids and with a molecular weight of ~ 19kDa. It contains a carbohydrate recognition domain (CRD) at its C-terminus which is found within galectin family proteins (Figure 4.1A and B), however its sequence is altered at 5 of the 7 residues required for carbohydrate binding. Therefore, unlike all other galectin proteins, LGALSL is thought to not facilitate carbohydrate binding, indicating there may be an alternative role for this protein (Zhou et al., 2008; Wälti et al., 2008). This predicted alternative function however has not been identified, and no connection of LGALSL/GRP and microtubules is apparent within the literature.

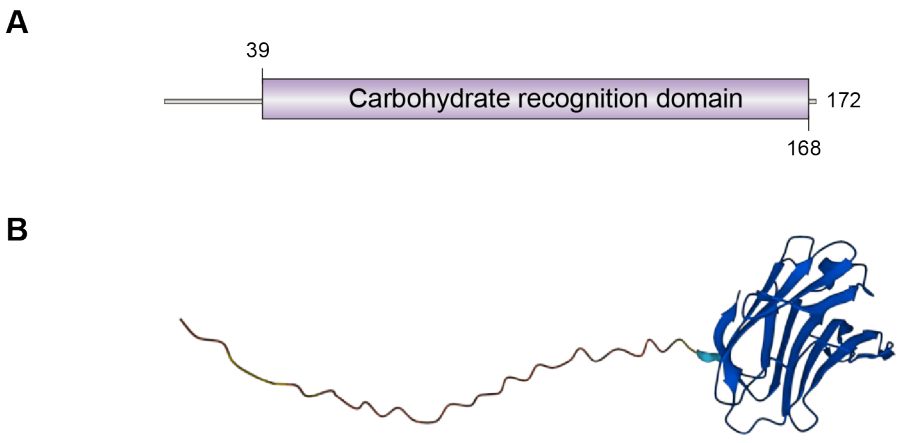

Figure 4.1 – LGALSL domain map and structure

A. Schematic diagram of domains in LGALSL. **B.** AlphaFold structure of LGALSL: AF-Q3ZCW2-F1. AlphaFold2 DB version 2022-11-01.

4.2.2 Cloning and generation of GFP tagged LGALSL

In order to easily visualise the localisation of LGALSL, I generated a GFP-tagged version, illustrated in Figure 4.1A. The GFP was inserted at the N-terminus of LGALSL based on the predicted protein structure from alpha fold (Figure 4.1B), to not interfere with the CRD. The cloning process for generating this construct is detailed within section 2.3.2.

4.2.3 LGALSL displays microtubule localisation

Having generated the GFP-tagged version, transfection into U2OS cells revealed that LGALSL localisation is largely cytosolic, however some filamentous structures, which may reflect microtubules, can be seen (Figure 4.2A). In order to verify this, I transfected GFP-LGALSL into Hela cells which stably express cherry tubulin to visualise colocalisation with the microtubule network (Figure 4.2B). These results suggests that overexpressed GFP-LGALSL can interact with microtubules.

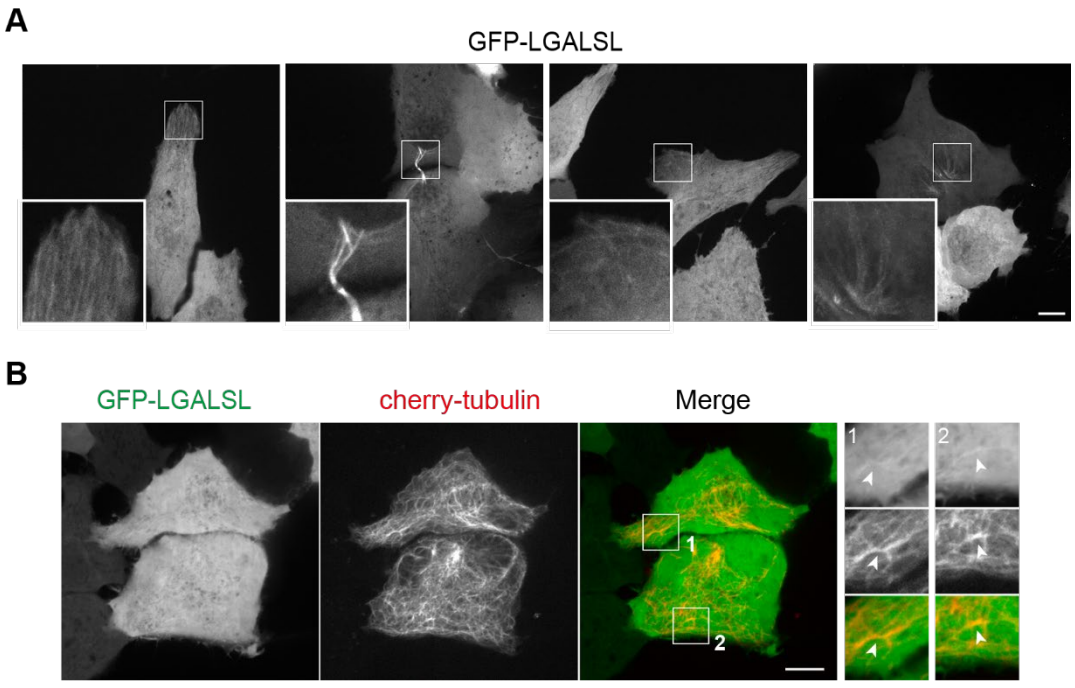

Figure 4.2 – LGALSL may localise to microtubules

A. U2OS cells and **B.** HeLa cherry-tubulin cells were transfected with 1 µg GFP-LGALSL plasmid DNA. Images were acquired from live cells in ibidi dishes using a 3i spinning disc confocal microscope. Scale bars = 10 µm.

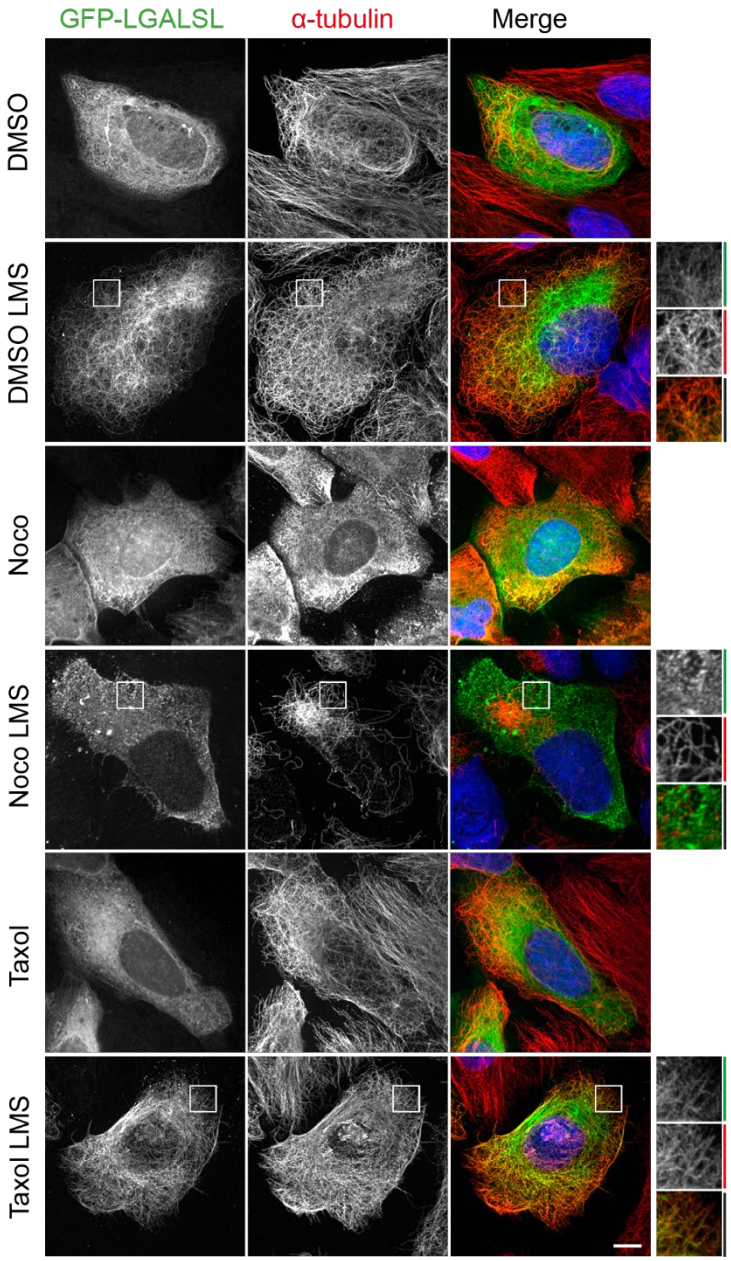

Figure 4.3 – GFP-LGALSL shows clear colocalisation with microtubules

U2OS cells were transfected with 1 µg DNA of GFP-LGALSL for 21 hours. Cells were then treated with 6 µM Nocodazole (Noco, 1 hour) or 6 µM taxol (30 minutes) alongside a DMSO control. Lysis and microtubule stabilisation buffer (LMS) was then either added or not for 5 minutes at 4°C. Cells were then fixed with ice cold methanol and stained for α-tubulin. Visualisation was performed with a 3i spinning disk confocal microscope. Scale bar = 10 µm.

To see whether removal of the cytosol allowed for better visualisation of GFP-LGALSL on microtubules, I performed the microtubule extraction protocol as detailed in section 2.4.9 on transfected cells and fixed and stained them for α-tubulin. Nocodazole and taxol treated cells were also visualised alongside for comparison. Figure 4.3 shows

that when either treatment is added, localisation to microtubules is difficult to detect. However, when lysis and microtubule stabilisation (LMS) is added, clear microtubule localisation is seen for both control and taxol treated cells but is lost in nocodazole treated cells. Under these conditions, the morphology of the microtubule network is altered, adopting a curlier structure, although the same is not observed under Taxol-treated conditions. This confirms that LGALSL is a novel microtubule binding protein successfully identified following differential microtubule extraction.

4.3 RMDN3

From the proteomic results displayed in section 3.5.4, RMDN3 (Regulator of Microtubule Dynamics protein 3) was enriched in the microtubule fraction compared to nocodazole. Furthermore, it is also taxol sensitive, with less RMDN3 being extracted following treatment with taxol. It was the second most taxol sensitive protein in the whole data set behind MAPRE3 (EB3), a microtubule end-binding protein. As this was the most taxol sensitive novel candidate protein identified, further characterisation was performed.

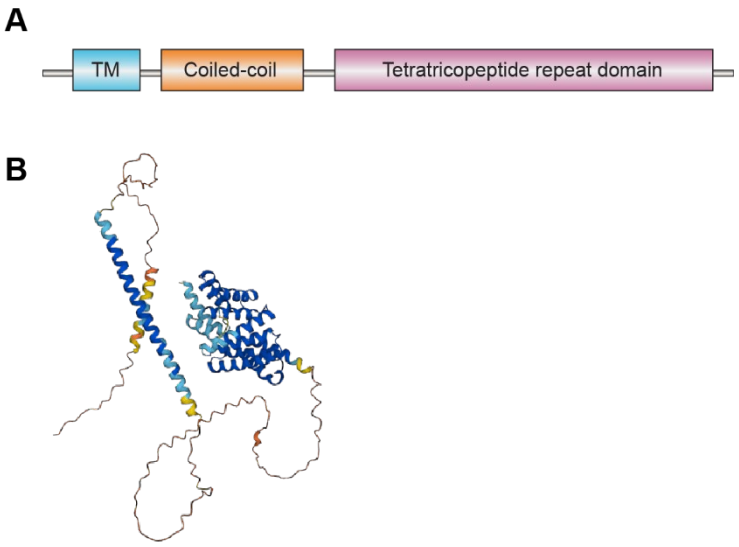

Figure 4.4 – RMDN3 domain map and structure

A. Schematic diagram of domains in RMDN3. **B.** Alpha fold structure of RMDN3. AF-Q96TC7-F1, AlphaFold2 DB version 2022-11-01.

4.3.1 Structure and function of RMDN3

RMDN3, also known as PTPIP51 (protein tyrosine phosphatase-interacting protein 51) is a transmembrane protein which localises within the outer mitochondrial membrane (OMM). It is made up of a transmembrane domain and a coiled-coil at its

N-terminus, and a tetratricopeptide repeat (TPR) domain at its C-terminus (Stoica et al., 2014). The transmembrane domain facilitates its insertion into the OMM, the coiled-coil domain may mediate tetramerization and lipid binding activity, and the TPR domain is required for protein-protein and lipid interactions (Yeo et al., 2021). This structure is shown in Figure 4.4A and B. It is involved in phospholipid binding and transfer, of phosphatidic acid in particular, at mitochondria-associated ER membranes (Yeo et al., 2021). It has been shown to associate with VAPB (vesicle-associated membrane-associated protein B) to regulate calcium homeostasis, as loss of either protein reduces the uptake of calcium from released ER stores into the mitochondria (De vos et al., 2012). An additional role for RMDN3 in initiation of apoptosis has also been shown. RMDM3 overexpression resulted in a decrease in the mitochondrial membrane potential, release of cytochrome c, caspase-3 activation and PARP cleavage, eventually leading to mitochondrial-dependent apoptosis (Lv et al., 2006). This apoptotic initiation is most likely the result of an influx of Ca^{2+} following upregulated RMDN3 (Yeo et al., 2021).

In *C. elegans*, 5 related proteins have been identified, with RMDN1, 2 and 3 being conserved in humans. RMDN1 associates with microtubules in *C. elegans* embryos, and one figure within this paper shows possible localisation of human HA-RMDN3 and HA-RMDN2 to microtubules and the mitotic spindle in Hela cells (Oishi et al., 2007). These results seem contradictory to others within the literature which detail mitochondrial localisation of RMDN3, and also the presence of the transmembrane domain (De vos et al., 2012). RMDN3 was therefore further investigated in this chapter to confirm these observations.

4.3.2 Alignment of RMDN3 and RMDN1

To identify the similarities between RMDN1 and RMDN3, I performed an alignment of the human protein sequences (Figure 4.5). RMDN1 is lacking the first 129 amino acids present in RMDN3, which includes the mitochondrial transmembrane domain and the coiled-coil region. The greatest sequence similarity between the 2 proteins occurs towards the end of the protein sequence. This is consistent with the structural data showing that both RMDN1 and RMDN3 have tetratricopeptide repeats towards the C-terminus (Yeo et al., 2021).

```
RMDN1  ------------------------------------------------------------ 0
RMDN3  MSRLGALGGARAGLGLLLGTAAGLGFLCLLYSQRWKRTQRHGRSQSLPNSLDYTQTSDPG 60

RMDN1  ------------------------------------------------------------ 0
```

```
RMDN3  RHVMLLRAVPGGAGDASVLPSLPREGQEKVLDRLDFVLTSLVALRREVEELRSSLRGLAG 120


RMDN1  ---------MALAAR--LWRLLPFRRGAAP--GSRLP--AGTSGSRGHCGPCRFRGFEVM 45
RMDN3  EIVGEVRCHMEENQRVARRRFPFVRERSDSTGSSSVYFTASSGAT-FTDAESEGGYTTA 179
                *    *    * :** *  :   **     :.:**:  . .     *: .

RMDN1  G-------------NPGTF---KRGLLLSALSYLGFETYQVIS--Q---AAVVHATAKVE 84
RMDN3  NAESDNERDSDKESEDGEDEVSCETVKMGRKDSLDLEEEAASGASSALEAGGSSGLEDVL 239
       .             : *      . : :.  . *.:*   . .  .   *.   .  .*

RMDN1  EILEQADYLYESGETE--KLYQLL--TQYKESEDAELLWRLARASRDVAQLSRTSEEEKK 140
RMDN3  PLLQQADELHRGDEQGKREGFQLLLNNKLVYGSRQDFLWRLARAYSDMCELTEEVSEKK- 298
        :*:*** *:...*    : :***  .:   ..  ::******  *:.:*:.  .*:*

RMDN1  LLVYEALEYAKRALEKNESSFASHKWYAICLSDVGDYEGIKAKIANAYIIKEHFEKAIEL 200
RMDN3  SYALDGKEEAEAALEKGDESADCHLWYAVLCGQLAEHESIQRRIQSGFSFKEHVDKAIAL 358
         . :. * *: ****.:.*  .* ***:  .::.::*.*: :* ..: :***.:*** *

RMDN1  NPKDATSIHLMGIWCYTFAEMPWYQRRIAKMLFATPPSSTYEKALGYFHRAEQVDPNFYS 260
RMDN3  QPENPMAHFLLGRWCYQVSHLSWLEKKTATALLESPLSATVEDALQSFLKAEELQPGFSK 418
       :*::  : .*:* *** .:.: * ::: *. *: :* *:* *.**  * :**:::*.* .

RMDN1  KNLLLLGKTYLKLHNKKLAAFWLMKAKDYPAHTEEDKQIQTEAAQLLTSFSEKN       314
RMDN3  AGRVYISKCYRELGKNSEARWWMKLALELPDVTKEDLAIQKDLEELEVILRD--       470
        . : :.* * :* ::. * :*:  * : *  *:**  **.:  :* . : :
```

Figure 4.5 – Alignment of human RMDN1 and RMDN3

4.3.3 RMDN3 localises to mitochondria

I first wanted to confirm the localisation of endogenous RMDN3. U2OS cells were either fixed with ice cold methanol and co-stained for α-tubulin (Figure 4.6A, top), or fixed with paraformaldehyde (PFA) and co-stained for the mitochondrial marker TOMM20 (translocase of outer mitochondrial membrane 20, Figure 4.6A, bottom). Colocalisation was observed with TOMM20 but not with α-tubulin, confirming that endogenous RMDN3 localises to the mitochondria as previously suggested (Stoica et al., 2014). It should be noted that staining of RMDN3 differs slightly with different fixation methods, with PFA providing better visualisation of mitochondrial colocalisation, but MeOH allowing better tubulin staining. I next wanted to see whether overexpressed RMDN3 replicates the same localisation pattern as the endogenous protein. A construct expressing RMDN3 containing a HA tag at the C-terminus (obtained from MRC PPU as detailed in 2.3.2) was transiently transfected into U2OS cells and fixed and stained for HA and either α-tubulin (MeOH fixation, Figure 4.6B top) or TOMM20 (PFA fixation, Figure 4.6B bottom). As expected, RMDN3-HA localises to the mitochondria as clear co-localisation with TOMM20. There are however some instances which suggest mitochondrial-located RMDN3-HA may be tracking along microtubules, as highlighted in the enlarged section.

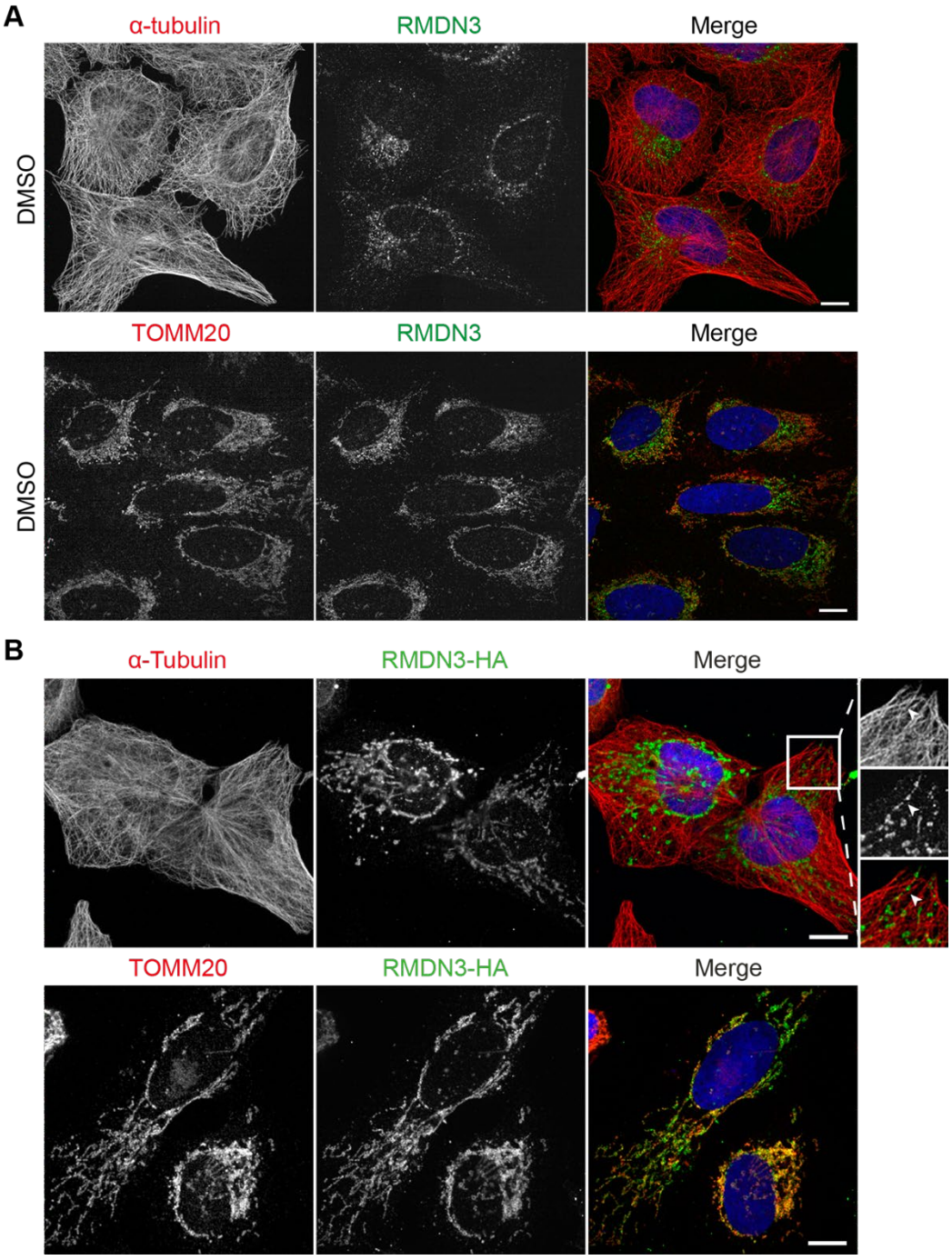

Figure 4.6 – RMDN3 colocalises with the mitochondrial network

A. Endogenous RMDN3. U2OS cells were fixed with ice cold methanol and stained for α-tubulin (red, top panel), or fixed with PFA and stained for TOMM20 (red, bottom panel). Both sets were co-stained with RMDN3 (green) and DAPI (blue). **B.** Overexpressed RMDN3-HA. U2OS cells were transfected with 1 µg of RMDN3-HA plasmid DNA for 21 hours. Cells were fixed with ice cold methanol and stained for α-tubulin (red, top panel), or fixed with PFA and stained for TOMM20 (red, bottom panel). Both sets were co-stained with HA (green) and DAPI (blue). Possible tracking along microtubules is indicated with an arrow. Images were acquired using a 3i spinning disc confocal microscope. Scale bars = 10 µm.

4.3.4 Cloning and generation of GFP tagged RMDN3

In order to more easily visualise the localisation of RMDN3, I decided to generate a GFP-tagged version. A GFP tagged version allows for easier visualisation as live-cell imaging can be performed. The cloning process for generating this construct is detailed within section 2.3.2. As the transmembrane domain for mitochondrial insertion resides at the N-terminus of the protein, and the TPR domain for protein-protein interactions is found at the C-terminus, the GFP-tag was incorporated at either end of the protein so the impact of its presence could be analysed. Furthermore, an additional construct containing a C-terminally tagged version of RMDN3 lacking the transmembrane domain (by deleting amino acids 2-41) which targets RMDN3 to the OMM was also generated. These constructs are illustrated in Figure 4.7.

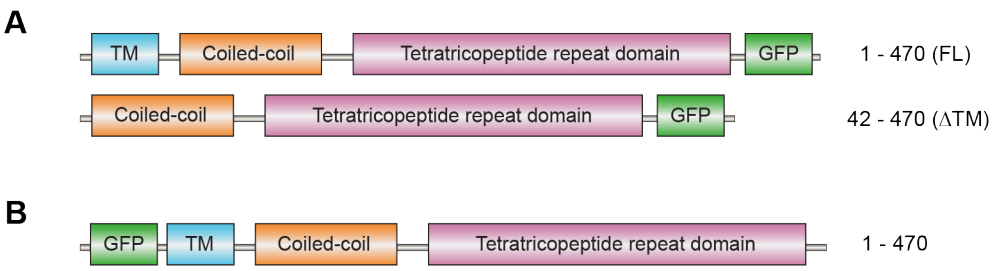

Figure 4.7 – Generated GFP-tagged RMDN3 constructs

A. Schematic representation of the full length (FL) and truncated RMDN3 (ΔTM) constructs with a C-terminal GFP tag. **B.** Schematic representation of full length RMDN3 with an N-terminal GFP tag.

4.3.5 C-terminally tagged RMDN3 localises to mitochondria via the transmembrane domain

I first wanted to visualise the C-terminally tagged construct to confirm mitochondria localisation. Additionally, I compared the full-length construct to a truncation lacking the transmembrane domain (ΔTM) to visualise its localisation when mitochondrial targeting was abolished. Figure 4.8A shows that RMDN3-GFP successfully localises to the mitochondria as colocalisation with TOMM20 was observed (top panel). Upon removing the transmembrane domain however, mitochondrial targeting is obliterated, and the protein adopts a cytosolic localisation (bottom panel). For comparison, co-staining of both constructs with α-tubulin was also performed (Figure 4.8B) and confirms that neither the full-length of the ΔTM are able to localise to microtubules.

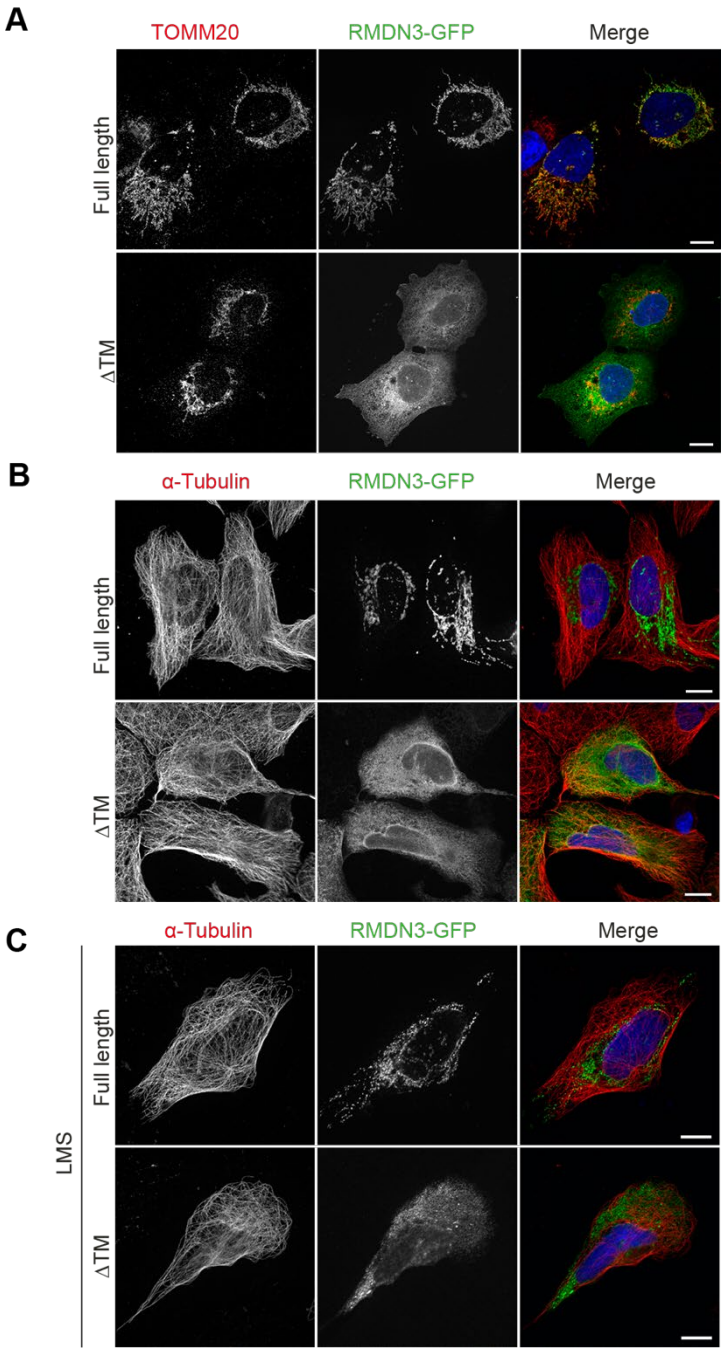

Figure 4.8 – Removal of the RMDN3 transmembrane domain prevents mitochondrial localisation.

U2OS cells were transfected with 1 µg of RMDN3-GFP plasmid DNA (full length or the ΔTM truncation) for 21 hours. **A.** Cells were fixed with paraformaldehyde and stained for TOMM20 (red) and DAPI (blue). **B.** Cells were fixed with ice cold methanol and stained for α-tubulin (red) and DAPI (blue). **C.** Cells were treated with lysis and microtubule stabilisation buffer (LMS) for 5 minutes at 4°C to wash away the cytosolic proteins whilst retaining microtubules. Cells were then fixed with ice cold methanol and stained for α-tubulin (red) and DAPI (blue). Visualisation was performed with a 3i spinning disk confocal microscope. Scale bar = 10 µm.

As LGALSL could be visualised on the microtubule network by removing the cytosolic proteins (shown in Figure 4.3), I performed the microtubule extraction protocol on cells transfected with the FL or ΔTM RMDM3 in a similar manner before fixing and staining for α-tubulin (Figure 4.8C). Despite reducing the levels of cytosolic proteins, microtubule localisation was still not observed with either construct. As the TPR domain resides at the C-terminal end of the protein, it is possible that the addition of the GFP tag directly interferes with the RMDN3-microtubule interaction, or induces a conformational change in the structure, preventing their association.

4.3.6 N-terminally tagged RMDN3 localises to microtubules

To further investigate RMDN3 as a novel microtubule binding protein, I confirmed the localisation of the generated construct with the GFP-tag incorporated at the N-terminus of the protein. As the transmembrane domain is predicted to occur between the amino acid positions 20 to 42, the insertion of the GFP tag here may prevent successful insertion into the OMM. The TPR domain is expected to be unaffected by the addition of GFP at this end of the protein. Figure 4.9A illustrates that GFP-RMDN3 does not localise to the mitochondria but does in fact localise to what appears to be the microtubule network. I further confirmed this by visualising its localisation within Hela cells which stably express cherry-tubulin (Figure 4.9B). Co-localisation is observed, indicating that tagging RMDN3 at the N-terminus facilitates microtubule binding. As this construct allowed me to visualise the association of RMDN3 with microtubules, this was used for all subsequent analysis.

4.3.7 GFP-RMDN3 stabilises microtubules and prevents their depolymerisation

To confirm that GFP-RMDN3 displays the typical characteristics of a microtubule binding protein, its localisation following nocodazole-induced microtubule depolymerisation was analysed. Figure 4.10A shows that unexpectedly, RMDN3 tubular structures persist under these conditions. Interestingly, the microtubules which are bound by this overexpressed RMDN3 are unable to undergo depolymerisation. To test whether these decorated microtubules are resistant to depolymerisation in general, cold treatment was applied. The same result is observed with cold-induced depolymerisation, as shown in Figure 4.10B. It can therefore be hypothesised that the overexpression and induced microtubule bundling by GFP-RMDN3 causes microtubules to resist depolymerisation from nocodazole treatment and cold temperatures.

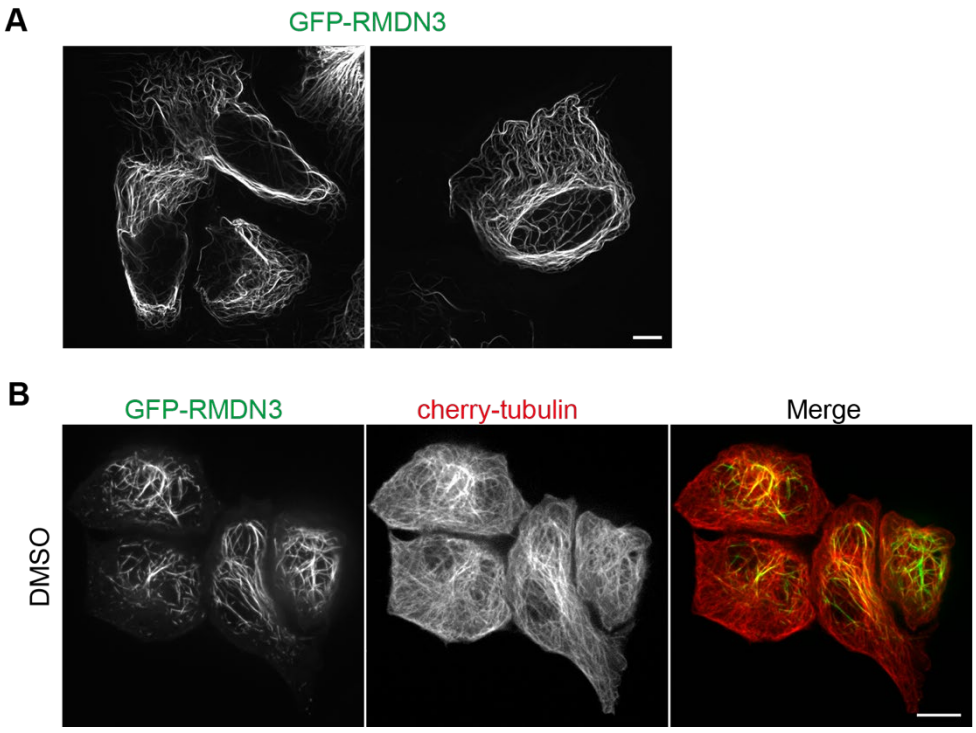

Figure 4.9 – GFP-RMDN3 localises to microtubules

Cells were transfected with 1 µg of GFP-RMDN3 plasmid DNA for 21 hrs. **A.** U2OS cells. **B.** Hela cells expressing stable mCherry-tubulin. Visualisation was performed live with a 3i spinning disk confocal microscope. Scale bars = 10 µm.

I also noticed that in control cells, clear co-localisation was not fully observed between the GFP-RMDN3 and the α-tubulin antibody. Overexpressed GFP-RMDN3 induces significant microtubule bundling when transiently transfected into both U2OS cells and Hela cherry tubulin cells (shown in Figure 4.9). As colocalisation is observed with the cherry tubulin, it is possible that the high level of protein bound to the microtubule lattice and the induced bundling may reduce access for the antibody to bind properly. Following taxol and nocodazole treatment, co-localisation between the GFP tag and the α-tubulin staining is increased as a greater overlap can be seen. The proteomic results shown in section 3.5.6 revealed that RMDN3 is also taxol sensitive, with treatment causing a loss in microtubule binding. Taxol treatment was therefore expected to reduce colocalisation of RMDN3 with microtubules however this was not observed.

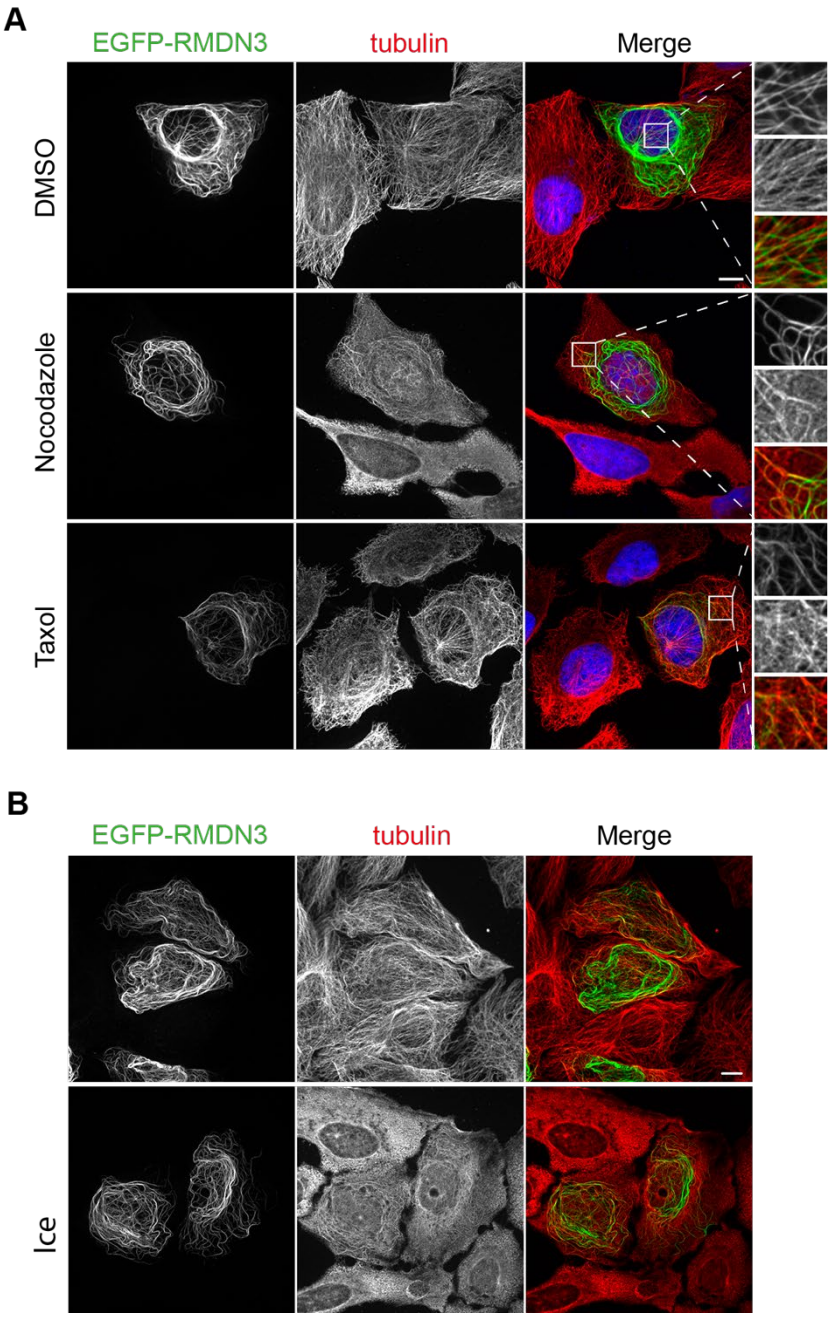

Figure 4.10 – GFP-RMDN3 localisation is not lost with nocodazole or cold treatment

U2OS cells were transfected with 1 µg of GFP-RMDN3 plasmid DNA for 21 hours. **A**. Cells were then treated with nocodazole (6 µM, 1 hour), taxol (6 µM, 30 minutes) or DMSO (1 hour) before being fixed with ice cold methanol and stained for α-tubulin. **B.** Cells were either incubated on ice at 4ºC or not for 1 hour before being fixed with ice cold methanol and stained for α-tubulin. Images were acquired using a 3i spinning disc confocal microscope. Scale bar = 10 µm.

4.3.8 GFP-RMDN3 localises to modified microtubules

Microtubules are highly decorated in post-translational modifications (PTMs). These include both common PTMs such as phosphorylation, acetylation and ubiquitylation, and unique modifications such as detyrosination, glutamylation and glycylation. These modifications are described in more detail in section 1.1.10.2. It was noticed that RMDN3 does not localise to the whole microtubule network, as the α-tubulin staining extends further than the GFP signal in all cells show in Figure 4.10. Furthermore, localisation is restricted to the perinuclear region, indicating its presence on more stable microtubules. As modified microtubules are enriched at the perinuclear region (Akisaka et al., 2011), I therefore wanted to check different microtubule populations to see whether RMDN3 displayed greater colocalisation with these. Acetylated α-tubulin (AcTub) and detyrosinated (DetyTub) were tested, and RMDN3 can be seen to localise closely with both (Figure 4.11A). Pearson's colocalisation coefficient was calculated for each using the JACoP plugin in Fiji and compared with that of the whole microtubule network (Figure 4.11B). A relatively low colocalisation coefficient value was observed for the whole tubulin network, with an average of 0.52. These values were increased for both acetylated and detyrosinated with values of 0.71 and 0.78 respectively, indicating that RMDN3 has a greater overlap with both modified microtubule networks.

4.3.9 GFP-RMDN3 does not localise to the centrosome

Most microtubules originate from a microtubule organising centre (MTOC), with the most dominant one being the centrosome. The centrosome is a complex globular structure and contains the gamma-tubulin ring complex (y-TuRC), formed from y-tubulin and several other proteins, which acts as a scaffold for microtubule nucleation (Liu et al., 2020). As this organelle is rich in growing microtubules, many microtubule-associated proteins are commonly found here. To determine whether GFP-RMDN3 is among these proteins, colocalisation with the centrosome marker pericentrin was performed. Figure 4.12 confirms that GFP-RMDN3 is not found at the centrosome as no overlap with the marker is observed.

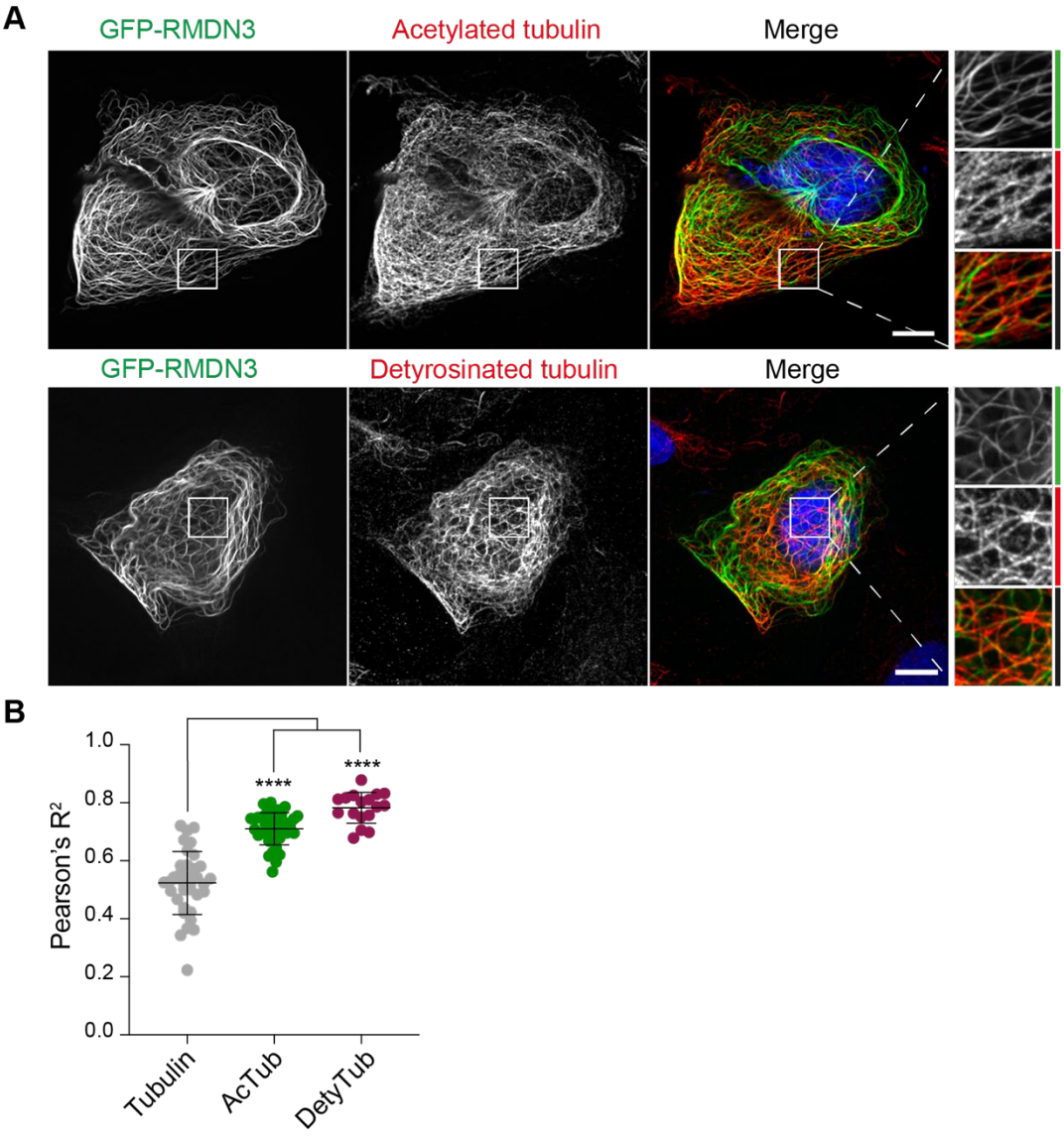

Figure 4.11 – RMDN3 localises on acetylated and detyrosinated microtubules

A. U2OS cells were transfected with 1 µg of either GFP-RMDN3 plasmid DNA for 21 hours. Cells were then fixed with ice cold methanol and stained for acetylated tubulin (top panel) or detyrosinated tubulin (bottom panel). Scale bar = 10 µm. **B**. Pearson's colocalisation coefficient was calculated using JaCoP plugin in Fiji. Mean and standard deviation is shown. Cell number: Tubulin (36), AcTub (43), DetyTub (17). Statistical significance was performed via one-way ANOVA using Dunnet's multiple comparison: **** = $p \leq 0.001$.

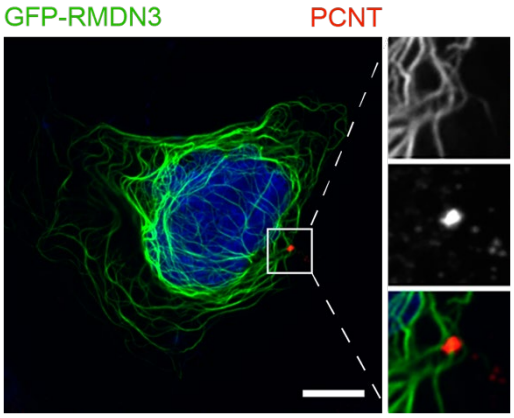

Figure 4.12 – GFP-RMDN3 does not bind to the centrosome

U2OS cells were transfected with 1 µg of GFP-RMDN3 plasmid DNA for 21 hours. Cells were then fixed with ice cold methanol and stained for pericentrin (red) and DAPI (blue). Images were acquired using a 3i spinning disc confocal microscope. Scale bar = 10 µm.

4.3.10 Taxol affects the mitochondria network

As both RMDN3 and SAMM50 are mitochondrial associated proteins which were specifically identified in my proteome to be sensitive to taxol, I speculated that there may be some interplay between taxol treatment, microtubule stability and the mitochondrial network. Mitochondrial networks are similar to microtubule networks in that they are highly dynamic, allowing them to regulate their shape, size and distribution across the cell (Tilokani et al., 2018). Furthermore, there are processes called mitochondrial fusion and fission which result in the joining of adjacent mitochondria and separating of a single mitochondria into two, respectively, which also occur to regulate the mitochondrial network (Tilokani et al., 2018). To determine whether taxol influences mitochondrial dynamics, networks labelled with a fluorescent dye called MitoTracker (detailed in 2.1.9) were visualised before and after treatment. Figure 4.13A shows that the mitochondrial network can clearly be visualised in U2OS cells using MitoTracker staining. Following taxol treatment this network appears more fragmented, confirming that taxol does alter mitochondrial dynamics by increasing fission events. Quantitation using MiNa analysis (described in section 2.2.3) confirms that taxol treatment decreases both the branch length and the overall network. This suggests that taxol-induced microtubule stabilisation alters the mitochondrial network and may thereby reduce the binding ability of RMDN3 to microtubules. On the other hand, taxol may increase the dynamics of the mitochondrial network by an alternative action.

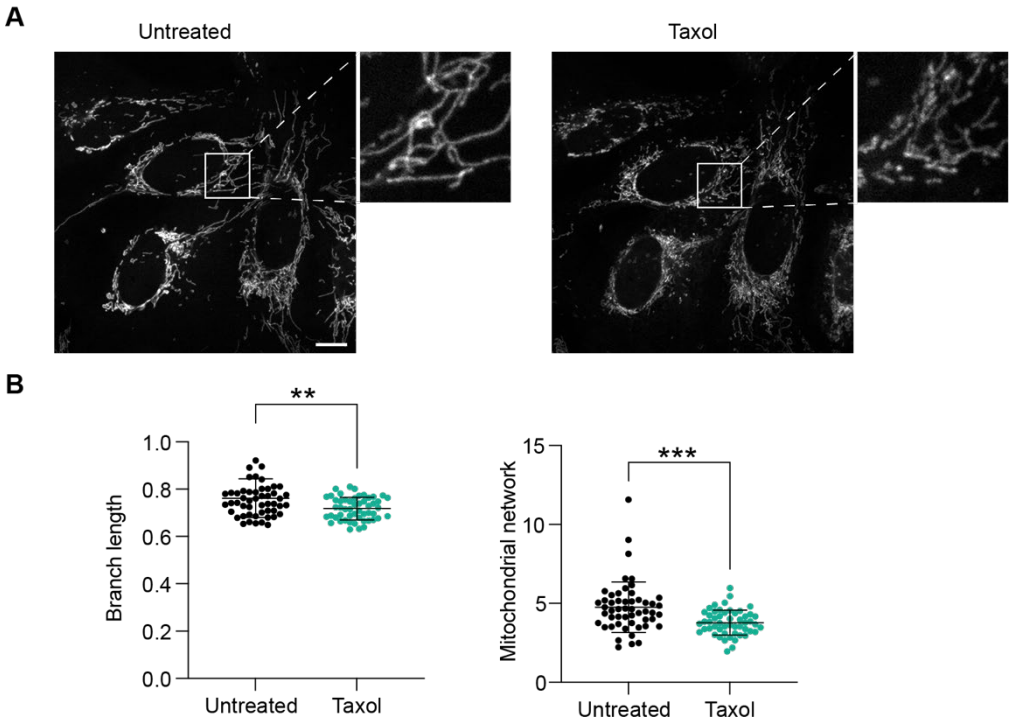

Figure 4.13 – Mitochondrial network is disrupted after Taxol treatment

A. U2OS cells were stained with 50nM of MitoTracker™ Green FM for 30 minutes. Mitochondrial networks were imaged before and after being treated with 6 μM taxol. Images were acquired using a spinning disc confocal microscope. Scale = 10 μm. **B.** Quantification using Mina analysis shows the mean branch length and the network. 52 cells were analysed before and after taxol treatment. Error bars represent standard deviation. Statistical significance was performed via student's t-test: ** = $p \leq 0.01$, *** = $p \leq 0.001$.

4.4 TRIM3

From the proteomic results displayed in section 3.5.6, TRIM3 was shown to be enriched in the control microtubule fraction compared to nocodazole, identifying it as a potential novel microtubule binding protein. Furthermore, it also displayed some sensitivity to taxol compared to control cells, with TRIM3 binding being reduced upon taxol treatment. Although it was only identified within two out of the three repeats, the ratios obtained within these repeats were of similar values (Figure 3.18) suggesting it may be a true hit.

4.4.1 Introduction to TRIM3

TRIM3, also known as BERP (brain-expressed RING finger protein), is a member of the tripartite-motif containing protein (TRIM) superfamily (El-Husseini et al., 2000; El-Husseini and Vincent, 1999). This family is defined by the presence of the TRIM or RBCC domain which is formed from a Really Interesting New Gene (RING) domain, one or two B-box zinc finger domains (BB1, BB2) and a coiled-coil region. Further details on this E3-ligase family can be found within section 1.3.6.

TRIM3 is a member of the VII sub-class of TRIM family proteins. Along with the family specific RBCC domains, it also contains a filamin-like domain and an NHL-repeat domain situated at the C-terminus of the protein (Figure 4.14) (Williams et al., 2019). The presence of the NHL-domain is what classifies the VII subfamily and facilitates a variety of interactions. This domain was given its name due to being first identified in the three proteins NCL-1, HT2A and LIN-41 (Slack and Ruvkun, 1998). The NHL-domain is formed from 6 blades which can fold into a β-propellor structure (Tocchini and Ciosk, 2015; Loedige et al., 2015). Each blade consists of around 40 residues folded into 4 β-stands to create a barrel-like structure (Tocchini and Ciosk, 2015). This NHL-repeat is known for inducing protein-protein interactions and has also been implicated in RNA-binding (Williams et al., 2019), with the positive charge on the surface of this fold interacting with the negative charge of RNA (Loedige et al., 2014). The filamin domains adopts an immunoglobulin-like structure, thought to be involved in dimerisation and to facilitate interactions with the actin cytoskeleton (Ozato et al., 2008). TRIM3 has been previously shown to display E3 ligase activity in the turnover of GKAP (Hung et al., 2010), although its activity is significantly lower than its closest paralogue, TRIM2, and dimerisation is required to restore catalytic activity of TRIM3 (Esposito et al., 2022).

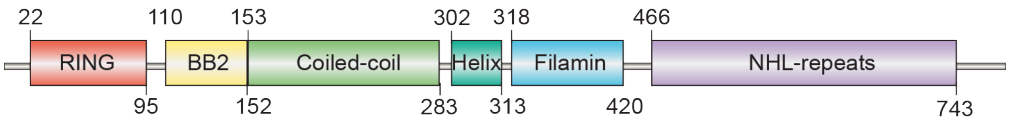

Figure 4.14 – Structure of TRIM3

Schematic showing domains found within TRIM3. Diagram is not to scale.

TRIM3 is a relatively understudied protein, although some of its functions have been identified. It associates with myosin V, actinin-4 and Hrs to form a tetrameric complex called the CART complex (cytoskeleton-associated recycling or transport), which is

required for transferrin receptor recycling (Yan et al., 2005). It has also been shown to regulate hippocampal plasticity, learning and memory by controlling the levels of synaptic γ-actin in a ubiquitin-dependent manner (Schreiber et al., 2015). Additionally, it directly associates with the motor protein KIF21B and controls its functional motility (Labonté et al., 2013). Toll-like receptor 3 (TLR3) is also ubiquitinated by TRIM3 to form K63 chains to mediate trafficking to endolysosomes via the ESCRT (endosomal sorting complex required for transport) pathway. TRIM3 has therefore been proposed to provide a positive regulatory mechanism for the innate immune system (Li et al., 2020). Functional relevance has also been determined for TRIM3 in cancer. TRIM3 acts as a tumour suppressor in glioblastoma by suppressing c-myc expression and regulating the Musashi-notch pathway (Chen et al., 2014), and ubiquitinating p21 *in vitro*, inducing growth arrest (Raheja et al., 2014). It has also been implicated as an oncogene in breast cancer by promoting p53 degradation (Wang et al., 2020) and activating and stabilising oestrogen receptor signalling by SUMOylation (Ye et al., 2021) and K63 polyubiquitination (Zhuang et al., 2022).

A number of TRIM proteins have been confirmed to localise to microtubules. Alignment and phylogenetic analysis of FN3 domain containing proteins revealed a region of 67 amino acids positioned from the end of the coiled-coil, first identified in the C-I subfamily. This region was termed the COS (C-terminal subgroup One Signature) box and is found in 10 RBCC proteins across subfamilies C-I, C-II and C-III, and 1 BCC protein, illustrated in Figure 1.16. It was shown that manipulation of 3 conserved amino acids towards the start and end of this region caused loss of microtubule binding, and insertion of this region into TRIM37 was sufficient to induce microtubule binding (Short and Cox, 2006). All members of subfamily CI and C-II associate with the microtubule cytoskeleton, however TRIM42, the single member of the C-III subfamily remains poorly characterised (Cox, 2012). In the rest of this Chapter, I will provide the first characterisation of TRIM3 as a novel microtubule binding protein.

4.4.2 TRIM3 gene and protein

TRIM proteins are conserved across the metazoan kingdom. The number of family members has rapidly increased during vertebrate evolution (Ozato et al., 2008), with greater than 70 proteins being found within humans (Williams et al., 2019). Figure 4.15 shows the alignment of human TRIM3 amino acid sequence with chimpanzee, cow, mouse, rat and zebra fish. TRIM3 is highly conserved across all species with the

exception of the zebra fish which differs at a number of positions throughout the sequence.

```
Human     ----MAKRED -SPGPEVQPM DKQFLVCSIC LDRYQCPKVL PCLHTFCERC LQNYIPAQSL TLSCPVCRQT SILPEQGVSA LQNNFFISSL  85
Chimp     ----MAKRED -SPGPEVQPM DKQFLVCSIC LDRYQCPKVL PCLHTFCERC LQNYIPAQSL TLSCPVCRQT SILPEQGVSA LQNNFFISSL  85
Bovine    ----MAKRED -SPGPEVQPM DKQFLVCSIC LDRYRCPKVL PCLHTFCERC LQNYIPAQSL TLSCPVCRQT SILPEQGVSA LQNNFFISSL  85
Mouse     ----MAKRED -SPGPEVQPM DKQFLVCSIC LDRYRCPKVL PCLHTFCERC LQNYIPPQSL TLSCPVCRQT SILPEQGVSA LQNNFFISSL  85
Rat       ----MAKRED -SPGPEVQPM DKQFLVCSIC LDRYRCPKVL PCLHTFCERC LQNYIPPQSL TLSCPVCRQT SILPEQGVSA LQNNFFISSL  85
ZebraF    MPLTMAKRES GSTSPVVRQI DKQFLVCSIC LEHYHNPKVL PCLHTFCERC LQNYIPPQSL TLSCPVCRQT SILPEKGVAA LQNNFFITNL  90

Human     MEAMQQAPDG AHDPEDPHPL SVVAGR---P LSCPNHEGKT MEFYCEACET AMCGECRAGE HREHGTVLLR DVVEQHKAAL QRQLEAVRGR  172
Chimp     MEAMQQAPDG AHDPEDPHPL SVVAGR---P LSCPNHEGKT MEFYCEACET AMCGECRAGE HREHGTVLLR DVVEQHKAAL QRQLEAVRGR  172
Bovine    MEAMQQAPDG AHDPEDPHPL SAVAGR---P LSCPNHEGKT MEFYCEACET AMCGECRAGE HREHGTVLLR DVVEQHKAAL QRQLEAVRGR  172
Mouse     MEAMQQAPEG AHDPEDPHPL SAVAGR---P LSCPNHEGKT MEFYCEACET AMCGECRAGE HREHGTVLLR DVVEQHKAAL QRQLEAVRGR  172
Rat       MEAMQQAPDG AHDPEDPHPL SAVAGR---P LSCPNHEGKT MEFYCEACET AMCGECRAGE HREHGTVLLR DVVEQHKAAL QRQLEAVRGR  172
ZebraF    MEVLQREQDC TRSEASSGLE SAGAATYAPP LSCPNHEGKV MEFYCESCET AMCLECTEGE HREHVTVPLR DVLEQHKAAL KNQLDAIRNR  180

Human     LPQLSAAIAL VGGISQQLQE RKAEALAQIS AAFEDLEQAL QQRKQALVSD LETICGAKQK VLQSQLDTLR QGQEHIGSSC SFAEQALRLG  262
Chimp     LPQLSAAIAL VGGISQQLQE RKAEALAQIS AAFEDLEQAL QQRKQALVSD LETICGAKQK VLQSQLDTLR QGQEHIGSSC SFAEQALRLG  262
Bovine    LPQLSAAIAL VGGISQQLQE RKAEALAQIS SAFEDLEQAL QQRKQALVSD LEAICGAKQK VLQTQLDTLR QGQEHIGSSC SFAEQALRLG  262
Mouse     LPQLSAAIAL VGGISQQLQE RKAEALAQIS AAFEDLEQAL QQRKQALVSD LESICGAKQK VLQTQLDTLR QGQEHIGSSC SFAEQALRLG  262
Rat       LPQLSAAIAL VGGISQQLQE RKAEALAQIS AAFEDLEQAL QQRKQALVSD LESICGAKQK VLQTQLDTLR QGQEHIGSSC SFAEQALRLG  262
ZebraF    LPQLTAAIEL VNEISKQLTD RKNEAVTEIS NTFEELEKAL HQRKTTLITD LENICSTKQK VLQGQLAALM QGKENIQSSC SFTEQALNHG  270

Human     SAPEVLLVRK HMRERLAALA AQAFPERPHE NAQLELVLEV DGLRRSVLNL GALLTTSATA HETVATGEGL RQALVGQPAS LTVTTKDKDG  352
Chimp     SAPEVLLVRK HMRERLAALA AQAFPERPHE NAQLELVLEV DGLRRSVLNL GALLTTSATA HETVATGEGL RQALVGQPAS LTVTTKDKDG  352
Bovine    SAPEVLLVRK HMRERLAALA AQAFPERPHE NAQLELVLEV DGLRRSVLNL GALLTTSATA HETVATGEGL RQALVGQPAS LTVTTKDKDG  352
Mouse     SAPEVLLVRK HMRERLAALA AQAFPERPHE NAQLELVLEV DGLRRSVLNL GALLTTSATA HETVATGEGL RQALVGQPAS LTVTTKDKDG  352
Rat       SAPEVLLVRK HMRERLAALA AQAFPERPHE NAQLELVLEV DGLRRSVLNL GALLTTSAAA HETVATGEGL RQALVGQPAS LTVTTKDKDG  352
ZebraF    SPTEVLLVQK QMGERMGALA RHAFPEQPHE NGHLDCQVET EGLRRSIQNL GVLLTTSSVG HTSVATGEGL RHAVVGQNTT VTVTTKDKDG  360

Human     RLVRTGSAEL RAEITGPDGT RLPVPVVDHK NGTYELVYTA RTEGELLLSV LLYGQPVRGS PFRVRALRPG DLPPSPDDVK RRVKSP---G  439
Chimp     RLVRTGSAEL RAEITGPDGT RLPVPVVDHK NGTYELVYTA RTEGELLLSV LLYGQPVRGS PFRVRALRPG DLPPSPDDVK RRVKSP---G  439
Bovine    RLVRTGSAEL RAEITGPDGT RLPVPVVDHK NGTYELVYTA RTEGELLLSV LLYGQPVRGS PFRVRALRPG DLPPSPDDVK RRVKSP---G  439
Mouse     RLVRTGSAEL CAEITGPDGV RLAVPVVDHK NGTYELVYTA RTEGDLLLSV LLYGQPVRGS PFRVRALRPG DLPPSPDDVK RRVKSP---G  439
Rat       RLVRTGSAEL CAEITGPDGM RLAVPVVDHK NGTYELVYTA RTEGDLLLSV LLYGQPVRGS PFRVRALRPG DLPPSPDDVK RRVKSP---G  439
ZebraF    ELVKTGNAAL RAQISGADGG VTETDVTDNK NGTYEIGYTL RSEGEFSFSV LLYGRHVRGS PFRLRAVKAC DAPQSPDDVK RRVKSPGGGG  450

Human     GPGSHVRQKA VRRPSSMYST GGKRKDNPIE DELVFRVGSR GREKGEFTNL QGVSAASSGR IVVADSNNQC IQVFSNEGQF KFRFGVRGRS  529
Chimp     GPGSHVRQKA VRRPSSMYST GGKRKDNPIE DELVFRVGSR GREKGEFTNL QGVSAASSGR IVVADSNNQC IQVFSNEGQF KFRFGVRGRS  529
Bovine    GPGSHVRQKA VRRPSSMYST GGKRKDNPIE DELVFRVGSR GREKGEFTNL QGVSAASSGR IVVADSNNQC IQVFSNEGQF KFRFGVRGRS  529
Mouse     GPGSHVRQKA VRRPSSMYST GGKRKDNPIE DELVFRVGSR GREKGEFTNL QGVSAASSGR IVVADSNNQC IQVFSNEGQF KFRFGVRGRS  529
Rat       GPGSHVRQKA VRRPSSMYST GGKRKDNPIV DELVFRVGSR GREKGEFTNL HPLSAASSGR IVVADSNNQC IQVFSNEGQF KFRFGVRGRS  529
ZebraF    GAGGHVRQKA VRRPSSMYST -TKKKENPIE DELIFRVGTR GRERGEFSNL QGISTTSSGR IVVADSNNQC IQVFSNDGQF KLKFGVRGRS  539

Human     PGQLQRPTGV AVDTNGDIIV ADYDNRWVSI FSPEGKFKTK IGAGRLMGPK GVAVDRNGHI IVVDNKSCCV FTFQPNGKLV GRFGGRGATD  619
Chimp     PGQLQRPTGV AVDTNGDIIV ADYDNRWVSI FSPEGKFKTK IGAGRLMGPK GVAVDRNGHI IVVDNKSCCV FTFQPNGKLV GRFGGRGATD  619
Bovine    PGQLQRPTGV AVDTNGDIIV ADYDNRWVSI FSPEGKFKTK IGAGRLMGPK GVAVDRNGHI IVVDNKSCCV FTFQPNGKLV GRFGGRGATD  619
Mouse     PGQLQRPTGV AVDTNGDIIV ADYDNRWVSI FSPEGKFKTK IGAGRLMGPK GVAVDRNGHI IVVDNKSCCV FTFQPNGKLV GRFGGRGATD  619
Rat       PGQLQRPTGV AVDTNGDIIV ADYDNRWVSI FSPEGKFKTK IGAGRLMGPK GVAVDRNGHI IVVDNKSCCV FTFQPNGKLV GRFGGRGATD  619
ZebraF    PGQLQRPTGV AVDMNGDIIV ADYDNRWLSI FSPDGKFKNK IGAGRLMGPK GVAVDKNGHI ITADNKACCV FIFQSNGKLV TKFGAKGTSE  629

Human     RHFA------ ---------- ----GPHFVA VNNKNEIVVT DFHNHSVKVY SADGEFLFKF GSHGEGNGQF NAPTGVAVDS NGNIIVADWG  689
Chimp     RHFA------ ---------- ----GPHFVA VNNKNEIVVT DFHNHSVKVY SADGEFLFKF GSHGEGNGQF NAPTGVAVDS NGNIIVADWG  689
Bovine    RHFA------ ---------- ----GPHFVA VNNKNEIVVT DFHNHSVKVY SADGEFLFKF GSHGEGNGQF NAPTGVAVDS NGNIIVADWG  689
Mouse     RHFA------ ---------- ----GPHFVA VNNKNEIVVT DFHNHSVKVY SADGEFLFKF GSHGEGNGQF NAPTGVAVDS NGNIIVADWG  689
Rat       RHFA------ ---------- ----GPHFVA VNNKNEIVVT DFHNHSVKVY SADGEFLFKF GSHGEGNGQF NAPTGVAVDS NGNIIVADWG  689
ZebraF    RQFADKSAPN TPTEPKQSKS GPAFSPHFVA INNKNEIVVT DFHNHSVKVY NADGEFLFKF GSHGEGNGQF NAPTGVAVDS NGNIIVADWG  719

Human     NSRIQVFDSS GSFLSYINTS AEPLYGPQGL ALTSDGHVVV ADAGNHCFKA YRYLQ          744
Chimp     NSRIQVFDSS GSFLSYINTS AEPLYGPQGL ALTSDGHVVV ADAGNHCFKA YRYLQ          744
Bovine    NSRIQVFDSS GSFLSYINTS AEPLYGPQGL ALTSDGHVVV ADAGNHCFKA YRYLQ          744
Mouse     NSRIQVFDSS GSFLSYINTS AEPLYGPQGL ALTSDGHVVV ADAGNHCFKA YRYLQ          744
Rat       NSRIQVFDSS GSFLSYINTS AEPLYGPQGL ALTSDGHVVV ADAGNHCFKA YRYLQ          744
ZebraF    NSRIQVFDSS GSFLSYINTT ADPLYGPQGL ALTSDGHVAV ADSGNHCFKV YRYLQ          774
```

Figure 4.15 – Alignment of TRIM3 across species

4.4.3 TRIM3 expression levels in different cell lines

It was intriguing to me that TRIM3 was extracted within this data set, yet no other TRIM proteins already shown to bind to microtubules were identified. I therefore analysed the expression levels of TRIM3 proteins compared to other TRIMs identified within Hela cells using the proteomic data set published by Bekker-Jensen *et al.* in 2017 (Bekker-Jensen et al., 2017). This data set provides values for the copy number of individual proteins, calculated using iBAQ proteomics. Copy numbers for 34 TRIM family members were identified. Of these, TRIM3 was the 14th most abundant, with ~21,000 copies present per cell. TRIM28 was the most abundant member with ~2,200,000 copies. Of the 10 TRIM proteins known to contain a microtubule-binding cos box domain (as described in section 4.4.1), only 2 were present within this data set: TRIM54 and TRIM46 with much lower copy numbers of around 570 each. To put these numbers into context, the most abundant protein in Hela cells was histone 4 with a copy number of ~60,000,000.

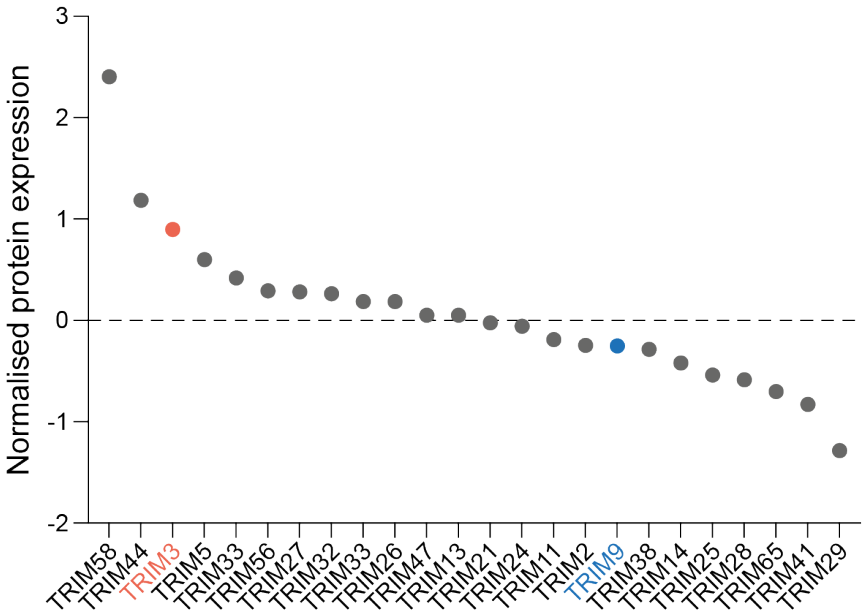

Figure 4.16 – Normalised expression levels of TRIM proteins in U2OS cells

Expression levels of TRIM proteins in U2OS cells were compared to that within a protein lysate pool from 11 different cell lines. Ratios of normalised protein expression levels are shown. TRIM3 is highlighted in orange, and TRIM9 (cos-box containing TRIM protein) is shown in blue. Data obtained from Nusinow *et al* (2020).

To analyse the TRIM proteins within U2OS cells, another proteomics dataset was used. This analysis provides ratios of normalised protein expression levels compared to a pool of protein lysates from 11 different cell lines (Nusinow et al., 2020). Therefore, rather than providing individual copy numbers, this data gives an idea of how much a particular protein is expressed in a certain cell line compared to the 'average' cell line. The TRIM proteins and their ratio values are shown in Figure 4.16. TRIM3 is shown to be expressed in higher levels in U2OS cells compared to the average cell line (orange). The data was filtered for microtubule binding cos-box TRIM proteins, with only TRIM9 being identified (blue). This protein is expressed in lower levels in U2OS in comparison to the control. Taken together, these data suggest that TRIM3 is more highly enriched compared to other microtubule binding TRIM family members, possibly suggesting why it was the only one identified in my dataset. Furthermore, the absence of the other cos-box containing proteins within these 2 datasets may indicate that mass spectrometry detection is difficult for these proteins, explaining their absence in my proteome.

4.4.4 TRIM3 is extracted in a nocodazole-sensitive manner

To show that TRIM3 is a novel hit and does bind to microtubules, I first confirmed its differential extraction across the control, nocodazole and taxol treated cells. Figure 4.17 shows that more TRIM3 is removed within the nocodazole cytosolic fraction compared to both the control and taxol fractions. In addition, TRIM3 levels are greater in both control and taxol microtubule fractions mirroring the same pattern as both α-tubulin and EML4, indicating that TRIM3 is successfully enriched for in a similar manner to microtubule proteins.

4.4.5 TRIM3 localisation

4.4.5.1 TRIM3 localises to microtubules

To determine whether TRIM3 is able to bind to microtubules, visualisation of its localisation was required. As the commercially available antibody against TRIM3 did not provide reliable staining for immunofluorescence (data not shown), the use of a tagged protein construct was required. Professor Germana Meroni kindly provided me with 2 constructs expressing a mouse version of TRIM3 tagged with either GFP or HA at the N-terminus of the protein. In addition to these, she was also kind enough to supply the same constructs for human TRIM2, the closest family member to TRIM3, as a control.

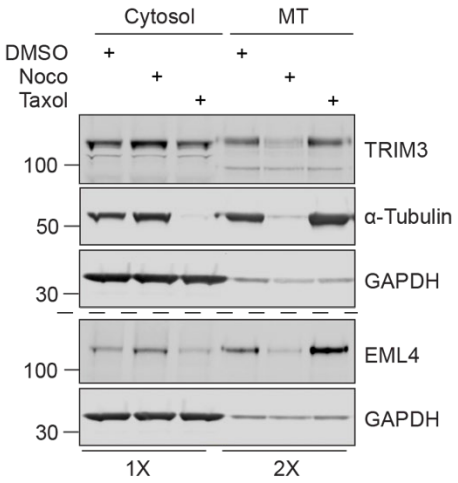

Figure 4.17 – Confirmation of TRIM3 extraction in control and taxol treated cells

U2OS cells were treated with 6 μM Nocodazole for 1 hour or Taxol for 30 minutes alongside a DMSO control. Lysis and microtubule stabilisation buffer was then added (5 minutes at 4°C) to remove cytosolic proteins (cytosol). Remaining microtubules were then collected using 8M urea (MT). Western blot analysis of α-tubulin, GAPDH and EML4. Sample concentrations are as indicated.

Using both these HA- and GFP-tagged constructs, I therefore checked TRIM3 subcellular localisation. Figure 4.18A confirms that GFP-mTRIM3 shows clear colocalisation with α-tubulin (top panel). Furthermore, treatment with nocodazole shows loss of microtubule localisation in line with their depolymerisation (middle panel), and treatment with Taxol allows GFP-mTRIM3 colocalisation with microtubules to remain (bottom panel). To confirm this localisation is specific to TRIM3 and not the attached GFP tag, cells were transfected with HA-mTRIM3 and stained using either the TRIM3 or the HA antibody alongside the α-tubulin microtubule marker. As expected, clear microtubule colocalisation can be seen with this construct using both antibodies in Figure 4.18B. As a final verification that TRIM3 displays microtubule localisation, microtubule depolymerisation was induced by cold-treating cells for 1 hour. Figure 4.19 confirms that as microtubule structures are lost, so is the TRIM3 localisation. TRIM3 is therefore confirmed as a novel microtubule binding protein identified using my optimised extraction protocol.

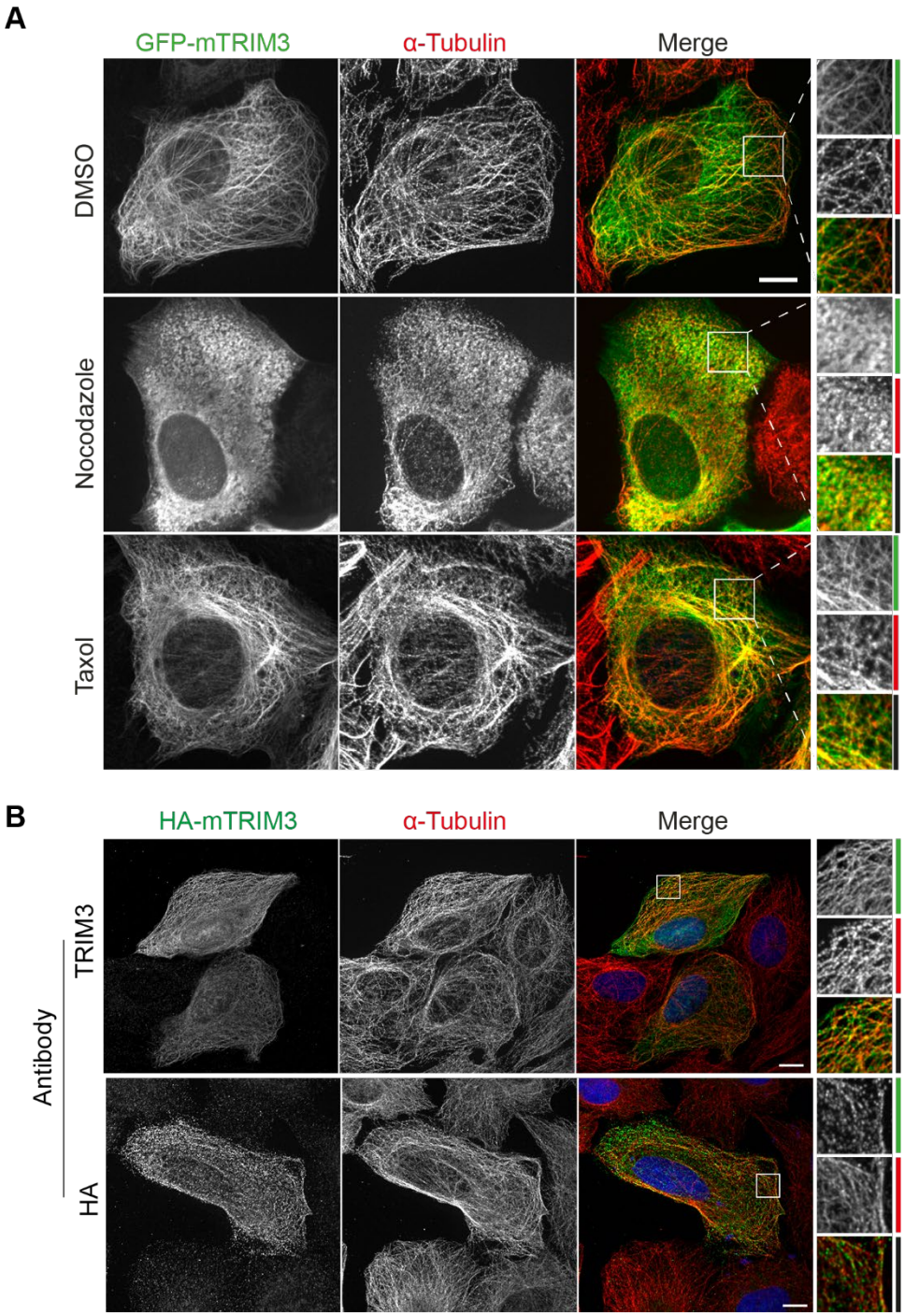

Figure 4.18 – TRIM3 localises to microtubules

A. U2OS cells were transfected with 1 µg of GFP-mTRIM3 plasmid DNA for 21 hours. Cells were then treated with nocodazole (6 µM, 1 hour), taxol (6 µM, 30 minutes) or DMSO (1 hour) before being fixed with ice cold methanol and stained for α-tubulin. **B.** U2OS cells were transfected with 1 µg HA-mTRIM3. Cells were fixed with ice cold methanol and stained for α-tubulin and either TRIM3 or HA. Images were acquired using a 3i spinning disc confocal microscope. Scale bars = 10 µm.

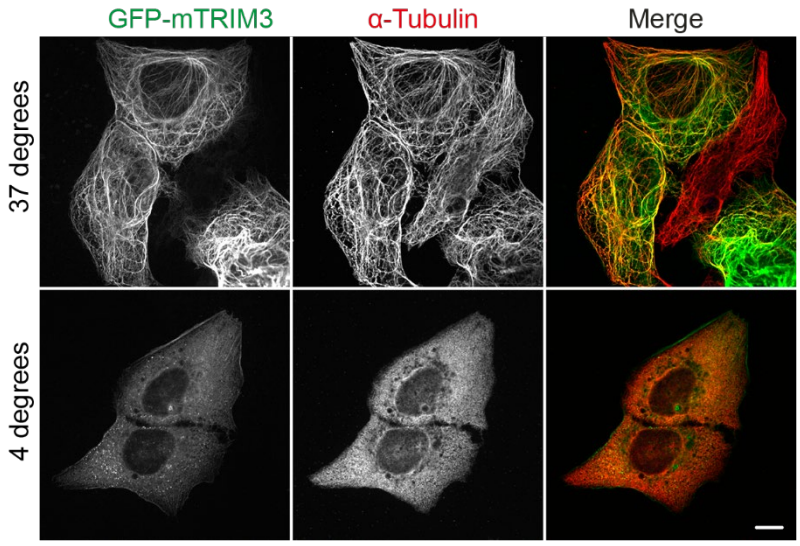

Figure 4.19 – TRIM3 localisation is lost with cold-induced microtubule depolymerisation

U2OS cells were transfected with 1 µg of GFP-mTRIM3 plasmid DNA for 21 hrs. Cells were then cold treated to depolymerise microtubules before being fixed with ice cold methanol and stained for α-tubulin. Images were acquired using a 3i spinning disc confocal microscope. Scale bars = 10 µm.

4.4.5.2 TRIM2 also colocalises with microtubules

TRIM2 is another tripartite motif containing protein which is classified within the same subfamily as TRIM3. It is the closest paralogue to TRIM3 out of all other family members. As I was also gifted tagged constructs for this protein, I wanted to see whether TRIM2 also possesses the ability to colocalise with microtubules. U2OS cells were therefore transfected with GFP-TRIM2. Figure 4.20 confirms that microtubule colocalisation can also be observed with TRIM2. Furthermore, treatment with nocodazole causes microtubule depolymerisation and loss of TRIM2 localisation, whereas taxol treatment allows its localisation to be retained. These results confirm that TRIM2 has also been identified as a novel microtubule binding protein.

4.4.5.3 TRIM3 does not bind to the centrosome

To confirm whether TRIM3 localises to the centrosome, colocalisation with pericentrin was performed. Figure 4.21 confirms that TRIM3 (top panel) is not found at the centrosome as no overlap with the marker is observed. Similar results are seen for TRIM2 (bottom panel).

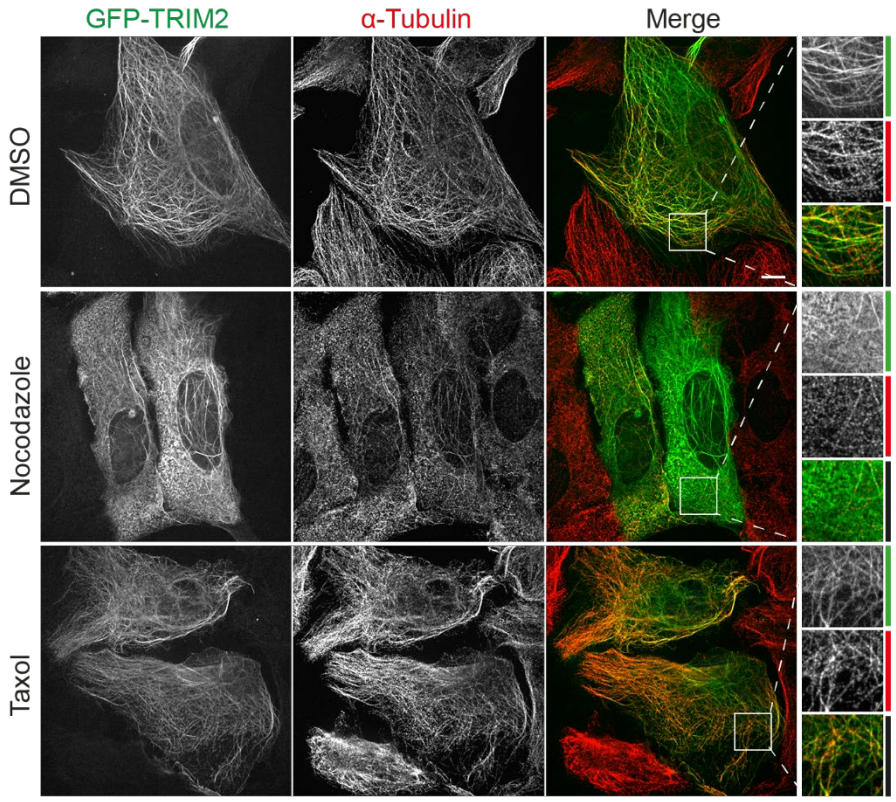

Figure 4.20 – TRIM2 localises to microtubules

U2OS cells were transfected with 1 µg of GFP-TRIM2 plasmid DNA for 21 hours. Cells were then treated with nocodazole (6 µM, 1 hour), taxol (6 µM, 30 minutes) or DMSO (1 hour) before being fixed with ice cold methanol and stained for α-tubulin. Images were acquired using a 3i spinning disc confocal microscope. Scale bar = 10 µm.

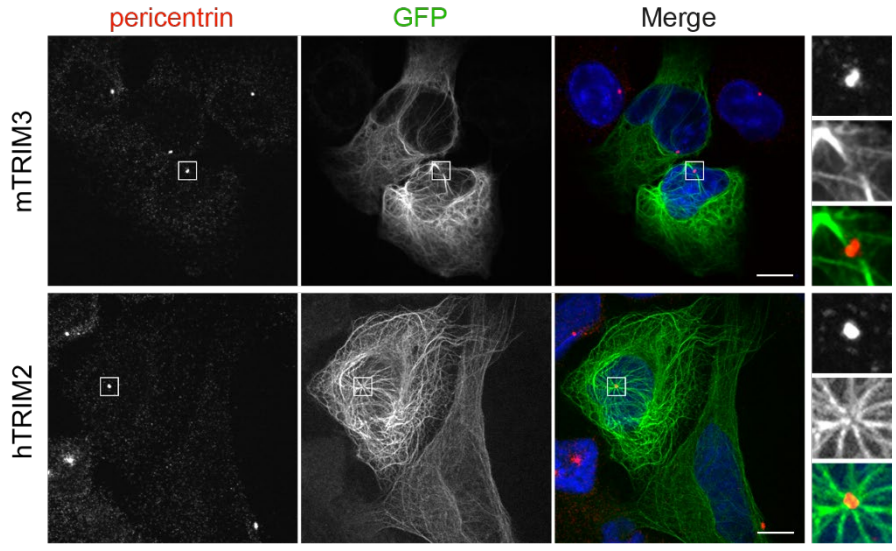

Figure 4.21 – TRIM3 and TRIM2 do not localise to the centrosome

U2OS cells were transfected with 1 µg of either GFP-mTRIM3 or GFP-TRIM2 plasmid DNA for 21 hours. Cells were then fixed with ice cold MeOH and stained for and pericentrin (red) and DAPI (blue). Images were acquired using a 3i spinning disc confocal microscope. Scale bar = 10 µm.

4.4.5.4 TRIM3 colocalises to the whole microtubule network

As mentioned in section 1.1.10.2, microtubules are highly decorated with a number of PTMs. TRIM3 and TRIM2 both appear to occupy the whole microtubule network observed when co-staining with α-tubulin. As microtubule modifications have been implicated in regulating the interactions between microtubule binding proteins and microtubules, I wanted to confirm that TRIM3 could also bind to these modified microtubule subsets. Colocalisation of TRIM3 and TRIM2 was performed with acetylated α-tubulin (AcTub, Figure 4.22A) and detyrosinated α-tubulin (DetyTub, Figure 4.22B). Both proteins are able to localise to both acetylated and detyrosinated microtubule subsets. Pearson's colocalisation coefficient was calculated for each using the JACoP plugin in Fiji and compared with that of the whole microtubule network (tubulin). High colocalisation coefficient values were obtained for all, with TRIM3 giving mean values of 0.81, 0.78 and 0.73, and TRIM2 with 0.82, 0.81 and 0.73, for α-tubulin, AcTub and DetyTub respectively. These results confirm that TRIM3 has a greater overlap with the whole microtubule network compared to both modified networks, whereas TRIM2 colocalises least with the detyrosinated network.

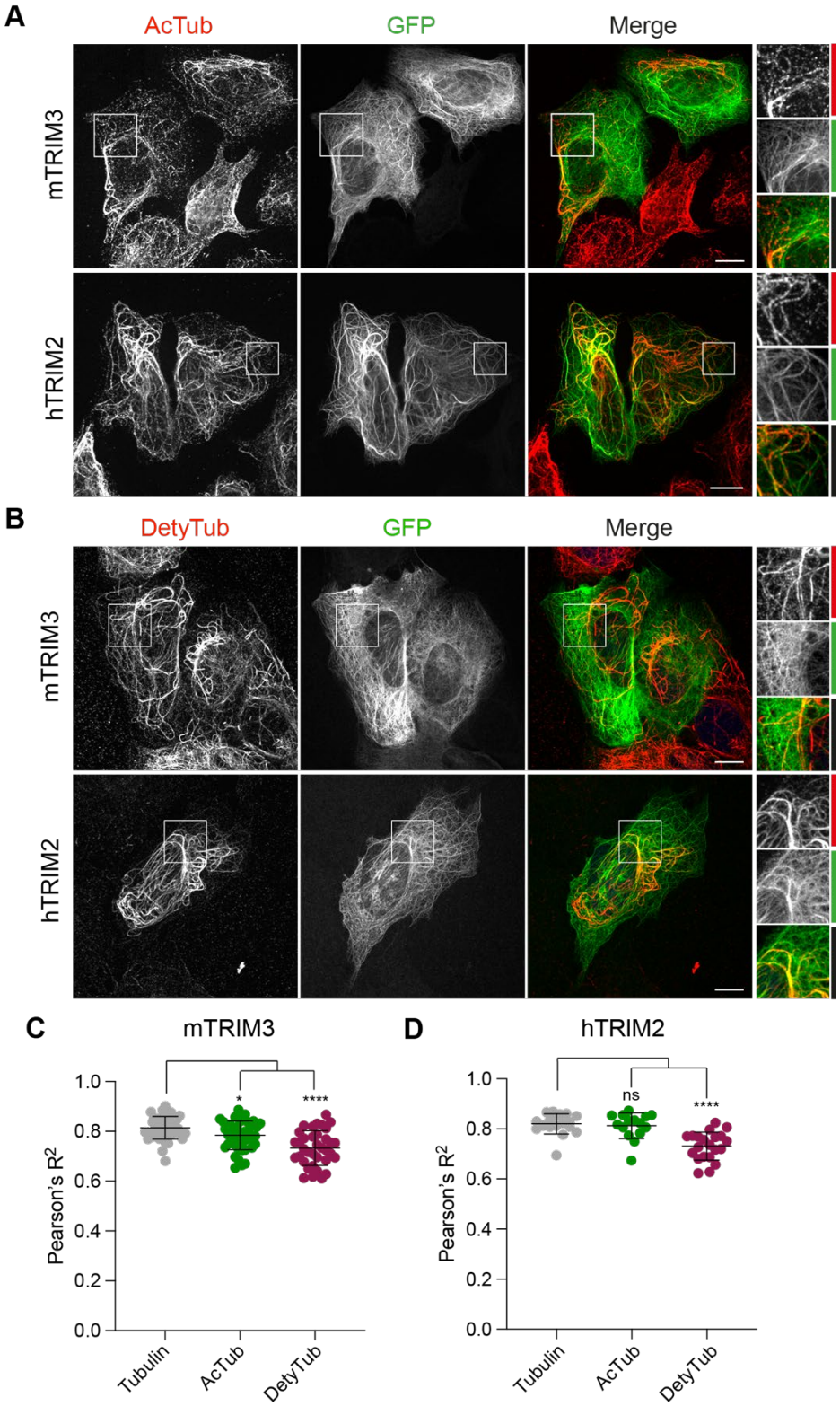

Figure 4.22 – TRIM3 and TRIM3 colocalise with modified microtubules

U2OS cells were transfected with 1 µg of either GFP-mTRIM3 or GFP-TRIM2 plasmid DNA for 21 hours. Cells were then fixed with ice cold methanol and stained for **A.** acetylated tubulin, or **B.** detyrosinated tubulin. Scale bar = 10 µm. **C/D.** Pearson's colocalisation coefficient was calculated using JACoP plugin in Fiji. Mean and standard deviation is indicated. Statistical significance was performed via one-way ANOVA: ns (not significant) = $p>0.05$, * = $p\leq0.05$, **** = $p\leq0.001$.

4.4.5.5 TRIM3 colocalises with the mitotic spindle

Microtubules make up the major structural component of the mitotic spindle. The spindle is formed from astral microtubules, kinetochore microtubules and interpolar microtubules and is described in further detail in section 1.2.1. As previous results have confirmed that overexpressed TRIM3 can colocalise to microtubules within interphase, I therefore wanted to confirm whether it could also colocalise to the spindle microtubules as well. GFP-TRIM3 can localise to the mitotic spindle at metaphase (Figure 4.23A), with this localisation persisting throughout anaphase and telophase (Figure 4.23B).

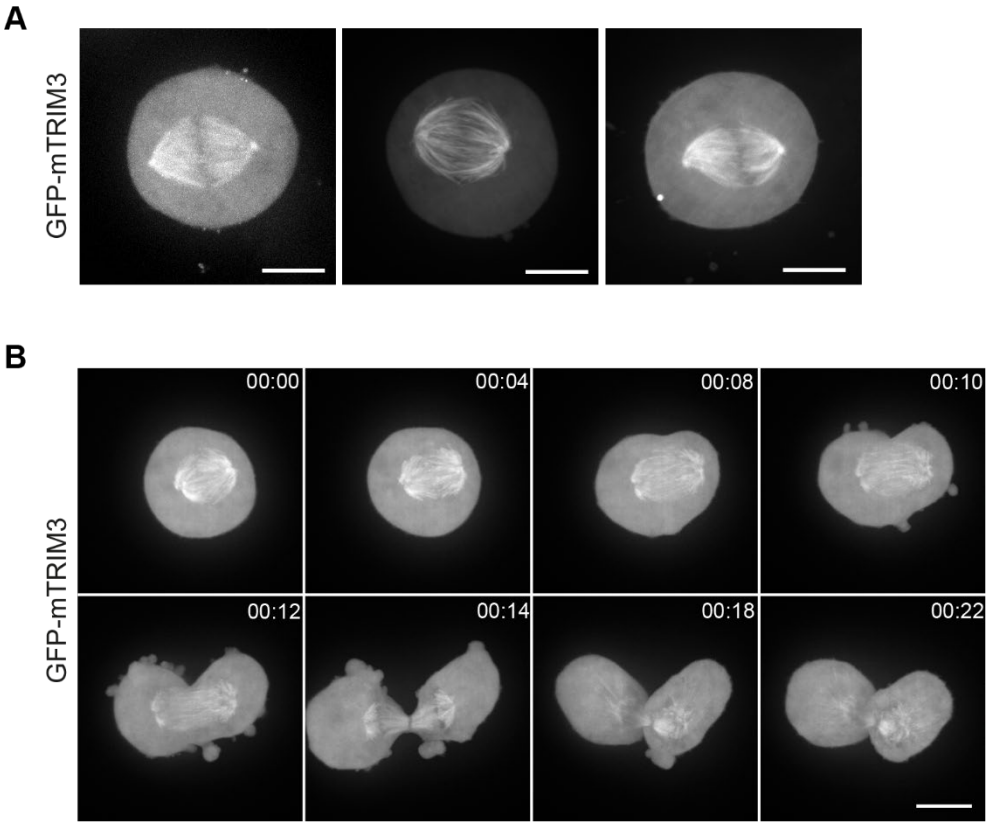

Figure 4.23 – TRIM3 localises to the mitotic spindle

U2OS cells were synchronised to prometaphase using thymidine for 24 hours and nocodazole for 18 hours as described. Transfection with GFP-mTRIM3 was performed alongside nocodazole addition. Cells were released into fresh DMEM to allow mitotic progression and Z-stacks were acquired using a 3i spinning disc confocal microscope. Maximum projections are shown. Scale bars = 10 μm. **A.** Cells selected at metaphase. **B.** Cells were imaged every minute as they progressed through mitosis. Time is hh:mm.

4.4.5.6 The TRIM family cos box domain

As mentioned previously the cos-box is a sequence motif found within 10 TRIM family members and has been shown to be required for their localisation to microtubules. The paper published in 2006 by Short and Cox shows that the cos-box is a 67 amino acid long sequence motif which occurs just after the coiled-coil domain within TRIM proteins. Furthermore, if 3 conserved amino acids at both the start (FLQ) and the end (LDY) of the sequence are mutated then microtubule localisation is lost (Short and Cox, 2006). With this in mind, I therefore wanted to investigate the sequence of TRIM3 to confirm whether this may also have a cos box sequence which facilitates the microtubule localisation seen. Figure 4.24A shows a sequence alignment of these 67 amino acids within 9 TRIM proteins which contain the cos box, TRIM2 and TRIM3 proteins, and an additional number of TRIM family members which also share a similar helical structure at this region. Mafft multiple sequence alignment was utilised here with L-INS-I to improve the search for one conserved domain. The sequence alignment reveals that although some sequence similarity is observed, TRIM3 and TRIM2 do not contain the conserved 3 amino acids at the start and end of the cos-box sequence, indicated with a * in Figure 4.24A. The confirms what the original authors found (Short and Cox, 2006): TRIM3 and TRIM2 do not contain a cos box sequence and must localise to microtubules via an alternative domain.

Using AlphaFold2, I was able to visualise the predicted 3D structures of TRIM proteins containing a cos box. In all of these proteins, the cos box sequence results in a short helical turn just after the coiled-coil domain, followed by an unstructured region and finishes with another short alpha helix structure. This is shown in Figure 4.24B, with TRIM18 (MID1) used as an example, with the cos box and conserved amino acids labelled. I was intrigued to see that TRIM3 also contains this helical region at the same point. This was intriguing and suggested that this similarly structural region to the cos-box may still be involved in the localisation of TRIM3 to microtubules. This structure is illustrated in Figure 4.24C. The term ‘helix’ refers to the short helical region at the end of the cos-box domain and is labelled in the alpha fold diagram. To determine which region is responsible for TRIM3 interaction with microtubules, GFP-tagged truncations and deletions were created.

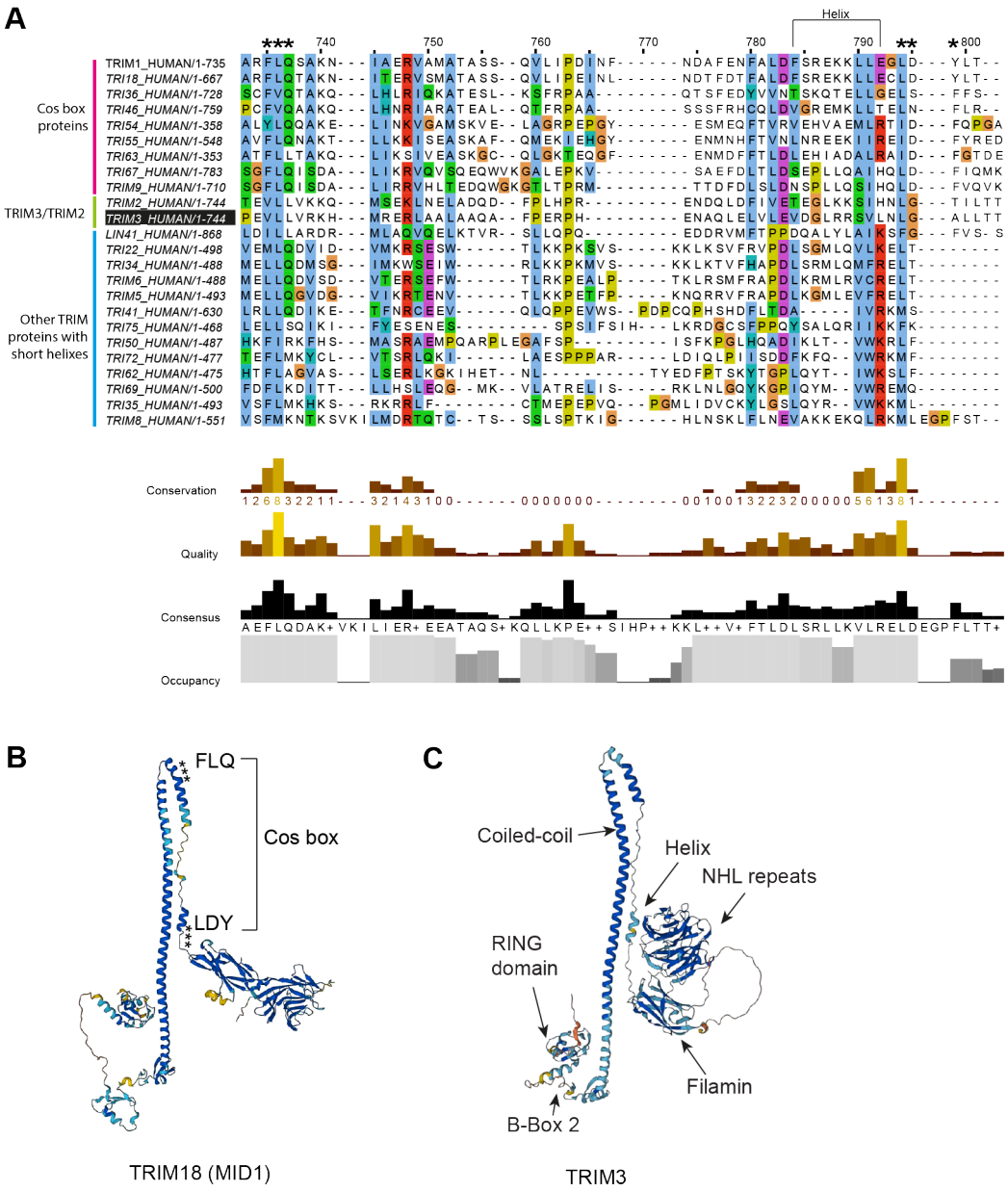

Figure 4.24 – TRIM3 does not contain a cos-box domain

A. Alignment of TRIM3 compared to the COS-box containing proteins and other proteins containing a similar helical structure. The COS-box sequence was compared across all selected proteins using MAFFT alignment using L-INS-I iterative refinement. Sequences were viewed and the figure created in Jalview. Conserved amino acids are indicated with a *. **B.** AlphaFold2 structure of cos-box containing protein TRIM18 (MID1, AF-O15344-F1). **C.** AlphaFold2 structure of TRIM3 (AF-O75382-F1).

4.4.5.7 Generation of TRIM3 truncations and deletion mutations

The cloning process for generating constructs containing the desired truncations and deletions is detailed within section 2.3.2 and section 2.3.3 respectively. First, dependence of the N-terminal region was investigated by removing the domains at this end of the protein sequentially. The RING domain and the B-box 2 domain (BB2) were first removed to create ΔRBD. The coiled-coil domain was then also removed to create ΔRBDC, followed by the additional removal of the short helix structure to created ΔRBDCH. Finally, the filamin domain was also removed to create ΔRBDCHF. The same was then done for the domains at the C-terminus of the protein with the NHL repeats first being removed to give ΔNHL, then the filamin domain also being removed to give ΔFNHL, followed by the additional removal of the helix structure to give ΔHFNLH. In addition to the removal of these terminal domains, the filamin domain (del filamin) and the helix structure (del helix) were also both in turn removed from the middle of the structure to confirm any independence from them in microtubule localisation. A schematic of these constructs and the amino acid locations of each of them are shown in Figure 4.25.

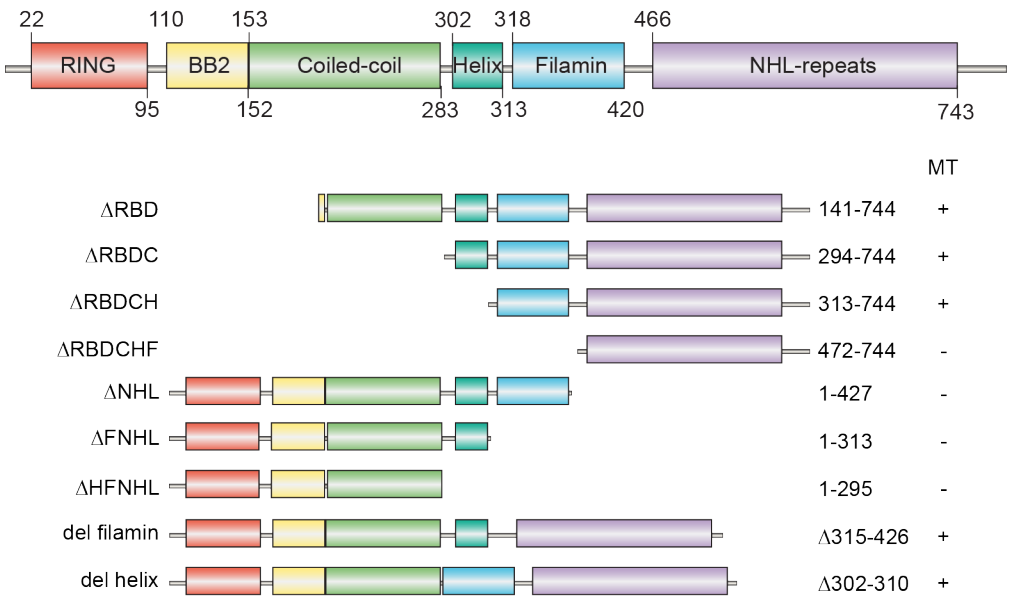

Figure 4.25 – Generation of TRIM3 truncations and deletions

Schematic representation of the full length and truncated TRIM3 constructs that were used for the study and a summary of their localisation. Schematics are not to scale.

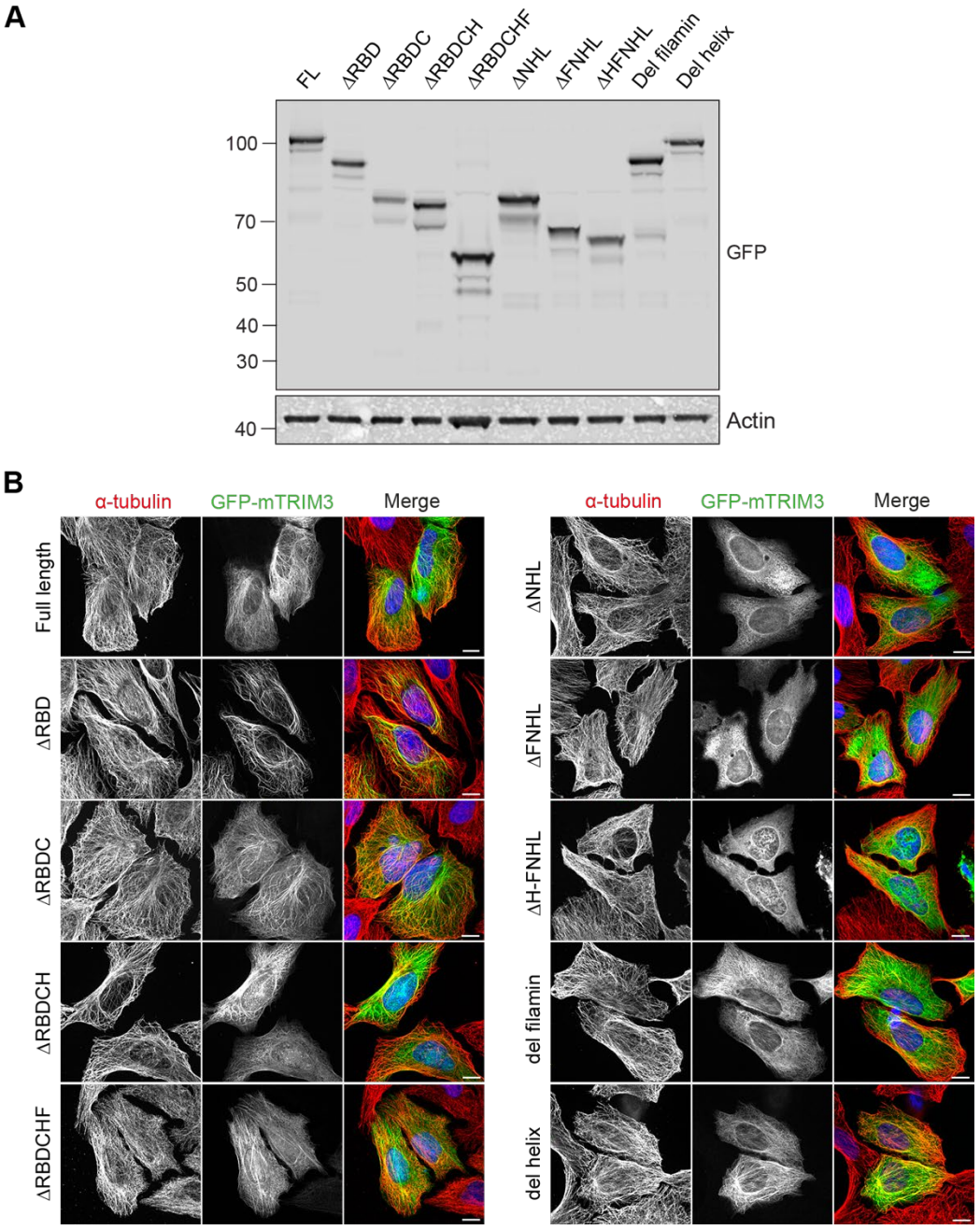

Figure 4.26 – TRIM3 localises to microtubules via the NHL repeats

A. U2OS cells were transfected with 1 µg DNA for 21 hours and lysed in RIPA buffer. Western blot showing GFP expression levels. **B.** Representative images of the differential localisation of the constructs on microtubules. U2OS cells were transfected with 1 µg DNA for 21 hours, fixed with ice-cold MeOH and stained for α-tubulin. Images were acquired with a 3i spinning disk confocal. Scale bar: 10µm

4.4.5.8 TRIM3 localises to microtubules via the NHL repeats

Upon generation of these constructs, U2OS cells were transfected and lysed to determine successful protein expression. Western blot analysis confirms that a successful GFP-tagged protein can be expressed from each of the constructs at the expected size (Figure 4.26A). Maintenance of microtubule localisation was then analysed in U2OS cells by co-staining for α-tubulin. Figure 4.26B shows that microtubule localisation is retained within constructs lacking the N-terminal domains, as ΔRBD, ΔRBDC and ΔRBDCH are all still able to colocalise with α-tubulin. The constructs which lack the C-terminal domains however are unable to retain their microtubule localisation. Cytosolic GFP staining can be seen for the ΔNHL, ΔFNHL and the ΔHFNHL, and colocalisation with tubulin is lost. Deletion of either the filamin or the helix does not disrupt TRIM3 colocalisation with microtubules. Interestingly however, expression of the NHL repeats on their own (represented by ΔRDBCHF), is no longer sufficient to retain microtubule binding. A filamentous localisation is still observed with this construct however this does not co-localise with α-tubulin so is predicted to be another cytoskeletal form. Taken together, this indicates that the NHL repeat is required for microtubule binding of TRIM but is not sufficient on its own.

4.4.5.9 TRIM3 colocalises with HRS

Earlier studies have suggested that TRIM3 is part of complex which is required for transferrin receptor recycling (Yan et al., 2005). I therefore wanted to investigate whether I could reproduce this observation of the CART complex. GFP-mTRIM3 was transfected into U2OS cells and Hrs localisation was visualised (Figure 4.27). In untransfected cells, Hrs shows no distinct microtubule localisation and appears to be on early endosomes, however when TRIM3 is overexpressed, Hrs shifts to colocalise with TRIM3 and microtubules. USP31 is a microtubule binding protein described in Chapter 5 and was used here as a control. Overexpression shows no microtubule localisation of Hrs was observed, indicating this result is specific for TRIM3 and not just microtubule binding proteins. This therefore confirms that TRIM3 is part of the CART complex. Other components of the CART complex were not tested here due to lack of reagents.

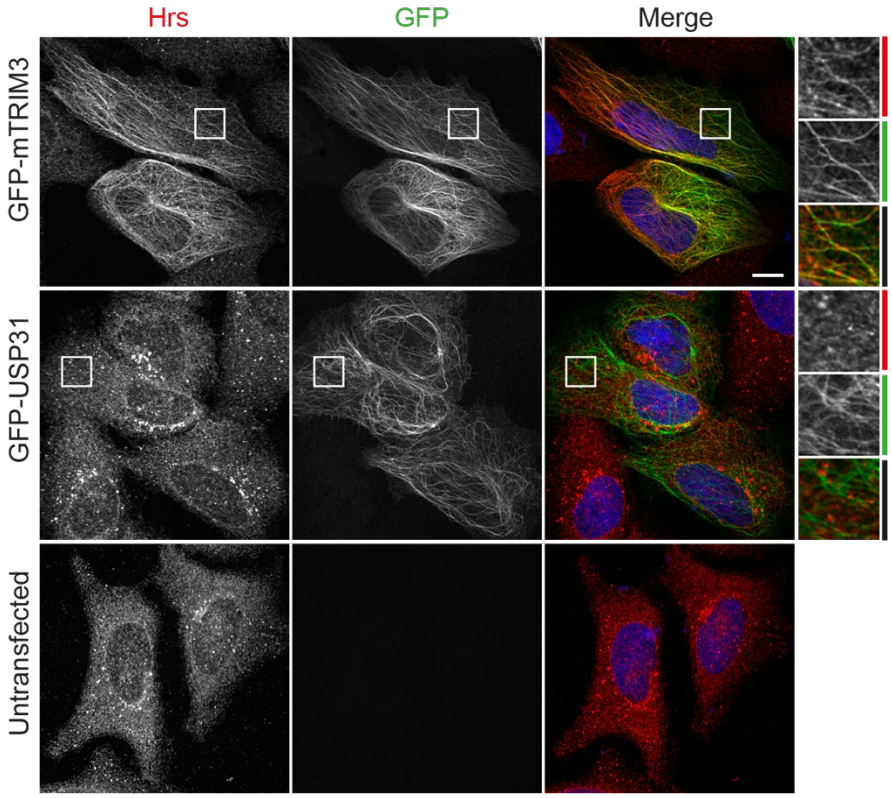

Figure 4.27 – TRIM3 colocalises with Hrs

U2OS cells were transfected with 1 µg DNA for 21 hours, fixed with ice-cold MeOH and stained for Hrs (red) and DAPI (blue). Images were acquired with a 3i spinning disk confocal microscope. Scale bar: 10µm

4.4.5.10 TRIM3 may colocalise with actin

As TRIM3 was also shown to associate with myosin V (Yan et al., 2005), it was hypothesised that TRIM3 may also localise to actin. Furthermore, when microtubules are depolymerised, some GFP-TRIM3 can be seen to localise to potential filamentous structures towards the edge of the cell which do not colocalise with α-tubulin. This can be seen in Figure 4.18 and Figure 4.19 towards the top edges of the cells. To determine whether this filamentous structure is actin and confirm that TRIM3 can also bind to the actin cytoskeleton, GFP-mTRIM3 transfected cells were stained with Phalloidin-594 to visualise filamentous actin. Figure 4.28 shows that TRIM3 displays clear localisation to microtubules (top panel), however some cells (around 5-10% of those transfected) also display localisation with actin (second panel), indicating a possible cross-link between the microtubule and actin cytoskeleton.

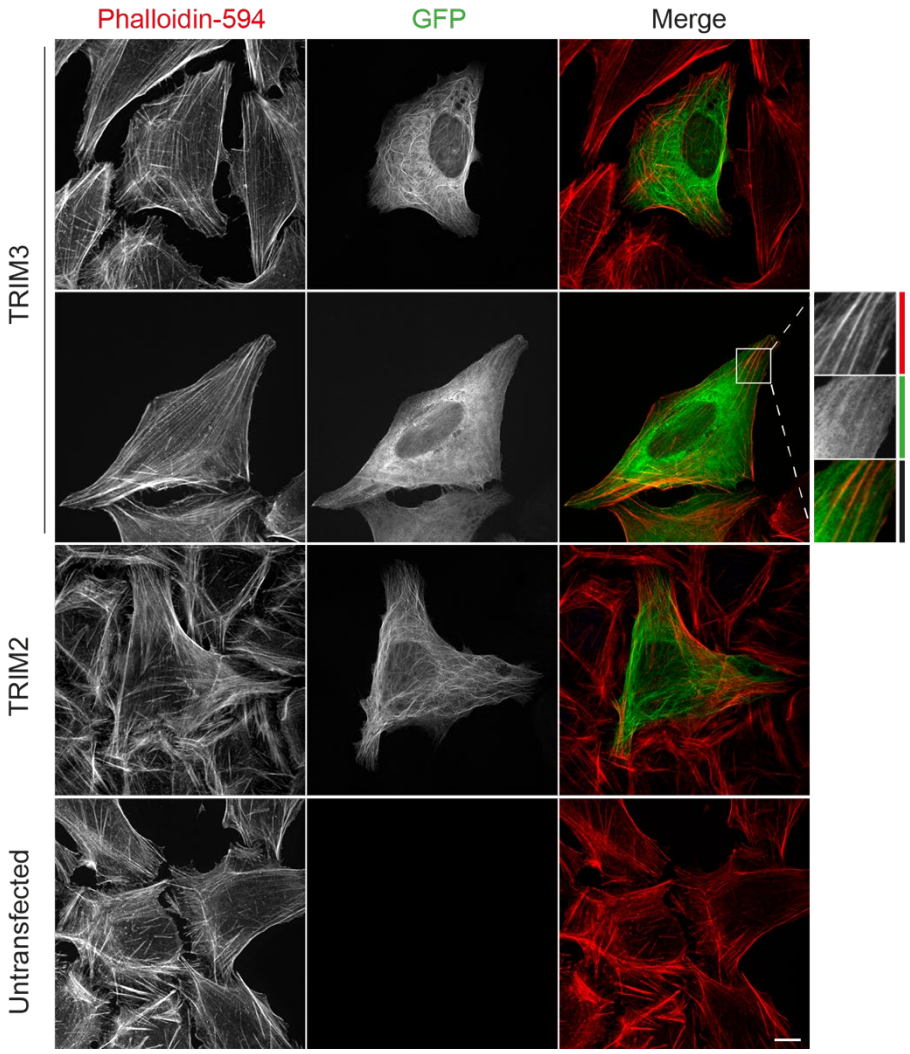

Figure 4.28 – TRIM3 may also colocalise with actin

U2OS cells were transfected with 1 µg of either GFP-mTRIM3 or GFP-TRIM2 plasmid DNA for 21 hours. Cells were then fixed with PFA and stained for Phalloidin-594 (red). Images were acquired using a 3i spinning disc confocal microscope. Scale bar = 10 µm.

4.4.6 Phenotypic effects of TRIM3 depletion

4.4.6.1 TRIM3 depletion and tubulin levels

Microtubule binding proteins are known to regulate the structure, dynamics and function of the microtubule network. As TRIM3 localises to microtubules, I therefore wanted to see whether its depletion affects the global microtubule network. This was first assessed by analysing the expression levels of tubulin proteins and its modifications. TRIM3 was depleted for indicated time points using an siRNA pool. As shown in Figure 4.29A and B, levels of tubulin, acetylated α-tubulin and detyrosinated α-tubulin are unaffected by TRIM3 depletion at all of the timepoints tested.

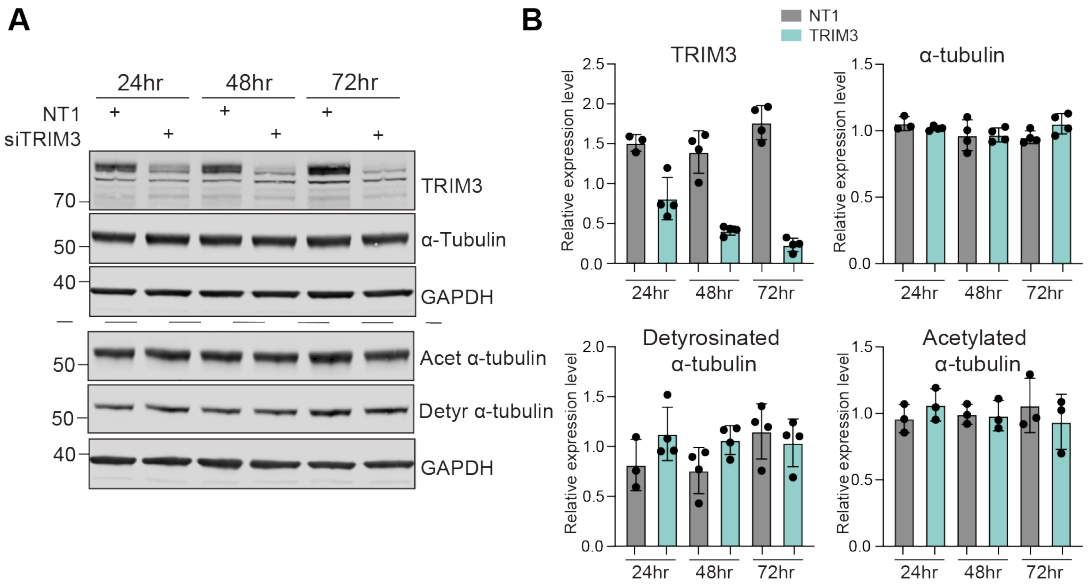

Figure 4.29 – TRIM3 depletion does not affect tubulin levels

A. U2OS cells were transfected with 40 nM siRNA against TRIM3 or a non-targeting control (NT1) for 24, 48 or 72 hours. Samples were lysed and analysed by western blotting and probed for indicated proteins. Shown is a representative experiment. **B.** Quantification of western blots illustrated in **A**. Graph shows results from 3-4 independent experiments. Mean and standard deviation is shown.

I next checked whether TRIM3 affects the microtubule network density. Observing immunofluorescent images by eye gave no indication of a denser or sparser microtubule network following TRIM3 depletion, as shown in Figure 4.30A. To confirm this conclusion, quantitation using 2 different measurements was performed (Figure 4.30B). First, the corrected total cell fluorescence (CTCF) was determined (left graph) as described in section 2.2.2. No change in the CTCF was seen following TRIM3 depletion, suggesting microtubule bunding is not altered under these conditions. The second analysis looked at the density of the network (see section 2.2.1). Control samples were used to determine a threshold which was applied to all images and the percentage of the area that was not occupied by a pixel was measured. This analysis allowed for the percentage of empty space to be calculated and compared. Similar to the CTCF analysis, no change in the density was observed. Taken together, these results suggest that TRIM3 does not play a role in regulating the assembly of microtubules and the density of the network.

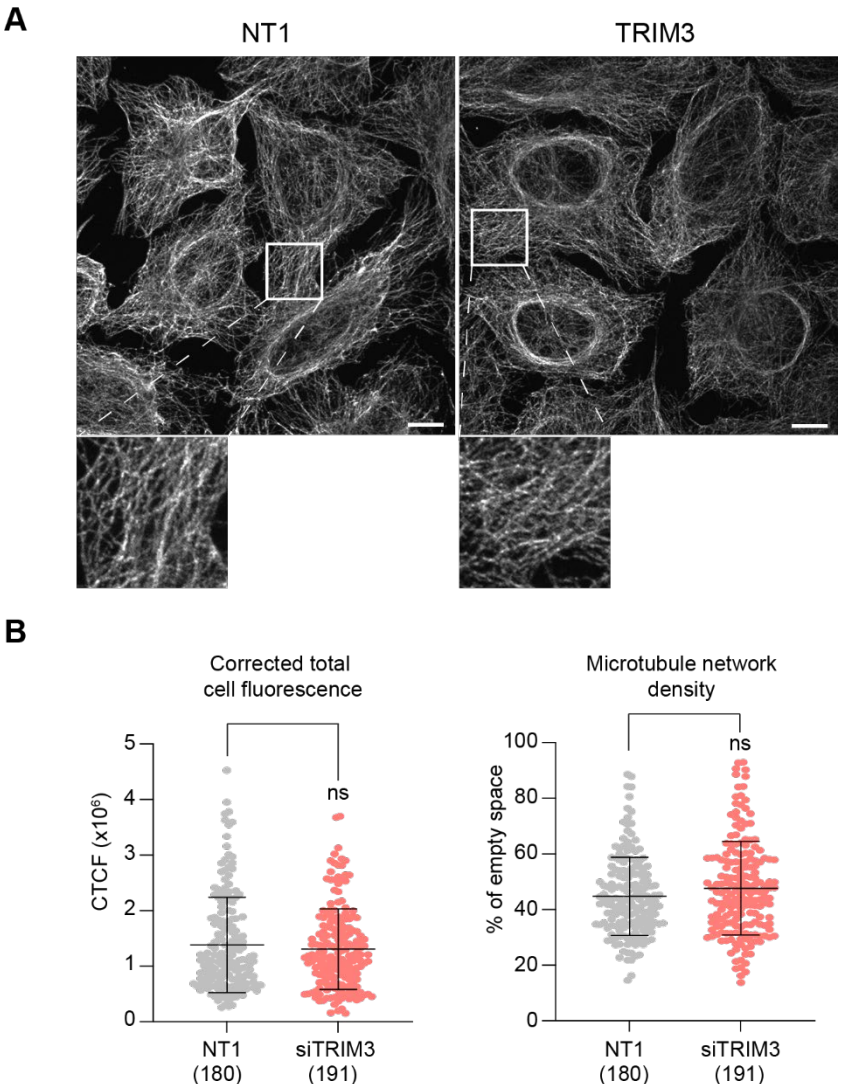

Figure 4.30 – TRIM3 and the microtubule density

A. U2OS cells were transfected with 40 nM siRNA against TRIM3 or a non-targeting control (NT1) for 48 hours then fixed with ice-cold methanol and stained for α-tubulin. Images were acquired using a 3i spinning disk confocal microscope. Scale bar = 10 µm. **B.** Graphs showing quantification of microtubule network by measuring the corrected total cell fluorescence (CTCF, left) and the % of empty space (right) from 3 independent repeats. Mean and standard deviation are shown from the indicated number of cells. Unpaired t-test confirmed the statistical significance. ns (not significant) = p>0.05.

4.4.6.2 TRIM3 affects the accumulation of acetylation on α-tubulin

Microtubule modifications accumulate on stable microtubules, with acetylation of α-tubulin being a well-known marker of microtubule stability (Gadadhar et al., 2017a). Treatment with taxol leads to an increase in both the polymerisation and the stability of microtubules, as previously described in section 1.1.5. Taxol treatment thereby

causes an increase in the levels of modifications present along the microtubule lattice. Although basal levels of both acetylation and detyrosination were not affected by TRIM3 depletion, it was possible that their accumulation rate may still be. Cells were therefore treated with taxol for indicated time points and the levels of acetylation and detyrosination were monitored.

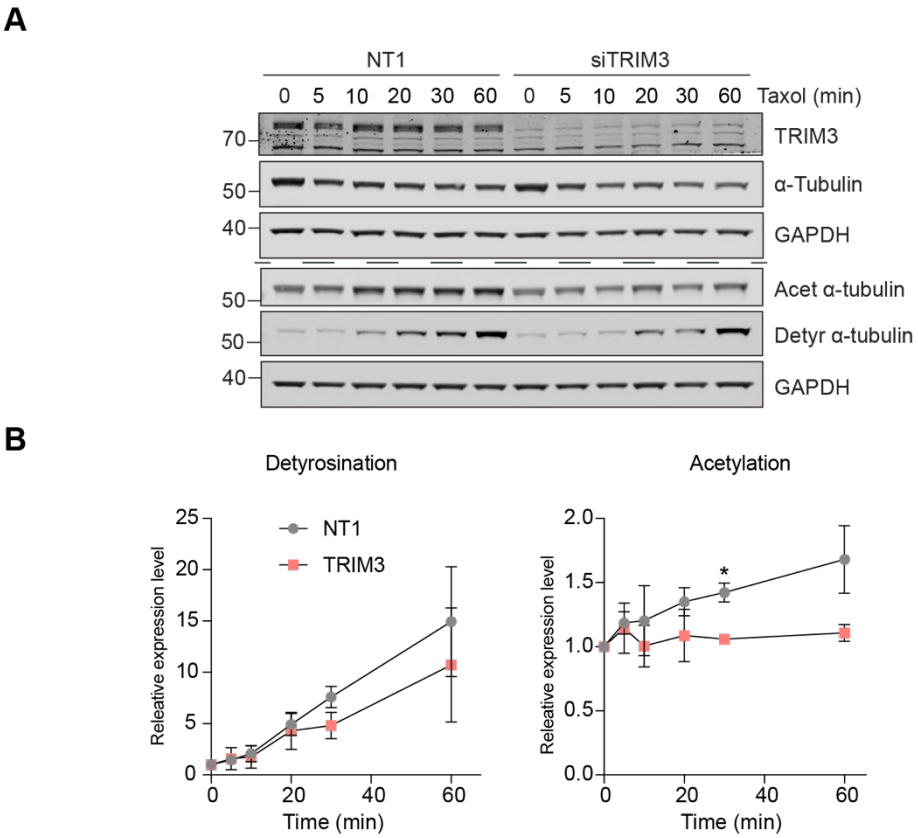

Figure 4.31 – TRIM3 depletion prevents accumulation of acetylated α-tubulin

A. U2OS cells were transfected with 40nM of either control (NT1) or siRNA targeting TRIM3 for 72 hours. Transfected cells were treated with 0.5 µg/ml Taxol for indicated timepoints and expression levels of tubulin and modified tubulin were analysed. **B.** Quantification of detyrosinated and acetylated tubulin levels. Mean and standard deviation is shown for each time point. Significance was determined using two-way ANOVA, * = $p \leq 0.05$. n=3 for detyrosination, n=4 for acetylation.

Figure 4.31A shows that for both control and TRIM3 depleted cells, treatment with taxol causes a decrease in the total levels of α-tubulin. Within the control cells an increase in both acetylation and detyrosination is observed as expected, with levels of both continuing to increase right up to the 1-hour timepoint. However, when TRIM3 levels are depleted, whilst an increase in detyrosination is still observed, albeit at a

slightly decreased rate, acetylation does not accumulate. Acetylation levels remain comparable to the 0-hour time point after 1 hour taxol treatment. Quantitation of these levels (Figure 4.31B) confirms that accumulation of acetylation does not occur following TRIM3 depletion compared to the 50% increase observed under control conditions. For detyrosination, although a slight delay in the accumulation is observed, this difference is not statistically significant. Overall, TRIM3 does not affect the accumulation of microtubule modifications as a whole following taxol treatment, but specifically regulates the accumulation of acetylated α-tubulin.

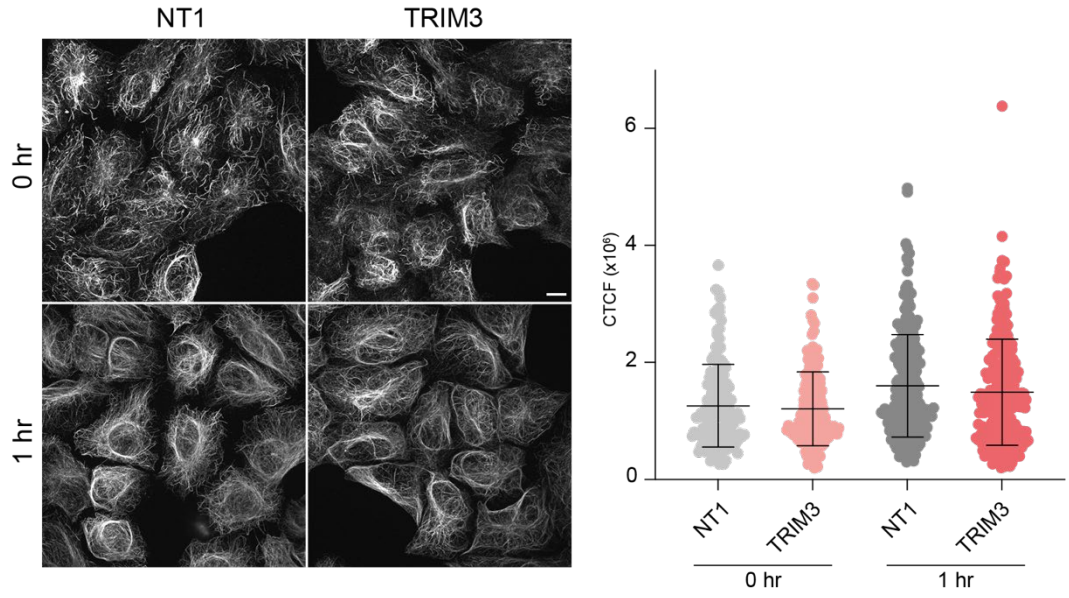

Figure 4.32 – TRIM3 depletion and visualisation of accumulation of acetylated α-tubulin

U2OS cells were transfected with 40 nM siRNA against TRIM3 or a non-targeting control (NT1) for 72 hours. Transfected cells were treated with 0.5 µg/ml Taxol for 1hr before being fixed with ice-cold methanol and stained for acetylated α-tubulin. Images were acquired using a 3i spinning disk confocal microscope. Scale bar = 10 µm. Quantitation of the acetylated network is shown in the graph. The acetylated microtubule network was measuring the corrected total cell fluorescence (CTCF). Mean and standard deviation are shown. Number of cells analysed: 0 hr - NT1 (181), TRIM3 (160); 1 hr – NT1 (224), TRIM3 (226), from 2 independent repeats.

Immunofluorescence was performed to visualise the acetylated microtubule network before and after treatment with Taxol in TRIM3 depleted cells compared to an NT1 control. Figure 4.32 shows that at the 0-hour timepoint, U2OS cells display relatively high levels of acetylated microtubules, with no differences in the CTCF between control and TRIM3 depleted cells. Unexpectedly, following taxol treatment, an

increase in the acetylated microtubule network can be visualised in both control and depleted cells. This therefore contradicts the observations obtained from western blot analysis in Figure 4.31, suggesting that only a subset of the acetylated microtubule network may be affected by TRIM3 activity.

4.4.6.3 TRIM3 depletion affects the acetylation of stable microtubules

α-tubulin acetylation of lysine 40 (K40) is a marker of microtubule stability. This modification accumulates on stable microtubules and has been shown to increase mechanical resilience and prevent breakage, allowing for persistence of long-lived microtubules (Xu et al., 2017). As the immunofluorescence results observed in Figure 4.32 were contradictory to the results observed in Figure 4.31, it is possible that TRIM3 may not regulate the whole acetylated microtubule network, but only a subset of it. As long-lived microtubules represent a small population of the acetylated microtubule network, I therefore hypothesised that these may be lost when TRIM3 levels are reduced.

To specifically visualise these stable microtubules, cells were first treated with nocodazole to depolymerise the dynamic microtubules. Cells were then washed using PHEM buffer to remove the depolymerised microtubules, leaving behind the long-lived, nocodazole-resistant microtubules. Depletion of ATAT1 (α-tubulin acetyltransferase), the enzyme responsible for tubulin acetylation (Akella et al., 2010; Shida et al., 2010), was performed alongside for comparison. In control cells, stable microtubules are observed and typically display high levels of acetylation and a curvy morphology (Figure 4.33A, left panels). When ATAT1 was depleted, very few microtubules remained, and even fewer acetylated microtubules. Those that did remain displayed short fragments distributed across each cell (right panels). Following TRIM3 depletion, the number of acetylated microtubules remaining is reduced, albeit not to as great an extent as siATAT1 (middle panels). Furthermore, the curvature observed in control cells appears reduced, with microtubules adopting an overall straighter configuration. To quantify this result, I employed the MINA plugin in Fiji (previously described in 2.2.3) to evaluate the overall network size and the branch length of the acetylated network in each condition. Though this plugin was previously designed to interpret the mitochondrial network, sufficient mapping of the microtubule network could also be achieved (Figure 2.1).

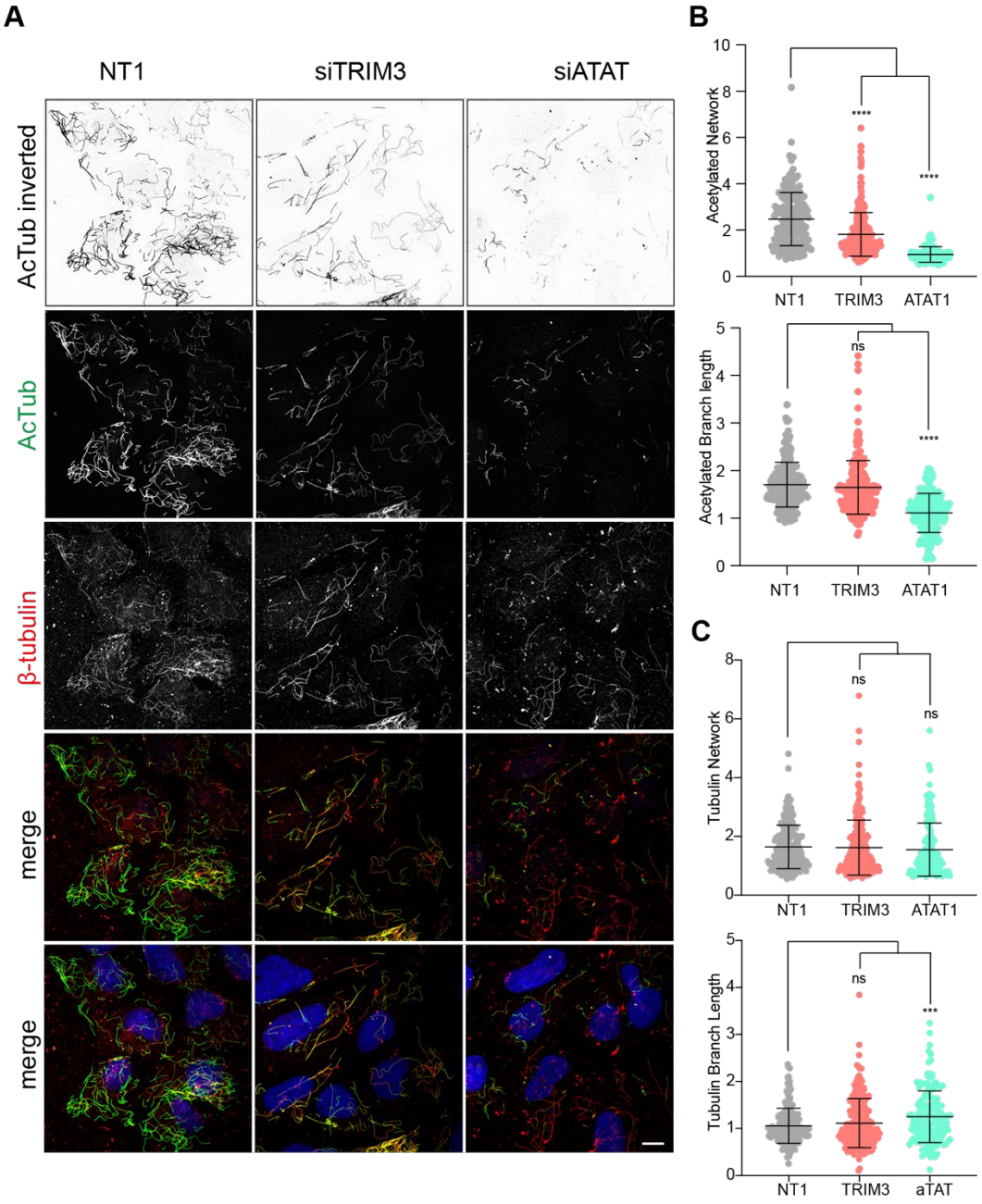

Figure 4.33 – TRIM3 depletion affects the stable acetylated tubulin network

A. U2OS cells were transfected with 40nM of either control (NT1) or siRNA targeting TRIM3 or ATAT1 for 72 hrs. Cells were then treated with nocodazole (6 μM, 1 hr) before being washed in PHEM buffer to remove the soluble microtubules, leaving behind only nocodazole-resistant microtubules. Cells were fixed with ice cold MeOH and stained for β-tubulin (red) and acetylated tubulin (green). **B/C.** Quantification using MiNa analysis shows the mean network and branch length of **B.** acetylated microtubules and **C.** the whole microtubule network (β-tubulin). Mean and standard deviation from 3 independent repeats is shown. Cell number analysed: NT1 (194), siTRIM3 (219), siATAT1 (167). Significance was determined using a one-way ANOVA via Dunnet's multiple comparison, ns = not significant ($p>0.05$), *** = $p\leq0.005$, **** = $p\leq0.001$.

Figure 4.33B shows the results for the acetylated network. For ATAT1 depleted cells, this analysis showed that the overall network was reduced alongside the length of the microtubules. For TRIM3 depleted cells, whilst the overall acetylated network was reduced (top graph), the overall branch length was not affected. To confirm whether this was specific to acetylation or all the remaining microtubules, the same analysis was performed on the β-tubulin staining (Figure 4.33C). Although ATAT1 depletion appeared to cause a slight increase in microtubule branch length, TRIM3 depletion has no effect on the β-tubulin network or the branch length. Taken together, these results suggest that TRIM3 specifically reduces the level of acetylation on stable microtubules.

4.4.6.4 TRIM3 depletion affects ATAT1 expression levels

As TRIM3 depletion regulates the levels of acetylated microtubules, I next investigated whether the levels of the responsible acetylase enzyme, ATAT1, were also affected. To confirm the specificity of the ATAT1 antibody and identify which band on the western blot is representative, ATAT1 was first depleted using an siRNA pool and probed for the protein to identify the band of interest. Figure 4.34A (left panel) shows a band just above the 50 kDa marker which is decreased following ATAT1 depletion. When TRIM3 is depleted (right panel), this same band is also reduced, indicating that TRIM3 affects the expression levels of ATAT1. Western blot quantification confirms that ATAT1 expression levels are reduced by half following TRIM3 depletion (Figure 4.34B).

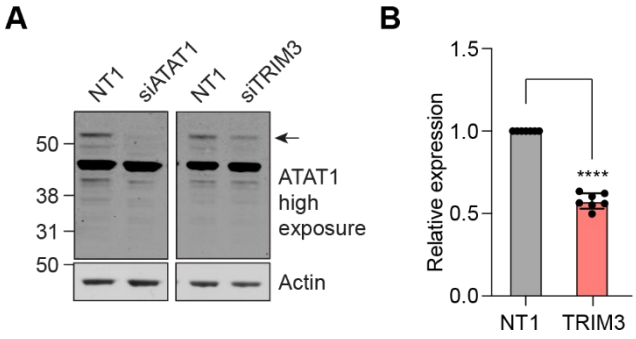

Figure 4.34 – TRIM3 depletion affects ATAT1 expression levels

U2OS cells were transfected with 40nM of either control (NT1) or siRNA targeting TRIM3 or aTAT for 72 hours. Cells were lysed in RIPA buffer and ATAT1 expression levels were analysed. Graph shows quantification from 7 independent repeats. Mean and SD is shown. Significance was determined using an unpaired t-test, **** = $p \leq 0.001$.

To confirm whether changes in ATAT1 expression levels occurred at a transcriptional level, RT-qPCR was performed on extracted mRNA following depletion of both TRIM3 and ATAT1. Figure 4.35 confirms that as expected, both TRIM3 and ATAT1 display reduced mRNA levels when each are depleted respectively. Upon depletion of ATAT1 however, TRIM3 mRNA levels remain consistent compared to the NT1 control (left graph). Furthermore, following TRIM3 depletion, ATAT1 mRNA levels are also not reduced and are comparable to control levels (right graph). These results indicate that TRIM3 is able to regulate the expression levels of ATAT1 via a post-transcriptional mechanism.

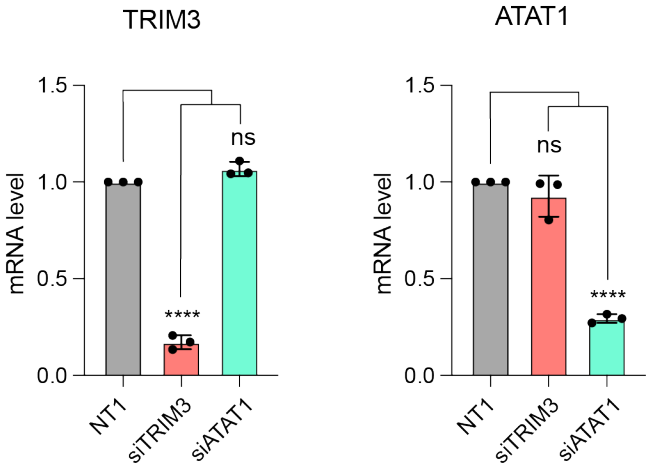

Figure 4.35 – TRIM3 regulates ATAT1 levels on a post-transcriptional level

U2OS cells were transfected with 40 nM of control or siRNA pools targeting either TRIM3 of ATAT1 for 72 hours. mRNA was extracted then reverse transcribed before qPCR was performed using primers specific for TRIM3 and ATAT1. mRNA levels are shown relative to those of GAPDH. Error bars: mean, SD. Statistical analysis was performed using one-way ANOVA with Dunnett's multiple comparison, n=3, ns (not significant) = $p>0.05$, **** = $p\leq0.001$.

4.4.6.5 TRIM3 does not affect the stability of ATAT1

As TRIM3 is an E3-ligase enzyme and has been shown to display catalytic activity, it is able to regulate the stability of its substrates by altering their ubiquitin status. To determine whether ATAT1 is a substrate of TRIM3 and is targeted for degradation via TRIM3-dependent ubiquitination, TRIM3 was depleted from cells for 72 hours before a cycloheximide chase experiment was performed. Cycloheximide (CHX) inhibits protein synthesis by binding to the 60S ribosome and blocking the final step of

translational elongation (Schneider-Poetsch et al., 2010). As protein synthesis has been inhibited, protein turnover can be monitored by measuring the expression levels of the protein of interest after increasing incubation times with the inhibitor. Over the indicated time-course, the expression levels of both ATAT1 and TRIM3 remain relatively stable in control cells, with only a slight decrease observed after 8 hours treatment. TRIM3 depletion leads to equivalent turnover kinetics of ATAT1 compared to the control, indicating that it does not have any control on ATAT1 expression at the protein level during this time course. As ATAT1 appears to be a relatively long-lived protein, protein stability is difficult to judge.

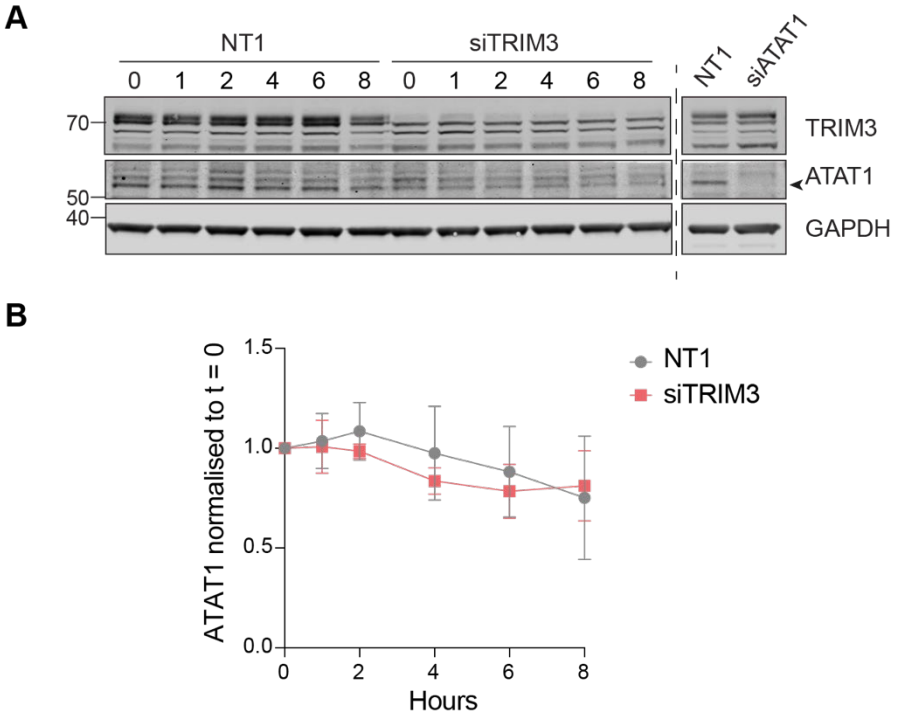

Figure 4.36 – TRIM3 does not change the protein stability of ATAT1

U2OS cells were transfected with 40nM of control or siRNA pools targeting TRIM3 for 72 hours. Cells were then treated with 100 µg/ml cycloheximide (CHX) for the indicated time points then lysed in RIPA buffer. ATAT1 expression levels were analysed. siRNA against ATAT1 was performed alongside to identify the correct band representing ATAT1. **A.** Representative western blot. **B.** Graph showing the reduction of ATAT1 in control cells (grey) compared TRIM3 depleted cells (pink). Mean and standard deviation is shown.

4.4.6.6 TRIM3 does not affect EB1 distribution on microtubule plus ends

As previously mentioned, acetylation is a well-known marker of microtubule stability as it has been shown to accumulate on long-lived microtubules. As TRIM3 plays a role in regulating the levels of α-tubulin acetylation, it could be hypothesised that TRIM3 is involved in microtubule stability and dynamics. Plus-end tracking proteins are known to decorate the dynamic growing ends of microtubules. EB1 (end-binding protein 1) is referred to as the master plus-end tracking protein as it is able to autonomously associate with the growing microtubule end (Akhmanova and Steinmetz, 2010) and interact with other plus-tip binding proteins to facilitate their binding (Dixit et al., 2009; Fong et al., 2017). Plus-tip proteins are described in more detail in section 1.1.9.2. Work carried out in Thomas Surrey's lab showed that the abundance of EB1 proteins at microtubule plus tips are indicative of microtubule dynamics, with larger caps representing greater microtubule stability (Duellberg et al., 2016). EB1 cap lengths can therefore be used as a readout for changes in microtubule stability. To determine whether TRIM3 has a role in regulating this stability, the EB1 caps of microtubules within cells depleted of TRIM3 were measured and compared to control cells. Figure 4.37 shows that cap length does not change following TRIM3 depletion, with the average cap length per cell measuring at 2.86 µm for control cells and 2.92 µm for those treated with siRNA against TRIM3.

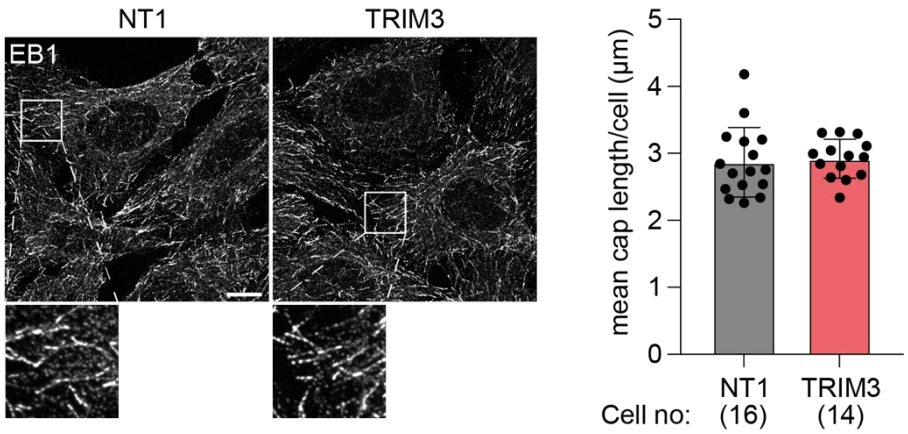

Figure 4.37 – TRIM3 depletion does not affect EB1-cap length

U2OS cells were transfected with 40 nM siRNA against TRIM3 or a non-targeting control (NT1) for 48 hrs then fixed with ice-cold methanol and stained for EB1. Images were acquired using a 3i spinning disk confocal microscope. Scale bar = 10 µm. Quantitation of the average EB1 comet length per cell is shown in the graph. The length of 30-40 comets per cell was measured manually using the measure line tool in Fiji. Mean and standard deviation are shown.

4.4.6.7 TRIM3 and microtubule dynamics

Despite EB1 cap length being unaffected by TRIM3 depletion, I wanted to confirm whether microtubule dynamics also remained unaffected. Microtubules are constantly growing and shrinking and remodelling their network to allow for rapid regulation of their cellular function. Plus-tips can therefore be monitored in real-time, and GFP-EB3 was used as a marker for polymerising microtubule ends to assess the parameters of microtubule growth. Cells were imaged continuously at 500ms intervals to capture the plus tip migration. Figure 4.38A shows representative regions of GFP-EB3 at microtubule ends and their movements across 10 seconds. The acquired time-lapse videos were analysed using the plusTipTracker add-on in Matlab which is able to automatically detect and measure the movement of plus-tip proteins (Applegate et al., 2011). This analysis shows that no changes in the growth speed, growth lifetime or the growth length are observed following TRIM3 depletion (Figure 4.38B). Taken together, TRIM3 does not regulate microtubule stability and dynamics.

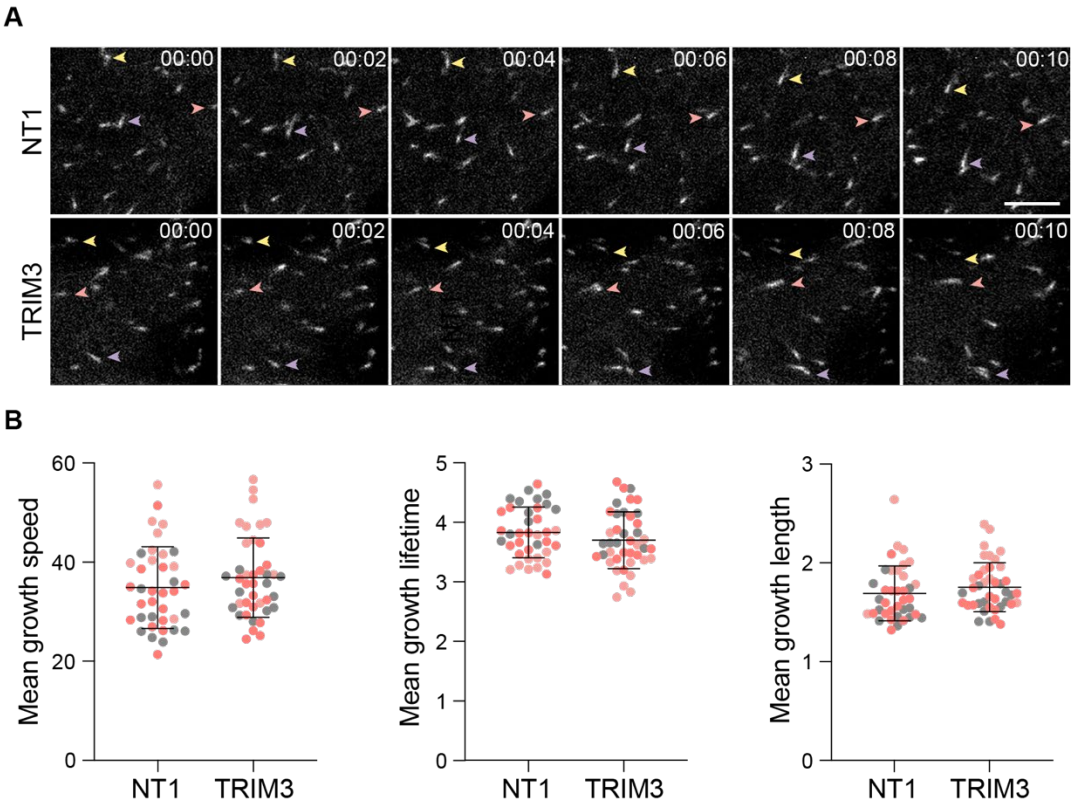

Figure 4.38 – TRIM3 depletion does not regulate microtubule dynamics

U2OS cells were transfected with 40 nM siRNA against TRIM3 or a non-targeting control (NT1) for 72 hours. 51 hours after siRNA treatment, cells were transfected with 1 µg GFP-EB3 plasmid DNA. Cells were then imaged on a 3i spinning disc confocal microscope at 500ms intervals for 2 minutes. **A.** Representative regions

of EB3 comets are shown. Arrows are used to track selected individual comets. Scale bar = 5 μm. Time is in mm:ss. **B.** EB3 comets were tracked using the plusTipTracker extension on Matlab and parameters are shown in the graphs. Mean and standard deviation of 3 independent repeats is show with each colour representing a single repeat.

4.4.6.8 TRIM3 depletion does not affect mitotic progression

TRIM3 was shown to localise with the mitotic spindle from metaphase right through to telophase (Figure 4.23). I therefore wanted to investigate whether TRIM3 plays a role within mitosis. To do this, TRIM3 was depleted for 72 hours in U2OS cells stably expressing mRFP-H2B and cells were imaged live to observe their mitotic progression. Imaging was performed over a 16-hour period, with images being captured at 5-minute intervals. These were then analysed manually to determine whether any delays in mitotic progression occurred, and if so, at what stage. Representative images of cells entering through mitosis, beginning at nuclear envelope breakdown (NEB) and ending when chromosomes decondense and the cells 'sit down' again, are shown in Figure 4.39A. The time taken for cells to reach prometaphase, metaphase, anaphase, and to eventually sit back down again, was analysed. The median time taken to reach each of these stages are shown in Figure 4.39B. No difference in the time taken to reach any of these stages was observed between the control cells and those depleted from TRIM3. These results therefore suggest that TRIM3 does not play a role in regulating mitotic progression.

To confirm further that no defects or delays in chromosome segregation are induced when TRIM3 is depleted, cells stably expressing GFP-CENP-A and mCherry-tubulin were utilised. These cells are described in (Barisic et al., 2015). As the centromere is used to direct the segregation of chromosomes during mitosis, this protein can be used as a marker for successful chromosome separation. TRIM3 was depleted for 72 hours alongside an NT1 control. Cells at late prometaphase and metaphase were selected for and imaged at 1-minute intervals. Figure 4.40 shows the progression from the last stage in metaphase into anaphase, and through to telophase, allowing for chromosome segregation to be observed. Representative images of control and TRIM3 depleted cells are shown, with no obvious differences apparent between them. Cells progress from metaphase into anaphase and late anaphase between the 00:00 and 00:08 time points. Furrow ingression, seen from the mCherry-tubulin marker, then begins at 00:10, with early and late telophase occurring between the 00:12 and 00:18 time frames. Both cells are seen to have a few lagging centromeres between the

00:02 and 00:06 time points, however these are corrected at 00:08. Taken together, these results confirm that TRIM3 does not play a role within mitotic progression, and its depletion does not affect the chromatid separation.

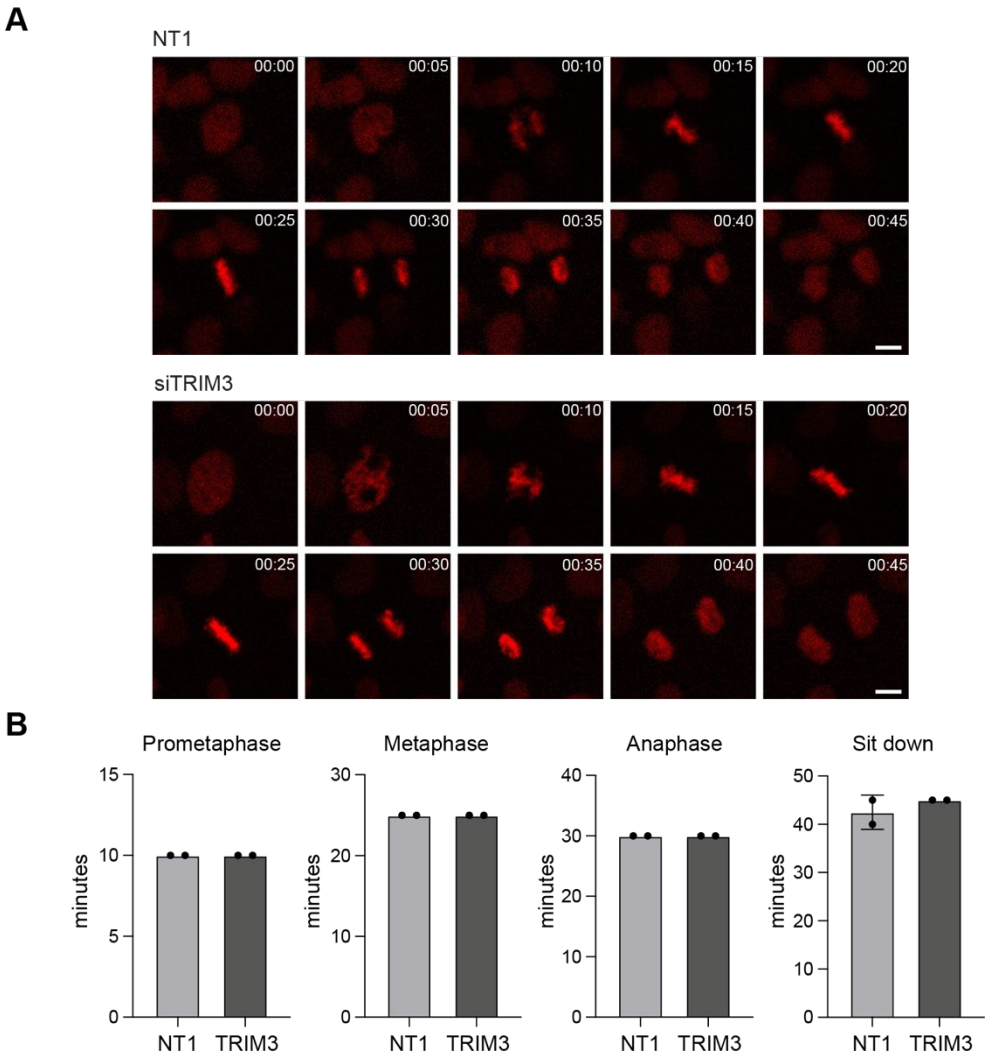

Figure 4.39 – TRIM3 depletion does not affect mitotic progression

U2OS cells stably expressing mRFP-H2B were transfected with 40 nM of either control (NT1) or siRNA targeting TRIM3. At 72 hours post-transfection, cells were imaged live using a Nikon TI-Eclipse microscope with a 20x objective at 5-minute intervals for 16 hours. **A.** Representative images of the cells analysed through mitosis. Time = hh:mm. Scale bar = 10 µm. **B.** Graphs showing the median time taken for cells to reach the indicated phases across 2 independent repeats. 323 cells were analysed per condition.

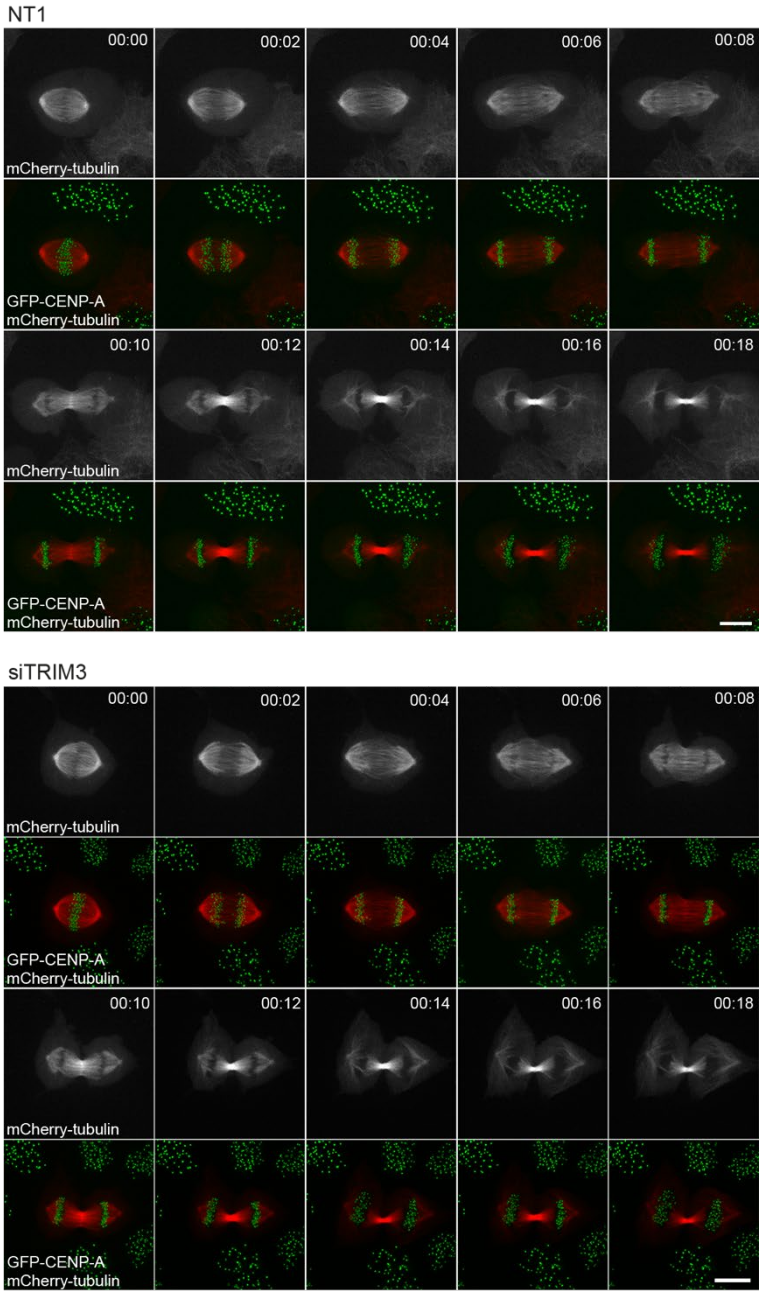

Figure 4.40 – TRIM3 depletion does not affect chromosome segregation

U2OS cells stably expressing GFP-CENPA and mCherry-tubulin were transfected with 40 nM of either control (NT1) or siRNA targeting TRIM3. At 72 hours post-transfection, cells at late prometaphase and metaphase were selected for an imaged using a 3i spinning disc confocal microscope (63x objective). Images were acquired using a z-stack at 1-minute intervals with a 16 µm range and a step size of 1 µm. Maximum projections are shown. Time = hh:mm. Scale bars = 10µm.

4.5 Discussion

As microtubules form a network which expands across the whole cell surface area, and they have a central role in one of the most regulated processes, mitosis, it is understandable that a large number of proteins are able to interact with them, with many still yet to be discovered. Identification of further novel microtubule binding proteins will aid our understanding into microtubule functions. Furthermore, a large number of already identified proteins are lacking further characterisation past their ability to associate with microtubules (Bodakuntla et al., 2019). Understanding this complex picture in greater detail is required to determine the mechanisms, functions and pathologies associated with microtubules. Within this chapter I have provided the initial characterisation of 2 novel microtubule binding protein: LGALSL and TRIM3. These results therefore validate the approach described Chapter 3.

4.5.1 LGALSL

LGALSL was identified as the most nocodazole-sensitive non-tubulin protein in the proteomics dataset and has been confirmed here as a novel microtubule binding protein. Galectin proteins are primarily known for binding to carbohydrates via their conserved carbohydrate recognition domains (CRDs), allowing them to associate with glycosylated proteins (Johannes et al., 2018). Microtubules can be modified by sialyloligosaccharide groups (Hino et al., 2003) and O-linked β-N-acetylglucosamine on both tubulin subunits (Ji et al., 2011). Glycosylation may therefore be involved in protein-protein interactions (Song and Brady, 2015). The galectin-like protein LGALSL may therefore interact with microtubules via these carbohydrate additions.

LGALSL has been reported to lack conserved resides within its CRD, so its carbohydrate binding ability may be limited (Zhou et al., 2008; Wälti et al., 2008). Direct microtubule binding could be a possibility as other galectin family members have been shown to associate with non-galactose-containing partners, such as the association of galectin-8 with the autophagic receptor NDP52 (Kim et al., 2013). Additionally, LGALSL is reported to interact with GALNT9 in HCT116 cells (Huttlin et al., 2021). GALNT9, also known as GalNAc-T9, is part of the UDP-N acetyl-α-D-galactosamine:polypeptide N-acetyl-galactosaminyl-transferase family of enzymes which catalyse the addition of O-glycan carbohydrate chains (Raman et al., 2012). This association may support a role for LGALSL in glycoprotein association and regulation.

4.5.2 RMDN3

RMDN3 was selected as a protein of interest due to it being one of the most Taxol-sensitive proteins identified within my dataset. Additionally, it was extracted in a similar manner to the protein SAMM50 which localises to the same subcellular region as RMDN3 and shares binding partners (Galmes et al., 2016; Monteiro-Cardoso et al., 2022) suggesting these are true candidates for microtubule binding. RMDN3, also known as PTPIP51, is a mitochondrial protein which localises to the outer mitochondrial membrane (Stoica et al., 2014). I have confirmed this result and shown that it is driven by its N-terminal transmembrane domain.

During generation of GFP-tagged constructs of RMDN3, a GFP tag was incorporated at the N-terminus of the protein without considering the transmembrane domain. This disrupted the mitochondrial targeting, and clear microtubule binding is observed. It can be hypothesised that the C-terminal tetratricopeptide repeat (TPR) may therefore be responsible for this microtubule binding. Within RMDN3, this domain is involved in phospholipid binding and transfer (Yeo et al., 2021), however these repeats are also able to act as scaffolds to allow for protein-protein interactions with great binding versatility (Zeytuni and Zarivach, 2012). TPRs are formed from repeating arrays of 34-amino acid motifs to create a coiled-coil structure (Perez-Riba and Itzhaki, 2019). These have been likened to structural repeats found in Tau proteins for interacting with microtubules (Butner and Kirschner, 1991; Smith et al., 1995), supporting the hypothesis that the RMDN3 TPR domain may facilitate microtubule binding. To confirm the dependence of the TPR domain for microtubule association, an N-terminally tagged construct lacking the transmembrane domain of RMDN3 needs to be generated.

RMDN1 associates with microtubules in *C elegans*, and implications that RMDN3 can do the same were also previously made (Oishi et al., 2007). Sequence comparisons between these 2 proteins revealed that RMDN1 lacks the transmembrane domain and the coiled-coil domain found within the first 129 amino acids present in RMDN3. RMDN1 is therefore free to associate with microtubules, further supporting the role of the TPR domain for microtubule interactions. Furthermore, an additional isoform consisting of 341 amino acids, which also lacks the first 129 amino acids, has been identified for RMDN3. As all the peptides identified within the proteomics data reside after residue 129, it is possible it was the detection of this isoform which allowed for its identification as a microtubule binding protein. Generating a construct of RMDN3

which has these first 129 amino acids removed would allow us to determine whether this hypothesis and the dependence on the TPR domain is correct.

GFP-RMDN3 overexpression induced microtubule bundling, indicating a functional role in microtubule network organisation, stability and dynamics in a similar way to MAP65 (Walczak and Shaw, 2010). Additionally, a strong colocalisation with both acetylated and detyrosinated microtubules was also seen. Recent advances within the microtubule field have proposed the concept of a 'tubulin code' which is the idea that microtubule PTM's generate different sub populations of networks which can influence the plethora of proteins that associate with them (Gadadhar et al., 2017a; Janke and Magiera, 2020). RMDN3 may therefore display a preference for modified microtubules over unmodified ones. Investigations of additional sub populations such as polyglycylation and polyglutamylation could also be checked to determine whether this preference is specific to all modifications or just those analysed here. On the other hand, acetylation and detyrosination are also known to accumulate on stable microtubules (Portran et al., 2017; Khawaja et al., 1988; Peris et al., 2009). As RMDN3 overexpression induces microtubule bundling and hence stability, this could in turn lead to the accumulation of these modifications. Further research is therefore required to determine the order of events connecting RMDN3, microtubule bundling and the accumulation of PTMs. Moreover, determining a role for RMDN3 in microtubule dynamics via EB3 plus-tip tracking or regrowth following nocodazole depolymerisation could also be performed under conditions of RMDN3 depletion.

One of the main functions of microtubules is to transport cargo around the cell via kinesin and dynein motor proteins (Endow et al., 2010). Mitochondria are known to be transported by kinesin-1 with a preference to acetylated microtubules. Furthermore, endoplasmic reticulum (ER) sliding also preferentially occurs on acetylated microtubules allowing for increased ER-mitochondrial contacts (Friedman et al., 2010). RMDN3 may therefore be involved in this transport mechanism by its ability to specifically recognise acetylated microtubules. It's interaction with the ER-associated protein VAPB (Stoica et al., 2014) further supports this hypothesis. As acetylation alone does not influence kinesin-1 motility and preferences (Balabanian et al., 2017; Kaul et al., 2014; Walter et al., 2012), specificity to these microtubule subsets may be provided via an additional mechanism involving RMDN3. This could be investigated via live cell imaging using MitoTracker and a newly developed stain for acetylated microtubules (Jansen et al., 2023) in the presence and depletion of RMDN3. An association between mitochondrial motility and the intracellular Ca^{2+}

levels has also been proposed (Barlan and Gelfand, 2017). The mitochondrial protein Miro interacts with the kinesin tail under physiological levels of Ca^{2+}. Elevated levels of Ca^{2+} induces a conformational change, causing kinesin-1 to switch into an inactive state and its association with microtubules is prevented (Wang and Schwarz, 2009). As RMDN3 is involved in calcium homeostasis (De vos et al., 2012), it is well placed to be involved within this regulatory mechanism of mitochondrial motility.

4.5.3 TRIM3

The tripartite motif containing E3 ligase enzyme, TRIM3, is relatively poorly characterised within the literature. My work has confirmed that TRIM3, and its closest family member TRIM2, clearly localise to microtubules. A number of other TRIM proteins also associate with microtubule through their cos box domains (Short and Cox, 2006). Only 2 of these, TRIM54 and TRIM46, were identified within my proteomics dataset, and neither were specifically extracted in a nocodazole-sensitive manner. The detection of TRIM3 may be accounted for by its relatively high expression levels in both Hela and U2OS cells. Functional roles relating to microtubules have been identified for other cos box-containing TRIMs. TRIM46 controls neuronal polarity and regulates microtubule organisation by forming closely-spaced microtubule bundles (Van Beuningen et al., 2015). TRIM55, also known as MURF2 (muscle RING finger protein 2) associated with glutamylated microtubules and functions in the alignment and extension of sarcomeres in muscle cells by transiently associating with sarcomeric myosin during myogenesis (Pizon et al., 2002). My work has identified a role for TRIM3 in the regulation of the acetylated network.

TRIM2 is the closest family member to TRIM3 as they share the same domain structure throughout, with their RING and B-box domains sharing 71% sequence homology, and their NHL domain sharing 81% (Esposito et al., 2022). This combined with my work suggests the TRIM2 NHL repeat is responsible for its microtubule localisation. TRIM32 and TRIM71 should also be investigated for microtubule interactions as they both contain an NHL repeat domain (Williams et al., 2019). Both TRIM2 and TRIM3 have been reported to associate with myosin V (Ohkawa et al., 2001; Yan et al., 2005), indicating they share binding partners. As heterodimerisation occurs between these family members (Esposito et al., 2022), co-dependency may also occur between these 2 proteins. Simultaneous depletion of both proteins should be investigated to determine whether greater phenotypic responses are achieved.

Extensive research has been carried out to elucidate the functional roles of the acetylation of K40 on the α-tubulin subunit which resides within the microtubule lumen (Fernández-Barrera and Alonso, 2018). Recently it has been identified to be involved in the stability of long-lived microtubules, and its absence leads to increased mechanical breakage (Xu et al., 2017). TRIM3 may therefore play a role in regulating microtubule stability, and further investigations could be made using *in vitro* techniques to determine this. Cilia and flagellar are highly acetylated structures and its presence is required for the kinetics of their assembly (Shida et al., 2010). TRIM3 may therefore disrupt ciliogenesis by altering the acetylation levels. Axonal transport is highly dependent on microtubule acetylation and reduced levels have been associated with various disease phenotypes (Eshun-Wilson et al., 2019). HDAC6 inhibition, which results in an increase in axonal acetylation levels, has been shown to reverse the transport defects observed in Huntington's Disease (Dompierre et al., 2007), Charcot-Marie-Tooth disease (D'Ydewalle et al., 2011), distal hereditary motor neuropathy (Kim et al., 2016), Parkinson's disease (Godena et al., 2014) and Alzheimer's disease (Mao et al., 2017). Despite this, the mechanisms for how acetylation affects axonal growth and transport remains elusive (Eshun-Wilson et al., 2019). Acetylated microtubules have been shown to enhance bundling which can increase the processivity of kinesin-1 motors (Balabanian et al., 2017). KIF21B is a kinesin motor protein which is specifically expressed in spleen and brain tissue. TRIM3 deletion in mouse hippocampal derived neurons lead to reduced axonal motility of KIF21B, via an independent method to its E3-ligase activity (Labonté et al., 2013). Taken together, TRIM3 may therefore indirectly regulate motor function of KIF21B by altering the levels of acetylated microtubules and reducing microtubule bundling in neurons. As mutations of this motor protein have been implicated in neurodevelopmental disorders (Asselin et al., 2020), understanding of this mechanistic hypothesis may allow for therapeutic treatments for KIF21B-related neurodevelopmental disorders.

TRIM3 regulates the levels of acetylated microtubules by altering the expression levels of ATAT1 in a post-transcriptional manner. With TRIM3 being an E3 ligase, direct ubiquitination of ATAT1 by TRIM3 would result in its destabilisation: ATAT1 levels would decrease in the presence of TRIM3 and increase in its absence. As the opposite is observed, it suggests that if TRIM3 is regulating the stability of ATAT1, it does so in an indirect manner, possibly by altering the activity of a deubiquitylase (DUB) which in turn removes ATAT1 ubiquitination, thereby stabilising it. Further investigations into the substrates of TRIM3 need to be performed before the full

mechanistic details can be elucidated. A rescue experiment and the use a catalytic mutant of TRIM3 would provide further insights into whether this phenotype is performed by the E3 ligase activity. With TRIM3 and TRIM2 being closely related family members, interplay has been observed between them. TRIM proteins are known to dimerise via their coiled-coil domains (Fiorentini et al., 2020) and a recent study shows that TRIM3 and TRIM2 dimerisation occurs via the coiled-coil and filamin domain of the respective protein (Esposito et al., 2022). Despite their high sequence similarity, TRIM3 displays reduced catalytic activity when expressed as a monomer compared to TRIM2, which was restored by homo- or hetero-dimerisation (Esposito et al., 2022). The potential co-dependency between these proteins may explain why basal acetylation levels are unaffected by TRIM3 depletion, and why only a small decrease in ATAT1 expression levels is observed. Further investigations into the dual role of TRIM3 and TRIM2 is therefore required.

There are emerging roles for TRIM proteins in RNA-binding, facilitated by the NHL-repeat domains, or in the case of TRIM25, the PRY-SPRY domain. These TRIM proteins can associate with mRNA to allow for rapid alterations in protein translation (Williams et al., 2019). Brat (BRAin Tumour) is the Drosophila orthologue of TRIM3 and TRIM2 and has been shown to associate with several hundred mRNA in *Drosophila* embryos via its highly specific RNA-binding motif (Loedige et al., 2015). As TRIM3 is the mammalian orthologue of Brat, RNA binding may occur via its NHL-repeat domain (Esposito et al., 2022). TRIM3 has been identified in RNA-transporting granules, supporting the idea of TRIM3-RNA interactions (Kanai et al., 2004). If TRIM3 RNA-binding occurs for ATAT1 mRNA, to align with the results obtained here, its association would need to enhance protein expression, with TRIM3 depletion leading to reduced ATAT1 translation. This would therefore fit with the unaffected mRNA levels, the ATAT1 downregulation and the unaffected ATAT1 stability seen following CHX treatment in TRIM3 depleted cells. Although most instances of TRIM-mRNA binding results in the negative regulation of protein expression via translational repression (Loedige et al., 2013), the reverse cannot be ruled out. Identifying whether TRIM3 and TRIM2 are capable of interacting with RNA is crucial to understanding their functional roles better and may assist with the mechanistic details connecting TRIM3 and ATAT1.

Chapter 5 – USP31 and its role in mitosis

5.1 Introduction

In parallel to my discovery-based approach, detailed in Chapter 3, I also decided to pursue mechanistic studies of a novel microtubule-associated protein previously discovered in the laboratory. Due to covid restrictions in place within the laboratory, some of this was carried out as a team effort alongside Erithelgi Bertsoulaki and Joana Gomes Neto. This research builds on foundational and preliminary observations made by Erithelgi Bertsoulaki as part of her PhD thesis work (Bertsoulaki, 2018).

USP31 is a deubiquitylase (DUB) which is poorly characterised in the literature. Erithelgi Bertsoulaki revealed that an overexpressed version of GFP-USP31 displays clear association with microtubules (Bertsoulaki, 2018). Additionally, she also observed a dramatic relocalisation of USP31 onto the mitotic spindle during late anaphase. She showed that depletion of USP31 causes cells to become arrested at G2/M phase, causing them to take much longer to divide than control cells. These results indicated that USP31 must play a significant role within mitosis, and this has been further explored with the work described in this chapter. I have therefore characterised the dynamics of USP31 during mitosis, showing that it is both upregulated 2-3-fold and phosphorylated in a CDK1-dependent manner during mitosis. Analysis of a catalytically inactive version of USP31 shows the formation of multiple ectopic cleavage furrows. Furthermore, under anaphase-like conditions USP31 depletion reduces the expression levels of multiple chromosomal passenger complex components, in particular, INCENP, as well as impairing its translocation from the centromeres to the central spindle. This data represents the first investigation into a regulatory role for USP31 during mitosis.

5.2 USP31 expression during mitosis

5.2.1 USP31 levels increase during mitosis

A study which investigated DUB expression levels during the cell cycle did not reveal any evidence indicating certain DUBs are highly expressed in mitosis compared to interphase (Darling, 2017). This study also did not include any comprehensive analysis of USP31. Analysis of the expression levels of this DUB across the cell cycle was therefore undertaken.

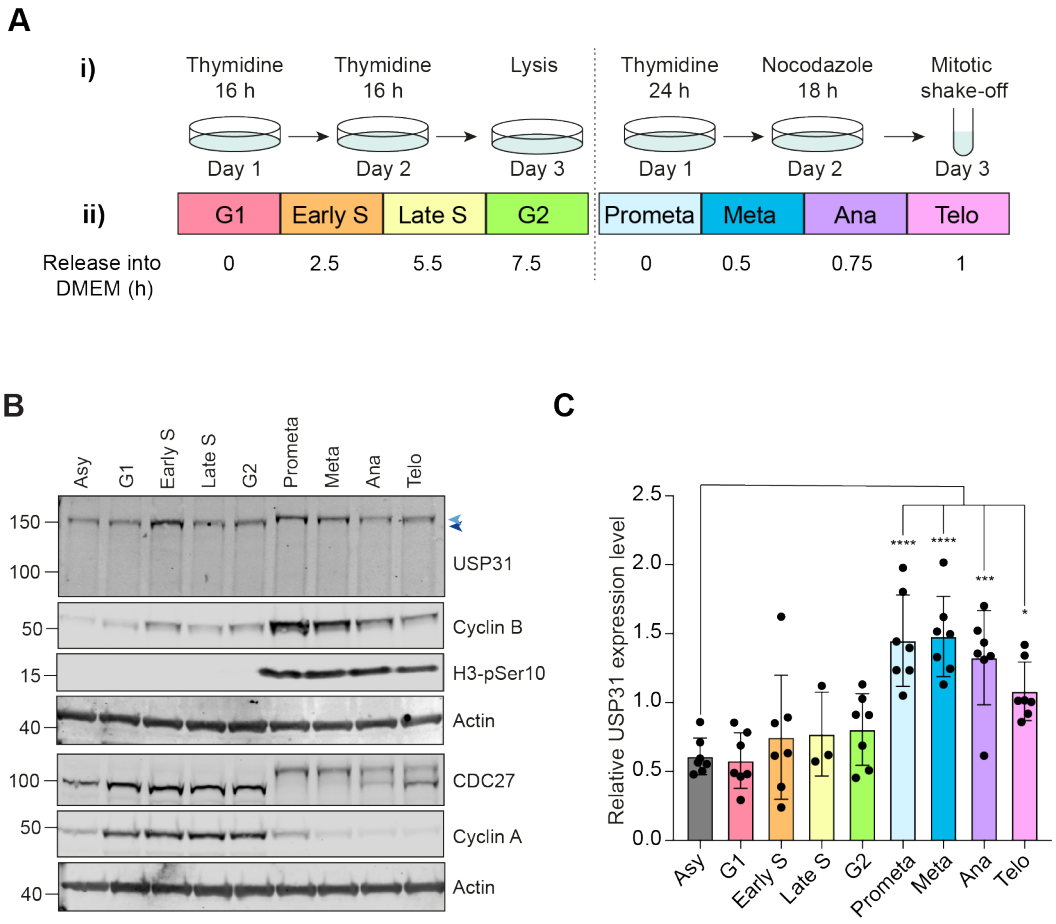

Figure 5.1 – USP31 expression levels increase during mitosis

A. Schematic showing cell synchronisation protocols, separated by a dashed line. **i)** schedules for double thymidine block or single thymidine block followed by nocodazole treatment are shown. **ii)** Lysis timing for each stage is shown. **B.** USP31 expression during the cell cycle. U2OS urea cell lysates were collected upon either synchronisation protocol at the time-points specified in A. Dark blue arrow shows the unphosphorylated band, light blue arrow shows the phosphorylated. **C:** Western blot quantitation of **B**. Graph shows individual values from 3 (Late S) or 7 (all others) independent biological repeats. Error bars indicate SD; one-way ANOVA with Dunnett's multiple comparisons test, *p≤0.05, ***p≤0.001, ****p≤0.0001

To increase the number of cells occupying different phases of the cell cycle, 2 methods of cell synchronisation were adopted as illustrated in Figure 5.1A. Cells were synchronised either by a double thymidine block to collect cells within G1, Early S, Late S and G2 phases, whereas synchronisation with thymidine followed by nocodazole was used to arrest cells during early mitosis (also described as mitotic shake off). Mitotic shake off refers to the removal of the rounded-up, dividing cells from the surface of the plate by carefully detaching them using the current cell culture medium. This therefore enriches for cells which have entered into mitosis and are

arrested at prometaphase whilst avoiding those in other phases of the cell cycle. Cells were then lysed at these different time points following release into fresh culture medium and probed for USP31. The results displayed in Figure 5.1B show that levels of USP31 are relatively low within asynchronous cells and cell cycle phases between G1 and G2. However, levels of USP31 are seen to increase significantly during early mitosis, with levels remaining high as cells progress into late mitosis. Western blot quantification in Figure 5.1C confirms there is a 2 to 3-fold increase in mitosis compared to asynchronous cells. Expression levels of USP31 are therefore significantly increased at mitotic entry. Blots shown were generated by me, with additional data contributed by Joana Gomes Neto incorporated into the quantitation for statistical analysis.

5.2.2 USP31 displays a shift in molecular weight during mitosis

In addition to the increase in USP31 expression levels during mitosis, I also observed an upshift in molecular weight (MW), which persists throughout mitosis. Figure 5.2A shows the band displayed for asynchronous cells lies just under the 150 kDa marker (dark blue arrow), whereas the band observed for all the mitotic stages lies just above the 150 kDa marker (light blue arrow). This same upshift can also be seen for a lower MW form which runs at ~100 kDa, indicated with the green arrows.

To analyse at what stage upon mitotic entry this higher MW band is first observed, cells were synchronised using a single thymidine block. Cells were then released from thymidine into fresh media containing 100ng/ml nocodazole and lysed at specified time points as they transition into prometaphase. Figure 5.2B indicates the higher MW band first appears 14 hours after release into nocodazole and continues to increase in intensity up to the 18-hour timepoint. The presence of this band correlates with cyclin B expression levels, and phosphorylation of CDC27 and INCENP. To determine the kinetics of the depletion and presence of the higher MW band as cells exit mitosis, a mitotic shake off was performed and USP31 was analysed for up to 6 hours following release from nocodazole. Data presented in Figure 5.2C confirms that after 6 hours, the expression level of USP31 has almost decreased back to that of the asynchronous cells. This pattern mirrors that of cyclin B, confirming cells are returning to interphase by this point. Additionally, the observed higher MW band gradually decreases in MW over time, displaying a stepwise pattern. After 6 hours, the shift in MW has reverted back to that seen for asynchronous cells, indicated by the blue arrows. The lower MW isoform of USP31 (green arrows) follows the same pattern.

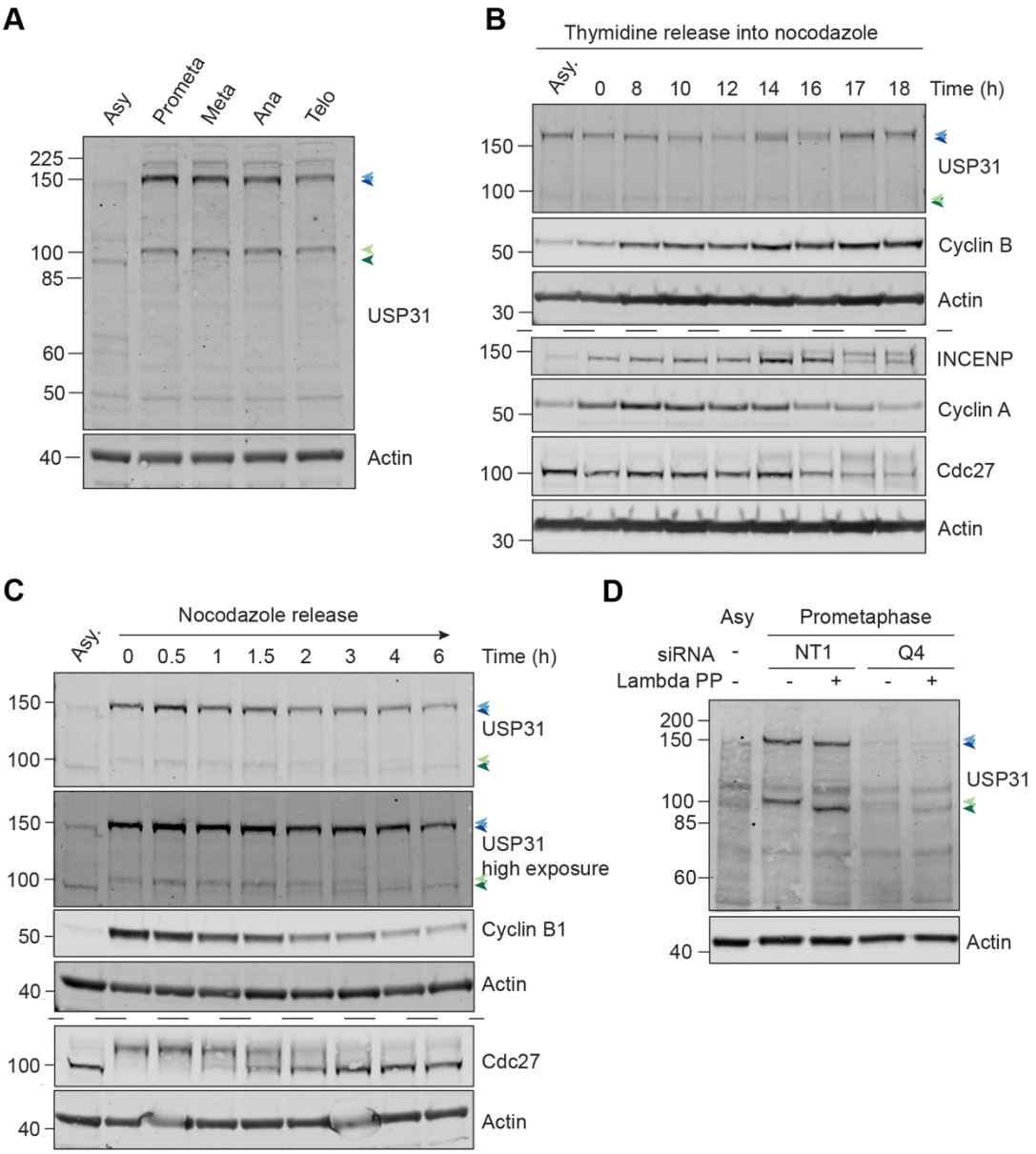

Figure 5.2 – USP31 is phosphorylated during mitosis

A. U2OS cells were synchronised using a single thymidine block followed by nocodazole. Samples were released into fresh DMEM and lysed after 0 (prometa), 30 (meta), 45 (ana) and 60 (telo) minutes. **B.** U2OS cells were treated with thymidine for 24 h before being released into fresh DMEM containing nocodazole and incubated for the indicated time points. **C.** USP31 depletion and MW shift occurs as cells exit mitosis. U2OS cells were synchronised with a single thymidine block followed by nocodazole to prometaphase and then released into fresh DMEM to allow cells to proceed through mitosis. **D.** U2OS cells were transfected with either control (NT1) or an siRNA oligos targeting USP31 (Q4) for 48h and synchronised using a single thymidine block followed by nocodazole treatment. Cells were lysed and samples were treated with 400 units of lambda phosphatase for 30 min. Blue arrows represent full length USP31 whereas green arrows represent a proposed shorter isoform. Top arrows (light) and bottom arrows (dark) indicate the phosphorylated and dephosphorylated USP31 species respectively.

5.3 USP31 is phosphorylated in mitosis

Phosphorylation frequently occurs within mitosis to allow for the fast and controlled regulation of this highly important process, as discussed in section 1.2.3. Many proteins such as CDC27, Securin and INCENP are phosphorylated upon entry into mitosis, and dephosphorylated as cells return to interphase (Agarwal and Cohen-Fix, 2002; Bishop and Schuniacher, 2002; Huang et al., 2007). I speculated that this upshift in MW may represent a phosphorylated version of USP31. Cells were therefore synchronised to prometaphase and lysed before being treated with or without lambda phosphatase. Lambda phosphatase is an enzyme derived from bacteriophage and is a dual specificity manganese-dependent protein phosphatase which displays activity towards phosphorylated serine, threonine and tyrosine residues. Treatment with this phosphatase removes any phosphate groups present from any proteins within the lysate. As a control, USP31 was depleted using the siRNA oligo, Q4, to confirm specificity of the USP31 band. Figure 5.2D shows that lambda phosphatase treatment causes a downward shift in the high MW band for both full length USP31 (blue arrows) and the isoform (green arrows) in both the NT1 and Q4 samples. Taken together, this confirms that USP31 is phosphorylated during mitosis.

5.3.1 Kinase activity during mitosis

There are a number of kinases known to function within mitosis which could be responsible for USP31 phosphorylation such as Cyclin-dependent kinases (CDK), Polo like kinases (PLK) and Aurora kinases. As CDK1, aurora B and PLK1 are highly active during mitosis (Nigg, 2001), I hypothesised that it could be one of these performing this role. Cyclin B is an activator of CDK1 and CDC27 is a known substrate (Huang et al., 2007). USP31 phosphorylation increases at a similar rate to cyclin B levels and the presence of CDC27 phosphorylation (Figure 5.2B), supporting the notion that CDK1 may be the responsible kinase. INCENP is a member of the chromosomal passenger complex (CPC) and plays a role within the spindle assembly checkpoint and cytokinesis (Aleem et al., 2015). INCENP has been previously shown to be phosphorylated both by CDK1 (Goto et al., 2005) and aurora B (Bishop and Schuniacher, 2002) upon mitotic entry. In Figure 5.2B, INCENP phosphorylation mirrors that of USP31, making either CDK1 or aurora B potential candidates as the responsible kinase.

5.3.2 USP31 is phosphorylated by CDK1

Initial experiments using inhibitors were carried out to establish whether CDK1, aurora B or PLK1 was responsible for USP31 phosphorylation. Firstly, cells were synchronised using thymidine and nocodazole and arrested at entry to mitosis. The aurora B inhibitor, ZM477439, was added alongside nocodazole, thereby preventing its activity as cells enter mitosis. Aurora B inhibition still allows spindle formation however chromosomes are unable to align at the metaphase plate as kinetochore attachments cannot be maintained (Doodhi et al., 2021). As aurora B also regulates cytokinesis, its inhibition causes the cells to exit mitosis prematurely (Keen and Taylor, 2009). Upon release from nocodazole, mitotic cells were incubated for the specified time points for western blot analysis. Figure 5.3A shows ZM477439 treatment successfully inhibited aurora B, as histone 3 phosphorylation at serine 10 (H3-pSer10), a site specific for aurora B phosphorylation (Hirota et al., 2005) was not observed. USP31 MW does shift downwards slightly in a stepwise fashion over the analysed time frame. However, as phosphorylated USP31 is observed at the onset of mitosis (0 minutes) despite the inhibitor being present for 18 hours prior to this, it suggests that this dephosphorylation observed may be due premature mitotic exit.

This same approach could not be used to test for CDK1 phosphorylation as inhibition during synchronisation would prevent cells from entering mitosis. Cells were therefore synchronised to prometaphase prior to treatment with either RO3306, ZM447439 or BI2536 to inhibit CDK1, aurora B or PLK1 respectively upon release from nocodazole. The results from CDK1 and aurora B inhibition are shown in Figure 5.3B, and PLK1 inhibition in Figure 5.3C. CDK1 inhibition leads to complete loss of phosphorylation after 30 minutes. A slight downshift is seen after aurora B inhibition, although much less prominent than CDK1 inhibition. USP31 remained phosphorylated after PLK1 inhibition. These results suggest that either CDK1 or aurora B, or both, may be responsible for USP31 phosphorylation.

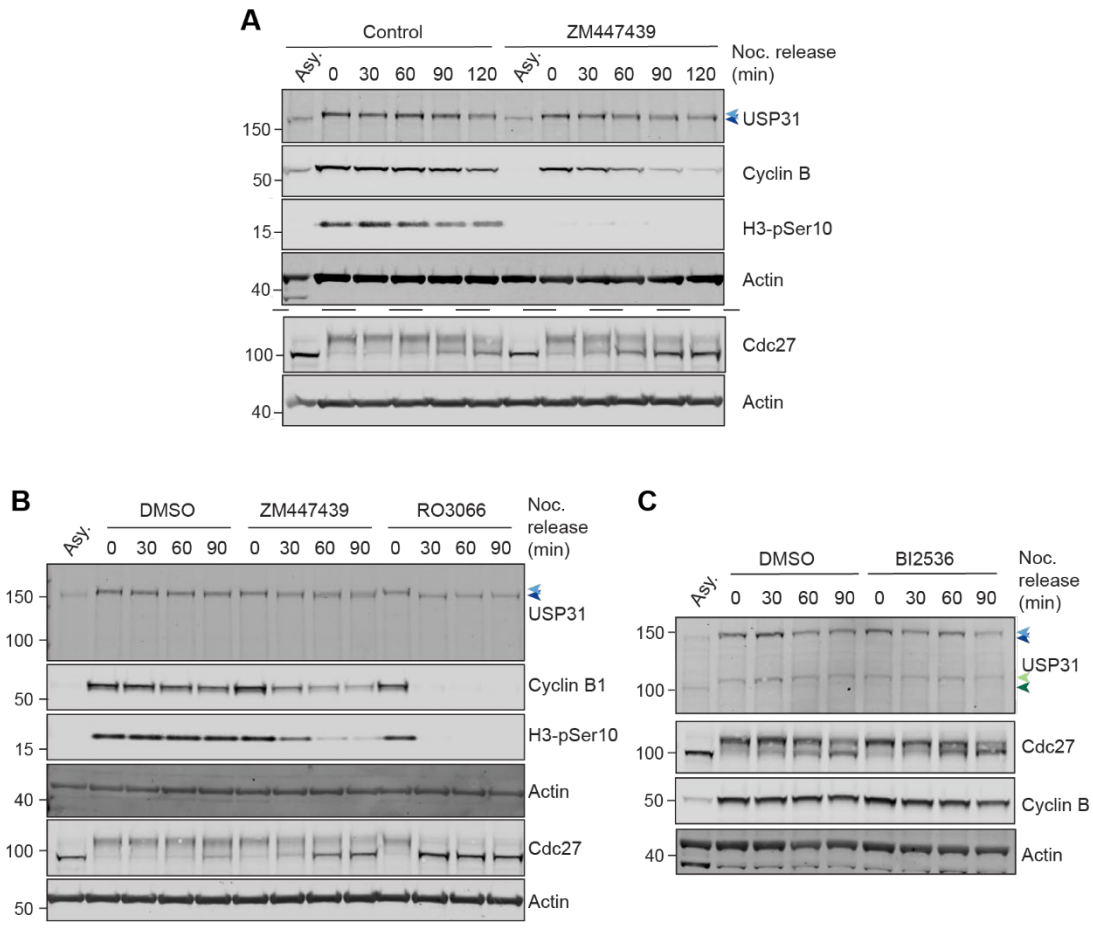

Figure 5.3 – USP31 is not phosphorylated by PLK1

A. U2OS cells were synchronised with single thymidine block followed by treatment with nocodazole and the aurora B inhibitor ZM447439 (10 μM) or DMSO for 18 hrs. Samples were released from nocodazole and samples taken after indicated times. **B.** U2OS cells were synchronised with single thymidine block followed by nocodazole, then released from nocodazole into fresh DMEM. Samples were treated with either the aurora B inhibitor ZM447439 (10 μM) or the CDK1 inhibitor RO3306 (10 μM), or DMSO for the indicated timepoints. **C.** U2OS cells were synchronised as in B then released from nocodazole into fresh DMEM. Samples were treated with either PLK1 inhibitor BI2536 (100nM) or DMSO for the indicated timepoints. Blue and green arrows indicate full length USP31 and a proposed shorter isoform, respectively. Top arrows (light) and bottom arrows (dark) indicate the phosphorylated and dephosphorylated USP31 species respectively.

Inhibiting CDK1 or aurora B causes cells to prematurely exit mitosis, allowing for activation of mitotic phosphatases (Keen and Taylor, 2009). USP31 dephosphorylation may therefore be a result of cells exiting mitosis rather than a direct response from kinase inhibition. To combat this possible caveat, upon release from nocodazole, cells were treated with MG132 for 1 hour to inhibit the proteasomal

degradation pathway. This prevents mitotic regulators such as cyclin B and securin from being degraded, arresting cells at the metaphase plate and inhibiting anaphase onset (Afonso et al., 2019). Either RO3306 or ZM447439 were then added, causing the cytoplasm to enter into an anaphase like state, while maintaining the spindle in a metaphase conformation. As a control, the MG132 wash-out was performed alongside, allowing cells to naturally enter into anaphase, albeit taking slightly longer than usual. This protocol is illustrated in Figure 5.4A. Figure 5.4B shows that when RO3306 is added, dephosphorylation of USP31 is still observed. This result is not seen following aurora B inhibition (Figure 5.4C). To further confirm this observation, synchronised cells were either treated immediately with the inhibitors or pre-treated with MG132 before inhibitor addition. Figure 5.4D shows that CDK1 inhibition results in USP31 dephosphorylation whereas no change is observed following aurora B inhibition. Taken together, these results suggest that CDK1 phosphorylates USP31, whereas aurora B and PLK1 do not. *In vitro* investigations could be performed to further confirm CDK1 as the sole responsible kinase.

5.3.3 GFP-USP31 in the stable cell lines is also phosphorylated during mitosis

Erithelgi Bertsoulaki generated U2OS cell lines which stably overexpress GFP-USP31 either in its wild-type form (WT13) or a catalytically inactive mutant (CA1) whereby the catalytic cysteine has been mutated to an alanine (Bertsoulaki, 2018). To confirm that over expressed GFP-USP31 is also phosphorylated during mitosis, mitotic cells were treated with lambda phosphatase and the downshift in MW was analysed. Figure 5.5A confirms that in both WT13 and CA1 cells, the overexpressed GFP-USP31 is also phosphorylated as the downshift in MW was observed following lambda phosphatase treatment.

To confirm that CDK1 is responsible for phosphorylation of the GFP-USP31 expressed within these cell lines, cells were arrested at prometaphase and treated with either RO3306 or ZM447439 directly after release from nocodazole or after a 1-hour treatment with MG132. Figure 5.5B shows that within both cell lines, dephosphorylation is observed following RO3306 CDK1 inhibition but not with ZM443479 aurora B inhibition. These results therefore indicate that GFP-USP31 is also dephosphorylated upon CDK1 inhibition but not aurora B inhibition.

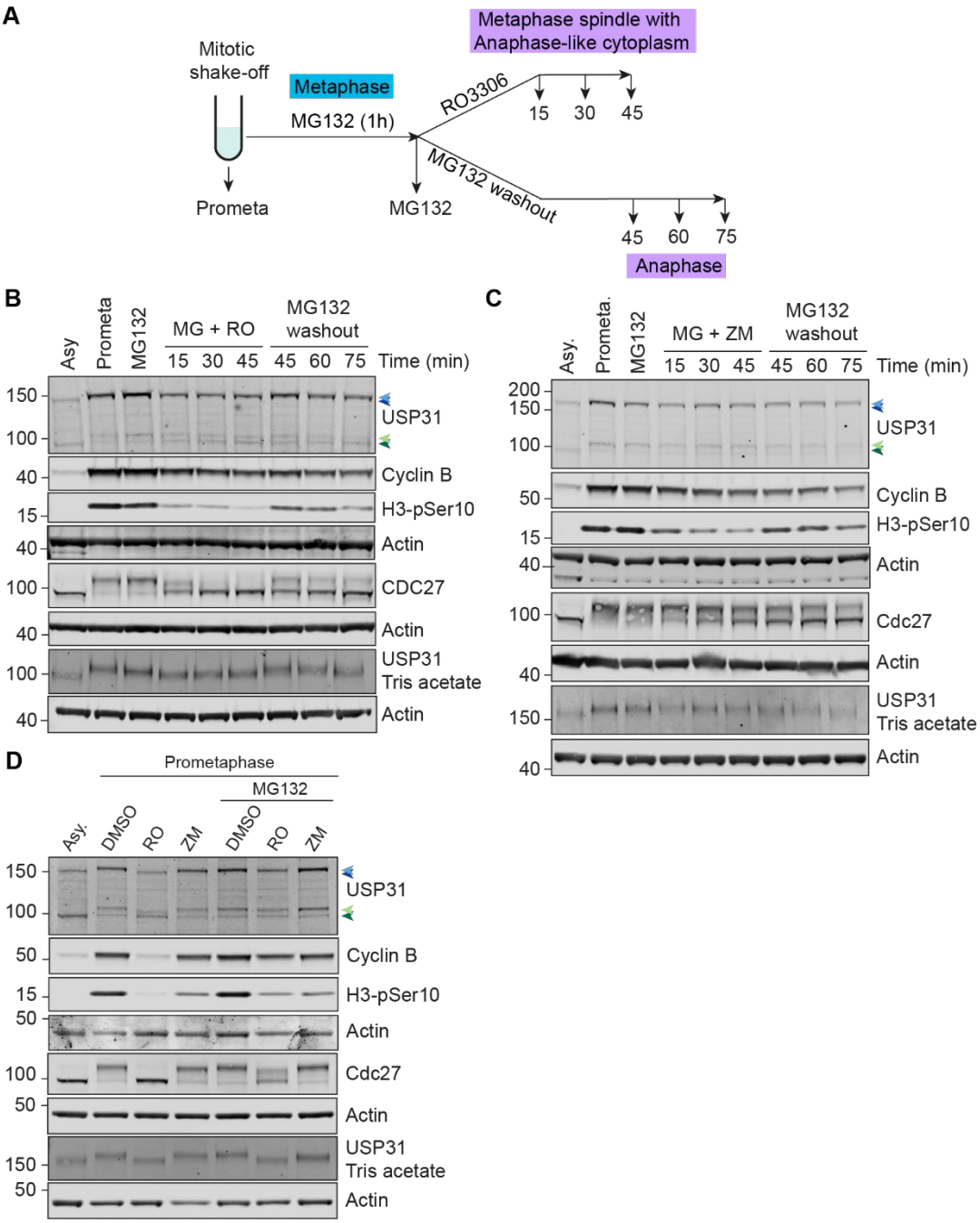

Figure 5.4 –USP31 is phosphorylated by CDK1 during mitosis

A. Schematic diagram for experimental procedure in B and C. **B.** U2OS cells were synchronised using thymidine and nocodazole then released into fresh DMEM. One sample was lysed immediately (Prometa). MG132 (MG, 5 μM) was added to all other samples for 1 hour to arrest cells at metaphase. CDK1 inhibitor (RO3306, RO, 10 μM) was then added for specified times. For control cells, MG132 washout was performed for specified times to allow re-entry into mitosis. Asy: Asynchronous cell lysates. **C.** Same as in B but using aurora B inhibitor (ZM447439, ZM, 10 μM). **D.** U2OS cells were synchronised as in B and released into fresh DMEM. Samples were treated immediately with either DMSO, RO (10 μM) or ZM (10 μM) for 30 min, or were first pre-treated with MG132 (MG, 5μM) for 1 h before RO or ZM addition.

Blue and green arrows indicate full length USP31 and a proposed shorter isoform, respectively. Top arrows (light) and bottom arrows (dark) indicate the phosphorylated and dephosphorylated USP31 species respectively.

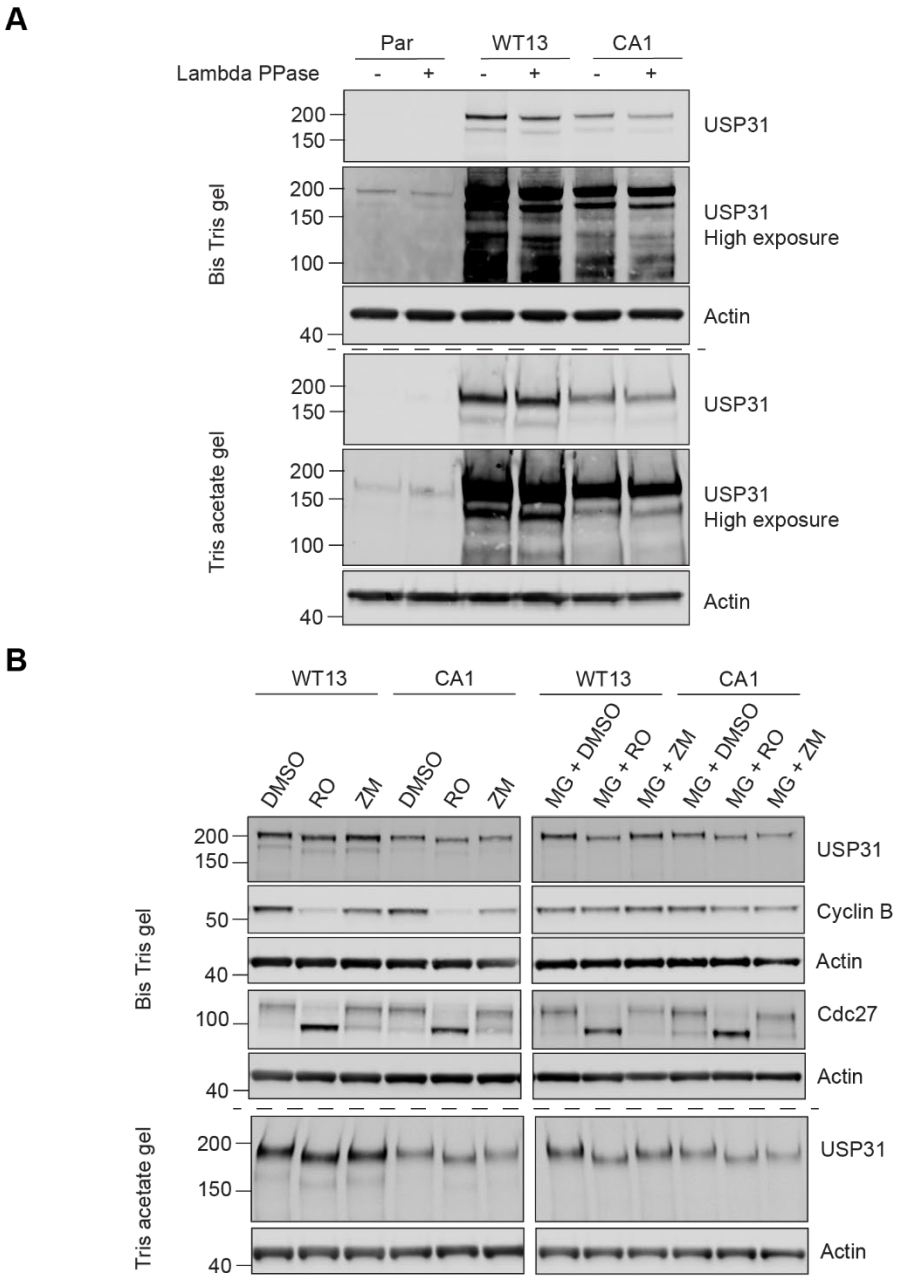

Figure 5.5 – GFP-tagged USP31 in stably expressing cell lines is phosphorylated in mitosis by CDK1

A. Parental U2OS cells and stably expressing GFP-USP31 WT13 and CA1 cells were synchronised using a single thymidine block followed by nocodazole and released into fresh DMEM. Cells were lysed and samples were treated with 400 units of lambda phosphatase for 30 minutes. **B.** WT13 and CA1 cells were synchronised as in B. Samples were treated immediately with either DMSO, RO3306 (RO, 10 μM) or ZM447439 (ZM, 10 μM) for 30 minutes, or were first pre-treated with MG132 (MG, 5μM) for 1 hour before RO or ZM addition.

5.3.4 USP31 phosphorylation may regulate its localisation to the mitotic spindle

Previous research performed by Erithelgi Bertsoulaki has shown that transiently transfected GFP-USP31 is able to localise to the mitotic spindle (Bertsoulaki, 2018). She observed that during metaphase, USP31 is largely cytosolic however some localisation can be seen at kinetochore microtubules. As cells transition into anaphase and telophase there is a rapid relocalisation of USP31 from the cytosol onto the central spindle which persists as cells enter cytokinesis. I have confirmed this result using different clones which stably express GFP-USP31 (Figure 5.6). Both WT13 and WT9 cell lines show slight spindle localisation during metaphase and early anaphase, with both displaying a clear relocalisation to the kinetochore microtubules and central spindle after anaphase onset at 9 and 10 minutes respectively. Imaging of WT8 shows that relocalisation is less dramatic in this clone but can still be observed on the central spindle microtubules during telophase at 9 minutes. No spindle localisation of GFP-USP31 can be seen in the WT10 clones.

The expression levels of these clones are shown in Figure 5.7. WT13 and WT9 express the highest levels of GFP-USP31, explaining why spindle localisation is clearer in these cells compared to WT8. Additionally, GFP-USP31 cannot be detected with the USP31 antibody in WT10 cells, and GFP staining shows a species which runs at a slightly lower MW compared to the other clones. As the USP31 antibody detects the last 98 amino acids at the C-terminal (1254-1352) it is thought this may express a truncated version of USP31 which lacks the C-terminus. As this is the region required for microtubule binding (Bertsoulaki, 2018), this would explain the lack of spindle localisation within this clone. Sequencing would be required to confirm this hypothesis.

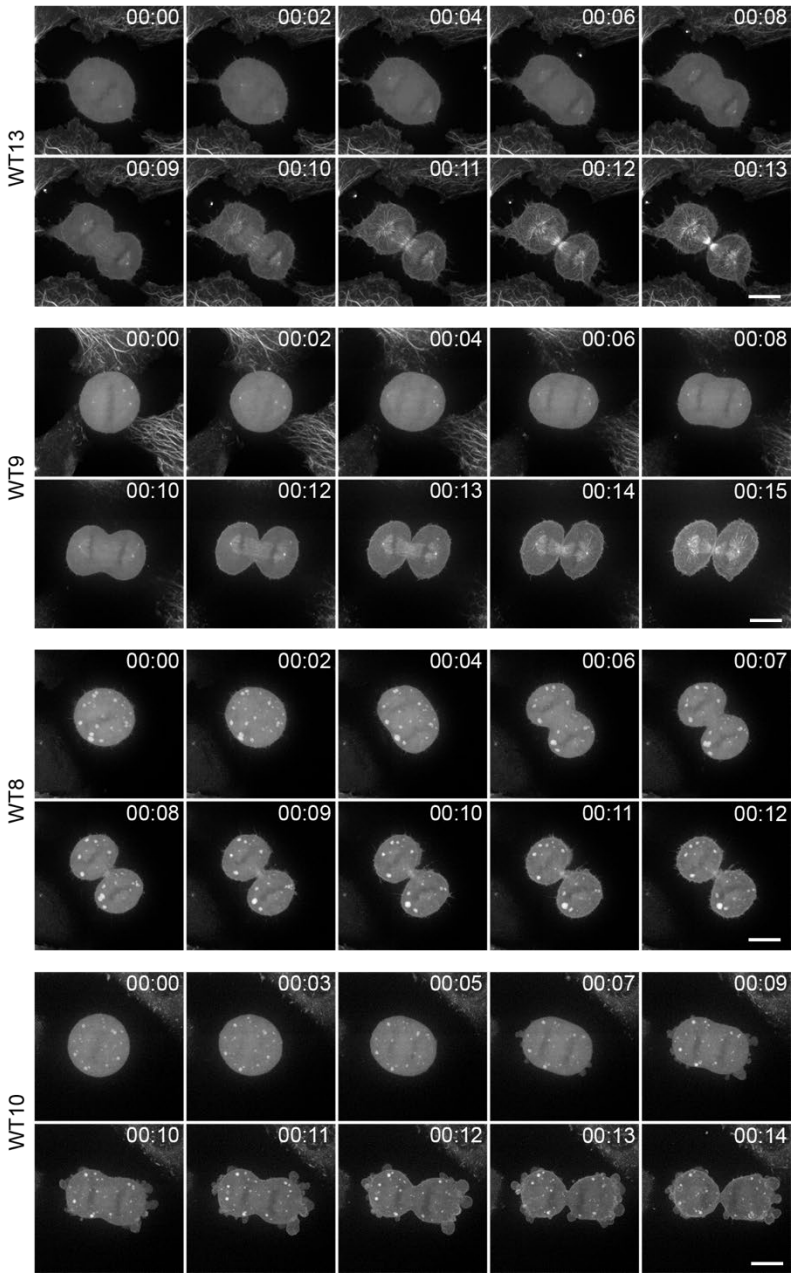

Figure 5.6 – GFP-USP31 relocalises to the central spindle during anaphase

U2OS cells stably expressing wild-type USP31 (WT13, WT9, WT8 or WT10) were selected at metaphase and imaged as they progress through mitosis using a 3i-spinning disk confocal. Z-stacks were acquired every minute (16µm range, 1 µm steps), and the maximum projection for the selected time-points are shown (hh:mm). Scale bar: 10 µm.

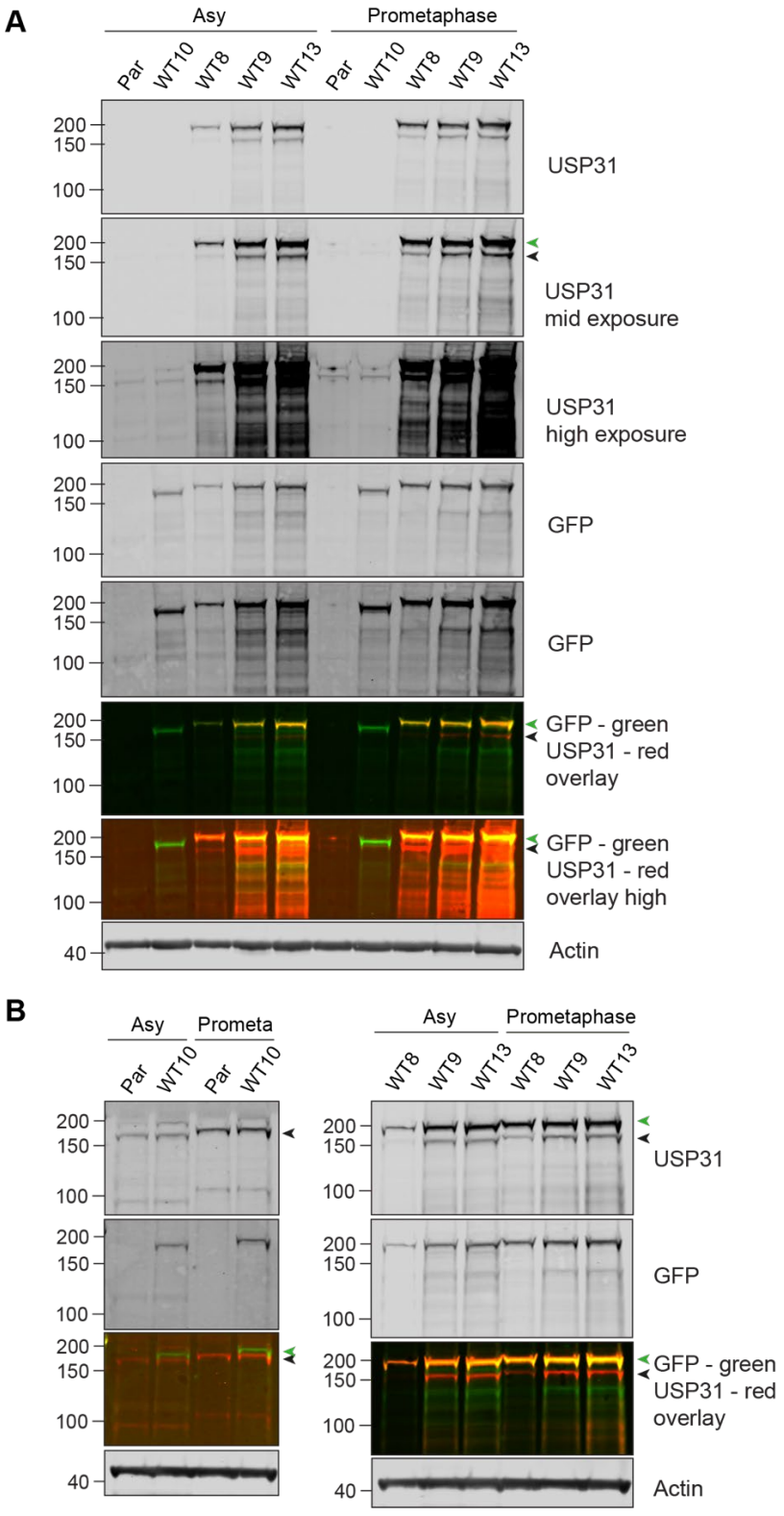

Figure 5.7 – USP31 expression levels in U2OS cells stably expressing GFP-USP31

U2OS cells stably expressing GFP-USP31 (WT10, WT8, WT9, WT13) were lysed at both asynchronous or prometaphase and compared to parental U2OS cells (par). **A.** All cell lines. **B.** Cell lines on separate blots for easier visualisation of low expression bands. Left – Parental and WT10, right – WT8, WT9 and WT10. Black and green arrows represent endogenous and GFP-tagged USP31 respectively.

5.3.5 Localisation of USP31 on the mitotic spindle is controlled by CDK1

The rapid relocalisation of USP31 to the spindle microtubules during anaphase coincides with the loss of CDK1 activity. As USP31 is phosphorylated in a CDK1-dependent manner as the cells enter mitosis (Figure 5.4), I speculated that phosphorylation could regulate spindle localisation. To investigate this hypothesis, stably expressing wild type GFP-USP31 cell lines (WT13) were imaged during mitosis. Cells were treated with MG132 for 1hr to arrest cells at metaphase (00:00 time point). The CDK1 inhibitor RO3306 was then added to allow the cell to assume an anaphase-like cytoplasm, whilst maintaining a metaphase plate. Imaging began at the addition of this inhibitor. A schematic of this protocol is illustrated in Figure 5.8A. At metaphase, USP31 was not observed on the spindle, and its localisation appears largely cytosolic (Figure 5.8B). Upon addition of CDK inhibitor, USP31 is rapidly recruited onto the kinetochore microtubules. These results confirm that USP31 spindle localisation is controlled by CDK1 inactivity, supporting the hypothesis that phosphorylation prevents microtubule binding of USP31.

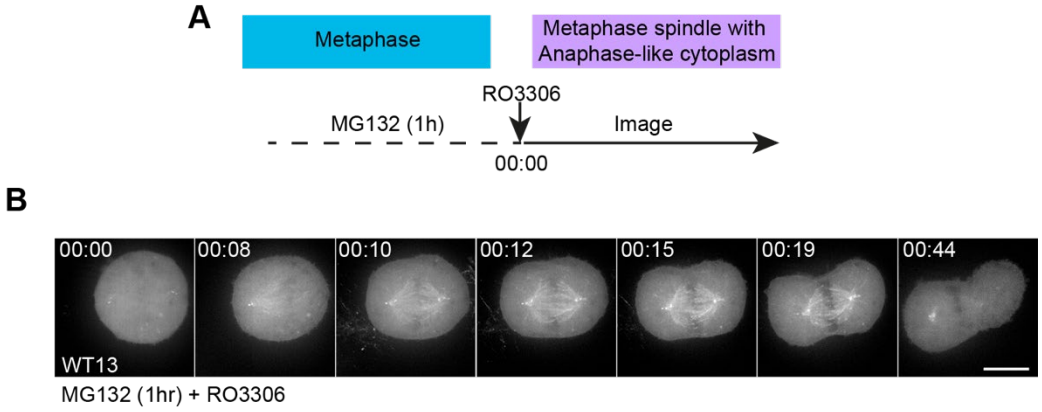

Figure 5.8 – Localisation of USP31 on the spindle is controlled by CDK1

A. Schematic diagram showing the experimental protocol used in B. **B.** U2OS cells stably expressing wild-type (WT13) USP31 were arrested in metaphase using MG132 (5 μM) for 1 h. Cells were imaged immediately after the addition of RO3306 (CDK1 inhibitor; 10 μM) using a 3i-spinning disk confocal. Z-stacks were acquired every minute (14μm range, 1μm steps), and the maximum projection for the selected time-points are shown (hours:mm). Scale bar: 10 μm.

5.4 Determination of USP31 phosphorylation sites

5.4.1 Conjugating the GFP nanobody to the beads

In order to determine which residues within USP31 are phosphorylated during mitosis, I decided to perform mass spectrometry analysis. In order to do this, immunoprecipitation of USP31-GFP from the WT13 cells using a GFP nano-trap pulldown assay was required to enrich for the protein. GFP nano-trap protein can be produced in Rosetta *E. coli* cells and purified before binding to NHS activated Sepharose beads. Purified protein was kindly gifted from previous PhD students within the laboratory, Douglas Grimes and Hannah Elcocks, and was therefore ready to be conjugated to the Sepharose beads. The GFP nano-trap protein was first dialysed overnight into the coupling solution before association to the beads was performed.

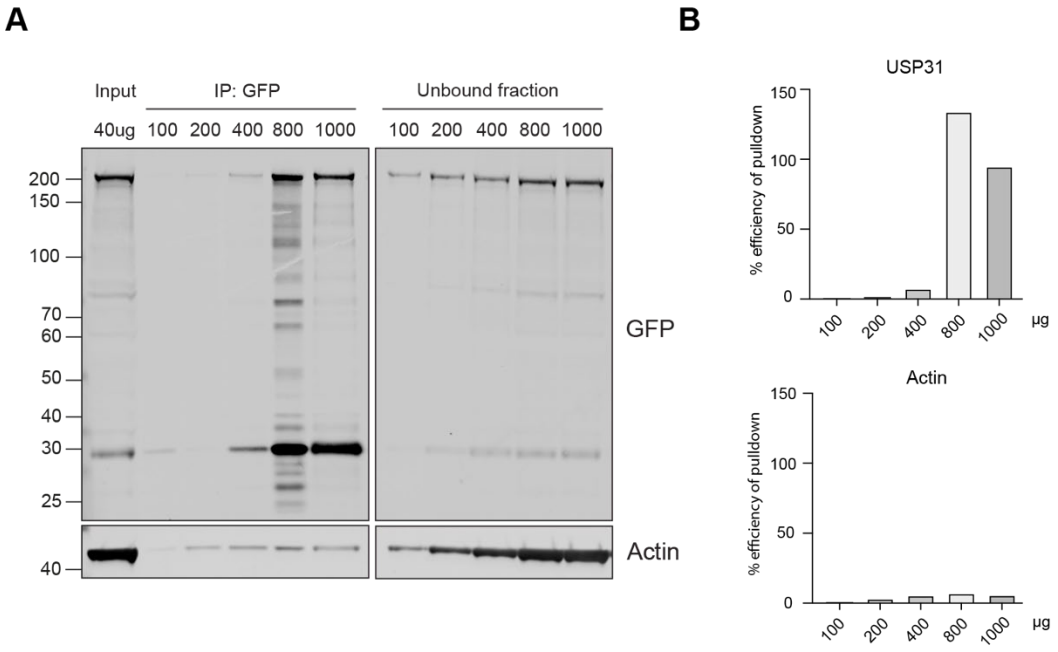

Figure 5.9 – Generation of GFP pulldown beads

WT13 cells were lysed in 8M urea before different protein concentrations were incubated with the newly prepared GFP nanotrap conjugated NHS Sepharose beads overnight. Samples were eluted using 2x SB and analysed. **A.** Western blot samples of pulled-down protein compared to 40 µg input and unbound fraction. **B.** Western blot quantification showing the percentage efficiency of the pulldown compared to the input sample.

An initial test was done to confirm the new beads could capture the GFP-USP31 protein from the WT13 cells and determine the required concentration to achieve enrichment. Cells were lysed in 8M urea lysis buffer and incubated with the nano-trap beads at different concentrations as specified to allow for a titration. Figure 5.9A shows these beads successfully bind GFP-USP31 as there is a large band visible at ~ 200 kDa. The 800 and 1000 µg concentrations show a high level of enrichment compared to the lower concentration levels and therefore either concentration would be suitable for further experiments. Western blot quantification (Figure 5.9B) confirms that an equal or greater percentage of GFP-USP31 is captured via the beads compared to the input using these 2 concentrations. The greatest enrichment achieved was only 133% however actin levels are significantly reduced compared to the input. This confirms the pulldown was specific for GFP-USP31 and therefore reduces the background proteins present.

5.4.2 Phosphoproteomics of USP31

In order to identify specific residues phosphorylated during mitosis, WT13 cells were arrested at prometaphase then treated with either DMSO, RO3306 or ZM447439 for 30 minutes. An asynchronous sample was also collected alongside as a control. These samples were separated by SDS-PAGE and the bands corresponding to GFP-USP31 were excised. In-gel digest and tryptic digestion was performed before being analysed via mass spectrometry. A schematic of this workflow is illustrated in Figure 5.10.

This analysis only managed to identify Ser-433 as a phosphorylation site of USP31. The peptide containing this residue was only identified within the ZM447439 sample. It can therefore be concluded that this residue is not phosphorylated by aurora B as it is still present following aurora B inhibition. The probability score for phosphorylation at this residue was predicted as 0.741, as shown in Table 5.1.

Table 5.1 – Phospho-proteomics of USP31 during mitosis

Gene	Position	Asy	DMSO	RO3306	ZM447439	Amino Acid	Sequence window	Phospho (STY) Probability
USP31	433	-	-	-	0.740671	S	NLNHLKFGLDYHRLSSPTQTAAKQGKMDSPT	LS(0.256)S(0.741)PT(0.003)QTAAK

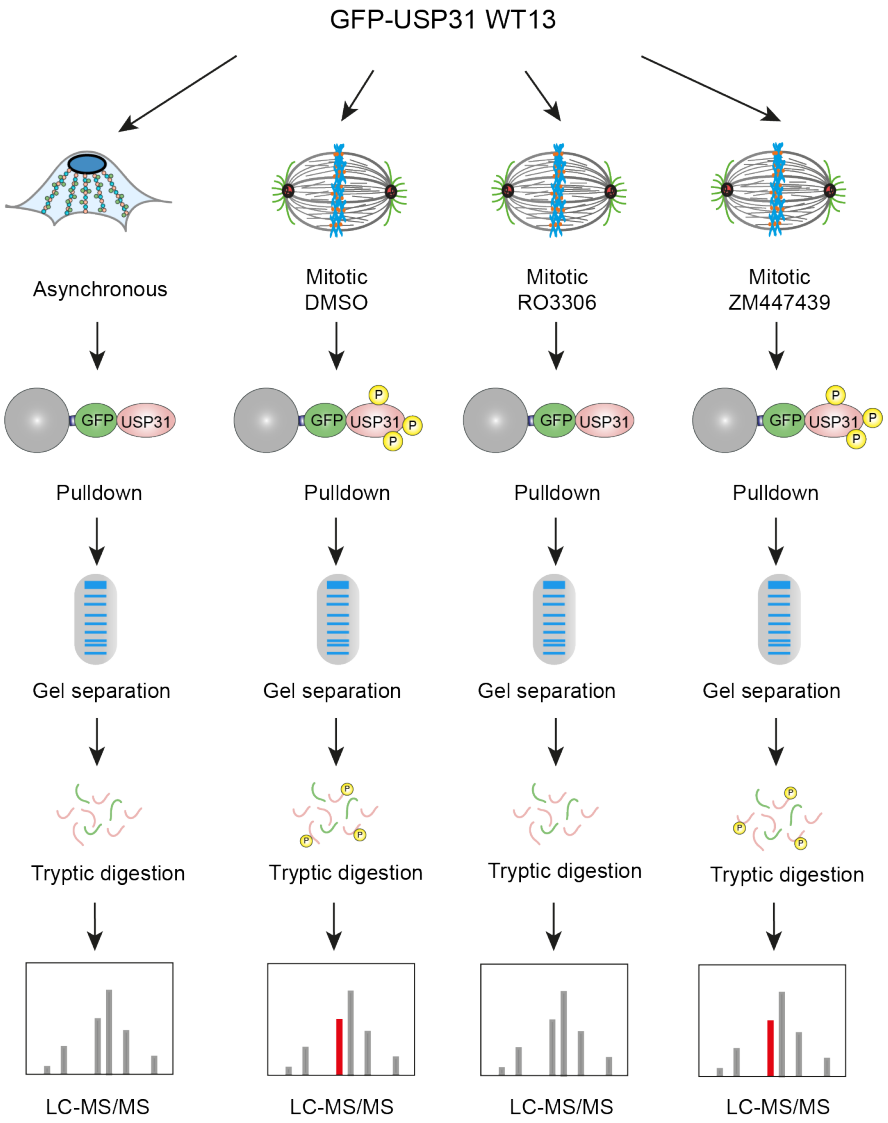

Figure 5.10 – GFP-USP31 pulldown workflow

Schematic diagram showing the workflow for mass spectrometry analysis of USP31 phosphorylation sites. Mitotic cells were treated with either DMSO, RO3306 or ZM447439 for 30 minutes before being lysed. Asynchronous cells were lysed as a control. A GFP-nano-trap pulldown was performed to extract GFP-USP31. The band of interest was then subjected to in gel digest for phosphoproteomic analysis.

As CDK1 has been shown to phosphorylate USP31, the CDK1 census sequence can be used to predict other possible residues. This consensus sequence is S/T*-P, or more specifically S/T*-P-x-K/R (Holt et al., 2009). Serine 433 is followed by a proline and would therefore qualify. Other residues which fit within this more specific consensus sequence include S879 and S1001. These sites are situated at the C-terminal domain of USP31 which is required for microtubule binding (Bertsoulaki, 2018). Confirmation of these phosphorylation sites using this method of identification

is not possible due to the length of the peptides created around these regions when digested with trypsin. The S879 containing peptide is only 6 amino acids long, rendering it too small for specific identification, whereas the S1001 peptide is 29 amino acids which is too long for analysis. For these predictions to be confirmed, an alternative protease would need to be utilised. Chymotrypsin which cleaves after tryptophan, tyrosine and phenylalanine would be a suitable choice to isolate S879, creating a peptide of 16 amino acids. AspN combined with LysN could also be used, creating a peptide of 14 amino acids. For S1001 combination of AspN and GluC could be used to produce a 7 residue peptide (Giansanti et al., 2016).

5.4.3 Generation of USP31 phospho-mutants

In order to test the hypothesis that USP31 phosphorylation regulates microtubule binding, site directed mutagenesis was used to incorporate point mutations into the GFP-USP31 plasmid. Single amino acid changes were introduced at the predicted phosphorylation sites, S433, S879 and S1001. At all 3 positions, the serine residue was coded for by a TCT codon. Both alanine and glutamate point mutations were created by mutating this codon to GCT and GAA respectively at each of the 3 points as illustrated in Figure 5.11A. Alanine (A) is used as it is similar in structure to serine however it can no longer be phosphorylated, referred to as a phospho-null site, and glutamate (E) is used to mimic continuous phosphorylation, referred to as a phospho-mimetic site. Successful mutagenesis, and the absence of undesired mutations was confirmed via whole construct sequencing. The point mutations created are illustrated within Figure 5.11B and their expression within U2OS cells was confirmed in Figure 5.11C, with all expressing a protein at the expected size of ~180 kDa.

Once these mutated plasmids had been created, I performed an initial analysis to confirm whether microtubule binding could still be achieved in interphase by transiently transfecting U2OS cells. Figure 5.12 shows that microtubule binding is still observed for all USP31 mutants: these phosphorylation sites therefore have no effect on localisation during interphase. To determine whether localisation was affected during mitosis, cells were synchronised with thymidine and nocodazole treatments and transfected with all mutated plasmids at the same time as nocodazole addition. After 16-18 hours, cells were washed to remove the nocodazole and released into fresh media to allow for cells to re-enter into mitosis. The results in Figure 5.13 confirm that all phosphorylation mutants are able to localise to the mitotic spindle at metaphase, anaphase and telophase, confirming that these phosphorylation sites do

not play a role in the spatial regulation of USP31 during mitosis. Further mutants using alternative predicted sites for phosphorylation would therefore need to be tested to confirm this hypothesis.

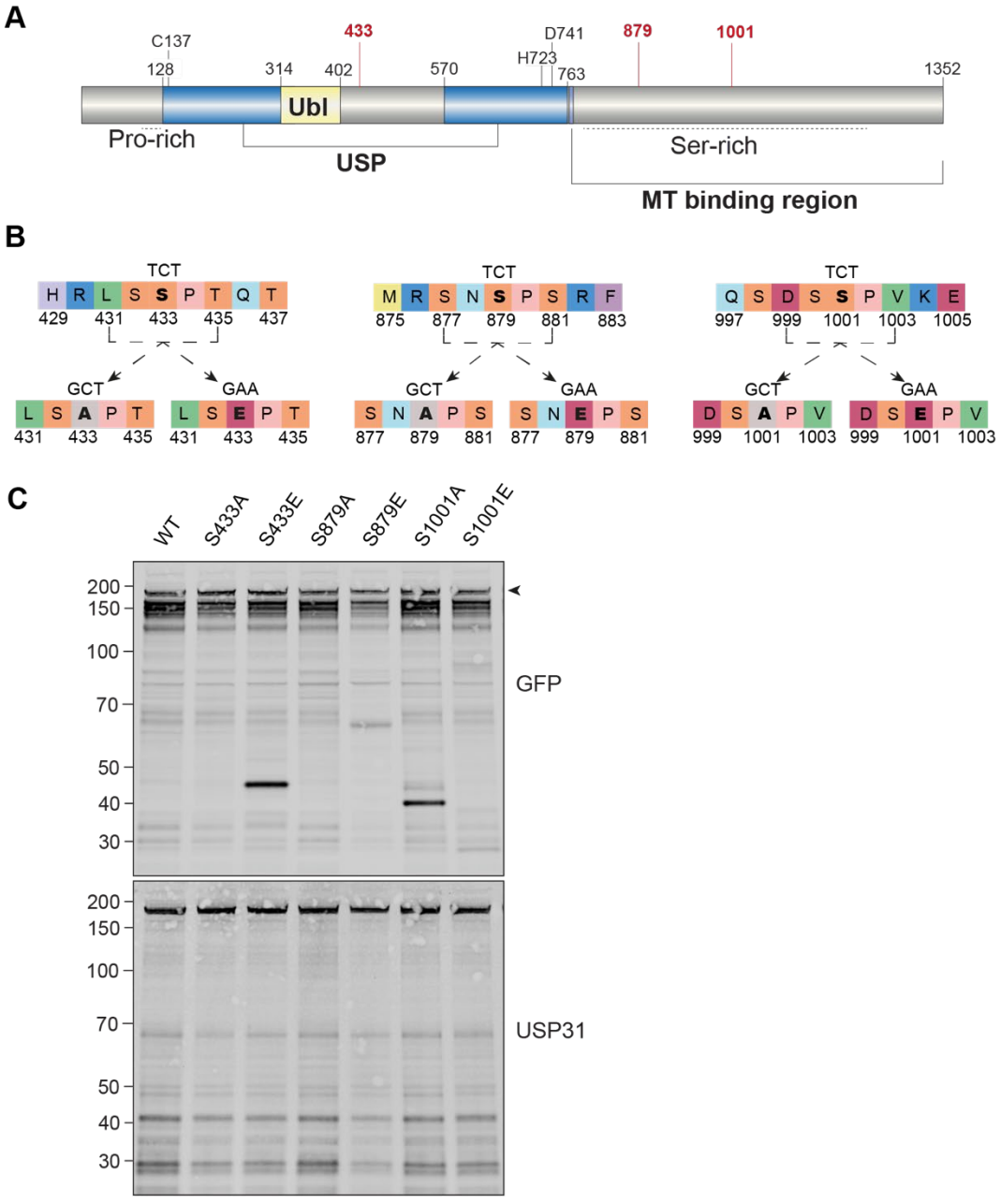

Figure 5.11 - Generation of USP31 phospho-mutants

A. Schematic diagram of the domain structure of USP31. Positions of predicted phosphorylation sites are shown in red. **B.** Schematic diagram showing the original amino acid sequence of USP31 (top row) and the changes to be made by site directed mutagenesis (bottom row). **C.** U2OS cells were transfected with GFP-USP31 containing each of the generated mutations compared to the wild-type (WT) for 21 hours and analysed for their expression levels and MW. Arrow indicates band representing GFP-USP31.

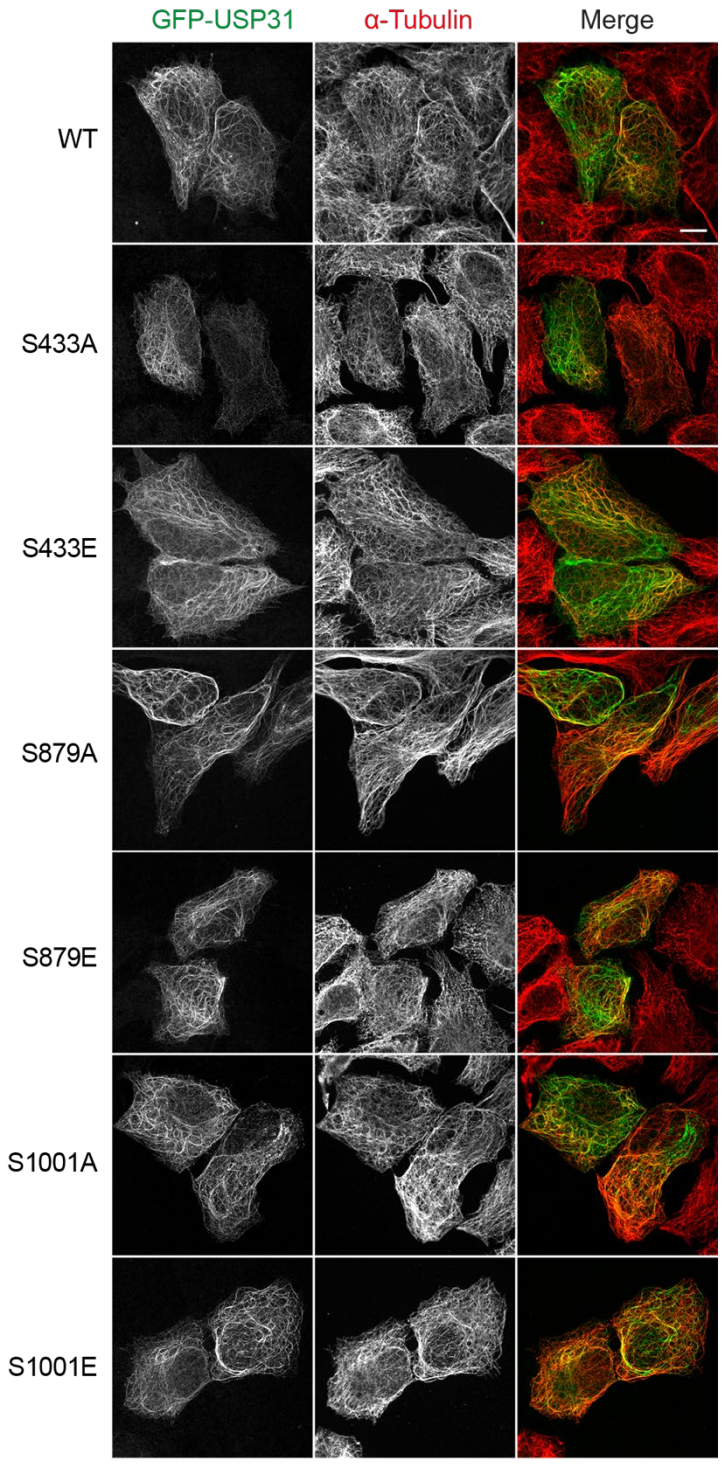

Figure 5.12 – USP31 phospho-mutants all localise to microtubules

U2OS cells were transiently transfected with the wild type (WT) and the GFP-USP31 phospho-mutants as indicated and fixed with ice cold MeOH before being stained for α-tubulin. Images were acquired on a 3i spinning disk confocal microscope. Scale bar: 10 μm.

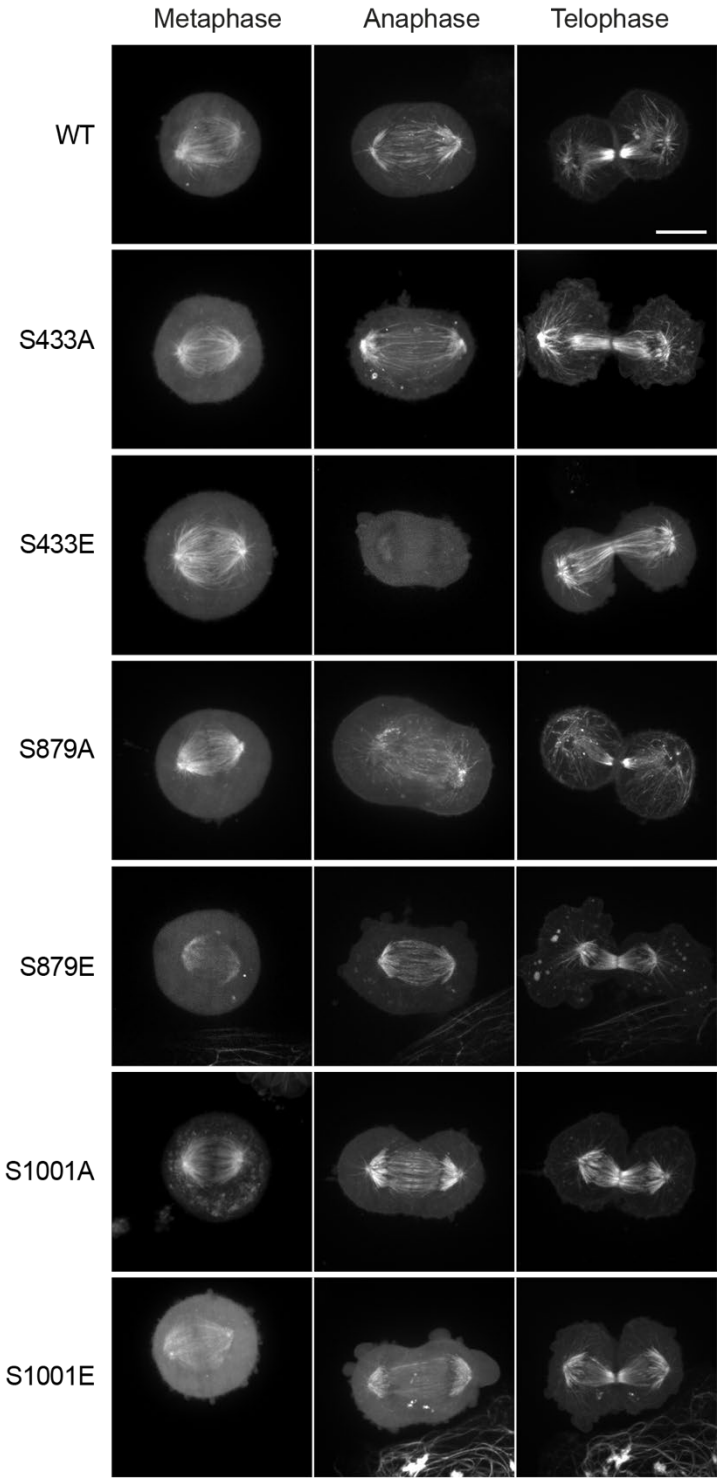

Figure 5.13 - USP31 phospho-mutants all localise to the spindle

U2OS cells were transiently transfected with 1µg of DNA of the wild type (WT) and the GFP-USP31 phospho-mutants as indicated for 18 hours. Cells were synchronise using nocodazole, added at the same time as the transfection reagent. Nocodazole washout into fresh DMEM was performed an hour before imaging, and cells were selected and imaged live at metaphase, anaphase and telophase. Images were acquired on a 3i spinning disk confocal microscope. Maximum projection is shown (range: 15 µm, step size: 1 µm). Scale bar: 10 µm.

5.5 USP31 and the chromosomal passenger complex

5.5.1 USP31 catalytic inactive mutant displays ectopic furrowing during anaphase-like conditions

When analysing the USP31 localisation in response to the CDK1 inhibitor (Figure 5.8B), the cells expressing a catalytic inactive version of GFP-USP31 (CA1) was also analysed alongside. Similar results were observed with regards to USP31 localisation onto the spindle, shown in Figure 5.14. In addition, I also observed a peculiar phenotype within these catalytically inactive mutant cell lines: CDK1 inhibition leads to multiple ectopic furrowing points, which is not observed in the WT13 cells. This phenotype was observed in 38/45 cells for CA1 (84%) whereas only in 6/40 cells for WT13 (15%). This result suggests that cytokinesis may be disrupted as furrow ingression occurs at multiple areas in addition to the midbody when USP31 is inactive. The chromosomal passenger complex (CPC, described in section 1.2.4), plays a role in the spindle checkpoint and the initiation of furrow ingression for cytokinesis (Aleem et al., 2015; Carmena et al., 2012). It is this role within cytokinesis that highlighted this complex and its possible connection to USP31.

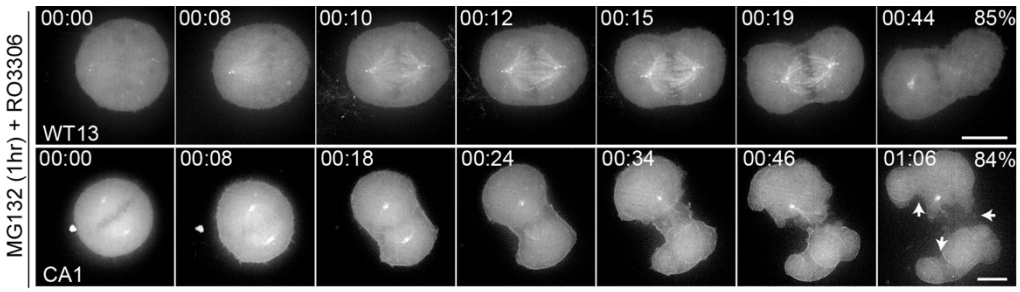

Figure 5.14 – USP31 CA1 cells show ectopic furrowing during cytokinesis

U2OS cells stably expressing wild-type (WT13) or catalytically inactive (CA1) USP31 were arrested in metaphase using MG132 (5 μM) for 1 h. Cells were imaged immediately after the addition of RO3306 (CDK1 inhibitor; 10 μM) using a 3i-spinning disk confocal. Z-stacks were acquired every minute (14 μm range, 1 μm step size) and the maximum projection for the selected time-points are shown (hours:mm). Arrows point to furrow positions in the CA1 cell line. Scale bar: 10 μm.

5.5.2 USP31 depletion causes reduced levels of the CPC and the associated motor proteins in mitosis

As USP31 is a DUB, and therefore can prevent proteasomal degradation of its protein targets via the removal of ubiquitin chains, I speculated that USP31 may lead to stabilisation of the CPC proteins. USP31 was therefore depleted using 2 separate oligonucleotides (Q1 and Q4) alongside a non-targeting control (NT1) and mitotic cells were collected for analysis of interested proteins. The levels of all 4 monomers of the CPC tetramer INCENP, aurora B, borealin and survivin (Carmena et al., 2012), were analysed, alongside the mitotic kinesin-like proteins, MKLP1 (Zhu et al., 2005) and MKLP2 (Gruneberg et al., 2004), and the Kelch-like protein KLHL21 (Maerki et al., 2009). These proteins are all described in more detail section 1.2.4. Figure 5.15 shows that following transfection with the Q4 oligonucleotide, all proteins except survivin and MKLP2 are significantly downregulated. As for Q1, statistical significance is observed for INCENP, aurora B, KLHL21 and MKLP1. Discrepancy between oligonucleotides could be accounted for by Q4 causing a greater reduction in both the full length and isoform of USP31. Overall, these results suggest that USP31 may act to stabilise some members of the CPC, associated motor proteins and the E3 ligase which acts upon it. Blots shown were generated by me, with additional data contributed by Joana Gomes Neto incorporated into the quantitation for statistical analysis.

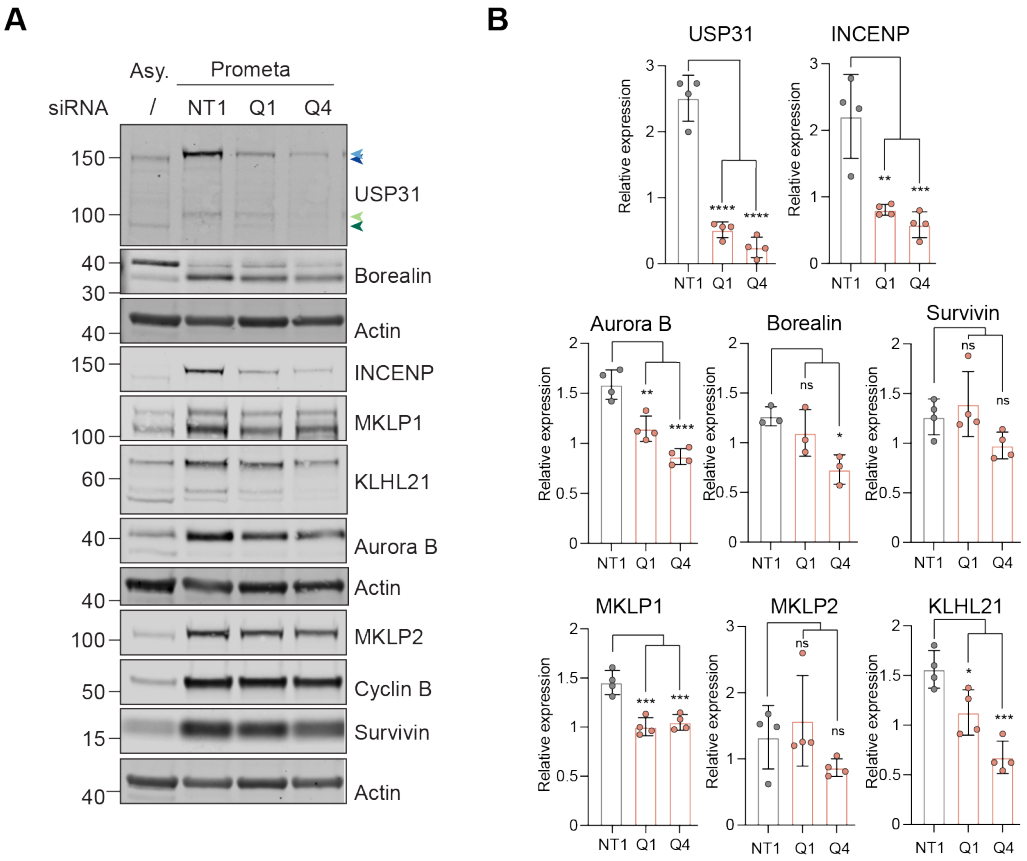

Figure 5.15 – USP31 depletion affects CPC protein levels

A. U2OS cells were transfected with siRNA against USP31 (Q1 and Q4) or a non-targeting control (NT1) for 48 hours. Cells were synchronized to prometaphase (Prometa) using thymidine and nocodazole and then lysed immediately. Samples were analysed by western blotting and probed for indicated proteins. Asy: Asynchronous cell lysates. Shown is a representative experiment. Blue and green arrows indicate full length USP31 and a proposed shorter isoform, respectively. Top arrows (light) and bottom arrows (dark) indicate the phosphorylated and unphosporylated USP31 species respectively. **B.** Quantification of western blots illustrated in A. Graph shows results from 4 independent experiments. Statistical analysis carried out via one-way ANOVA with Dunnett's multiple comparisons test. ns=not significant, *p≤0.05, **p≤0.01, ***p≤0.001, ****p≤0.0001.

5.5.3 USP31 depletion causes mislocalisation of the CPC components in a CDK1 dependent manner

Spatiotemporal regulation of the CPC is crucial for its proper function within mitosis (Carmena et al., 2012; Aleem et al., 2015). With this in mind, and due to the ectopic furrowing phenotype observed in Figure 5.14, I therefore speculated whether USP31 may also be involved in the spatiotemporal regulation of the CPC. To investigate this, USP31 was depleted for 48 hours before treating with MG132 for 1 hour to arrest cells

in metaphase. To induce an anaphase-like cytoplasm, CDK1 inhibitor, RO3306, was then added for 8 minutes before cells were fixed for imaging via immunofluorescence. The localisations of aurora B (top panels) and INCENP (bottom panels) were analysed (Figure 5.16A). In control cells, localisation of both proteins analysed can be seen at the spindle midzone as expected. Following USP31 depletion, this localisation is altered, and the CPC components fail to transition to the midzone. For both oligonucleotides, the levels at the midzone are visibly reduced, confirming the results observed in Figure 5.15. For quantification purposes, the cells analysed have been divided into 3 phenotypes: normal midzone staining, reduced midzone staining and no midzone staining. Figure 5.16B shows that cells with reduced or no midzone staining are observed more frequently following USP31 depletion compared to the NT1 control for both CPC proteins analysed. The same experiment was repeated to analyse borealin localisation under these same conditions. Similar results are observed in Figure 5.16C however due to sensitivity of the antibody for immunofluorescence, this result is less clear. In NT1-treated cells, borealin staining accumulates more at the midzone as expected. This accumulation is reduced for Q1 and even more so for Q4, confirming that 3 of the CPC components are affected by USP31 depletion. Analysis of survivin localisation was not achievable due to the antibody not being sensitive enough for immunofluorescence. Taken together, these results indicate that USP31 plays a role in not only stabilising the components of the CPC complex, but also regulating their localisation to the spindle midzone in the absence of CDK1 activity. Images shown were generated by me, with additional data contributed by Joana Gomes Neto incorporated into the quantitation.

5.5.4 Aurora B inhibition does not lead to mislocalisation of the CPC proteins in USP31 depleted cells

To confirm that this mislocalisation observed following USP31 depletion is dependent on CDK1 inhibition, the same experiment as above was performed whilst inhibiting aurora B. USP31 depleted cells were treated with MG132 for 1 hour followed by ZM447439 for either 8 minutes or 40 minutes. Cells were then fixed in ice cold methanol and stained for INCENP and β-tubulin. Figure 5.17 confirms that following USP31 depletion, aurora B inhibition does not lead to the same mislocalisation of INCENP as was previously seen following CDK1 inhibition after either 8 minutes (A) or 40 minutes (B) incubation. This suggests that this mislocalisation occurs specifically in a CDK1 dependent manner, possibly indicating a connection to the phosphorylation status of USP31 at anaphase onset.

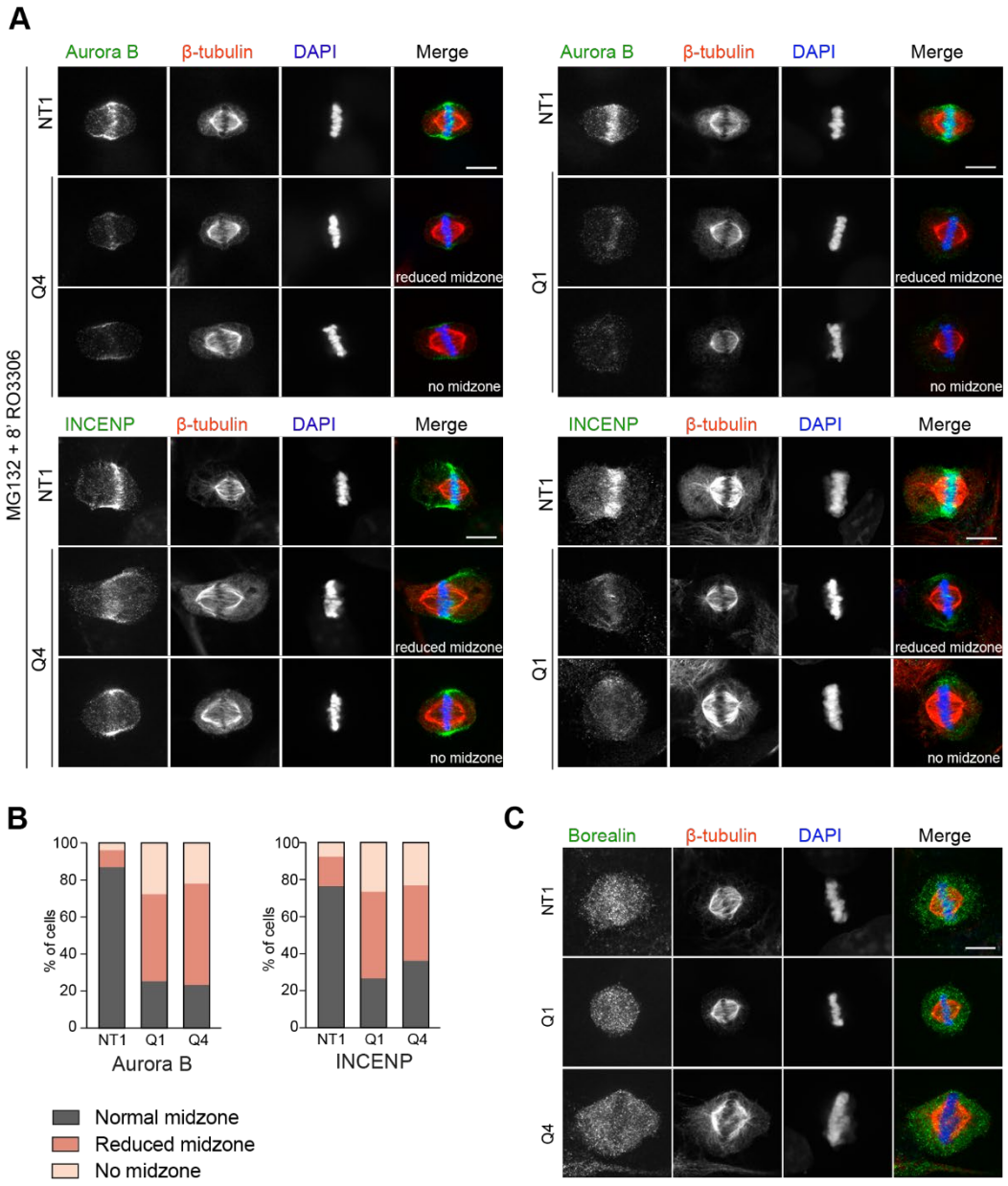

Figure 5.16 – USP31 depletion affects CPC localisation

A. U2OS cells were transfected with siRNA against USP31 (Q4, Q1) or a non-targeting control (NT1) for 48 hours, then treated with MG132 (5 μM) for 1 hour and subsequently treated with RO3306 (10μ M) for 8 minutes. Cells were fixed with MeOH and stained for the indicated antibodies. Images were acquired with a 3i spinning disk confocal; a single confocal slice is shown. Scale bar 10 μm. **B.** Bar graph show the quantification of the frequency of phenotypes observed in A (% cells showing each phenotype; cells analysed per condition: Aurora B: NT1 (76), Q1 (83), Q4 (73). INCENP: NT1 (119), Q1 (109), Q4 (160)). **C.** U2OS cells were treated as in A and stained for borealin. Images were acquired with a 3i spinning disk confocal; a single confocal slice is shown. Scale bar = 10 μm.

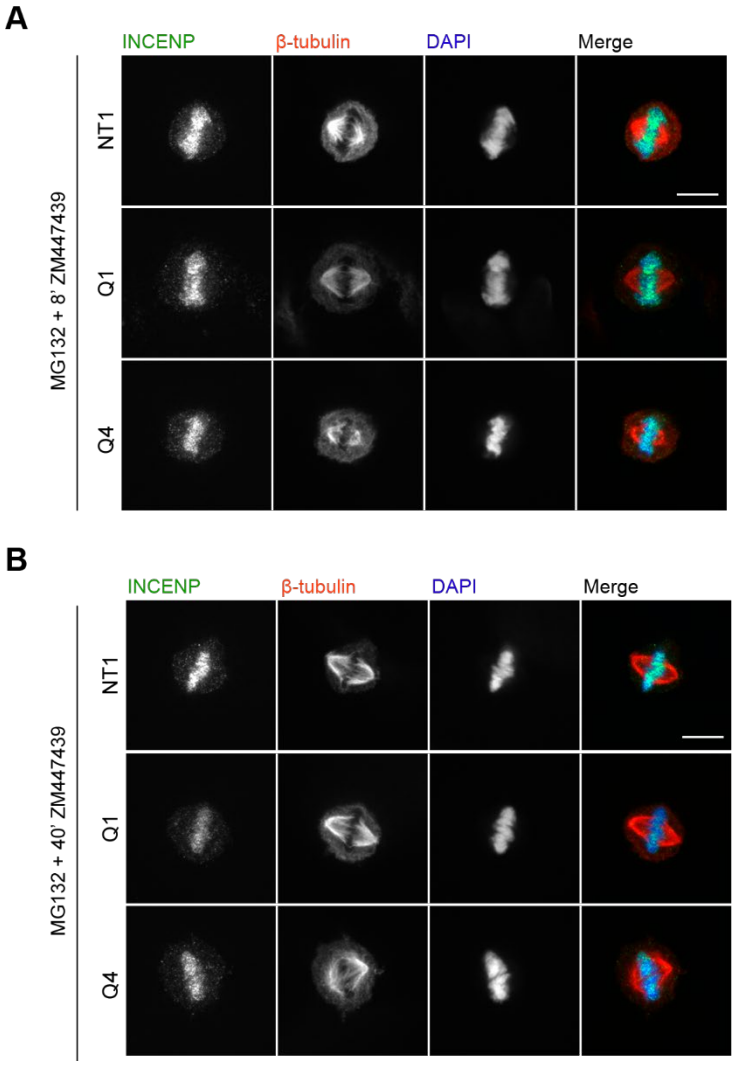

Figure 5.17 – Aurora B inhibition does not affect the localisation of the CPC in USP31 depleted cells

U2OS cells were transfected with siRNA against USP31 (Q4) or a non-targeting control (NT1) for 48 hours, then treated with MG132 (5 μM) for 1 hour and subsequently treated with ZM447439 (10 μM) for either 8 minutes (**A**) or 40 min (**B**). Cells were fixed with MeOH and stained for the indicated antibodies. Images were acquired with a 3i spinning disk confocal; a single confocal slice is shown. Scale bar = 10 μm.

5.5.5 USP31 depletion does not cause this effect on the CPC by disrupting the detyrosinated or acetylated networks

Previous work from Erithelgi Bertsoulaki showed that USP31 depletion has a dramatic effect on the detyrosinated and the acetylated microtubule network: both are reduced and disrupted in the absence of USP31 (Bertsoulaki, 2018). Microtubule post translational modifications (PTMs) are highly abundant within the mitotic spindle.

Previous research has shown that if you disrupt the detyrosinated network during mitosis then chromosome segregation is compromised. CENP-E motor proteins recognise detyrosinated kinetochore microtubules, whereas dynein motor proteins recognise tyrosinated astral microtubules (Barisic and Maiato, 2016). Depletion of tubulin tyrosine ligase (TTL), the enzyme required for restoring the α-tubulin c-terminal tyrosine detailed in section 1.1.10.3, causes CENP-E to transport chromosomes away from the spindle poles in random directions, preventing successful segregation (Barisic et al., 2015). In this model (Figure 5.18A), detyrosination acts as a guide to navigate motor proteins to the correct localisation during cell division to allow for precise segregation of chromosomes (Barisic et al., 2015; Barisic and Maiato, 2016).

I therefore speculated that the CPC mislocalisation observed following siRNA depletion of USP31 may be due to the defects observed on the detyrosinated and acetylated networks. This rationale was based on the knowledge that the MKLP2 transports the CPC along microtubules during anaphase onset from the centromeres to the central spindle midzone to allow for cytokinesis initiation (Adriaans et al., 2020). Either of these PTMs may play a role in directing this microtubule-dependent transport. I therefore transfected cells with siRNA corresponding to α-tubulin acetyl transferase (ATAT1), and the cofactor protein which complexes to VASH1/2, small vasohibin-binding protein (SVBP). These depletions lead to a reduction in the levels of K40 acetylated α-tubulin and detyrosinated α-tubulin respectively, as shown in Figure 5.18B. To confirm whether the CPC is mislocalised following microtubule PTM disruption, cells were treated with MG132 for 1 hour followed by treatment with CDK1 inhibitor, RO3306, for 8 minutes to recreate the same conditions as in section 5.5.3. Figure 5.18C and D confirms that INCENP sufficiently transitions to the midzone under these conditions. This concludes that USP31-dependent mislocalisation of the CPC is not regulated by microtubule PTMs.

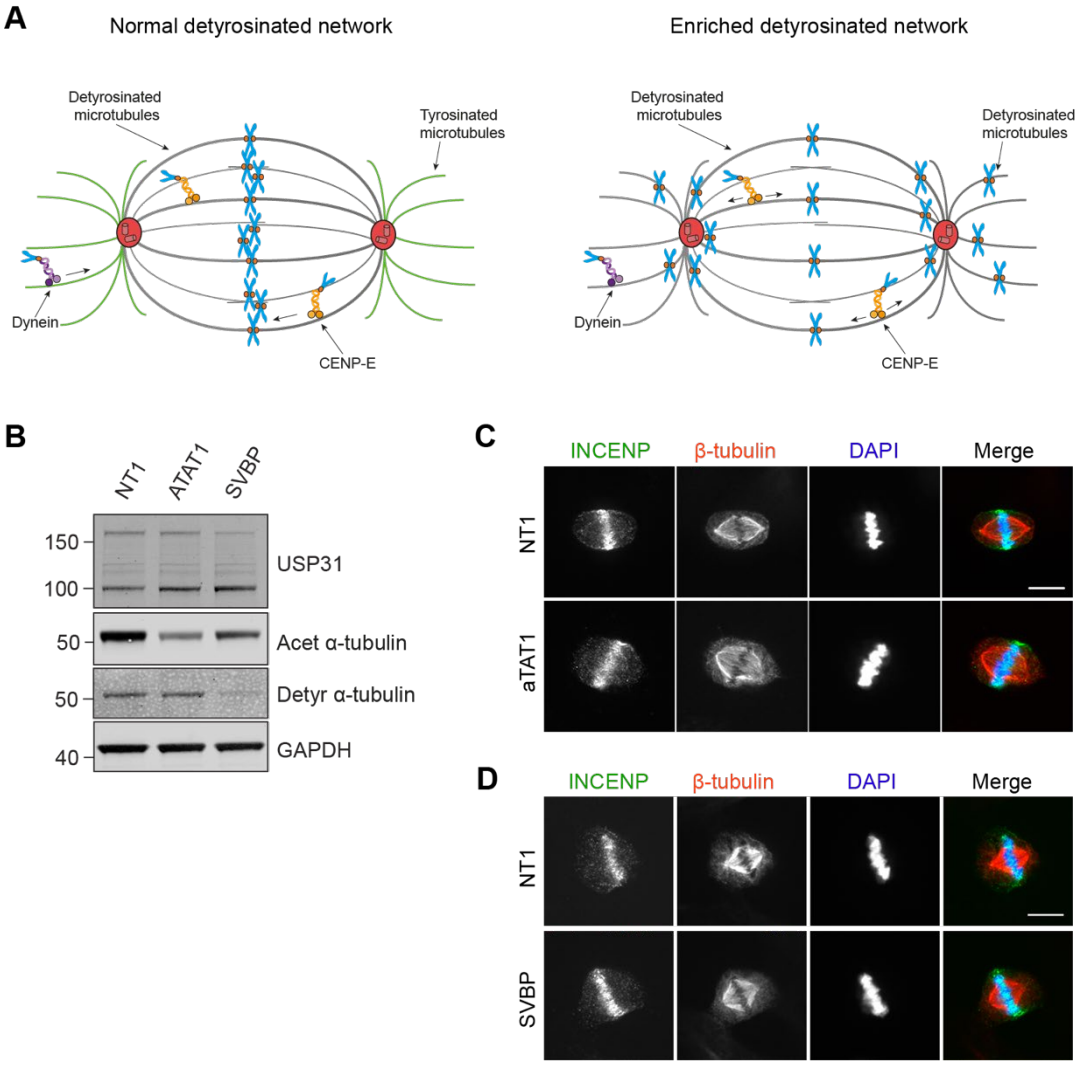

Figure 5.18 – Disruption of the detyrosinated and acetylated microtubule networks does not affect CPC mislocalisation

A. Schematic showing spindle organisation with normal levels of detyrosinated tubulin (left) and enriched levels of detyrosinated tubulin (right). **B.** U2OS cells were depleted with ATAT1 or SVBP for 48 hours Samples were analysed by western blotting and probed for indicated proteins. **C/D.** U2OS cells were transfected with siRNA against a non-targeting control (NT1), ATAT1 (**C**) or SVBP (**D**) for 48 hours. Cells were then treated with MG132 (5 μM) for 1 hour and subsequently treated with RO3306 (10 μM) for 8 minutes. Cells were fixed with MeOH and stained for the indicated antibodies. Images were acquired with a 3i spinning disk confocal; a single confocal slice is shown. Scale bar = 10 μm.

5.5.6 USP31 affects the CPC expression and localisation during anaphase but not telophase

USP31-dependent CPC mislocalisation occurs in the presence of the CDK1 inhibitor RO3306. I therefore wanted to confirm whether the same result can be seen in physiological anaphase conditions as well. This will allow for better differentiation between kinetochore- and midzone-localised CPC components, as chromosome separation will occur normally as opposed to under MG132 treatment where it is prevented. To investigate this, USP31 depleted cells were synchronised to prometaphase following thymidine-nocodazole block and released into fresh DMEM to allow them to re-enter into mitosis. Methanol-fixed cells were then stained for INCENP to represent the CPC localisation and results are shown in Figure 5.19A. The CPC transitions from the centromeres to the midzone during anaphase in NT1 control cells (top panel). In some instances, a slight delay in this transport is apparent, as some residual INCENP staining is observed still on the chromosomes (lower NT1 example). Following USP31 depletion with the Q1 oligonucleotide, reduced INCENP staining at the midzone is observed alongside incomplete relocalisation from the centromeres to the midzone. Under these conditions, more residual staining which overlaps with the chromosome staining is seen. USP31 depletion with Q4 shows that INCENP levels are significantly reduced at the midzone, however less residual staining is observed still at the centromeres. This mislocalisation previously observed with this oligonucleotide is therefore less striking when under this configuration. Taken together, it can be concluded that USP31 depletion does lead to a reduction of the CPC levels at the spindle midzone, and a mislocalisation or a delay in transition can also be observed for at least 1 oligonucleotide.

I next wanted to confirm whether this mislocalisation of the CPC persists into telophase. During this stage of mitosis, the CPC is expected to localise to the midbody arms which flank the midbody core and the central spindle microtubules (Carmena et al., 2012; Capalbo et al., 2019). To investigate this, the same experimental setup as above was employed. Figure 5.19B confirms that the INCENP does indeed localise to the midbody arms during telophase in USP31 depleted cells. This therefore suggests that the absence of CPC staining at the midzone observed in Figure 5.16 and Figure 5.19B suggests this may be a delay in its transition rather than a complete mislocalisation.

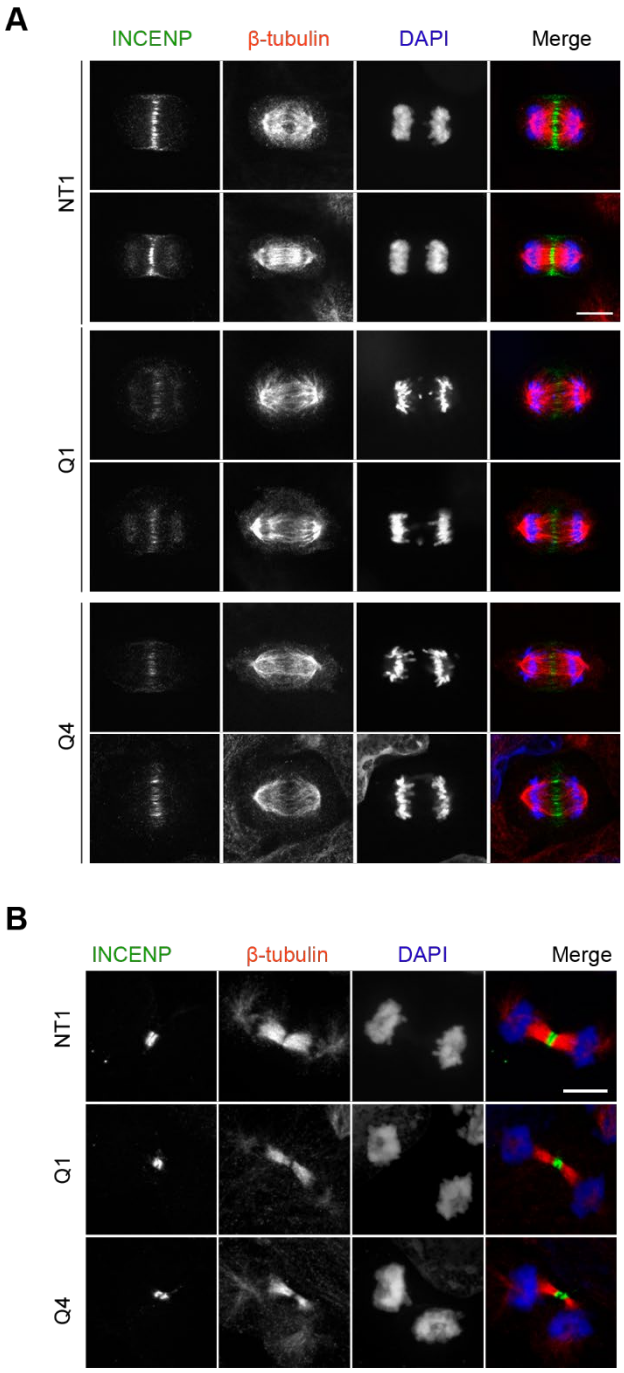

Figure 5.19 – CPC localisation during anaphase and telophase

U2OS cells were transfected with siRNA against USP31 (Q1 or Q4) or a non-targeting control (NT1) for 48 hours and synchronised to prometaphase with a single thymidine block followed by nocodazole. Cells were then washed and released into fresh DMEM for 2-3 hours to allow progression through mitosis. Cells were fixed with MeOH and stained for the indicated proteins. Images were acquired with a 3i spinning disk confocal. Scale bar = 10 μm. **A.** Single confocal slice of representative cells in anaphase, **B.** Maximum projection of representative cells in telophase.

5.5.7 USP31 does not affect cytokinesis

The CPC plays a critical role in cytokinesis by regulating the timing of the abscission that leads to the complete separation of the 2 daughter cells (Aleem et al., 2015). As USP31 regulates both expression levels and subcellular localisation of the CPC components during prometaphase and anaphase, it is possible that defects in cytokinesis may also occur. This would correlate with the ectopic furrowing phenotype observed in the stable cell lines expressing the catalytic inactive version of GFP-USP31 (CA1) shown in section 5.5.1. To confirm whether USP31 depletion causes cytokinesis defects, cells were fixed and co-stained for α-tubulin and pericentrin, a frequently used marker of the centrosome. If cytokinesis was defective in these cells, an increase in the number of centrosomes per cell would be observed. Centrosome numbers were therefore counted for each of the 2 oligos used and compared to the control cells. Representative images of a field of cells for each condition is shown in Figure 5.20, with selected insets showing the centrosomes. The quantitation of 238, 164 and 164 cells for NT1, Q1 and Q4 respectively is shown in the graph and confirms that no significant difference if observed in the centrosome numbers following USP31 depletion. A slight increase in the number of cells containing 2 centrosomes is observed for both oligos, (40% of control cells compared to 45% for both Q1 and Q4). This could be attributed to the increase in the number of cells seen in G2 phase following USP31 depletion, as observed by Erithelgi Bertsoulaki (Bertsoulaki, 2018). This therefore indicates that USP31 does not play a role in cytokinesis.

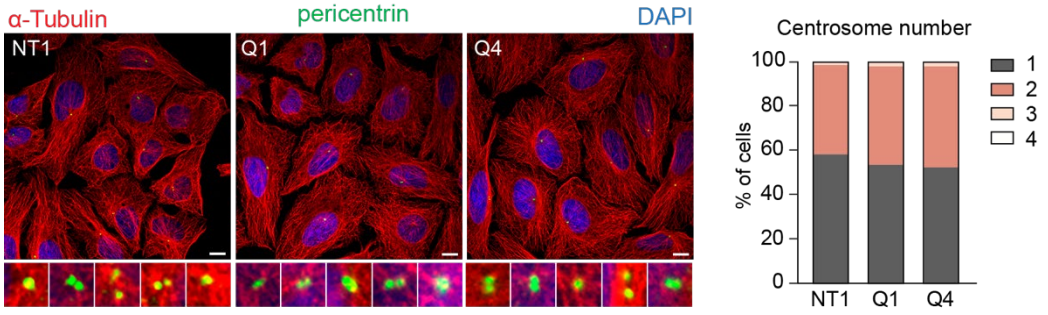

Figure 5.20 – USP31 depletion does not affect centrosome number

U2OS cells were transfected with siRNA against USP31 (Q1 or Q4) or a non-targeting control (NT1) for 48 hours. Cells were fixed using ice cold methanol and stained for α-tubulin (red), pericentrin (green) and DNA (DAPI, blue). Representative images and insets are shown. Images were acquired using a 3i spinning disk confocal. 40X objective. Scale bars = 10 μm. The number of centrosomes per cell is quantitated in the graph.

5.5.8 USP31 depletion leads to a delay in the transition of INCENP from the centromeres to the spindle midzone

It is clear that USP31 has a role within the regulation of the CPC expression levels and its localisation during anaphase onset. This mislocalisation does however appear to rectify itself during telophase as the CPC proteins are able to successfully localise to the spindle midbody arms as shown in section 5.5.6. This therefore suggests that rather than a complete mislocalisation of the CPC during mitosis, USP31 depletion may cause a delay in the translocation of it from the centromeres to the central spindle midzone during anaphase onset. To investigate this, I utilised U2OS cells which stably express doxycycline inducible VSV-INCENP-GFP, kindly gifted to us from Professor Susanna Lens (UMC Utrecht, The Netherlands).

I first confirmed whether USP31 depletion could reduce expression levels of the induced VSV-INCENP-GFP protein in a similar manner to the endogenous protein. Cells were therefore synchronised to prometaphase, and INCENP expression was induced using doxycycline for 3 hours before cells were lysed. Asynchronous samples were also taken to compare to the expression levels in mitosis. INCENP-GFP can successfully be induced following 3 hours of doxycycline treatment in both asynchronous and mitotic cells (Figure 5.21A). Furthermore, the impact of USP31 depletion on INCENP expression levels can be recapitulated with the inducible INCENP-GFP protein levels, as both oligos lead to a reduction in levels compared to the NT1 control. This result supports the suggestion that USP31 has a direct role in stabilising INCENP expression levels and argues against it being a transcriptional change.

I then went on to follow the kinetics of INCENP translocation from the centromeres at metaphase, to the spindle midzone during anaphase, and then to the midbody arms during telophase in real-time. INCENP-GFP expression was induced in asynchronous cells and live cell imaging was performed. Cells in late prometaphase and metaphase were selected and a z-stack was acquired every minute throughout anaphase and telophase. Figure 5.21B shows images from representative cells following USP31 depletion, with the first frame of each starting at metaphase (one frame before anaphase onset commenced). To complement the results shown in Figure 5.21A, a decrease in the protein expression is observed with both oligonucleotides.

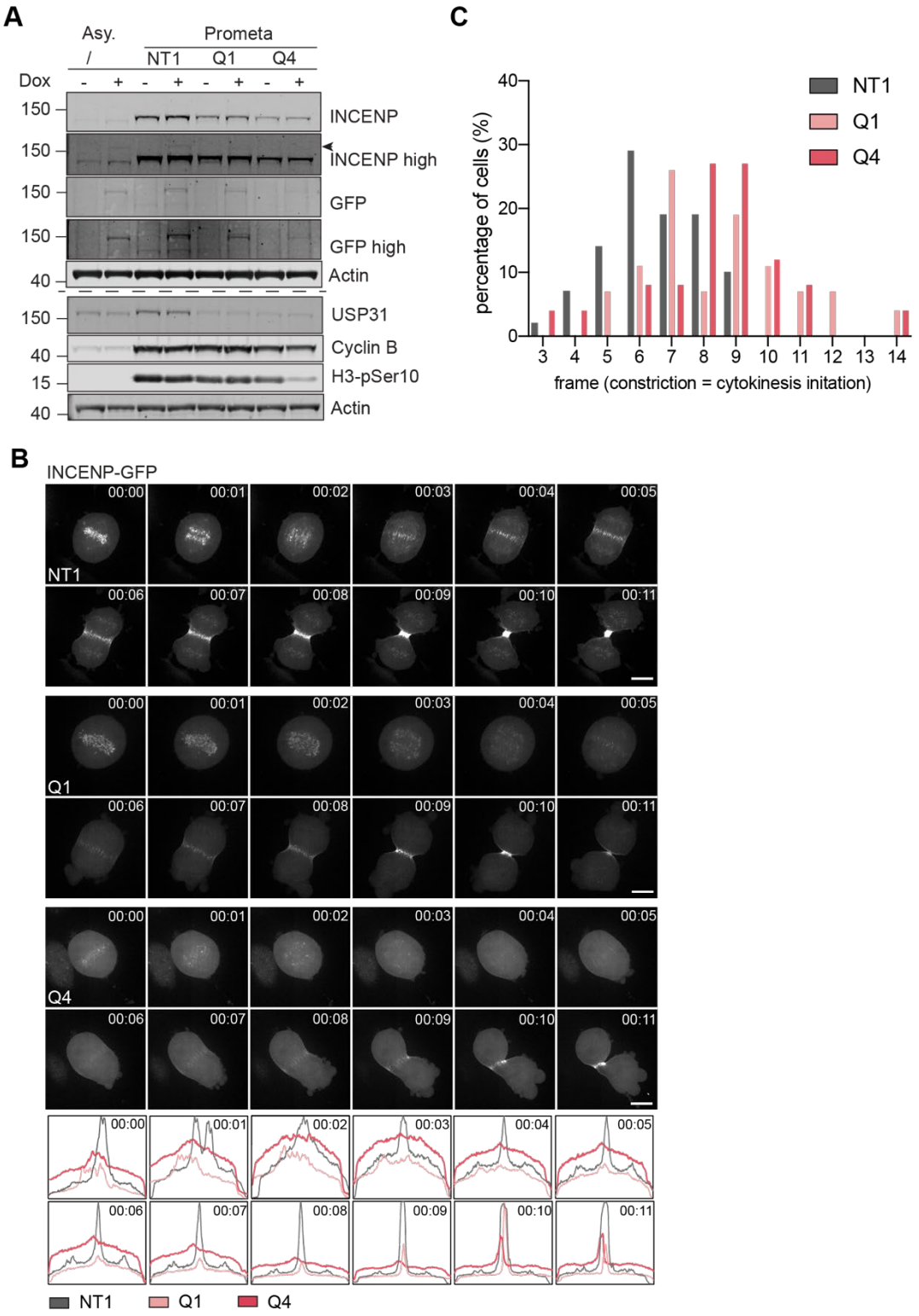

Figure 5.21 – USP31 depletion effects the transition of GFP-INCENP

A. U2OS cells expressing inducible INCENP-GFP were transfected with siRNA against USP31 (Q1, Q4) or a non-targeting control (NT1) and synchronised with a single thymidine block followed by nocodazole to prometaphase. INCENP-GFP (arrowheads) expression was induced for 3 hours with doxycycline (1 µg/ml) prior to lysis and processing for western blotting with the indicated antibodies. **B.** U2OS

cells inducibly expressing INCENP-GFP were transfected with siRNA against USP31 (Q1, Q4) or a non-targeting control (NT1) for 45 hours, then treated with doxycycline (1 µg/ml) for 3 hours to induce expression of INCENP-GFP. Cells were then imaged on a 3i spinning disc confocal microscope as they transition from metaphase to anaphase. Z-stacks (range 17µm, 1µm steps) were acquired every minute. Shown is a sequence of representative Z-stack maximum projections (17 µm range, 1 µm step size) starting one frame before anaphase onset. Scale bar = 10 µm. Time is shown in hh:mm. Quantitation of intensity levels of GFP-INCENP expression. Fiji was used to produce trace graphs across each cell from pole to pole at each timepoint. **C.** Quantitation of all cells imaged for B. The percentage of cells that undergo initiation of furrow ingression at each timepoint is shown in the graph. NT1 (42 cells), Q1 (27 cells), Q4 (26 cells).

In the NT1 control cells, INCENP-GFP localisation can clearly be seen at the centromeres at the 00:00 time frame, and as the cells pass through anaphase, the expected relocalisation to the spindle midzone occurs between 00:02 and 00:04. After the 00:05 time frame, spindle elongation and cleavage furrow formation occurs at the equatorial cortex. Furrow ingression and compacting of the central spindle then occurs after this point, causing INCENP-GFP to accumulate at the spindle midbody. These timings however are not replicated in USP31 depleted cells. For the cells treated with Q1, relocalisation from the centromeres to the spindle midzone is not completed until the 00:06 timepoint, with cleavage furrow formation and spindle elongation not being initiated until 00:07. Accumulation at the midbody then occurs at 00:10. Similar results are seen with the second Q4 oligonucleotide. Upon anaphase onset, the INCENP-GFP is released from the centromeres after 00:04 but appears to dissipate (possibly into the cytoplasm) before faintly relocalising to the spindle midzone at the 00:06 time frame. Elongation and cleavage furrow ingression occurs after 00:07 before accumulation at the midbody at 00:10. The expression levels of GFP-INCENP across the width of the cell (from pole to pole) were analysed and trace graphs for each timepoint are illustrated (Figure 5.21B). Trace levels illustrate that in control cells, INCENP levels peak at the equator of the cell throughout the duration of imaging. Following USP31 depletion however, the peak level at the equator is reduced during metaphase (00:00). Furthermore, INCENP levels do not display a sharp peak at the equator as they progress through anaphase but appear more constant across the width of the cell. This peak at the equator does reappear for both Q1 and Q4 cells however not until after 00:09 and 00:10 respectively. Quantitation of the timeframe where initial furrow ingression is observed was performed and is shown in Figure 5.21C, confirming this delay is representative.

These results confirm that USP31 regulates INCENP expression levels in a post-transcriptional manner. Furthermore, a delay in the release and redistribution of INCENP from the centromeres to the spindle midzone during the transition from metaphase to telophase is observed. Taken together, USP31 therefore regulates both the abundance and the dynamics of the CPC.

5.6 Discussion

Deubiquitylases (DUBs) play a complex and highly choreographed role within mitosis. It has been reported that USP44 regulates the spindle assembly checkpoint by stabilising the Mad2-Cdc20 complex (Stegmeier et al., 2007), USP9X controls centrosome duplication (Wang et al., 2017b; Li et al., 2017), the spindle assembly checkpoint (Skowyra et al., 2018) and survivin relocalisation (Vong et al., 2005), whilst USP35 stabilises aurora B (Park et al., 2018). USP31 is a DUB which is poorly characterised in the literature. Previous work by Erithelgi Bertsoulaki showed that it localises to microtubules and to the mitotic spindle, and its depletion leads to mitotic defects. The work presented in this chapter provides a detailed investigation of the role of USP31 during cellular division.

5.6.1 USP31 expression levels

The fluctuations in expression levels of deubiquitylases throughout the cell cycle have been previously investigated, however, no specific DUBs emerged as being highly expressed in mitosis in comparison to other cell cycle phases (Darling, 2017). Furthermore, this study did not include any comprehensive analysis of USP31. I have shown here that USP31 increases its expression levels 2-3-fold during mitosis compared to asynchronous cells. This therefore makes USP31 the DUB which changes its expression levels the most over the course of the cell cycle, as no other DUB has been reported to vary its levels to this degree (Darling, 2017). This is a typical characteristic seen with other proteins which have a primary and crucial function in mitosis (Nath et al., 2015). For example, cyclin B, which associates with CDK1 and allows for the phosphorylation of proteins required for entry into mitosis and the spindle assembly checkpoint (SAC), is highly upregulated upon entry into mitosis and reduced as cells progress to mitotic exit (Ding et al., 2020; Fung and Poon, 2005). Furthermore, members of the CPC such as INCENP also follow this pattern. As these mentioned proteins are crucial for mitosis, and their perturbation/depletion leads to delays in mitotic progression, this transcriptional upregulation is essential for successful chromosome segregation (Hümmer and

Mayer, 2009). From the results shown in this chapter, it is fitting that USP31 would also undergo an increase in expression and that it is a crucial mitotic regulator.

5.6.2 USP31 phosphorylation

As well as mitotic-induced upregulation of USP31, I also confirmed the phosphorylation of the whole USP31 population during M-phase. Phosphorylation is a key regulatory mechanism within mitosis (Nigg, 2001), with 30% of the mitotic proteome being modified with a phosphate group (Welburn and Jeyaprakash, 2018). USP31 phosphorylation coincides with its increased expression levels, and therefore may influence its stabilisation (Nishi et al., 2011), however further research is required to confirm this hypothesis. This phosphorylation has also been shown to occur in a CDK1-dependent manner. A possible drawback of this conclusion is the lack of dephosphorylation observed as the cells enter into anaphase and telophase (Figure 5.1B). However, in conjunction with previous studies (Afonso et al., 2019), complete degradation of cyclin B has also not occurred at these stages in our hands, indicating continued CDK1 activation and prolonged USP31 phosphorylation. In vitro investigations could be performed to confirm CDK1 as the sole kinase. Additionally, investigations into whether phosphorylation increases the activity levels of USP31 could also be employed.

During metaphase, USP31 localises mainly to the cytosol and its microtubule binding abilities have been lost. Upon inhibition of CDK1 however, USP31 relocalises onto the mitotic spindle, leading to the hypothesis that CDK1-dependent phosphorylation prevents USP31 associating to the spindle microtubules. There are other proteins which have their microtubule binding ability regulated by the presence of phosphorylation which would support this hypothesis. For example, Ipl1 aurora kinase in yeast cells is able to associate with Bim1, the yeast homolog of EB1 when it has been dephosphorylated at anaphase onset, allowing it to associate with the mitotic spindle at this point (Zimniak et al., 2012). An additional example is provided by CLASP2 proteins where phosphorylation at multiple sites inhibits the electrostatic attractions it forms with EB1 +tip proteins and thereby prevents is association with microtubules and plus-tip tracking during mitosis (Kumar et al., 2012). As Ipl1, CLASP2 and USP31 are all thought to be phosphorylated by CDK1, it is therefore possible that USP31 may act in a similar way, allowing for microtubule association when it is dephosphorylated. USP31 is therefore subjected to spatiotemporal regulation and may not perform some functions until spindle localisation is restored.

USP31 residues S433, S879 and S1001 were mutated to confirm their roles in phosphorylation and microtubule association, however no evidence for this was identified. USP31 has been shown to be phosphorylated at other residues in addition to those analysed in this chapter. A previous study performed large-scale quantitative phosphoproteomics using small-molecule inhibitors for both aurora B and PLK1 on cells arrested in mitosis. Phosphorylated residues for USP31 identified here included S877, S887, S1057, S1060, T1122, Y1123, S1126 and S1221 however none were shown to meet the cut-off requirement of at least 2.5-fold reduction following inhibitor treatment (Kettenbach et al., 2011). PhosphoSitePlus® shows 59 residues which could be phosphorylated. The residue with the most experimental evidence is S1323, where immunoaffinity beads to detect phospho-MAPK and CDK substrates have been utilised (Hornbeck et al., 2015). Of these other identified sites, none of them fit the specific CDK1 consensus sequence except S690 and S1111 (Sharma et al., 2014; Klammer et al., 2012; Christensen et al., 2010; Hornbeck et al., 2015). There are also a further 20 sites which fit the less specific consensus of S/T*-P. Other sites may therefore be involved in the regulation of USP31 phosphorylation and could be mutated to confirm the role in spindle association. A caveat to the point mutations generated here is that there are additional serine residues in close proximity to all 3 predicted positions. Serine residues are also located at position 432, 877, 881 and 1000. It is therefore possible that because phosphorylation cannot occur on 433, 879 and 1001 due to the introduced point mutations, these other surrounding residues have been phosphorylated to overcome this, thus possibly altering the observed localisation. In order to eliminate this possibility, additional mutations at these positions would need to be introduced.

5.6.3 USP31 and the chromosomal passenger complex

I have shown that USP31 plays a significant role in regulating the stability of the chromosomal passenger complex (CPC) during mitosis. The CPC is a crucial complex which regulates the attachment of microtubules to kinetochores, activates the spindle assembly checkpoint and initiates cytokinesis (Carmena et al., 2012; Aleem et al., 2015). INCENP is the most significantly affected by USP31 depletion, although a decrease in expression levels is also seen for aurora B and borealin. As the CPC proteins are involved within the same complex, it is possible that the destabilisation of only one of these proteins leads to the indirect downregulation of the others (Honda et al., 2003). Thereby, some or all of the CPC components may be a substrate of USP31. Tandem Ubiquitin Binding Entities (TUBEs) protein domains which

specifically bind to polyubiquitin chains (Hjerpe et al., 2009) and could be utilised here to determine whether CPC components are polyubiquitinated and whether this changes following USP31 depletion. An alternative approach could be the use of his10-tagged ubiquitin pulldown experiments (Trulsson et al., 2022). These methods may identify changes in polyubiquitination following USP31 depletion, providing evidence that USP31 prevents their targeted degradation. This decrease in protein expression could also be attributed to reduced transcription. However, as this same result is recapitulated using the doxycycline-inducible GFP-INCENP cells lines via both western blot and live cell imaging, this suggestion seems less likely. Furthermore, unpublished data performed by Joana Gomes Neto has shown that the cells stably expressing the catalytic inactive form of USP31 display similar reductions in INCENP levels. This result supports the suggestion that USP31 has a direct role in stabilising INCENP expression levels and argues against it being a transcriptional change. This change could be further confirmed by the use of qPCR-RT experiments.

I have shown that cells stably expressing doxycycline-inducible GFP-INCENP exhibit a transitional delay of the CPC between anaphase onset and telophase. The addition and removal of ubiquitin is required for the extraction of the CPC from the chromosomes. Survivin is targeted to the centromeres via K63 ubiquitination, mediated by the ubiquitin binding protein, Ufd1 (ubiquitin fusion degradation 1). USP9X-dependent deubiquitylation of survivin is required for release of the CPC from the kinetochores and subsequent relocalisation to the midzone during anaphase (Vong et al., 2005). In parallel, aurora B ubiquitination by Cul-3-KLHL9-KLHL13 facilitates its removal from the chromosomes (Sumara et al., 2007), whereas the Cul3-KLHL21-mediated ubiquitination targets it to the midzone (Maerki et al., 2009). These cycles of ubiquitination and deubiquitination of the CPC components are present on multiple levels, thereby controlling its dynamic behaviour and coordinating mitotic progression. USP31 has been shown here to also play a role in this relocalisation, suggesting that action from both DUBs may be required for sufficient relocalisation. As USP9X is involved in survivin release, it could be hypothesised that USP31 activity is required for the subsequent recruitment to the midzone. USP31 activity may therefore further add to the numerous mechanisms required for critical spatiotemporal regulation of the CPC (Van Der Horst and Lens, 2014).

MKLP1 and MKLP2 motor proteins are known to transport the CPC from kinetochores to the midzone, and regulate spindle midzone formation respectively (Gruneberg et al., 2004). Disruption of MKLP2 levels, although not statistically significant, was seen

with 1 oligonucleotide. Transport of the CPC to the midzone via this motor protein may therefore be impaired, resulting in an indirect effect on CPC localisation. On the other hand, as MKLP2 processivity increases with CPC expression levels (Adriaans et al., 2020), CPC destabilisation observed may in turn reduce MKLP2 activity, hence impairing relocalisation. In addition, INCENP is also required for survivin localisation (Wheatley et al., 2001), the recruitment of MKLP1 to the midzone and midbody (Zhu et al., 2005), and the transport of MKLP2 to the ends of stable microtubules in the spindle midzone (Serena et al., 2020; Hümmer and Mayer, 2009). As INCENP is reduced significantly following USP31 depletion, this loss could also cause an indirect effect on CPC relocalisation by any of these mechanisms. Due to these multiple layers of dependence on each other, further investigation is required to determine which of these proteins are direct substrates of USP31.

In addition to this mechanistic delay observed during the later stages of mitosis, Erithelgi Bertsoulaki also observed a delay between nuclear envelope breakdown and anaphase onset. She saw that USP31 depleted cells take on average between 32 and 40 minutes to reach anaphase onset, whereas control cells only take 25 minutes (Bertsoulaki, 2018). The CPC also has a role during these early mitotic stages by controlling chromosome alignment and the SAC (Carmena et al., 2012; Aleem et al., 2015). Following its localisation at the inner centromeres, aurora B activity leads to the recruitment of a number of proteins to centromeres and kinetochores. This includes proteins involved in the SAC such as Mad1, Mad2, Bub1, BubR1, Mps1 and CENP-E (Ditchfield et al., 2003; Kelly and Funabiki, 2009). Additionally, the attachment and stabilisation of kinetochore microtubules is tightly regulated by aurora B activity in response to tension defects (Kalantzaki et al., 2015). The CPC therefore functions to repair incorrect kinetochore-microtubule attachments (Kelly and Funabiki, 2009). Additionally, aurora B regulates the localisation and activity of MCAK (mitotic centromere associated kinesin), the kinesin-13 microtubule depolymerase (Andrews et al., 2004; Lan et al., 2004), allowing for microtubule depolymerisation upon erroneous kinetochore attachments. USP31 stabilisation and spatiotemporal regulation of one or more of the CPC components may therefore reduce the effectiveness of either of these mechanisms, causing a delay in early mitosis. Furthermore, USP31 depletion disrupts the detyrosinated microtubule network (Bertsoulaki, 2018). Detyrosination is required for suppressing MCAK activity (Peris et al., 2009; Sirajuddin et al., 2014) at the centromeres, allowing for stabilisation of correct kinetochore-microtubule attachments (Ferreira et al., 2020). USP31-dependent loss of detyrosination may therefore result in the inability to suppress

MCAK activity, which in turn would prevent stabilisation of correct kinetochore-microtubule attachments. This hypothesis would correlate with the data from Erithelgi Bertsoulaki which reveals reduced kinetochore microtubule half-lives in USP31 depleted spindles (Bertsoulaki, 2018). Further investigation of MCAK activity would be required to confirm this.

5.6.4 Next steps for USP31

This research has provided the first in-depth analysis of the expression, localisation and mechanistic roles of USP31 during mitosis, and therefore provides a foundation for further investigations into this DUB. USP31 localisation on the mitotic spindle has been visualised using overexpressed, GFP-tagged versions of USP31. Although this provides useful insights into the protein function, the ability to confirm this result with the endogenous protein is desirable. USP21 is another DUB which displays microtubule localising abilities when transiently overexpressed (Urbé et al., 2012). Further studies of this protein however revealed that USP21 primarily localises to the centrosome (Heride et al., 2016). An endogenously tagged version of USP31 would therefore provide us with more reliable information to confirm its microtubule localisation. A caveat of this however is that USP31 protein copy numbers within cells are low, with an estimate of only ~350 copies in Hela cells (Bekker-Jensen et al., 2017). Given this, GFP-tagged endogenous USP31 may be expressed at too low levels to clearly determine the localisation via immunofluorescence. Despite this, USP31 has been identified in a previous study which performed proteomic analysis of mitotic spindles within *Xenopus* egg extracts, suggesting its involvement in self-organisation of microtubules during M-phase (Rosas-Salvans et al., 2018). This finding further reinforces the claim that USP31 localises to the spindle and is a key regulator of mitosis.

The next steps will be to fully confirm substrates of USP31 to uncover its mechanistic roles within mitosis. This can be explored using mass spectrometry analysis of mitotic cells following siRNA depletion of USP31 to determine proteins stabilised by USP31 activity. Furthermore, biotin proximity labelling (BioID) (Roux et al., 2012) or TurboID (Cho et al., 2020) could be utilised to identify proteins which directly interact with USP31.

Chapter 6 - Conclusions

6.1 Novel microtubule binding proteins

In this thesis I have introduced a new protocol for identifying microtubule associated proteins (MAPs) and shown its ability to identify both LGALSL and TRIM3 as novel microtubule binding proteins. These results confirm that there are still microtubule binding proteins to be identified. A number of other proteins were also identified as potential candidates including 2 members of the syndecan family of transmembrane proteogylcans, syndecan-1 and syndecan-4. Syndecan proteins are cell surface receptors that mediate adhesion between the cell and the extracellular matrix (ECM). They also function as receptors for ECM proteins and growth factors (Morgan et al., 2007). Syndecan-4 is required for the formation of focal adhesions (Woods and Couchman, 2001), and microtubules are involved in stimulating focal adhesion disassembly (Ezratty et al., 2005). Syndecan-1, -2 and -4 have all been reported to associate with tubulin within the mitotic spindle (Brockstedt et al., 2002). It would therefore be interesting to see whether syndecan proteins have any further roles which involve the microtubule network both in interphase and mitosis.

Despite extracting many microtubule binding proteins, not all known MAPs were identified. EB2 and other plus tip proteins such as CLIP170 and CLIP115 were missing from the dataset, although EB3 was readily detected. Some proteins with high off rates which undergo transient microtubule association may therefore be missed using this method of extraction. It should therefore be expected that some novel microtubule binding proteins will also go undetected and additional protocol optimisation may be required to achieve a more complete proteome.

6.2 Future applications for microtubule differential extraction

During the development of this differential extraction protocol, it was envisioned that it could be utilised for further applications such as investigating readers of the tubulin code. Additionally, as it was easily applied to RPE1 and SKN-BE2 cells, this protocol could also be utilised within neuronal systems.

6.2.1 The tubulin code

The tubulin code has been described to influence the association and activity of microtubule binding proteins such as CENP-E favouring detyrosinated microtubules (Barisic et al., 2015), and spastin activity regulation by polyglutamylation (Lacroix et

al., 2010; Valenstein and Roll-Mecak, 2016). All instances to date have reported a direct link between a specific microtubule PTM and individual proteins but are yet to be performed on a global scale. This novel proteomics method provides a useful tool to facilitate this investigation in cells with manipulated PTMs. U2OS cell lines which have been deleted for either TTL or VASH1 and VASH2 using CRISPR/Cas9, kindly gifted from Dr Helder Maiato (Ferreira et al., 2020), display complete or diminished detyrosination networks respectively (Figure 6.1). Comparisons of the microtubule fractions within each cell line can be made to parental control cells to determine any changes. Functional roles for detyrosinated microtubule networks could then be elucidated following further investigations into identified proteins. This system can be easily manipulated for investigations into other microtubule PTMs and even combinations. One potential caveat is that it will only allow for investigations into proteins which have increased or diminished binding in response to changes in PTM and will not account for protein activity differences such as motor processivity or altered directionality.

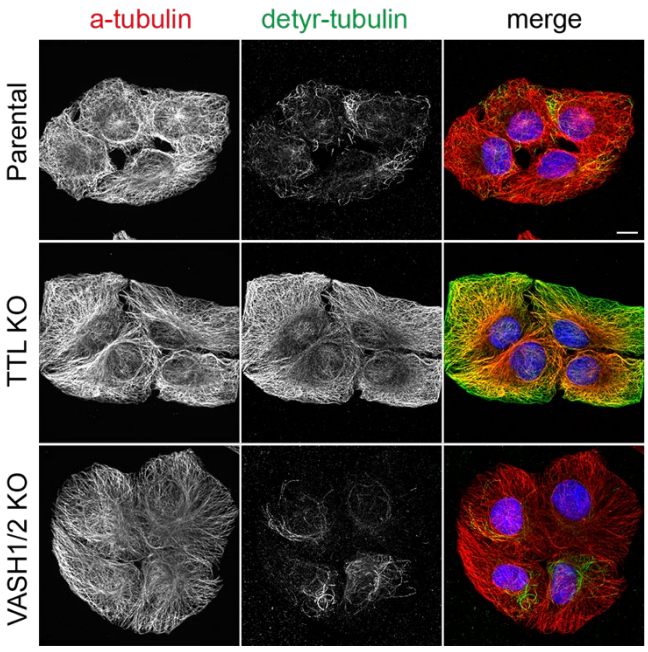

Figure 6.1 – Detyrosination networks in TTL and VASH1/2 knock-out cell lines

U2OS cells deleted from tubulin tyrosine ligase (TTL KO) or Vasohibin 1 and Vasohibin 2 (VASH1/2 KO) were fixed in ice cold methanol and stained for α-tubulin (red) and detyrosinated α-tubulin (green) to visualise the differences in detyrosination network compared to parental U2OS cells.

6.2.2 The neuronal microtubule proteome

Microtubules are critical for neuronal development, maintenance, and function. This protocol could be applied to neuronal systems allowing for identification of the neuronal microtubule proteome. Additionally, the tubulin code plays a crucial role within neurons, and modifications are spatiotemporally regulated during development. Despite their high presence, their functional relevance remains largely unknown (Moutin et al., 2020). Manipulation of different aspects of the microtubule code could be performed via siRNA depletion of the responsible enzymes followed by differential extraction. Further applications could also be performed in a i3 (isogenic, integrated, inducible) neuronal system previously developed by Michael Ward and colleagues (NIH, USA) (Wang et al., 2017a). These cells contain a CRISPRi system for mediated depletion of target genes and could be used to perturb tubulin modifications and investigate their affects throughout neuronal development. This tool could be applied in combination with the differential extraction protocol to specifically identify binding proteins which associate to particular subsets of neuronal microtubules. Further optimisation of microtubule extraction will be required within neuronal cells due to their anticipated increase in nocodazole-resistant stable microtubules. However, a recent study revealed that 15 minutes nocodazole treatment was sufficient to achieve 50% depolymerisation of the microtubule network, which could be sufficient (Qiang et al., 2018).

6.3 TRIMs and microtubules

Of the ~80 TRIM family members present within humans, greater than 10% of them localise to microtubules via a 67 amino acid sequence motif called the cos-box (Short and Cox, 2006). This family must have important roles associated with the microtubule cytoskeleton to explain the large number of family members that localise to them.

Functions have been identified for the C-I subfamily members. MID1 (TRIM18) and MID2 (TRIM1) are both involved in cytokinesis (Gholkar et al., 2016) and axon development (Lu et al., 2013), whilst MID1 has also been reported to target PP2Ac and Alpha4 for degradation (Trockenbacher et al., 2001). TRIM9 is recruited to microtubule plus ends by EB1 in *Drosophila* S2 cells and promotes microtubule growth and prevents catastrophe (Feng et al., 2021) and also regulates synaptic vesicle exocytosis by binding to SNAP25 and inhibiting SNARE complex assembly (Li et al., 2001). TRIM36 has been reported to influence cytoskeletal organisation and assembly in *Xenopus* egg development (Mascaro et al., 2022), and also interacts with

the kinetochore protein CENP-H and delays cell cycle progression when overexpressed (Miyajima et al., 2009). TRIM46 organises parallel microtubules during initial neuronal polarisation and asissts with the formation of parallel, closely spaced, microtubule bundles (Van Beuningen et al., 2015). Finally, TRIM67, alongside TRIM9, interacts with MAP1B and KIF1A and regulates neuronal morphogenesis in response to netrin-1 axon guidance cues (Menon et al., 2021). The C-II muscle proteins TRIM63, TRIM55 and TRIM54 are involved in muscle tissue remodelling by mediating turnover of muscle proteins (Perera et al., 2012). The single family member of the C-III subfamily, TRIM42, remains poorly characterised. Despite sharing similar C-terminal domain architecture, these proteins display a wide array of different functions (Cox, 2012). It also still remains unclear why so many TRIM proteins are targeted to microtubules. Microtubule ubiquitylation has been previously reported (Xu et al., 2010), however its functional role remains unclear. TRIM proteins therefore may provide a good starting point for further investigations into α- and β- tubulin ubiquitylation.

TRIM3 differs from other microtubule-associated TRIMs as it does not contain a cos box domain (Short and Cox, 2006): its microtubule localising region has been mapped to the NHL-repeats. There is therefore an additional domain capable of targeting more TRIMs to microtubules. From my data, it can be hypothesised that TRIM2 localises to microtubules through this same domain, and it will be interesting to see whether any of the other C-VII family members also contain this ability and if they have microtubule-related functions.

6.4 TRIM3 in neurons

TRIM3 is highly expressed in the brain where some functional relevance has been identified for it (Esposito et al., 2022), including the regulation of the neuronal kinesin KIF21B (Labonté et al., 2013). Additionally, the molluscan orthologue of TRIM2/3 has been implicated in neuronal differentiation as its depletion reduced neurite outgrowth (Van Diepen et al., 2005). My data has shown that TRIM3 plays a role in regulating the acetylated microtubule network by altering the expression levels of the responsible acetylase, ATAT1, in a post-transcriptional manner. Alterations in KIF21B processivity could be a result of this perturbed microtubule code as motors display subset preferences. Additionally, the acetylation of microtubules is responsible for inducing microtubule stabilisation (Eshun-Wilson et al., 2019) and promoting microtubule bundling (Balabanian et al., 2017), both important features within

neuronal axons. As loss of acetylation has also been shown to increase axonal and dendritic branching (Jenkins et al., 2017; Wei et al., 2018), investigations into whether TRIM3 is involved in regulating any of these aspects may lead to interesting findings.

6.5 USP31 in neurons

USP31 expression levels are also high in neuroblastoma cells (Bertsoulaki, 2018) and may therefore be involved in the development and differentiation of neurons. Yeast two-hybrid investigations to identify USP31 binding partners have revealed Ankyrin 2/B (AnkB) and Myc binding protein 2 (MYCBP2) as two of the top hits. AnkB has been shown to link dynein-dynactin motor proteins with their cargoes in primary hippocampal neurons and its loss resulted in shortened axon tracks (Lorenzo et al., 2014). Additionally, it can directly associate with microtubules (Davis and Bennett, 1984) and giant AnkB couples axonal microtubules to plasma membranes (Yang et al., 2019). MYCBP2 is an unconventional E3 ligase enzyme which ubiquitylates threonine and serine residues (Pao et al., 2018) and mutations have been shown to alter microtubule morphology in zebrafish forebrain neurons (Hendricks and Jesuthasan, 2009). USP31 may therefore be involved in these processes if either of these proteins are confirmed to be a substrate. Further investigations should therefore be performed using target specific CRISPRi within the i3 iPSC neuronal system (Wang et al., 2017a).

6.6 Microtubule-related diseases

A number of different diseases have been associated with microtubules and their binding proteins (Matamoros and Baas, 2016). Microtubule dynamics and post-translational modifications are highly regulated in neurons to ensure axonal transport and maintain their polarity (Moutin et al., 2020). Perturbations in these characteristics have been reported in neurodegenerative diseases such as Alzheimer's disease (Fernandez-Valenzuela et al., 2020), Parkinson's disease (Pellegrini et al., 2017) and Amyotrophic Lateral Sclerosis (Liu and Henty-Ridilla, 2022). Identifying and characterising all microtubule binding proteins involved in dynamic regulation may therefore lead to the development of therapeutics by providing alternative druggable targets.

Dysregulation of microtubule binding proteins also lead to disease phenotypes. Dysfunctional tau proteins can aggregate to form fibrillary tangles which are the key feature in Alzheimer's disease and other tauopathies (Iqbal et al., 2016). Mutations

within the microtubule binding protein LRRK2 (leucine rich repeat kinase 2) are the leading genetic cause for Parkinson's disease. LRRK2 mutants preferentially binds to dynamic, deacetylated microtubules (Law et al., 2014), inhibiting axonal transport which can be rescued with HDAC6 inhibitors (Godena et al., 2014). Additionally, mouse embryonic fibroblasts with deleted LRRK2 have high levels of acetylated microtubules indicating some interplay between this protein and microtubule dynamics and modifications. It is proposed that LRRK2 mutations lead to alterations in microtubule stability which in turn may contribute to the disease phenotype (Law et al., 2014). This further highlights the importance of identifying all microtubule binding proteins, their regulatory roles in microtubule dynamics and any associations with diseases they may have. Furthermore, as alterations within acetylation levels has been linked with neurodegenerative diseases, it will be interesting to determine whether TRIM3 activity or expression levels are altered during disease progression, and whether further mechanistic understanding can result in alternative therapeutics.

6.7 USP31 as a drug target

Over recent years, DUBs have emerged as attractive targets for small molecule inhibitors. This is due to many being directly associated with disease phenotypes or regulating the stability of disease-related substrates. Small molecule inhibitors can therefore be used to target DUBs to aid the degradation of a protein which may not usually be druggable (Harrigan et al., 2017). The selection of which DUB to target is based on there being strong supporting biology and a potential clinical hypothesis. Inhibitors for USP30 have been developed as it is well established for its role in the PINK1/Parkin mitophagy pathway and its connections to Parkinson's disease (Rusilowicz-Jones et al., 2020; Phu et al., 2020). This comprehensive study on USP31 has significantly contributed to a greater understanding of its functional role within mitosis and could therefore promote a screening campaign for specific inhibitors. The mitotic defects observed from USP31 depletion indicate its potential as an enzymatic target for cancer therapeutics. Aurora B inhibitors have been developed as potential therapeutic strategies for cancer, however they are all yet to meet the clinic and many have been shown to display off-target effects (Borah and Reddy, 2021). As USP31 regulates the stability of both aurora B and INCENP, inhibition of USP31 may provide an alternative therapeutic method as dysregulation and overexpression of aurora B is frequently observed in cancer (Borah and Reddy, 2021). The use of small molecule inhibitors can also aid the discovery of new biology. For example, a specific inhibitor against USP9X facilitated the identification of a role in ribosomal stalling (Clancy et

al., 2021). The development of a USP31-specific inhibitor will therefore aid further advances into understanding its mitotic functions and will assist with identifying specific roles related to USP31 catalytic activity. Additionally, acute inhibition of USP31 could be applied at any point during the cell cycle to identify more specific roles.

References

Adams, R.R., S.P. Wheatleya, A.M. Gouldsworthy, S.E. Kandels-Lewis, M. Carmena, C. Smythe, D.L. Gerloff, and W.C. Earnshaw. 2000. INCENP binds the Aurora-related kinase AIRK2 and is required to target it to chromosomes, the central spindle and cleavage furrow. *Curr. Biol.* 10:1075–1078. doi:10.1016/S0960-9822(00)00673-4.

Adriaans, I.E., A. Basant, B. Ponsioen, M. Glotzer, and S.M. Lens. 2019. PLK1 plays dual roles in centralspindlin regulation during cytokinesis. *J. Cell Biol.* 218:1250–1264. doi:10.1083/jcb.201805036.

Adriaans, I.E., P.J. Hooikaas, A. Aher, M.J.M. Vromans, R.M. van Es, I. Grigoriev, A. Akhmanova, and S.M.A. Lens. 2020. MKLP2 Is a Motile Kinesin that Transports the Chromosomal Passenger Complex during Anaphase. *Curr. Biol.* 30:2628-2637.e9. doi:10.1016/j.cub.2020.04.081.

Aebersold, R. 2003. A mass spectrometric journey into protein and proteome research. *J. Am. Soc. Mass Spectrom.* 14:685–695. doi:10.1016/S1044-0305(03)00289-7.

Afonso, O., C.M. Castellani, L.P. Cheeseman, J.G. Ferreira, B. Orr, L.T. Ferreira, J.J. Chambers, E. Morais-De-Sá, T.J. Maresca, and H. Maiato. 2019. Spatiotemporal control of mitotic exit during anaphase by an aurora B-Cdk1 crosstalk. *Elife*. 8. doi:10.7554/eLife.47646.

Agarwal, R., and O. Cohen-Fix. 2002. Phosphorylation of the mitotic regulator Pds1/securin by Cdc28 is required for efficient nuclear localization of Esp1/separase. *Genes Dev.* 16:1371–1382. doi:10.1101/gad.971402.

Aillaud, C., C. Bosc, L. Peris, A. Bosson, P. Heemeryck, J. Van Dijk, J. Le Friec, B. Boulan, F. Vossier, L.E. Sanman, S. Syed, N. Amara, Y. Couté, L. Lafanechère, E. Denarier, C. Delphin, L. Pelletier, S. Humbert, M. Bogyo, and A. Andrieux. 2017. Vasohibins/SVBP are tubulin carboxypepidases (TCPs) that regulate neuron differentiation. *Science (80-.).* 358:1448–1453.

Akella, J.S., D. Wloga, J. Kim, N.G. Starostina, S. Lyons-Abbott, N.S. Morrissette, S.T. Dougan, E.T. Kipreos, and J. Gaertig. 2010. MEC-17 is an α-tubulin acetyltransferase. *Nature*. 467:218–222. doi:10.1038/nature09324.

Akhmanova, A., and H. Maiato. 2017. Closing the tubulin detyrosination cycle. *Science (80-.).* 358:1381–1382. doi:10.1007/BF02285261.

Akhmanova, A., and M.O. Steinmetz. 2010. Microtubule +TIPs at a glance. *J. Cell Sci.* 123:3415–3419. doi:10.1242/jcs.062414.

Akisaka, T., H. Yoshida, and T. Takigawa. 2011. Differential distribution of posttranslationally modified microtubules in osteoclasts. *J. Histochem. Cytochem.* 59:630–638. doi:10.1369/0022155411405334.

Akutsu, M., I. Dikic, and A. Bremm. 2016. Ubiquitin chain diversity at a glance. *J. Cell Sci.* 129:875–880. doi:10.1242/jcs.183954.

Al-Bassam, J., H. Kim, G. Brouhard, A. van Oijen, S.C. Harrison, and F. Chang. 2010. CLASP

promotes microtubule rescue by recruiting tubulin dimers to the microtubule. *Dev. Cell*. 19:245–258. doi:10.1016/j.devcel.2010.07.016.

Aleem, E., V.M. Draviam, M. Mendoza, S.H. Lee, and M. Kitagawa. 2015. The chromosomal passenger complex (CPC) as a key orchestrator of orderly mitotic exit and cytokinesis. *Front. Cell Dev. Biol.* | *www.frontiersin.org*. 3:14. doi:10.3389/fcell.2015.00014.

Alfaro-Aco, R., and S. Petry. 2017. How TPX2 helps microtubules branch out. *Cell Cycle*. 16:1560–1561. doi:10.1080/15384101.2017.1348080.

Andrews, P.D., Y. Ovechkina, N. Morrice, M. Wagenbach, K. Duncan, L. Wordeman, and J.R. Swedlow. 2004. Aurora B regulates MCAK at the mitotic centromere. *Dev. Cell*. 6:253–268. doi:10.1016/S1534-5807(04)00025-5.

Applegate, K.T., S. Besson, A. Matov, M.H. Bagonis, K. Jaqaman, and G. Danuser. 2011. PlusTipTracker: Quantitative image analysis software for the measurement of microtubule dynamics. *J. Struct. Biol.* 176:168–184. doi:10.1016/j.jsb.2011.07.009.

Arce, C.A., C.H. Casale, and H.S. Barra. 2008. Submembraneous microtubule cytoskeleton: Regulation of ATPases by interaction with acetylated tubulin. *FEBS J.* 275:4664–4674. doi:10.1111/j.1742-4658.2008.06615.x.

Arce, C.A., M.E. Hallak, J.A. Rodriguez, H.S. Barra, and R. Caputio. 1978. Capability of tubulin and microtubules to incorporate and to release tyrosine and phenylalanine and the effect of the incorporation of these amino acids on tubulin assembly. *J. Neurochem.* 31:205–210. doi:10.1111/j.1471-4159.1978.tb12449.x.

Arce, C.A., J.A. Rodriguez, H.S. Barra, and R. Caputto. 1975. Incorporation of l-Tyrosine, l-Phenylalanine and l-3,4-Dihydroxyphenylalanine as Single Units into Rat Brain Tubulin. *Eur. J. Biochem.* 59:145–149. doi:10.1111/j.1432-1033.1975.tb02435.x.

Arendt, C.S., and M. Hochstrasser. 1997. Identification of the yeast 20S proteasome catalytic centers and subunit interactions required for active-site formation. *Proc. Natl. Acad. Sci. U. S. A.* 94:7156–7161. doi:10.1073/pnas.94.14.7156.

Arnal, I., and R.H. Wade. 1995. How does taxol stabilize microtubules? *Curr. Biol.* 5:900–908. doi:10.1016/S0960-9822(95)00180-1.

Asai, D.J., and M.P. Koonce. 2001. The dynein heavy chain: Structure, mechanics and evolution. *Trends Cell Biol.* 11:196–202. doi:10.1016/S0962-8924(01)01970-5.

Asselin, L., J. Rivera Alvarez, S. Heide, C.S. Bonnet, P. Tilly, H. Vitet, C. Weber, C.A. Bacino, K. Baranaño, A. Chassevent, A. Dameron, L. Faivre, N.A. Hanchard, S. Mahida, K. McWalter, C. Mignot, C. Nava, A. Rastetter, H. Streff, C. Thauvin-Robinet, M.M. Weiss, G. Zapata, P.J.G. Zwijnenburg, F. Saudou, C. Depienne, C. Golzio, D. Héron, and J.D. Godin. 2020. Mutations in the KIF21B kinesin gene cause neurodevelopmental disorders through imbalanced canonical motor activity. *Nat. Commun. 2020 111*. 11:1–18. doi:10.1038/s41467-020-16294-6.

Aumeier, C., L. Schaedel, J. Gaillard, K. John, L. Blanchoin, and M. Théry. 2016. Self-repair promotes microtubule rescue. *Nat. Cell Biol.* 18:1054–1064. doi:10.1038/ncb3406.

Badin-Larçon, A.C., C. Boscheron, J.M. Soleilhac, M. Piel, C. Mann, E. Denarier, A. Fourest-

Lieuvin, L. Lafanechère, M. Bornens, and D. Job. 2004. Suppression of nuclear oscillations in Saccharomyces cerevisiae expressing Glu tubulin. *Proc. Natl. Acad. Sci. U. S. A.* 101:5577–5582. doi:10.1073/pnas.0307917101.

Balabanian, L., C.L. Berger, and A.G. Hendricks. 2017. Acetylated Microtubules Are Preferentially Bundled Leading to Enhanced Kinesin-1 Motility. *Biophysj*. 113:1551–1560. doi:10.1016/j.bpj.2017.08.009.

Banerjee, S., and S. Mazumdar. 2012. Electrospray Ionization Mass Spectrometry: A Technique to Access the Information beyond the Molecular Weight of the Analyte. *Int. J. Anal. Chem.* 2012:40. doi:10.1155/2012/282574.

Bantscheff, M., M. Schirle, G. Sweetman, J. Rick, and B. Kuster. 2007. Quantitative mass spectrometry in proteomics: A critical review. *Anal. Bioanal. Chem.* 389:1017–1031. doi:10.1007/s00216-007-1486-6.

Barber, M., R.S. Bordoli, R.D. Sedgwick, and A.N. Tyler. 1981. Fast atom bombardment of solids (F.A.B.): A new ion source for mass spectrometry. *J. Chem. Soc. Chem. Commun.* 0:325–327. doi:10.1039/C39810000325.

Bard, J.A.M., E.A. Goodall, E.R. Greene, E. Jonsson, K.C. Dong, and A. Martin. 2018. Structure and Function of the 26S Proteasome. *Annu. Rev. Biochem.* 87:697–724. doi:10.1146/annurev-biochem-062917-011931.

Barisic, M., and H. Maiato. 2016. The Tubulin Code: A Navigation System for Chromosomes during Mitosis. *Trends Cell Biol.* 26:766–775. doi:10.1016/J.TCB.2016.06.001.

Barisic, M., R.S. e Sousa, S.K. Tripathy, M.M. Magiera, A. V. Zaytsev, A.L. Pereira, C. Janke, E.L. Grishchuk, and H. Maiato. 2015. Microtubule detyrosination guides chromosomes during mitosis. *Science*. 348:799. doi:10.1126/SCIENCE.AAA5175.

Barlan, K., and V.I. Gelfand. 2017. Microtubule-based transport and the distribution, tethering, and organization of organelles. *Cold Spring Harb. Perspect. Biol.* 9. doi:10.1101/cshperspect.a025817.

Barra, H.S., C.A. Arce, J.A. Rodríguez, and R. Caputto. 1974. Some common properties of the protein that incorporates tyrosine as a single unit and the microtubule proteins. *Biochem. Biophys. Res. Commun.* 60:1384–1390. doi:10.1016/0006-291X(74)90351-9.

Basnet, N., H. Nedozralova, A.H. Crevenna, S. Bodakuntla, T. Schlichthaerle, M. Taschner, G. Cardone, C. Janke, R. Jungmann, M.M. Magiera, C. Biertümpfel, and N. Mizuno. 2018. Direct induction of microtubule branching by microtubule nucleation factor SSNA1. *Nat. Cell Biol.* 20:1172–1180. doi:10.1038/s41556-018-0199-8.

Bekker-Jensen, D.B., C.D. Kelstrup, T.S. Batth, S.C. Larsen, C. Haldrup, J.B. Bramsen, K.D. Sørensen, S. Høyer, T.F. Ørntoft, C.L. Andersen, M.L. Nielsen, and J. V. Olsen. 2017. An Optimized Shotgun Strategy for the Rapid Generation of Comprehensive Human Proteomes. *Cell Syst.* 4:587-599.e4. doi:10.1016/J.CELS.2017.05.009.

Bertsoulaki, E. 2018. Characterisation of USP31- the 3rd microtubule localising Deubiquitylase. University of Liverpool. 328 pp.

Van Beuningen, S.F.B., L. Will, M. Harterink, A. Chazeau, E.Y. Van Battum, C.P. Frias, M.A.M.

Franker, E.A. Katrukha, R. Stucchi, K. Vocking, A.T. Antunes, L. Slenders, S. Doulkeridou, P. Sillevis Smitt, A.F.M. Altelaar, J.A. Post, A. Akhmanova, R.J. Pasterkamp, L.C. Kapitein, E. de Graaff, and C.C. Hoogenraad. 2015. TRIM46 Controls Neuronal Polarity and Axon Specification by Driving the Formation of Parallel Microtubule Arrays. *Neuron*. 88:1208–1226. doi:10.1016/J.NEURON.2015.11.012.

Bhabha, G., G.T. Johnson, C.M. Schroeder, and R.D. Vale. 2016. How Dynein Moves Along Microtubules. *Trends Biochem. Sci.* 41:94–105. doi:10.1016/j.tibs.2015.11.004.

Bieling, P., S. Kandels-Lewis, I.A. Telley, J. Van Dijk, C. Janke, and T. Surrey. 2008. CLIP-170 tracks growing microtubule ends by dynamically recognizing composite EB1/tubulinbinding sites. *J. Cell Biol.* 183:1223–1233. doi:10.1083/jcb.200809190.

Biggins, S., and C.E. Walczak. 2003. Captivating capture: How microtubules attach to kinetochores. *Curr. Biol.* 13:R449–R460. doi:10.1016/S0960-9822(03)00369-5.

Bishop, J.D., and J.M. Schuniacher. 2002. Phosphorylation of the carboxyl terminus of inner centromere protein (INCENP) by the Aurora B kinase stimulates Aurora B kinase activity. *J. Biol. Chem.* 277:27577–27580. doi:10.1074/jbc.C200307200.

Blajeski, A.L., V.A. Phan, T.J. Kottke, and S.H. Kaufmann. 2002. G1 and G2 cell-cycle arrest following microtubule depolymerization in human breast cancer cells. *J. Clin. Invest.* 110:91–99. doi:10.1172/JCI13275.

Bobinnec, Y., M. Moudjou, J.P. Fouquet, E. Desbruyères, B. Eddé, and M. Bornens. 1998. Glutamylation of centriole and cytoplasmic tubulin in proliferating non-neuronal cells. *Cell Motil. Cytoskeleton*. 39:223–232. doi:10.1002/(SICI)1097-0169(1998)39:3<223::AID-CM5>3.0.CO;2-5.

Bodakuntla, S., A.S. Jijumon, C. Villablanca, C. Gonzalez-Billault, and C. Janke. 2019. Microtubule-Associated Proteins: Structuring the Cytoskeleton. *Trends Cell Biol.* 29:804–819. doi:10.1016/j.tcb.2019.07.004.

Bolte, S., and F.P. Cordelières. 2006. A guided tour into subcellular colocalization analysis in light microscopy. *J. Microsc.* 224:213–232. doi:10.1111/j.1365-2818.2006.01706.x.

Bonner, M.K., D.S. Poole, T. Xu, A. Sarkeshik, J.R. Yates, and A.R. Skop. 2011. Mitotic spindle proteomics in Chinese hamster ovary cells. *PLoS One*. 6. doi:10.1371/journal.pone.0020489.

Borah, N.A., and M.M. Reddy. 2021. Aurora kinase B inhibition: A potential therapeutic strategy for cancer. *Molecules*. 26. doi:10.3390/molecules26071981.

Borden, K.L.B., S.R. Martin, N.J. O'Reilly, J.M. Lally, B.A. Reddy, L.D. Etkin, and P.S. Freemont. 1993. Characterisation of a novel cysteine/histidine-rich metal binding domain from Xenopus nuclear factor XNF7. *FEBS Lett.* 335:255–260. doi:10.1016/0014-5793(93)80741-C.

Borisy, G.G., and J.B. Olmsted. 1972. Nucleated assembly of microtobules in porcine brain extracts. *Science (80-.).* 177:1196–1197. doi:10.1126/science.177.4055.1196.

Borisy, G.G., and E.W. Taylor. 1967. The mechanism of action of colchicine. Binding of colchincine-3H to cellular protein. *J. Cell Biol.* 34:525–533. doi:10.1083/jcb.34.2.525.

Bosson, A., J.-M. Soleilhac, O. Valiron, D. Job, A. Andrieux, and M.-J. Moutin. 2012. Cap-Gly Proteins at Microtubule Plus Ends: Is EB1 Detyrosination Involved? *PLoS One*. 7:e33490. doi:10.1371/journal.pone.0033490.

De Brabander, M., R. Van de Veire, F. Aerts, G. Geuens, M. Borgers, L. Desplenter, and J. DeCree. 1975. Oncodazole (R 17934): a new anti-cancer drug interfering with microtubules. Effects on neoplastic cellscultured in vitro and in vivo. *New York Am. Elsevier*. 509–522.

Brady, S.T. 1985. A novel brain ATPase with properties expected for the fast axonal transport motor. *Nature*. 317:73–75. doi:10.1038/317073a0.

Brady, S.T., R.J. Lasek, and R.D. Allen. 1985. Video microscopy of fast axonal transport in extruded axoplasm: A new model for study of molecular mechanisms. *Cell Motil.* 5:81–101. doi:10.1002/cm.970050203.

Brinkley, W.B.R. 1997. Microtubules: A brief historical perspective. *In* Journal of Structural Biology. Academic Press Inc. 84–86.

Brockstedt, U., K. Dobra, M. Nurminen, and A. Hjerpe. 2002. Immunoreactivity to cell surface syndecans in cytoplasm and nucleus: Tubulin-dependent rearrangements. *Exp. Cell Res.* 274:235–245. doi:10.1006/EXCR.2002.5477.

Browne, T.R., A. Van Langenhove, C.E. Costello, K. Biemann, and D.J. Greenblatt. 1981. Kinetic equivalence of stable-isotope-labeled and unlabeled phenytoin. *Clin. Pharmacol. Ther.* 29:511–515. doi:10.1038/clpt.1981.71.

Brust-Mascher, I., and J.M. Scholey. 2011. Mitotic motors and chromosome segregation: The mechanism of anaphase B. *Biochem. Soc. Trans.* 39:1149–1153. doi:10.1042/BST0391149.

Budhidarmo, R., Y. Nakatani, and C.L. Day. 2012. RINGs hold the key to ubiquitin transfer. *Trends Biochem. Sci.* 37:58–65. doi:10.1016/J.TIBS.2011.11.001.

Buey, R.M., R. Mohan, K. Leslie, T. Walzthoeni, J.H. Missimer, A. Menzel, S. Bjelić, K. Bargsten, I. Grigoriev, I. Smal, E. Meijering, R. Aebersold, A. Akhmanova, and M.O. Steinmetz. 2011. Insights into EB1 structure and the role of its c-terminal domain for discriminating microtubule tips from the lattice. *Mol. Biol. Cell*. 22:2912–2923. doi:10.1091/mbc.E11-01-0017.

Bulinski, J.C., and G.G. Borisy. 1979. Self-assembly of microtubules in extracts of cultured HeLa cells and the identification of HeLa microtubule-associated proteins. *Proc. Natl. Acad. Sci. U. S. A.* 76:293–297. doi:10.1073/pnas.76.1.293.

Butner, K.A., and M.W. Kirschner. 1991. Tau protein binds to microtubules through a flexible array of distributed weak sites. *J. Cell Biol.* 115:717–730. doi:10.1083/JCB.115.3.717.

Capalbo, L., Z.I. Bassi, M. Geymonat, S. Todesca, L. Copoiu, A.J. Enright, G. Callaini, M.G. Riparbelli, L. Yu, J.S. Choudhary, E. Ferrero, S. Wheatley, M.E. Douglas, M. Mishima, and P.P. D'Avino. 2019. The midbody interactome reveals unexpected roles for PP1 phosphatases in cytokinesis. *Nat. Commun. 2019 101*. 10:1–17. doi:10.1038/s41467-019-12507-9.

Carlier, M.F., and D. Pantaloni. 1981. Kinetic Analysis of Guanosine 5'-Triphosphate Hydrolysis Associated with Tubulin Polymerization. *Biochemistry*. 20:1918–1924. doi:10.1021/bi00510a030.

Carmena, M., S. Ruchaud, and W.C. Earnshaw. 2009. Making the Auroras glow: regulation of Aurora A and B kinase function by interacting proteins. *Curr. Opin. Cell Biol.* 21:796–805. doi:10.1016/J.CEB.2009.09.008.

Carmena, M., M. Wheelock, H. Funabiki, and W.C. Earnshaw. 2012. The chromosomal passenger complex (CPC): From easy rider to the godfather of mitosis. *Nat. Rev. Mol. Cell Biol.* 13:789–803. doi:10.1038/nrm3474.

Carter, A.P., C. Cho, L. Jin, and R.D. Vale. 2011. Crystal structure of the dynein motor domain. *Science (80-.).* 331:1159–1165. doi:10.1126/science.1202393.

Carvalho, A., M. Carmena, C. Sambade, W.C. Earnshaw, and S.P. Wheatley. 2003. Survivin is required for stable checkpoint activation in taxol-treated HeLa cells. *J. Cell Sci.* 116:2987–2998. doi:10.1242/jcs.00612.

Caudron, M., G. Bunt, P. Bastiaens, and E. Karsenti. 2005. Spatial coordination of spindle assembly by chromosome-mediated signaling gradients. *Science (80-.).* 309:1373–1376. doi:10.1126/science.1115964.

Chakraborty, M., A. Toleikis, N. Siddiqui, R.A. Cross, and A. Straube. 2020. Activation of cytoplasmic dynein through microtubule crossbridging. *bioRxiv*. 2020.04.13.038950. doi:10.1101/2020.04.13.038950.

Chalfie, M., and J.N. Thomson. 1982. Structural and functional diversity in the neuronal microtubules of Caenorhabditis elegans. *J. Cell Biol.* 93:15–23. doi:10.1083/jcb.93.1.15.

Chang, C.L., Y.J. Chen, C.G. Quintanilla, T.S. Hsieh, and J. Liou. 2018. EB1 binding restricts STIM1 translocation to ER-PM junctions and regulates store-operated Ca2+ entry. *J. Cell Biol.* 217:2047–2058. doi:10.1083/JCB.201711151/VIDEO-2.

Chang, P., and T. Stearns. 2000. δ-Tubulin and ε-tubulin: Two new human centrosomal tubulins reveal new aspects of centrosome structure and function. *Nat. Cell Biol.* 2:30–35. doi:10.1038/71350.

Chen, G., J. Kong, C. Tucker-Burden, M. Anand, Y. Rong, F. Rahman, C.S. Moreno, E.G. Van Meir, C.G. Hadjipanayis, and D.J. Brat. 2014. Human Brat ortholog TRIM3 is a tumor suppressor that regulates asymmetric cell division in glioblastoma. *Cancer Res.* 74:4536. doi:10.1158/0008-5472.CAN-13-3703.

Chen, Z.J., and L.J. Sun. 2009. Nonproteolytic Functions of Ubiquitin in Cell Signaling. *Mol. Cell*. 33:275–286. doi:10.1016/j.molcel.2009.01.014.

Chiang, A.P., J.S. Beck, H.J. Yen, M.K. Tayeh, T.E. Scheetz, R.E. Swiderski, D.Y. Nishimura, T.A. Braun, K.Y.A. Kim, J. Huang, K. Elbedour, R. Carmi, D.C. Slusarski, T.L. Casavant, E.M. Stone, and V.C. Sheffield. 2006. Homozygosity mapping with SNP arrays identifies TRIM32, an E3 ubiquitin ligase, as a Bardet–Biedl syndrome gene (BBS11). *Proc. Natl. Acad. Sci. U. S. A.* 103:6287. doi:10.1073/PNAS.0600158103.

Cho, K.F., T.C. Branon, N.D. Udeshi, S.A. Myers, S.A. Carr, and A.Y. Ting. 2020. Proximity

labeling in mammalian cells with TurboID and split-TurboID. *Nat. Protoc.* 15:3971–3999. doi:10.1038/s41596-020-0399-0.

Choi, Y.K., P. Liu, S.K. Sze, C. Dai, and R.Z. Qi. 2010. CDK5RAP2 stimulates microtubule nucleation by the γ-tubulin ring complex. *J. Cell Biol.* 191:1089–1095. doi:10.1083/jcb.201007030.

Christensen, G.L., C.D. Kelstrup, C. Lyngsø, U. Sarwar, R. Bøgebo, S.P. Sheikh, S. Gammeltoft, J. V. Olsen, and J.L. Hansen. 2010. Quantitative phosphoproteomics dissection of seven-transmembrane receptor signaling using full and biased agonists. *Mol. Cell. Proteomics*. 9:1540–1553. doi:10.1074/MCP.M900550-MCP200.

Chu, C.W., F. Hou, J. Zhang, L. Phu, A. V. Loktev, D.S. Kirkpatrick, P.K. Jackson, Y. Zhao, and H. Zou. 2011. A novel acetylation of β-tubulin by San modulates microtubule polymerization via down-regulating tubulin incorporation. *Mol. Biol. Cell*. 22:448–456. doi:10.1091/mbc.E10-03-0203.

Clague, M.J., I. Barsukov, J.M. Coulson, H. Liu, D.J. Rigden, and S. Urbé. 2013. Deubiquitylases from genes to organism. *Physiol. Rev.* 93:1289–1315. doi:10.1152/PHYSREV.00002.2013/SUPPL_FILE/TABLES2.PDF.

Clague, M.J., C. Heride, and S. Urbé. 2015. The demographics of the ubiquitin system. *Trends Cell Biol.* 25:417–426. doi:10.1016/j.tcb.2015.03.002.

Clague, M.J., S. Urbé, and D. Komander. 2019. Breaking the chains: deubiquitylating enzyme specificity begets function. *Nat. Rev. Mol. Cell Biol.* 20:338–352. doi:10.1038/s41580-019-0099-1.

Clancy, A., C. Heride, A. Pinto-Fernández, H. Elcocks, A. Kallinos, K.J. Kayser-Bricker, W. Wang, V. Smith, S. Davis, S. Fessler, C. McKinnon, M. Katz, T. Hammonds, N.P. Jones, J. O'Connell, B. Follows, S. Mischke, J.A. Caravella, S. Ioannidis, C. Dinsmore, S. Kim, A. Behrens, D. Komander, B.M. Kessler, S. Urbé, and M.J. Clague. 2021. The deubiquitylase USP9X controls ribosomal stalling. *J. Cell Biol.* 220. doi:10.1083/JCB.202004211.

Clark, R.H., J.C. Stinchcombe, A. Day, E. Blott, S. Booth, G. Bossi, T. Hamblin, E.G. Davies, and G.M. Griffiths. 2003. Adaptor protein 3-dependent microtubule-mediated movement of lytic granules to the immunological synapse. *Nat. Immunol.* 4:1111–1120. doi:10.1038/ni1000.

Consolati, T., J. Locke, J. Roostalu, Z.A. Chen, J. Gannon, J. Asthana, W.M. Lim, F. Martino, M.A. Cvetkovic, J. Rappsilber, A. Costa, and T. Surrey. 2020. Microtubule Nucleation Properties of Single Human γTuRCs Explained by Their Cryo-EM Structure. *Dev. Cell*. 53:603-617.e8. doi:10.1016/j.devcel.2020.04.019.

Cook, W.J., L.C. Jeffrey, E. Kasperek, and C.M. Pickart. 1994. Structure of tetraubiquitin shows how multiubiquitin chains can be formed. *J. Mol. Biol.* 236:601–609. doi:10.1006/jmbi.1994.1169.

Cooke, C.A., M.M.S. Heck, and W.C. Earnshaw. 1987. The inner centromere protein (INCENP) antigens: movement from inner centromere to midbody during mitosis. *J. Cell*

Biol. 105:2053. doi:10.1083/JCB.105.5.2053.

Coombes, C., A. Yamamoto, M. McClellan, T.A. Reid, M. Plooster, G.W.G. Luxton, J. Alper, J. Howard, and M.K. Gardner. 2016. Mechanism of microtubule lumen entry for the α-tubulin acetyltransferase enzyme αTAT1. *Proc. Natl. Acad. Sci.* 113:E7176–E7184. doi:10.1073/pnas.1605397113.

Cox, J., and M. Mann. 2008. MaxQuant enables high peptide identification rates, individualized p.p.b.-range mass accuracies and proteome-wide protein quantification. *Nat. Biotechnol.* 26:1367–1372. doi:10.1038/nbt.1511.

Cox, J., and M. Mann. 2009. Computational Principles of Determining and Improving Mass Precision and Accuracy for Proteome Measurements in an Orbitrap. *J. Am. Soc. Mass Spectrom.* 20:1477–1485. doi:10.1016/j.jasms.2009.05.007.

Cox, J., A. Michalski, and M. Mann. 2011a. Software Lock Mass by Two-Dimensional Minimization of Peptide Mass Errors. *J. Am. Soc. Mass Spectrom.* 22:1373–1380. doi:10.1007/s13361-011-0142-8.

Cox, J., N. Neuhauser, A. Michalski, R.A. Scheltema, J. V. Olsen, and M. Mann. 2011b. Andromeda: A peptide search engine integrated into the MaxQuant environment. *J. Proteome Res.* 10:1794–1805. doi:10.1021/pr101065j.

Cox, T.C. 2012. The microtubule-associated C-I subfamily of TRIM proteins and the regulation of polarized cell responses. *Adv. Exp. Med. Biol.* 770:105–118. doi:10.1007/978-1-4614-5398-7_8.

Cstorer, A., and R. Ménard. 1994. [33] Catalytic mechanism in papain family of cysteine peptidases. *Methods Enzymol.* 244:486–500. doi:10.1016/0076-6879(94)44035-2.

Cunningham, C.N., J.M. Baughman, L. Phu, J.S. Tea, C. Yu, M. Coons, D.S. Kirkpatrick, B. Bingol, and J.E. Corn. 2015. USP30 and parkin homeostatically regulate atypical ubiquitin chains on mitochondria. *Nat. Cell Biol. 2014 172*. 17:160–169. doi:10.1038/ncb3097.

D'Ydewalle, C., J. Krishnan, D.M. Chiheb, P. Van Damme, J. Irobi, A.P. Kozikowski, P. Vanden Berghe, V. Timmerman, W. Robberecht, and L. Van Den Bosch. 2011. HDAC6 inhibitors reverse axonal loss in a mouse model of mutant HSPB1-induced Charcot-Marie-Tooth disease. *Nat. Med.* 17:968–974. doi:10.1038/nm.2396.

Dalbeth, N., T.J. Lauterio, and H.R. Wolfe. 2014. Mechanism of action of colchicine in the treatment of gout. *Clin. Ther.* 36:1465–1479. doi:10.1016/j.clinthera.2014.07.017.

Darling, S. 2017. Profiling deubiquitylase activity during the cell cycle reveals phosphorylation-dependent regulation of USP7 activity at G1/S.

Davis, J.Q., and V. Bennett. 1984. Brain ankyrin. A membrane-associated protein with binding sites for spectrin, tubulin, and the cytoplasmic domain of the erythrocyte anion channel. *J. Biol. Chem.* 259:13550–13559. doi:10.1016/S0021-9258(18)90728-3.

Delgehyr, N., J. Sillibourne, and M. Bornens. 2005. Microtubule nucleation and anchoring at the centrosome are independent processes linked by ninein function. *J. Cell Sci.* 118:1565–1575. doi:10.1242/jcs.02302.

Delphin, C., D. Bouvier, M. Seggio, E. Couriol, Y. Saoudi, E. Denarier, C. Bosc, O. Valiron, M. Bisbal, I. Arnal, and A. Andrieux. 2012. MAP6-F is a temperature sensor that directly binds to and protects microtubules from cold-induced depolymerization. *J. Biol. Chem.* 287:35127–35138. doi:10.1074/jbc.M112.398339.

Deng, L., C. Wang, E. Spencer, L. Yang, A. Braun, J. You, C. Slaughter, C. Pickart, and Z.J. Chen. 2000. Activation of the IκB Kinase Complex by TRAF6 Requires a Dimeric Ubiquitin-Conjugating Enzyme Complex and a Unique Polyubiquitin Chain. *Cell*. 103:351–361. doi:10.1016/S0092-8674(00)00126-4.

Desai, A., and T.J. Mitchison. 1997. Microtubule polymerisation dynamics. *Annu. Rev. Cell Dev. Biol.* 13:83–117. doi:10.1146/annurev.cellbio.13.1.83.

Deshaies, R.J., and C.A.P. Joazeiro. 2009. RING domain E3 ubiquitin ligases. *Annu. Rev. Biochem.* 78:399–434. doi:10.1146/annurev.biochem.78.101807.093809.

Van Diepen, M.T., G.E. Spencer, J. Van Minnen, Y. Gouwenberg, J. Bouwman, A.B. Smit, and R.E. Van Kesteren. 2005. The molluscan RING-finger protein L-TRIM is essential for neuronal outgrowth. *Mol. Cell. Neurosci.* 29:74–81. doi:10.1016/J.MCN.2005.01.005.

Dikic, I., S. Wakatsuki, and K.J. Walters. 2009. Ubiquitin-binding domains from structures to functions. *Nat. Rev. Mol. Cell Biol.* 10:659–671. doi:10.1038/nrm2767.

Dimitrov, A., M. Quesnoit, S. Moutel, I. Cantaloube, C. Poüs, and F. Perez. 2008. Detection of GTP-tubulin conformation in vivo reveals a role for GTP remnants in microtubule rescues. *Science (80-.).* 322:1353–1356. doi:10.1126/science.1165401.

Ding, L., J. Cao, W. Lin, H. Chen, X. Xiong, H. Ao, M. Yu, J. Lin, and Q. Cui. 2020. The roles of cyclin-dependent kinases in cell-cycle progression and therapeutic strategies in human breast cancer. *Int. J. Mol. Sci.* 21. doi:10.3390/ijms21061960.

Ditchfield, C., V.L. Johnson, A. Tighe, R. Ellston, C. Haworth, T. Johnson, A. Mortlock, N. Keen, and S.S. Taylor. 2003. Aurora B couples chromosome alignment with anaphase by targeting BubR1, Mad2, and Cenp-E to kinetochores. *J. Cell Biol.* 161:267–280. doi:10.1083/jcb.200208091.

Dixit, R., B. Barnett, J.E. Lazarus, M. Tokito, Y.E. Goldman, and E.L.F. Holzbaur. 2009. Microtubule plus-end tracking by CLIP-170 requires EB1. *Proc. Natl. Acad. Sci. U. S. A.* doi:10.1073/pnas.0807614106.

Dompierre, J.P., J.D. Godin, B.C. Charrin, F.P. Cordelieres, S.J. King, S. Humbert, and F. Saudou. 2007. Histone Deacetylase 6 Inhibition Compensates for the Transport Deficit in Huntington's Disease by Increasing Tubulin Acetylation. *J. Neurosci.* 27:3571–3583. doi:10.1523/JNEUROSCI.0037-07.2007.

Donoso, J.A., L.S. Green, I.E. Heller-Bettinger, and F.E. Samson. 1977. Action of the Vinca Alkaloids Vincristine, Vinblastine, and Desacetyl Vinblastine Amide on Axonal Fibrillar Organelles in Vitro. *Cancer Res.* 37:1401–1407.

Doodhi, H., T. Kasciukovic, L. Clayton, and T.U. Tanaka. 2021. Aurora b switches relative strength of kinetochore–microtubule attachment modes for error correction. *J. Cell Biol.* 220. doi:10.1083/jcb.202011117.

Dósa, A., and T. Csizmadia. 2022. The role of K63-linked polyubiquitin in several types of autophagy. *Biol. Futur.* 73:137–148. doi:10.1007/s42977-022-00117-4.

Douglas, M.E., T. Davies, N. Joseph, and M. Mishima. 2010. Aurora B and 14-3-3 Coordinately Regulate Clustering of Centralspindlin during Cytokinesis. *Curr. Biol.* 20:927–933. doi:10.1016/J.CUB.2010.03.055.

Duellberg, C., N.I. Cade, D. Holmes, and T. Surrey. 2016. The size of the EB cap determines instantaneous microtubule stability. *Elife*. 5. doi:10.7554/ELIFE.13470.

Duerr, A., D. Pallas, and F. Solomon. 1981. Molecular analysis of cytoplasmic microtubules in situ: Identification of both widespread and specific proteins. *Cell*. 24:203–211. doi:10.1016/0092-8674(81)90516-X.

Dunn, S., E.E. Morisson, T.B. Liverpool, C. Molina-París, R.A. Cross, M.C. Alonso, and M. Peckham. 2008. Differential trafficking of Kif5c on tyrosinated and detyrosinated microtubules in live cells. *J. Cell Sci.* 121:1085–1095. doi:10.1242/jcs.026492.

Dunsch, A.K., E. Linnane, F.A. Barr, and U. Gruneberg. 2011. The astrin-kinastrin/SKAP complex localizes to microtubule plus ends and facilitates chromosome alignment. *J. Cell Biol.* 192:959–968. doi:10.1083/jcb.201008023.

Ebneth, A., R. Godemann, K. Stamer, S. Illenberger, B. Trinczek, E.M. Mandelkow, and E. Mandelkow. 1998. Overexpression of tau protein inhibits kinesin-dependent trafficking of vesicles, mitochondria, and endoplasmic reticulum: Implications for Alzheimer's disease. *J. Cell Biol.* 143:777–794. doi:10.1083/jcb.143.3.777.

Eddé, B., J. Rossier, J.P. Le Caer, E. Desbruyères, F. Gros, and P. Denoulet. 1990. Posttranslational glutamylation of α-tubulin. *Science (80-.).* 247:83–85. doi:10.1126/science.1967194.

Edman, P. 1949. A method for the determination of amino acid sequence in peptides. *Arch. Biochem.* 22:475.

Edman, P., and G. Begg. 1967. A Protein Sequenator. *In* European Journal of Biochemistry. Springer Berlin Heidelberg. 80–91.

El-Husseini, A.E.D., D. Kwasnicka, T. Yamada, S. Hirohashi, and S.R. Vincent. 2000. BERP, a Novel Ring Finger Protein, Binds to α-Actinin-4. *Biochem. Biophys. Res. Commun.* 267:906–911. doi:10.1006/BBRC.1999.2045.

El-Husseini, A.E.D., and S.R. Vincent. 1999. Cloning and characterization of a novel RING finger protein that interacts with class V myosins. *J. Biol. Chem.* 274:19771–19777. doi:10.1074/jbc.274.28.19771.

Elowe, S., S. Hümmer, A. Uldschmid, X. Li, and E.A. Nigg. 2007. Tension-sensitive Plk1 phosphorylation on BubR1 regulates the stability of kinetochore-microtubule interactions. *Genes Dev.* 21:2205–2219. doi:10.1101/gad.436007.

Endow, S.A., F.J. Kull, and H. Liu. 2010. Kinesins at a glance. *J. Cell Sci.* 123:3420. doi:10.1242/jcs.082667doi:10.

Eng, J.K., A.L. McCormack, and J.R. Yates. 1994. An approach to correlate tandem mass spectral data of peptides with amino acid sequences in a protein database. *J. Am. Soc.*

Mass Spectrom. 5:976–989. doi:10.1016/1044-0305(94)80016-2.

Erck, C., L. Peris, A. Andrieux, C. Meissirel, A.D. Gruber, M. Vernet, A. Schweitzer, Y. Saoudi, H. Pointu, C. Bosc, P.A. Salin, D. Job, and J. Wehland. 2005. A vital role of tubulin-tyrosine-ligase for neuronal organization. *Proc. Natl. Acad. Sci. U. S. A.* 102:7853–7858. doi:10.1073/pnas.0409626102.

Erickson, B.K., J. Mintseris, D.K. Schweppe, J. Navarrete-Perea, A.R. Erickson, D.P. Nusinow, J.A. Paulo, and S.P. Gygi. 2019. Active Instrument Engagement Combined with a Real-Time Database Search for Improved Performance of Sample Multiplexing Workflows. *J. Proteome Res.* 18:1299–1306. doi:10.1021/ACS.JPROTEOME.8B00899/SUPPL_FILE/PR8B00899_SI_004.XLSX.

Eshun-Wilson, L., R. Zhang, D. Portran, M. V. Nachury, D.B. Toso, T. Löhr, M. Vendruscolo, M. Bonomi, J.S. Fraser, and E. Nogales. 2019. Effects of α-tubulin acetylation on microtubule structure and stability. *Proc. Natl. Acad. Sci. U. S. A.* 116:10366–10371. doi:10.1073/pnas.1900441116.

Esposito, D., J. Dudley-Fraser, A. Garza-Garcia, and K. Rittinger. 2022. Divergent self-association properties of paralogous proteins TRIM2 and TRIM3 regulate their E3 ligase activity. *Nat. Commun.* 13. doi:10.1038/s41467-022-35300-7.

Ezratty, E.J., M.A. Partridge, and G.G. Gundersen. 2005. Microtubule-induced focal adhesion disassembly is mediated by dynamin and focal adhesion kinase. *Nat. Cell Biol.* 7:581–590. doi:10.1038/ncb1262.

Faesen, A.C., M.P.A. Luna-Vargas, P.P. Geurink, M. Clerici, R. Merkx, W.J. Van Dijk, D.S. Hameed, F. El Oualid, H. Ovaa, and T.K. Sixma. 2011. The differential modulation of USP activity by internal regulatory domains, interactors and eight ubiquitin chain types. *Chem. Biol.* 18:1550–1561. doi:10.1016/J.CHEMBIOL.2011.10.017.

Fawcett, D.W., and K.R. Porter. 1954. A study of the fine structure of ciliated epithelia. *J. Morphol.* 94:221–281. doi:10.1002/jmor.1050940202.

Feng, C., J.M. Cleary, G.O. Kothe, M.C. Stone, A.T. Weiner, J.I. Hertzler, W.O. Hancock, and M.M. Rolls. 2021. Trim9 and Klp61F promote polymerization of new dendritic microtubules along parallel microtubules. *J. Cell Sci.* 134. doi:10.1242/jcs.258437.

Fenn, J.B., M. Mann, C.K. Meng, S.F. Wong, and C.M. Whitehouse. 1989. Electrospray ionization for mass spectrometry of large biomolecules. *Science (80-.).* 246:64–71. doi:10.1126/science.2675315.

Fernández-Barrera, J., and M.A. Alonso. 2018. Coordination of microtubule acetylation and the actin cytoskeleton by formins. *Cell. Mol. Life Sci.* 75:3181–3191. doi:10.1007/s00018-018-2855-3.

Fernandez-Valenzuela, J.J., R. Sanchez-Varo, C. Muñoz-Castro, V. De Castro, E. Sanchez-Mejias, V. Navarro, S. Jimenez, C. Nuñez-Diaz, A. Gomez-Arboledas, I. Moreno-Gonzalez, M. Vizuete, J.C. Davila, J. Vitorica, and A. Gutierrez. 2020. Enhancing microtubule stabilization rescues cognitive deficits and ameliorates pathological phenotype in an amyloidogenic Alzheimer's disease model. *Sci. Rep.* 10:14776.

doi:10.1038/s41598-020-71767-4.

Ferreira, L.T., B. Orr, G. Rajendraprasad, A.J. Pereira, C. Lemos, J.T. Lima, C. Guasch Boldú, J.G. Ferreira, M. Barisic, and H. Maiato. 2020. α-Tubulin detyrosination impairs mitotic error correction by suppressing MCAK centromeric activity. *J. Cell Biol.* 219. doi:10.1083/jcb.201910064.

Findeisen, P., S. Mühlhausen, S. Dempewolf, J. Hertzog, A. Zietlow, T. Carlomagno, and M. Kollmar. 2014. Six subgroups and extensive recent duplications characterize the evolution of the eukaryotic tubulin protein family. *Genome Biol. Evol.* 6:2274–88. doi:10.1093/gbe/evu187.

Fiorentini, F., D. Esposito, and K. Rittinger. 2020. Does it take two to tango? RING domain self-association and activity in TRIM E3 ubiquitin ligases. *Biochem. Soc. Trans.* 48:2615–2624. doi:10.1042/BST20200383.

Fong, K.W., F.K.C. Au, Y. Jia, S. Yang, L. Zhou, and R.Z. Qi. 2017. Microtubule plus-end tracking of end-binding protein 1 (EB1) is regulated by CDK5 regulatory subunit-associated protein 2. *J. Biol. Chem.* 292:7675–7687. doi:10.1074/jbc.M116.759746.

Fourest-Lieuvin, A., L. Peris, V. Gache, I. Garcia-Saez, C. Juillan-Binard, V. Lantez, and D. Job. 2006. Microtubule regulation in mitosis: Tubulin phosphorylation by the cyclin-dependent kinase Cdk1. *Mol. Biol. Cell*. 17:1041–1050. doi:10.1091/mbc.E05-07-0621.

Fox, J.C., A.E. Howard, J.D. Currie, S.L. Rogers, and K.C. Slep. 2014. The XMAP215 family drives microtubule polymerization using a structurally diverse TOG array. *Mol. Biol. Cell*. 25:2375–2392. doi:10.1091/mbc.E13-08-0501.

Friedman, J.R., B.M. Webster, D.N. Mastronarde, K.J. Verhey, and G.K. Voeltz. 2010. ER sliding dynamics and ER-mitochondrial contacts occur on acetylated microtubules. *J. Cell Biol.* 190:363–375. doi:10.1083/jcb.200911024.

Frosk, P., T. Weiler, E. Nylen, T. Sudha, C.R. Greenberg, K. Morgan, T.M. Fujiwara, and K. Wrogemann. 2002. Limb-Girdle Muscular Dystrophy Type 2H Associated with Mutation in TRIM32, a Putative E3-Ubiquitin–Ligase Gene. *Am. J. Hum. Genet.* 70:663. doi:10.1086/339083.

Fu, J., I.M. Hagan, and D.M. Glover. 2015. The centrosome and its duplication cycle. *Cold Spring Harb. Perspect. Med.* 5:a015800. doi:10.1101/cshperspect.a015800.

Fukata, Y., T.J. Itoh, T. Kimura, C. Ménager, T. Nishimura, T. Shiromizu, H. Watanabe, N. Inagaki, A. Iwamatsu, H. Hotani, and K. Kaibuchi. 2002. CRMP-2 binds to tubulin heterodimers to promote microtubule assembly. *Nat. Cell Biol. 2002 48*. 4:583–591. doi:10.1038/ncb825.

Fung, T.K., and R.Y.C. Poon. 2005. A roller coaster ride with the mitotic cyclins. *Semin. Cell Dev. Biol.* 16:335–342. doi:10.1016/J.SEMCDB.2005.02.014.

Gache, V., P. Waridel, C. Winter, A. Juhem, M. Schroeder, A. Shevchenko, and A. V. Popov. 2010. Xenopus meiotic microtubule-associated interactome. *PLoS One*. 5. doi:10.1371/journal.pone.0009248.

Gadadhar, S., S. Bodakuntla, K. Natarajan, and C. Janke. 2017a. The tubulin code at a glance.

J. Cell Sci. 130:1347–1353. doi:10.1242/jcs.199471.

Gadadhar, S., H. Dadi, S. Bodakuntla, A. Schnitzler, I. Bièche, F. Rusconi, and C. Janke. 2017b. Tubulin glycylation controls primary cilia length. *J. Cell Biol.* 216:2701–2713. doi:10.1083/jcb.201612050.

Galjart, N. 2010. Plus-End-Tracking Proteins and Their Interactions at Microtubule Ends. *Curr. Biol.* 20:R528–R537. doi:10.1016/J.CUB.2010.05.022.

Galmes, R., A. Houcine, A.R. Vliet, P. Agostinis, C.L. Jackson, and F. Giordano. 2016. ORP5/ORP8 localize to endoplasmic reticulum–mitochondria contacts and are involved in mitochondrial function. *EMBO Rep.* 17:800–810. doi:10.15252/embr.201541108.

Ganguly, A., R. Bhattacharya, and F. Cabral. 2008. Cell cycle dependent degradation of MCAK: Evidence against a role in anaphase chromosome movement. *Cell Cycle*. 7:3187–3193. doi:10.4161/cc.7.20.6814.

Gao, J., L. Huo, X. Sun, M. Liu, D. Li, J.T. Dong, and J. Zhou. 2008. The tumor suppressor CYLD regulates microtubule dynamics and plays a role in cell migration. *J. Biol. Chem.* 283:8802–8809. doi:10.1074/jbc.M708470200.

Gardner, M.K., M. Zanic, and J. Howard. 2013. Microtubule catastrophe and rescue. *Curr. Opin. Cell Biol.* 25:14–22. doi:10.1016/j.ceb.2012.09.006.

Garner, C.C., A. Garner, G. Huber, C. Kozak, and A. Matus. 1990. Molecular Cloning of Microtubule-Associated Protein 1 (MAP1A) and Microtubule-Associated Protein 5 (MAP1B): Identification of Distinct Genes and Their Differential Expression in Developing Brain. *J. Neurochem.* 55:146–154. doi:10.1111/j.1471-4159.1990.tb08832.x.

Gassmann, R., A. Carvalho, A.J. Henzing, S. Ruchaud, D.F. Hudson, R. Honda, E.A. Nigg, D.L. Gerloff, and W.C. Earnshaw. 2004. Borealin a novel chromosomal passenger required for stability of the bipolar mitotic spindle. *J. Cell Biol.* 166:179–191. doi:10.1083/JCB.200404001.

Gelfman, S., S. Dugger, C. de Araujo Martins Moreno, Z. Ren, C.J. Wolock, N.A. Shneider, H. Phatnani, E.T. Cirulli, B.N. Lasseigne, T. Harris, T. Maniatis, G.A. Rouleau, R.H. Brown, A.D. Gitler, R.M. Myers, S. Petrovski, A. Allen, D.B. Goldstein, and M.B. Harms. 2019. A new approach for rare variation collapsing on functional protein domains implicates specific genic regions in ALS. *Genome Res.* 29:809–818. doi:10.1101/GR.243592.118/-/DC1.

Genova, M., L. Grycova, V. Puttrich, M.M. Magiera, Z. Lansky, C. Janke, and M. Braun. 2023. Tubulin polyglutamylation differentially regulates microtubule-interacting proteins. *EMBO J.* 42. doi:10.15252/EMBJ.2022112101.

Gerlitz, G., O. Reiner, and M. Bustin. 2013. Microtubule dynamics alter the interphase nucleus. *Cell. Mol. Life Sci.* 70:1255–1268. doi:10.1007/s00018-012-1200-5.

Gholkar, A.A., S. Senese, Y.C. Lo, E. Vides, E. Contreras, E. Hodara, J. Capri, J.P. Whitelegge, and J.Z. Torres. 2016. The X-Linked-Intellectual-Disability-Associated Ubiquitin Ligase Mid2 Interacts with Astrin and Regulates Astrin Levels to Promote Cell Division. *Cell Rep.* 14:180–188. doi:10.1016/J.CELREP.2015.12.035.

Giansanti, P., L. Tsiatsiani, T.Y. Low, and A.J.R. Heck. 2016. Six alternative proteases for mass spectrometry-based proteomics beyond trypsin. *Nat. Protoc.* 11:993–1006. doi:10.1038/nprot.2016.057.

Gibbons, I.R. 1963. STUDIES ON THE PROTEIN COMPONENTS OF CILIA FROM TETRAHYMENA PYRIFORMIS. *Proc. Natl. Acad. Sci. United States*. 50:1002–1010. doi:10.1073/pnas.50.5.1002.

Gibbons, I.R. 1981. Cilia and flagella of eukaryotes. *J. Cell Biol.* 91. doi:10.1083/jcb.91.3.107s.

Gibbons, I.R., and A.J. Rowe. 1965. Dynein: A protein with adenosine triphosphatase activity from cilia. *Science (80-.).* 149:424–426. doi:10.1126/science.149.3682.424.

Gill, S.R., T.A. Schroer, I. Szilak, E.R. Steuer, M.P. Sheetz, and D.W. Cleveland. 1991. Dynactin, a conserved, ubiquitously expressed component of an activator of vesicle motility mediated by cytoplasmic dynein. *J. Cell Biol.* 115:1639–1650. doi:10.1083/jcb.115.6.1639.

Gillingham, A.K., and S. Munro. 2000. The PACT domain, a conserved centrosomal targeting motif in the coiled-coil proteins AKAP450 and pericentrin. *EMBO Rep.* 1:524. doi:10.1093/EMBO-REPORTS/KVD105.

Giustiniani, J., V. Daire, I. Cantaloube, G. Durand, C. Poüs, D. Perdiz, and A. Baillet. 2009. Tubulin acetylation favors Hsp90 recruitment to microtubules and stimulates the signaling function of the Hsp90 clients Akt/PKB and p53. *Cell. Signal.* 21:529–539. doi:10.1016/j.cellsig.2008.12.004.

Godena, V.K., N. Brookes-Hocking, A. Moller, G. Shaw, M. Oswald, R.M. Sancho, C.C.J. Miller, A.J. Whitworth, and K.J. De Vos. 2014. Increasing microtubule acetylation rescues axonal transport and locomotor deficits caused by LRRK2 Roc-COR domain mutations. *Nat. Commun. 2014 51*. 5:1–11. doi:10.1038/ncomms6245.

Goldspink, D.A., C. Rookyard, B.J. Tyrrell, J. Gadsby, J. Perkins, E.K. Lund, N. Galjart, P. Thomas, T. Wileman, and M.M. Mogensen. 2017. Ninein is essential for apico-basal microtubule formation and CLIP-170 facilitates its redeployment to non-centrosomal microtubule organizing centres. *Open Biol.* 7. doi:10.1098/rsob.160274.

Goodenough, U., and J. Heuser. 1984. Structural comparison of purified dynein proteins with in situ dynein arms. *J. Mol. Biol.* 180:1083–1118. doi:10.1016/0022-2836(84)90272-9.

Goshima, G., M. Mayer, N. Zhang, N. Stuurman, and R.D. Vale. 2008. Augmin: A protein complex required for centrosome-independent microtubule generation within the spindle. *J. Cell Biol.* 181:421–429. doi:10.1083/jcb.200711053.

Goto, H., T. Kiyono, Y. Tomono, A. Kawajiri, T. Urano, K. Furukawa, E.A. Nigg, and M. Inagaki. 2005. Complex formation of Plk1 and INCENP required for metaphase–anaphase transition. *Nat. Cell Biol. 2005 82*. 8:180–187. doi:10.1038/ncb1350.

Grayson, M.A. 2011. John Bennett Fenn: a curious road to the prize. *J. Am. Soc. Mass Spectrom.* 22:1301–1308. doi:10.1007/s13361-011-0136-6.

Greer, C.A., and G.M. Shepherd. 1982. Selective synthesis and utilization of flagellar tubulin. The multi-tubulin hypothesis. *In* Brain Research. 156–161.

Grover, S., and E. Hamel. 1994. The magnesium–GTP interaction in microtubule assembly. *Eur. J. Biochem.* 222:163–172. doi:10.1111/j.1432-1033.1994.tb18854.x.

Gruneberg, U., R. Neef, R. Honda, E.A. Nigg, and F.A. Barr. 2004. Relocation of Aurora B from centromeres to the central spindle at the metaphase to anaphase transition requires MKlp2. *J. Cell Biol.* 166:167–172. doi:10.1083/jcb.200403084.

Gundersen, G.G., and J.C. Bulinski. 1986. Distribution of tyrosinated and nontyrosinated alpha-tubulin during mitosis. *J. Cell Biol.* 102:1118–26. doi:10.1083/jcb.102.3.1118.

Gundersen, G.G., M.H. Kalnoski, and J.C. Bulinski. 1984. Distinct populations of microtubules: Tyrosinated and nontyrosinated alpha tubulin are distributed differently in vivo. *Cell*. 38:779–789. doi:10.1016/0092-8674(84)90273-3.

Gygi, S.P., G.L. Corthals, Y. Zhang, Y. Rochon, and R. Aebersold. 2000. Evaluation of two-dimensional gel electrophoresis-based proteome analysis technology. *Proc. Natl. Acad. Sci. U. S. A.* 97:9390–9395. doi:10.1073/pnas.160270797.

Gygi, S.P., B. Rist, S.A. Gerber, F. Turecek, M.H. Gelb, and R. Aebersold. 1999. Quantitative analysis of complex protein mixtures using isotope-coded affinity tags. *Nat. Biotechnol.* 17:994–999. doi:10.1038/13690.

Habura, A., I. Tikhonenko, R.L. Chisholm, and M.P. Koonce. 1999. Interaction mapping of a dynein heavy chain. Identification of dimerization and intermediate-chain binding domains. *J. Biol. Chem.* 274:15447–15453. doi:10.1074/jbc.274.22.15447.

Haglund, K., S. Sigismund, S. Polo, I. Szymkiewicz, P.P. Di Fiore, and I. Dikic. 2003. Multiple monoubiquitination of RTKs is sufficient for their endocytosis and degradation. *Nat. Cell Biol. 2003 55*. 5:461–466. doi:10.1038/ncb983.

Harrigan, J.A., X. Jacq, N.M. Martin, and S.P. Jackson. 2017. Deubiquitylating enzymes and drug discovery: emerging opportunities. *Nat. Publ. Gr.* 17. doi:10.1038/nrd.2017.152.

Hatakeyama, S. 2011. TRIM proteins and cancer. *Nat. Rev. Cancer 2011 1111*. 11:792–804. doi:10.1038/nrc3139.

Hatakeyama, S. 2017. TRIM Family Proteins: Roles in Autophagy, Immunity, and Carcinogenesis. *Trends Biochem. Sci.* 42:297–311. doi:10.1016/J.TIBS.2017.01.002.

Hausrat, T.J., J. Radwitz, F.L. Lombino, P. Breiden, and M. Kneussel. 2021. Alpha- and beta-tubulin isotypes are differentially expressed during brain development. *Dev. Neurobiol.* 81:333–350. doi:10.1002/DNEU.22745.

Heald, R., and A. Khodjakov. 2015. Thirty years of search and capture: The complex simplicity of mitotic spindle assembly. *J. Cell Biol.* 211:1103. doi:10.1083/JCB.201510015.

Hendricks, M., and S. Jesuthasan. 2009. PHR regulates growth cone pausing at intermediate targets through microtubule disassembly. *J. Neurosci.* 29:6593–6598. doi:10.1523/JNEUROSCI.1115-09.2009.

Henzel, W.J., T.M. Billeci, J.T. Stults, S.C. Wong, C. Grimley, and C. Watanabe. 1993. Identifying proteins from two-dimensional gels by molecular mass searching of peptide fragments in protein sequence databases. *In* Proceedings of the National Academy of Sciences of the United States of America. National Academy of Sciences. 5011–5015.

Henzel, W.J., C. Watanabe, and J.T. Stults. 2003. Protein identification: The origins of peptide mass fingerprinting. *J. Am. Soc. Mass Spectrom.* 14:931–942. doi:10.1016/S1044-0305(03)00214-9.

Heride, C., D.J. Rigden, E. Bertsoulaki, D. Cucchi, E. De Smaele, M.J. Clague, and S. Urbé. 2016. The centrosomal deubiquitylase USP21 regulates Gli1 transcriptional activity and stability. *J. Cell Sci.* 129:4001. doi:10.1242/JCS.188516.

Herzog, W., and K. Weber. 1978. Fractionation of Brain Microtubule-Associated Proteins: Isolation of Two Different Proteins which Stimulate Tubulin Polymerization in vitro. *Eur. J. Biochem.* 92:1–8. doi:10.1111/j.1432-1033.1978.tb12716.x.

Hicke, L. 2001. Protein regulation by monoubiquitin. *Nat. Rev. Mol. Cell Biol.* 2:195–201. doi:10.1038/35056583.

Hino, M., I. Kijima-Suda, Y. Nagai, and H. Hosoya. 2003. Glycosylation of the alpha and beta tubulin by sialyloligosaccharides. *Zoolog. Sci.* 20:709–715. doi:10.2108/zsj.20.709.

Hipp, M.S., P. Kasturi, and F.U. Hartl. 2019. The proteostasis network and its decline in ageing. *Nat. Rev. Mol. Cell Biol.* 20:421–435. doi:10.1038/s41580-019-0101-y.

Hirota, T., J.J. Lipp, B.H. Toh, and J.M. Peters. 2005. Histone H3 serine 10 phosphorylation by Aurora B causes HP1 dissociation from heterochromatin. *Nat. 2005 4387071*. 438:1176–1180. doi:10.1038/nature04254.

Hjerpe, R., F. Aillet, F. Lopitz-Otsoa, V. Lang, P. England, and M.S. Rodriguez. 2009. Efficient protection and isolation of ubiquitylated proteins using tandem ubiquitin-binding entities. *EMBO Rep.* 10:1250–1258. doi:10.1038/EMBOR.2009.192.

Hochegger, H., N. Hégarat, and J.B. Pereira-Leal. 2013. Aurora at the pole and equator: Overlapping functions of Aurora kinases in the mitotic spindle. *Open Biol.* 3. doi:10.1098/rsob.120185.

Hoebeke, J., G. Van Nijen, and M. De Brabander. 1976. Interaction of oncodazole (R 17934), a new anti-tumoral drug, with rat brain tubulin. *Biochem. Biophys. Res. Commun.* 69:319–324. doi:10.1016/0006-291X(76)90524-6.

Holt, L.J., B.B. Tuch, J. Villen, A.D. Johnson, S.P. Gygi, and D.O. Morgan. 2009. Global analysis of cdk1 substrate phosphorylation sites provides insiqhts into evolution. *Science (80-.).* 325:1682–1686. doi:10.1126/SCIENCE.1172867/SUPPL_FILE/HOLT-SOM.PDF.

Honda, R., R. Körner, and E.A. Nigg. 2003. Exploring the functional interactions between Aurora B, INCENP, and survivin in mitosis. *Mol. Biol. Cell*. 14:3325–3341. doi:10.1091/mbc.E02-11-0769.

Honnappa, S., S.M. Gouveia, A. Weisbrich, F.F. Damberger, N.S. Bhavesh, H. Jawhari, I. Grigoriev, F.J.A. van Rijssel, R.M. Buey, A. Lawera, I. Jelesarov, F.K. Winkler, K. Wüthrich, A. Akhmanova, and M.O. Steinmetz. 2009. An EB1-Binding Motif Acts as a Microtubule Tip Localization Signal. *Cell*. 138:366–376. doi:10.1016/j.cell.2009.04.065.

Hooikaas, P.J., M. Martin, T. Mühlethaler, G.J. Kuijntjes, C.A.E. Peeters, E.A. Katrukha, L. Ferrari, R. Stucchi, D.G.F. Verhagen, W.E. Van Riel, I. Grigoriev, A.F.M. Altelaar, C.C.

Hoogenraad, S.G.D. Rüdiger, M.O. Steinmetz, L.C. Kapitein, and A. Akhmanova. 2019. MAP7 family proteins regulate kinesin-1 recruitment and activation. *J. Cell Biol.* 218:1298–1318. doi:10.1083/JCB.201808065/VIDEO-2.

Höök, P., and R.B. Vallee. 2006. The dynein family at a glance. *J. Cell Sci.* 119:4369–4371. doi:10.1242/jcs.03176.

Hornbeck, P. V., B. Zhang, B. Murray, J.M. Kornhauser, V. Latham, and E. Skrzypek. 2015. PhosphoSitePlus, 2014: mutations, PTMs and recalibrations. *Nucleic Acids Res.* 43:D512. doi:10.1093/NAR/GKU1267.

Van Der Horst, A., and S.M.A. Lens. 2014. Cell division: Control of the chromosomal passenger complex in time and space. *Chromosoma*. 123:25–42. doi:10.1007/s00412-013-0437-6.

van der Horst, A., M.J. Vromans, K. Bouwman, M.S. van der Waal, M.A. Hadders, and S.M.A. Lens. 2015. Inter-domain Cooperation in INCENP Promotes Aurora B Relocation from Centromeres to Microtubules. *Cell Rep.* 12:380–387. doi:10.1016/j.celrep.2015.06.038.

Horwitz, S.B. 1994. Taxol (paclitaxel): mechanisms of action. *Ann. Oncol.* 5 Suppl 6.

Houtman, S.H., M. Rutteman, C.I. De Zeeuw, and P.J. French. 2007. Echinoderm microtubule-associated protein like protein 4, a member of the echinoderm microtubule-associated protein family, stabilizes microtubules. *Neuroscience*. 144:1373–1382. doi:10.1016/J.NEUROSCIENCE.2006.11.015.

Howes, S.C., G.M. Alushin, T. Shida, M. V. Nachury, and E. Nogales. 2014. Effects of tubulin acetylation and tubulin acetyltransferase binding on microtubule structure. *Mol. Biol. Cell*. 25:257–266. doi:10.1091/mbc.E13-07-0387.

Hrdinka, M., B.K. Fiil, M. Zucca, D. Leske, K. Bagola, M. Yabal, P.R. Elliott, R.B. Damgaard, D. Komander, P.J. Jost, and M. Gyrd-Hansen. 2016. CYLD Limits Lys63- and Met1-Linked Ubiquitin at Receptor Complexes to Regulate Innate Immune Signaling. *Cell Rep.* 14:2846. doi:10.1016/J.CELREP.2016.02.062.

Huang, D.W., B.T. Sherman, and R.A. Lempicki. 2009. Systematic and integrative analysis of large gene lists using DAVID bioinformatics resources. *Nat. Protoc.* 4:44–57. doi:10.1038/nprot.2008.211.

Huang, J.Y., G. Morley, D. Li, and M. Whitaker. 2007. Cdk1 phosphorylation sites on Cdc27 are required for correct chromosomal localisation and APC/C function in syncytial Drosophila embryos. *J. Cell Sci.* 120:1990. doi:10.1242/JCS.006833.

Hubbert, C., A. Guardiola, R. Shao, Y. Kawaguchi, A. Ito, A. Nixon, M. Yoshida, X.F. Wang, and T.P. Yao. 2002. HDAC6 is a microtubule-associated deacetylase. *Nature*. 417:455–458. doi:10.1038/417455a.

Hughes, J.R., A.M. Meireles, K.H. Fisher, A. Garcia, P.R. Antrobus, A. Wainman, N. Zitzmann, C. Deane, H. Ohkura, and J.G. Wakefield. 2008. A microtubule interactome: Complexes with roles in cell cycle and mitosis. *PLoS Biol.* 6:785–795. doi:10.1371/journal.pbio.0060098.

Hümmer, S., and T.U. Mayer. 2009. Cdk1 Negatively Regulates Midzone Localization of the

Mitotic Kinesin Mklp2 and the Chromosomal Passenger Complex. *Curr. Biol.* 19:607–612. doi:10.1016/j.cub.2009.02.046.

Hung, A.Y., C.C. Sung, I.L. Brito, and M. Sheng. 2010. Degradation of Postsynaptic Scaffold GKAP and Regulation of Dendritic Spine Morphology by the TRIM3 Ubiquitin Ligase in Rat Hippocampal Neurons. *PLoS One*. 5:9842. doi:10.1371/JOURNAL.PONE.0009842.

Huttlin, E.L., R.J. Bruckner, J. Navarrete-Perea, J.R. Cannon, K. Baltier, F. Gebreab, M.P. Gygi, A. Thornock, G. Zarraga, S. Tam, J. Szpyt, B.M. Gassaway, A. Panov, H. Parzen, S. Fu, A. Golbazi, E. Maenpaa, K. Stricker, S. Guha Thakurta, T. Zhang, R. Rad, J. Pan, D.P. Nusinow, J.A. Paulo, D.K. Schweppe, L.P. Vaites, J.W. Harper, and S.P. Gygi. 2021. Dual proteome-scale networks reveal cell-specific remodeling of the human interactome. *Cell*. 184:3022-3040.e28. doi:10.1016/J.CELL.2021.04.011.

Iida, J., T.J. Itoh, H. Hotani, K.I. Nishiyama, H. Murofushi, J.C. Bulinski, and S.I. Hisanaga. 2002. The projection domain of MAP4 suppresses the microtubule-bundling activity of the microtubule-binding domain. *J. Mol. Biol.* 320:97–106. doi:10.1016/S0022-2836(02)00402-3.

Ikegami, K., and M. Setou. 2009. TTLL10 can perform tubulin glycylation when co-expressed with TTLL8. *FEBS Lett.* 583:1957–1963. doi:10.1016/j.febslet.2009.05.003.

Imamula, K., T. Kon, R. Ohkura, and K. Sutoh. 2007. The coordination of cyclic microtubule association/dissociation and tail swing of cytoplasmic dynein. *Proc. Natl. Acad. Sci. U. S. A.* 104:16134–16139. doi:10.1073/pnas.0702370104.

Iqbal, K., F. Liu, and C.X. Gong. 2016. Tau and neurodegenerative disease: The story so far. *Nat. Rev. Neurol.* 12:15–27. doi:10.1038/nrneurol.2015.225.

Ishii, T., K. Ohnuma, A. Murakami, N. Takasawa, T. Yamochi, S. Iwata, M. Uchiyama, N.H. Dang, H. Tanaka, and C. Morimoto. 2003. SS-A/Ro52, an autoantigen involved in CD28-mediated IL-2 production. *J. Immunol.* 170:3653–3661. doi:10.4049/JIMMUNOL.170.7.3653.

Issaq, H.J., and T.D. Veenstra. 2008. Two-dimensional polyacrylamide gel electrophoresis (2D-PAGE): Advances and perspectives. *Biotechniques*. 44:697–700. doi:10.2144/000112823.

Jaishankar, A., N.L.S. Tang, M. Jelani, A.M. Mabb, A.J. George, Y.C. Hoffiz, A.J. Charles, and Y. Zhu. 2018. A Comprehensive Atlas of E3 Ubiquitin Ligase Mutations in Neurological Disorders. *Front. Genet.* | *www.frontiersin.org*. 9:29. doi:10.3389/fgene.2018.00029.

Janke, C., and J.C. Bulinski. 2011. Post-translational regulation of the microtubule cytoskeleton: Mechanisms and functions. *Nat. Rev. Mol. Cell Biol.* 12:773–786. doi:10.1038/nrm3227.

Janke, C., and M.M. Magiera. 2020. The tubulin code and its role in controlling microtubule properties and functions. *Nat. Rev. Mol. Cell Biol.* 1–20. doi:10.1038/s41580-020-0214-3.

Janke, C., and G. Montagnac. 2017. Causes and Consequences of Microtubule Acetylation. *Curr. Biol.* 27:R1287–R1292. doi:10.1016/j.cub.2017.10.044.

Janke, C., K. Rogowski, D. Wloga, C. Regnard, A. V. Kajava, J.M. Strub, N. Temurak, J. Van Dijk, D. Boucher, A. Van Dorsselaer, S. Suryavanshi, J. Gaertig, and B. Eddé. 2005. Tubulin polyglutamylase enzymes are members of the TTL domain protein family. *Science (80-.).* 308:1758–1762. doi:10.1126/science.1113010.

Jansen, K.I., M.K. Iwanski, M. Burute, and L.C. Kapitein. 2023. A live-cell marker to visualize the dynamics of stable microtubules throughout the cell cycle. *J. Cell Biol.* 222. doi:10.1083/JCB.202106105.

Jenkins, B. V., H.A.J. Saunders, H.L. Record, D.M. Johnson-Schlitz, and J. Wildonger. 2017. Effects of mutating α-tubulin lysine 40 on sensory dendrite development. *J. Cell Sci.* 130:4120–4131. doi:10.1242/jcs.210203.

Jeyaprakash, A.A., U.R. Klein, D. Lindner, J. Ebert, E.A. Nigg, and E. Conti. 2007. Structure of a Survivin-Borealin-INCENP Core Complex Reveals How Chromosomal Passengers Travel Together. *Cell*. 131:271–285. doi:10.1016/J.CELL.2007.07.045.

Ji, S., J.G. Kang, S.Y. Park, J. Lee, Y.J. Oh, and J.W. Cho. 2011. O-GlcNAcylation of tubulin inhibits its polymerization. *Amino Acids*. 40:809–818. doi:10.1007/s00726-010-0698-9.

Jin, J., X. Li, S.P. Gygi, and J.W. Harper. 2007. Dual E1 activation systems for ubiquitin differentially regulate E2 enzyme charging. *Nature*. 447:1135–1138. doi:10.1038/nature05902.

Johannes, L., R. Jacob, and H. Leffler. 2018. Galectins at a glance. *J. Cell Sci.* 131. doi:10.1242/JCS.208884/57083.

Joo, H.M., J.Y. Kim, J.B. Jeong, K.M. Seong, S.Y. Nam, K.H. Yang, C.S. Kim, H.S. Kim, M. Jeong, S. An, and Y.W. Jin. 2011. Ret finger protein 2 enhances ionizing radiation-induced apoptosis via degradation of AKT and MDM2. *Eur. J. Cell Biol.* 90:420–431. doi:10.1016/J.EJCB.2010.12.001.

Jordan, M.A., D. Thrower, and L. Wilson. 1992. Effects of vinblastine, podophyllotoxin and nocodazole on mitotic spindles. Implications for the role of microtubule dynamics in mitosis. *J. Cell Sci.* 102:401–416.

Kaitna, S., M. Mendoza, V. Jantsch-Plunger, and M. Glotzer. 2000. Incenp and an Aurora-like kinase form a complex essential for chromosome segregation and efficient completion of cytokinesis. *Curr. Biol.* 10:1172–1181. doi:10.1016/S0960-9822(00)00721-1.

Kalantzaki, M., E. Kitamura, T. Zhang, A. Mino, B. Novák, and T.U. Tanaka. 2015. Kinetochore-microtubule error correction is driven by differentially regulated interaction modes. *Nat. Cell Biol.* 17:421. doi:10.1038/ncb3128.

Kanai, Y., N. Dohmae, and N. Hirokawa. 2004. Kinesin Transports RNA: Isolation and Characterization of an RNA-Transporting Granule. *Neuron*. 43:513–525. doi:10.1016/J.NEURON.2004.07.022.

Kapitein, L.C., E.J.G. Peterman, B.H. Kwok, J.H. Kim, T.M. Kapoor, and C.F. Schmidt. 2005. The bipolar mitotic kinesin Eg5 moves on both microtubules that it crosslinks. *Nat. 2005 4357038*. 435:114–118. doi:10.1038/nature03503.

Karas, M., and F. Hillenkamp. 1988. Laser Desorption Ionization of Proteins with Molecular

Masses Exceeding 10 000 Daltons. *Anal. Chem.* 60:2299–2301. doi:10.1021/ac00171a028.

Kardon, J.R., and R.D. Vale. 2009. Regulators of the cytoplasmic dynein motor. *Nat. Rev. Mol. Cell Biol.* 10:854–865. doi:10.1038/nrm2804.

Kaseda, K., H. Higuchi, and K. Hirose. 2003. Alternate fast and slow stepping of a heterodimeric kinesin molecule. *Nat. Cell Biol.* 5:1079–1082. doi:10.1038/ncb1067.

Kaul, N., V. Soppina, and K.J. Verhey. 2014. Effects of α-tubulin K40 acetylation and detyrosination on kinesin-1 motility in a purified system. *Biophys. J.* doi:10.1016/j.bpj.2014.05.008.

Keates, R.A.B. 1980. Effects of glycerol on microtubule polymerization kinetics. *Biochem. Biophys. Res. Commun.* 97:1163–1169. doi:10.1016/0006-291X(80)91497-7.

Kedar, V., H. McDonough, R. Arya, H.H. Li, H.A. Rockman, and C. Patterson. 2004. Muscle-specific RING finger 1 is a bona fide ubiquitin ligase that degrades cardiac troponin I. *Proc. Natl. Acad. Sci. U. S. A.* 101:18135–18140. doi:10.1073/pnas.0404341102.

Keen, N., and S. Taylor. 2009. Mitotic drivers-inhibitors of the Aurora B Kinase. *Cancer Metastasis Rev.* 28:185–195. doi:10.1007/s10555-009-9184-9.

Kellogg, E.H., N.M.A. Hejab, S. Poepsel, K.H. Downing, F. DiMaio, and E. Nogales. 2018. Near-atomic model of microtubule-tau interactions. *Science (80-.).* 360:1242–1246. doi:10.1126/science.aat1780.

Kelly, A.E., and H. Funabiki. 2009. Correcting aberrant kinetochore microtubule attachments: an Aurora B-centric view. *Curr. Opin. Cell Biol.* 21:51–58. doi:10.1016/j.ceb.2009.01.004.

Kemphues, K.J., T.C. Kaufman, R.A. Raff, and E.C. Raff. 1982. The testis-specific β-tubulin subunit in drosophila melanogaster has multiple functions in spermatogenesis. *Cell*. 31:655–670. doi:10.1016/0092-8674(82)90321-X.

Kettenbach, A.N., D.K. Schweppe, B.K. Faherty, D. Pechenick, A.A. Pletnev, and S.A. Gerber. 2011. Quantitative phosphoproteomics identifies substrates and functional modules of Aurora and Polo-like kinase activities in mitotic cells. *Sci. Signal.* 4. doi:10.1126/SCISIGNAL.2001497.

Khawaja, S., G.G. Gundersen, and J.C. Bulinski. 1988. Enhanced stability of microtubules enriched in detyrosinated tubulin is not a direct function of detyrosination level. *J. Cell Biol.* 106:141–149. doi:10.1083/jcb.106.1.141.

Khazaei, M.R., M.-P. Girouard, R. Alchini, S.O. Tone, T. Shimada, S. Bechstedt, M. Cowan, D. Guillet, P.W. Wiseman, G. Brouhard, J.F. Cloutier, and A.E. Fournier. 2014. Collapsin Response Mediator Protein 4 Regulates Growth Cone Dynamics through the Actin and Microtubule Cytoskeleton. *J. Biol. Chem.* 289:30133. doi:10.1074/JBC.M114.570440.

Kikuchi, K., Y. Sakamoto, A. Uezu, H. Yamamoto, K.I. Ishiguro, K. Shimamura, T. Saito, S.I. Hisanaga, and H. Nakanishi. 2022. Map7D2 and Map7D1 facilitate microtubule stabilization through distinct mechanisms in neuronal cells. *Life Sci. Alliance*. 5. doi:10.26508/lsa.202201390.

Kim, B.W., S. Beom Hong, J. Hoe Kim, D. Hoon Kwon, and H.K. Song. 2013. Structural basis

for recognition of autophagic receptor NDP52 by the sugar receptor galectin-8. *Nat. Commun.* 4. doi:10.1038/ncomms2606.

Kim, J.Y., S.Y. Woo, Y. Bin Hong, H. Choi, J. Kim, H. Choi, I. Mook-Jung, N. Ha, J. Kyung, S.K. Koo, S.C. Jung, and B.O. Choi. 2016. HDAC6 Inhibitors Rescued the Defective Axonal Mitochondrial Movement in Motor Neurons Derived from the Induced Pluripotent Stem Cells of Peripheral Neuropathy Patients with HSPB1 Mutation. *Stem Cells Int.* 2016. doi:10.1155/2016/9475981.

Kimura, Y., N. Kurabe, K. Ikegami, K. Tsutsumi, Y. Konishi, O.I. Kaplan, H. Kunitomo, Y. Iino, O.E. Blacque, and M. Setou. 2010. Identification of tubulin deglutamylase among Caenorhabditis elegans and mammalian cytosolic carboxypeptidases (CCPs). *J. Biol. Chem.* 285:22936–22941. doi:10.1074/jbc.C110.128280.

Kirschner, M., and T. Mitchison. 1986. Beyond self-assembly: From microtubules to morphogenesis. *Cell*. 45:329–342. doi:10.1016/0092-8674(86)90318-1.

Klammer, M., M. Kaminski, A. Zedler, F. Oppermann, S. Blencke, S. Marx, S. Müller, A. Tebbe, K. Godl, and C. Schaab. 2012. Phosphosignature predicts dasatinib response in non-small cell lung cancer. *Mol. Cell. Proteomics*. 11:651–668. doi:10.1074/MCP.M111.016410.

Klose, J. 1975. Protein mapping by combined isoelectric focusing and electrophoresis of mouse tissues - A novel approach to testing for induced point mutations in mammals. *Hum. Genet.* 26:231–243. doi:10.1007/BF00281458.

Kobayashi, T., T. Ikeda, R. Ota, T. Yasukawa, and H. Itoh. 2022. The atypical small GTPase RABL3 interacts with RAB11 to regulate early ciliogenesis in human cells. *J. Cell Sci.* 135. doi:10.1242/jcs.260021.

Kolla, S.D.D., M. Ye, K.G. Mark, and M. Rapé. 2022. Assembly and function of branched ubiquitin chains. *Trends Biochem. Sci.* 47:759–771. doi:10.1016/j.tibs.2022.04.003.

Kollman, J.M., J.K. Polka, A. Zelter, T.N. Davis, and D.A. Agard. 2010. Microtubule nucleating γ 3-TuSC assembles structures with 13-fold microtubule-like symmetry. *Nature*. 466:879–882. doi:10.1038/nature09207.

Komander, D., M.J. Clague, and S. Urbé. 2009a. Breaking the chains: Structure and function of the deubiquitinases. *Nat. Rev. Mol. Cell Biol.* 10:550–563. doi:10.1038/nrm2731.

Komander, D., and M. Rape. 2012. The Ubiquitin Code. *Annu. Rev. Biochem.* 81:203–229. doi:10.1146/annurev-biochem-060310-170328.

Komander, D., F. Reyes-Turcu, J.D.F. Licchesi, P. Odenwaelder, K.D. Wilkinson, and D. Barford. 2009b. Molecular discrimination of structurally equivalent Lys 63-linked and linear polyubiquitin chains. *EMBO Rep.* 10:466–473. doi:10.1038/embor.2009.55.

Komarova, Y., G. Lansbergen, N. Galjart, F. Grosveld, G.G. Borisy, and A. Akhmanova. 2005. EB1 and EB3 Control CLIP Dissociation from the Ends of Growing Microtubules □ D. *Mol. Biol. Cell*. 16:5334–5345. doi:10.1091/mbc.E05-07-0614.

Kong, H.J., D.E. Anderson, C.H. Lee, M.K. Jang, T. Tamura, P. Tailor, H.K. Cho, J. Cheong, H. Xiong, H.C. Morse, and K. Ozato. 2007. Cutting Edge: Autoantigen Ro52 Is an

Interferon Inducible E3 Ligase That Ubiquitinates IRF-8 and Enhances Cytokine Expression in Macrophages. *J. Immunol.* 179:26–30. doi:10.4049/JIMMUNOL.179.1.26.

Krauhs, E., M. Little, T. Kempf, R. Hofer-Warbinek, W. Ade, and H. Ponstingl. 1981. Complete amino acid sequence of β-tubulin from porcine brain. *Proc. Natl. Acad. Sci. U. S. A.* 78:4156–4160. doi:10.1073/pnas.78.7.4156.

Kull, F.J., E.P. Sablin, R. Lau, R.J. Fletterick, and R.D. Vale. 1996. Crystal structure of the kinesin motor domain reveals a structural similarity to myosin. *Nature*. 380:550–555. doi:10.1038/380550a0.

Kull, F.J., and R.D. Sloboda. 2014. A Slow Dance for Microtubule Acetylation. *Cell*. 157:1255–1256. doi:10.1016/j.cell.2014.05.021.

Kumar, N. 1981. Taxol-induced polymerization of purified tubulin. Mechanism of action. *J. Biol. Chem.* 256:10435–10441. doi:10.1016/s0021-9258(19)68639-4.

Kumar, P., M.S. Chimenti, H. Pemble, A. Schönichen, O. Thompson, M.P. Jacobson, and T. Wittmann. 2012. Multisite phosphorylation disrupts arginine-glutamate salt bridge networks required for binding of cytoplasmic linker-associated protein 2 (CLASP2) to end-binding protein 1 (EB1). *J. Biol. Chem.* 287:17050–17064. doi:10.1074/jbc.M111.316661.

Kunjappu, M.J., and M. Hochstrasser. 2014. Assembly of the 20S proteasome. *Biochim. Biophys. Acta - Mol. Cell Res.* 1843:2–12. doi:10.1016/J.BBAMCR.2013.03.008.

L'Hernault, S.W., and J.L. Rosenbaum. 1983. Chlamydomonas α-tubulin is posttranslationally modified in the flagella during flagellar assembly. *J. Cell Biol.* 97:258–263. doi:10.1083/jcb.97.1.258.

L'Hernault, S.W., and J.L. Rosenbaum. 1985. Chlamydomonas α-Tubulin Is Posttranslationally Modified by Acetylation on the ε-Amino Group of a Lysine. *Biochemistry*. 24:473–478. doi:10.1021/bi00323a034.

Labonté, D., E. Thies, Y. Pechmann, A.J. Groffen, M. Verhage, A.B. Smit, R.E. van Kesteren, and M. Kneussel. 2013. TRIM3 Regulates the Motility of the Kinesin Motor Protein KIF21B. *PLoS One*. 8:75603. doi:10.1371/journal.pone.0075603.

Lacroix, B., J. Van Dijk, N.D. Gold, J. Guizetti, G. Aldrian-Herrada, K. Rogowski, D.W. Gerlich, and C. Janke. 2010. Tubulin polyglutamylation stimulates spastin-mediated microtubule severing. *J. Cell Biol.* 189:945–954. doi:10.1083/jcb.201001024.

Lampert, F., P. Hornung, and S. Westermann. 2010. The Dam1 complex confers microtubule plus end-tracking activity to the Ndc80 kinetochore complex. *J. Cell Biol.* 189:641–649. doi:10.1083/jcb.200912021.

Lan, W., X. Zhang, S.L. Kline-Smith, S.E. Rosasco, G.A. Barrett-Wilt, J. Shabanowitz, D.F. Hunt, C.E. Walczak, and P.T. Stukenberg. 2004. Aurora B Phosphorylates Centromeric MCAK and Regulates Its Localization and Microtubule Depolymerization Activity. *Curr. Biol.* 14:273–286. doi:10.1016/J.CUB.2004.01.055.

Landskron, L., J. Bak, A. Adamopoulos, K. Kaplani, M. Moraiti, L.G. van den Hengel, J.-Y. Song, O.B. Bleijerveld, J. Nieuwenhuis, T. Heidebrecht, L. Henneman, M.-J. Moutin, M.

Barisic, S. Taraviras, A. Perrakis, and T.R. Brummelkamp. 2022. Posttranslational modification of microtubules by the MATCAP detyrosinase. *Science (80-.).* doi:10.1126/SCIENCE.ABN6020.

Lane, J., and V. Allan. 1998. Microtubule-based membrane movement. *Biochim. Biophys. Acta - Rev. Biomembr.* 1376:27–55. doi:10.1016/S0304-4157(97)00010-5.

Lara-Gonzalez, P., J. Pines, and A. Desai. 2021. Spindle assembly checkpoint activation and silencing at kinetochores. *Semin. Cell Dev. Biol.* 117:86–98. doi:10.1016/j.semcdb.2021.06.009.

Lasek, R.J., and S.T. Brady. 1985. Attachment of transported vesicles to microtubules in axoplasm is facilitated by AMP-PNP. *Nature*. 316:645–647. doi:10.1038/316645a0.

Latremoliere, A., L. Cheng, M. DeLisle, C. Wu, S. Chew, E.B. Hutchinson, A. Sheridan, C. Alexandre, F. Latremoliere, S.H. Sheu, S. Golidy, T. Omura, E.A. Huebner, Y. Fan, M.C. Whitman, E. Nguyen, C. Hermawan, C. Pierpaoli, M.A. Tischfield, C.J. Woolf, and E.C. Engle. 2018. Neuronal-Specific TUBB3 Is Not Required for Normal Neuronal Function but Is Essential for Timely Axon Regeneration. *Cell Rep.* 24:1865-1879.e9. doi:10.1016/J.CELREP.2018.07.029.

Law, B.M.H., V.A. Spain, V.H.L. Leinster, R. Chia, A. Beilina, H.J. Cho, J.M. Taymans, M.K. Urban, R.M. Sancho, M.B. Ramírez, S. Biskup, V. Baekelandt, H. Cai, M.R. Cookson, D.C. Berwick, and K. Harvey. 2014. A direct interaction between leucine-rich repeat kinase 2 and specific β-Tubulin isoforms regulates tubulin acetylation. *J. Biol. Chem.* 289:895–908. doi:10.1074/JBC.M113.507913.

Ledbetter, M.C., and K.R. Porter. 1964. Morphology of microtubules of plant cells. *Science (80-.).* 144:872–874. doi:10.1126/science.144.3620.872.

LeDizet, M., and G. Piperno. 1987. Identification of an acetylation site of Chlamydomonas alpha-tubulin. *Proc. Natl. Acad. Sci. U. S. A.* 84:5720–5724. doi:10.1073/pnas.84.16.5720.

Lee, J.C., D.J. Field, and L.L.Y. Lee. 1980. Effects of Nocodazole on Structures of Calf Brain Tubulin. *Biochemistry*. 19:6209–6215. doi:10.1021/bi00567a041.

Lee, J.S., G.D. Burkholder, L.J. P Latimer, B.L. Haug, R.P. Braun, D. Horowitz, F. Johnston, E. Lund, G.Q. Pcnnabble, J.H. White, V. Chau, J.W. Tobias, A. Bachmair, D. MARRIOTr, D.J. EcKER, D.K. Gonda, A. Varshavsky, V. Chau, D. Marriott are, J.W. Tobias, A. Bachmair, D.K. Gonda, and A. Varshavsky are. 1989. A Multiubiquitin Chain Is Confined to Specific Lysine in a Targeted Short-Lived Protein. *Science (80-.).* 243:1576–1583. doi:10.1126/SCIENCE.2538923.

de Leenheer, A.P., and L.M. Thienpont. 1992. Applications of isotope dilution-mass spectrometry in clinical chemistry, pharmacokinetics, and toxicology. *Mass Spectrom. Rev.* 11:249–307. doi:10.1002/mas.1280110402.

Lewellyn, L., A. Carvalho, A. Desai, A.S. Maddox, and K. Oegema. 2011. The chromosomal passenger complex and centralspindlin independently contribute to contractile ring assembly. *J. Cell Biol.* 193:155. doi:10.1083/JCB.201008138.

Li, J., Z. Cai, R.D. Bomgarden, I. Pike, K. Kuhn, J.C. Rogers, T.M. Roberts, S.P. Gygi, and J.A. Paulo. 2021. TMTpro-18plex: The Expanded and Complete Set of TMTpro Reagents for Sample Multiplexing. *J. Proteome Res.* 20:2964–2972. doi:10.1021/ACS.JPROTEOME.1C00168/SUPPL_FILE/PR1C00168_SI_005.XLSX.

Li, W.W., Y. Nie, Y. Yang, Y. Ran, W.W. Luo, M.G. Xiong, S.Y. Wang, Z.S. Xu, and Y.Y. Wang. 2020. Ubiquitination of TLR3 by TRIM3 signals its ESCRTmediated trafficking to the endolysosomes for innate antiviral response. *Proc. Natl. Acad. Sci. U. S. A.* 117:23707–23716. doi:10.1073/pnas.2002472117.

Li, X., N. Song, L. Liu, X. Liu, X. Ding, X. Song, S. Yang, L. Shan, X. Zhou, D. Su, Y. Wang, Q. Zhang, C. Cao, S. Ma, N. Yu, F. Yang, Y. Wang, Z. Yao, Y. Shang, and L. Shi. 2017. USP9X regulates centrosome duplication and promotes breast carcinogenesis. *Nat. Commun.* 8. doi:10.1038/ncomms14866.

Li, Y., L.S. Chin, C. Weigel, and L. Li. 2001. Spring, a Novel RING Finger Protein That Regulates Synaptic Vesicle Exocytosis. *J. Biol. Chem.* 276:40824–40833. doi:10.1074/jbc.M106141200.

Liao, G., and G.G. Gundersen. 1998. Kinesin is a candidate for cross-bridging microtubules and intermediate filaments: Selective binding of kinesin to detyrosinated tubulin and vimentin. *J. Biol. Chem.* 273:9797–9803. doi:10.1074/jbc.273.16.9797.

Lin, S.X., G.G. Gundersen, and F.R. Maxfield. 2002. Export from pericentriolar endocytic recycling compartment to cell surface depends on stable, detyrosinated (GGlu) microtubules and kinesin. *Mol. Biol. Cell*. 13:96–109. doi:10.1091/mbc.01-05-0224.

Linck, R., X. Fu, J. Lin, C. Ouch, A. Schefter, W. Steffen, P. Warren, and D. Nicastro. 2014. Insights into the structure and function of ciliary and flagellar doublet microtubules: Tektins, Ca2+-binding proteins, and stable protofilaments. *J. Biol. Chem.* 289:17427–17444. doi:10.1074/jbc.M114.568949.

Liu, N., Y. Xiong, Y. Ren, L. Zhang, X. He, X. Wang, M. Liu, D. Li, W. Shui, and J. Zhou. 2015. Proteomic Profiling and Functional Characterization of Multiple Post-Translational Modifications of Tubulin. *J. Proteome Res.* 14:3292–3304. doi:10.1021/acs.jproteome.5b00308.

Liu, P., W. Gan, S. Su, A. V Hauenstein, T.M. Fu, B. Brasher, C. Schwerdtfeger, A.C. Liang, M. Xu, and W. Wei. 2018. K63-linked polyubiquitin chains bind to DNA to facilitate DNA damage repair. *Sci. Signal.* 11. doi:10.1126/scisignal.aar8133.

Liu, P., E. Zupa, A. Neuner, A. Böhler, J. Loerke, D. Flemming, T. Ruppert, T. Rudack, C. Peter, C. Spahn, O.J. Gruss, S. Pfeffer, and E. Schiebel. 2020. Insights into the assembly and activation of the microtubule nucleator γ-TuRC. *Nature*. 578:467–471. doi:10.1038/s41586-019-1896-6.

Liu, S.-T., and H. Zhang. 2016. The mitotic checkpoint complex (MCC): looking back and forth after 15 years. *AIMS Mol. Sci.* 3:597–634. doi:10.3934/molsci.2016.4.597.

Liu, X., and J.L. Henty-Ridilla. 2022. Multiple roles for the cytoskeleton in ALS. *Exp. Neurol.* 355:114143. doi:10.1016/j.expneurol.2022.114143.

Loedige, I., D. Gaidatzis, R. Sack, G. Meister, and W. Filipowicz. 2013. The mammalian TRIM-NHL protein TRIM71/LIN-41 is a repressor of mRNA function. *Nucleic Acids Res.* 41:518–532. doi:10.1093/nar/gks1032.

Loedige, I., L. Jakob, T. Treiber, D. Ray, M. Stotz, N. Treiber, J. Hennig, K.B. Cook, Q. Morris, T.R. Hughes, J.C. Engelmann, M.P. Krahn, and G. Meister. 2015. The Crystal Structure of the NHL Domain in Complex with RNA Reveals the Molecular Basis of Drosophila Brain-Tumor-Mediated Gene Regulation. *Cell Rep.* 13:1206–1220. doi:10.1016/J.CELREP.2015.09.068.

Loedige, I., M. Stotz, S. Qamar, K. Kramer, J. Hennig, T. Schubert, P. Löffler, G. Längst, R. Merkl, H. Urlaub, and G. Meister. 2014. The NHL domain of BRAT is an RNA-binding domain that directly contacts the hunchback mRNA for regulation. *Genes Dev.* 28:749–764. doi:10.1101/gad.236513.113.

Lopata, M.A., and D.W. Cleveland. 1987. In vivo microtubules are copolymers of available beta-tubulin isotypes: localization of each of six vertebrate beta-tubulin isotypes using polyclonal antibodies elicited by synthetic peptide antigens. *J. Cell Biol.* 105:1707–1720. doi:10.1083/jcb.105.4.1707.

López, M.P., F. Huber, I. Grigoriev, M.O. Steinmetz, A. Akhmanova, G.H. Koenderink, and M. Dogterom. 2014. Actin-microtubule coordination at growing microtubule ends. *Nat. Commun.* 5:1–9. doi:10.1038/ncomms5778.

Lorenzo, D.N., A. Badea, J. Davis, J. Hostettler, J. He, G. Zhong, X. Zhuang, and V. Bennett. 2014. A PIK3C3–Ankyrin-B–Dynactin pathway promotes axonal growth and multiorganelle transport. *J. Cell Biol.* 207:735. doi:10.1083/JCB.201407063.

Louie, R.K., S. Bahmanyar, K.A. Siemers, V. Votin, P. Chang, T. Stearns, W.J. Nelson, and A.I.M. Barth. 2004. Adenomatous polyposis coli and EB1 localize in close proximity of the mother centriole and EB1 is a functional component of centrosomes. *J. Cell Sci.* 117:1117–1128. doi:10.1242/jcs.00939.

Lu, T., R. Chen, T.C. Cox, R.X. Moldrich, N. Kurniawan, G. Tan, J.K. Perry, A. Ashworth, P.F. Bartlett, L. Xu, J. Zhang, B. Lu, M. Wu, Q. Shen, Y. Liu, L.J. Richards, and Z. Xiong. 2013. X-linked microtubule-associated protein, Mid1, regulates axon development. *Proc. Natl. Acad. Sci. U. S. A.* 110:19131–19136. doi:10.1073/PNAS.1303687110/SUPPL_FILE/PNAS.201303687SI.PDF.

Lüders, J., U.K. Patel, and T. Stearns. 2006. GCP-WD is a γ-tubulin targeting factor required for centrosomal and chromatin-mediated microtubule nucleation. *Nat. Cell Biol.* 8:137–147. doi:10.1038/ncb1349.

Luo, Y., and L. Pelletier. 2014. Pericentrin: Critical for spindle orientation. *Curr. Biol.* 24:R962–R964. doi:10.1016/J.CUB.2014.08.062.

Lv, B.F., C.F. Yu, Y.Y. Chen, Y. Lu, J.H. Guo, Q.S. Song, D.L. Ma, T.P. Shi, and L. Wang. 2006. Protein tyrosine phosphatase interacting protein 51 (PTPIP51) is a novel mitochondria protein with an N-terminal mitochondrial targeting sequence and induces apoptosis. *Apoptosis*. 11:1489–1501. doi:10.1007/s10495-006-8882-9.

Maday, S., A.E. Twelvetrees, A.J. Moughamian, and E.L.F. Holzbaur. 2014. Axonal Transport: Cargo-Specific Mechanisms of Motility and Regulation. *Neuron*. 84:292–309. doi:10.1016/J.NEURON.2014.10.019.

Madiraju, C., J.P. Novack, J.C. Reed, and S. ichi Matsuzawa. 2022. K63 ubiquitination in immune signaling. *Trends Immunol.* 43:148–162. doi:10.1016/j.it.2021.12.005.

Maerki, S., M.H. Olma, T. Staubli, P. Steigemann, D.W. Gerlich, M. Quadroni, I. Sumara, and M. Peter. 2009. The Cul3-KLHL21 E3 ubiquitin ligase targets Aurora B to midzone microtubules in anaphase and is required for cytokinesis. *J. Cell Biol.* 187:791–800. doi:10.1083/jcb.200906117.

Magdeldin, S., S. Enany, Y. Yoshida, B. Xu, Y. Zhang, Z. Zureena, I. Lokamani, E. Yaoita, and T. Yamamoto. 2014. Basics and recent advances of two dimensional-polyacrylamide gel electrophoresis. *Clin. Proteomics*. 11:16. doi:10.1186/1559-0275-11-16.

Magiera, M.M., P. Singh, and C. Janke. 2018. SnapShot: Functions of Tubulin Posttranslational Modifications. *Cell*. doi:10.1016/j.cell.2018.05.032.

Maier, B., M. Kirsch, S. Anderhub, H. Zentgraf, and A. Krämer. 2013. The novel actin/focal adhesion-associated protein MISP is involved in mitotic spindle positioning in human cells. *Cell Cycle*. 12:1457. doi:10.4161/CC.24602.

Makrantoni, V., and A.L. Marston. 2018. Cohesin and chromosome segregation. *Curr. Biol.* 28:R688–R693. doi:10.1016/j.cub.2018.05.019.

Mao, C.-X., X. Wen, S. Jin, and Y.Q. Zhang. 2017. Increased acetylation of microtubules rescues human tau-induced microtubule defects and neuromuscular junction abnormalities in Drosophila. *Dis. Model. Mech.* 10:1245–1252. doi:10.1242/dmm.028316.

Markus, S.M., and W.-L. Lee. 2011. Microtubule-dependent path to the cell cortex for cytoplasmic dynein in mitotic spindle orientation. *Bioarchitecture*. 1:209–215. doi:10.4161/bioa.18103.

Martin, M., and A. Akhmanova. 2018. Coming into Focus: Mechanisms of Microtubule Minus-End Organization. *Trends Cell Biol.* doi:10.1016/j.tcb.2018.02.011.

Martinez-Fonts, K., C. Davis, T. Tomita, S. Elsasser, A.R. Nager, Y. Shi, D. Finley, and A. Matouschek. 2020. The proteasome 19S cap and its ubiquitin receptors provide a versatile recognition platform for substrates. *Nat. Commun.* 11. doi:10.1038/s41467-019-13906-8.

Mascaro, M., I. Lages, and G. Meroni. 2022. Microtubular TRIM36 E3 Ubiquitin Ligase in Embryonic Development and Spermatogenesis. *Cells*. 11. doi:10.3390/cells11020246.

Matamoros, A.J., and P.W. Baas. 2016. Microtubules in health and degenerative disease of the nervous system. *Brain Res. Bull.* 126:217–225. doi:10.1016/j.brainresbull.2016.06.016.

Mazia, D., and K. Dan. 1952. The Isolation and Biochemical Characterization of the Mitotic Apparatus of Dividing Cells. *Proc. Natl. Acad. Sci.* 38:826–838. doi:10.1073/pnas.38.9.826.

McKenney, R.J., W. Huynh, M.E. Tanenbaum, G. Bhabha, and R.D. Vale. 2014. Activation of cytoplasmic dynein motility by dynactin-cargo adapter complexes. *Science (80-.).* 345:337–341. doi:10.1126/science.1254198.

Melkov, A., and U. Abdu. 2018. Regulation of long-distance transport of mitochondria along microtubules. *Cell. Mol. Life Sci.* 75:163–176. doi:10.1007/s00018-017-2590-1.

Menon, S., D. Goldfarb, C.T. Ho, E.W. Cloer, N.P. Boyer, C. Hardie, A.J. Bock, E.C. Johnson, J. Anil, M. Ben Major, and S.L. Gupton. 2021. The TRIM9/TRIM67 neuronal interactome reveals novel activators of morphogenesis. *Mol. Biol. Cell*. 32:314–330. doi:10.1091/mbc.E20-10-0622.

Meroni, G., and G. Diez-Roux. 2005. TRIM/RBCC, a novel class of “single protein RING finger” E3 ubiquitin ligases. *BioEssays*. 27:1147–1157. doi:10.1002/BIES.20304.

Metzger, M.B., J.N. Pruneda, R.E. Klevit, and A.M. Weissman. 2014. RING-type E3 ligases: Master manipulators of E2 ubiquitin-conjugating enzymes and ubiquitination. *Biochim. Biophys. Acta - Mol. Cell Res.* 1843:47–60. doi:10.1016/J.BBAMCR.2013.05.026.

Meunier, S., and I. Vernos. 2012. Microtubule assembly during mitosis - from distinct origins to distinct functions? *J. Cell Sci.* 125:2805–2814. doi:10.1242/jcs.092429.

Miki, H., Y. Okada, and N. Hirokawa. 2005. Analysis of the kinesin superfamily: Insights into structure and function. *Trends Cell Biol.* 15:467–476. doi:10.1016/j.tcb.2005.07.006.

Miller, A.L. 2011. The contractile ring. *Curr. Biol.* 21. doi:10.1016/J.CUB.2011.10.044.

Mitchell Wells, J., and S.A. McLuckey. 2005. Collision-induced dissociation (CID) of peptides and proteins. *Methods Enzymol.* 402:148–185. doi:10.1016/S0076-6879(05)02005-7.

Mitchison, T., and M. Kirschner. 1984. Dynamic instability of microtubule growth. *Nature*. 312:237–242. doi:10.1038/312237a0.

Mitchison, T.J. 1989. Polewards microtubule flux in the mitotic spindle: Evidence from photoactivation of fluorescence. *J. Cell Biol.* 109:637–652. doi:10.1083/jcb.109.2.637.

Mitchison, T.J. 1993. Localization of an exchangeable GTP binding site at the plus end of microtubules. *Science (80-.).* 261:1044–1047. doi:10.1126/science.8102497.

Miyajima, N., S. Maruyama, K. Nonomura, and S. Hatakeyama. 2009. TRIM36 interacts with the kinetochore protein CENP-H and delays cell cycle progression. *Biochem. Biophys. Res. Commun.* 381:383–387. doi:10.1016/j.bbrc.2009.02.059.

Mogensen, M.M., A. Malik, M. Piel, V. Boukson-Castaing, and M. Bornens. 2000. Microtubule minus-end anchorage at Centrosomal and non-centrosomal sites: The role of ninein. *J. Cell Sci.* 113:3013–3023.

Mohan, N., E.M. Sorokina, I.V. Verdeny, A.S. Alvarez, and M. Lakadamyali. 2019. Detyrosinated microtubules spatially constrain lysosomes facilitating lysosome-autophagosome fusion. *J. Cell Biol.* 218:632–643. doi:10.1083/jcb.201807124.

Mohri, H. 1968. Amino-acid composition of “tubulin” constituting microtubules of sperm flagella. *Nature*. 217:1053–1054. doi:10.1038/2171053a0.

Monda, J.K., and I.M. Cheeseman. 2018. The kinetochore-microtubule interface at a glance. *J. Cell Sci.* 131. doi:10.1242/jcs.214577.

Monteiro-Cardoso, V.F., L. Rochin, A. Arora, A. Houcine, E. Jääskeläinen, A.M. Kivelä, C. Sauvanet, R. Le Bars, E. Marien, J. Dehairs, J. Neveu, N. El Khallouki, E. Santonico, J. V. Swinnen, D. Tareste, V.M. Olkkonen, and F. Giordano. 2022. ORP5/8 and MIB/MICOS link ER-mitochondria and intra-mitochondrial contacts for non-vesicular transport of phosphatidylserine. *Cell Rep.* 40. doi:10.1016/J.CELREP.2022.111364.

Montenegro Gouveia, S., K. Leslie, L.C. Kapitein, R.M. Buey, I. Grigoriev, M. Wagenbach, I. Smal, E. Meijering, C.C. Hoogenraad, L. Wordeman, M.O. Steinmetz, and A. Akhmanova. 2010. In Vitro Reconstitution of the Functional Interplay between MCAK and EB3 at Microtubule Plus Ends. *Curr. Biol.* 20:1717–1722. doi:10.1016/J.CUB.2010.08.020.

Moores, C.A., and R.A. Milligan. 2006. Lucky 13 - Microtubule depolymerisation by kinesin-13 motors. *J. Cell Sci.* 119:3905–3913. doi:10.1242/jcs.03224.

Morgan, M.R., M.J. Humphries, and M.D. Bass. 2007. Synergistic control of cell adhesion by integrins and syndecans. *Nat. Rev. Mol. Cell Biol.* 8:957–969. doi:10.1038/nrm2289.

Morley, S.J., Y. Qi, L. Iovino, L. Andolfi, D. Guo, N. Kalebic, L. Castaldi, C. Tischer, C. Portulano, G. Bolasco, K. Shirlekar, C.M. Fusco, A. Asaro, F. Fermani, M. Sundukova, U. Matti, L. Reymond, A. De Ninno, L. Businaro, K. Johnsson, M. Lazzarino, J. Ries, Y. Schwab, J. Hu, and P.A. Heppenstall. 2016. Acetylated tubulin is essential for touch sensation in mice. *Elife*. 5:25. doi:10.7554/ELIFE.20813.

Moutin, M.J., C. Bosc, L. Peris, and A. Andrieux. 2020. Tubulin post-translational modifications control neuronal development and functions. *Dev. Neurobiol.* dneu.22774. doi:10.1002/dneu.22774.

Mukai, M., K. Ikegami, Y. Sugiura, K. Takeshita, A. Nakagawa, and M. Setou. 2009. Recombinant mammalian Tubulin polyglutamylase TTLL7 performs both initiation and elongation of polyglutamylation on ß-Tubulin through a random sequential pathway. *Biochemistry*. 48:1084–1093. doi:10.1021/bi802047y.

Murata, T., S. Sonobe, T.I. Baskin, S. Hyodo, S. Hasezawa, T. Nagata, T. Horio, and M. Hasebe. 2005. Microtubule-dependent microtubule nucleation based on recruitment of γ-tubulin in higher plants. *Nat. Cell Biol.* 7:961–968. doi:10.1038/ncb1306.

Nakata, T., S. Niwa, Y. Okada, F. Perez, and N. Hirokawa. 2011. Preferential binding of a kinesin-1 motor to GTP-tubulin-rich microtubules underlies polarized vesicle transport. *J. Cell Biol.* 194:245–255. doi:10.1083/jcb.201104034.

Nath, S., D. Ghatak, P. Das, and S. Roychoudhury. 2015. Transcriptional control of mitosis: Deregulation and cancer. *Front. Endocrinol. (Lausanne).* 6. doi:10.3389/fendo.2015.00060.

Neef, R., C. Preisinger, J. Sutcliffe, R. Kopajtich, E.A. Nigg, T.U. Mayer, and F.A. Barr. 2003. Phosphorylation of mitotic kinesin-like protein 2 by polo-like kinase 1 is required for cytokinesis. *J. Cell Biol.* 162:863–875. doi:10.1083/jcb.200306009.

Neumayer, G., C. Belzil, O.J. Gruss, and M. Dang Nguyen. 2014. TPX2: of spindle assembly, DNA damage response, and cancer. *Cell. Mol. Life Sci*. 71:3027–3047.

doi:10.1007/s00018-014-1582-7.

Nieuwenhuis, J., A. Adamopoulos, O.B. Bleijerveld, A. Mazouzi, E. Stickel, P. Celie, M. Altelaar, P. Knipscheer, A. Perrakis, V.A. Blomen, and T.R. Brummelkamp. 2017. Vasohibins encode tubulin detyrosinating activity. *Science (80-.).* 358:1453–1456. doi:10.1126/science.aao5676.

Nieuwenhuis, J., and T.R. Brummelkamp. 2018. The Tubulin Detyrosination Cycle: Function and Enzymes. *Trends Cell Biol.* S0962-8924:30141–7. doi:10.1016/j.tcb.2018.08.003.

Nigg, E.A. 2001. Mitotic kinases as regulators of cell division and its checkpoints. *Nat. Rev. Mol. Cell Biol.* 2:21–32. doi:10.1038/35048096.

Nirschl, J.J., M.M. Magiera, J.E. Lazarus, C. Janke, and E.L.F. Holzbaur. 2016. α-Tubulin Tyrosination and CLIP-170 Phosphorylation Regulate the Initiation of Dynein-Driven Transport in Neurons. *Cell Rep.* 14:2637–2652. doi:10.1016/j.celrep.2016.02.046.

Nishi, H., K. Hashimoto, and A.R. Panchenko. 2011. Phosphorylation in protein-protein binding: Effect on stability and function. *Structure*. 19:1807–1815. doi:10.1016/j.str.2011.09.021.

Nogales, E. 1998. Structure of the alpha/beta tubulin dimer by electron crystallography. *Acta Crystallogr. Sect. B Struct. Sci.* 52:753–769. doi:10.1107/S0108768196005599.

Nogales, E. 2000. Structural Insights into Microtubule Function. *Annu. Rev. Biophys. Biomol. Struct.* 69:277–302. doi:10.1146/annurev.biophys.30.1.397.

Nogales, E., M. Whittaker, R.A. Milligan, and K.H. Downing. 1999. High-resolution model of the microtubule. *Cell*. 96:79–88. doi:10.1016/S0092-8674(00)80961-7.

Nogales, E., S.G. Wolf, and K.H. Downing. 1998. Structure of the αβ tubulin dimer by electron crystallography. *Nature*. 391:199–203. doi:10.1038/34465.

Norden, C., M. Mendoza, J. Dobbelaere, C. V. Kotwaliwale, S. Biggins, and Y. Barral. 2006. The NoCut Pathway Links Completion of Cytokinesis to Spindle Midzone Function to Prevent Chromosome Breakage. *Cell*. 125:85–98. doi:10.1016/J.CELL.2006.01.045.

North, B.J., B.L. Marshall, M.T. Borra, J.M. Denu, and E. Verdin. 2003. The human Sir2 ortholog, SIRT2, is an NAD+-dependent tubulin deacetylase. *Mol. Cell*. 11:437–44. doi:10.1016/s1097-2765(03)00038-8.

Nusinow, D.P., J. Szpyt, M. Ghandi, C.M. Rose, E.R. McDonald, M. Kalocsay, J. Jané-Valbuena, E. Gelfand, D.K. Schweppe, M. Jedrychowski, J. Golji, D.A. Porter, T. Rejtar, Y.K. Wang, G. V. Kryukov, F. Stegmeier, B.K. Erickson, L.A. Garraway, W.R. Sellers, and S.P. Gygi. 2020. Quantitative Proteomics of the Cancer Cell Line Encyclopedia. *Cell*. 180:387-402.e16. doi:10.1016/J.CELL.2019.12.023/ATTACHMENT/564C2B29-7019-423B-A0BB-487D969188B7/MMC7.XLSX.

O'Brien, E.T., E.D. Salmon, R.A. Walker, and H.P. Erickson. 1990. Effects of Magnesium on the Dynamic Instability of Individual Microtubules. *Biochemistry*. 29:6648–6656. doi:10.1021/BI00480A014/ASSET/BI00480A014.FP.PNG_V03.

O'Connell, P.A., D.M. Pinto, K.A. Chisholm, and T.H. MacRae. 2006. Characterization of the microtubule proteome during post-diapause development of Artemia franciscana.

Biochim. Biophys. Acta - Proteins Proteomics. 1764:920–928. doi:10.1016/j.bbapap.2006.03.003.

O'Farrell, P.H. 1975. High resolution two-dimensional electrophoresis of Proteins. *J. Biol. Chem.* 250:4007–4021. doi:10.1002/elps.201400060.

Oakley, B.R., V. Paolillo, and Y. Zheng. 2015. γ-tubulin complexes in microtubule nucleation and beyond. *Mol. Biol. Cell*. 26:2957–2962. doi:10.1091/mbc.E14-11-1514.

Oakley, C.E., and B.R. Oakley. 1989. Identification of γ-tubulin, a new member of the tubulin superfamily encoded by mipA gene of Aspergillus nidulans. *Nature*. 338:662–664. doi:10.1038/338662a0.

Oda, Y., K. Huang, F.R. Cross, D. Cowburn, and B.T. Chait. 1999. Accurate quantitation of protein expression and site-specific phosphorylation. *Proc. Natl. Acad. Sci. U. S. A.* 96:6591–6596. doi:10.1073/pnas.96.12.6591.

Ohkawa, N., K. Kokura, T. Matsu-ura, T. Obinata, Y. Konishi, and T.A. Tamura. 2001. Molecular cloning and characterization of neural activity-related RING finger protein (NARF): A new member of the RBCC family is a candidate for the partner of myosin V. *J. Neurochem.* 78:75–87. doi:10.1046/J.1471-4159.2001.00373.X.

Oishi, K., H. Okano, and H. Sawa. 2007. RMD-1, a novel microtubule-associated protein, functions in chromosome segregation in Caenorhabditis elegans. *J. Cell Biol.* 179:1149–1162. doi:10.1083/jcb.200705108.

Olenick, M.A., and E.L.F. Holzbaur. 2019. Cell science at a glance dynein activators and adaptors at a glance. *J. Cell Sci.* 132. doi:10.1242/jcs.227132.

Ong, S.E., B. Blagoev, I. Kratchmarova, D.B. Kristensen, H. Steen, A. Pandey, and M. Mann. 2002. Stable isotope labeling by amino acids in cell culture, SILAC, as a simple and accurate approach to expression proteomics. *Mol. Cell. Proteomics*. 1:376–386. doi:10.1074/mcp.M200025-MCP200.

Ong, S.E., I. Kratchmarova, and M. Mann. 2003. Properties of 13C-substituted arginine in stable isotope labeling by amino acids in cell culture (SILAC). *J. Proteome Res.* 2:173–181. doi:10.1021/pr0255708.

Ott, C., K. Ross, S. Straub, B. Thiede, M. Götz, C. Goosmann, M. Krischke, M.J. Mueller, G. Krohne, T. Rudel, and V. Kozjak-Pavlovic. 2012. Sam50 Functions in Mitochondrial Intermembrane Space Bridging and Biogenesis of Respiratory Complexes. *Mol. Cell. Biol.* 32:1173. doi:10.1128/MCB.06388-11.

Ouyang, Z., Z. Takáts, T.A. Blake, B. Gologan, A.J. Guymon, J.M. Wiseman, J.C. Oliver, V.J. Davisson, and R.G. Cooks. 2003. Preparing protein microarrays by soft-landing of mass-selected ions. *Science (80-.).* 301:1351–1354. doi:10.1126/science.1088776.

Ozato, K., D.M. Shin, T.H. Chang, and H.C. Morse. 2008. TRIM family proteins and their emerging roles in innate immunity. *Nat. Rev. Immunol. 2008 811*. 8:849–860. doi:10.1038/nri2413.

Pagliuca, F.W., M.O. Collins, A. Lichawska, P. Zegerman, J.S. Choudhary, and J. Pines. 2011. Quantitative Proteomics Reveals the Basis for the Biochemical Specificity of the Cell

Cycle Machinery. *Mol. Cell*. 43:406. doi:10.1016/J.MOLCEL.2011.05.031.

Pagnamenta, A.T., P. Heemeryck, H.C. Martin, C. Bosc, L. Peris, I. Uszynski, S. Gory-Fauré, S. Couly, C. Deshpande, A. Siddiqui, A.A. Elmonairy, S. Jayawant, S. Murthy, I. Walker, L. Loong, P. Bauer, F. Vossier, E. Denarier, T. Maurice, E.L. Barbier, J.C. Deloulme, J.C. Taylor, E.M. Blair, A. Andrieux, and M.J. Moutin. 2019. Defective tubulin detyrosination causes structural brain abnormalities with cognitive deficiency in humans and mice. *Hum. Mol. Genet.* 28:3391–3405. doi:10.1093/hmg/ddz186.

Palazzo, A., B. Ackerman, and G.G. Gundersen. 2003. Tubulin acetylation and cell motility. *Nat. 2003 4216920*. 421:230–230. doi:10.1038/421230a.

Pao, K.C., N.T. Wood, A. Knebel, K. Rafie, M. Stanley, P.D. Mabbitt, R. Sundaramoorthy, K. Hofmann, D.M.F. Van Aalten, and S. Virdee. 2018. Activity-based E3 ligase profiling uncovers an E3 ligase with esterification activity. *Nat. 2018 5567701*. 556:381–385. doi:10.1038/s41586-018-0026-1.

Park, J., M.S. Kwon, E.E. Kim, H. Lee, and E.J. Song. 2018. USP35 regulates mitotic progression by modulating the stability of Aurora B. *Nat. Commun.* 9. doi:10.1038/s41467-018-03107-0.

Park, K., K.J. Hoff, L. Wethekam, N. Stence, M. Saenz, and J.K. Moore. 2021. Kinetically Stabilizing Mutations in Beta Tubulins Create Isotype-Specific Brain Malformations. *Front. Cell Dev. Biol.* 9:3281. doi:10.3389/FCELL.2021.765992/BIBTEX.

Paša-Tolic, L., P.K. Jensen, G.A. Anderson, M.S. Lipton, K.K. Peden, S. Martinović, N. Tolić, J.E. Bruce, and R.D. Smith. 1999. High throughput proteome-wide precision measurements of protein expression using mass spectrometry [10]. *J. Am. Chem. Soc.* 121:7949–7950. doi:10.1021/ja991063o.

Paschal, B.M., H.S. Shpetner, and R.B. Vallee. 1987. MAP 1C is a microtubule-activated ATPase which translocates microtubules in vitro and has dynein-like properties. *J. Cell Biol.* 105:1273–1282. doi:10.1083/jcb.105.3.1273.

Patel, P.C., K.H. Fisher, E.C.C. Yang, C.M. Deane, and R.E. Harrison. 2009. Proteomic Analysis of Microtubule-associated Proteins during Macrophage Activation* □ S. *Mol. Cell. Proteomics*. 8:2500–14. doi:10.1074/mcp.M900190-MCP200.

Paturle-Lafanechère, L., D. Job, B. Eddé, P. Denoulet, A. Van Dorsselaer, H. Mazarguil, J.P. Le Caer, and J. Wehland. 1991. Characterization of a Major Brain Tubulin Variant Which Cannot Be Tyrosinated. *Biochemistry*. 30:10523–10528. doi:10.1021/bi00107a022.

Paturle-Lafanechère, L., M. Manier, N. Trigault, F. Pirollet, H. Mazarguil, and D. Job. 1994. Accumulation of delta 2-tubulin, a major tubulin variant that cannot be tyrosinated, in neuronal tissues and in stable microtubule assemblies. *J. Cell Sci.* 107:1529–1543.

Pellegrini, L., A. Wetzel, S. Grannó, G. Heaton, and K. Harvey. 2017. Back to the tubule: microtubule dynamics in Parkinson's disease. *Cell. Mol. Life Sci.* 74:409–434. doi:10.1007/s00018-016-2351-6.

Peng, J., D. Schwartz, J.E. Elias, C.C. Thoreen, D. Cheng, G. Marsischky, J. Roelofs, D. Finley, and S.P. Gygi. 2003. A proteomics approach to understanding protein

ubiquitination. *Nat. Biotechnol. 2003 218*. 21:921–926. doi:10.1038/nbt849.

Perdiz, D., R. Mackeh, C. Poüs, and A. Baillet. 2011. The ins and outs of tubulin acetylation: More than just a post-translational modification? *Cell. Signal.* 23:763–771. doi:10.1016/j.cellsig.2010.10.014.

Perera, S., B. Mankoo, and M. Gautel. 2012. Developmental regulation of MURF E3 ubiquitin ligases in skeletal muscle. *J. Muscle Res. Cell Motil.* 33:107–122. doi:10.1007/s10974-012-9288-7.

Perez-Riba, A., and L.S. Itzhaki. 2019. The tetratricopeptide-repeat motif is a versatile platform that enables diverse modes of molecular recognition. *Curr. Opin. Struct. Biol.* 54:43–49. doi:10.1016/J.SBI.2018.12.004.

Perez, F., G.S. Diamantopoulos, R. Stalder, and T.E. Kreis. 1999. CLIP-170 highlights growing microtubule ends in vivo. *Cell*. 96:517–527. doi:10.1016/S0092-8674(00)80656-X.

Peris, L., J. Parato, X. Qu, J.M. Soleilhac, F. Lante, A. Kumar, M.E. Pero, J. Martínez-Hernández, C. Corrao, G. Falivelli, F. Payet, S. Gory-Faure, C. Bosc, M. Blanca Ramirez, A. Sproul, J. Brocard, B. Di Cara, P. Delagrange, A. Buisson, Y. Goldberg, M.J. Moutin, F. Bartolini, and A. Andrieux. 2022. Tubulin tyrosination regulates synaptic function and is disrupted in Alzheimer's disease. *Brain*. 145:2486–2506. doi:10.1093/BRAIN/AWAB436.

Peris, L., M. Thery, J. Fauré, Y. Saoudi, L. Lafanechère, J.K. Chilton, P. Gordon-Weeks, N. Galjart, M. Bornens, L. Wordeman, J. Wehland, A. Andrieux, and D. Job. 2006. Tubulin tyrosination is a major factor affecting the recruitment of CAP-Gly proteins at microtubule plus ends. *J. Cell Biol.* 174:839–849. doi:10.1083/jcb.200512058.

Peris, L., M. Wagenbach, L. Lafanechère, J. Brocard, A.T. Moore, F. Kozielski, D. Job, L. Wordeman, and A. Andrieux. 2009. Motor-dependent microtubule disassembly driven by tubulin tyrosination. *J. Cell Biol.* 185:1159–1166. doi:10.1083/jcb.200902142.

Perkins, D.N., D.J.C. Pappin, D.M. Creasy, and J.S. Cottrell. 1999. Probability-based protein identification by searching sequence databases using mass spectrometry data. *Electrophoresis*. 20:3551–3567. doi:10.1002/(SICI)1522-2683(19991201)20:18<3551::AID-ELPS3551>3.0.CO;2-2.

Peters, J.M. 2006. The anaphase promoting complex/cyclosome: a machine designed to destroy. *Nat. Rev. Mol. Cell Biol. 2006 79*. 7:644–656. doi:10.1038/nrm1988.

Petrovic, A., J. Keller, Y. Liu, K. Overlack, J. John, Y.N. Dimitrova, S. Jenni, S. van Gerwen, P. Stege, S. Wohlgemuth, P. Rombaut, F. Herzog, S.C. Harrison, I.R. Vetter, and A. Musacchio. 2016. Structure of the MIS12 Complex and Molecular Basis of Its Interaction with CENP-C at Human Kinetochores. *Cell*. 167:1028-1040.e15. doi:10.1016/J.CELL.2016.10.005.

Petry, S. 2016. Mechanisms of Mitotic Spindle Assembly. *Annu. Rev. Biochem.* 85:659–683. doi:10.1146/annurev-biochem-060815-014528.

Petry, S., A.C. Groen, K. Ishihara, T.J. Mitchison, and R.D. Vale. 2013. Branching microtubule nucleation in xenopus egg extracts mediated by augmin and TPX2. *Cell*. 152:768–777.

doi:10.1016/j.cell.2012.12.044.

Petry, S., and R.D. Vale. 2015. Microtubule nucleation at the centrosome and beyond. *Nat. Cell Biol.* 17:1089–1093. doi:10.1038/ncb3220.

Phu, L., C.M. Rose, J.S. Tea, C.E. Wall, E. Verschueren, T.K. Cheung, D.S. Kirkpatrick, and B. Bingol. 2020. Dynamic Regulation of Mitochondrial Import by the Ubiquitin System. *Mol. Cell*. 77:1107-1123.e10. doi:10.1016/j.molcel.2020.02.012.

Pizon, V., A. Iakovenko, P.F.M. van der Ven, R. Kelly, C. Fatu, D.O. Fürst, E. Karsenti, and M. Gautel. 2002. Transient association of titin and myosin with microtubules in nascent myofibrils directed by the MURF2 RING-finger protein. *J. Cell Sci.* 115:4469–4482. doi:10.1242/JCS.00131.

Ponstingl, H., E. Krauhs, M. Little, and T. Kempf. 1981. Complete amino acid sequence of alpha-tubulin from porcine brain. *Proc. Natl. Acad. Sci. U. S. A.* 78:2757–2761. doi:10.1073/pnas.78.5.2757.

Poole, C.A., C.G. Jensen, J.A. Snyder, C.G. Gray, V.L. Hermanutz, and D.N. Wheatley. 1997. Confocal analysis of primary cilia structure and colocalization with the Golgi apparatus in chondrocytes and aortic smooth muscle cells. *Cell Biol. Int.* 21:483–494. doi:10.1006/cbir.1997.0177.

Portran, D., L. Schaedel, Z. Xu, M. Théry, and M. V. Nachury. 2017. Tubulin acetylation protects long-lived microtubules against mechanical ageing. *Nat. Cell Biol.* 19:391–398. doi:10.1038/ncb3481.

Prota, A.E., M.M. Magiera, M. Kuijpers, K. Bargsten, D. Frey, M. Wieser, R. Jaussi, C.C. Hoogenraad, R.A. Kammerer, C. Janke, and M.O. Steinmetz. 2013. Structural basis of tubulin tyrosination by tubulin tyrosine ligase. *J. Cell Biol.* 200:259–270. doi:10.1083/jcb.201211017.

Qiang, L., X. Sun, T.O. Austin, H. Muralidharan, D.C. Jean, M. Liu, W. Yu, and P.W. Baas. 2018. Tau Does Not Stabilize Axonal Microtubules but Rather Enables Them to Have Long Labile Domains. *Curr. Biol.* 28:2181-2189.e4. doi:10.1016/J.CUB.2018.05.045.

Qiang, L., W. Yu, A. Andreadis, M. Luo, and P.W. Baas. 2006. Tau protects microtubules in the axon from severing by katanin. *J. Neurosci.* 26:3120–3129. doi:10.1523/JNEUROSCI.5392-05.2006.

Raaijmakers, J.A., M.E. Tanenbaum, and R.H. Medema. 2013. Systematic dissection of dynein regulators in mitosis. *J. Cell Biol.* 201:201. doi:10.1083/JCB.201208098.

Radwitz, J., T.J. Hausrat, F.F. Heisler, P.C. Janiesch, Y. Pechmann, M. Rübhausen, and M. Kneussel. 2022. Tubb3 expression levels are sensitive to neuronal activity changes and determine microtubule growth and kinesin-mediated transport. *Cell. Mol. Life Sci.* 79:575. doi:10.1007/s00018-022-04607-5.

Raheja, R., Y. Liu, E. Hukkelhoven, N. Yeh, and A. Koff. 2014. The ability of TRIM3 to induce growth arrest depends on RING-dependent E3 ligase activity. *Biochem. J.* 458:537. doi:10.1042/BJ20131288.

Raman, J., Y. Guan, C.L. Perrine, T.A. Gerken, and L.A. Tabak. 2012. UDP-N-acetyl α-d-

galactosamine: Polypeptide N- acetylgalactosaminyltransferases: Completion of the family tree. *Glycobiology*. 22:768–777. doi:10.1093/glycob/cwr183.

Ramirez-Rios, S., S.R. Choi, C. Sanyal, T.B. Blum, C. Bosc, F. Krichen, E. Denarier, J.-M. Soleilhac, B. Blot, C. Janke, V. Stoppin-Mellet, M.M. Magiera, I. Arnal, M.O. Steinmetz, and M.-J. Moutin. 2023. VASH1–SVBP and VASH2–SVBP generate different detyrosination profiles on microtubules. *J. Cell Biol.* 222. doi:10.1083/JCB.202205096/213744.

Ramkumar, A., B.Y. Jong, and K.M. Ori-McKenney. 2018. ReMAPping the microtubule landscape: How phosphorylation dictates the activities of microtubule-associated proteins. *Dev. Dyn.* 247:138–155. doi:10.1002/dvdy.24599.

Rao, S., S.B. Horwitz, and I. Ringel. 1992. Direct photoaffinity labeling of tubulin with taxol. *J. Natl. Cancer Inst.* 84:785–8. doi:10.1093/jnci/84.10.785.

Rao, S.R., N. Flores-Rodriguez, S.L. Page, C. Wong, P.J. Robinson, and M. Chircop. 2016. The clathrin-dependent spindle proteome. *Mol. Cell. Proteomics*. 15:2537–2553. doi:10.1074/mcp.M115.054809.

Rappsilber, J., Y. Ishihama, and M. Mann. 2003. Stop And Go Extraction tips for matrix-assisted laser desorption/ionization, nanoelectrospray, and LC/MS sample pretreatment in proteomics. *Anal. Chem.* 75:663–670. doi:10.1021/ac026117i.

Ravelli, R.B.G., B. Gigant, P.A. Curmi, I. Jourdain, S. Lachkar, A. Sobel, and M. Knossow. 2004. Insight into tubulin regulation from a complex with colchicine and a stathmin-like domain. *Nature*. 428:198–202. doi:10.1038/nature02393.

Ravichandran, K.S. 2001. Signaling via Shc family adapter proteins. *Oncogene*. 20:6322–6330. doi:10.1038/SJ.ONC.1204776.

Raybin, D., and M. Flavin. 1977. Enzyme Which Specifically Adds Tyrosine to the α Chain of Tubulin. *Biochemistry*. 16:2189–2194. doi:10.1021/bi00629a023.

Reck-Peterson, S.L., W.B. Redwine, R.D. Vale, and A.P. Carter. 2018. The cytoplasmic dynein transport machinery and its many cargoes. *Nat. Rev. Mol. Cell Biol.* 19:382–398. doi:10.1038/s41580-018-0004-3.

Redeker, V., N. Levilliers, J.M. Schmitter, J.P. Le Caer, J. Rossier, A. Adoutte, and M.H. Bré. 1994. Polyglycylation of tubulin: A posttranslational modification in axonemal microtubules. *Science (80-.).* 266:1688–1691. doi:10.1126/science.7992051.

Reed, N.A., D. Cai, T.L. Blasius, G.T. Jih, E. Meyhofer, J. Gaertig, and K.J. Verhey. 2006. Microtubule Acetylation Promotes Kinesin-1 Binding and Transport. *Curr. Biol.* 16:2166–2172. doi:10.1016/j.cub.2006.09.014.

Rice, S., A.W. Lin, D. Safer, C.L. Hart, N. Naber, B.O. Carragher, S.M. Cain, E. Pechatnikova, E.M. Wilson-Kubalek, M. Whittaker, E. Pate, R. Cooke, E.W. Taylor, R.A. Milligan, and R.D. Vale. 1999. A structural change in the kinesin motor protein that drives motility. *Nature*. 402:778–784. doi:10.1038/45483.

Robzyk, K., J. Recht, and M.A. Osley. 2000. Rad6-Dependent Ubiquitination of Histone H2B in Yeast. *Science (80-.).* 287:501–504. doi:10.1126/SCIENCE.287.5452.501.

Rodríguez-Feo, J.A., J. Gallego-Delgado, M. Puerto, F. Wandosell, and J. Osende. 2016. Reticulon-4B/Nogo-B acts as a molecular linker between microtubules and actin cytoskeleton in vascular smooth muscle cells. *Biochim. Biophys. Acta - Mol. Cell Res.* 1863:1985–1995. doi:10.1016/j.bbamcr.2016.04.025.

Rogers, G.C., S.L. Rogers, T.A. Schwimmer, S.C. Ems-McClung, C.E. Walczak, R.D. Vale, J.M. Scholey, and D.J. Sharp. 2004. Two mitotic kinesins cooperate to drive sister chromatid separation during anaphase. *Nature*. 427:364–370. doi:10.1038/nature02256.

Rogowski, K., J. van Dijk, M.M. Magiera, C. Bosc, J.C. Deloulme, A. Bosson, L. Peris, N.D. Gold, B. Lacroix, M.B. Grau, N. Bec, C. Larroque, S. Desagher, M. Holzer, A. Andrieux, M.J. Moutin, and C. Janke. 2010. A family of protein-deglutamylating enzymes associated with neurodegeneration. *Cell*. 143:564–578. doi:10.1016/j.cell.2010.10.014.

Rogowski, K., F. Juge, J. van Dijk, D. Wloga, J.M. Strub, N. Levilliers, D. Thomas, M.H. Bré, A. Van Dorsselaer, J. Gaertig, and C. Janke. 2009. Evolutionary Divergence of Enzymatic Mechanisms for Posttranslational Polyglycylation. *Cell*. 137:1076–1087. doi:10.1016/j.cell.2009.05.020.

Rosas-Salvans, M., T. Cavazza, G. Espadas, E. Sabido, and I. Vernos. 2018. Proteomic profiling of microtubule self-organization in m-phase. *Mol. Cell. Proteomics*. 17:1991–2004. doi:10.1074/mcp.RA118.000745.

Rosenblatt, J. 2005. Spindle assembly: Asters part their separate ways. *Nat. Cell Biol.* 7:219–222. doi:10.1038/ncb0305-219.

Roth, D., B.P. Fitton, N.P. Chmel, N. Wasiluk, and A. Straube. 2019. Spatial positioning of EB family proteins at microtubule tips involves distinct nucleotide-dependent binding properties. *J. Cell Sci.* 132. doi:10.1242/JCS.219550/265683/AM/SPATIAL-POSITIONING-OF-EB-FAMILY-PROTEINS-AT.

Rotin, D., and S. Kumar. 2009. Physiological functions of the HECT family of ubiquitin ligases. *Nat. Rev. Mol. Cell Biol. 2009 106*. 10:398–409. doi:10.1038/nrm2690.

Roux, K.J., D.I. Kim, M. Raida, and B. Burke. 2012. A promiscuous biotin ligase fusion protein identifies proximal and interacting proteins in mammalian cells. *J. Cell Biol.* 196:801–810. doi:10.1083/JCB.201112098.

Rusilowicz-Jones, E. V., J. Jardine, A. Kallinos, A. Pinto-Fernandez, F. Guenther, M. Giurrandino, F.G. Barone, K. McCarron, C.J. Burke, A. Murad, A. Martinez, E. Marcassa, M. Gersch, A.J. Buckmelter, K.J. Kayser-Bricker, F. Lamoliatte, A. Gajbhiye, S. Davis, H.C. Scott, E. Murphy, K. England, H. Mortiboys, D. Komander, M. Trost, B.M. Kessler, S. Ioannidis, M.K. Ahlijanian, S. Urbé, and M.J. Clague. 2020. USP30 sets a trigger threshold for PINK1–PARKIN amplification of mitochondrial ubiquitylation. *Life Sci. Alliance*. 3. doi:10.26508/LSA.202000768.

Sahara, S., M. Aoto, Y. Eguchi, N. Imamoto, Y. Yoneda, and Y. Tsujimoto. 1999. Acinus is a caspase-3-activated protein required for apoptotic chromatin condensation. *Nature*. 401:168–173. doi:10.1038/43678.

Salina, D., K. Bodoor, D.M. Eckley, T.A. Schroer, J.B. Rattner, and B. Burke. 2002.

Cytoplasmic dynein as a facilitator of nuclear envelope breakdown. *Cell*. 108:97–107. doi:10.1016/S0092-8674(01)00628-6.

Sandoval, I. V., and K. Weber. 1978. Calcium-Induced Inactivation of Microtubule Formation in Brain Extracts: Presence of a Calcium-Dependent Protease Acting on Polymerization-Stimulating Microtubule-Associated Proteins. *Eur. J. Biochem.* 92:463–470. doi:10.1111/j.1432-1033.1978.tb12768.x.

Sankaran, S., L.M. Starita, A.M. Simons, and J.D. Parvin. 2006. Identification of Domains of BRCA1 Critical for the Ubiquitin-Dependent Inhibition of Centrosome Function. *Cancer Res*. 66:4100–4107. doi:10.1158/0008-5472.CAN-05-4430.

Sasaki, T., S.J. Rodig, L.R. Chirieac, and P.A. Jänne. 2010. The biology and treatment of EML4-ALK non-small cell lung cancer. *Eur. J. Cancer*. 46:1773–1780. doi:10.1016/J.EJCA.2010.04.002.

Sauer, G., R. Körner, A. Hanisch, A. Ries, E.A. Nigg, and H.H.W. Silljé. 2005. Proteome analysis of the human mitotic spindle. *Mol. Cell. Proteomics*. 4:35–43. doi:10.1074/mcp.M400158-MCP200.

Schaedel, L., K. John, J. Gaillard, M. V. Nachury, L. Blanchoin, and M. Thery. 2015. Microtubules self-repair in response to mechanical stress. *Nat. Mater.* 14:1156–1163. doi:10.1038/nmat4396.

Schiff, P.B., and S.B. Horwitz. 1980. Taxol stabilizes microtubules in mouse fibroblast cells. *Proc. Natl. Acad. Sci. U. S. A.* 77:1561–1565. doi:10.1073/pnas.77.3.1561.

Schiff, P.B., and S.B. Horwitz. 1981. Taxol Assembles Tubulin in the Absence of Exogenous Guanosine 5'-Triphosphate or Microtubule-Associated Proteins. *Biochemistry*. 20:3247–3252. doi:10.1021/bi00514a041.

Schmit, T.L., and N. Ahmad. 2007. Regulation of mitosis via mitotic kinases: New opportunities for cancer management. *Mol. Cancer Ther.* 6:1920–1931. doi:10.1158/1535-7163.MCT-06-0781.

Schneider-Poetsch, T., J. Ju, D.E. Eyler, Y. Dang, S. Bhat, W.C. Merrick, R. Green, B. Shen, and J.O. Liu. 2010. Inhibition of eukaryotic translation elongation by cycloheximide and lactimidomycin. *Nat. Chem. Biol.* 6:209–217. doi:10.1038/nchembio.304.

Scholey, J.M. 1996. Kinesin-II, a membrane traffic motor in axons, axonemes, and spindles. *J. Cell Biol.* 133:1–4. doi:10.1083/jcb.133.1.1.

Schreiber, J., M.J. Végh, J. Dawitz, T. Kroon, M. Loos, D. Labonté, K.W. Li, P. Van Nierop, M.T. Van Diepen, C.I. De Zeeuw, M. Kneussel, R.M. Meredith, A.B. Smit, and R.E. Van Kesteren. 2015. Ubiquitin ligase TRIM3 controls hippocampal plasticity and learning by regulating synaptic γ-actin levels. *J. Cell Biol.* 211:569–586. doi:10.1083/JCB.201506048.

Schroeder, C.M., and R.D. Vale. 2016. Assembly and activation of dynein-dynactin by the cargo adaptor protein Hook3. *J. Cell Biol.* 214:309–318. doi:10.1083/jcb.201604002.

Schroer, T.A. 2000. Motors, Clutches and Brakes for Membrane Traffic: A Commemorative Review in Honor of Thomas Kreis. *Traffic*. 1:3–10. doi:10.1034/j.1600-

0854.2000.010102.x.

Schroer, T.A. 2004. Dynactin. *Annu. Rev. Cell Dev. Biol.* 20:759–779. doi:10.1146/annurev.cellbio.20.012103.094623.

Schroer, T.A., and M.P. Sheetz. 1991. Two activators of microtubule-based vesicle transport. *J. Cell Biol.* 115:1309–1318. doi:10.1083/jcb.115.5.1309.

Schubert, O.T., H.L. Röst, B.C. Collins, G. Rosenberger, and R. Aebersold. 2017. Quantitative proteomics: Challenges and opportunities in basic and applied research. *Nat. Protoc.* 12:1289–1294. doi:10.1038/nprot.2017.040.

Schulman, B.A., and J. Wade Harper. 2009. Ubiquitin-like protein activation by E1 enzymes: The apex for downstream signalling pathways. *Nat. Rev. Mol. Cell Biol.* 10:319–331. doi:10.1038/nrm2673.

Schulze, W.X., and M. Mann. 2004. A Novel Proteomic Screen for Peptide-Protein Interactions. *J. Biol. Chem.* 279:10756–10764. doi:10.1074/jbc.M309909200.

Schweppe, D.K., J.K. Eng, Q. Yu, D. Bailey, R. Rad, J. Navarrete-Perea, E.L. Huttlin, B.K. Erickson, J.A. Paulo, and S.P. Gygi. 2020. Full-Featured, Real-Time Database Searching Platform Enables Fast and Accurate Multiplexed Quantitative Proteomics. *J. Proteome Res.* 19:2026–2034. doi:10.1021/acs.jproteome.9b00860.

Semenova, I., K. Ikeda, K. Resaul, P. Kraikivski, M. Aguiar, S. Gygi, I. Zaliapin, A. Cowan, and V. Rodionov. 2014. Regulation of microtubule-based transport by MAP4. *Mol. Biol. Cell*. 25:3119–3132. doi:10.1091/mbc.E14-01-0022.

Serena, M., R.N. Bastos, P.R. Elliott, and F.A. Barr. 2020. Molecular basis of MKLP2-dependent Aurora B transport from chromatin to the anaphase central spindle. *J. Cell Biol.* 219. doi:10.1083/JCB.201910059.

Shao, Q., and Y.Q. Gao. 2006. On the hand-over-hand mechanism of kinesin. *Proc. Natl. Acad. Sci. U. S. A.* 103:8072–8077. doi:10.1073/pnas.0602828103.

Sharma, K., R.C.J. D'Souza, S. Tyanova, C. Schaab, J.R. Wiśniewski, J. Cox, and M. Mann. 2014. Ultradeep Human Phosphoproteome Reveals a Distinct Regulatory Nature of Tyr and Ser/Thr-Based Signaling. *Cell Rep.* 8:1583–1594. doi:10.1016/J.CELREP.2014.07.036.

Sharp, D.J., G.C. Rogers, and J.M. Scholey. 2000. Cytoplasmic dyein is required for poleward chromosome movement during mitosis in Drosophila embryos. *Nat. Cell Biol.* 2:922–930. doi:10.1038/35046574.

Sherman, B.T., M. Hao, J. Qiu, X. Jiao, M.W. Baseler, H.C. Lane, T. Imamichi, and W. Chang. 2022. DAVID: a web server for functional enrichment analysis and functional annotation of gene lists (2021 update). *Nucleic Acids Res.* 50:W216. doi:10.1093/NAR/GKAC194.

Shida, T., J.G. Cueva, Z. Xu, M.B. Goodman, and M. V Nachury. 2010. The major α-tubulin K40 acetyltransferase αTAT1 promotes rapid ciliogenesis and efficient mechanosensation. *PNAS*. 107:21517–22. doi:10.1073/pnas.1013728107.

Short, K.M., and T.C. Cox. 2006. Subclassification of the RBCC/TRIM superfamily reveals a novel motif necessary for microtubule binding. *J. Biol. Chem.* 281:8970–8980.

doi:10.1074/jbc.M512755200.

Sikirzhytski, V., F. Renda, I. Tikhonenko, V. Magidson, B.F. McEwen, and A. Khodjakov. 2018. Microtubules assemble near most kinetochores during early prometaphase in human cells. *J. Cell Biol.* 217:2647–2659. doi:10.1083/jcb.201710094.

Sirajuddin, M., L.M. Rice, and R.D. Vale. 2014. Regulation of microtubule motors by tubulin isotypes and post-translational modifications. *Nat. Cell Biol.* 16:335–344. doi:10.1038/ncb2920.

Skowyra, A., L.A. Allan, A.T. Saurin, and P.R. Clarke. 2018. USP9X Limits Mitotic Checkpoint Complex Turnover to Strengthen the Spindle Assembly Checkpoint and Guard against Chromosomal Instability. *Cell Rep.* 23:852–865. doi:10.1016/j.celrep.2018.03.100.

Slack, F.J., and G. Ruvkun. 1998. A novel repeat domain that is often associated with RING finger and B-box motifs. *Trends Biochem. Sci.* 23:474–475. doi:10.1016/S0968-0004(98)01299-7.

Slep, K.C. 2009. The role of TOG domains in microtubule plus end dynamics. *In* Biochemical Society Transactions. 1002–1006.

Sloboda, R.D., S.A. Rudolph, J.L. Rosenbaum, and P. Greengard. 1975. Cyclic AMP dependent endogenous phosphorylation of a microtubule associated protein. *Proc. Natl. Acad. Sci. U. S. A.* 72:177–181. doi:10.1073/pnas.72.1.177.

Smith, J.B. 2001. Peptide Sequencing by Edman Degradation. *In* Encyclopedia of Life Sciences. John Wiley & Sons, Ltd, Chichester, UK.

Smith, R.L., M.J. Redd, and A.D. Johnson. 1995. The tetratricopeptide repeats of Ssn6 interact with the homeo domain of α2. *Genes Dev.* 9:2903–2910. doi:10.1101/gad.9.23.2903.

Smithies, O., and M.D. Poulik. 1956. Two-dimensional electrophoresis of serum proteins. *Nature*. 177:1033. doi:10.1038/1771033a0.

Song, Y., and S.T. Brady. 2015. Post-translational modifications of tubulin: Pathways to functional diversity of microtubules. *Trends Cell Biol.* 25:125–136. doi:10.1016/j.tcb.2014.10.004.

Souphron, J., S. Bodakuntla, A.S. Jijumon, G. Lakisic, A.M. Gautreau, C. Janke, and M.M. Magiera. 2019. Purification of tubulin with controlled post-translational modifications by polymerization–depolymerization cycles. *Nat. Protoc.* 14:1634–1660. doi:10.1038/s41596-019-0153-7.

Spencer, V.A., and J.R. Davie. 1999. Role of covalent modifications of histones in regulating gene expression. *Gene*. 240:1–12. doi:10.1016/S0378-1119(99)00405-9.

Splinter, D., D.S. Razafsky, M.A. Schlager, A. Serra-Marques, I. Grigoriev, J. Demmers, N. Keijzer, K. Jiang, I. Poser, A.A. Hyman, C.C. Hoogenraad, S.J. King, and A. Akhmanova. 2012. BICD2, dynactin, and LIS1 cooperate in regulating dynein recruitment to cellular structures. *Mol. Biol. Cell*. 23:4226–4241. doi:10.1091/mbc.E12-03-0210.

Splinter, D., M.E. Tanenbaum, A. Lindqvist, D. Jaarsma, and A. Flotho. 2010. Bicaudal D2, Dynein, and Kinesin-1 Associate with Nuclear Pore Complexes and Regulate Centrosome and Nuclear Positioning during Mitotic Entry. *PLoS Biol*. 8:1000350.

doi:10.1371/journal.pbio.1000350.

Starita, L.M., Y. Machida, S. Sankaran, J.E. Elias, K. Griffin, B.P. Schlegel, S.P. Gygi, and J.D. Parvin. 2004. BRCA1-Dependent Ubiquitination of y-Tubulin Regulates Centrosome Number. *Mol. Cell. Biol.* 24:8457–8466. doi:10.1128/mcb.24.19.8457-8466.2004.

Steen, H., and M. Mann. 2004. The ABC's (and XYZ's) of peptide sequencing. *Nat. Rev. Mol. Cell Biol.* 5:699–711. doi:10.1038/nrm1468.

Stegmeier, F., M. Rape, V.M. Draviam, G. Nalepa, M.E. Sowa, X.L. Ang, E.R. McDonald, M.Z. Li, G.J. Hannon, P.K. Sorger, M.W. Kirschner, J.W. Harper, and S.J. Elledge. 2007. Anaphase initiation is regulated by antagonistic ubiquitination and deubiquitination activities. *Nature*. 446:876–881. doi:10.1038/nature05694.

Stevens, R.E., F.L. Renaud, and I.R. Gibbons. 1967. Guanine nucleotide associated with the protein of the outer fibers of flagella and cilia. *Science (80-.).* 156:1606–1608. doi:10.1126/science.156.3782.1606.

Stewart, M.D., T. Ritterhoff, R.E. Klevit, and P.S. Brzovic. 2016. E2 enzymes: More than just middle men. *Cell Res.* 26:423–440. doi:10.1038/cr.2016.35.

Stewart, S., and G. Fang. 2005. Destruction box-dependent degradation of Aurora B is mediated by the anaphase-promoting complex/cyclosome and Cdh1. *Cancer Res.* 65:8730–8735. doi:10.1158/0008-5472.CAN-05-1500.

Stoica, R., K.J. De Vos, S. Paillusson, S. Mueller, R.M. Sancho, K.F. Lau, G. Vizcay-Barrena, W.L. Lin, Y.F. Xu, J. Lewis, D.W. Dickson, L. Petrucelli, J.C. Mitchell, C.E. Shaw, and C.C.J. Miller. 2014. ER-mitochondria associations are regulated by the VAPB-PTPIP51 interaction and are disrupted by ALS/FTD-associated TDP-43. *Nat. Commun.* 5. doi:10.1038/ncomms4996.

Sumara, I., and M. Peter. 2007. Cell Cycle A Cul3-Based E3 Ligase Regulates Mitosis and is Required to Maintain the Spindle Assembly Checkpoint in Human Cells Extra View A Cul3-Based E3 Ligase Regulates Mitosis and is Required to Maintain the Spindle Assembly Checkpoint in Human Cells. *Cell Cycle*. 6:24. doi:10.4161/cc.6.24.5068.

Sumara, I., M. Quadroni, C. Frei, M.H. Olma, G. Sumara, R. Ricci, and M. Peter. 2007. A Cul3-Based E3 Ligase Removes Aurora B from Mitotic Chromosomes, Regulating Mitotic Progression and Completion of Cytokinesis in Human Cells. *Dev. Cell*. 12:887–900. doi:10.1016/J.DEVCEL.2007.03.019/ATTACHMENT/3A3C426C-9978-4BB8-BFBF-9D14E792354D/MMC1.PDF.

Szczesna, E., E.A. Zehr, S.W. Cummings, A. Szyk, K.K. Mahalingan, Y. Li, and A. Roll-Mecak. 2022. Combinatorial and antagonistic effects of tubulin glutamylation and glycylation on katanin microtubule severing. *Dev. Cell*. 57:2497-2513.e6. doi:10.1016/J.DEVCEL.2022.10.003.

Tai, H.C., and E.M. Schuman. 2008. Ubiquitin, the proteasome and protein degradation in neuronal function and dysfunction. *Nat. Rev. Neurosci.* 9:826–838. doi:10.1038/nrn2499.

Takahara, T., Y. Arai, Y. Kono, H. Shibata, and M. Maki. 2018. A microtubule-associated protein MAP1B binds to and regulates localization of a calcium-binding protein ALG-2.

Biochem. Biophys. Res. Commun. 497:492–498. doi:10.1016/j.bbrc.2018.02.048.

Tanaka, K. 2009. The proteasome: Overview of structure and functions. *Proc. Japan Acad. Ser. B Phys. Biol. Sci.* 85:12–36. doi:10.2183/pjab.85.12.

Tanaka, T.U., N. Rachidi, C. Janke, G. Pereira, M. Galova, E. Schiebel, M.J.R. Stark, and K. Nasmyth. 2002. Evidence that the Ipl1-Sli15 (Aurora Kinase-INCENP) Complex Promotes Chromosome Bi-orientation by Altering Kinetochore-Spindle Pole Connections. *Cell*. 108:317–329. doi:10.1016/S0092-8674(02)00633-5.

Tanenbaum, M.E., N. Galjart, M.A.T.M. Van Vugt, and R.H. Medema. 2006. CLIP-170 facilitates the formation of kinetochore-microtubule attachments. *EMBO J.* 25:45–57. doi:10.1038/sj.emboj.7600916.

Tang, B.L., T. Zhang, D.Y.H. Low, E.T. Wong, H. Horstmann, and W. Hong. 2000. Mammalian homologues of yeast sec31p. An ubiquitously expressed form is localized to endoplasmic reticulum (ER) exit sites and is essential for ER-Golgi transport. *J. Biol. Chem.* 275:13597–13604. doi:10.1074/JBC.275.18.13597.

Tas, R.P., A. Chazeau, B.M.C. Cloin, M.L.A. Lambers, C.C. Hoogenraad, and L.C. Kapitein. 2017. Differentiation between Oppositely Oriented Microtubules Controls Polarized Neuronal Transport. *Neuron*. 96:1264-1271.e5. doi:10.1016/j.neuron.2017.11.018.

Taylor, E.W. 1965. THE MECHANISM OF COLCHICINE INHIBITION OF MITOSIS. I. KINETICS OF INHIBITION AND THE BINDING OF H3-COLCHICINE. *J. Cell Biol.* 25:145–160. doi:10.1083/jcb.25.1.145.

Thein, K.H., J. Kleylein-Sohn, E.A. Nigg, and U. Gruneberg. 2007. Astrin is required for the maintenance of sister chromatid cohesion and centrosome integrity. *J. Cell Biol.* 178:345–354. doi:10.1083/JCB.200701163/VIDEO-2.

Thoma, C.R., A. Matov, K.L. Gutbrodt, C.R. Hoerner, Z. Smole, W. Krek, and G. Danuser. 2010. Quantitative image analysis identifies pVHL as a key regulator of microtubule dynamic instability. *J. Cell Biol.* 190:991–1003. doi:10.1083/jcb.201006059.

Thompson, A., J. Schäfer, K. Kuhn, S. Kienle, J. Schwarz, G. Schmidt, T. Neumann, and C. Hamon. 2003. Tandem mass tags: A novel quantification strategy for comparative analysis of complex protein mixtures by MS/MS. *Anal. Chem.* 75:1895–1904. doi:10.1021/ac0262560.

Thrower, J.S., L. Hoffman, M. Rechsteiner, and C.M. Pickart. 2000. Recognition of the polyubiquitin proteolytic signal. *EMBO J.* 19:94. doi:10.1093/EMBOJ/19.1.94.

Tilokani, L., S. Nagashima, V. Paupe, and J. Prudent. 2018. Mitochondrial dynamics: overview of molecular mechanisms. *Essays Biochem.* 62:341–360. doi:10.1042/EBC20170104.

Timothy O'brien, E., E.D. Salmon, and H.P. Erickson. 1997. How Calcium Causes Microtubule Depolymerization. *Cytoskeleton*. 36:125–135. doi:10.1002/(SICI)1097-0169(1997)36:2.

Tischfield, M.A., and E.C. Engle. 2010. Distinct α- and β-tubulin isotypes are required for the positioning, differentiation and survival of neurons: New support for the "multi-tubulin" hypothesis. *Biosci. Rep.* 30:319–330. doi:10.1042/BSR20100025.

Tocchini, C., and R. Ciosk. 2015. TRIM-NHL proteins in development and disease. *Semin.*

Cell Dev. Biol. 47–48:52–59. doi:10.1016/j.semcdb.2015.10.017.

Toniato, E., X. Peter Chen, J. Losman, V. Flati, L. Donahue, and P. Rothman. 2002. TRIM8/GERP RING Finger Protein Interacts with SOCS-1. *J. Biol. Chem.* 277:37315–37322. doi:10.1074/JBC.M205900200.

Torok, M., and L.D. Etkin. 2001. Two B or not two B? Overview of the rapidly expanding B-box family of proteins. *Differentiation*. 67:63–71. doi:10.1046/J.1432-0436.2001.067003063.X.

Torosantucci, L., M. De Luca, G. Guarguaglini, P. Lavia, and F. Degrassi. 2008. Localized RanGTP accumulation promotes microtubule nucleation at kinetochores in somatic mammalian cells. *Mol. Biol. Cell*. 19:1873–1882. doi:10.1091/mbc.E07-10-1050.

Tracz, M., and W. Bialek. 2021. Beyond K48 and K63: non-canonical protein ubiquitination. *Cell. Mol. Biol. Lett. 2021 261*. 26:1–17. doi:10.1186/S11658-020-00245-6.

Trockenbacher, A., V. Suckow, J. Foerster, J. Winter, S. Krauß, H.H. Ropers, R. Schneider, and S. Schweiger. 2001. MID1, mutated in Opitz syndrome, encodes an ubiquitin ligase that targets phosphatase 2A for degradation. *Nat. Genet.* 29:287–294. doi:10.1038/ng762.

Trulsson, F., V. Akimov, M. Robu, N. van Overbeek, D.A.P. Berrocal, R.G. Shah, J. Cox, G.M. Shah, B. Blagoev, and A.C.O. Vertegaal. 2022. Deubiquitinating enzymes and the proteasome regulate preferential sets of ubiquitin substrates. *Nat. Commun. 2022 131*. 13:1–17. doi:10.1038/s41467-022-30376-7.

Tyanova, S., T. Temu, and J. Cox. 2016. The MaxQuant computational platform for mass spectrometry-based shotgun proteomics. *Nat. Protoc.* 11:2301–2319. doi:10.1038/nprot.2016.136.

Ünlü, M., M.E. Morgan, and J.S. Minden. 1997. Difference gel electrophoresis: A single gel method for detecting changes in protein extracts. *Electrophoresis*. 18:2071–2077. doi:10.1002/elps.1150181133.

Urbé, S., H. Liu, S.D. Hayes, C. Heride, D.J. Rigden, and M.J. Clague. 2012. Systematic survey of deubiquitinase localization identifies USP21 as a regulator of centrosome-and microtubule-associated functions. *Mol. Biol. Cell*. 23:1095–1103. doi:10.1091/mbc.E11-08-0668.

Vale, R.D., T.S. Reese, and M.P. Sheetz. 1985a. Identification of a novel force-generating protein, kinesin, involved in microtubule-based motility. *Cell*. 42:39–50. doi:10.1016/S0092-8674(85)80099-4.

Vale, R.D., B.J. Schnapp, T.S. Reese, and M.P. Sheetz. 1985b. Organelle, bead, and microtubule translocations promoted by soluble factors from the squid giant axon. *Cell*. 40:559–569. doi:10.1016/0092-8674(85)90204-1.

Vale, R.D., B.J. Schnapp, T.S. Reese, and M.P. Sheetz. 1985c. Movement of organelles along filaments dissociated from the axoplasm of the squid giant axon. *Cell*. 40:449–454. doi:10.1016/0092-8674(85)90159-X.

Valenstein, M.L., and A. Roll-Mecak. 2016. Graded Control of Microtubule Severing by Tubulin

Glutamylation. *Cell*. 164:911–921. doi:10.1016/j.cell.2016.01.019.

Valente, A.J., L.A. Maddalena, E.L. Robb, F. Moradi, and J.A. Stuart. 2017. A simple ImageJ macro tool for analyzing mitochondrial network morphology in mammalian cell culture. *Acta Histochem.* 119:315–326. doi:10.1016/J.ACTHIS.2017.03.001.

Vallee, R.B., and G.S. Bloom. 1983. Isolation of sea urchin egg microtubules with taxol and identification of mitotic spindle microtubule-associated proteins with monoclonal antibodies. *Proc. Natl. Acad. Sci. U. S. A.* 80:6259–6263. doi:10.1073/pnas.80.20.6259.

Vallee, R.B., J.C. Williams, D. Varma, and L.E. Barnhart. 2004. Dynein: An Ancient Motor Protein Involved in Multiple Modes of Transport. *J. Neurobiol.* 58:189–200. doi:10.1002/neu.10314.

Venuto, S., and G. Merla. 2019. E3 ubiquitin ligase TRIM proteins, cell cycle and mitosis. *Cells*. 8:510. doi:10.3390/cells8050510.

Verhey, K.J., and J. Gaertig. 2007. The tubulin code. *Cell Cycle*. 6:2152–2160. doi:10.4161/cc.6.17.4633.

Verhey, K.J., and J.W. Hammond. 2009. Traffic control: Regulation of kinesin motors. *Nat. Rev. Mol. Cell Biol.* 10:765–777. doi:10.1038/nrm2782.

Vong, Q.P., K. Cao, H.Y. Li, P.A. Iglesias, and Y. Zheng. 2005. Chromosome alignment and segregation regulated by ubiquitination of survivin. *Science (80-.).* 310:1499–1504. doi:10.1126/science.1120160.

De vos, K.J., G.M. Mórotz, R. Stoica, E.L. Tudor, K.F. Lau, S. Ackerley, A. Warley, C.E. Shaw, and C.C. Miller. 2012. VAPB interacts with the mitochondrial protein PTPIP51 to regulate calcium homeostasis. *Hum. Mol. Genet.* 21:1299–1311. doi:10.1093/hmg/ddr559.

Waizenegger, I.C., J.F. Giménez-Abián, D. Wernic, and J.M. Peters. 2002. Regulation of human separase by securin binding and autocleavage. *Curr. Biol.* 12:1368–1378. doi:10.1016/S0960-9822(02)01073-4.

Walczak, C.E., and S.L. Shaw. 2010. A MAP for bundling microtubules. *Cell*. 142:364–367. doi:10.1016/j.cell.2010.07.023.

Walker, R.A., E.T. O'Brien, N.K. Pryer, M.F. Soboeiro, W.A. Voter, H.P. Erickson, and E.D. Salmon. 1988. Dynamic instability of individual microtubules analyzed by video light microscopy: rate constants and transition frequencies. *J. Cell Biol.* 107:1437–1448. doi:10.1083/jcb.107.4.1437.

Walter, W.J., V. Beránek, E. Fischermeier, and S. Diez. 2012. Tubulin Acetylation Alone Does Not Affect Kinesin-1 Velocity and Run Length In Vitro. *PLoS One*. 7:e42218. doi:10.1371/journal.pone.0042218.

Wälti, M.A., S. Thore, M. Aebi, and M. Künzler. 2008. Crystal structure of the putative carbohydrate recognition domain of human galectin-related protein. *Proteins Struct. Funct. Bioinforma.* 72:804–808. doi:10.1002/PROT.22078.

Wang, C., M.E. Ward, R. Chen, K. Liu, T.E. Tracy, X. Chen, M. Xie, P.D. Sohn, C. Ludwig, A. Meyer-Franke, C.M. Karch, S. Ding, and L. Gan. 2017a. Scalable Production of iPSC-Derived Human Neurons to Identify Tau-Lowering Compounds by High-Content

Screening. *Stem Cell Reports*. 9:1221–1233. doi:10.1016/j.stemcr.2017.08.019.

Wang, H.W., and E. Nogales. 2005. Nucleotide-dependent bending flexibility of tubulin regulates microtubule assembly. *Nature*. 435:911–915. doi:10.1038/nature03606.

Wang, N., C. Bosc, S. Ryul Choi, B. Boulan, L. Peris, N. Olieric, H. Bao, F. Krichen, L. Chen, A. Andrieux, V. Olieric, M.J. Moutin, M.O. Steinmetz, and H. Huang. 2019a. Structural basis of tubulin detyrosination by the vasohibin–SVBP enzyme complex. *Nat. Struct. Mol. Biol.* 26:571–582. doi:10.1038/s41594-019-0241-y.

Wang, Q., A.H. Crevenna, I. Kunze, and N. Mizuno. 2014. Structural basis for the extended CAP-Gly domains of p150glued binding to microtubules and the implication for tubulin dynamics. *Proc. Natl. Acad. Sci. U. S. A.* 111:11347–11352. doi:10.1073/pnas.1403135111.

Wang, Q., Z. Peng, H. Long, X. Deng, and K. Huang. 2019b. Polyubiquitylation of α-tubulin at K304 is required for flagellar disassembly in Chlamydomonas. *J. Cell Sci.* 132. doi:10.1242/jcs.229047.

Wang, Q., Y. Tang, Y. Xu, S. Xu, Y. Jiang, Q. Dong, Y. Zhou, and W. Ge. 2017b. The X-linked deubiquitinase USP9X is an integral component of centrosome. *J. Biol. Chem.* 292:12874–12884. doi:10.1074/jbc.M116.769943.

Wang, X., and T.L. Schwarz. 2009. The Mechanism of Ca2+-Dependent Regulation of Kinesin-Mediated Mitochondrial Motility. *Cell*. 136:163–174. doi:10.1016/J.CELL.2008.11.046.

Wang, X., Y. Zhang, X. Pei, G. Guo, B. Xue, X. Duan, and D. Dou. 2020. TRIM3 inhibits P53 signaling in breast cancer cells. *Cancer Cell Int.* 20. doi:10.1186/s12935-020-01630-z.

Wang, Z., T. Wu, L. Shi, L. Zhang, W. Zheng, J.Y. Qu, R. Niu, and R.Z. Qi. 2010. Conserved motif of CDK5RAP2 mediates its localization to centrosomes and the Golgi complex. *J. Biol. Chem.* 285:22658–22665. doi:10.1074/jbc.M110.105965.

Wani, M.C., H.L. Taylor, M.E. Wall, P. Coggon, and A.T. Mcphail. 1971. Plant Antitumor Agents.VI.The Isolation and Structure of Taxol, a Novel Antileukemic and Antitumor Agent from Taxus brevifolia2. *J. Am. Chem. Soc.* 93:2325–2327. doi:10.1021/ja00738a045.

Watrin, E., A. Schleiffer, K. Tanaka, F. Eisenhaber, K. Nasmyth, and J.M. Peters. 2006. Human Scc4 Is Required for Cohesin Binding to Chromatin, Sister-Chromatid Cohesion, and Mitotic Progression. *Curr. Biol.* 16:863–874. doi:10.1016/j.cub.2006.03.049.

Watson, E.R., N.G. Brown, J.M. Peters, H. Stark, and B.A. Schulman. 2019. Posing the APC/C E3 Ubiquitin Ligase to Orchestrate Cell Division. *Trends Cell Biol.* 29:117–134. doi:10.1016/j.tcb.2018.09.007.

Wei, D., N. Gao, L. Li, J.X. Zhu, L. Diao, J. Huang, Q.J. Han, S. Wang, H. Xue, Q. Wang, Q.F. Wu, X. Zhang, and L. Bao. 2018. α-Tubulin Acetylation Restricts Axon Overbranching by Dampening Microtubule Plus-End Dynamics in Neurons. *Cereb. Cortex*. 28:3332–3346. doi:10.1093/CERCOR/BHX225.

Weingarten, M.D., A.H. Lockwood, S.Y. Hwo, and M.W. Kirschner. 1975. A protein factor

essential for microtubule assembly. *Proc. Natl. Acad. Sci. U. S. A.* 72:1858–1862. doi:10.1073/pnas.72.5.1858.

Weisbrich, A., S. Honnappa, R. Jaussi, O. Okhrimenko, D. Frey, I. Jelesarov, A. Akhmanova, and M.O. Steinmetz. 2007. Structure-function relationship of CAP-Gly domains. *Nat. Struct. Mol. Biol.* 14:959–967. doi:10.1038/nsmb1291.

Weisenberg, R.C. 1972. Microtubule formation in vitro in solutions containing low calcium concentrations. *Science (80-.).* 177:1104–1105. doi:10.1126/science.177.4054.1104.

Weisenberg, R.C., G.G. Borisy, and E.W. Taylor. 1968. The Colchicine-Binding Protein of Mammalian Brain and Its Relation to Microtubules. *Biochemistry*. 7:4466–4479. doi:10.1021/bi00852a043.

Welburn, J.P.I., and A.A. Jeyaprakash. 2018. Mechanisms of mitotic kinase regulation: A structural perspective. *Front. Cell Dev. Biol.* 6:6. doi:10.3389/fcell.2018.00006.

Welburn, J.P.I., M. Vleugel, D. Liu, J.R. Yates, M.A. Lampson, T. Fukagawa, and I.M. Cheeseman. 2010. Aurora B Phosphorylates Spatially Distinct Targets to Differentially Regulate the Kinetochore-Microtubule Interface. *Mol. Cell*. 38:383–392. doi:10.1016/J.MOLCEL.2010.02.034.

Wendell, K.L., L. Wilson, and M.A. Jordan. 1993. Mitotic block in HeLa cells by vinblastine: Ultrastructural changes in kinetochore-mcirotubule attachment and in centrosomes. *J. Cell Sci.* 104:261–274.

Wheatley, S.P., A. Carvalho, P. Vagnarelli, and W.C. Earnshaw. 2001. INCENP is required for proper targeting of Survivin to the centromeres and the anaphase spindle during mitosis. *Curr. Biol.* 11:886–890. doi:10.1016/S0960-9822(01)00238-X.

White, C.M., B.K. Martin, L.F. Lee, J.S. Haskill, and J.P.Y. Ting. 1998. Effects of paclitaxel on cytokine synthesis by unprimed human monocytes, T lymphocytes, and breast cancer cells. *Cancer Immunol. Immunother.* 46:104–112. doi:10.1007/s002620050468.

Wichmann, C., F. Meier, S.V. Winter, A.D. Brunner, J. Cox, and M. Mann. 2019. MaxQuant.live enables global targeting of more than 25,000 peptides. *Mol. Cell. Proteomics*. 18:982–994. doi:10.1074/mcp.TIR118.001131.

Wickstead, B., and K. Gull. 2011. The evolution of the cytoskeleton. *J. Cell Biol.* 194:513–525. doi:10.1083/jcb.201102065.

Wickström, S.A., K.C. Masoumi, S. Khochbin, R. Fässler, and R. Massoumi. 2010. CYLD negatively regulates cell-cycle progression by inactivating HDAC6 and increasing the levels of acetylated tubulin. *EMBO J.* 29:131–144. doi:10.1038/emboj.2009.317.

Wieczorek, M., S. Bechstedt, S. Chaaban, and G.J. Brouhard. 2015. Microtubule-associated proteins control the kinetics of microtubule nucleation. *Nat. Cell Biol.* 17:907–916. doi:10.1038/ncb3188.

Wijk, S.J.L., and H.T.M. Timmers. 2010. The family of ubiquitin-conjugating enzymes (E2s): deciding between life and death of proteins. *FASEB J.* 24:981–993. doi:10.1096/fj.09-136259.

Wilkins, M.R., E. Gasteiger, J.C. Sanchez, A. Bairoch, and D.F. Hochstrasser. 1998. Two-

dimensional gel electrophoresis for proteome projects: The effects of protein hydrophobicity and copy number. *Electrophoresis*. 19:1501–1505. doi:10.1002/elps.1150190847.

Willems, E., M. Dedobbeleer, M. Digregorio, A. Lombard, P.N. Lumapat, and B. Rogister. 2018. The functional diversity of Aurora kinases: a comprehensive review. *Cell Div. 2018 131*. 13:1–17. doi:10.1186/S13008-018-0040-6.

Williams, F.P., K. Haubrich, C. Perez-Borrajero, and J. Hennig. 2019. Emerging RNA-binding roles in the TRIM family of ubiquitin ligases. *Biol. Chem.* 400:1443–1464. doi:10.1515/hsz-2019-0158.

Wilm, M., and M. Mann. 1996. Analytical properties of the nanoelectrospray ion source. *Anal. Chem.* 68:1–8. doi:10.1021/ac9509519.

Witt, S.H., H. Granzier, C.C. Witt, and S. Labeit. 2005. MURF-1 and MURF-2 Target a Specific Subset of Myofibrillar Proteins Redundantly: Towards Understanding MURF-dependent Muscle Ubiquitination. *J. Mol. Biol.* 350:713–722. doi:10.1016/J.JMB.2005.05.021.

Wloga, D., J. Gaertig, A.J. Akella, D. Wloga, J. Kim, N.G. Starostina, S. Lyons-Abbott, N.S. Morrissette, S.T. Dougan, E.T. Kipreos, J. Gaertig, C.E. Argarana, H.S. Barra, R. Caputto, C.E. Argarana, H.S. Barra, R. Caputto, S. Audebert, E. Desbruyeres, C. Gruszczynski, A. Koulakoff, F. Gros, P. Denoulet, B. Edde, H.S. Barra, J.A. Rodriguez, C.A. Arce, R. Caputto, Y. Bobinnec, A. Khodjakov, L.M. Mir, C.L. Rieder, B. Edde, M. Bornens, Y. Bobinnec, M. Moudjou, J.P. Fouquet, E. Desbruyeres, B. Edde, M. Bornens, C. Bonnet, D. Boucher, S. Lazereg, B. Pedrotti, K. Islam, P. Denoulet, J.C. Larcher, D. Boucher, J.C. Larcher, F. Gros, P. Denoulet, C. Boyault, K. Sadoul, M. Pabion, S. Khochbin, M.H. Bre, B. de Nechaud, A. Wolff, A. Fleury, M.H. Bre, V. Redeker, M. Quibell, J. Darmanaden-Delorme, C. Bressac, J. Cosson, P. Huitorel, J.M. Schmitter, J. Rossler, T. Johnson, M.H. Bre, V. Redeker, J. Vinh, J. Rossier, N. Levilliers, D. Cai, D.P. McEwen, J.R. Martens, E. Meyhofer, K.J. Verhey, P.K. Campbell, K.G. Waymire, R.L. Heier, C. Sharer, D.E. Day, H. Reimann, J.M. Jaje, G.A. Friedrich, M. Burmeister, T.J. Bartness, J.M. Caron, A.P. Carter, J.E. Garbarino, E.M. Wilson-Kubalek, W.E. Shipley, C. Cho, R.A. Milligan, R.D. Vale, I.R. Gibbons, et al. 2010. Post-translational modifications of microtubules. *J. Cell Sci.* 123:3447–55. doi:10.1242/jcs.083576.

Wloga, D., E. Joachimiak, and H. Fabczak. 2017a. Tubulin post-translational modifications and microtubule dynamics. *Int. J. Mol. Sci.* 18. doi:10.3390/ijms18102207.

Wloga, D., E. Joachimiak, P. Louka, and J. Gaertig. 2017b. Posttranslational modifications of Tubulin and cilia. *Cold Spring Harb. Perspect. Biol.* 9. doi:10.1101/cshperspect.a028159.

Wloga, D., K. Rogowski, N. Sharma, J. Van Dijk, C. Janke, B. Eddé, M.H. Bré, N. Levilliers, V. Redeker, J. Duan, M.A. Gorovsky, M. Jerka-Dziadosz, and J. Gaertig. 2008. Glutamylation on α-tubulin is not essential but affects the assembly and functions of a subset of microtubules in Tetrahymena thermophila. *Eukaryot. Cell*. 7:1362–1372. doi:10.1128/EC.00084-08.

Wloga, D., D.M. Webster, K. Rogowski, M.H. Bré, N. Levilliers, M. Jerka-Dziadosz, C. Janke,

S.T. Dougan, and J. Gaertig. 2009. TTLL3 Is a Tubulin Glycine Ligase that Regulates the Assembly of Cilia. *Dev. Cell*. 16:867–876. doi:10.1016/j.devcel.2009.04.008.

Wolfson, M., C.P.H. Yang, and S.B. Horwitz. 1997. Taxol induces tyrosine phosphorylation of SHC and its association with Grb2 in murine RAW 264.7 cells. *Int. J. Cancer*. 70:248–252. doi:10.1002/(SICI)1097-0215(19970117)70:2<248::AID-IJC17>3.0.CO;2-E.

Woods, A., and J.R. Couchman. 2001. Syndecan-4 and focal adhesion function. *Curr. Opin. Cell Biol.* 13:578–583. doi:10.1016/S0955-0674(00)00254-4.

Worden, E.J., K.C. Dong, and A. Martin. 2017. An AAA Motor-Driven Mechanical Switch in Rpn11 Controls Deubiquitination at the 26S Proteasome. *Mol. Cell*. 67:799-811.e8. doi:10.1016/J.MOLCEL.2017.07.023.

Wu-Baer, F., K. Lagrazon, W. Yuan, and R. Baer. 2003. The BRCA1/BARD1 heterodimer assembles polyubiquitin chains through an unconventional linkage involving lysine residue K6 of ubiquitin. *J. Biol. Chem.* 278:34743–34746. doi:10.1074/JBC.C300249200.

Wu, T., Y. Merbl, Y. Huo, J.L. Gallop, A. Tzur, and M.W. Kirschner. 2010. UBE2S drives elongation of K11-linked ubiquitin chains by the anaphase-promoting complex. *Proc. Natl. Acad. Sci. U. S. A.* 107:1355–1360. doi:10.1073/PNAS.0912802107/SUPPL_FILE/PNAS.0912802107_SI.PDF.

Würtz, M., E. Zupa, E.S. Atorino, A. Neuner, A. Böhler, A.S. Rahadian, B.J.A. Vermeulen, G. Tonon, S. Eustermann, E. Schiebel, and S. Pfeffer. 2022. Modular assembly of the principal microtubule nucleator γ-TuRC. *Nat. Commun. 2022 131*. 13:1–16. doi:10.1038/s41467-022-28079-0.

Xu, G., J.S. Paige, and S.R. Jaffrey. 2010. Global analysis of lysine ubiquitination by ubiquitin remnant immunoaffinity profiling. *Nat. Biotechnol. 2010 288*. 28:868–873. doi:10.1038/nbt.1654.

Xu, K., P.M. Schwarz, and R.F. Ludueña. 2002. Interaction of nocodazole with tubulin isotypes. *Drug Dev. Res.* 55:91–96. doi:10.1002/ddr.10023.

Xu, P., D.M. Duong, N.T. Seyfried, D. Cheng, Y. Xie, J. Robert, J. Rush, M. Hochstrasser, D. Finley, and J. Peng. 2009. Quantitative Proteomics Reveals the Function of Unconventional Ubiquitin Chains in Proteasomal Degradation. *Cell*. 137:133–145. doi:10.1016/j.cell.2009.01.041.

Xu, Z., L. Schaedel, D. Portran, A. Aguilar, J. Gaillard, M. Peter Marinkovich, M. Théry, and M. V. Nachury. 2017. Microtubules acquire resistance from mechanical breakage through intralumenal acetylation. *Science (80-.).* 356:328–332. doi:10.1126/science.aai8764.

Yan, Q., W. Sun, P. Kujala, Y. Lotfi, T.A. Vida, and A.J. Bean. 2005. CART: An hrs/actinin-4/BERP/myosin V protein complex required for efficient receptor recycling. *Mol. Biol. Cell*. 16:2470–2482. doi:10.1091/mbc.E04-11-1014.

Yanagisawa, T., S. Hasegawa, and H. Mohri. 1968. The bound nucleotides of the isolated microtubules of sea-urchin sperm flagella and their possible role in flagellar movement. *Exp. Cell Res.* 52:86–100. doi:10.1016/0014-4827(68)90549-1.

Yang, C., J. Wu, C. de Heus, I. Grigoriev, N. Liv, Y. Yao, I. Smal, E. Meijering, J. Klumperman, R.Z. Qi, and A. Akhmanova. 2017. EB1 and EB3 regulate microtubule minus end organization and Golgi morphology. *J. Cell Biol.* 216:3179–3198. doi:10.1083/jcb.201701024.

Yang, J.T., R.A. Laymon, and L.S.B. Goldstein. 1989. A three-domain structure of kinesin heavy chain revealed by DNA sequence and microtubule binding analyses. *Cell*. 56:879–889. doi:10.1016/0092-8674(89)90692-2.

Yang, Q., J. Zhao, D. Chen, and Y. Wang. 2021. E3 ubiquitin ligases: styles, structures and functions. *Mol. Biomed.* 2:1–17. doi:10.1186/s43556-021-00043-2.

Yang, R., K.K. Walder-Christensen, N. Kim, D. Wu, D.N. Lorenzo, A. Badea, Y.H. Jiang, H.H. Yin, W.C. Wetsel, and V. Bennett. 2019. ANK2 autism mutation targeting giant ankyrin-B promotes axon branching and ectopic connectivity. *Proc. Natl. Acad. Sci. U. S. A.* 116:15262–15271. doi:10.1073/PNAS.1904348116/VIDEO-2.

Yau, K.W., S.F.B. vanBeuningen, I. Cunha-Ferreira, B.M.C. Cloin, E.Y. vanBattum, L. Will, P. Schätzle, R.P. Tas, J. vanKrugten, E.A. Katrukha, K. Jiang, P.S. Wulf, M. Mikhaylova, M. Harterink, R.J. Pasterkamp, A. Akhmanova, L.C. Kapitein, and C.C. Hoogenraad. 2014. Microtubule Minus-End Binding Protein CAMSAP2 Controls Axon Specification and Dendrite Development. *Neuron*. 82:1058–1073. doi:10.1016/J.NEURON.2014.04.019.

Ye, R., N.J. AiErken, X. Kuang, H. Zeng, N. Shao, Y. Lin, P. Liu, and S. Wang. 2021. Tripartite motif-containing 3 (TRIM3) enhances ER signaling and confers tamoxifen resistance in breast cancer. *Oncogenesis*. 10. doi:10.1038/s41389-021-00350-x.

Ye, Y., and M. Rape. 2009. Building ubiquitin chains: E2 enzymes at work. *Nat. Rev. Mol. Cell Biol.* 10:755–764. doi:10.1038/nrm2780.

Yeo, H.K., T.H. Park, H.Y. Kim, H. Jang, J. Lee, G.-S. Hwang, S.E. Ryu, S.H. Park, H.K. Song, H.S. Ban, H.-J. Yoon, and B. Il Lee. 2021. Phospholipid transfer function of PTPIP51 at mitochondria-associated ER membranes. *EMBO Rep.* 22. doi:10.15252/embr.202051323.

Yu, I., C.P. Garnham, and A. Roll-Mecak. 2015. Writing and reading the tubulin code. *J. Biol. Chem.* 290:17163–17172. doi:10.1074/jbc.R115.637447.

Yu, Q., X. Liu, M.P. Keller, J. Navarrete-Perea, T. Zhang, S. Fu, L.P. Vaites, S.R. Shuken, E. Schmid, G.R. Keele, J. Li, E.L. Huttlin, E.H. Rashan, J. Simcox, G.A. Churchill, D.K. Schweppe, A.D. Attie, J.A. Paulo, and S.P. Gygi. 2023. Sample multiplexing-based targeted pathway proteomics with real-time analytics reveals the impact of genetic variation on protein expression. *Nat. Commun.* 14. doi:10.1038/s41467-023-36269-7.

Zeytuni, N., and R. Zarivach. 2012. Structural and functional discussion of the tetra-trico-peptide repeat, a protein interaction module. *Structure*. 20:397–405. doi:10.1016/J.STR.2012.01.006.

Zhai, Y., P.J. Kronebusch, and G.G. Borisy. 1995. Kinetochore microtubule dynamics and the metaphase-anaphase transition. *J. Cell Biol.* 131:721–734. doi:10.1083/jcb.131.3.721.

Zheng, Y., M.L. Wong, B. Alberts, and T. Mitchison. 1995. Nucleation of microtubule assembly by a γ-tubulin-containing ring complex. *Nature*. 378:578–583. doi:10.1038/378578a0.

Zhou, D., H. Ge, J. Sun, Y. Gao, M. Teng, and L. Niu. 2008. Crystal structure of the C-terminal conserved domain of human GRP, a galectin-related protein, reveals a function mode different from those of galectins. *Proteins Struct. Funct. Bioinforma.* 71:1582–1588. doi:10.1002/PROT.22003.

Zhu, C., E. Bossy-Wetzel, and W. Jiang. 2005. Recruitment of MKLP1 to the spindle midzone/midbody by INCENP is essential for midbody formation and completion of cytokinesis in human cells. *Biochem. J.* 389:373–381. doi:10.1042/BJ20050097.

Zhu, W., J.W. Smith, and C.-M. Huang. 2010. Mass Spectrometry-Based Label-Free Quantitative Proteomics. *J. Biomed. Biotechnol.* 2010. doi:10.1155/2010/840518.

Zhuang, T., B. Wang, X. Tan, L. Wu, X. Li, Z. Li, Y. Cai, R. Fan, X. Yang, C. Zhang, Y. Xia, Z. Niu, B. Liu, Q. Cao, Y. Ding, Z. Zhou, Q. Huang, and H. Yang. 2022. TRIM3 facilitates estrogen signaling and modulates breast cancer cell progression. *Cell Commun. Signal.* 20:45. doi:10.1186/S12964-022-00861-Z.

Zimmermann, F., M. Serna, A. Ezquerra, R. Fernandez-Leiro, O. Llorca, and J. Luders. 2020. Assembly of the asymmetric human γ-tubulin ring complex by RUVBL1-RUVBL2 AAA ATPase. *Sci. Adv.* 6:894–912. doi:10.1126/SCIADV.ABE0894/SUPPL_FILE/ABE0894_TABLE_S1.XLSX.

Zimniak, T., V. Fitz, H. Zhou, F. Lampert, S. Opravil, K. Mechtler, P. Stolt-Bergner, and S. Westermann. 2012. Spatiotemporal regulation of Ipl1/aurora activity by direct Cdk1 phosphorylation. *Curr. Biol.* 22:787–793. doi:10.1016/j.cub.2012.03.007.

Zitouni, S., C. Nabais, S.C. Jana, A. Guerrero, and M. Bettencourt-Dias. 2014. Polo-like kinases: structural variations lead to multiple functions. *Nat. Rev. Mol. Cell Biol. 2014 157*. 15:433–452. doi:10.1038/nrm3819.